Cleavage pattern architecture in early embryos : a quantitative approach

Anaëlle Pierre

NNT : 2017SACLS038

THESE DE DOCTORAT
DE
L'UNIVERSITE PARIS-SACLAY
PREPAREE A
L'UNIVERSITE PARIS-SUD

ECOLE DOCTORALE N°577
Structure et Dynamique des Systèmes Vivants

Spécialité : Sciences de la Vie et de la Santé

Par

Anaëlle Pierre

Architecture des plans de clivage pendant l'embryogenèse : une approche quantitative

Thèse présentée et soutenue publiquement le 7 mars 2017 devant un jury composé de :

Mme Nadine PEYRIERAS	DR, Neuro-PSI, (CNRS Gif-sur-Yvette, France)	Présidente du Jury
M. Julien DUMONT	DR, Institut Jacques Monod (France)	Rapporteur
M. Pierre-François LENNE	DR, IBDM (France)	Rapporteur
Mme Jenifer CROCE	CR, LBDV (France)	Examinatrice
M. François NEDELEC	DR, EMBL (Allemagne)	Examinateur
M. Nicolas MINC	CR, Institut Jacques Monod (France)	Directeur de thèse

REMERCIEMENTS

Avant tout, j'aimerais remercier mes parents, ainsi que tous les enseignants qui m'ont donné le goût de la recherche et un solide bagage scientifique, et sans qui je n'aurais pas pu envisager cette thèse. Un grand merci en particulier à Emmanuelle Deleporte, directrice du département de physique de l'ENS Cachan, qui m'a aidée à prendre le cap de la biophysique.

Ensuite, je voudrais bien sûr remercier Nico, qui m'a proposé un sujet de thèse à la fois original, passionnant, et publiable. Ces trois années de thèse (et demi) se sont déroulées presque sans accroc ni galère ! Merci aussi pour m'avoir fait confiance et m'avoir laissé une grande liberté dans mon travail et mes initiatives, et ce malgré nos différences (flagrantes) d'organisation. Enfin, merci pour avoir toujours été disponible pour mes questions et autres problèmes que j'ai pu rencontrer, et pour toutes tes idées ! Je tiens ici à remercier également mes tuteurs, Juliette et Zoher, pour avoir suivi de loin l'avancement de mon projet, et veillé à ce que Nico ne me maltraite pas trop…

Merci aussi aux membres de mon jury, Nadine Peyrieras, Julien Dumont, Pierre-François Lenne, Jenifer Croce et François Nédélec, qui ont gentiment accepté de lire mon manuscrit et de braver les kilomètres pour venir m'évaluer depuis Heidelberg, Cambridge, Villefranche-sur-mer ou même Gif-sur-Yvette ! Merci tout particulièrement à Julien et à Pierre-François pour avoir accepté le rôle de rapporteurs.

Au cours de ces presque quatre années passées au labo Minc, j'ai pu voir l'équipe s'agrandir et changer de visages. Mais l'ambiance y est toujours restée excellente, et j'ai beaucoup apprécié de pouvoir compter sur mes co-labos à la fois dans le cadre de mon travail (merci en particulier à la team oursins ! For the win !) et pour les pauses et after-labs. Un grand merci, donc, à Valeria, Jérémy, Armin, Dmitry, Hiro, Aurélien, la demi-Héliciane, et aux anciens qui sont partis voguer vers d'autres horizons : Daria, Henry, Marguerite, Louise et François. Je voudrais tout particulièrement remercier Armin, non pour ses calendriers abscons ou son bureau-supermarché, mais pour avoir agréablement partagé (et décoré) mon aquarium pendant trois ans.

Merci aussi aux membres des autres équipes, qui ont su rendre l'institut Jacques Monod vivant et convivial. Je pense en particulier (mais pas que !) à Charlène et au labo Borghi, aux GRAJ, à Julie, à Junie, à Benoît, à la joyeuse bande de la plate-forme d'imagerie, et bien sûr aux gentils organisateurs des after hours : Antonin, Kim et Hugo (et Philippon).

Et parce que ces années de thèse ne se résument pas aux seuls linos bleus de l'institut Jacques Monod, je voudrais remercier également tous ceux qui m'ont accompagnée des cinémas parisiens aux festivals des pays Baltes, à pied, à skis ou en Autolib'... A savoir ma famille, Coco et Robert, Isa, les vieux de PSB et de l'ENS Cachan, et tout particulièrement les grands adeptes de piscine-pancakes : Mémé, Clairette, Flavien, Alexis, Andreea, et Poussinet.

Pour finir, je tiens à remercier les oubliés de cette page de remerciements, pour avoir mis un peu de piquant dans ma thèse : nos petits oursins, le PC commun, et ma guitare.

Merci à tous !

TABLE OF CONTENTS

INTRODUCTION

"[The larva] then metamorphoses into a baby sea urchin and settles on the ocean floor, where its main predators are sea otters and Japanese restaurants."

Sandra Blakeslee, for the New York Times, 1984

I. THE CLEAVAGE PATTERNS

1. The cleaving embryo

a. The egg

In animals, the development of a new organism starts with the fertilization of the egg by the sperm. Both gametes contain equal haploid genetic material, as a result of meiosis. However, while the sperm gets rid of most of its cytoplasmic material during its maturation, the maturating egg accumulates cytoplasmic material that will be necessary for future embryonic development. It even increases the amount of cytoplasm it contains through asymmetric meiotic divisions, that gather all the cytoplasm in one cell instead of separating it into two daughter cells (Figure I.1.). The small cells that result from these asymmetric divisions are called polar bodies, and sometimes remain next to the egg during its early development. This cytoplasm accumulation yields an enormous egg, which can reach up to ~1 mm diameter in some species. As a comparison, the order of magnitude of the sperm head diameter is ~5 μm.

In addition to organelles, the egg cytoplasm contains yolk and other nutritive proteins, which provide the embryo with the energy and amino acids it needs to develop, before it can feed itself. In some species the amount of yolk can represent most of the egg volume (birds, fish). The egg cytoplasm also contains protective chemicals like DNA repair enzymes, UV filters or antibodies that help the developing embryo to face the dangers of its environment. The egg is also accumulating ribosomes, tRNA and mRNA that allow the embryo to synthetize its own enzymes and structural proteins in the early stages of development, when there is no gene expression in most species. Those mRNA often have a specific spatial distribution in the egg. In addition, in most species, morphogenetic factors (transcription factors, paracrine factors) that drive further cell differentiation are also present and non-isotropically distributed in the cytoplasm. These anisotropies in the cytoplasm composition yield an intrinsic polarity of the egg, and will determine cell fate as further cleavage segregates those components into different cells.

The cell membrane is surrounded by an extracellular matrix made of various glycoproteins, called the vitelline envelope in invertebrates, that recognizes and attaches sperm in a species-specific manner. Around it is usually a layer of egg jelly, also made of glycoproteins, which main function is to attract or activate sperm.

b. The process of fertilization

Depending on species, the fertilization of the egg happens at a different stage of egg maturation (Figure I.1.). Upon contact with the egg surface, the sperm head releases proteolytic enzymes and proteasomes from its acrosomal vesicle, in an exocytose process called the acrosome reaction. The released acrosomal enzymes digest proteins and make a path through the surrounding layers of the egg, up to the cell membrane. The sperm and egg membranes then fuse, allowing the male pronucleus to enter the egg, and to bring the chromosome number in the egg cell to its appropriate diploid value. Usually, only the content of the sperm head is let into the egg. However in many species, like insects, nematodes, mollusks or some annelids, the whole sperm, including the flagella, enters the egg. Shortly after entrance, the sperm nucleus enlarges and forms a male pronucleus.

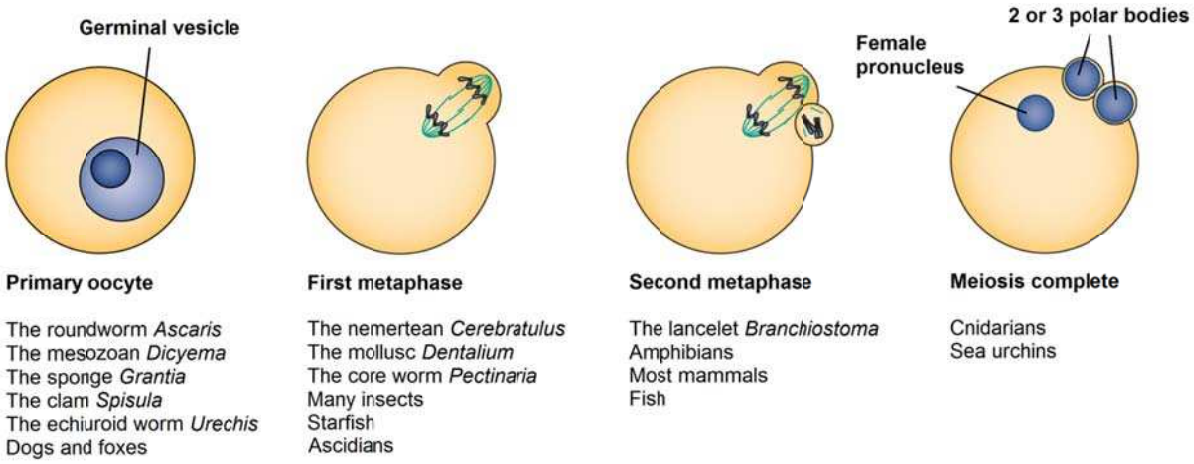

Figure I.1. : *The oocyte undergoes meiosis to give a haploid egg. The two divisions of meiosis are asymmetric, yielding small polar bodies, and an egg with an accumulation of cytoplasm. Fertilization occurs at a different stage of egg maturation, depending on species. (Adapted from (Clift and Schuh, 2013; Gilbert, 2000))*

If several pronuclei from different sperm heads fertilize the egg at once, the further development of the embryo is highly compromised, as it can result in malformations and malfunctions of the division machinery, and in the distribution of a wrong number and type of chromosomes in the daughter cells. There are exceptions to this, like the case of pleurodeles, that have a mechanism (still unknown) to destroy excess male pronuclei (Fankhauser, 1948; Iwao, 1989). The entrance of multiple sperm pronuclei, called polyspermy, can be avoided by restricting the possible sperm entry sites, like in insects where sperm can only pass one at a time in a tunnel in the chorion, called the micropyle. In most embryos, however, sperm can enter almost everywhere on the surface of the egg, and polyspermy is generally avoided by two mechanisms. The first mechanism is a transient fast block that happens typically seconds after the binding of egg and sperm, and usually consists of a change in the membrane potential of the egg (Longo et al., 1986). It is not observed in some species, like mammals, where the amount of sperm reaching the egg at once is rather low.

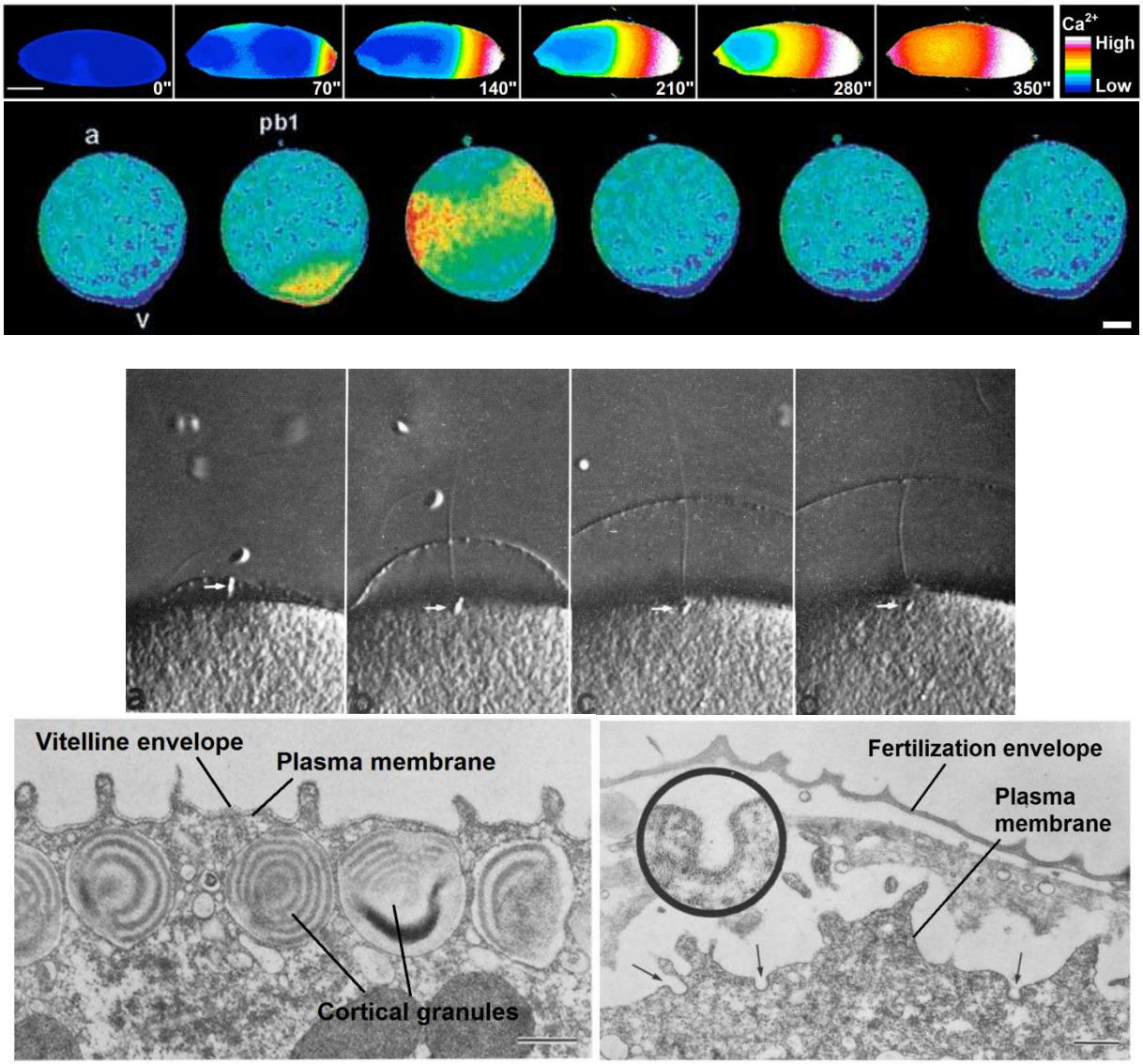

Figure I.2. : *The slow block process and egg activation.* ***Top*** *: calcium waves following fertilization in eggs of drosophila (top, Scale bar : 100 µm, image every 70 seconds, from (York-Andersen et al., 2015)) and ascidian (bottom, Scale bar : 20 µm, animal-vegetal axis and polar body indicated, image every 10 seconds, adapted from (Roegiers et al., 1999)). The ascidian egg undergoes a second calcium wave 1 minute after (not shown).* ***Bottom :*** *detachment and spreading of the vitelline envelope induced by exocytosis of the cortical granules in the sea urchin embryo. Time lapse in differential interference light microscopy (top, images taken at : 25 s (a), 35 s (b), 60 s (c) and 80 s (d) after fertilization, arrows indicate sperm head, from (Saiki Hamaguchi and Hiramoto, 1980)). Transmission electron micrographs showing the cortex before (left) and after (right) fertilization (bottom, arrows and inset show the sites of cortical granules exocytosis on the plasma membrane, Scale bar : 0.5 µm, adapted from (Chandler and Heuser, 1979)).*

The second mechanism is slower, as it takes place about 1 minute after egg-sperm contact. Upon fertilization (whether at sperm-egg contact or at the entry of sperm, depending on species), the egg cytoplasm shows an important increase in Ca^{2+} concentration, that originates at the point of fertilization and spreads through the egg as a wave, called the calcium wave (Figure I.2.) (Steinhardt et al., 1977). This calcium wave is often accompanied by a wave of cytoplasmic contraction. This rise in Ca^{2+} concentration triggers the exocytosis of the cortical granules, that are vesicles bound to the egg membrane, and contain digestive enzymes, hyalin proteins and mucopolysaccharides. This mechanism can block polyspermy in a chemical way, as in mammals where the released enzymes inhibit the binding of sperm to the egg surrounding cells (the zona pellucida), by modifying the sperm receptors. It can also create a mechanical barrier to sperm as the exocytosis occurs underneath the vitelline envelope, causing it to detach from the egg surface (Figure I.2.). The detached envelope then spreads away with the osmose-driven incorporation of external water between it and the egg. Finally, the envelope is strengthened by peroxydases and transglutaminases, to form a protective membrane called the fertilization envelope (Wong et al., 2004). Hyalin protein, like the adhesive glycoproteins that are also released by cortical granules, later helps cell adhesion and proper orientation of cells in the embryo.

The calcium wave, or a succession of calcium waves in some species, also acts as a trigger to the embryo's development. In particular it ends the repression of nuclear division and DNA synthesis, resumes meiosis (if not complete) and restores the mitotic cell cycle, presumably through the degradation of cyclins and the inactivation of MAP kinases (Carroll et al., 2000). It also releases the inhibitors from mRNAs, leading to a burst in protein synthesis (Winkler et al., 1980), in particular, cytoskeleton proteins and morphogenetic factors that are crucial for the upcoming morphogenesis. Another effect of the calcium wave(s) is the activation of NAD^+ kinases, resulting in the conversion of NAD^+ into $NADP^+$, a coenzyme for lipid biosynthesis, and thus allowing the formation of the extra membranes required by the process of cleavage (Epel et al., 1981). In the case of insects, the calcium waves happen at ovulation (though there are no cortical granules), and the sperm enter an already activated egg (Heifetz et al., 2001).

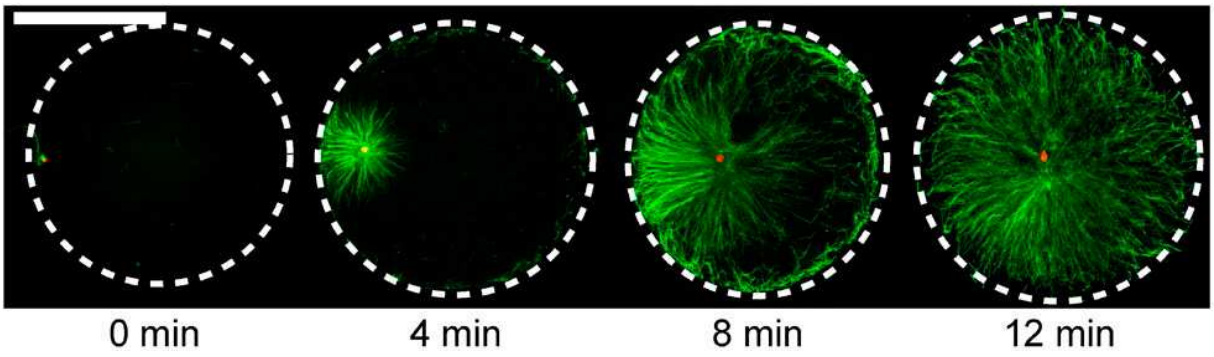

Figure I.3. : *Immunostaining images showing sperm aster growth and migration in the sea urchin embryo after fertilization. Microtubules are marked in green and centrosome in red. White dotted line indicates the egg surface. Scale bar : 50 µm. (From (Tanimoto et al., 2016))*

After the fusion of the egg and sperm membranes, the centriole brought by the sperm head nucleates an aster of microtubules (MTs), and the male pronucleus starts migrating toward the cell center (Figure I.3.) where it meets the female pronucleus. In rodents, the

centration is performed without centrioles and is thought to be actin-dependent (Chapter II.1.a.). In eggs where meiosis was complete at the time of fertilization, the two pronuclei fuse (Dan and Ito, 1984), usually forming a diploid zygote nucleus. The centrosomes of the future embryo usually originate from the sperm centriole.

c. Size and timing

After fertilization of the egg by the sperm and the gathering of the two pronuclei, the egg initiates a series of rapid successive divisions. Indeed, the mitotic cell cycle was restored by the calcium waves of fertilization, in particular through a release of the inhibition of mRNAs coding for cyclin B, leading to the activation and cycling activity of the mitosis-promoting factor. At these early stages of development, the cell cycle consists in two phases only : a phase where the cell divides (M) and a phase where DNA is replicated (S). Therefore the divisions are fast and embryos usually do not grow much or not at all, and early development proceeds solely by dividing the volume of the egg cell into smaller and smaller blastomeres (the cells within an embryo).

As cyclin B and its regulators are generally deposited in the egg cytoplasm, the division is only controlled by maternal cues and is independent on the embryo's genome, not yet expressed. This maternally driven cell cycle without gap phases yields a synchrony of the divisions, where all the blastomeres of an embryo divide at the same time. Later on, when after several rounds of division the maternal mRNAs get degraded, the embryo's DNA starts to be expressed and compensates for the shortage of maternal cytoplasmic components. It now also synthetizes new proteins via mRNAs, many of them having a crucial role in the next stages of embryogenesis. During this transition, referred to as the mid-blastula transition, the cell cycle switches from biphasic to quadriphasic, with the addition of two gap phases (G1 and G2) between the M and S phases (Edgar and Schubiger, 1986; Newport and Kirschner, 1982). As a direct consequence, the division rate slows down, and as each cell now expresses different cell cycle regulators, the divisions become asynchronous. It is interesting to note, however, that in some species the asynchrony of divisions occurs before the mid-blastula transition. It is the case during micromeres formation in echinoderm embryos for instance, where the four vegetal cells divide before the four animal cells at the 8-cell stage (Chapter I.3.b.).

d. Mitosis

Cell division consists of a repartition of the previously duplicated chromosomes into the two daughter cells, in a process called karyokinesis, coordinated with a cytoplasm division called cytokinesis. Prior to mitosis (in S phase, that identifies with interphase for early embryos), the chromosomes duplicate to form pairs of sisters chromatids bound together at the centromeres. In the centromere region, each chromatid has a protein structure called kinetochore, that is composed of two regions : a permanent region, called the inner kinetochore, tightly bound to the centromere DNA and a dynamic region, the outer kinetochore, that is assembled only for mitosis and will participate in chromosome segregation. After checking that the chromosomes duplication is complete, without DNA damage (G_2 checkpoint), the cell enters mitosis (Figure I.4.).

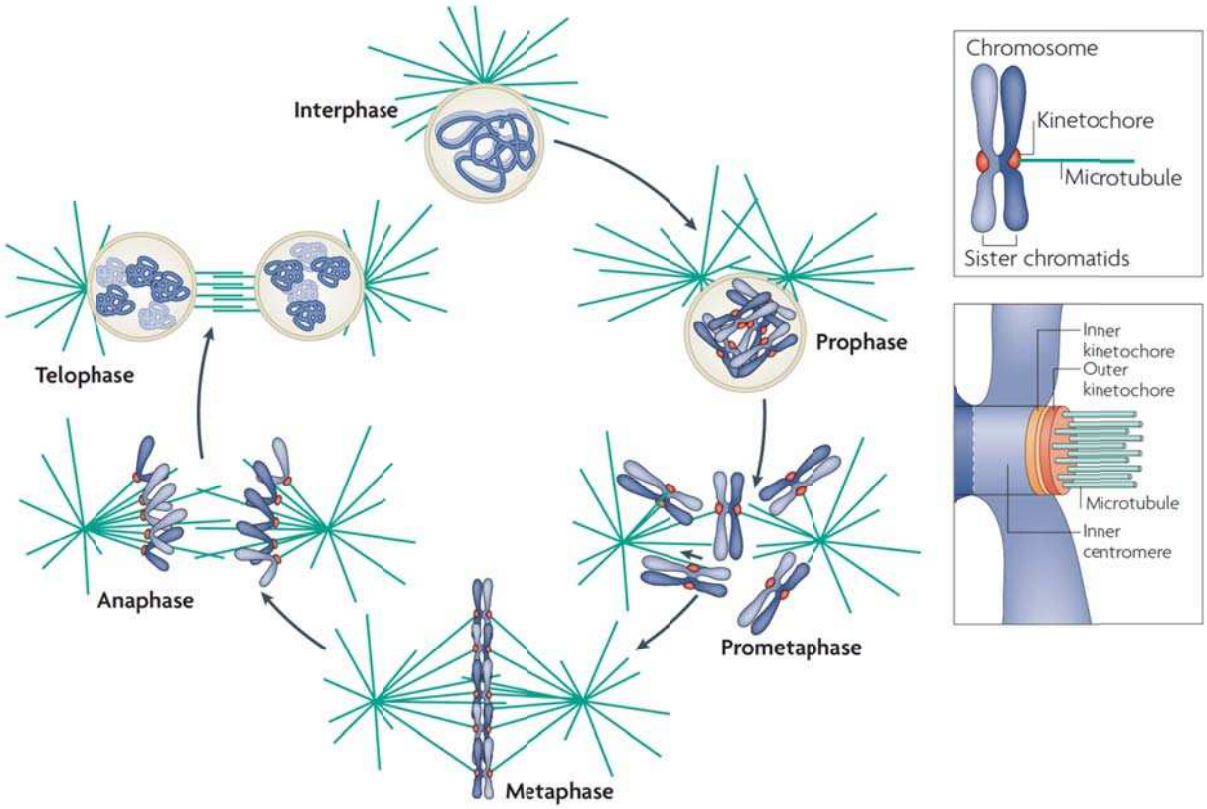

Figure I.4. : *The stages of mitosis. Note the centrosome duplication occurring prior to mitosis, generating a bipolar aster from the monopolar aster of interphase. In metaphase, the chromosomes align on the metaphase plate. In anaphase, the MTs that catch the chromosomes pull via a MT depolymerization at the kinetochores, while the polar MTs in-between push the centrosomes apart. Insets show MT-chromosome attachment via the kinetochores (top), and the structure of the kinetochores (bottom). (Adapted from (Cheeseman and Desai, 2008))*

In the beginning of mitosis (during a phase called prophase), chromosomes condense into long and thin shapes, and the cell starts to assemble the mitotic spindle, that is the structure that performs chromatids separation and karyokinesis. The mitotic spindle is made of microtubules organized by two centrosomes that position symmetrically around the nucleus (Chapter II.2.b.). Then, in prometaphase, the nuclear envelope disintegrates and the spindle spreads into the nuclear space toward the chromosomes, which now have clear X-shapes. The tips of the MTs attach to the outer kinetochores, so that the two sister chromatids are anchored to MTs growing from opposite centrosomes. In metaphase, as the MTs exert tension on the chromosomes, all the chromosomes align in a plane centered between the two centrosomes, and perpendicular to the centrosomes axis, called the metaphase plate. The spindle assembly checkpoint occurs at this stage, checking that all chromatids are attached and under bipolar tension, so that the cell can proceed to anaphase (Khodjakov and Pines, 2010). In anaphase, the bond (made of cohesins) between the two sister chromatids breaks. The MTs binding the chromosomes shrink (anaphase A), and in-between the chromosomes, the remaining MTs push the two centrosomes toward opposite ends of the cell (anaphase B). As a result, the chromatids are pulled toward opposite centrosomes, and getting separated into the two future daughter cells. At this stage, chromosomes reach their denser state to prepare for nucleus reformation. Finally, in telophase, the new nuclei form from the remaining fragments of the

old one and chromosomes start to decondense. The two daughter cells are separated by cytokinesis.

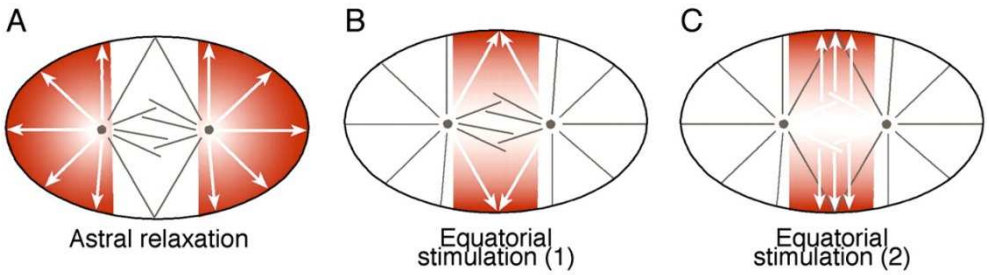

Figure I.5. : *The three main hypotheses for equatorial positioning of the cleavage furrow.* ***A :*** *the proximity of the centrosomes may induce a surface relaxation at the poles, leading to a contraction of the equator that has a higher surface tension/contractility.* ***B :*** *the astral MTs growing from the two centrosomes meet at the equator, defining the equator and inducing furrow constriction via MT depletion or ring-assembly factors recruitment.* ***C :*** *the higher proximity of the chromosomes at the equator due to the diamond shape of the mitotic spindle leads to the recruitment of specific factors at the equator, by diffusion or transport along astral MTs. (From (Kaltschmidt and Brand, 2002))*

The process of cytokinesis is triggered during the transition from metaphase to anaphase. The validation of the spindle assembly checkpoint leads to the inactivation of Cdk1 through the degradation of cyclin B. This causes a rearrangement of the cytoskeleton that paves the way for the further steps of cytokinesis. The link between karyokinesis and cytokinesis position is not clear, and seems to rely on various and complementary mechanisms depending of cell type (reviewed in (von Dassow, 2009; Oliferenko et al., 2009)) (Figure I.5.). In some embryos the cytokinetic zone has been proposed to depend on astral microtubules growing from the two opposite centrosomes, following an old observation (Chapter IV.3.c., 24). The two asters would not interpenetrate, and their cortical meeting zone would define the cytokinetic ring, whether due to microtubule depletion, or by recruitment of specific factors at the tips. A more general hypothesis rather implies the spindle midzone. As Cdk1 phosphoryles MKLP1, reducing its affinity for MTs, the inactivation of Cdk1 leads to a localization of MKLP1 at the mitotic spindle (Mishima et al., 2004). Two MKLP1 proteins, in association with two MgcRacGAP, form the Centralspindlin complex (White and Glotzer, 2012) that binds ECT2 (on MgcRacGAP), a RhoA activator (Tatsumoto et al., 1999). As a consequence, RhoA is locally activated at the spindle. As in anaphase the equatorial microtubules of the spindle reach the vicinity of the cell cortex at the metaphase plate (due to the diamond shape of the spindle), the Centralspindlin and activated RhoA are brought to the cortex in the shape of a ring in the plane that bisects the spindle perpendicular. Another pathway implies the Chromosomal Passenger Complex, recruited by chromosome proximity to midzone MT bundles (Field et al., 2015). The Chromosome Passenger Complex activates RhoA, forming a ring of activated RhoA at the equatorial vicinity of the cortex (Carmena et al., 2012). The cytokinesis will occur at this ring, causing the cleavage plane to be defined by the spindle position in most species. Moving a spindle by physical manipulation has been shown to change the cytokinesis plane (Bringmann and Hyman, 2005; Rappaport, 1985). Also, when the spindle is not at the center of the cell during anaphase, like during the early development of fishes or amphibians for instance (Chapter I.3.b.), cytokinesis starts in the

region where the spindle is close to the cell cortex (Hara, 1977), and then progresses to complete the ring (amphibians) or remains incomplete (fishes). In early embryos, the centrosomes are duplicated and positioned on both sides of the nucleus before the nuclear envelope breakdown, and the spindle assembles at the place where the nucleus was, keeping the same centrosome orientation. As a consequence, the position and orientation of the mitotic spindle and cytokinetic ring are generally set by the position of the nucleus at the onset of mitosis.

The first effects of activated RhoA are the polymerization of actin and the activation of myosin II (Chapter II.1.a.), yielding the assembly of a ring of actin and myosin at the cell cortex (Figure I.6.). The ring is about 0.1 µm large and extends 8-10 µm into the cytoplasm, for the early blastomeres. The mDia formin, an effector of RhoA, and profilin generate this ring-shaped network by polymerizing parallel non-branched actin (Watanabe et al., 1997). In addition, MgcRacGAP inhibits Rac, a GTPase that promotes actin branching through a pathway involving the Arp2/3 branching complex (Canman et al., 2008). This dynamic actin structure, in association with activated myosin II (through the activation of the ROCK kinase by RhoA, that phosphoryles the light chain of myosin II) that is able to generate force, leads to a contractility of the ring (Amano et al., 1996). During telophase, the ring contracts and splits the cell in two in a "purse-string" fashion. MTs are also present around the cleavage furrow to bring new material from the cytoplasm to the site of scission, allowing the required synthesis of extra membrane. Finally, the narrowing furrow forms an intercellular bridge from which actin withdraws, and that contains mostly MTs and other remnants of the spindle (Elad et al., 2011). The cleavage of the bridge by MTs severing and membrane fusion, in a process called abscission, is the longest step of cytokinesis.

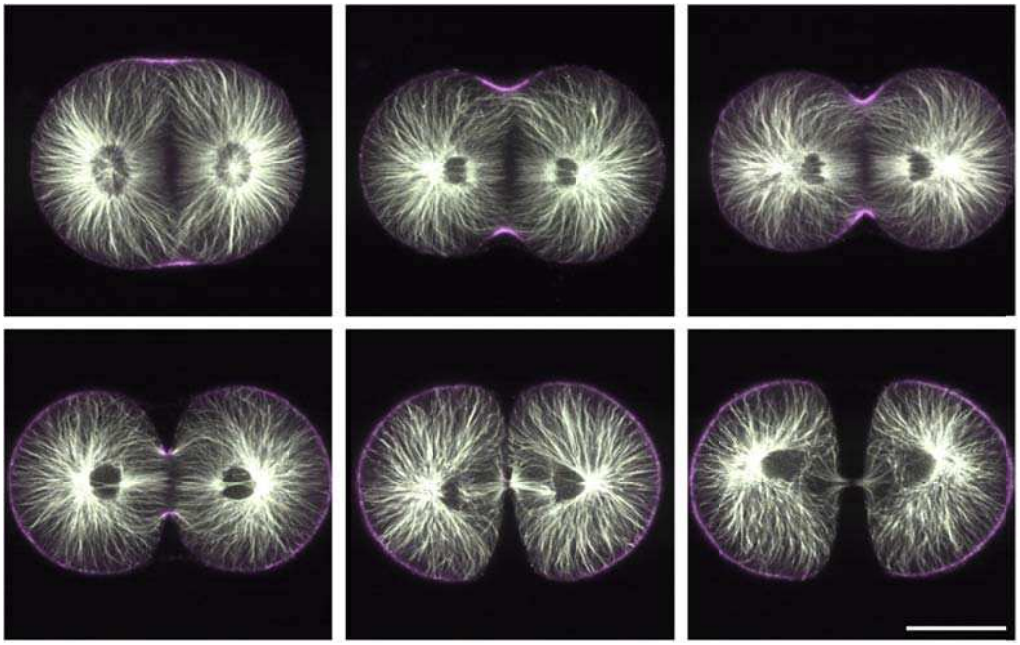

Figure I.6. : *Immunostaining images showing cytokinesis in a sea urchin egg, from the end of anaphase (first image) to the beginning of the next interphase (last image). MTs are marked in white and pRLC (showing activated myosin) in violet. The ring of acto-myosin contracts and forms an intercellular bridge. Note the MT bundle at the bridge and the interpenetrating MT asters in the first image. (Scale bar : 20 µm, from (Foe and von Dassow, 2008))*

2. Functions of the cleavage

a. Polarity establishment

In most species, early embryonic cleavage is associated with axes definition and cell fate determination. As the zygote divides, it segregates its cytoplasmic and cortical components into different blastomeres. Since some of these components do not have an isotropic distribution, the blastomeres do not share the same composition. In particular, maternal mRNAs and morphogenetic factors that will define further cell differentiation get segregated into different blastomeres, which will consequently end up with different fates, and form the different tissues of the future embryo. On top of this passive segregation mechanism, some patterning molecules can also be actively transported along the cytoskeleton toward a specific cell, or be associated with one of the centrosomes and follow it in one of the daughter cells (Lambert and Nagy, 2002).

Another way of specifying cell fate is by a precise spatial arrangement of blastomeres within the embryo. Blastomeres from different lineages interact to induce the formation of specific tissues. It is the case for instance in the nematode *C. elegans* (Chapter II.5.e.) where posterior stem cells induce the differentiation of anterior blastomeres. A tightly controlled division orientation in the early stages in thus crucial to bring interacting cells in contact and specify later cell fates.

Early cleavage generally serves to define the main axes of the embryo. Most animal classes display a bilateral symmetry, with tree main axes that are the dorso-ventral axis, the antero-posterior axis and the lateral (left-right) axis. However there can be less axes in some classes, like cnidarians that have a radial symmetry (one axis) or ctenophores that have a biradial symmetry (two axes). In many cases, the cleavage pattern defines one axis at a time, through successive rounds of divisions. In some rare cases the identity of the axes is set after they are defined, like in nemerteans where the first cleavage defines the dorso-ventral axis in 50% of the cases and the lateral axis in another 50% of the cases (Martindale and Henry, 1995). Usually however the identity of the newly defined axis is invariant, and the different axes are defined in a specific order, one after the other through successive division rounds (Goldstein and Freeman, 1997). Exceptions to this are the case of insects, where a multinucleated cell divides to form a multicellular blastoderm in one round of divisions, and the case of mammals, where the axis are defined later, after the separation between the cells that will form the fetus and the ones that will form the placenta. In this last particular case the main axes of the embryo are defined through cells reorganization.

It is interesting to note, however, that in most cases the embryonic axes were already defined before the first division of the zygote, by the intrinsic polarity of the egg. In some cases this polarity is set before fertilization, as the cytoplasm and cortical components of the egg get specifically distributed in the maturating egg. Sometimes the egg undergoes cytoplasmic and/or cortical rearrangements after fertilization. These rearrangements are often dependent on the point of sperm entry.

b. Conservation and variations

Since the egg cell generally has an intrinsic polarity, that the cleavage pattern follows to orient the first rounds of division and define the embryonic axes, it is not surprising to observe that all embryos of a same species usually follow the same cleavage pattern. In those species where successive rounds of division define the main axes, early embryos follow a cellular logic in which each cell originates from a precise cell lineage, and has to divide specifically with respect to its localization and developmental stage. Later on, as cells get more numerous and start to express their own genome and morphogens, the embryo switches to a tissular logic, where the behavior of individual cells is more stochastic. From this stage, morphogenesis is a result of the combined actions of multiple cells and is controlled at the level of the group of cells. Mammals and insects seem to follow a tissular logic directly, and do not display a reproducible early cleavage pattern. In species where early embryos follow a cellular logic however, the individual behavior of cells is important, and the cleavage pattern is generally highly reproducible, typically up to the 16 to 64-cell stage.

Cleavage patterns can also be conserved across closely related species, and even through animal classes. This is the case for instance of the cleavage of amphibians, that almost all follow the same mesolecithal pattern (Chapter I.3.b.), or of fishes, that follow close variations of the discoidal cleavage (Chapter I.3.a.) (Desnitskiy, 2014). However, in some animal classes, like mollusks or nematodes worms, the cleavage pattern, yet very reproducible within a species, is not well conserved between closely related species (Figure I.7.). A possible explanation for these variations would be that these patterns mostly rely on a complex maternal signalization, which is subject to genetic variation. On the other hand, the more reproducible patterns would rather rely on self-organization of the embryo, with respect to cues like gravity or simple maternal signalization, thus being less prone to variation.

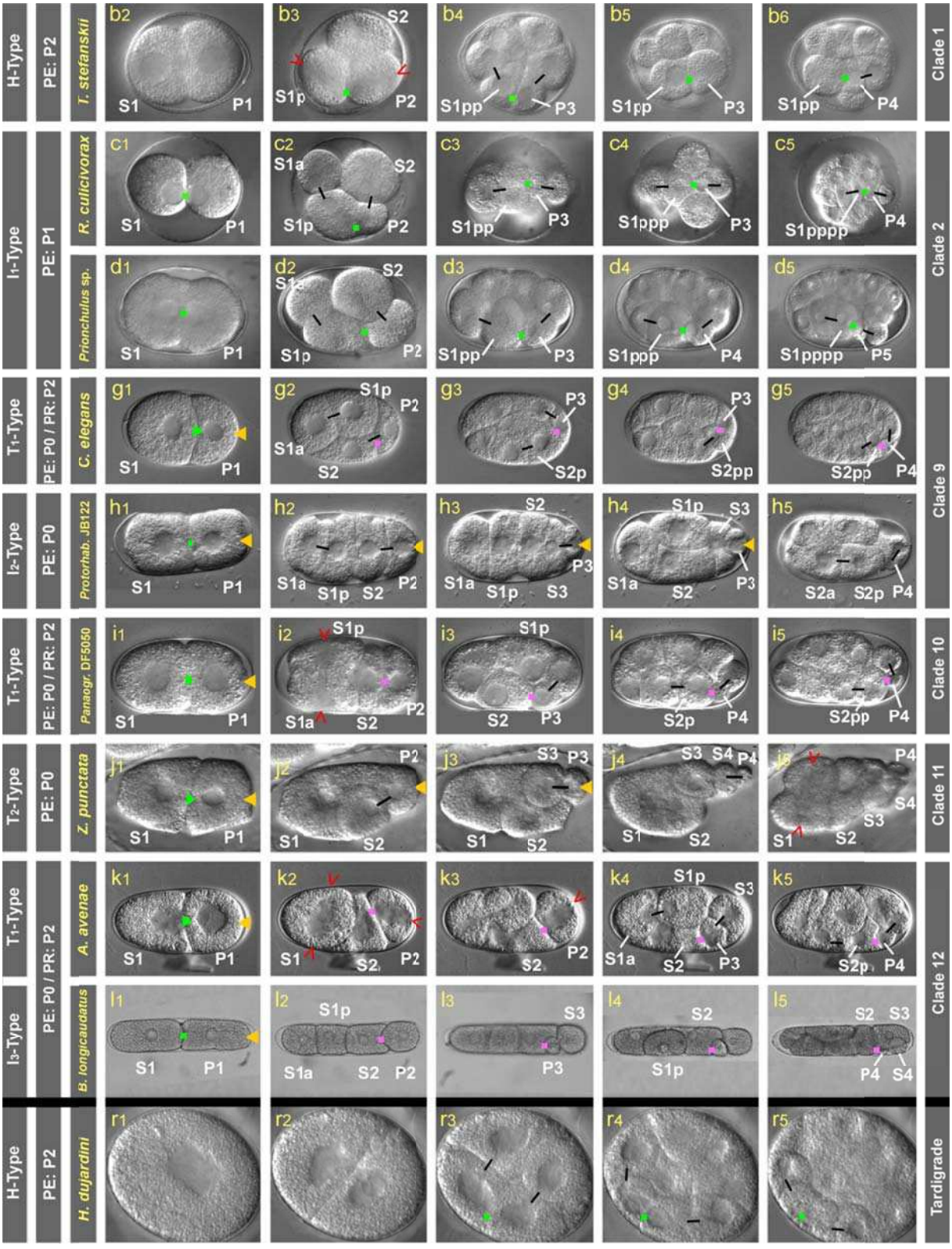

Figure I.7. : *Various cleavage patterns of nematodes species and closely related tardigrades. The clades which the represented species belong to are indicated on the right. On the left are indicated the type of cleavage pattern, of polarity specification, and the species. Concerning polarity specification, PE indicates the stage when visible polarity is established and, when applicable, PR indicates the stage when polarity is reversed in the germline, that is when the germ line cell is less posterior than its somatic cell sister. On the images, cells names are in*

white, open red arrowheads indicate spindle orientation and black bars connect sister cells. From cell behavior, the positions of polarity organizing centers (that orient mitotic spindles along the antero-posterior axis) are marked. Dots indicate primary polarity organizing centers (POCs) acting on two adjacent cells, and arrowheads show POCs acting on the germline cell only. Green stands for primary POC, purple for secondary and yellow for tertiary. (Adapted from (Gabriel et al., 2007; Schulze and Schierenberg, 2011))

3. The classical cleavage patterns

There are 8 main types of cleavage patterns (Figure I.8.). They can be classified in two main groups, depending on the completion of cytokinesis.

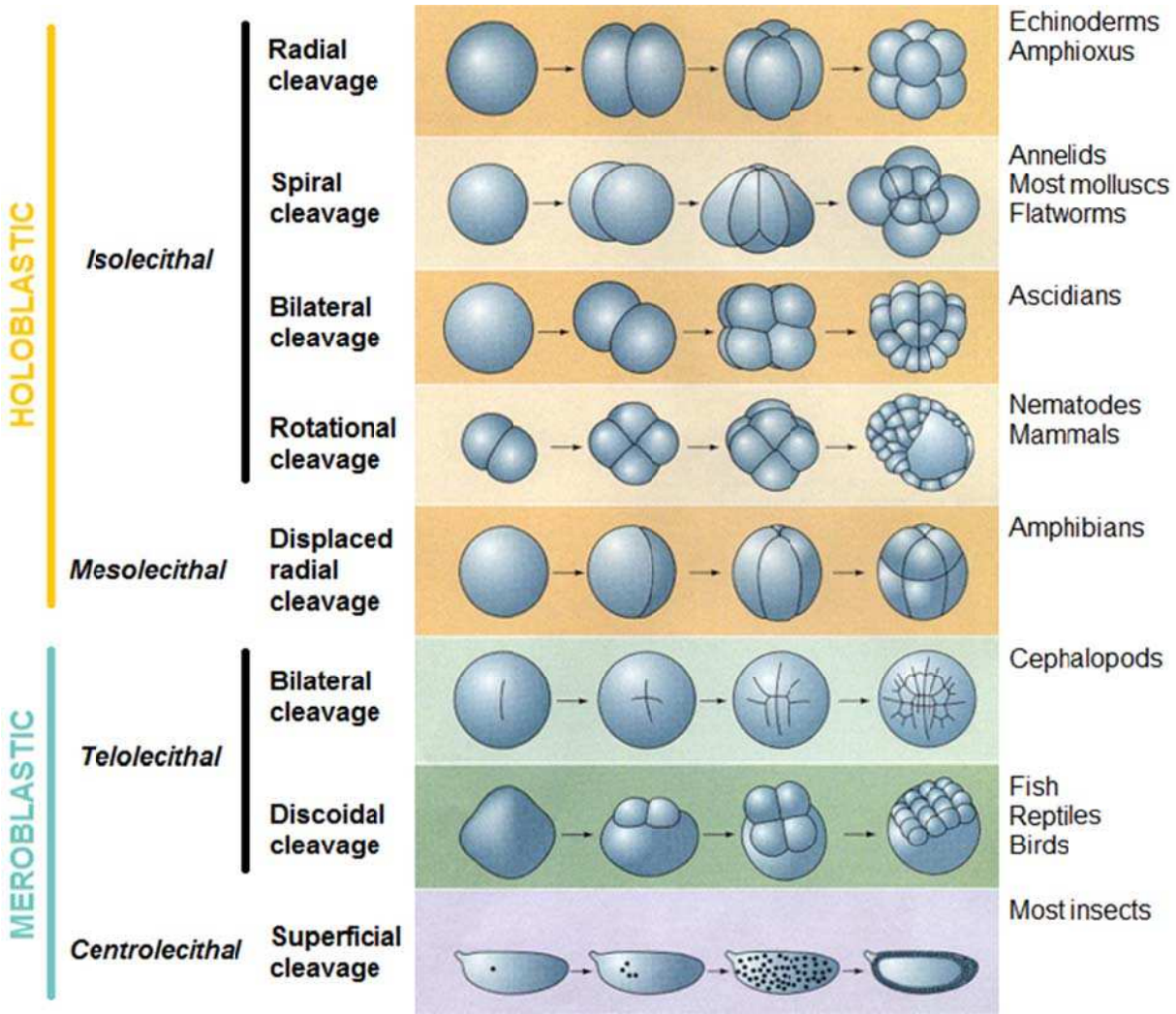

Figure I.8. : *Overview of the main classical cleavage patterns. Classification is shown on the left, and depends on completion of cleavage and position of yolk. Examples of species exhibiting these cleavage patterns are given on the right. (Adapted from (Gilbert, 2000))*

a. The meroblastic cleavages

Eggs that contain a huge accumulation of yolk tend to cleave only partially, as the yolky part is not cleaved. This type of cleavage is called meroblastic, and can be divided in two main cases, as the yolky part can be on one side of the egg (telolecithal cleavage), or in the center (centrolecithal cleavage).

The centrolecithal cleavage

The centrolecithal cleavage is displayed by most insects. Typically, the egg cell undergoes a series of karyokinesis, which are not associated with any cytokinesis, giving rise to a plurinucleated cell, known as syncytium. In drosophila, after 8 cycles of karyokinesis, the syncytium contains 256 nuclei. After the next karyokinesis, five nuclei migrate to the posterior pole where cellularization happens, that is, simultaneous cytokinesis enclosing those nuclei into five distinct cells, the pole cells, which will become the gametes of the adult fly. At the next karyokinesis round, all the other nuclei migrate toward the cell cortex (Foe and Alberts, 1983), bringing their cytoplasmic surrounding and the maternal patterning factors it contains with them (Karr and Alberts, 1986). The nuclear divisions continue there, until at the 13^{th} round of karyokinesis partial cytokinesis occurs, where all the nuclei get enclosed between membrane invaginations. This creates one layer of cells at the embryo's periphery, called the cellular blastoderm. The main axes of the embryo are set by the cytoplasmic content of the cells within the blastoderm, originating from the gradients of patterning factors that are present in the egg cytoplasm from the egg maturation.

The telolecithal cleavage

There are two main types of telolecithal cleavage : the bilateral cleavage that is displayed by cephalopod mollusks, and the discoidal cleavage that is found in fish, reptiles and birds. In both cases, only the non-yolky superficial side of the embryo is being cleaved, in a partial manner as the cleavage furrow does not progress into the yolk. The yolk/blastodisc separation often appears to be an active process where the actin cytoskeleton contracts to push the non-yolky cytoplasm on one side of the embryo (Leung et al., 2000). There are also MTs growing inside the yolk and organizing transport along their lattice. The cleaving blastodisc first forms a single layer of cells on the yolk, and then give rise to additional layers (Olivier et al., 2010). In birds, the cells in the center of the blastoderm then die, and only the superficial cells, known as the area pellucida, the peripheric cells, the area opaca, and the layer of cells between them, the marginal zone (Arendt and Nübler-Jung, 1999), give rise to the embryo (Figure I.9.). The antero-posterior axis is formed later on, as cells accumulate at the lower side of the blastodisc by gravity, forming the future head of the chick from a radially symmetrical embryo.

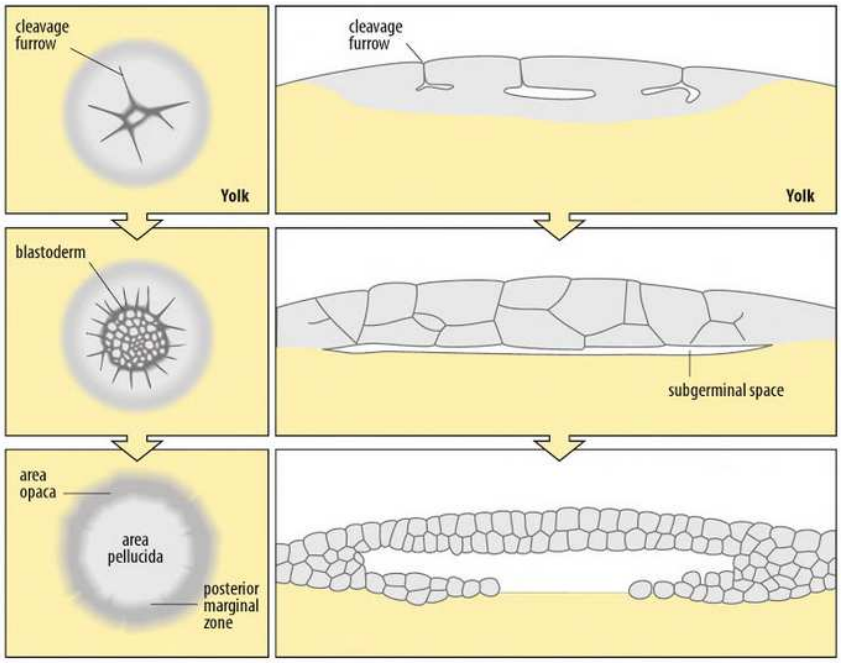

Figure I.9. : *Development of the blastodisc in birds. The embryo is radially symmetric. Cells from the inner layers of the blastoderm die and the remaining cells will reorganize to define the antero-posterior axis.* ***Left :*** *view from the animal pole.* ***Right :*** *side view. (From (Wolpert et al., 2015))*

b. The holoblastic cleavages

In species where the egg cell does not contain much yolk, cytokinesis can be complete and the cleavage is called holoblastic. In the case where the yolk distribution is not isotropic, generally associated with a spindle shifted toward the non-yolky part of the embryo, cleavage is complete but the furrow starts from the non-yolky side and slowly ingresses toward the other part. The next cytokinesis usually begins before the completion of the previous one. This type of holoblastic cleavage is called mesolecithal. On the other hand, if the yolk distribution is isotropic or near-isotropic, and the furrow directly forms a ring shape, the cleavage is called isolecithal. The isolecithal cleavage comes in four main variations : the radial cleavage, found in echinoderms and amphioxus, the spiral cleavage found in mollusks, flatworms and annelids, the bilateral cleavage found in ascidians, and the rotational cleavage found in mammals and nematodes.

The mesolecithal cleavage

The mesolecithal cleavage is found in most amphibian species. The two first cleavages are meridional and perpendicular to each other, while the third one is equatorial and asymmetric, yielding smaller cells at the animal pole, that is the pole with less yolk (Yokota et al., 2004). Then divisions alternate between meridional and equatorial orientations, with the more vegetal cells being bigger and dividing at a slower rate than the more animal ones. This yields an animal region made of numerous small cells and a vegetal region made of fewer yolky large cells (Gilbert, 2000).

The radial isolecithal cleavage

The radial isolecithal cleavage consists of three rounds of perpendicular symmetric divisions, the two first ones being meridional and the third one equatorial. In some species like holothurians, the next rounds of cleavage are symmetric, alternating between meridional and equatorial divisions. In some others like sea urchins, the fourth round of divisions meridionally splits the animal cells into equal blastomeres, while the vegetal cells divide asymmetrically to form smaller cells, called micromeres, toward the vegetal pole, and bigger cells called macromeres (Figure I.10.). This asymmetric division is preceded by a migration of the vegetal nuclei toward the vegetal pole at the very end of interphase (Holy and Schatten, 1991). The micromeres then divide asymmetrically to form big macromeres and small micromeres at the vegetal pole, while the macromeres divide symmetrically and meridionally, and the animal cells divide symmetrically and equatorially. Afterwards, the small micromeres divide once more and then stop, and the other cells alternate between meridional and equatorial cleavages (Summers et al., 1993). It is believed that the micromeres specification implies the Wnt pathway, as Dishevelled and β-catenin are found at the vegetal pole (Peng and Wikramanayake, 2013; Weitzel et al., 2004), and as embryos display abnormal micromeres and form ectodermal balls when β-catenin is prevented from entering the nuclei (ectoderm formation is the normal fate of animal cells) (Logan and McClay, 1998). These maternal polar effectors, located at the vegetal pole, would then define the animal-vegetal (future antero-posterior) axis.

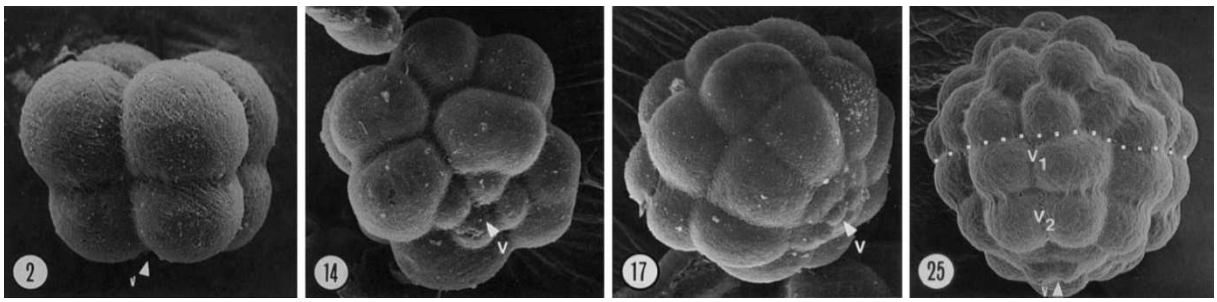

Figure I.10. : *Scanning electron microscopy images of sea urchin embryos at the 8-cell stage (2), late 16-cell stage (14), 32-cell stage (17) and 56-cell stage (25). Arrows indicate the vegetal pole. In the 56-cell stage, dotted line shows the separation between animal and vegetal blastomeres from the 8-cell stage. The two rings of daughter cells, originating from the equatorial division of the large blastomeres at the 32-cell stage, are identified (v1 and v2). (From (Summers et al., 1993))*

The spiral isolecithal cleavage

The spiral cleavage displays more variations between species. The first two divisions are almost meridional, yielding four blastomeres rearranged from a pure square configuration to a slightly more tetraedric configuration. Importantly, those four blastomeres (referred to as A, B, C and D) already differ in terms of cell fate, due to the specific segregation of patterning factors. In many cases, this segregation is made by association of the factors with distinct centrosomes (Lambert and Nagy, 2002). Some species develop a protrusion shortly before the

two first divisions, where patterning factors are bound (Figure I.11.). The maternal molecules are presumably bound at the cytoskeleton, or in the cortical cortex, as cytoplasm manipulation does not affect cell fate and overall embryonic development (van den Biggelaar, 1977; Clement, 1968). This protrusion, called the polar lobe, forms a bulb and remains attached to the egg cell by a thin tube, thus isolating the mRNAs and morphogens while the rest of the cell undergoes division. The lobe then fuses again with the daughter cell to which it is attached (CD), and reforms before the second division (only in this CD daughter cell). At the 4-cell stage the polar lobe is absorbed by the D cell to which it is attached, and does not form again (Wilson, 1904). As a consequence, in many species, blastomeres at the 4-cell stage have different sizes, and the D cell has a larger volume than the other cells. Among the patterning factors delivered by the polar lobe to the D blastomere are morphogenetic factors for endoderm and mesoderm formation, and for the determination of the dorso-ventral axis. A differential accumulation of yolk is also seen in most species, with more yolk at the vegetal pole.

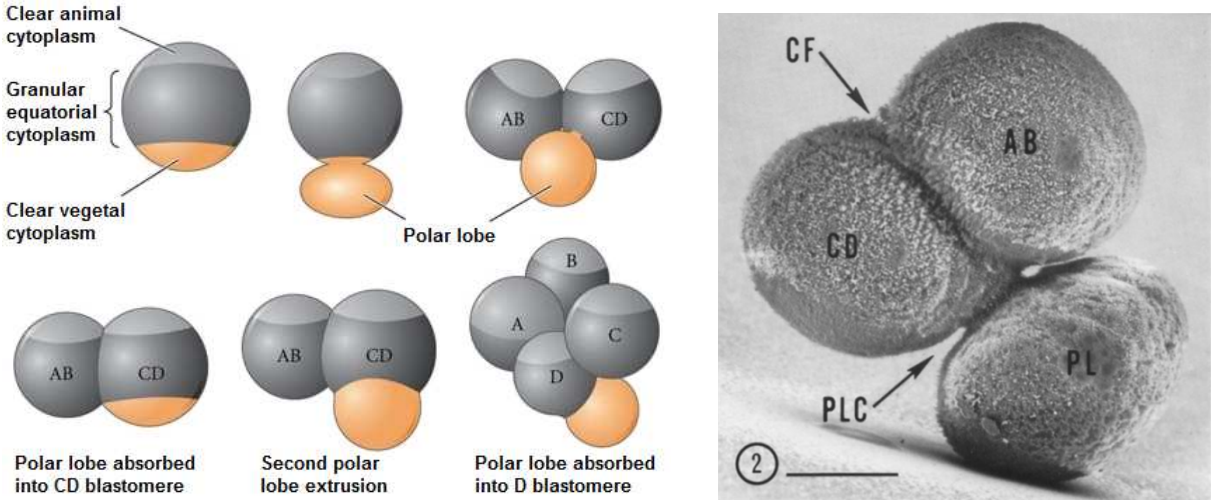

Figure I.11. : *Polar lobe formation in some species, that allows to segregate morphogens into the D blastomere.* ***Left :*** *the two rounds of lobe extrusion and absorption. The blastomeres are identified. (From (Gilbert, 2000))* ***Right :*** *scanning electron micrograph of an* Ilyanassa *egg during the first cleavage. The two daughter cells are identified, as well as the polar lobe (PL), the cleavage furrow (CF) and the polar lobe constriction (PLC). (Scale bar : 50 µm, from (Conrad et al., 1973))*

Contrary to the radial cleavage pattern, the next division is not oriented along the animal-vegetal axis, but slightly biased to the right or to the left. It is asymmetric, and yields a micromere at the animal pole, that is sitting both on its sister macromere and on one of the neighboring macromeres, due to the angle of the division. It is interesting to note that the resulting configuration is close to the most thermodynamically stable packing, contrary to the radial pattern. The following rounds of cleavage also give asymmetric oblique divisions, yielding smaller and smaller micromeres at the animal pole, and bigger blastomeres near the vegetal pole, with a densely packed structure (Figure I.12.). The angles of division alternate between the successive rounds, with all the micromeres of the embryo budding off the right of the macromeres, then off the left, and so on (Lambert, 2010). Interestingly, in snails, the orientation of the first near radial division (that is the third division of the zygote) determines

the future orientation of the animal's shell (Morgan, 1927). If the micromeres bud to the right, the coil opens to the right of the shell (dextral coiling), while a budding to the left yields a left opening (sinistral coiling). In most species, all or most animals have the same coiling orientation. This orientation is thought to be determined by maternal cytoplasmic factors (Chapter II.5.b.).

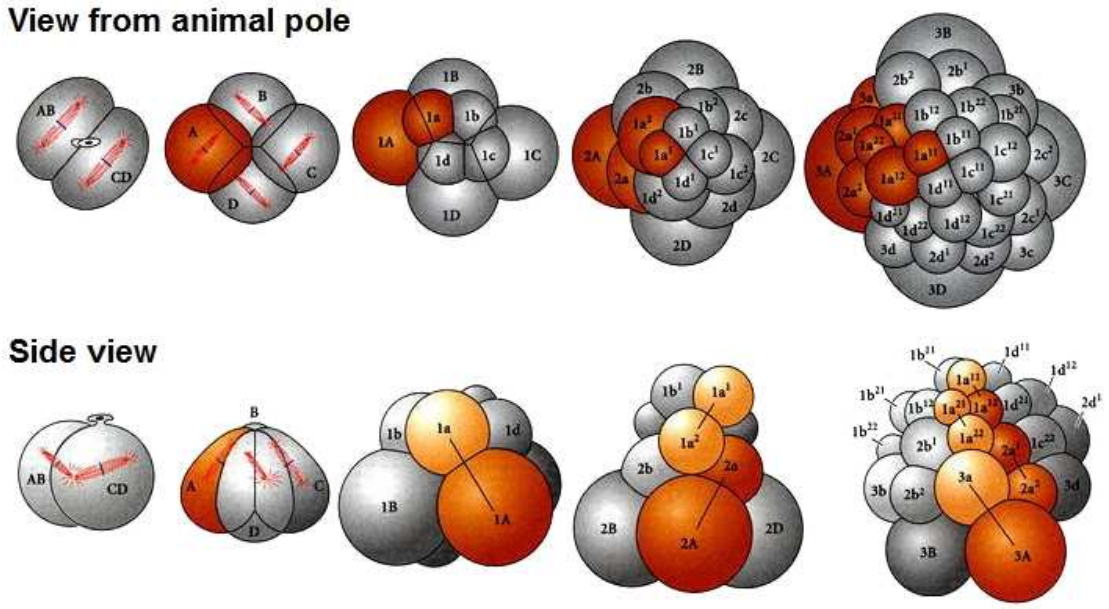

Figure I.12. : *Cell fate during spiral cleavage in a right-coiling species. Left-coiling species exhibit a mirror image of this pattern. In the early stages, spindles are represented in red. The lineage of the A blastomere is followed in orange, and black bars connect sister cells. The rounds of cleavage alternate between a division orientation to the left and to the right. Divisions are asymmetric. (From (Gilbert, 2000))*

The bilateral isolecithal cleavage

The bilateral cleavage starts with a meridional division, that sets the future left and right sides of the embryo. The two sides then behave symmetrically during the following early cleavage. The two other axes of the embryo were defined before the first cleavage, as the egg undergoes cytoplasmic rearrangement upon fertilization. The cortical yellow cytoplasm, that contains lipid inclusions, as well as the clear cytoplasm originating from the nucleus breakdown during meiosis, migrate toward the vegetal pole, that will become the dorsal side of the embryo (Sardet et al., 2005). This vegetal cytoplasmic cap contains yolk, mitochondria and endoplasmic reticulum components, as well as maternal mRNAs. As the sperm migrates along the future posterior side of the embryo, the sperm aster induces a cytoplasm rotation, leaving the yolk toward the anterior side and dragging the yellow and clear cytoplasms toward the posterior side (Figure I.13.). This cytoplasmic rotation, that finishes during the first cleavage, sets the future antero-posterior axis of the embryo (Roegiers et al., 1999; Sawada and Schatten, 1989). From the now posterior cytoplasm, the posterior cells assemble a cortical structure called the centrosome attracting body (CAB), at the two-cell stage. The CAB is making about a 30° angle with the vegetal pole. It is thought to play a crucial role in cell differentiation, as it attracts specific maternal mRNAs (Hibino et al., 1998; Negishi et al.,

2007). The next division is orthogonal to the first one, and almost meridional, separating the anterior and posterior sides of the embryo. Yet the spindles appear to be tilted from a purely horizontal orientation (that would give a meridional division), rather pointing toward the newly formed CAB. This division is also slightly asymmetric, yielding smaller anterior cells. In some species, the membranes separating the anterior and posterior cells adopt a concave shape prior to the next division. The third division is roughly equatorial, both for the anterior and posterior cells. However, the posterior spindles are pointing toward the CAB, so that the division makes an angle from a pure equatorial division. This angle causes the four cells within each lateral side of the embryo to arrange into a more thermodynamically stable packing, with a contact between the animal posterior cell and the vegetal anterior one (Figure I.13.). The divisions are asymmetric, with four smaller animal cells. The fourth division is near-meridional and near-symmetric in all blastomeres, except in the two vegetal posterior blastomeres that contain the CAB. Those perform asymmetric divisions, yielding smaller posterior cells, as the mitotic spindles get displaced toward the CAB and point toward it. From the fourth division, the posterior blastomeres that inherit the CAB only do asymmetric divisions, yielding smaller posterior daughter cells (Conklin, 1905; Nishida, 2005; Satoh, 1979).

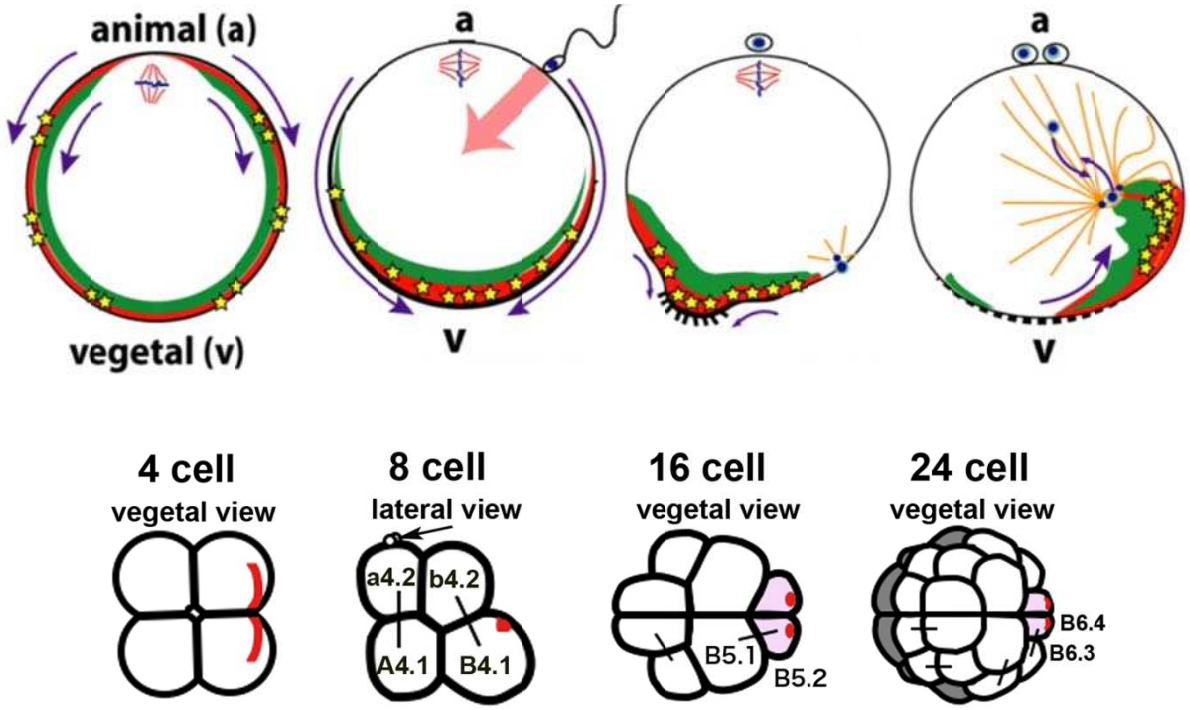

Figure I.13. : *Polarity specification in the ascidian embryo.* ***Top :*** *The two cytoplasmic waves that determine embryonic axes upon fertilization. Cytoplasm movement is indicated by blue arrows. Myoplasm is shown in green, cortical endoplasmic reticulum in red, and stars indicate postplasmic PEM RNAs. The sperm MT aster is shown in orange, and the movements of the two pronuclei are indicated by blue arrows on the last image. The animal-vegetal axis is indicated. (Adapted from (Sardet et al., 2007))* ***Bottom :*** *Localization of the CAB (in red) from the 4-cell stage to the 24-cell stage. Micromeres are in violet, black bars connect sister cells, cells are identified. The successive spindle orientations and positions seem to be influenced by the CAB, as the cells containing the CAB undergo asymmetric divisions. The arrow shows the polar bodies. (From (Negishi et al., 2007))*

The rotational isolecithal cleavage

The rotational cleavage is characterized by a second division leading to a tetraedric blastomeres arrangement. This feature is however found in very different cleavage patterns, originating from different mechanisms. The two mainly studied rotational patterns are the mammal and *C. elegans* nematode patterns.

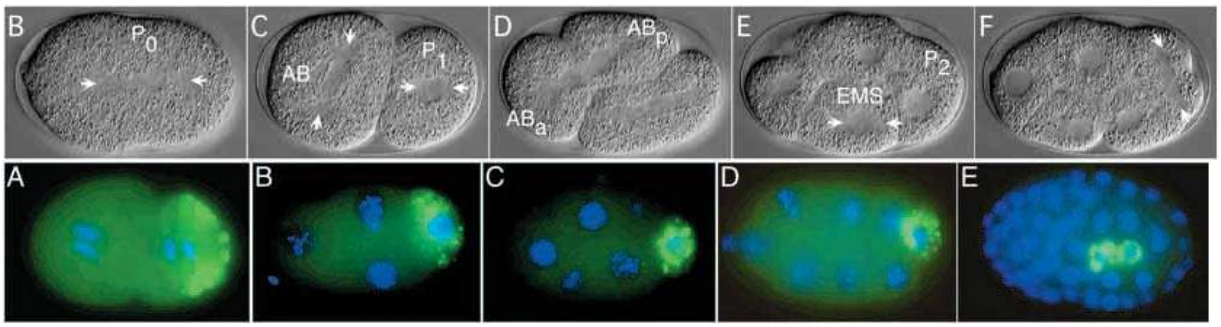

Figure I.14. : *Development and germ line specification in the* C. elegans *embryo.* ***Top :*** *development of the embryo, with spindle orientations indicated by arrows. The germ line cells (P1 and P2) are smaller than their sister somatic cell.* ***Bottom :*** *Epifluorescent micrographs showing the segregation of the P-granules (in green) in the germ cells. DNA is marked in blue. (Both images from (Gomes et al., 2001))*

The cleavage pattern of nematodes shows huge variations between closely related species (Figure I.7.). In the *C. elegans* worm, the first axis to be set is the antero-posterior axis (Figure I.14.). The egg has an oblong shape, and after entering the egg, the sperm pronucleus is pushed by cytoplasmic movements (initiated by its centriole) toward the closest end of the egg, that will become the posterior side (Goldstein and Hird, 1996). The antero-posterior axis is thus determined by the point of sperm entry. Then the sperm pronucleus migrates toward the center of the cell where it meets the female pronucleus. The first division is oriented along the antero-posterior axis, and is asymmetric, with the posterior daughter cell (P1) being smaller than the anterior one (AB). All asymmetric divisions of the *C. elegans* embryo, systematically occurring at the posterior side of the embryo, yield a founder cell, that will give rise to a differentiated lineage, and a stem cell (Sulston and Horvitz, 1977). The posterior side contains P-granules, which are ribonucleoproteins complexes containing translation regulators that are responsible for the specification of germ cells. The P-granules migrate shortly after fertilization to end up in the cytoplasmic vicinity of the posterior pole (Strome and Wood, 1983). As the asymmetric divisions are posterior and oriented along the antero-posterior axis, it is the stem cell that inherits the P-granules at the first two divisions (Figure I.14.). During the next two divisions, the P-granules keep being segregated into the stem cell by associating with its nucleus. The posterior lineage thus gives rise to the germ cells of the adult worm. At the second division, while the posterior stem cell P1 divides asymmetrically along the antero-posterior axis to produce a smaller posterior stem cell (P2) and a bigger anterior founder cell (EMS), the founder cell AB divides symmetrically and perpendicular to the antero-posterior axis. However, the oblong shape of the embryo does not leave enough space for this orthogonal arrangement, causing one of the daughter cells to slide along the egg shell to a more favorable tetraedric arrangement. This cell that moves toward the posterior side to end

up above the EMS cell defines the future dorso-ventral axis of the embryo (Evans et al., 1994). Laterally, the side of this cell will be the dorsal pole, and the side of the EMS cell will be the ventral pole. The development of *C. elegans* from the 4-cell stage is also highly reproducible, yielding to an adult containing 959 somatic cells originating from an invariant lineage (Sulston and Horvitz, 1977).

On the contrary, the development of mammals is only reproducible up to the 4-cell stage, as the genome of the embryo takes over the maternal factors between the 2-cell stage and the 8-cell stage, depending on species (Braude et al., 1988; Piko and Clegg, 1982). On top of the non-reproducibility of the early development, this yields an early asynchrony of divisions, with occurrences of stages where embryos contain an odd number of cells. However, all divisions are symmetric up to the 8-cell stage, and during the second division, the two cleavage planes are orthogonal to each other, giving rise to a tetraedric arrangement of the blastomeres at the 4-cell stage (Figure I.15.) (Gulyas, 1975). An interesting feature of the development of mammals is the compaction occurring at the 8-cell stage in mice (Chapter III.2.c., Figure III.6.). The eight blastomeres, that were arranged in a loose packing, undergo a rapid compaction through an increase of cortical tension (Maître et al., 2015) and the expression of cell-cell adhesion proteins such as E-cadherins, and form a tight ball of cells (Fleming et al., 2001). This ball remains compact through the next divisions, and cells rearrange within the ball, presumably according to cells mechanical properties modulated by cell polarity, yielding polar cells at the surface and apolar cells inside the ball (Chapter III.2.c.). Most of the inner cells will form the future embryo, while most of the outer cells will give rise to the embryonic part of the placenta, called the chorion.

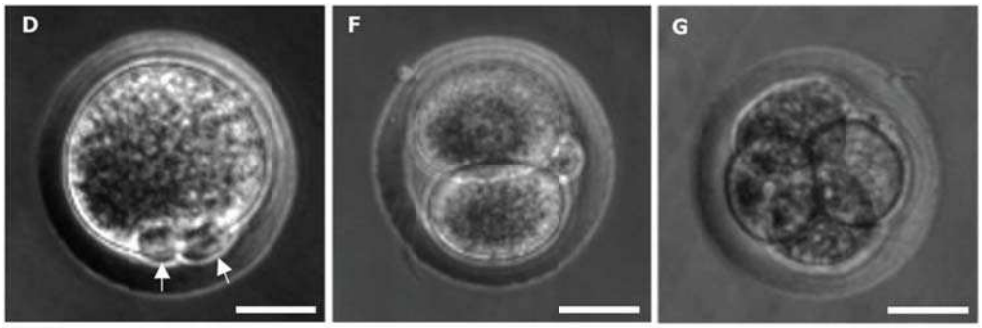

Figure I.15. : *Early development of the mammal embryo. Note the tetraedric arrangement of cells at the 4-cell stage. Arrows indicate the polar bodies. (Scale bar : 30 µm, adapted from (Choi and He, 2013))*

4. Empiric rules for division positioning

The question of the determination of the division planes, leading to the high reproducibility of the early cleavage patterns as well as to the formation and maintenance of specific tissular shapes during later morphogenesis, has been fascinating cell biologists and embryologists for years.

a. From the previous division

The first empirical rules to predict the position of the cleavage plane come from plant biology. In 1878, Julius Sachs proposed that cells typically tend to divide into equal parts, and that each new plane of division tends to intersect the preceding one at right angles (Sachs, 1878). An analogy to this in the development of early embryos of animals would be the frequent occurrence of successive orthogonal division planes in cleavage patterns. The most striking example of this is the radial isolecithal cleavage, which begins with three orthogonal symmetric divisions. The discoidal telolecithal cleavage of fishes also starts with a succession of orthogonal symmetric divisions within the plane of the blastodisc. As a third example, the mesolecithal cleavage features three orthogonal divisions, even though the third one is asymmetric. The idea that a cleavage plane orients orthogonal to the previous one can thus be proposed as a default rule, and would find an explanation in the dynamics of centrosomes duplication and organization (Chapter II.2.b.). Although widely observed, in animals as in plants, this rule based on the history of the cleaving embryo is not truly predictive, since several different planes are allowed at each round of divisions (Figure I.16.). Another idea, that was formulated by Hofmeister in 1867, states that plant cells tend to divide perpendicular to the cell's growth axis (Hofmeister, 1867). This rule refines Sachs' rule in some cases but still appears insufficient in many situations to accurately predict cell division.

b. The energy minimization rule

In 1886, Leo Errera adds a supplemental condition to the rules for plants divisions : cells divide along the surface of the least area that halves the cell's volume (Errera, 1886). From now on, the position of the division is well defined as being the shortest boundary that is orthogonal to the previous division plane, giving a real predictive power to Errera's rule (Figure I.16.). Interestingly, this idea is originally inspired by the behavior of soap bubbles, which tend to minimize their surface energy by minimizing their overall surface area. Errera's rule would then correspond to an energy minimization of the new cell boundary, whether to economize cell wall material, or because the mechanisms setting the new boundary reach an equilibrium position. It is indeed believed that in plants the cytoskeleton strands (made of actin and microtubules) that stabilize the future boundary site are under tension, and thus would naturally find the shortest way through the cell. The analogy can be made with the thermodynamically stable packing of cells observed in the spiral isolecithal cleavage, or with the tetraedric configuration of the 4-cell stage in the rotational isolecithal cleavage, both minimizing the overall energy of the system. Thermodynamic considerations could then be taken into account to predict cell division positioning in animal embryos. Yet, despite being remarkably accurate in most divisions of plant development, Errera's rule fails to predict the stochasticity in the choice of the division position in cases of a non-unique shortest boundary (Figure I.16.).

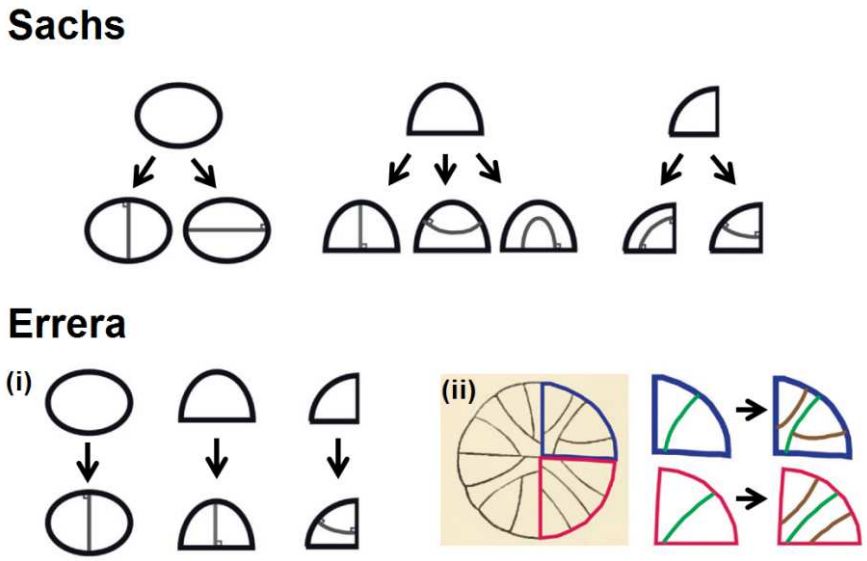

Figure I.16. : *Possible predictions of the division plane in plants, from cell geometry.* ***Top :*** *Sachs' rule yields several possibilities for a given geometry.* ***Bottom :*** *Errera's rule narrows the possibilities (i), but still fails to predict division plane positioning in some specific geometries, where the cells show variable behaviors (ii). (Adapted from (Minc and Piel, 2012))*

c. The long axis rule

In 1884, Oskar Hertwig proposes the first empirical rule to predict cell division in animals. This rule, known as the long axis rule, states that the typical position of the nucleus tends toward the center of its sphere of influence, that is, of the protoplasmic mass in which it lies. In addition the axis of the spindle typically lies in the longest axis of the protoplasmic mass, and division therefore tends to cut this axis transversely (Hertwig, 1884). This rule applies to many embryonic and tissular divisions, and still stands today as a general rule for cell division specification in many tissues. In addition, Hertwig and others performed shape manipulations experiments (Chapter IV.3.c.) that directly challenge and confirm this rule, thus establishing cell shape as a major cue for specifying animal cell division. However, Hertwig's rule remains imprecise in the definition of the cell long axis, allowing several possible cleavage planes in some ambiguous shapes. It also notably fails to predict any asymmetric divisions, raising the necessity of additional rules to predict the developmental patterns of early embryos. Finally, Hertwig's rule, as well as Errera's and Sachs' rules, is an empirical rule based on simple considerations of cell geometry and mechanics, but does not shed light on the underlying biological mechanisms that set the division plane.

5. Lability of the patterns

The nature of the cues setting the early cleavage patterns and the following cell differentiation has been widely investigated over the past 150 years. In addition to the previously cited shape-related rules for division specification, many perturbation experiments have been performed in the early years of embryology.

a. Separation of blastomeres

A simple experiment challenging the auto-specification of cells is the separation of the blastomeres within an embryo. In many cases, when the separation is performed at an early stage, each blastomere develops into a full embryo. This is the case for instance in some sea urchin species, for embryos separated at any stage earlier than the 8-cell stage (Hörstadius and others, 1973). Interestingly, the separated blastomeres follow the same series of division orientations as if they were still within an embryo, so that the resulting cleavage pattern differs from the one of complete embryos. However, this different cleavage pattern gives rise to a (smaller) larva that is not lacking any type of tissue. Moreover, even in the case when blastomeres are separated after cleavage has set the main axes of the embryo and/or specified different cell fates for blastomeres, some separated blastomeres can regenerate a complete embryo. For example, in cnidarian embryos, that determine their main axis at the first division by creating an anterior blastomere and a posterior one, each one of these two blastomeres is still able to form a complete embryo when separated. In sea urchins, the four vegetal cells at the 8-cell stage can generate a full larvae, yet smaller, even though most of the ectoderm of the normally developing embryo originates from the four animal cells. These experiments underlie an intrinsic adaptability of embryonic development and cell fate specification.

b. Shape manipulation

In order to challenge the shape-related divisions rules, experiments have been performed where early embryos are mechanically deformed. The first occurrences of such experiments consist in compressing the eggs between two glass slides and monitoring the divisions. The experiments have been done by Hertwig in Xenopus, by Dan in sea urchins and by Whittaker in ascidians. In both cases the eggs are compressed along various directions with respect to the animal-vegetal axis, and always yielded altered cleavage patterns (Dan, 1987; Hertwig, 1893; Whittaker, 1980). More recently, sea urchin eggs have been deformed to specific shapes by putting them in microfabricated wells (Minc et al., 2011). Here again the cleavage pattern was altered (Figure I.17.). Importantly, the division aligned with the long axis of the well rather than with any maternal cue within the egg, confirming Hertwig's rule for the role of shape as a major cue for division specification. Those results suggest an inherent plasticity of the cleavage patterns, where the choice of the division plane relies more on self-organization of the cell with respect to cues like shape rather than on a tight maternal genetic control. A similar illustration of this lability is the induction of spiral cleavage in snails. It is possible to switch the spindle orientation from dextral to sinistral at the 4-cell stage by mechanical perturbation (with needles). The whole morphogenesis then switches from dextral to sinistral, without requiring any further manipulation (Grande and Patel, 2009).

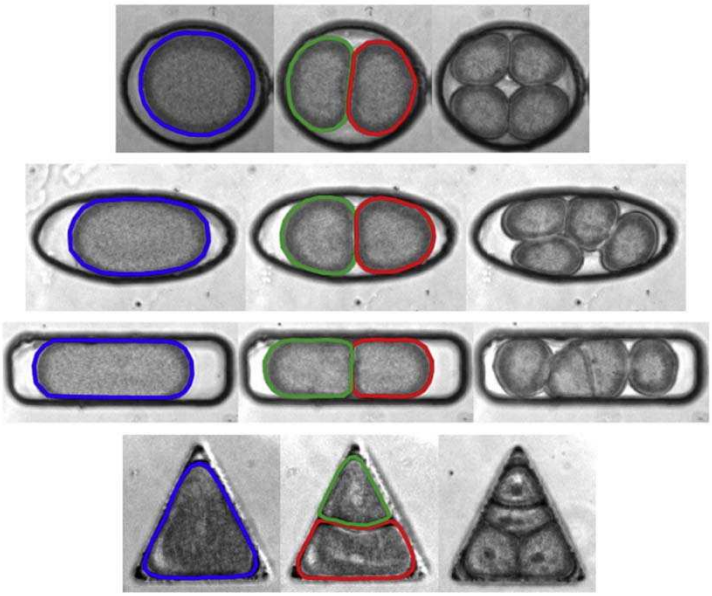

Figure I.17. : *Alteration of the cleavage pattern by shape manipulation. Sea urchin embryos are confined into microfabricated chambers of different shapes, and exhibit different cleavage patterns. (Adapted from (Minc et al., 2011))*

c. Cytoplasm displacement

Another type of classical embryo perturbation involves cytoplasm displacement. Many experiments are reported in the literature, where the eggs are centrifuged, supposedly segregating the cytoplasmic components along the direction of centrifugation, according to their density. These centrifugation experiments have been performed on eggs of Xenopus, sea urchins or ascidians. The cleavage pattern was usually altered, even if the centrifuged sea urchin eggs did not have a strong phenotype. Interestingly, centrifugation of Xenopus eggs packed the denser yolk content of the cytoplasm into one side of the egg, leading to a subsequent near-meroblastic cleavage. Another example of cytoplasm manipulation is the removal of cytoplasm from a part of the embryo. Cytoplasm ablation near the vegetal pole of ascidians after the first wave of cytoplasmic movement (condensation of yellow cytoplasm at the vegetal pole) has been shown to prevent the formation of the dorso-ventral axis and gastrulation (Nishida, 1996). After the second cytoplasmic movement that displaces the cytoplasmic cap toward the posterior side of the embryo, an ablation of cytoplasm near the future CAB yields a radialized embryo, with only anterior cell fates (Figure I.18.). On the contrary, when this cytoplasmic region is transplanted to the anterior region of another egg, the posterior cleavage pattern is duplicated, with the formation of an ectopic CAB at the site of injection, and spindle displacement toward this CAB yielding successive asymmetric divisions (Figure I.18.) (Nishida, 1994; Nishikata et al., 1999). These experiments highlight the importance of cytoplasmic components in division specification, but also show that it is possible to alter the cleavage patterns simply by reorganizing the cytoplasmic content of the eggs, illustrating how early embryos behave as self-organized systems, from cues deposited in the egg prior to fertilization.

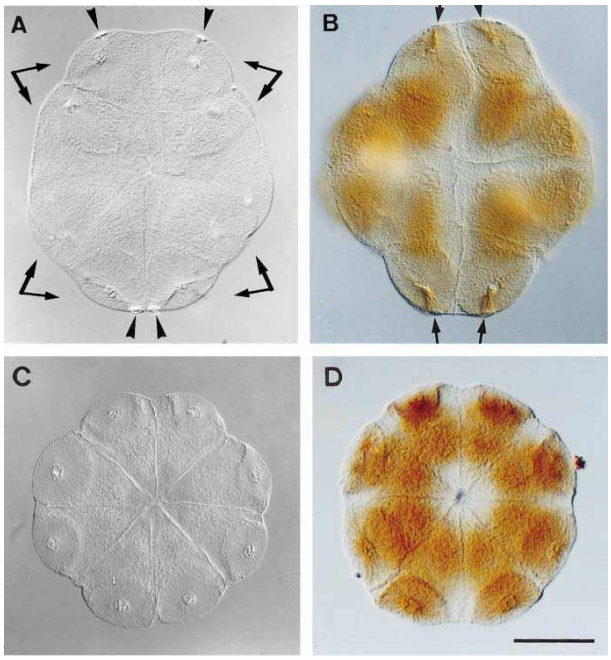

Figure I.18. : *Alteration of the cleavage pattern of the ascidian embryo by cytoplasm displacement. Fixed embryos are imaged using differential interference contrast (Nomarski) optics (A and C) and stained for tubulin (B and D).* ***Top :*** *induction of unequal cleavage on both the anterior and posterior sides after transplantation of posterior cytoplasm (from another egg) to the egg anterior side. Long arrows identify sister cells. Arrowheads show the CABs forming at both poles, and short arrows show the MT bundles linking the centrosomes to the CAB.* ***Bottom :*** *development of a radialized embryo after removal of posterior cytoplasm in the egg. (Scale bar : 50 µm, from (Nishikata et al., 1999))*

d. Membrane perturbation

Similarly, removing parts of the membrane of eggs can alter the cleavage patterns. A striking example is the vegetal cap ablation in sea urchins embryos, which prevent micromeres formation. A similar phenotype is observed when all membrane is perturbed by treating the eggs with SLS detergent from the 4-cell stage (Dan, 1979; Tanaka, 1976). In addition, when eggs are cut equatorially prior to fertilization, the vegetal half develops normally while the animal half only forms an ectoderm ball, similar to the 8-cell stage blastomeres separation experiment (Maruyama et al., 1985). However, transplanting a fragment of vegetal egg membrane to the animal half egg restores the normal development (Kiyomoto and Shirai, 1993), highlighting the importance of vegetal membrane for cell fate determination. Membrane manipulation can also challenge the relationship between fertilization and cleavage pattern, by simulating a calcium wave. For instance, local use of Ca^{2+} ionophore in ascidians eggs triggers the first cytoplasmic segregation independently from the animal-vegetal axis, thus setting the dorso-ventral axis away from the animal-vegetal axis (Jeffery, 1982). Altogether, these results suggest the same kind of specification of the cleavage patterns with regards to membrane as to cytoplasmic polarity.

e. Cell cycle perturbation

Another kind of embryonic perturbation challenges the timing of embryonic development. The most classical experiments are performed on the sea urchin embryo, and consist in retarding the cell cycle and monitoring the timing of micromeres formation. In a variant of this experiment performed by Hörstadius, the cell cycle is paused by putting the developing embryos in diluted sea water, thus skipping one or two cell cycles at different possible developmental stages and then resuming normal cell cycle (Hörstadius, 1939). The paused embryos display various cleavage patterns, according to the duration of the cell cycle pause and stage at which it happened, but always differed from the normal cleavage pattern,

with micromeres appearing precautiously (before the 16-cell stage). Similarly, retardation experiments have been performed by Dan at the 4-cell stage of the sea urchin embryo, where embryos are treated with UVs or disruptive chemicals that presumably induce a delay in cell cycle progression (Dan and Ikeda, 1971). The following division was asymmetric, yielding four smaller vegetal cells, with an animal/vegetal volume ratio that varied with the treatment. These two experiments suggest the existence of a clock for micromere apparition in sea urchin embryos. A similar clock seems to control the occurrence of the first asymmetric divisions, and the alternance between clockwise and counterclockwise divisions during the spiral cleavage. Indeed, when cleavages are reversely inhibited by actin disruption (cytochalasin B), the cleavage pattern is altered. When the second division is skipped, micromeres appear precautiously at the 4-cell stage, while when the third division is skipped, the first asymmetric division has the direction of rotation of the second asymmetric division in untreated embryos (Conklin, 1912; Freeman, 1983). Those classical experiments, yielding deeply altered cleavage patterns, thus highlight that some regulatory layers can be timing-dependent.

f. Sperm and polar bodies

Finally, it is interesting to note that in many embryos, the point of sperm entry serves to determine the main embryonic axes and subsequent cell fate (Goldstein and Hird, 1996; Roegiers et al., 1995). As the sperm usually has a wide zone of the egg surface where it can enter, the main embryonic axes remain labile in the unfertilized egg, to get eventually specified upon fertilization. The female pronucleus can also determine embryonic polarity in some cases. During meiosis, the female spindle is generally located at the animal pole, where it forms the polar bodies. In the gastropod *Limax*, it has been shown that mechanical displacement (by compression) of the meiotic spindle between the two rounds of meiosis was accompanied by a rotation of the animal-vegetal primordial axis (Guerrier, 1968). The following cleavage pattern of the embryo was oriented with respect to the final meiotic position, that is the site of the second polar body formation, pushed up to a 90° angle from the initial meiotic position and its first polar body. This last experiment confirms that the cleavage patterns and its associated axis and cell fate definition are labile and relying rather on self-organization of the embryo than on a tight genetic control.

As seen throughout the last examples of embryo manipulation, the cues determining division patterns and individual cell division are multiple. However it is possible to investigate on these as in many species early embryos behave as self-organized systems. Importantly, cell shape seems to play a major role in division plane specification, as most cells within the embryos divide according to Hertwig's long axis rule. Many possible biological mechanisms have been proposed to explain the positioning of the spindle (and thus of the division plane) with respect to cell shape and other cues. The second chapter presents an overview of these different mechanisms.

II. THE MECHANISMS OF NUCLEUS AND SPINDLE POSITIONING

1. The cytoskeleton

The cytoskeleton is a network of fibers located in the cell cytoplasm, that plays a major role in generating force within the cell. In particular, it is involved in cytoplasmic movements and transport of material through the cell's volume, as well as in the maintenance and evolutions of specific cell shape and mechanical properties. The cytoskeleton also seems to be the main effector of spindle positioning, in addition to segregating chromosomes and performing cytokinesis. In eukaryotes, it is composed of three main types of fibers, which are the actin filaments, the intermediate filaments and the microtubules.

a. Actin

Assembly and dynamics

Actin is present in the cell cytoplasm in two possible forms : as a monomeric globular protein, called G-actin, or as fibers (F-actin) that result from the polymerization of G-actin. G-actin assembles in a polar fashion, to form a right-handed double-stranded helical filament, measuring 6 nm in diameter, that has an arrowhead-like structure. The filament's end that is on the side where the tips of the arrows point is called the pointed end (+ end), and the other side is called the barbed end (- end). Upon the incorporation of G-actin, that is bound to adenosine triphosphate (ATP), ATP is hydrolyzed, so that the monomers subunits are now bound to an adenosine diphosphate (ADP), that mediates subunits dissociation. Actin filaments are thus highly dynamic structures, which preferentially polymerize at the barbed end, and depolymerize at the pointed end where older subunits have undergone ATP hydrolysis (Figure II.1.). The filaments elongate or shrink, depending on the balance between polymerization and depolymerization rates. When these two rates are similar, the filaments are in a state of dynamic equilibrium called treadmilling. The dynamic behavior of actin is highly regulated through interaction with various other proteins, such as stabilizing or destabilizing binding proteins, capping proteins, or severing proteins.

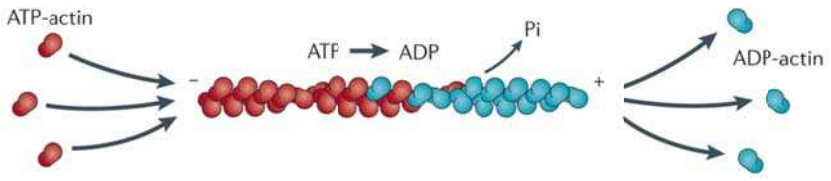

Figure II.1. : *Polymerization of actin at the barbed end and depolymerization at the pointed end. The actin subunits undergo ATP hydrolysis after incorporation. (Adapted from (Nürnberg et al., 2011))*

Some other proteins are implied in the formation and stabilization of an actin meshwork. The Arp2/3 complex, for instance, mediates the branching of filaments through the nucleation of new filaments along the existing ones. Some additional proteins, like filamin, α-actinin, fascin or fimbrin, crosslink the existing filaments to stabilize the meshwork. On the other hand, some proteins like formins induce the polymerization of unbranched actin filaments, yielding a network of parallel filaments. The tight regulation of these different mechanisms gives rise to a great variety of actin structures and dynamics (Figure II.2.), implied in various cellular functions.

Figure II.2. : *Examples of actin networks originating from the interaction of actin filaments with different regulatory proteins, yielding different modes of nucleation and crosslinking. (Adapted from (Pritchard et al., 2014))*

Force generation

In addition, the filaments are able to exert force within the cell, both from their dynamics of polymerization and assembly, and from their association with motor proteins. The motors that can bind actin all belong to the myosin family, a superfamily that contains 15 to 20 classes. Myosins are usually composed of one or two heavy chains, bound via their tails, and light chains (Figure II.3.). Each heavy chain has three functional domains. The tail, implied in the dimerization of some myosins, is also the attachment zone of subcellular structures, like cargos that the myosins transport along the actin strand. The attachment to actin occurs at the head of the myosin chains. It is mediated by ATP, which provides the energy for myosin processivity along the filament. Finally, the neck, which is localized between the head and the tail, acts as a lever during myosin motion, and is also interacting with light chains. Myosins usually walk toward the barbed end of the filaments, but some, like Myo6, move toward the pointed end, while some others, like Myo9, move in both directions.

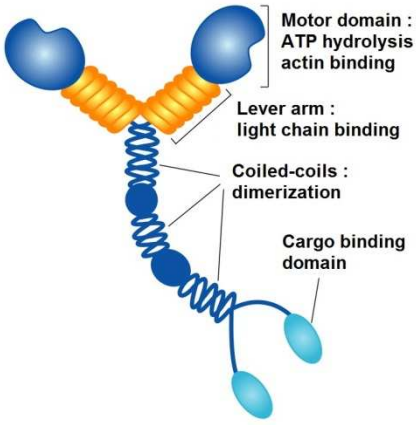

Figure II.3. : *Schematic representation of Myosin V. Myosins are formed by the dimerization of two heavy chains (in blue), bound to light chains (in orange). (From (Tóth et al., 2005))*

The motion of myosins along actin filaments allows cargo transport within the cell, but it is also often used to generate force. In particular, the contractile ring that squeezes the cell in two during cytokinesis is made of the crosslinking of myosin with a network of parallel actin filaments. Acto-myosin is also responsible for the cortical tension of the cell, and thus is important to define cell shape (Chapter III.2.). Actin appears to be implied in nuclear positioning in many cell types. For instance, migrating cells like fibroblasts position their nuclei at the rear of the cells, thanks to a retrograde flow of actin, depending on myosin activity (Gomes et al., 2005). During the migration of neurons, the nuclei are pushed forward by contraction of an acto-myosin network (Bellion et al., 2005). It is also actin that anchors the nuclei during oogenesis in Drosophila, preventing them to drift into the oocytes as the cells undergo rapid cytoplasmic flows (Robinson and Cooley, 1997). However, it is not clear whether actin plays a role in nuclear positioning in the early embryo, as actin depolymerization experiments generally do not affect nucleus centration after fertilization (Minc et al., 2011; Tanimoto et al., 2016) and positioning in interphase (Ajduk et al., 2014; Nishikata et al., 1999). An exception to this is the case of mouse embryonic development, where actin filaments appear to be important in nucleus centration (Chaigne et al., 2016). Actin has also been suggested to be responsible alone for nuclear migration in the syncytial Drosophila embryo (von Dassow and Schubiger, 1994). In addition, actin can be involved in the organization and force generation of maternal polarity cues, like in the *C. elegans* embryo. These polar domains are thought to have an influence on spindle positioning (Chapter II.5.a.).

b. Intermediate filaments

In addition to the actin microfilaments, the cytoskeleton also contains intermediate filaments, in vertebrates and some other animals, fungi, plants, and unicellular organisms. The fibrous proteins that compose these filaments are related, yet very diverse, showing little sequence similarity. Their secondary structure is however similar, as they feature a central α-helical rod domain and assemble by two to form a coiled coiled dimer by interaction of the rod domains. The N-terminal head and C-terminal tail are non-α-helical and display wide variation in their sequences and lengths. Identical dimers then assemble to form antiparallel tetramers that then assemble head-to-tail and laterally by 8 and form filaments of diameters ranging between 6 and 12 nm (Figure II.4.). The intermediate filaments are self-assembled (without ATP) and non-polar, and they form a dynamic network, possibly through their interactions with actin-based and MT-based motor proteins (Helfand et al., 2004).

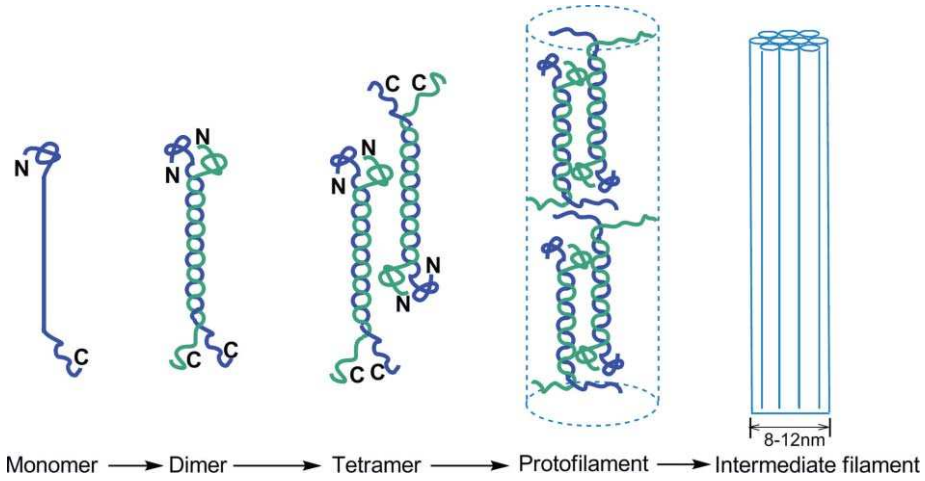

Figure II.4. : *Typical assembly of intermediate filaments. The monomers dimerize via their central rod domain, and assemble to generate fibers of about 8-12 nm in diameter. (From (Guharoy et al., 2013))*

A specific type of intermediate filaments, lamins, form the lamina that is a dense fiber network against the inside of the nuclear envelope. Intermediate filaments are also present in the cytoplasm, and link the cell-cell junctions to the outer nuclear membrane (Herrmann and Aebi, 2004). However, the role of these filaments in nuclear positioning is still unclear. In skeletal muscle fibers, desmin seems to be important to the clustering of nuclei at the sites of neuromuscular junctions, and to the proper spacing of the other peripheric nuclei (Ralston et al., 2006). In migrating astrocytes, the retrograde flow of actin could push on the nucleus via intermediate filaments located in front of it (Dupin et al., 2011). Similar mechanisms have been shown in other cell types, but the literature does not report a significant role played by intermediate filaments in nuclear positioning in the early embryo.

c. Microtubules

The MT cytoskeleton appears to play the most important role in nuclear positioning, especially in the early development of embryos. MT disruption with nocodazole has been shown to stop the centration of the male pronucleus after fertilization in the sea urchin embryo (Schatten and Schatten, 1981; Tanimoto et al., 2016), and to inhibit the formation of micromeres in ascidian embryos (Nishikata et al., 1999). In C. elegans embryos, nocodazole treatment at the 2-cell stage changes the location of the nucleus from centered to cortical in the anterior blastomere (Hyman and White, 1987). In zebrafish embryos, local depolymerization of MTs induces a movement of the centrosomes (Wühr et al., 2010). MTs are also involved in the formation of the mitotic apparatus, leading to chromosomes separation in eukaryotes.

Structure

Microtubules are fibers generated by the polymerization of a heterodimer of two globular proteins, α and β-tubulin. The αβ-tubulin dimers assemble into protofilaments in a

linear head-to-tail fashion. The protofilaments are polar, as they are composed of an alternance of α-tubulin and β-tubulin subunits, with an α-tubulin at one end (the minus end) and a β-tubulin at the other end (the plus end). Then 13 protofilaments assemble laterally and with the same polarity to form a hollow cylinder, with an outer diameter of 25 nm (Figure II.5.). Yet, *in vitro*, some MTs have been found to be formed by the parallel association of 10 to 16 protofilaments. Between two adjacent protofilaments, the contacts are made between two α-tubulin subunits or two β-tubulin subunits, yielding a left-handed helix inner structure. In order to laterally close the helix, one pair of adjacent protofilaments makes α-tubulin-β-tubulin contacts. The contact between those two protofilaments at the seam is usually the last lateral contact to form upon polymerization.

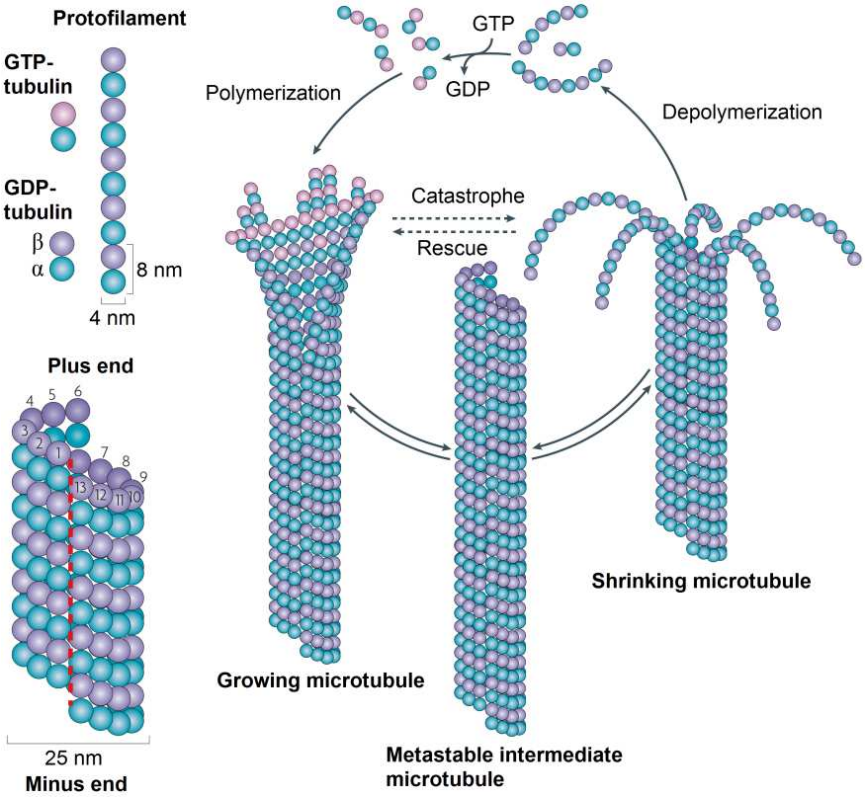

Figure II.5. : *Polar assembly of tubulin dimers to form protofilaments, and of 13 protofilaments to form microtubules. The seam is indicated in red. The microtubules are dynamic structures and exhibit a cycle of polymerization and depolymerization, mediated by the timely hydrolysis of GTP. (From (Akhmanova and Steinmetz, 2008))*

Dynamics

MTs are nucleated in the MT organizing centers (MTOCs, Chapter II.2.a.). They polymerize by addition of αβ-tubulin dimers at both ends, but the polymerization is faster at the plus end. Moreover, the minus end is often capped and anchored at MTOCs, restricting the MT dynamic behavior to the plus end. Prior to polymerization, both subunits of the αβ-tubulin heterodimer bind a guanosine triphosphate (GTP) via the N-terminus. When incorporated at the MT plus end, the GTP of the β-tubulin subunit is hydrolyzed into a

guanosine diphosphate (GDP). When the rate of GTP hydrolysis is lower than the rate of addition of αβ-tubulin dimers, a GTP cap forms at the tip, stabilizing the structure, and the MT keeps growing. MTs can grow up to 50 μm.

However, when the rate of GTP hydrolysis exceeds the rate of addition of αβ-tubulin dimers, the exposition of GDP-bound β-tubulin at the tip makes the MT unstable. This results in a rapid depolymerization, known as catastrophe, after a period without apparent growth or shrinkage, called dwell time. The depolymerization of the MT can stop, presumably as it reaches islands of GTP-bound β-tubulin that remain along the MT lattice (Dimitrov et al., 2008), and that could be remnants of previous cycles of growth and shrinkage. The growth then resumes, in an event called rescue. MTs usually undergo cycles of catastrophe and rescue (Figure II.5.), and have a half-life of 5-10 minutes.

The dynamics of MTs are tightly regulated by a number of MT-associated proteins (MAPs). They can interact with the MTs whether along the strand, by tracking the tips, or both. Some of them act as MTs stabilizers, by promoting rescue, like the CAP-Gly family (Arnal et al., 2004), by slowing down depolymerization, by stabilizing dimers or protofilament interactions to prevent catastrophe, like HURP (Silljé et al., 2006), or by suppressing catastrophe, like the EB plus-end tracking proteins (Tirnauer et al., 2002) or the structural MAPs (Ichihara et al., 2001). The γ-TuRC complex, found in the MTOCs, anchors the minus end and caps it, thus stabilizing it (Chapter II.2.a.). Some other MAPs are destabilizing MTs, whether by suppressing rescue, by accelerating depolymerization, or by promoting catastrophe, like katanin, spastin, the non-motile kinesin-13 motors, or some members of the kinesin-8 and kinesin-14 families. Finally, some MAPs, like the XMAP215/Stu2 (Gard and Kirschner, 1987) and EB families, increase the growth rate of MTs, while others, like stathmin (Jourdain et al., 1997), decrease it.

Organization

In interphase, MTs nucleate from the two centrosomes that are the main MTOCs at this stage (Chapter II.2.a.), and extend their plus ends through the cytoplasm. In early embryos, it is believed that these two asters of MTs extend up to the cell cortex, and thus fill up the whole cytoplasm, even in the extremely large eggs, like the Xenopus ones. It is not clear however whether the MTs that reach the cell cortex nucleate at the centrosome and cover the whole distance (Verde et al., 1992), as the actual length of individual MTs is still unknown. It is more likely that MTs are shorter, but additional MTs nucleate on the way between the centrosome and the cortex as a compensation, allowing the asters to still reach the cortex (Ishihara et al., 2016). This hypothesis is supported by experiments performed during mitosis in Drosophila S2 cells and Xenopus extracts, where the growing plus tips of MTs are labeled (with EB1) and appear within the spindle, away from the centrosomes, suggesting the existence of nucleation points along the existing MTs (Ishihara et al., 2014; Mahoney et al., 2006; Tirnauer et al., 2004). The nucleation of new MTs on the existing ones is thought to be mediated by Augmin, that is a hetero-octameric protein complex first identified in Drosophila (Goshima et al., 2008; Uehara et al., 2009). Augmin would bind to MTs and recruit γ-TuRC, a complex that acts as a scaffold for αβ-tubulin dimers to polymerize, and as a cap to stabilize the minus end of the new MT. Importantly, the new MTs are nucleated along the existing ones and thus generate MT branching, that creates a physical continuity of the MT network and allows the propagation of forces throughout the whole distance between the nucleus and the cortex. The MTs can also be crosslinked by proteins

from the MAP65/Ase1/PRC1 family, or kinesins (Chapter II.1.d.), stabilizing the network and allowing force propagation (Cahu and Surrey, 2009; Campbell et al., 1989; Lansky et al., 2015). In particular it is possible that some MTs are nucleated near the cell cortex, like it is observed in plants, yeast, oocytes or right after egg fertilization (Gard, 1994; Lüders and Stearns, 2007; Maro et al., 1985; Samejima et al., 2005; Schroeder and Gard, 1992), or slide from other parts of the cell, including from the centrosomes (Ahmad and Baas, 1995; Ishihara et al., 2014; Rusan et al., 2002), and would be linked to the astral MTs in such crosslinking events. The formation of a MT meshwork by nucleation of new MTs away from the centrosomes would allow the asters to span the whole cytoplasm even with short MTs, and could also compensate the dilution effect as the aster spreads from the centrosome across the cell volume, maintaining high MT density far from the centrosomes.

The MTs asters growing from the two centrosomes extend in all possible directions, and are generally interpenetrating (Asnes and Schroeder, 1979; Brinkley et al., 1981). However, in many other cases, in particular when cytokinesis is not complete at the time of the next interphase, like it is the case for many meroblastically cleaving embryos, the asters do not interpenetrate (Wühr et al., 2010). Instead, they seem to repel each other, and delimitate volumes of cytoplasm, with lower MT density planes in-between (Wühr et al., 2011) (Figure II.6.). Each pair of asters extends only within the volume that roughly corresponds to the future volume of its daughter cell after cytokinesis. It is believed that these large asters preposition the centrosome pair for the next cell cycle, through MT force generation mechanisms discussed in chapter II.3.. The mechanisms of aster-aster repelling are still debated. The overlap and interaction between anti-parallel microtubules could be what allows aster-aster recognition and repelling, via conserved midzone-organizing proteins like PRC1 or Kif23 (Mishima et al., 2002; Mollinari et al., 2002; Nislow et al., 1992; Subramanian et al., 2010). Aster growth could also be inhibited in the midzone. For instance, the Kif4 kinesin that moves toward plus ends of MTs, and has been shown to inhibit plus ends polymerization in vitro (Bringmann et al., 2004) and in somatic midzones (Hu et al., 2011), would be targeted to the midzone due to the abundance of plus ends. A recent study in Xenopus eggs extract suggests a role of the Aurora B subunit of the Chromosomal Passenger Complex, recruited via Kif4A and Kif20AE kinesins, to sharpen the aster-aster boundary (Nguyen et al., 2014).

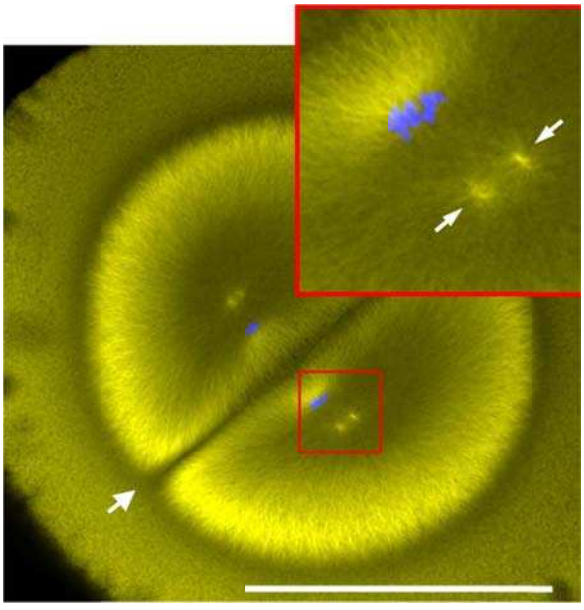

Figure II.6.: *Animal view of a Xenopus embryo, fixed at anaphase-telophase before the first cytokinesis. MTs are marked in yellow and DNA in blue. The two pairs of asters show a clear mutual exclusion, and the site of aster-aster interaction (indicated by an arrow) is positioned at the future division plane. Inset shows the duplicated centrosomes, which are already oriented for the second division (indicated by arrows). (Scale bar : 500 µm, adapted from (Wühr et al., 2010))*

In the early stages of mitosis, the MT asters shrink, to an average radius of ~30-40 µm in large eggs of Xenopus and Zebrafish in metaphase (Wühr et al., 2008, 2010) and smaller in smaller eggs and blastomeres, so that the aster radius is generally smaller than the cell radius (Figure II.7.). This transition is presumably mediated by Cdk1 kinase, that promotes catastrophe via a complex network of MAPs, resulting in a dramatic decrease of MT lengths (Belmont et al., 1990; Niethammer et al., 2007; Verde et al., 1992). Thus the whole cell volume is not probed by a significant amount of MTs, and in large eggs asters do not reach the cortex. Yet, in smaller blastomeres, like in sea urchins, nematodes or ascidians, some astral MTs still reach the cell cortex, though the cortical MT density is lower than in interphase. At the onset of anaphase, the levels of Cdk1 decrease and MT asters regrow.

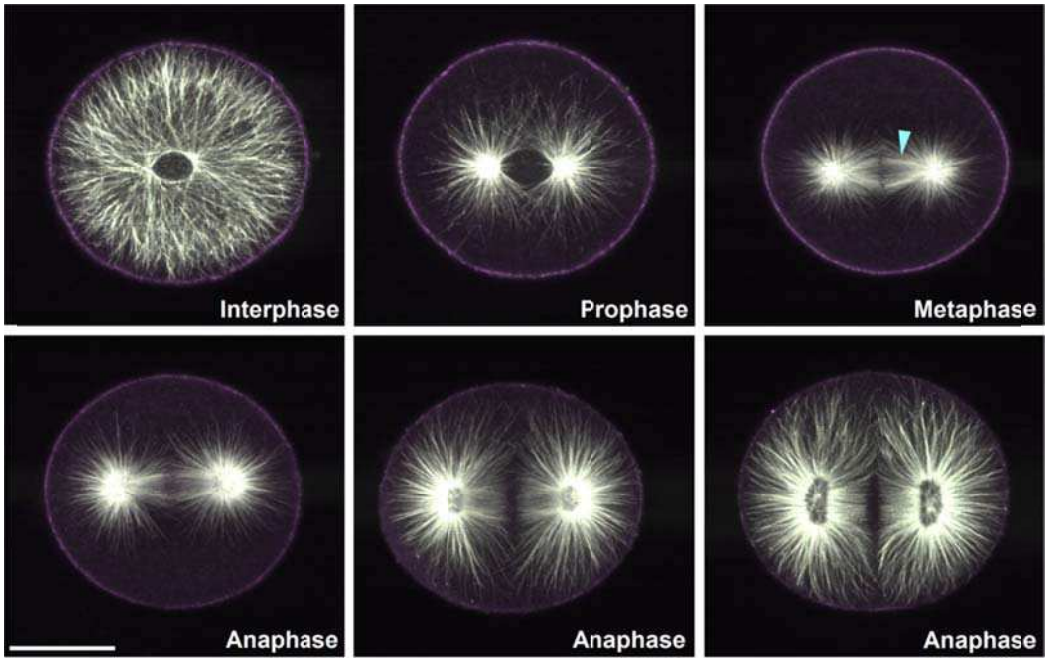

Figure II.7. : *Immunostaining images showing asters dynamics through the cell cycle in a sea urchin egg. MTs are marked in white and pRLC (showing activated myosin) in violet. Asters span the whole cell in interphase, and there is no aster-aster exclusion. Asters then shrink at the onset of mitosis and regrow in anaphase. Arrowhead shows the spindle MTs. (Scale bar : 20 µm, from (Foe and von Dassow, 2008))*

During mitosis, MTs also assemble the mitotic spindle, by nucleation at the centrosomes and polymerization of the plus tips toward the chromosomes. MTs are also found to nucleate along the existing MTs of the spindle (Mahoney et al., 2006; Tirnauer et al., 2004), possibly speeding up the spindle assembly by increasing the amount of available MTs, and favoring the establishment of spindle bipolarity by increasing the density of antiparallel MTs overlapping at the center (Petry et al., 2011, 2013). The MTs that reach the kinetochores bind to them and cluster in bundles, stabilized by MAPs. They depolymerize from their plus ends (at the kinetochores), and thus shrink, while MT-based molecular motors (dyneins, Chapter II.1.d.) at the kinetochores drag the chromatids along the MT lattice toward the centrosome. The remaining MTs interact at the metaphase plate, where plus-end directed motors (kinesins, Chapter II.1.d.) crosslink antiparallel filaments and cause them to slide, resulting in an elongation of the spindle (Brust-Mascher and Scholey, 2011).

d. MT-associated molecular motors

Similarly to actin filaments, MT filaments are able to generate force through the ATP-dependent movements of molecular motors along them. These motors are 50-100 nm long structures. There are two main groups of MT-based motors : dyneins, that walk toward the minus ends of MTs, and kinesins that mostly walk toward the plus ends.

Dynein

Dynein family can be divided in two groups, the cytoplasmic dyneins and the axonemal dyneins. Axonemal dyneins are found only in cells that have cilia or a flagella, and it mediates the beating of these structures by causing their inner MTs to slide. Cytoplasmic dynein is found in all animal cells (and fungi cells) and it is mainly involved in cargo transport toward the minus tips of the MTs.

Cytoplasmic dyneins are composed of two identical heavy chains, which are responsible for generating movement via ATP hydrolysis, of two intermediate chains involved in cargo attachment to the dynein motor, of two light intermediate chains and of several light chains (Figure II.8.). In each heavy chain, the ATPase activity occurs at the ring-shaped head made of six AAA domains. Yet, only four of these six proteins appear to bind ATP. From the head, one projection, the coiled-coil stalk, is implied in MT binding, while the N-terminal domain, called the stem, binds the intermediate, light intermediate and light chains. The stem is also mediating dynein homodimerization. The two heavy chains of the dynein complex undergo cycles of attachment to MTs and detachment, and their alternating activity allows dynein to walk along the MT without detaching. The processive behavior of dynein is however not clear, as the stepping and directionality appear to be partially stochastic (Reck-Peterson et al., 2006).

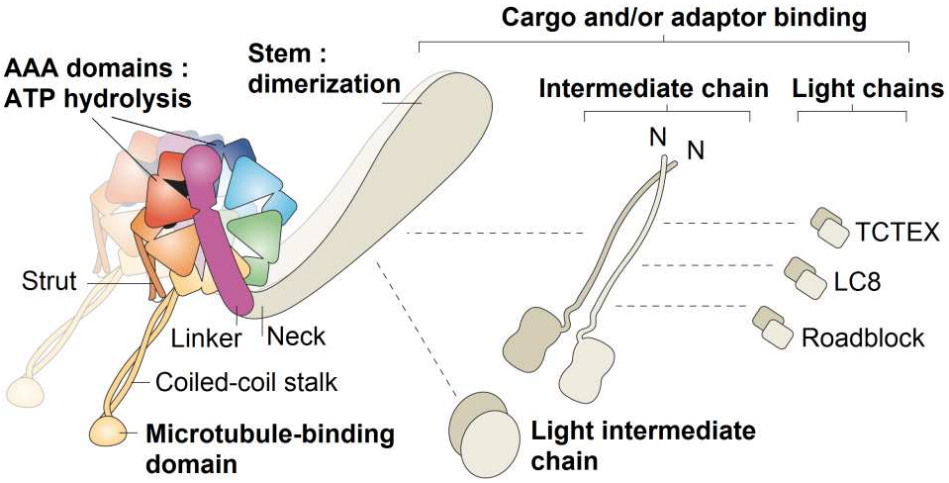

Figure II.8. : *Cytoplasmic dynein is composed of two heavy chains and of several light chains and intermediate chains. (Adapted from (Roberts et al., 2013))*

Axonemal dyneins are composed of one to three different heavy chains, each of them featuring a ring-shaped structure similar to the one of cytoplasmic dyneins, a coiled-coil MT-binding stalk and a stem that binds to a neighboring MT, thus leading to a crosslinking of MTs within the axoneme. The ATPase activity then leads to a conformational change of the dynein complex, yielding sliding between adjacent MTs and ciliary or flagellar movement.

Dynein recruitment and motor activity is regulated by various proteins. In particular, the dynactin complex acts as an activator of dynein processivity toward the MT minus tips. It also mediates cargo attachment, as its Arp1-filament interacts with spectrins that usually covers membranes, and thus targets dynein to the membranes of organelles or vesicles, or as its p150 subunit interacts with GTPases and GTPase-interacting proteins (Culver–Hanlon et al., 2006). As the dynactin complex is required for dynein processivity and cargo binding, it is essential to many cellular functions. Some other adaptor proteins target dynein to specific sites, like plus tips, kinetochores, cortex, centrosomes or nuclear envelope. These include for example Bicaudal D, the RZZ complex, or the LIS1/NudE complex that also seems to regulate dynein activity (Vallee et al., 2012).

Kinesin

The other MT-based motor family is the kinesin family, which is more diverse and includes both many plus-end directed motors, a few minus-end directed ones and some going in both directions. At least 14 subfamilies have been identified in eukaryotes so far. Most kinesins exhibit a dimer structure, where two identical heavy chains bind to light chains. The heavy chains come in various designs, but generally contain a conserved globular head, responsible for MT binding and motor activity, a C-terminal tail that binds the light chains, and an α-helical coiled-coil neck that acts as a flexible linker and mediates homodimerization (Figure II.9.). The variety of the light chains is responsible for the localization and cargo-specificity of kinesins. In some cases, the cargo binds directly to the kinesin C-terminal tail.

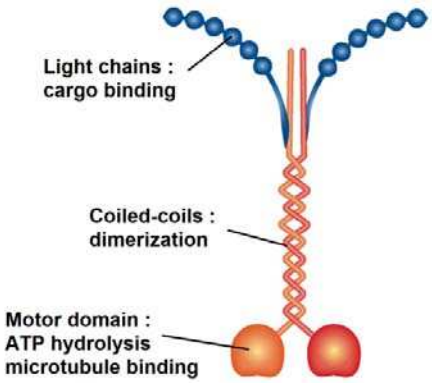

Figure II.9. : *Schematic representation of Kinesin I. Kinesins are various, but usually made of a dimer of heavy chains, bound to light chains that ensure cargo specificity. (Adapted from (Dodding and Way, 2011))*

Typically, kinesins walk in a unidirectional way along the MTs, by coordination of the MT-binding and detachment of its two subunits. In most kinesins, the motor domain is located toward the N-terminus. These kinesins, known as N-kinesins, usually exhibit a plus-end directed motion. Each step is powered by the hydrolysis of an ATP molecule, that gives the direction of the motor by a process called neck linker zippering. The length of the step is the length of a αβ-tubulin heterodimer. As N-kinesins are dimers, they remain attached to the MT by at least one of the two heavy chains, allowing kinesin processivity. It is interesting to note,

however, that processivity is also seen in some monomeric N-kinesins, like the kinesin-3 KIF1A. Here, the permanent attachment needed for processivity may come from electrostatic interactions between dynein and the MT (Okada and Hirokawa, 2000). In a few other kinesins, the motor domain is located near the C-terminus or at the middle. These kinesins, called C-kinesins and M-kinesins respectively, do not usually display a plus-end directed motion. M-kinesins from the kinesin-13 family are non-motile and have a MT depolymerization activity (Howard and Hyman, 2007). C-kinesins usually walk toward the minus-end of MTs, and the mechanism is generally different from the N-kinesin walking mechanism. This is thought to be due to the different architecture of the neck in these kinesins, allowing rotation toward the minus MT tip (Endow and Waligora, 1998). The C-kinesins are usually non-processive, taking only one step and detaching from the filament.

2. Centrosome positioning

Centrosomes are the main MTOCs in the animal developing embryos, and are flanking the nucleus. They are thus likely to be involved in MT-driven nuclear positioning.

a. Centrosomes structure

Animal centrosomes are composed of two centrioles, positioned orthogonally, surrounded by the pericentriolar matrix (PCM), which is an amorphous electro-dense mass of protein, involved in particular in MT nucleation (Figure II.10.). The centrioles are hollow cylinders made of nine microtubule triplets, assembled laterally. Exceptions to this are crabs and Drosophila embryos, which feature nine doublets, and *C. elegans* sperm cells and early embryos, which have nine singlets. The two centrioles are bound together by interconnecting fibers at their proximal ends. The mother centriole has two sets of nine appendages at the distal end, called the distal appendages and subdistal appendages, allowing it to anchor cytoplasmic MTs. The daughter centriole does not have such structures.

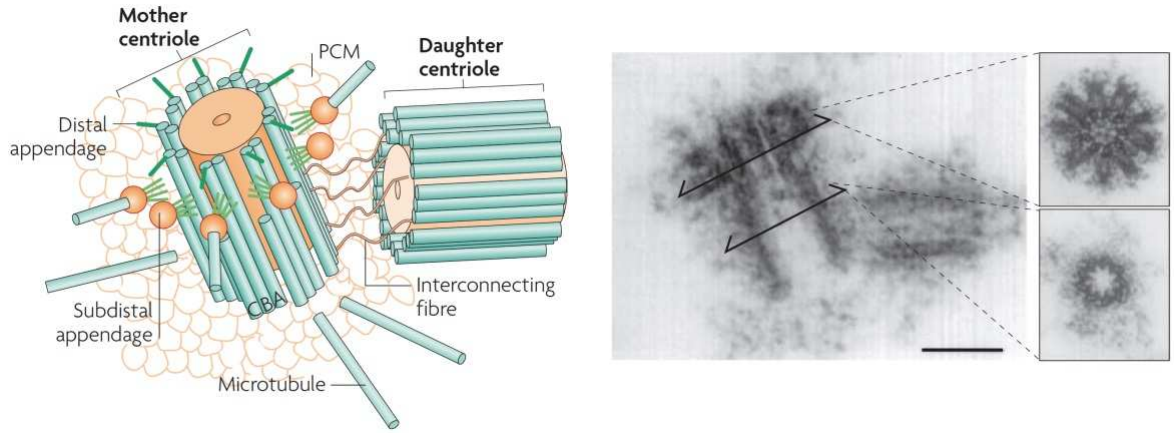

Figure II.10. : *Schematic representation of the centrosome. MTs assemble with a nine-fold symmetry to form the centrioles. Astral MTs nucleate in the surrounding PCM and the mother centriole can dock them via its distal appendages. The centrosome structure is apparent on electron micrographs on the left. Insets show proximal and distal cross sections of the mother centriole. (Scale bar : 0.2 µm, adapted from (Bettencourt-Dias and Glover, 2007))*

In the vicinity of the two centrioles, the PCM contains proteins that nucleate and tether the MTs, like γ-tubulin, pericentrin and ninein. γ-tubulin is a member of the tubulin family, that interacts with other PCM proteins to form a γ-tubulin ring complex (γ-TuRC). This complex displays a 13-fold symmetry that mimics the 13 protofilaments at the MT plus ends and acts as a template for αβ-tubulin dimers to polymerize, and as a cap to stabilize the minus end of the new MT and protect it from depolymerizing MAPs (Figure II.11.). The new MT thus only polymerizes from its plus end, and is anchored to the centrosome (to the mother centriole) by its minus end.

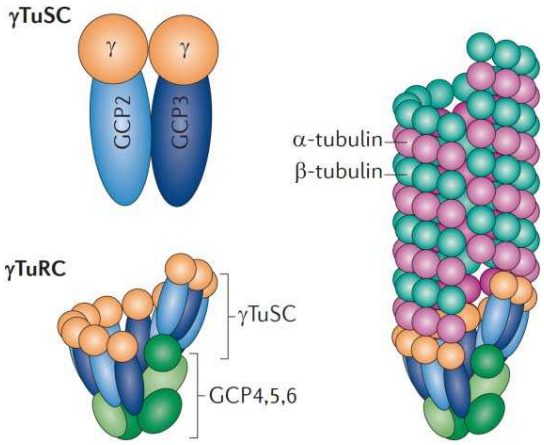

Figure II.11. : *The γ-TuRC complex forms a scaffold with a 13-fold symmetry for MT to grow on, allowing MT nucleation at the centrosomes. (From (Kollman et al., 2011))*

b. Centrosomes dynamics

The centrosomes duplicate during the cell cycle, to ensure that the dividing cell nucleates a bipolar spindle from two centrosomes, each of them ending up in one of the daughter cells (Figure II.12.). This duplication is tightly linked to the cell cycle progression via Cdk2 (Hinchcliffe et al., 1999). As soon as DNA replication starts, each daughter cell severs the tight link, potentially made of cohesins, between the two centrioles of its unique centrosome, leaving only a loose link that does not maintain the orthogonal arrangement of centrioles. The cell then starts assembling a new centriole in the vicinity of each older centriole. When the two new daughter centrioles have reached their final sizes (~400 nm in length), and the previous daughter centriole have grown appendages, thus becoming a mother centriole, the loose link between the mother centrioles is severed. The two new centrosomes mature and recruit the PCM around them, polymerizing the MT interphase aster. At the onset of mitosis, centrosomes are pulled apart by dynein activity and position on both sides of the nucleus. Consequently, the aster duplicates to form two asters, originating each from opposite sides of the nucleus. In anaphase, centrosomes are segregated into the two daughter cells. Centrosomes usually keep the orthogonal orientation of the centrioles, that favors spindle assembly, through mitosis. However, in some early embryos, the loss of centriolar orientation can happen from anaphase, as a compensation for the lack of gap phases in the cell cycle. In particular in the rapid syncytial divisions of the Drosophila embryo, centrioles have been found to split and position to opposite sides of the nucleus from previous telophase, before centriole duplication (Callaini and Riparbelli, 1990).

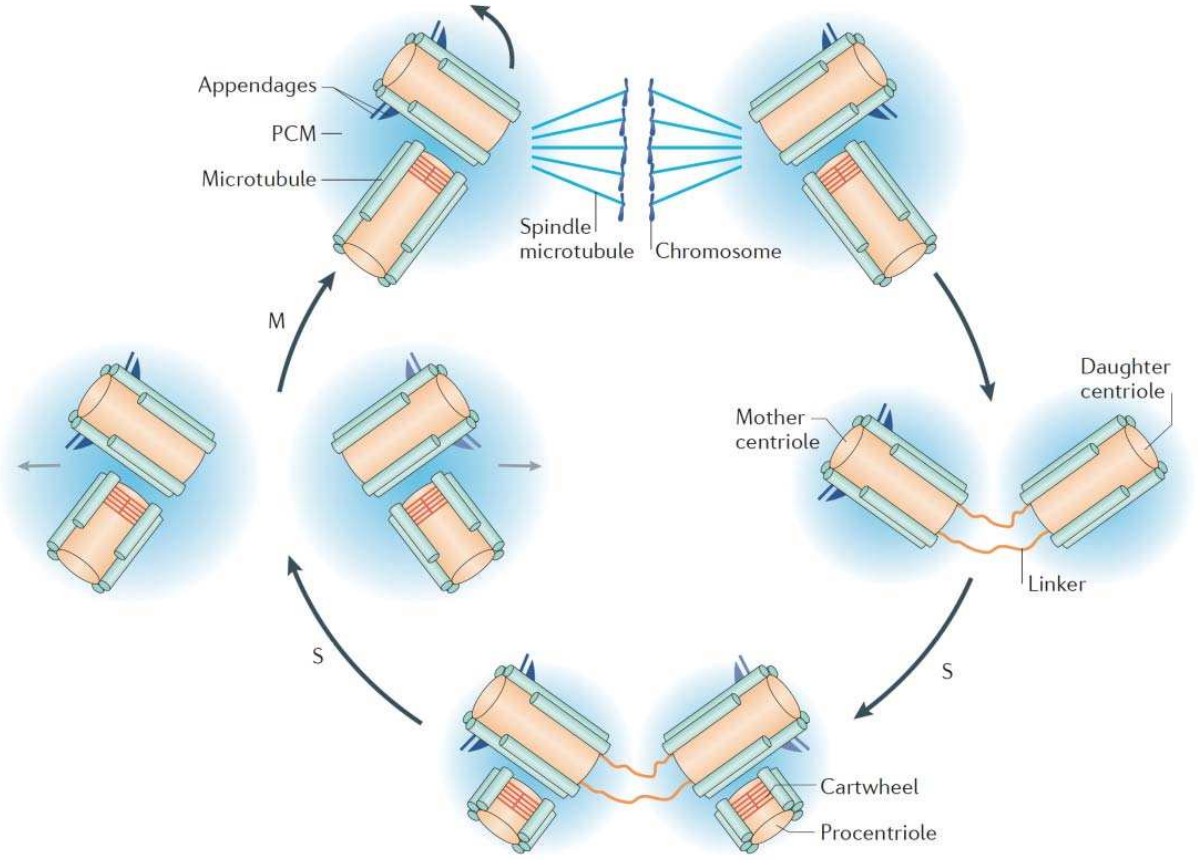

Figure II.12. : *The centrosome cycle. Centrosomes are segregated in the two daughter cells at the end of mitosis, and duplicate for the next round of divisions. The orthogonal arrangement of centrioles is generally kept through mitosis, but in some embryos the depicted cycle is modified to compensate for the lack of gap phases in early embryonic development. (Adapted from (Gönczy, 2015))*

In most embryos, the centrosomes both originate from the one or two centrioles brought by the sperm head, that duplicate once or twice to give the two centrosomes, each composes of two centrioles, of the first mitosis. The female pronucleus is sometimes associated with its own centriolar material, like in the sea urchin embryo, but only the male centrosome is able to generate a bipolar spindle (Schatten et al., 1988). Upon fertilization, the male centrosome assembles a single aster of MTs, which is thought to generate the migration of the male pronucleus toward the female pronucleus and the cell center in most embryos (Chapter II.4.b.). At the onset of the first mitosis, the centered centrosome duplicates, and the aster with it. However, the time of centrosome duplication is highly variable. In some species like sea urchins, centrosomes are separated long before mitosis. In nematodes, the centrosome is already duplicated even before pronuclear migration (O'Connell, 2000) and two MT asters center the pronucleus. In rodents however, the sperm contains one centriole but the sperm centration and the early divisions are performed without centrioles and associated MT asters, consistent with the exceptionally long duration of the centration and cleavage processes, taking about 12 hours and one or two days, respectively. As a comparison, these processes take about 10 minutes and 30 minutes to an hour respectively in the sea urchin embryo. The

absence of centrosomes and asters in rodents is also consistent with the observed role of actin in nuclear positioning in this system (Chaigne et al., 2016), contrary to most early embryos which seem to rely almost only on the MT cytoskeleton to position their nuclei. MTs could still be required in sperm centration in rodents (Schatten et al., 1985). The centrioles appear in a later stage of development, suggesting they are not sperm-derived (Szollosi et al., 1972).

In early embryos, the organization of the centrosomes is thought to be involved in nuclear positioning. The pair of centrosomes that assemble the spindle would be pre-positioned by the asters of MTs during the previous interphase. The single centrosome originating from the previous cell division would grow a large MT aster that probes the cell cortex and cytoplasm, and determine the position of the centrosome and associated nucleus with respect to cellular cues. Upon centrosome duplication, the same kind of self-organization mechanisms would determine the arrangement of the two centrosomes around the nucleus, thus setting the orientation of the future spindle and division plane. The nature of the mechanisms involved in the positioning and orientation of the aster pair is still debated. In most cases, it is believed that the MTs of the aster exert forces on the centrosomes, through their polymerization mechanism or their interaction with molecular motors. The positioning of the pair of centrosomes would then result from a mechanical equilibrium between aster forces. In the next chapters, different force generation mechanisms are described and compared.

3. Various mechanisms of mechanical nuclear positioning

a. Tracking

The first type of cytoplasmic-related nuclear positioning is the nuclear tracking along MTs. This mechanism is seen when the nucleus is not anchored to a MTOC, like it is generally the case for the female pronucleus. After fertilization, the male pronucleus grows an aster from its centrosome, that allows it to migrate, but the female pronucleus rather relies on the MTs from the male aster to reach the center of the cell and the male pronucleus. The movement of the female pronucleus along the MTs of the sperm aster is driven by molecular motors. The female pronucleus seems to behave like cargo (Figure II.13.), and the link between the nuclear envelope and dynein could be made by the dynactin complex. Evidence for such a mechanism are found for instance in the sea urchin, or *C. elegans* embryo, where suppression of the sperm aster or all MTs stopped the female pronucleus migration (Rouvière et al., 1994; Schatten, 1983; Strome and Hill, 1988; Wilson, 1901), and where the trajectories of the female pronucleus appeared to be always directed to the current center of the sperm aster (Chambers, 1939; Wilson, 1925). The directionality of the migration (towards the sperm center, at the minus ends of the MTs), as well as its speed (0.2 to 1.5 μm/second), are consistent with dynein being the implied motor (Rouvière et al., 1994; Schatten, 1981; Stewart-Savage and Grey, 1982). This hypothesis is supported by dynein inhibition performed in Xenopus extracts (Reinsch and Karsenti, 1997).

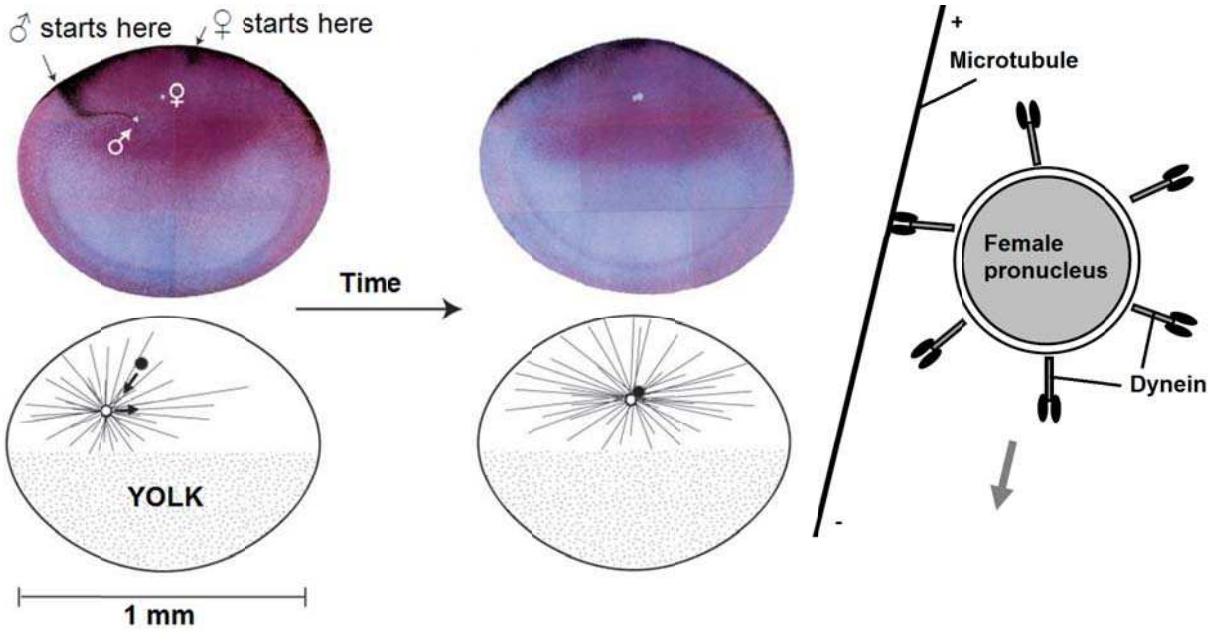

Figure II.13. : *The female pronucleus has been proposed to reach the male pronucleus by a MT tracking mechanism.* ***Left :*** *histological sections of Xenopus eggs 30 minutes (left) and 40 minutes (right) after fertilization, showing the gathering of the two pronuclei (indicated in white). Bottom panels show corresponding schematic views, with MT asters and pronuclei.* ***Right :*** *schematic representation of the nuclear MT tracking mechanism, where dyneins drag the female pronucleus along the MT lattice towards the minus end. (Adapted from (Hausen and Riebesell, 1991; Reinsch and Gönczy, 1998))*

The dynein-mediated nuclear tracking along MTs could also be responsible for the attraction of the nucleus to the centrosome, especially after nuclear reformation at the end of mitosis. In a Xenopus reconstituted system, nuclei that reform after mitosis migrate towards the center of asters (Murray et al., 1996). In the sea urchin embryo, one of the two centrosomes of the vegetal blastomeres at the 8-cell stage migrates toward the vegetal pole prior to micromeres formation. This leading centrosome is then followed by the nucleus, to give rise to an asymmetric division (DAN, 1984; Dan and Ito, 1984). This vegetal nuclear migration could be due to such a tracking mechanism.

For nuclei that are attached to a MTOC, nuclear positioning can be achieved by other mechanisms, which directly imply the positioning of the MTOC. Each centrosome is positioned by forces that apply on it, from the large aster it grows. As suggested by experiments where the nucleus is detached from the centrosomes, or where extra centrosomes are injected into the cell, this positioning mechanism does not seem to depend on the nucleus itself (Boveri, 1888; Heidemann and Kirschner, 1975; Lindeman and Pelegri, 2012). Thus the nucleus would be passively positioned through its attachment to an actively positioning MTOC. The unique centrosome of interphase, and later the pair of centrosomes bound together by the nucleus, would be positioned and oriented though MT forces.

b. Membrane pushing

Mechanism

The MTs can exert pushing forces on the centrosomes, when they reach the cortex of the cell. As the MT polymerizes against an obstacle, it pushes against it (Inoué and Salmon, 1995). But if the obstacle cannot be moved, the polymerization process leads to a backward sliding of the MT, resulting in a pushing force that is transmitted to the centrosome along the MT network. In the case of MTs growing against the cell cortex, this mechanism would cause the centrosome to move away from the cortex, presumably leading to the positioning of the centrosome at the center of the cell from a balance between the actions of all astral MTs. Such a centering mechanism has been obtained in vitro, by polymerization of a MT aster in a small chamber (Holy et al., 1997), and was observed in MT bundles in *S. pombe* (Tran et al., 2001). In the *C. elegans* zygote, cortical signaling has been suggested to yield an asymmetric division, with a nucleus displaced toward the posterior side (Chapter II.5.a.). A hypothesis is that the cortical signaling modulates MT stability, with MTs stabilized by PAR-3 at the anterior side (Cheng et al., 1995; Etemad-Moghadam et al., 1995) and depolymerizing MTs at the posterior side through the action of PAR-1 (Drewes et al., 1997; Ebneth et al., 1999). This idea is consistent with the pushing MTs mechanism, where MTs would push more on the anterior cortex and displace the centrosomes toward the posterior side of the egg. However, recent studies rather suggest a pulling mechanism to account for the first asymmetric division in this system (Chapter II.5.a.).

Length-dependence

The mechanism where MTs push against the cortex would account for the centering of the nucleus only if the pushing force is modulated, so that all MTs extending from the centrosome do not push with the same force. Otherwise, given the fact that the asters extend in all directions, all positions and orientations would generate the same net force on the centrosomes and the central position of the nucleus would not be favored (Figure II.14.).

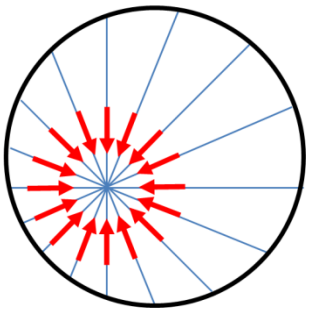

Figure II.14. : *If all MTs push with the same force on the centrosome, the forces compensate and do not center the nucleus. Length-dependence of force is a way to induce a nuclear centration by astral MT forces. MTs are depicted in blue and pushing forces in red.*

The MTs are fibers that have a rigidity of about 10^{-23} Nm^2, with variations over two orders of magnitude, depending on MT interaction with MAPs. As they push against the cell cortex, they can buckle. A longer MT is more subject to buckling than a short one, and since a buckled MT exerts less pushing force, the pushing force exerted by the MT depends on its length. Longer MTs would then push less than the shorter ones on the centrosome. If the

centrosome is close to the cortex, the MTs that extend toward this closer part of the cortex are limited in length, and thus push more, resulting in a nuclear centering process (Bjerknes, 1986) (Figure II.15.). It is interesting to take into account the bundling dynamics of MTs. Bundles of MTs are indeed more rigid than individual MTs, and the number and distribution of bundles may influence the length-dependency of the pushing forces.

A refinement of this mechanism takes into account the dynamic instabilities of MTs. As MTs undergo cycles of polymerization and depolymerization, they are more stable when they are short. Indeed, a longer MT would take longer to polymerize back to the cortex after depolymerizing to the center, and the instant number of MTs contacting the cortex within an aster would then decrease as the distance between the centrosome and the surface increases (Howard, 2006).

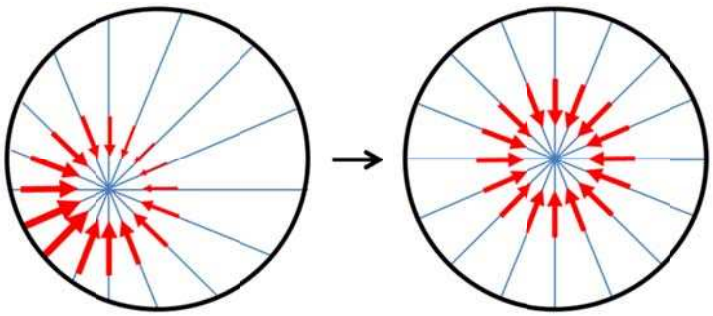

Figure II.15. : *If longer MTs push less than shorter ones, the asymmetry of forces induced by the decentering of the nucleus leads to a centration process. Such a length-dependence could be due to buckling of long MTs.*

Other refinements of this mechanism can be proposed, for instance by assuming that the angular distribution of MTs within the asters is not uniform. This can be due to a limit in the cytoplasmic density of available free tubulin or in the density of the MT mesh. In the context of a branched and crosslinked MT network, such limits would yield more MT tips reaching the cortex from a distant centrosome than from a closer one. Indeed, the MT density would be more homogeneous if the MTs form a dense network than if they radiate from the centrosomes and get diluted as they extend in the volume of the cell. The number of MT tips that each centrosome sends to the cortex would then be proportional to the cortical area that belongs to the centrosome, and thus be higher for the centrosome that is further away from the cortex. Similarly, if instead of forming a dense mesh MTs only radiate from the centrosome, but are regularly branched, the MT density may increase with the distance from the centrosome, again leading to more cortical MT tips belonging to the further centrosome. These mechanisms would counterbalance the centering effect of buckling in a MT pushing system, leading to more pushing on the further centrosome, that would act to increase the decentering of the nucleus.

An additional effect that may be taken into account is the sliding of MTs as they contact the cortex with an angle. The pushing MTs would then rip against the surface, and be redirected toward the further ends of the cell (Pavin et al., 2012). As a consequence, this mechanism would promote an alignment of the astral MTs with the long axis of the cell, and by gathering them along this axis would introduce inhomogeneities in the angular distribution of MTs within the asters. It is interesting to note, however, that the induced alignment of MTs along the cell long axis cannot explain Hertwig's long axis rule, as it would rather tend to increase the pushing force from the poles of the cell, orienting the pair of asters orthogonal to the long axis.

c. Membrane pulling

Mechanisms

An alternative to the pushing model is a mechanism in which MTs pull from the cell cortex. In *C. elegans*, the pair of centrosomes of the posterior blastomere at the 2-cell stage undergoes a near-90° rotation to align with the antero-posterior axis. This rotation is accompanied by a slight indentation of the cortex, and nocodazole treatment and laser cutting both inhibit the rotation, suggesting a MT link between the centrosome and the cell cortex (Hyman, 1989; Hyman and White, 1987). Actin also seems to be involved in the rotation (Waddle et al., 1994). As the actin barbed-end capping protein is enriched at the cortex, and is also involved in the dynactin complex, dynein has been proposed as an actor of the nuclear rotation. This hypothesis is supported by experiments where the levels of two orthologues of dynactin are reduced, leading to a misalignment of the centrosome pair (Skop and White, 1998). The proposed mechanism for dynein-mediated membrane pulling supposes an anchorage of dynein at the cell cortex, possibly via the dynactin complex. This attached dynein would capture MT tips that reach the cortex, and walk toward the minus ends (Skop and White, 1998; Waddle et al., 1994), as it is activated by dynactin. As dynein is bound to the cell cortex, its processivity yields a displacement of the MTs toward the cortex, and a pulling force on the centrosome (Figure II.16.). It is possible that the MT tips then slide along the surface, or get shortened through dynein-induced depolymerization. Dynein may indeed increase the polymerization and depolymerization rates, as well as promoting catastrophe (Carminati and Stearns, 1997). The destabilizing effect of dynein on MTs can be due to conformational changes induced by dynein binding along the MT lattice, or to exclusion of stabilizing MAPs.

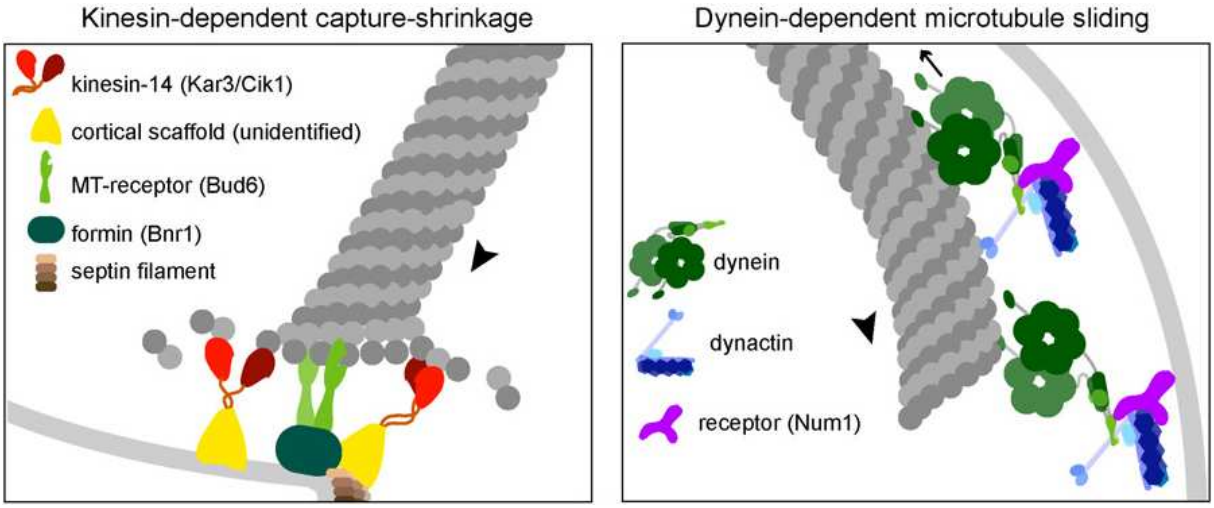

Figure II.16. : *Two mechanisms of cortical pulling, illustrated in budding yeast.* ***Left :*** *MTs that are anchored to the cortex by kinesins depolymerize and their shrinking generates a pulling force on the centrosome.* ***Right :*** *dyneins walk on the astral MTs and pull on them due to their anchorage to the cortex. MTs then slide along the cortex. (From (Moore and Cooper, 2010))*

Similarly, pulling forces could originate from the MT depolymerization itself. In this model, the depolymerization would not follow the MT drag toward the cortex, but drive it. The MTs are anchored to the cortex, likely by molecular motors, and undergo plus end depolymerization. Since the plus ends are bound to the surface, this shrinkage leads to a sliding of MTs toward the cortex and to a pulling force applied on the centrosome (Figure II.16.). Kinesins, dyneins and myosins have been suggested to be involved in this mechanism, since all these motors have the ability to anchor MTs at the cortex and to promote depolymerization. Such a mechanism has been observed *in vitro* (Grishchuk et al., 2005; Toba et al., 2006), in *C. elegans* (Kozlowski et al., 2007; Siller and Doe, 2009), budding yeast (Moore and Cooper, 2010; Siller and Doe, 2009) and in mammalian cells (Kwon et al., 2015).

Length-dependence

Both surface pulling mechanisms can depend on MT lengths. In the first mechanism, if the molecular motors are limiting, the pulling force is expected to increase with MT length. Indeed, MTs radiating from the centrosome get more and more spaced as they extent through the cytoplasm, so that when they reach the cell cortex, each MT recruits more dyneins. This scenario is only valid in the case of homogeneous cortical distribution of motors, or of evenly spaced cortical motors pulling on a fraction of astral MTs (Grill and Hyman, 2005; Howard, 2006) (Figure II.17.). If the MTs are limiting, all MTs will recruit the same number of motors and will pull with the same force. However, if MTs are branched, as it seems to be the case in large eggs and blastomeres (Ishihara et al., 2016; Petry et al., 2013), more tips originating from a single MT centrosomal minus end are expected to reach the surface when the MT is longer, thus the pulling force increases with MT length (Figure II.17.). In the second pulling mechanism, it is likely that only one or a few molecular motors are sufficient to anchor a MT tip to the cortex. Yet, the same kind of length-dependence is expected as in the pulling dynein mechanism. If the anchors are limiting, not all MT tips get attached and the more spaced MTs coming from a further centrosome are more likely to find an anchor and pull. If the MTs are limiting, a longer single MT generates more tips by branching than a shorter one, and exerts a higher pulling force. In any case, the pulling force of cortical mechanisms increases with MT length, allowing the nucleus to center. Indeed, if the nucleus is close to a side of the cortex, the MTs radiating toward the other side will be the longest MTs and thus the ones pulling the most on the centrosome, dragging it toward the cell center.

It is important to keep in mind, however, that these pulling mechanisms are mostly observed at specific areas of the cell cortex, where dynein or other depolymerization factors are enriched (Chapter II.5.a.). In those cases, nuclear positioning is generally asymmetric. Consequently, it is unlikely that nuclear centration relies on a balance between surface pulling forces originating from the whole surface. The idea of evenly distributed and limiting cortical motors is however what was proposed to account for observations made in some cultured mitotic cells, where newly separated centrosomes, still able to move independently, were systematically moving in the direction of the longest MTs of their respective asters (Waters et al., 1993).

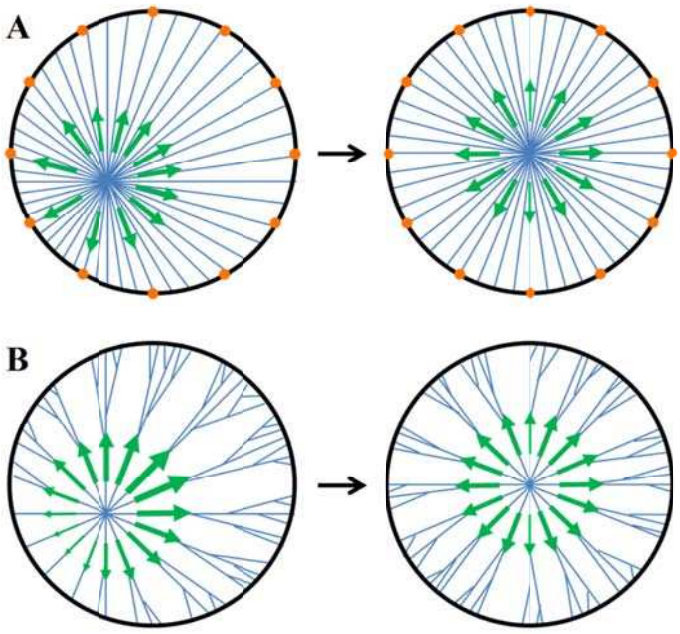

Figure II.17. : *Two possible mechanisms to induce a nuclear centration by cortical pulling MT forces (depicted in green).* ***A :*** *If the cortical anchors are limiting and evenly distributed (shown in orange), longer MTs are more sparse and have a better chance to find an anchor, resulting in an asymmetry in aster pulling force that tends to center the nucleus.* ***B :*** *If the MTs are limiting, the length-dependence of MT force required to center the nucleus can be achieved through MT branching. A longer MT will generate more branches and tips at the cortex, and thus will pull more.*

d. Cytoplasmic forces

Mechanisms

Another hypothesis for force generation of asters on centrosomes is that MTs exert force in bulk cytoplasm. Evidence for such a mechanism come from elegant experiments performed in sand dollar eggs (Hamaguchi and Hiramoto, 1986), where eggs were treated with a MT polymerization inhibitor, colcemid, that was inactivated by UV light in a specific area. When the colcemid was inactivated around the sperm aster, the aster centered within the inactivation zone, whether this area was contacting the cell cortex or not (Figure II.18.). As colcemid inactivation is not likely to create a mechanical interface between the UV illuminated cytoplasm and the surrounding cytoplasm, on which MTs can push by the polymerization mechanism, this experiment suggests that centering forces arise from bulk cytoplasm.

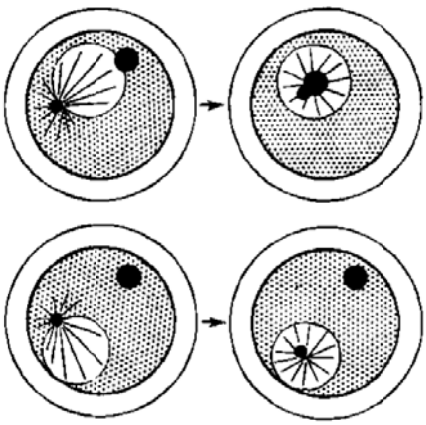

Figure II.18. : *Schematic representation of the local MT inhibition experiment performed by Hamaguchi and Hiramoto. Sand dollar eggs are treated with a MT depolymerizing factor (depicted in gray), that is photo-inactivated in a restricted area (in white) around the sperm aster. The sperm aster centers in the illuminated zone, independently of the female pronucleus or the cortex, suggesting a cytoplasmic force generation. (From (Hamaguchi and Hiramoto, 1986))*

The effectors of these forces are probably molecular motors. These motors would walk on astral MTs, whether toward the plus ends or the minus ends depending on the type of motors, and would be anchored in the cytoplasm, thus causing MTs to slide in the opposite direction (Hamaguchi and Hiramoto, 1986; Hamaguchi et al., 1986). Motors walking toward the plus end would then move the MTs towards their minus end, yielding a pushing force on the centrosome. Conversely, minus end-directed motors such as dynein would drag the MTs toward the plus ends and pull on the centrosomes. It is yet not clear how these motors are anchored in the cytoplasm. It is possible that they are bound to the actin and intermediate filaments network. The endoplasmic reticulum, that extends from the nuclear envelope up to the cortex, thus being present through whole cytoplasmic regions, could also play a role, as dynein has been found to bind its membrane in Xenopus extracts (Allan, 1995). Another possibility is that motors exert force when they bind to the cargos they transport across the cell to perform various cellular functions (Kimura and Kimura, 2011). Those vesicles and organelles are then dragged through the cytoplasm along the MT fibers, generating drag force from the intrinsic viscosity of the cytoplasm. These anchors for molecular motors would not be completely fixed, but the cytoplasmic resistance to their motion would be enough to generate a movement of the MT in the other direction (Figure II.19.). It is interesting to note that the movement of the female pronucleus toward the sperm centrosome, generated by a tracking mechanism mediated by dynein walking on MTs (Chapter II.3.a.), could in return participate in the motion of the sperm aster, as the female pronucleus has to move through a viscous cytoplasm. This vesicular anchorage mechanism is supported by observations of vesicles and injected polystyrene beads moving straight toward the sperm aster during the centration process in sea urchins (Hamaguchi et al., 1986).

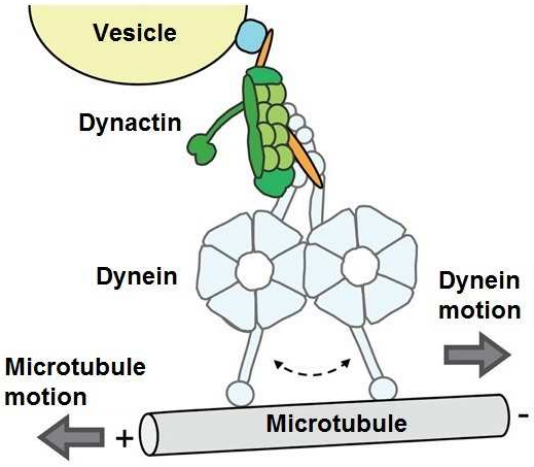

Figure II.19. : *Principle of the motor-mediated cytoplasmic pulling (illustrated with dynein). Dyneins or kinesins walking on MTs propel MTs in the other direction as the cargo they bind acts as an anchor. The resistive friction force of motor-bound vesicles in the cytoplasm generates an opposite force on the nucleus. In the case of dyneins, that walk toward the minus ends of MTs, the nucleus would be pulled. In the case of plus end-directed kinesins, it would be pushed. (Adapted from (Jaarsma and Hoogenraad, 2015))*

Another mechanism has been proposed in the nuclear migrations to the cortex in Drosophila syncytial embryos. The migrating nuclei appeared to leave MTs behind, thus migrating in the direction of the shortest front MTs (Baker et al., 1993). Here, the longer trailing MTs may interact with the ones of nuclei migrating toward the other side of the cortex. The anti-parallel arrays of MTs formed at the boundary may be crosslinked by plus end directed motors, consequently repelling each other and generating the pushing forces that move the nuclei toward the cortex.

Length-dependence

The force exerted by individual MTs on the centrosome is expected to increase with the MT length, as a longer MT must recruit more molecular motors within the hypothesis of a rather homogeneous cytoplasmic distribution of motors. If the MTs are limiting, this length-dependency should be even stronger in the context of branched MTs (Janson et al., 2007). Indeed, a single MT extending from the centrosome nucleates MT branches along its lattice, and thus longer MTs should generate more branches. It is also possible that longer MTs recruit even more motors, because of their longer lifetime (Seetapun and Odde, 2010) allowing tubulin posttranslational modifications (Cai et al., 2009).

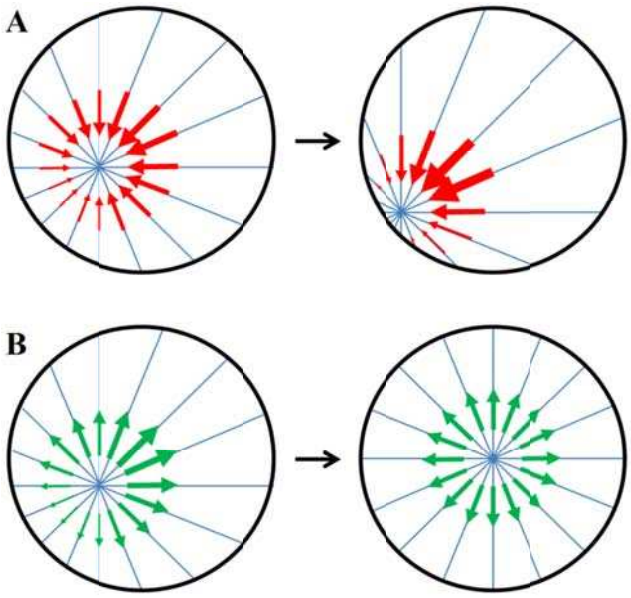

Figure II.20. : *If MT forces are generated in the bulk cytoplasm, a longer MT may recruit more motors and exert a bigger force.* ***A :*** *in the case of a kinesin-mediated pushing mechanism, the nucleus would be further decentered as longer MTs push more.* ***B :*** *a pulling mechanism tends to center the nucleus.*

In the case of a cytoplasmic pushing mechanism, based on plus end-directed motors, this length-dependency of force would lead to a decentering of the nucleus. If the nucleus is slightly closer to a side of the cortex, the MTs extending toward this closer side would indeed be shorter and push less than the others, yielding a force imbalance between all MT contribution, that would move the nucleus further toward this closer side of the cortex. Unless the cytoplasmic pushing mechanism is compensated by inhomogeneous angular distribution of MTs within the aster, or with pushing-induced buckling of MTs that would dramatically decrease the pushing force exerted by the longer MTs, it cannot account for the observed centration of the nucleus (Figure II.20.). In contrast, the cytoplasmic pulling mechanism, which relies on minus end-directed motors such as dynein, could center the nucleus if the pulling force increase with MT lengths. Indeed, if the nucleus is displaced toward a side of the cortex, the MTs extending toward the other side would be longer and pull more on the centrosome, recentering the nucleus (Figure II.20.). The length-dependence of the pulling force is consistent with the observation of centrosome movement toward the longest astral MTs in cultured mammalian cells, even though it was rather proposed to be due to a cortical

pulling mechanism (Waters et al., 1993). In the sea urchin egg, when the shape is elongated by putting eggs in PDMS microchambers, nuclei appear elongated along the centrosomes axis, that aligns with the shape long axis, and are rounded up by nocodazole treatment, consistent with a MT pulling mechanism with longer MTs pulling more. Moreover, considerations on the mechanical properties of the nucleus allowed to estimate the pulling forces exerted on the centered nucleus from elongation measurements. These forces were estimated to range from 10 to 30 pN, increasing with the shape anisotropy, in line with the length-dependent pulling hypothesis (Minc et al., 2011).

e. Pulling versus pushing

As seen in the previous paragraphs, centration of the nucleus could originate from polymerization-driven cortical pushing forces, dynein or depolymerization-driven cortical pulling forces, or motor-driven cytoplasmic pulling or pushing forces. As the anchors required by the cortical pulling mechanism do not seem to be evenly distributed around the cortex, but rather recruited in some areas, and as the cytoplasmic pushing would rather decenter the nucleus, the two main mechanisms that are considered are the cortical pushing and the cytoplasmic pulling mechanisms.

Depending on the system, one or the other, or both these two mechanisms are positioning the nucleus. To decipher between the two, direct experiments have been performed, like laser ablation. For instance, in *C. elegans* zygotes the central spindle was cut, dissociating the two centrosomes. Upon laser ablation, the centrosomes moved apart from each other, suggesting that the pulling forces may be dominant in this system (Grill et al., 2001). In zebrafish embryos, local induction of MT depolymerization was followed by a movement of the asters away from the depolymerization area, suggesting a pulling mechanism (Wühr et al., 2010). During the centering of the sperm aster in the sea urchin embryo, laser ablation at the front of the moving aster, where MTs do not contact any membrane, transiently stopped aster migration, suggesting that the front MTs were exerting most of the pulling forces necessary to aster motion. Similarly, a laser ablation on the side of the aster was followed by a movement of the aster away from the ablation line, suggesting a pulling mechanism (Tanimoto et al., 2016). Pushing forces were however found to be dominant in smaller cells (Howard, 2006; Tran et al., 2001). In bigger cells, the pulling mechanism seems to dominate, which is supported by mathematical evaluations. Indeed, in the large eggs of Xenopus or Zebrafish, the sperm aster is expected to become as large as the cell, yielding long MTs that are likely to buckle. The buckling critical force of such long MTs, calculated from the MT length and rigidity, can be compared to the drag force exerted on the centering aster, calculated from its radius and speed. This simple evaluation predicts that about 12 000 MTs would be required to center an aster by the cortical pushing mechanism, which is way higher than the number of MTs asters likely contain (Reinsch and Gönczy, 1998). In contrast, considering the typical force exerted by one dynein (about 1 pN (Gittes et al., 1993)), only a difference of 100 dyneins between both sides of the egg could compensate the previously calculated drag force (Reinsch and Gönczy, 1998), arguing in favor of the cytoplasmic pulling mechanism in these large cells. In the large eggs and blastomeres of early embryos, the positioning of the nucleus at the cell center would then be mainly, perhaps only, a result of cytoplasmic pulling forces (Gönczy et al., 1999; Grill and Hyman, 2005; Kimura and Kimura, 2011; Wühr et al., 2010).

4. Models for nuclear positioning

The positioning of the nucleus appears to result from a mechanical equilibrium between the forces exerted by astral MTs. Recent mathematical models are testing this hypothesis, by trying to predict the position and orientation of the sperm aster, or of the subsequent pair of asters.

a. A static model

Principle

As the positioning of the cleavage plane only depends on the final position and orientation of the aster pair, it is possible to predict it with a static model, that ignores the centration dynamics and only looks for the equilibrium position. In a model proposed by Minc et al. (Minc et al., 2011), the orientation of the aster pair is assessed, for an already centered nucleus. The modeling framework hypothesizes that the two MT asters fill up the whole volume of the cell, and radiate from the centrosomes with a constant astral MT angular density. The MTs are approximated to be straight, without branching, and the MT dynamics of polymerization and depolymerization are not taken into account, so that all MTs reach the cell cortex. In the model, the MTs pull on the centrosomes in a length-dependent manner, where longer MTs pull more, and since all MTs radiating from the centrosomes reach the cortex, the net force applied on the centrosomes only depends on cell shape.

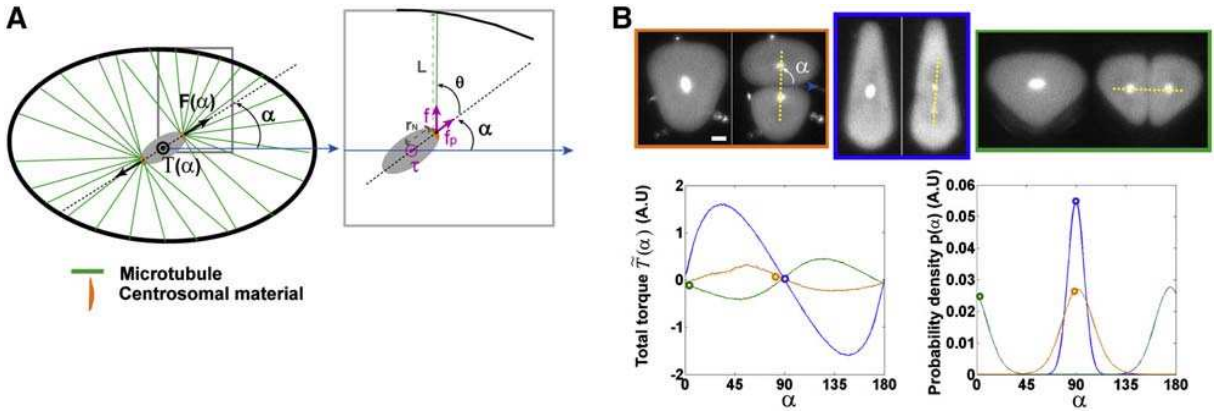

Figure II.21. : *A static model for nuclear positioning.* ***A :*** *Principle of the model. The lengths of MTs are inferred from their position within the aster and the geometry of the cell. Longer MTs are assigned a higher pulling force, consistent with a dynein-mediated cytoplasmic pulling mechanism, and the net torque on the aster pair is calculated.* ***B :*** *the model is tested on the different cell shapes of sea urchin eggs confined in microfabricated chambers (upper panels).The dotted line indicates the observed division axis of the cell. The torque and probability are plotted for all possible planar orientations in the model (lower panels), and experimental orientations are reported on the graphs (dots). (Scale bar : 20 µm, adapted from (Minc et al., 2011))*

The model predicts the orientation of the division in a 2D cell shape, by positioning the nucleus at the center of mass and exploring the possible orientations of the pair of asters (one variable angle in 2D). For each nuclear orientation, the lengths of individual MTs are inferred geometrically as the centrosome to cortex distances in the direction of the MTs. The forces of individual MTs are calculated as a function of their lengths, and summed up to give the net force applied on each aster, and the torque applied on the pair. As the net torque is calculated for every orientation of the nucleus, the equilibrium orientation can be found (Figure II.21.), and the orientation of the division plane is predicted to be perpendicular to the centrosomes axis at equilibrium.

Results

The probability of each division orientation is calculated from the torque potential (Théry et al., 2007), and compared to the observed orientations in sea urchin eggs dividing in PDMS microchambers of different shapes. The model was remarkably accurate in predicting cell division orientations (Figures II.21. and II.22.). In addition, it could account for the next divisions of the blastomeres within the chambers, and for an old observation of spindle orientations in a tissue section of the pigeon testis (Guyer, 1900) (Figure II.22.). The experimental results, as well as the model predictions, always followed Hertwig's long axis rule, confirming the role of shape in nuclear orientation. By demonstrating the ability of a length-dependent pulling mechanism to orient the nucleus consistently with observations, this modeling approach provides a mechanistic insight to Hertwig's empiric rule.

In addition, the nuclear shapes of eggs dividing in elliptic or rectangular microchambers of different shape anisotropies were used to estimate the pulling force exerted on centrosomes (Figure II.23.). These measurements were compared to the forces predicted by the model, under different hypotheses on the length-dependence of the force. The tested laws for the dependence of individual MT force to MT length were power laws : $F = L^{\delta}$. The exponent that gave the best fitting predictions through the increase of the shape anisotropy was ranging from 3 to 5. This result goes against the hypothesis of a pulling mechanism where dyneins would be anchored on the actin or intermediate filaments meshwork. Indeed, such a mechanism is expected to yield a force that is proportional to the MT length ($\delta = 1$), as the meshwork is rigid and supposedly homogeneous in filament density. The fitted exponent is also too big to account for a dynein-mediated cortical pulling mechanism, where dynein would be limiting. Such a mechanism would be surface-sensitive, as a single MT would recruit all available cortical dyneins within the solid angle it spans, thus corresponding to a square law ($\delta = 2$). The exponent is rather close to 3, arguing in favor of a cytoplasmic pulling mechanism where dynein would be evenly distributed in the cytoplasm (Mohri et al., 1976), and limiting. Individual MTs would then recruit all available dyneins within their own solid angle, thus probing the volume of the cell and yielding a cubic length-dependence.

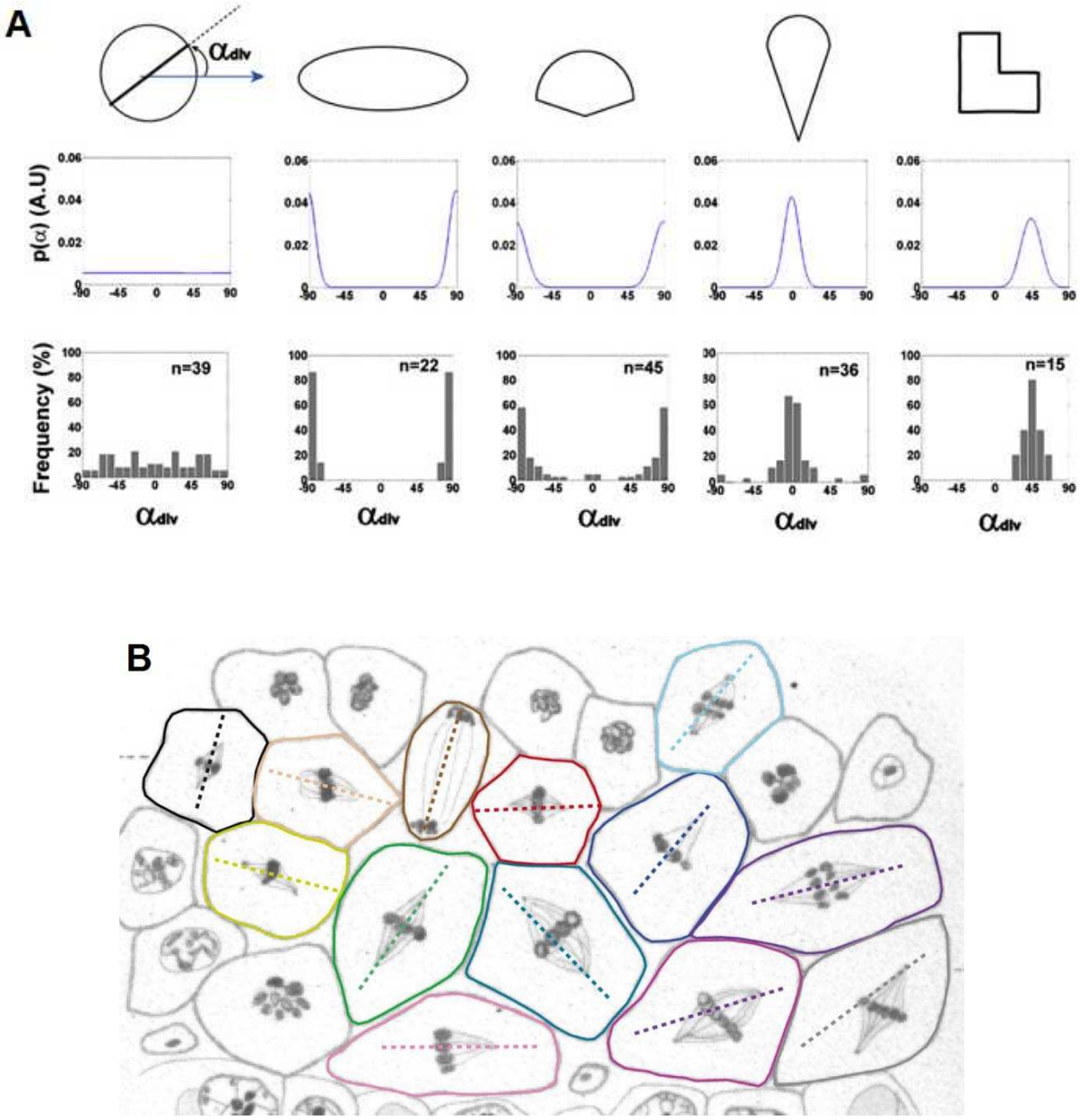

Figure II.22. : *The static 2D model predicts division orientation accurately.* ***A :*** *comparison of the angular probability, calculated for different cell shapes (upper panels), with the measured orientations of cell divisions in deformed sea urchin zygotes (lower panels).* ***B :*** *drawing of a tissue from pigeon testis, showing mitotic spindles (from (Guyer, 1900)). The predicted spindle orientation by the model is superimposed (dotted lines). (Adapted from (Minc et al., 2011))*

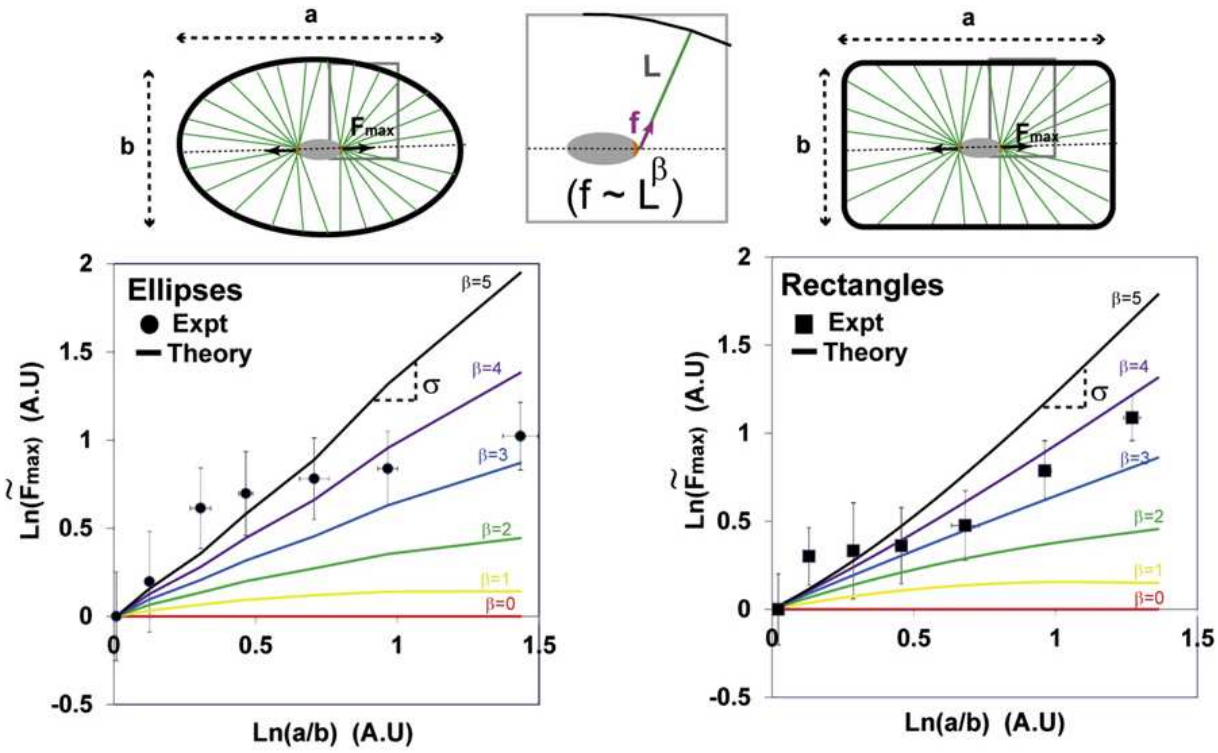

Figure II.23. : *Determination of the length-dependence of MT pulling forces. The deformation of the nucleus is calculated for different exponents and shape anisotropies (color curves), and compared to measures performed on sea urchin zygotes deformed in microchambers. The comparison suggests an exponent ranging from 3 to 5 for the length-dependence of MT forces. (Adapted from (Minc et al., 2011))*

The branching is not considered in this simple model. Consequently, the dependence of the force on the number of MT branches or tips in the context of limiting MTs is not assessed. This mechanism may account as well for the measured variations of MT forces with cell shape anisotropy, and cannot be ruled out. Yet, it is important to note that in the context of limiting dynein, the proposed cytoplasmic pulling mechanism does not depend on MT branches, as long as the branches nucleating on a single MT remain within the MT own solid angle. Under this approximation, the available dyneins will be recruited on the several branches of the MT instead of just one, but the overall number of motors pulling on each MT will remain unchanged, yielding the same pulling force as in the proposed radial model.

Limitations of this model are its 2-dimensionality, which may not accurately account for the observed divisions in more complex 3D blastomere shapes, and the fact that it ignores the centration and orientation processes. Indeed, the nucleus is supposed already centered, that does not account for a possible asymmetry of some divisions. Moreover, the centration process is dynamic, as the sperm aster migrates from the cortex to the center with a certain speed and trajectory, that this static model does not explain. In some embryos like the *C. elegans* embryo, the centered pair of asters undergoes oscillations, that possibly help probing the possible nuclear orientation and determining the final position. Here again the static model does not provide insight into the mechanisms responsible for such oscillations.

b. Centration dynamics

C. elegans

The dynamics of the centration process have been addressed by several models. In *C. elegans* embryos, Kimura et al. modeled the migration of the sperm pronucleus whether by a pushing or a pulling mechanism (Figure II.24.), and compared the results to in vivo measurements (Kimura and Onami, 2005). As the centrosomes are separated prior to sperm pronucleus migration in this system, the whole simulations were performed with a pair of asters. To calculate the MT lengths, the dynamics of MTs were taken into account (Nédélec, 2002). The modeling framework was iterative, comparing the centering forces to the aster drag force, evaluated from the cytoplasm viscosity and MT length, in small time steps, allowing to estimate the dynamics of the centration process. In the pushing mechanism, the MT force was evaluated from the polymerization dynamics according to a force-velocity relationship (Dogterom and Yurke, 1997; Hill, 1987; Peskin et al., 1993), and limited by the buckling threshold. The pair of asters centered in the simulation, both because the growing asters did not fill up the cell immediately, and thus only pushed toward the center in the beginning of the process, and because of buckling-related length-dependence of pushing forces. In the pulling mechanism, the motors were supposed to be anchored homogeneously throughout the cytoplasm, and thus the force was set proportional to the MT length. Here again the simulations showed a centration of the aster pair, because the rear MTs were limited in length by the cell cortex, and thus pulled less than the longer free-polymerizing front MTs. However, the distance versus time graph was sigmoidal for the pulling mechanism, where the aster accelerates and then slows down near the cell center, whereas the graph was convex for the pushing mechanism, where the aster moves fast right from the beginning and then decelerates (Figure II.24.). In vivo measurements of centering dynamics showed sigmoidal distance-time graphs, suggesting that the pulling mechanism may be dominant in this system.

A refinement of this pulling model has been proposed by Shinar et al. (Shinar et al., 2011), taking the effect of spindle migration on cytoplasm into account (Figure II.25.). The model supposes that the cytoplasm behaves like an incompressible Newtonian fluid. As previously, the motor anchorage into the cytoplasm generates the centering motion of the aster, described with a very similar modeling framework. But in addition, the motion generates cytoplasmic flows in the tightly confined egg, to meet an overall balance of forces. The velocity of MTs, calculated with the previous force-velocity relationship, is now the local relative MT velocity. This refined model still predicts the centration and rotation of the aster pair, although the required forces are increased by one order of magnitude due to the cytoplasmic resistance in this confined geometry. It also predicts the associated flows, including minus end-directed cytoplasmic flows along the MTs.

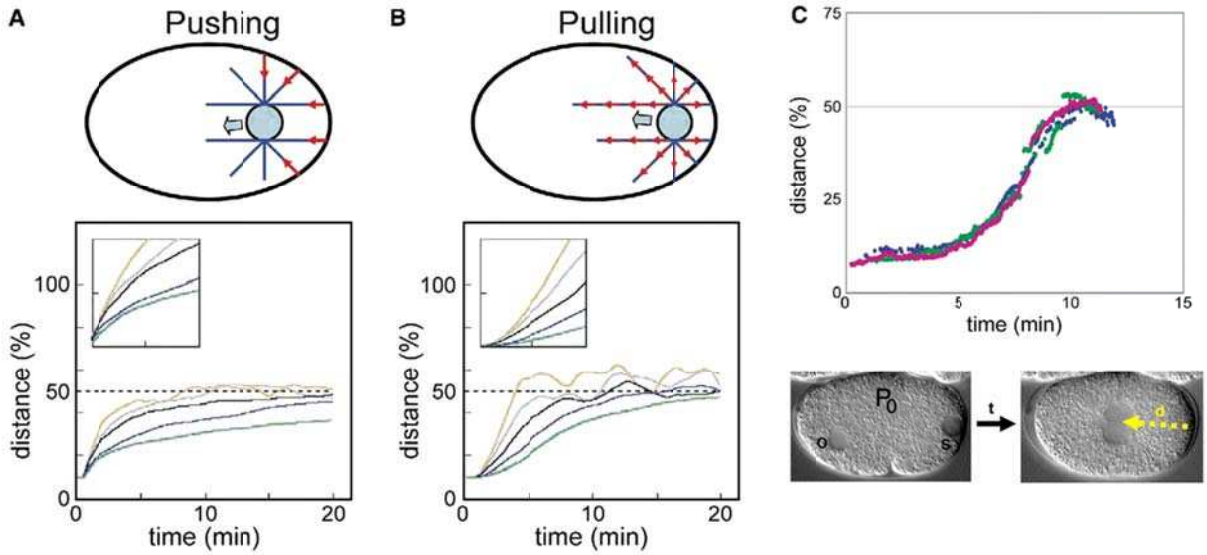

Figure II.24. : *The dynamics of male pronuclear centration in the* C. elegans *egg. Kimura et al. modeled the centration dynamics for different values of cytoplasm viscosity : 0.25 Ns/m^2 (orange), 0.5 Ns/m^2 (pink), 1.0 Ns/m^2 (black), 2.0 Ns/m^2 (blue), or 4.0 Ns/m^2 (green), in the case of a cortical pushing mechanism* ***(A)****, or a cytoplasmic pulling mechanism* ***(B)****. Insets show a zoom on the beginning of the curves.* ***C :*** *live measurement of pronuclear centration for three different* C. elegans *embryos (adapted from (Kimura and Onami, 2005)). The bottom panel illustrates the centration and measured distance (yellow dotted arrow) on live images (adapted from (Lyczak et al., 2002)).*

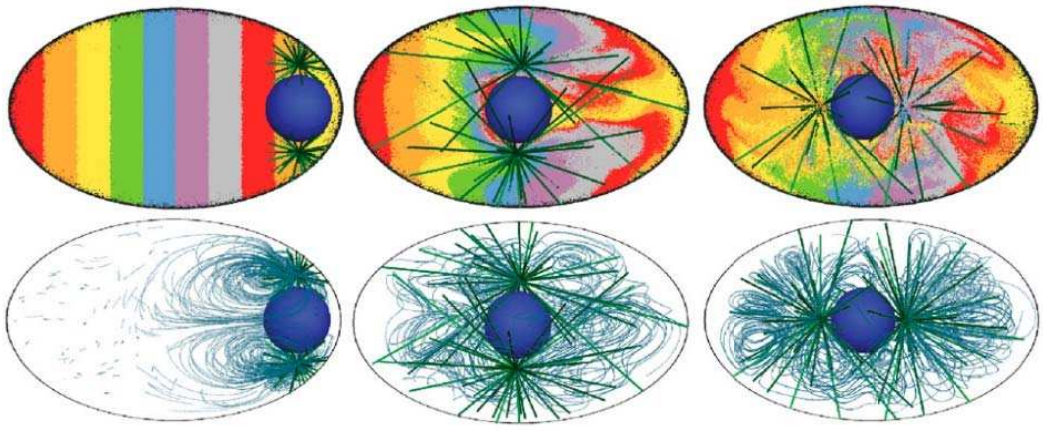

Figure II.25. : *Simulation of the cytoplasmic flows during the male pronuclear centration in the C. elegans egg. The modeling framework takes the interplay between MT (depicted in green) and cytoplasmic forces into account. The simulation accounts for pronuclear centering and rotation.* ***Top :*** *three frames from the simulation (at 0 s, 16:40 s and 66:40s) are shown with colored passive tracker particles to visualize cytoplasm flows.* ***Bottom :*** *the corresponding frames showing streamlines of the flows. (Adapted from (Shinar et al., 2011))*

Sea urchin

In the sea urchin embryo, a modeling framework has been recently proposed to explain how a cytoplasmic pulling mechanism may account for the observed constant speed of the centration (Tanimoto et al., 2016), a characteristic that is generally attributed to a pushing mechanism (Chambers, 1939; Saiki Hamaguchi and Hiramoto, 1980). Here, the MTs were proposed to grow at a constant speed, yet mechanically limited at the cortex. The possible MT length-dependences of pulling forces and drag forces were analyzed, as well as how they must compare to meet the constant speed condition. Two different mechanisms were inferred, where aster speed is expected to be equal to front MT polymerization rate, or inferior and dynein-dependent, respectively. Both solutions could account for the fast establishment of the constant speed regime in the high force limit, suggesting that forces may be higher in the embryos displaying a constant speed phase, such as the sea urchin and Xenopus embryos (Stewart-Savage and Grey, 1982; Wühr et al., 2009, 2010), than in embryos displaying long acceleration and deceleration phases, such as the *C. elegans* embryo (Kimura and Onami, 2005). Dynein inhibition did not affect the aster speed, arguing in favor of the first mechanism. In this mechanism, the aster moves at the polymerization speed, and the length difference between front and rear MTs is responsible for the motion. Interestingly, the simulations of aster centration in non-spherical cells could reproduce the trajectories observed in shape-manipulated eggs, that can be non-straight depending on the sperm entry point (Figure II.26.). This result shows that the aster moves according to its current geometry, changing direction upon contact with a new boundary, and that the positioning of the nucleus is an intrinsically self-organized process.

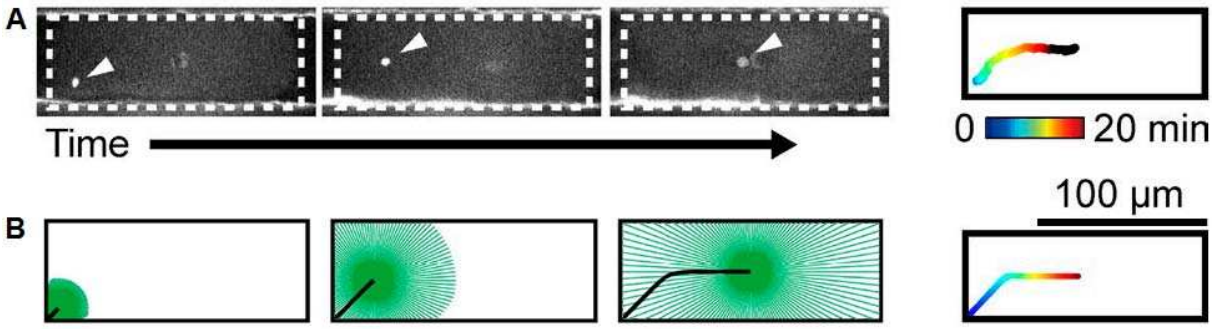

Figure II.26. : *Pronuclear centration on the sea urchin egg.* ***A :*** *fluorescence images of the centering sperm pronucleus (indicated by arrows, DNA marked in white), and corresponding trajectory (right). The egg develops in a rectangular microfabricated chamber, dotted lines indicate the cell surface.* ***B :*** *Simulation of sperm aster centration (MTs in green) in a similar shape, based on a dynein-mediated cytoplasmic pulling mechanism. The corresponding modeled trajectory is depicted on the right. (Adapted from (Tanimoto et al., 2016))*

c. Towards general cytoskeleton simulation

Given the high variety of possible MT behaviors and interaction, more general attempts have been made to model the dynamics of the cytoskeleton. The Cytosim software, currently under development in the cellular architecture group in EMBL, relies on a computationally efficient method (Hidalgo-Carcedo et al., 2011) to model MT and actin

dynamics. These filaments are considered incompressible and elastic, and their movements are simulated with regards to boundaries and objects within the cell, as well as fiber-fiber steric exclusion. The modeling framework takes the polymerization and depolymerization dynamics into account, as well as the possible nucleation and crosslinking events. Moreover, filaments can interact with molecular motors and binding molecules. Importantly, all these processes can be influenced by additional effectors, such as nucleation or severing agents, or MAP regulators promoting polymerization or depolymerization. These effectors can be activated or deactivated, or even adsorbed at surfaces.

The modularity of this modeling framework allows multiple effectors and parameter combinations, adapted to the variety of cell behaviors. Importantly, the model already accounts for the centration of nuclei, and could be used as a powerful tool to further explore the dynamics and mechanisms of spindle positioning.

In particular, even though it appears from Hertwig's experiments and the centration and division simulations described in this chapter that shape is a major cue for division positioning, it is important to keep in mind that the cues determining aster force are multiple, as suggested by many experimental results (see chapter I.5.). The length-dependent pulling or pushing models described here account for the centration and orientation of nuclei according to the long axis rule, and provide insight into the mechanisms that position nuclei with regard to cell shape. Given the accuracy of the model predictions, it is reasonable to consider cell shape as an important cue for cell division. However these models do not account for some observed nuclear positioning, like during asymmetric divisions. Additional cues have been proposed to bias the shape cues or even fully determine the position of the cleavage plane in some cases.

5. Additional polarity cues

a. Membrane polarity

The displacement of the nucleus away from the center of the cell, that is triggering asymmetric divisions, implies the establishment of a polarity within the cell. A possible way of polarizing the cell is by local recruitment of effectors at specific sites of the cortex. In the *C. elegans* worm, after fertilization and positioning of the sperm at the posterior pole, the sperm releases a GTPase activating protein, CYK-4, into the surrounding cytoplasm. This leads to a repositioning of cortical PAR proteins via cytoskeleton reorganization, where PAR-2 replaces PAR-3 in the vicinity of the sperm asters. PAR-3, that was initially homogeneously distributed over the whole cortex, is pushed toward the anterior side, in an actin-dependent fashion, and replaced by PAR-2 as the sperm pronucleus migrates toward the center of the egg. This causes an antero-posterior cortical asymmetry, with PAR-3 at the anterior half of the cortex and PAR-2 at the posterior half (Boyd et al., 1996; Etemad-Moghadam et al., 1995), that may be responsible for the asymmetric division of the zygote (Figure II.27.). In the sea urchin embryo, specific enrichment of factors at the vegetal cortex may cause the formation of micromeres at the vegetal pole, as suggested by detergent treatment experiments inhibiting micromere formation (Dan, 1979; Tanaka, 1976). As factors such as Dishevelled and β-catenin are enriched at the vegetal pole, the Wnt pathway may be implied in the asymmetric positioning of the vegetal nuclei. In ascidians embryos, a cortical structure called the CAB is

assembled at the posterior pole at the 2-cell stage, and the centrosome pairs appear to point toward it, and to be displaced toward it from the 4-cell stage, yielding asymmetric divisions. The CAB, assembled from the vegetal cytoplasm, appears to recruit kinesins, among many other factors like maternal mRNAs, and detergent treatment has been shown to disrupt both kinesin enrichment and micromere formation (Nishikata et al., 1999), consistent with a possible role for kinesin in asymmetric divisions. PEM mRNA inhibition also yields symmetric divisions.

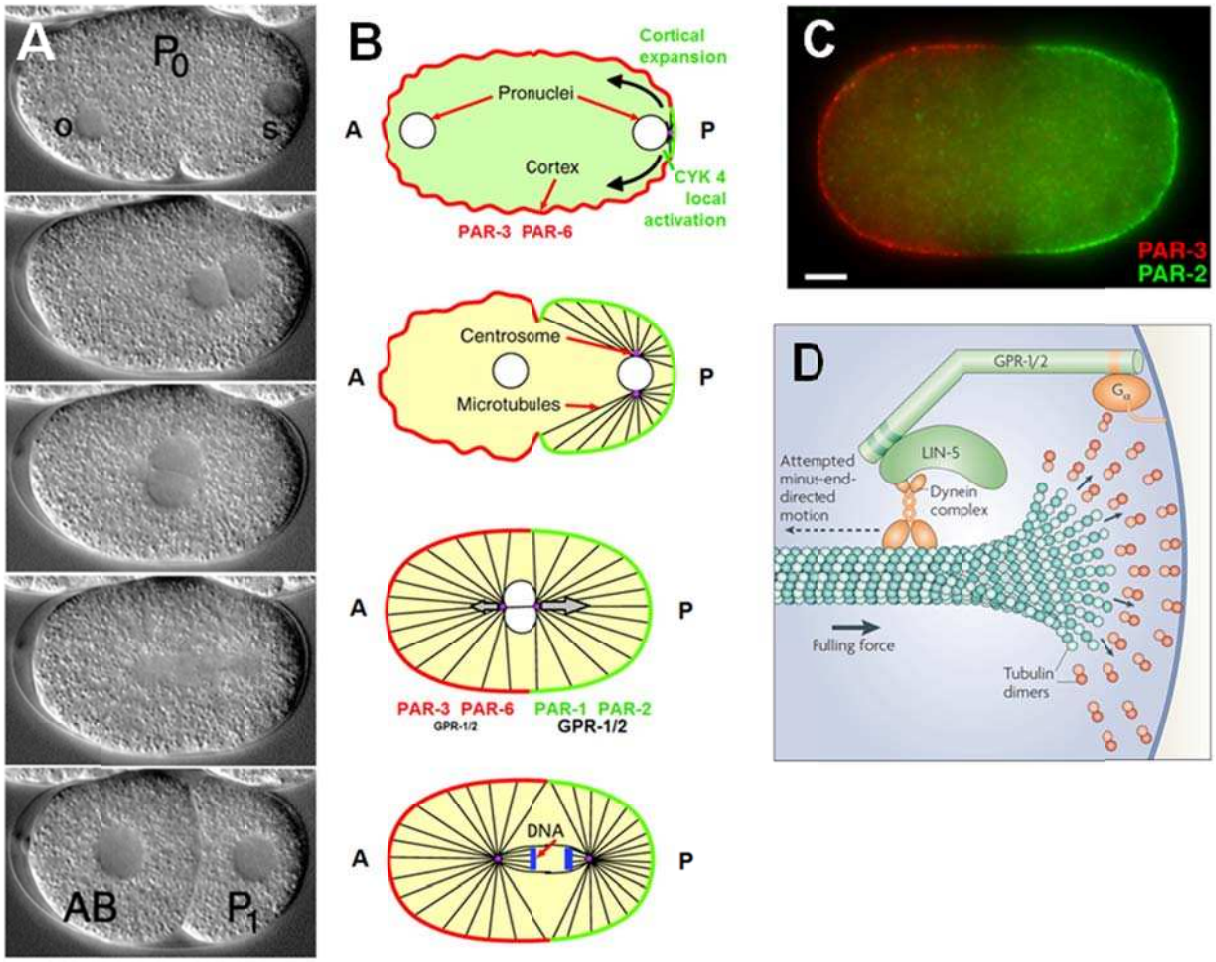

Figure II.27. : *Cortical polarity involved in the asymmetric division of the C. elegans zygote.* ***A :*** *time-lapse showing the pronuclear centration, the spindle decentering and the following asymmetric division of the zygote. Male and female pronuclei are indicated on the first image (S and O, respectively). (Adapted from (Lyczak et al., 2002))* ***B :*** *Schematic representation of the establishment of cortical polarity, relative to the anterior-posterior axis (indicated by A and P on the figure). PAR-2 domain expands in an actin-dependent process and excludes PAR-3. The resulting differential distribution of GPR-1 and 2 leads to different pulling forces on the spindle, shown as gray arrows, and to nuclear decentering.* ***C :*** *Immunostaining image of PAR-3 and PAR-2 cortical localizations. Scale bar : 5 µm. (B and C adapted from (Nance and Zallen, 2011))* ***D :*** *Hypothesized cortical pulling mechanism, dependent on dynein, GPR-1 and 2, G protein and LIN-5. (From (Gönczy, 2008))*

Several mechanisms have been proposed to induce a nuclear displacement from a cortical polarization. A first idea is that the nucleus is mechanically connected to specific cortical sites. In the worm *Chaeopterus* for instance, when the spindle is moved to a different location within the oocyte, using a needle, it comes back to its original position, suggesting a mechanical linkage of the spindle to a specific side of the cortex (Lutz et al., 1988). Some asymmetric divisions in embryos of mollusks also provide evidence for such a link (Conklin, 1917; Dan and Ito, 1984; Harvey, 1935). In ascidian posterior blastomeres, the nucleus appears linked to the CAB by a bundle of MTs (Nishikata et al., 1999) (Figure II.28.).

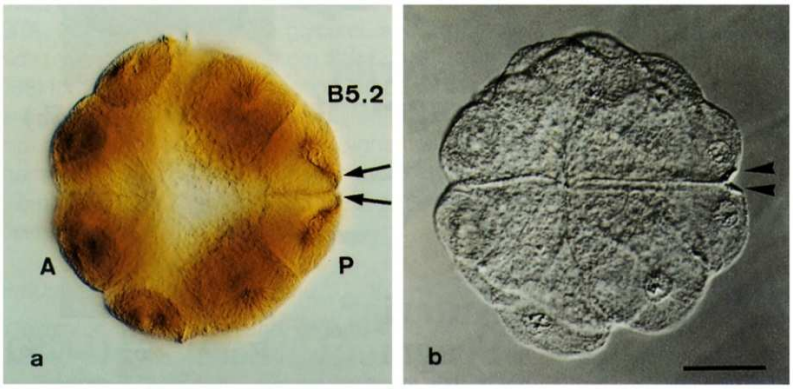

Figure II.28. : *Evidence of a MT link between the centrosomes and the CAB in ascidian embryos at the 16-cell stage. Fixed embryos are stained for tubulin* ***(a)*** *and imaged using differential interference contrast (Nomarski) optics* ***(b)****. Arrows indicate MT bundles between the CAB and the centrosome, and arrowheads show the CAB. The anteroposterior axis is indicated in (a). (Scale bar : 50 µm, from (Hibino et al., 1998))*

The link between the nucleus and specific sites of the cortex likely involves the cytoskeleton, and could thus not only be a passive bound, but exhibit a dynamic behavior. For instance in sea urchins the presence of the Wnt pathway suggests a recruitment of dynein, or a stabilization of MTs (Ciani et al., 2004), consistent with a dynein-mediated pulling mechanism (Chapter II.3.c.). In many other cell types, the local distribution of cortical effectors has been suggested to result in the recruitment of dynein, probably involving a cortical pulling mechanism that determines nuclear positioning (Figure II.29.). In the *C. elegans* zygote, a central spindle laser ablation experiment, where the centrosomes were dissociated, yielded a faster and further displacement of the posterior spindle pole toward the cortex, suggesting a larger pulling force at the posterior cortex (Grill et al., 2001). This is consistent with the observed asymmetric positioning of the nucleus, closer to the posterior side of the egg. The same experiment performed on par-2 or par-3 mutants, that have a centered nucleus, gave for both spindle poles the observed velocity of the WT anterior spindle pole or posterior spindle pole, respectively. The asymmetric distribution of PAR proteins is thought to lead to a preferentially posterior localization of the G protein regulators GPR-1 and GPR-2, thus activating dynein at the posterior pole, through association with Gα (Colombo et al., 2003; Gotta and Ahringer, 2001; Gotta et al., 2003; Srinivasan et al., 2003; Tsou et al., 2003) (Figure II.27.). The difference in the pulling activity of cortical dynein between the anterior and posterior poles would result in a bias of spindle positioning toward the posterior pole (Grill et al., 2001). Interestingly, the spindle oscillations associated with this positioning have been proposed to originate from localized cortical pulling, and to depend on the number or activity of force generators (Pecreaux et al., 2006).

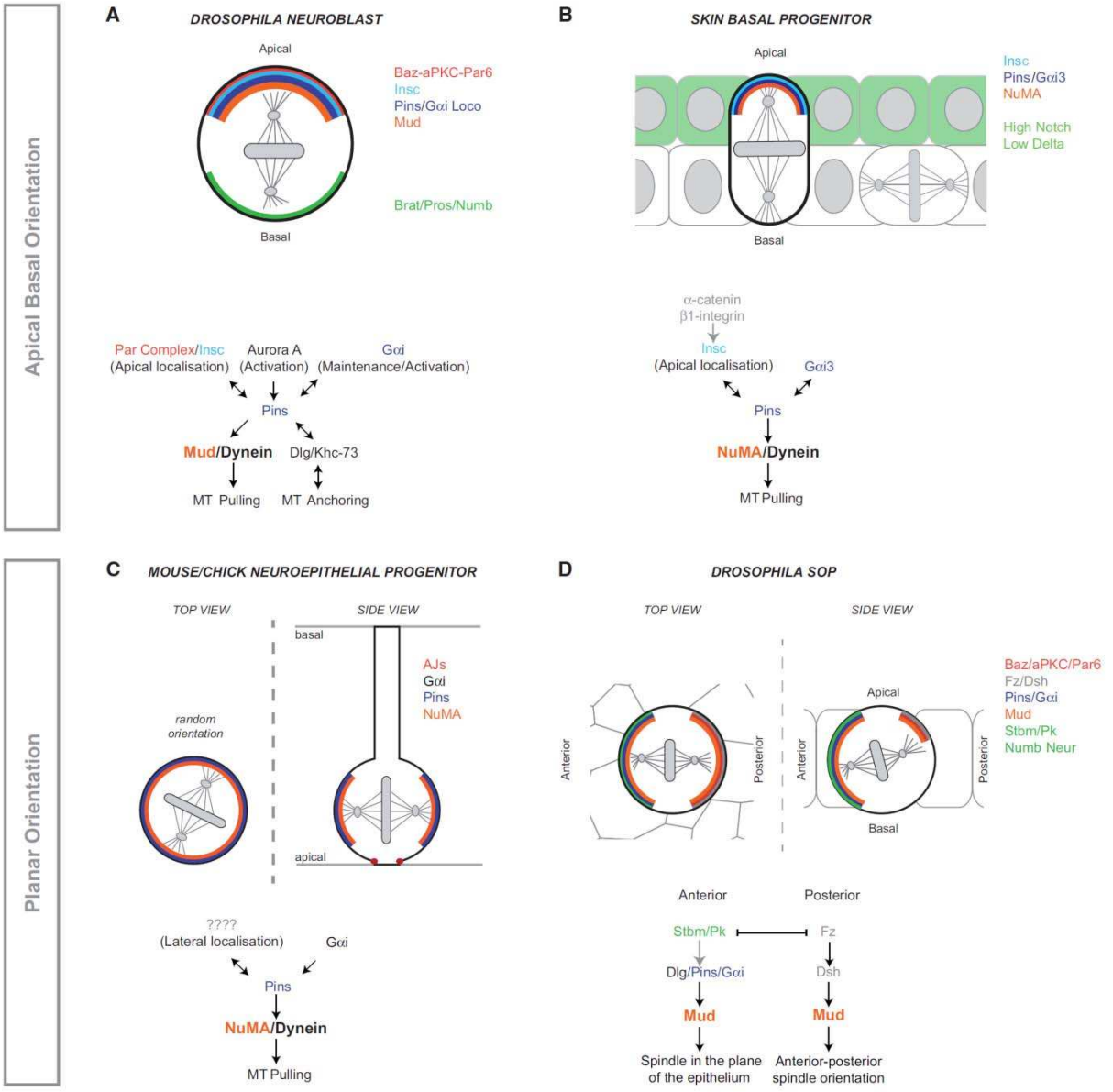

Figure II.29. : *Diverse signaling pathways, in different species and cell types, translating a cortical polarity into dynein differential recruitment and an alignment of mitotic spindles with regards to cell polarity. Upper panels describe two cases of apical-basal orientation, while on the lower panels, two other situations show a specific alignment of spindles within the orthogonal plane. (From (Morin and Bellaïche, 2011))*

In addition, the cortical tension could play a role in modulating the pulling forces. In the *C. elegans* zygote, the posterior cortex has a lower cortical tension than the anterior cortex (Mayer et al., 2010; Munro et al., 2004). A softer cortex may allow longer contacts between MTs and cortical motors, thus generating higher pulling forces (Kozlowski et al., 2007). This effect may have to be finely tuned, as a softer cortex also opposes less resistance to MT pulling, leading to the formation of membrane invaginations and generating less pulling force. In the *C. elegans* zygote, the acto-myosin network prevents membrane deformation by cortical motors, as shown by inhibition of myosin II, and of the G protein or its regulators GPR-1 and GPR-2 (Redemann et al., 2010).

Another possible effect of a cortical polarization is a modulation of MT dynamics. In the *C. elegans* zygote, MTs may be stabilized by PAR-3 at the anterior side (Cheng et al., 1995; Etemad-Moghadam et al., 1995) and depolymerized at the posterior side by PAR-1 (Drewes et al., 1997; Ebneth et al., 1999). The induced polarity in aster length or density could bias spindle positioning toward the posterior side of the egg, in particular in the context of a cortical pushing mechanism. Alternatively, the differential depolymerization dynamics may also lead to a differential pulling and thus to a spindle displacement if the MT tips are anchored to the cell cortex. Similarly, the presence of kinesins at the CAB in ascidians suggests that the MT bundle may shorten by kinesin-mediated depolymerization, pulling the nucleus toward the CAB.

b. Cytoplasmic polarity

The interaction between the cytoskeleton and a polarized membrane may bias the position and orientation of the centrosome pair, by modulating the forces at stake or by adding a cortical contribution to the force balance. In a similar way, a polarization of the cytoplasm could be involved in nuclear positioning, since cytoplasmic displacement appeared to modify the cleavage patterns (Chapter I.5.c.). A theoretical model involving cytoplasmic attractants and repellants near the vegetal and animal pole respectively, that displace the centrosomes, could reproduce the cleavage of normal and perturbed sea urchin embryos (Akiyama et al., 2010). In ascidians, the segregated posterior cytoplasm may be responsible for micromere formation, as its ablation yields symmetric divisions (Nishikata et al., 1999). However, it is not clear whether the cytoplasm itself contributes to the nuclear displacement, or if the displacement is generated by the CAB, that is assembled from this posterior cytoplasm. In snails, the coil orientation is thought to be determined by maternal cytoplasmic factors. The developmental pattern of the right-handed embryos in the right-handed species is generally a mirror image of the one of the left-handed embryos in the left-handed species. However, while the sinistral orientation of some embryos in the right-handed species often appears to be determined by the orientations (to the left) of the spindles at the 4-cell stage (CRAMPTON, 1894), in many cases the dextral orientation in the left-handed species seems to rather be due to a cell rearrangement during cytokinesis, from a radial spindle orientation (Shibazaki et al., 2004). In some species, the direction of coiling has been found to be genetically controlled (Sturtevant, 1923). Importantly, the coiling of the embryo is determined by the genotype of the mother. In addition, when cytoplasm from dextral embryos of a right-handed species is injected into eggs from mutant mothers of the same species (that are defective in the dextral coiling determinant), the dextral coiling is restored (Freeman and Lundelius, 1982). These elements indicate that the spiral division orientation is determined by maternal cytoplasmic factors.

However the mechanisms of cytoplasm-mediated nuclear positioning are unclear. It is possible to imagine that the segregation of the cytoplasm into distinct zones of distinct cytoplasmic compositions can lead to inhomogeneities in the local densities of MT regulators and molecular motors. The force generation of individual MTs would then be locally modulated, and potentially yield a bias from the long axis rule in the nuclear position and orientation. But in the case of spiral patterns for instance, the previously described injection of WT cytoplasm into sinistral mutants, that restores the dextral phenotype, is not likely to be performed with respect to existing cytoplasm segregation. It is not known whether the injected maternal factors may be targeted to specific places, possibly to the cortex.

c. Volume exclusion

An indirect way of modulating cytoskeleton force generation is by steric exclusion. The organelles or other vesicles within the cytoplasm would be equivalent to a dead volume for the division positioning machinery. For instance increasing the local density of vesicles could lead to a decrease in the cytoplasmic motor concentration, or in the number of MTs. In the Zebrafish embryo, most of the cytoplasmic volume is filled up by yolk, and the astral MTs nucleated at the centrosomes do not seem to grow in this yolky part of the embryo. The nuclear centration machinery would then be assembled only within the yolk-free blastodisc, and center the nucleus there. Alternatively, the vesicles and organelles may provide fixed interfaces for the astral MTs to push on. In the Xenopus embryo, a mathematical approach showed that the early cleavage pattern can be reproduced based on segregation of yolk at the vegetal pole (Bjerknes, 1986). The interface between the yolky vegetal part of the embryo and the animal part where the asters grow is supposed to behave as a membrane for MT pushing, and the centrosome pair is centered and oriented by a cortical pushing mechanism between the animal membranes and the vegetal interface. Yet very schematic, as the yolk-cytoplasm interface is modeled as net and rigid, the accuracy of the division predictions obtained by this approach suggests a possible role for volume exclusion in nuclear positioning (Figure II.30.).

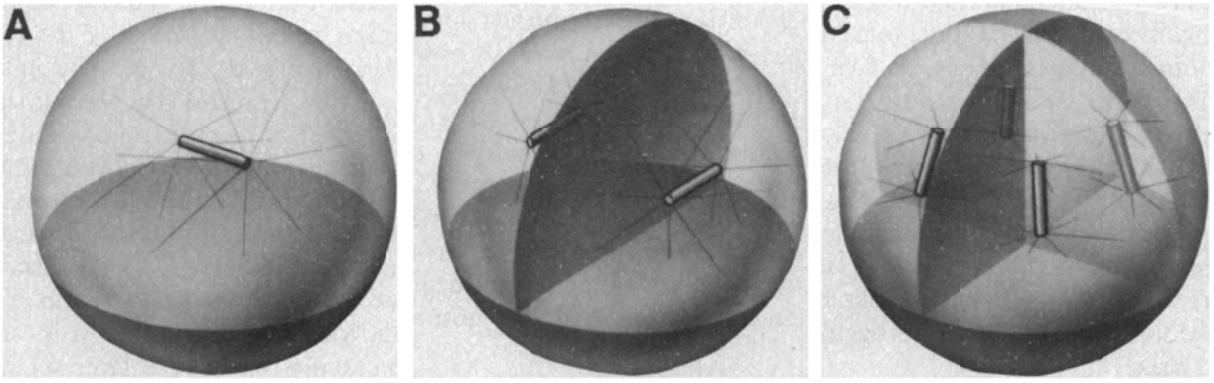

Figure II.30. : *Predicted spindle orientations in a spherical embryo, where the bottom third is filled with yolk, based on a cortical pushing mechanism. Rods indicate spindles, and thin lines schematically represent MTs. The simulations approach the amphibian cleavage pattern. (Adapted from (Bjerknes, 1986))*

d. Cleavage clock

As seen in chapter I.5.e., retardation of the cell cycle or inhibition of one round of divisions can alter the cleavage patterns. The embryonic cell cycle is paused, typically during the time of one or two rounds of divisions, in sea urchins or snails embryos (Conklin, 1912; Dan and Ikeda, 1971; Freeman, 1983; Horstadius, 1939). The observed modification of the cleavage pattern suggests that the positioning of the nucleus does not only rely on self-organization of the embryos, for instance with respect to shape and cytoplasmic or cortical composition, that would give a delayed non-altered cleavage pattern. Instead, these experiments highlight the presence of a clock for division specification, suggesting that the cues that determine nuclear positioning are under timely regulation. Importantly, the transcription and maturation dynamics of the egg patterning factors are presumably not

altered by the retardation experiments. It is thus possible that the cues that bias division positioning maturate through development, as suggested by some analysis of post-translational modifications of Dishevelled protein in the sea urchin embryo (Peng and Wikramanayake, 2013).

e. Adhesions

Division positioning appears to be determined by shape and additional cell-intrinsic polarity cues. However, cell-extrinsic factors may play a role in some cases. In many species, some cell lines are specified through interaction with other cells, in a process called conditional specification. In the 4-cell stage of the *C. elegans* embryo for instance, the P2 stem cell is essential to the proper orientation of the centrosome pair in its neighboring founder cell (EMS) (Goldstein, 1995). The P2 cell is thought to send a signal encoded by a Wnt protein homologue, received by the EMS cell via a homologue of the Frizzled Wnt receptor (Thorpe et al., 1997). The EMS then divides into a MS cell, that produces mesodermal muscles, and an E cell, that produces the intestinal endoderm. The removal of the P2 cell at the beginning of the 4-cell stage leads to the division of the EMS into two MS cells. The P2 cell also specifies the fates of the daughters of the AB cell, as only one of these blastomeres end up contacting the P2 cell. Experimental reversing of the two daughter cells reverse their fates, and the contact with the P2 cell seems to be necessary (Bowerman et al., 1992) and sufficient (Hutter and Schnabel, 1994; Mello et al., 1994) to cell fate determination of the posterior daughter. The mechanisms of spindle positioning mediated by the Wnt signaling cascade may involve cortical pulling on MTs, as MT drug-induced depolymerization prevents the correct spindle orientation. Consistent with that, the spindle positioning response to cell-cell contact does not require new transcription (Sclesinger et al 1999). Actin and the dynactin complex have been found at the cortical site (Waddle et al., 1994), as well as a dynein homolog (Gönczy et al., 1999), suggesting a dynein cortical pulling mechanism. Kinesin-like immunoreactivity has also been found at the centrosomes and cortical site, suggesting the possibility of a depolymerization-induced pulling mechanism (reviewed in (Goldstein, 2000)).

The polarity signal does not always depend on a direct cell-cell contact between an emitting cell and a receptor cell, but can propagate across tissues. For instance in the developing Drosophila wing, the Fat/Dachsous pathway determines the proximal-distal axis, as Dachsous forms a gradient along this axis. The polarized distribution of Dachsous leads to a localization of the myosin Dachs at the cells distal sides, and influences division orientation through cell shape (Mao et al., 2011; Rogulja et al., 2008). Changing the direction of the Dachsous gradient has been shown to alter the direction of cell division (Mao et al., 2011). Similarly, the core planar cell polarity pathway polarizes the localization of the transmembrane protein Frizzled and of the cytoplasmic proteins Dishevelled and Diego, among others, along the proximal-distal axis (Figure II.31.). The core planar cell polarity pathway is also present in the Zebrafish embryo during gastrulation, where an inhibition of Dishevelled activity gave rise to a randomization of cell division orientations (Gong et al., 2004).

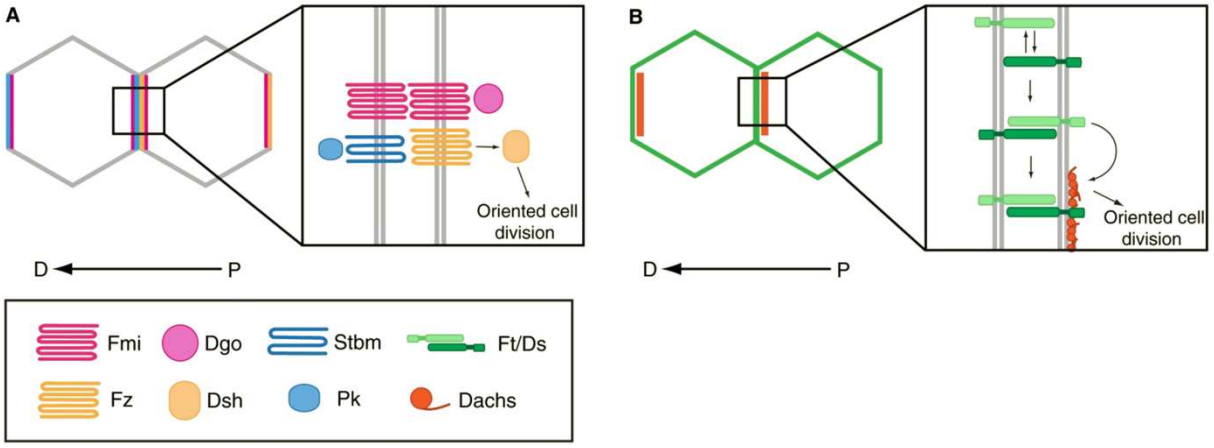

Figure II.31. : *Proximal-distal polarity in the drosophila epithelial tissues, leading to oriented cell divisions. The proximal-distal axis is indicated (D-P).* ***A :*** *the core planar cell polarity pathway.* ***B :*** *the Fat/Dachsous pathway. (From (Gillies and Cabernard, 2011))*

Regardless of any signaling, the interface itself may be used as a cue to polarize the embryo. In sea urchins for instance, the new membrane between two daughter cells does not have the same composition as the external membrane of the embryo, and lacks in particular integrins (Burke et al., 2004), hyalin, PAR6 and Cdc42 (Alford et al., 2009; Burke et al., 2004). In addition to a modification of cell shape due to the different mechanical properties of the outer and inner membranes (Chapter III.), this chemical difference may induce a difference in MT cortical force, and thus bias the centrosome positioning mechanisms.

Similarly, in Drosophila neuroblasts, the NuMA orthologue Mud localizes at the adherens junctions (Chapter III.1.a.) as it requires the adherent junction PDZ protein Canoe (Speicher et al., 2008), and its loss of function leads to a randomization of spindle orientation with regards to the internal polarity axis (Bowman et al., 2006; Izumi et al., 2006; Siller et al., 2006). It has been proposed that Mud interacts with dynein to control spindle orientation, even though this interaction has not been shown yet. However, dynein mutants exhibited the same phenotypes as Mud mutants (Siller and Doe, 2009), and NuMA has been shown to interact with dynein in Xenopus (Merdes et al., 1996). The distribution of patches of Mud around the cell may thus bias spindle orientation through a dynein cortical pulling mechanism.

Interestingly, cells within Drosophila epithelia round up before division. As the cell rounds up, the shape information is lost for the division machinery to orient the spindle with respect to the long axis rule. The Mud adhesion pattern would then be a way for the cell to remember its previous shape and still divide along its long axis. Indeed, within an epithelium, Mud forms patches around the tri-cellular junctions, marking the vertices of the cell in interphase. Alternatively, the rounding up process could be erasing cell shape in order to let the adhesion cues determine the division plane alone. In mammalian cells, a similar rounding is observed prior to division, and the geometry of the adhesion pattern has been shown to define the position of the division (Théry et al., 2005, 2007). Cells indeed remain attached to

their adhesive substrate via retraction fibers. The cell adhesion geometry could be modulated by micropatterning techniques, reproducibly defining zones of adhesion with the substrate. The adhesive pattern was changed, while the overall cell shape was not altered, and the observed orientation of the spindle suggested the adhesion pattern to be the dominant cue, over cell shape, for cell division in this system (Figure II.32.). It has been proposed that cortical pulling mechanisms occur at the zones of cell-substrate adhesion, as this assumption was sufficient to predict the orientation of the division (Théry et al., 2007). The generation of retraction fibers, linking the cortical force generators to the substrate according to the previous shape of the cell in interphase, would then allow the cell to remember its shape as it rounds up and performs mitosis.

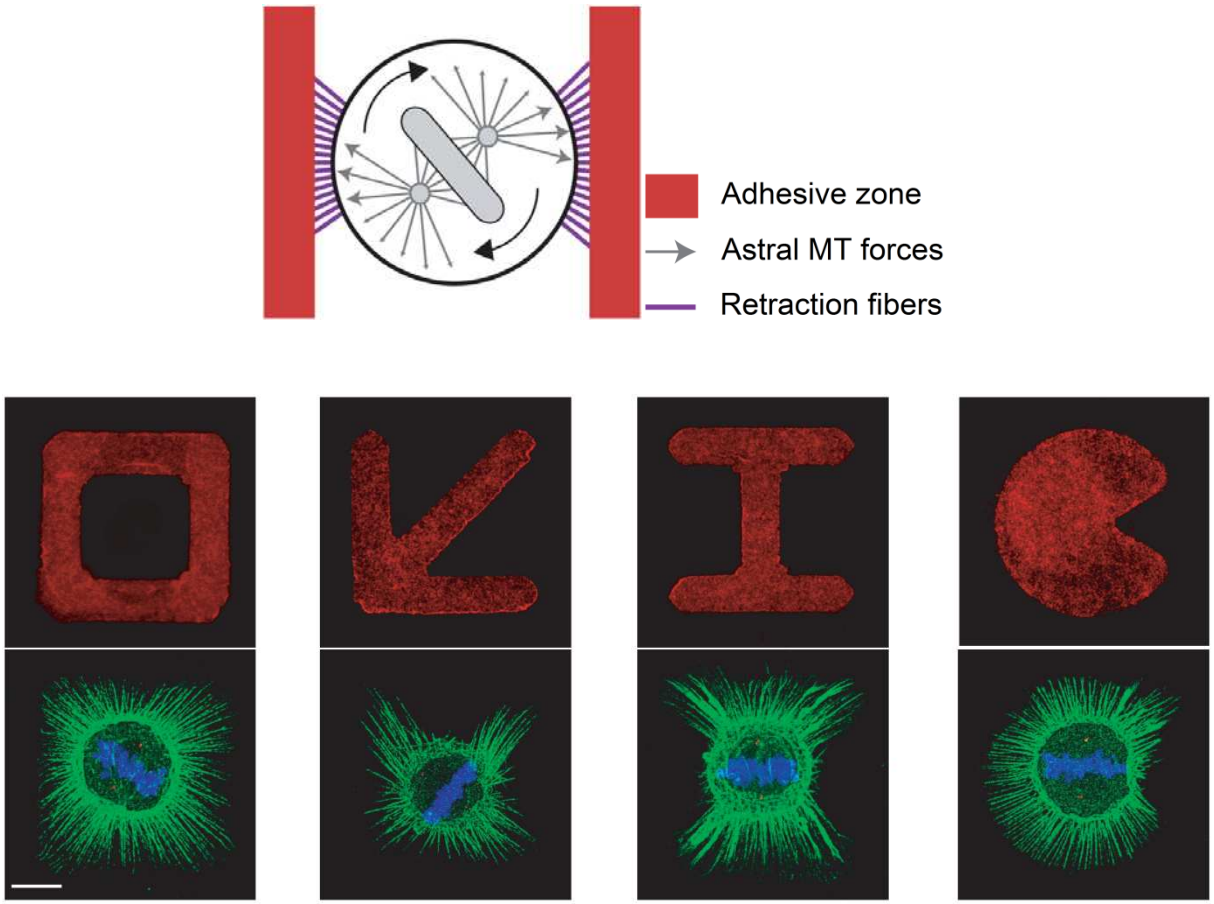

Figure II.32. : *Adhesions orient cell divisions.* ***Top :*** *schematic representation of cultured mammalian cells growing on a semi-adhesive substrate, and orienting their mitotic spindles with respect to the adhesive zone geometry. The cells round up during mitosis and keep a sense of the adhesion pattern through retraction fibers. (Adapted from (Morin and Bellaïche, 2011))* ***Bottom :*** *Microfabricated semi-adhesive substrates with different adhesive geometries (in red, upper panels), and fixed cells undergoing division on these patterns (lower panels), with actin stained in green, DNA in blue and spindle poles in red. The division axis is related to the adhesion pattern. (Scale bar : 10 µm adapted from (Théry et al., 2007))*

The mechanisms of cell division positioning thus appear to rely both on cell shape, through length-dependent astral MT forces that tend to center the nucleus, and on other additional intrinsic or extrinsic polar cues that bias the forces to yield a variety of division patterns. Concerning the extrinsic adhesion-related cues, it is interesting to note that the neighboring cells determine the shape of the dividing cell as they impose a contact plane, in a given packing. As cells divide according to the long axis rule, the arrangement of the embryo and the cell-cell mechanical interaction may bias the division, as seen in the next chapter.

III. CELL SHAPE

1. Cell-cell adhesion

a. Effectors

The adhesion of cells to their environment is mediated by several families of cell adhesion molecules, such as integrins, cadherins and syndecans. There are two main types of adhesion junctions : the tight junctions and the anchoring junctions.

The tight junctions are found for instance below the apical surface of epithelial cells, where they form a continuous band around the cell (Figure III.1.). They tightly link the neighboring cells to prevent the passage of ions and molecules trough the epithelium, so that materials must cross the cells to pass the epithelial layer, allowing transport specificity. They also constitute a barrier to the diffusion of membrane proteins between the apical and basal sides of the cells, maintaining the specialization of both surfaces. The tight junctions are composed of rows of transmembrane proteins, assembled in a branched network. The transmembrane proteins are various, but the four main families are the claudins, the occludins, the junctional adhesion molecules and the tricellulins. These proteins are embedded in both plasma membranes of the two adjacent cells, and they link the cytoskeletons of the two cells as their cytoplasmic parts interact with the actin cytoskeleton via several proteins (Günzel and Fromm, 2012). The transmembrane proteins interact with each other by their extracellular domains, whether between proteins of the same kind or between different types of proteins, to make an impermeable barrier to fluid.

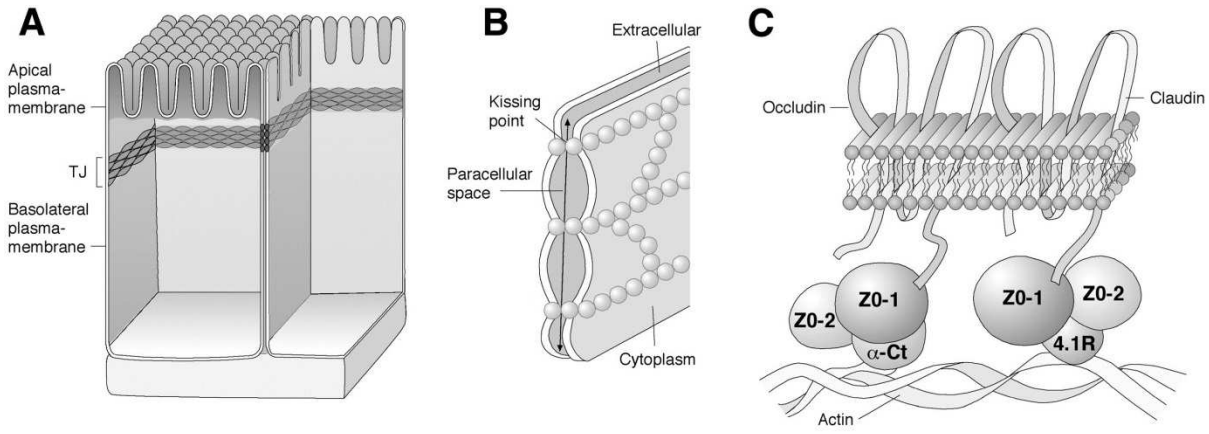

Figure III.1. : *Schematic representation of the tight junctions.* ***A :*** *tight junctions form a band at the apical side of epithelial tissues.* ***B :*** *The band is made of a branching network of rows of transmembrane proteins.* ***C :*** *The two main families of transmembrane proteins present in tight junctions are claudins and occludins, and they are linked to the cytoskeleton via various proteins. (Adapted from (Rajasekaran and Rajasekaran, 2003))*

The anchoring junctions are more permeable to fluids, and ensure the adhesion of cells to their neighbors or to the extracellular matrix. There are three types of anchoring junctions. The desmosomes link two neighboring cells via the interaction of trans-membrane cadherins coming from each cell. Cadherins depend on Ca^{2+} to function, and display calcium-binding domains in their extracellular bulk. In the cytoplasm, the cadherin tails are anchored to an outer structure made of membrane-associated attachment proteins such as plakoglobin and plakophilin, that is bound to an inner structure via the desmoplakin protein. In the inner structure, desmoplakin binds to the intermediate filament network, in particular to keratin or desmin filaments. The hemidesmosomes are another type of anchoring junctions, that link the cell to the extracellular matrix. They are found in particular in epithelial cells, where they attach the basal surface of the cell to the basal lamina. The link is made through trans-membrane integrins instead of cadherins. The extracellular domain of integrins can attach to various adhesive proteins of the extracellular matrix. The intracellular domain interacts with two rivet-like plaques (the inner and outer plaques) where keratin intermediate filaments are anchored. The structure and composition of the hemidesmosome, in particular of the plaques, is variable. Finally, the adherens junctions bind whether a neighboring cell or the extracellular matrix to the actin cytoskeleton of the cell (Figure III.2.). When binding adjacent cells, the junctions can form spots or bands around the cell. They involve trans-membrane cadherins, which interact in the extracellular zone to link the two cells together. In the cytoplasm, they bind to β-catenin, δ-catenin and γ-catenin, and anchor the actin filaments via α-catenin that attaches to β-catenin or γ-catenin (Harris and Tepass, 2010; Nelson et al., 2013). When binding a cell to the extracellular matrix, the adherens junctions form spots called focal adhesions. These focal adhesions can contain over 100 different proteins, but generally rely on trans-membrane integrins to link the cell to the matrix. In the cytoplasm, the integrins attach to the actin cytoskeleton via various adapter proteins, such as talin, α-actinin, filamin, vinculin or tensin.

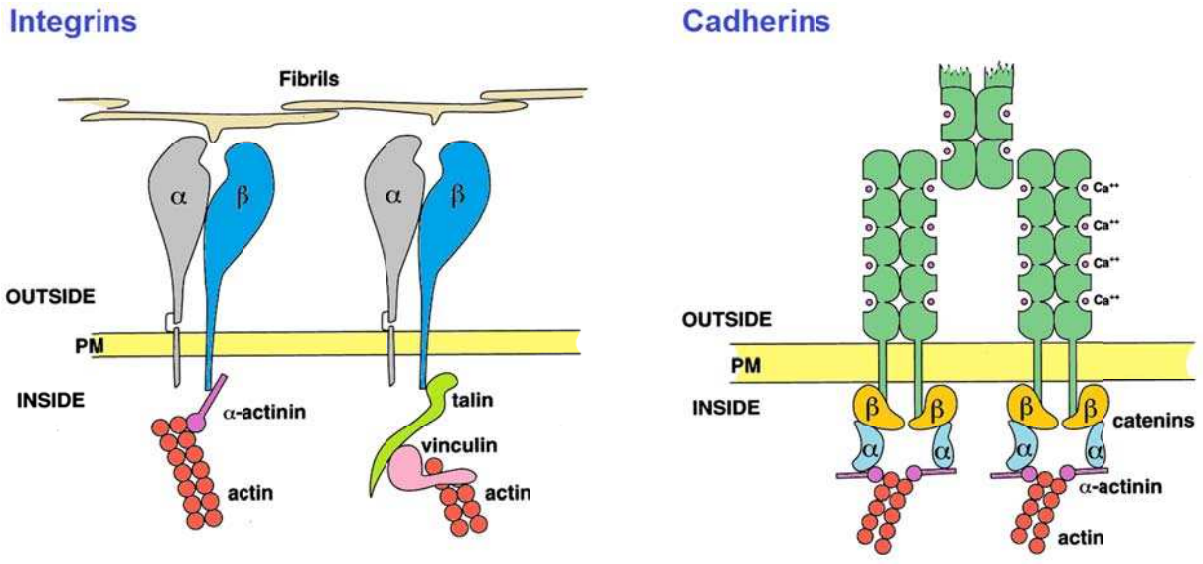

Figure III.2. : *The two main types of transmembrane proteins, found in adherens junctions, desmosomes and hemidesmosomes. The transmembrane proteins are linked to the cytoskeleton, whether to intermediate filaments via the desmosomes and hemidesmosomes rivet-like structures, or to actin as illustrated above. Integrins are generally involved in cell adhesion to the extracellular matrix, while cadherins mediate cell-cell adhesion. Cadherins are calcium-dependent. (Adapted from (Aplin et al., 1998))*

b. Effects on shape

The first effect of adhesion is to hold adjacent cells together. In the zebrafish embryo, the force required to separate cell doublets has been measured in different cell types (Maître et al., 2012), and found to be dependent on the accumulation of cadherins in the ring-shaped margin of the cell-cell contact, as well as on the mechanical resistance of the bond between cadherins and the actin cytoskeleton. The presence of such adhesions at the cell-cell contact prevents cell dissociation, and to a lesser extent cell rearrangement, since cadherins do not appear to diffuse freely within the membrane. Adhesions thus contribute to tissue viscosity.

In addition, the adhesion between adjacent cells generally tends to make the cell-cell interface bigger (Bertet et al., 2004; Hayashi and Carthew, 2004), resulting in a change in cell shape, as the cell keeps a constant volume. Such a modification of shape may bias the positioning of the pair of asters in the context of a cytoskeleton-dependent mechanism, like MT cortical pushing or cytoplasmic pulling, where the forces applied by individual MTs depend on MT lengths. In snails, by changing the Ca^{2+} concentration of the solution where the eggs were developing at the 2-cell stage, the area of the cell-cell contact was modified (Meshcheryakov, 1978). At the 8-cell stage, treatment with trypsin disrupted cell-cell contacts and changed cell shapes as well. These two experiments, that modified cell shape by changing in cell-cell adhesion, yielded a different cleavage orientation, with spindles oriented parallel to the longest interface, in line with Hertwig's long axis rule.

2. Cortical tension

a. Origin and measurement

Cortical tension appears to originate from the actin-myosin network underneath the cell membrane (Evans and Yeung, 1989; Pasternak et al., 1989; Stewart et al., 2011; Tinevez et al., 2009). It depends on both the density of the network and its structure (Clark et al., 2014; Salbreux et al., 2012). The definition of cortical tension usually comprises the contractility of the acto-myosin network and the tension of the membrane itself. Several methods have been developed to measure cortical tension. The most classic estimation is by micropipette aspiration, where the pressure required to suck the cell into the pipette is determined and linked to the surface tension under liquid behavior assumptions (Evans and Yeung, 1989) (Figure III.3.). Cortical tension can also be measured by atomic force measurement indentation, where the stiffness of the surface is assessed with a cantilever (Krieg et al., 2008), or by laser ablation. In blebbing cells, membrane tension has been measured by tethering the membrane with laser tweezers (Dai and Sheetz, 1999), allowing access to the tension of the membrane and the attachment force to the actin cytoskeleton, but not to the whole cortical tension. Membrane fluctuations have also been measured by interferometry, to assess the cortical tension of blebs (Peukes and Betz, 2014). In tissues, cortical tension could be estimated by compression between two plates, as the force required to maintain the compression, at tissular equilibrium, depends on surface tension (Davis et al., 1997). Finally, tissue surface tension can be measured by classic measurement techniques used for fluids, such as the gravity-induced droplet deformation (David et al., 2009). The measured cortical tensions range from 0.02 mJ/m^2 to 4.1 mJ/m^2, depending on species and cell type (Krieg et al., 2008; Lomakina et al., 2004; Pasternak et al., 1989).

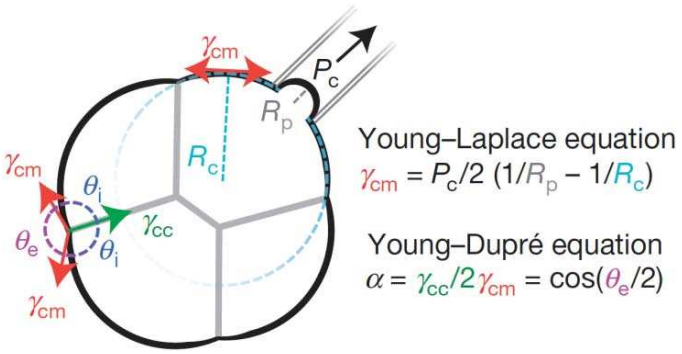

Figure III.3. : *Principle of the measurement of cortical tension by pipette aspiration. By adjusting the aspiration pressure P_c, and measuring curvature of the cell, the external tension is induced. The contact angles between adjacent cells link the cell-cell interface tension to the external tension. (From (Maître et al., 2015))*

b. Interplay with adhesion

Interestingly, cell-cell interfaces usually have a different surface tension than cell-medium interfaces. Upon separation of a Zebrafish cell doublet for instance, the curvature of the region where the cells were contacting increases abruptly and ends up higher that the curvature of the rest of the cell, suggesting a lower tension in this region compared to cell-medium tension (Maître et al., 2012). Consistently, the cortical accumulation of myosin II was found higher at the cell-medium interface than at the cell-cell contact. The actin density and/or myosin activity are downregulated at the cell-cell interfaces in many systems (Chaigne et al., 2013; Hidalgo-Carcedo et al., 2011; Maître et al., 2012; Toret et al., 2014; Yamada and Nelson, 2007). The cortex density at cell-cell interfaces has been shown to be inversely related to the expression level of cadherins in Xenopus aggregates (David et al., 2009). Adhesive molecules thus act as signaling molecules at the cell-cell interface to regulate cortical tension.

The observed difference in cortical contractility may be responsible for much of the cell-cell adhesion. Indeed, the binding energy of a cadherin pair has been estimated to be around 5×10^{-20} J (Sivasankar et al., 1999). Given the observed cadherin density, and the cells typical cortical tension, this adhering force is generally way lower than the adhesion required to bind cells together (Maître et al., 2012; Stirbat et al., 2013; Youssef et al., 2011). Cadherin adhesion alone would give the geometries of adhesive spheres, with small contact areas. To account for the observed spreading cell-cell interfaces, the difference in surface tensions between the cell-medium interface and the cell-cell contact should be higher. Indeed, the condition of equilibrium of the ring margin of the cell-cell contact imposes a balance between the surface tensions of the three connecting interfaces, modulated by contact angles (Figures III.3. and III.4.). A spread cell-cell interface then must have a low surface tension, compared to the cell-medium interface cortical tension. Adhesion alone does not lower the surface tension enough to account for observed contact areas and angles, and the effect of cortical elasticity has been shown to be negligible (Manning et al., 2010). The downregulation of actin at the cell-cell interface may thus be the main mechanism generating the wide cell-cell adhesive contacts that most tissues display. The process of cell-cell adhesion is thus an integration of the binding effect of adhesive molecules and of the modulation of cortical tension they induce by signaling (Amack and Manning, 2012).

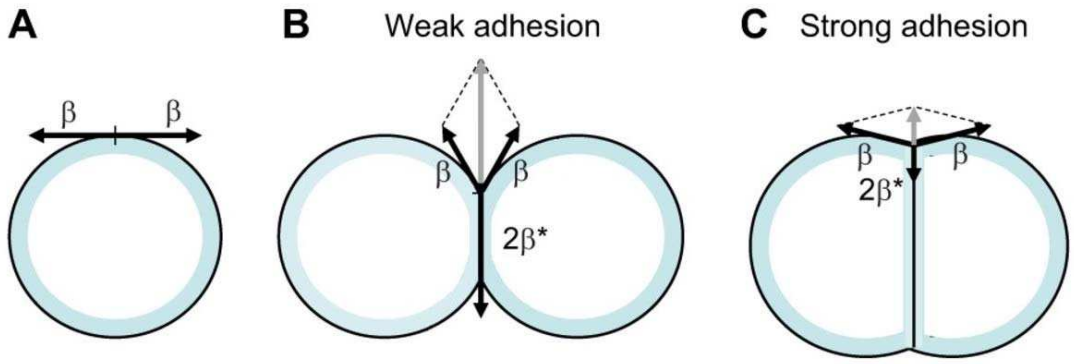

Figure III.4. : *The equilibrium of the ring margin of the cell-cell adhesion gives a relationship between the cell-medium cortical tension β, the cell-cell interface tension 2β* and the contact angle. A stronger adhesion, that reduces β*, increases the contact angle and widens the contact area. (From (Winklbauer, 2015))*

In the case of tissues or cell aggregates, cortical tension appears to influence cell shape in a liquid-like manner (Graner, 1993; Steinberg, 1978). Indeed, tissues can be described in terms of surface tension equilibriums, even though the underlying mechanisms are completely different since cells actively maintain their cortical tension by constant contraction of the acto-myosin network. The analogy between cell aggregates and liquids allows for instance to understand the observed rounding of the aggregates (Manning et al., 2010), that minimizes the tissue-medium area of contact to minimize the overall energy of the system. In particular, in an approximation known as the differential adhesion hypothesis, tissues or cell aggregates can be described as liquids, where surface tension is determined by the overall cohesion, that is, the interactions between the components. In this context, it is the depletion of neighboring interfaces induced by the creation of the tissue-medium interface that defines the cortical tension of the tissue (Figure III.5.). This cortical tension thus depends directly on cell-cell adhesion. The differential adhesion hypothesis has been shown to be valid in various cell lines (Borghi and James Nelson, 2009; Duguay et al., 2003; Forgacs et al., 1998; Foty and Steinberg, 1997; Foty et al., 1994, 1996, 1998; Schoetz, 2008; Schötz et al., 2008), and a linear relationship between the expression of cadherins and tissue cortical tension has been demonstrated for aggregates of L cells (Foty and Steinberg, 2005). A similar dependence has been found in zebrafish and Xenopus gastrula tissue (David et al., 2014; Schötz et al., 2008). This approximation of a liquid tissue behavior considers cells as point objects, only takes into account the number of cell-cell contacts and ignores their lengths. In some particular cases, where cells are stretched for instance, the differential adhesion hypothesis fails to account for observed behaviors (Manning et al., 2010; Stirbat et al., 2013; Wayne Brodland and Chen, 2000), and the actual cortical tension of individual cells must be considered, as described previously. In this alternative theory, it is the cortical tension of cells, instead of the cell-cell adhesion, that determines the surface tension of the tissue.

Tissue cortical tension displays a wide range of variations depending on cell type. Xenopus gastrula endoderm have a typical surface tension of about 0.05 mJ/m^2 (David et al., 2014), while limb bud tissue in chick embryos show surface tensions as high as 20 mJ/m^2 (Foty et al., 1996). Embryonic tissues generally have tensions within that range, but other cell types, such as cancer lines, can display even higher tensions. For instance the surface tension of ependymoma cells is about 56 mJ/m^2 (Hegedüs et al., 2006).

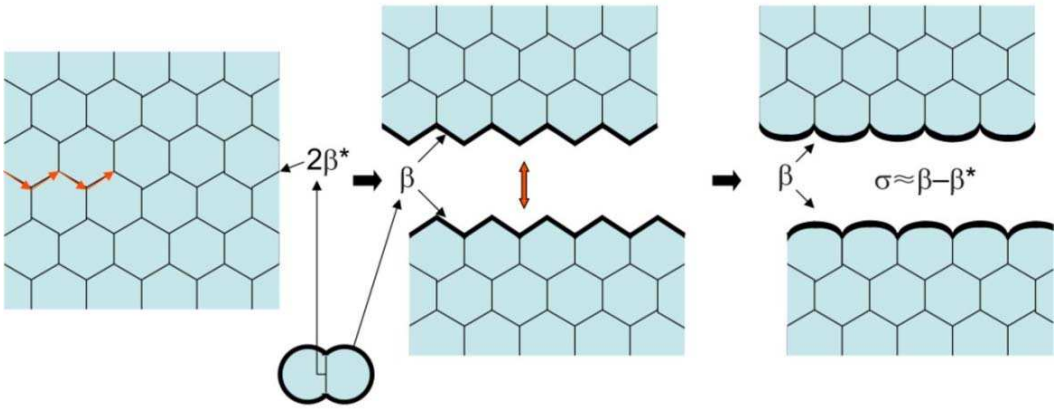

Figure III.5. : *In the differential adhesion hypothesis, cells aggregates are considered as liquids, where the creation of a cell-medium interface induces a depletion in the number of cell neighbors and increases the surface tension by β-β*, with β the cell-medium tension and β* the cell-cell tension. (From (Winklbauer, 2015))*

c. Effects

In addition to favoring the adhesion of adjacent cells, cortical tension mediated by acto-myosin is also involved in cell surface contractility. Prior to mitosis, the rounding of cells observed in many cell types such as mammal cultured cells or drosophila epithelia is a result of the global contractility of the surface. The contraction of the actin network increases the surface energy of the cell and induces a minimization of this energy by minimizing cell surface area, which, within the constraint of hydrostatic pressure, corresponds to a rounded up shape (Ramanathan et al., 2015; Stewart et al., 2011). In the 8-cell stage mouse embryo, the cells undergo compaction, that has been proposed to originate from an energy minimization process (Goel et al., 1986) dependent on cadherins within the differential adhesion hypothesis (Foty and Steinberg, 2005; Steinberg and Takeichi, 1994). Recent measurements of cortical tensions with micropipettes rather favor a role of the embryo-medium increasing cortical tension (Maître et al., 2015) (Figure III.6.), consistent with actin depolymerization and myosin inhibition experiments that block compaction.

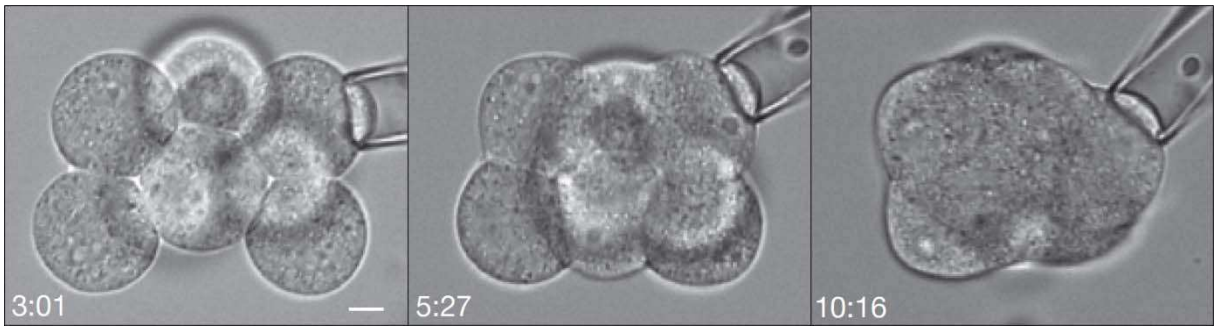

Figure III.6. : *The mouse embryo undergoes a compaction at the 8-cell stage, arising from an increase in cortical tension, that can be measured by pipette aspiration. (Scale bar : 10 µm, from (Maître et al., 2015))*

The spatial distribution of cortical contractility plays a major role in cell shape. During cytokinesis for instance, a ring of contractile acto-myosin squeezes the cell into two daughter cells (Chapter I.1.d.). During the blebbing-driven migration of cells, the blebbing behavior that allows the cell to protrude and move forward is generated by a difference in cortical tension between the bleb and the rest of the cortex (Paluch and Raz, 2013). The bleb is usually devoid of actin cortex, whether because the cortex is ruptured at the site of blebbing, or because the bleb is formed by detachment of the membrane from the cortex. Thus its surface tension is only due to the membrane resistance to deformation, and is lower than the acto-myosin-mediated tension of the non-blebbing surface, resulting in an expansion of the bleb under hydrostatic pressure. The cortical tension can also form gradients. In the sea urchin embryo, the vegetal pole displays a higher cortical tension than the animal pole. In the *C. elegans* zygote, the posterior cortex has a lower cortical tension than the anterior cortex (Mayer et al., 2010; Munro et al., 2004), possibly influencing MT nuclear positioning forces (Chapter II.5.a.).

In many epithelial tissues of developing embryos, such as Xenopus, chick or drosophila, the actin-myosin network contracts at the apical site during a process called apical constriction (Martin and Goldstein, 2014), yielding a shrinkage of the apical surface that allows to generate a folded epithelium from a plane one as the lateral sides of cells remain tightly bound (Alvarez and Navascués, 1990; Hardin and Keller, 1988; Kam et al., 1991; Lewis, 1947; Sweeton et al., 1991; Wallingford et al., 2013). The change in cell shape induced by apical constriction also plays a role in diverse epithelial mechanisms such as cell delamination or internalization, or wound healing (Davidson et al., 2002; Harrell and Goldstein, 2011; Toyama et al., 2008) (Figure III.7.). Cell rearrangement within tissues is also mediated by cortical tension. For instance in the case of neighbors exchange in epithelial tissues, the boundary between the two cells undergoes acto-myosin-driven constriction, until the formation of a 4-cellular junction (Bertet et al., 2004; Lecuit and Lenne, 2007; Marmottant et al., 2009), from which a new boundary can elongate (Figure III.8.). A last tissular mechanism mediated by a differential spatial distribution of cortical tension is the cell sorting or engulfment in cell aggregates. In the 16-cell stage mouse embryo, cells display differences in cortical contractility, due to the possibly asymmetric separation of the 8-cell stage apical domain between daughter cells. The unpolarized blastomeres, that display higher cortical levels of myosin, have been shown to be internalized into the embryo, supposedly as a result of their higher surface tension (Maître et al., 2016). Indeed, simulations based on geometrical balance of cortical tensions showed the engulfment of the cell with higher cortical tension into the other cell in the case of a cell doublet and its internalization in the case of a cell aggregate. This phenomenon was complete in both cases when the difference in external cortical tension between the cells in contact was reaching a given threshold (about 1.5 in tension ratio). These findings were confirmed by individual tracking of cells after having measured their surface tensions, and by transplant of low tension mutants (mMyh9) blastomeres into WT embryos, and of WT blastomeres into mutant embryos, showing a preferential internalization of the blastomeres of higher cortical tension, while the blastomeres of lower cortical tension preferentially stay outside.

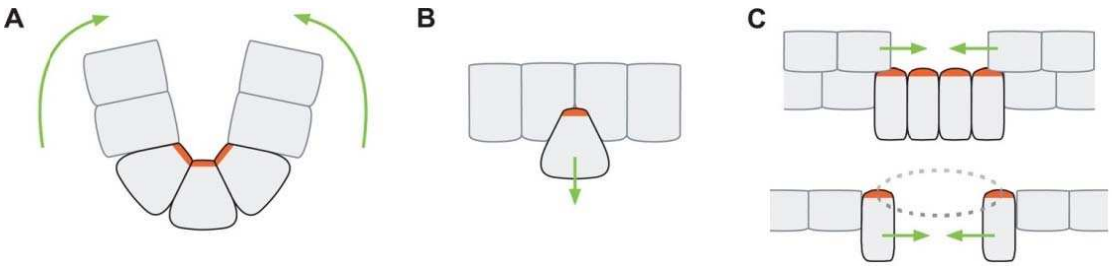

Figure III.7. : *Roles of apical constriction and its effect on cell shape. The contraction of one side of epithelial cells can give rise to folding and invaginations of the surface* ***(A)****, or to delamination of the contracting cells* ***(B)****. The narrowing of the apical surface is also implied in wound healing* ***(C)****. (Adapted from (Martin and Goldstein, 2014))*

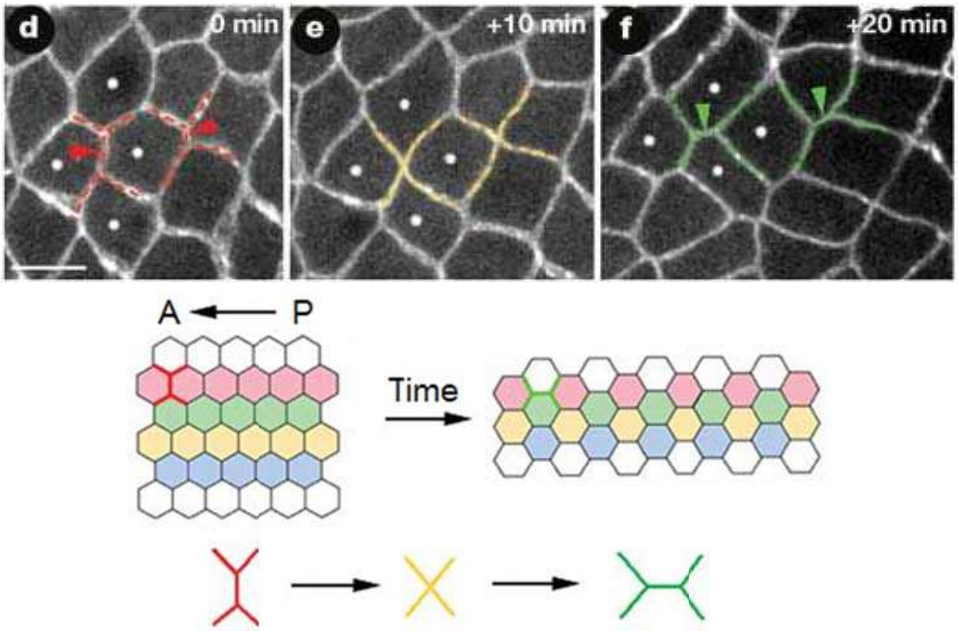

Figure III.8. : *Constriction of cell-cell contacts (indicated by red arrows), followed by relaxation of the contacts (green arrows) allows cell-cell intercalation within tissues. Upper panels show a cell-cell intercalation process in an epithelium of the developing drosophila, with cells of interest marked by a white dot. Lower panels show how such a mechanism contributes to tissue elongation, along the antero-posterior axis. (Scale bar : 5 µm, adapted from (Bertet et al., 2004))*

Interestingly, both the cortical tension and cell-cell adhesion approaches described in chapter III.2.b efficiently account for tissue behavior such as the rounding up of cell aggregates, cell sorting and engulfment. Altogether, these results suggest that the size of cell-cell contacts and the arrangement of the blastomeres depend on surface properties of the cells, that are cortical tension and adhesion, acting together with internal hydrostatic pressure. The resulting shapes of individual blastomeres within the cell packing can thus be accurately predicted from purely mechanical considerations.

IV. THE SEA URCHIN AS A MODEL ORGANISM

Sea urchin is a classic model organism to study embryonic development. It has been extensively used, as well as other echinoderms such as starfish and sand dollars, in the early studies of cleavage and gastrulation in the XIXth and XXth centuries.

1. General presentation

a. Phylogeny

Sea urchins are echinoderms, a phylum that is part of the deuterostome superphylum of animals, along with hemichordates and chordates (the phylum that contains vertebrates) (Figure IV.1.). The echinoderm phylum comprises five extant classes : echinoids (sea urchins), asteroids (starfish), holothurians (sea cucumbers), ophiuroids (brittlestars) and crinoids (sea lilies). Modern echinoderms find their origin in lower Cambrian, and the five groups radiate in a rather short period of time (525–480 Ma) (Erwin et al., 2011). However, modern subgroups and species apparition is more recent within each class. For instance crinoids and echinoids are thought to have radiated after the Permian/Triassic extinction (approx. 250 Ma) (Kroh and Smith, 2010; Rouse et al., 2013). At the same period, asteroid evolution may have undergone a bottleneck (Twitchett and Oji, 2005). As the separation of the five classes of modern echinoderms is ancient and happened in a relatively short time span, the phylogenetic relationship between these classes is unclear, in particular relative to the position of ophiuroids (Figure IV.2.). Recent studies support the hypothesis of an ophiuroids and asteroids common phylum (Telford et al., 2014). Within the echinoid class, species from most of the infraclasses display a five-fold symmetry, and are called regular echinoids. In the Irregularia infraclass however, this symmetric pattern is deformed to create a bilateral symmetry. Among these irregular echinoids are found sand dollars, sea biscuits, and heart urchins. The term sea urchin can refer whether to the whole echinoid class, or to the regular echinoids that do not form a monophyletic phylum.

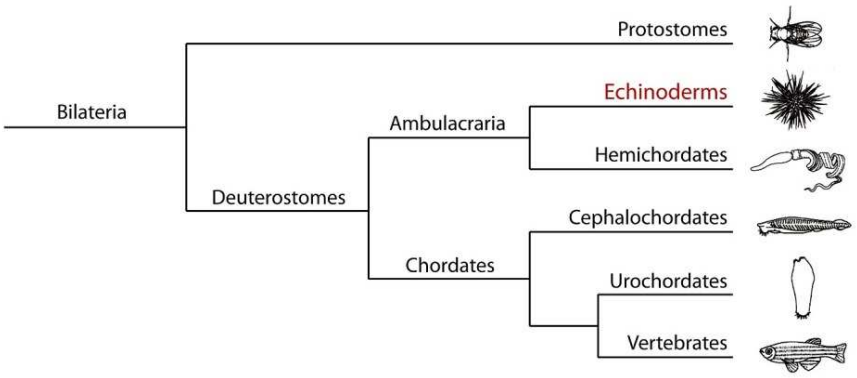

Figure IV.1. : *Position of echinoderms in the phylogenetic tree of bilaterians. (From (Lapraz et al., 2009))*

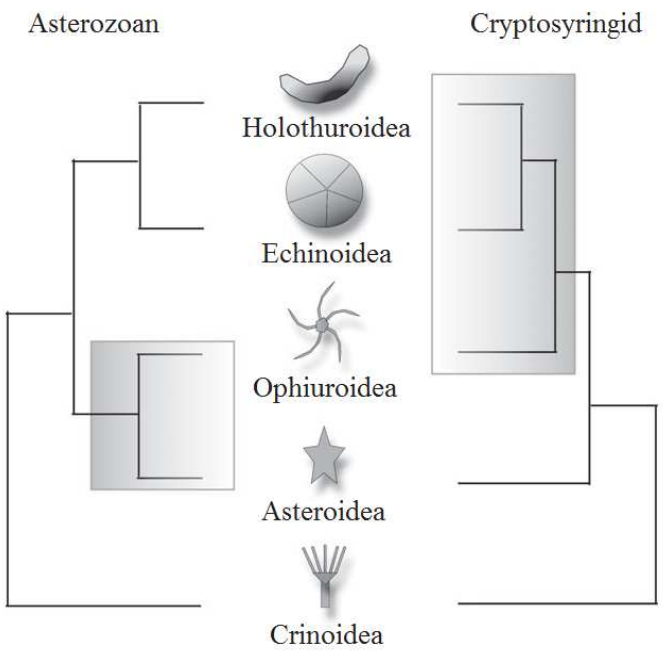

Figure IV.2. : *Two possible phylogenetic trees linking the five extant classes of echinoderms. The place of ophiuroids is debated although recent studies support the asterozoan hypothesis. (From (Telford et al., 2014))*

b. Life cycle

Sea urchins species are gonochoric, and usually spawn eggs or sperm into sea water. In some species, female urchins retain their eggs between their spines, offering them protection as they develop, but in most species the eggs are released directly into open water, where the fertilization occurs. Female urchins typically give millions of eggs, and the chances of fertilization are further increased by gathering of adults during the reproductive season and/or synchronization of eggs and sperm spawning, usually with respect to the lunar cycle and season. The eggs have a diameter of about 100 µm, and upon fertilization, they grow a rather broad fertilization envelope. Only the sperm head penetrates the egg, and the sperm aster centers typically within 10 minutes. The sea urchin egg does not display any anisotropic yolk accumulation in most species. Instead, yolk is homogeneously distributed within the cytoplasm, and the embryo cleaves in a radial holoblastic manner. Early divisions are rapid, taking usually about 30 min, yielding a swimming blastula within hours.

The blastula then undergoes gastrulation (Figure IV.3.). The gastrulation process starts with the epithelial-to-mesenchymal transition of the epithelial tissue, that is the ingression of some cells, called the primary mesenchyme cells, at the vegetal pole. This process is driven both by apical constriction (Chapter III.2.c.), and by a reduction of attachment to the lamina and the hyalin layer (Burdsal et al., 1991; Fink and McClay, 1985; Hertzler and McClay, 1999; Katow and Solursh, 1980) combined with an increase of affinity for the basal matrix (Burdsal et al., 1991). These internalized cells will later form the mesoderm. The epithelial-to-mesenchymal transition is followed by an invagination of the vegetal membrane, forming the anus, that progresses until the opening of the mouth. Gastrulation is usually complete within a day, and the swimming larva can feed. The mesoderm cells form the skeleton of the larva and enhance its cone-shape by growing up to 12 arms. At this stage, the sea urchin larva displays a bilateral symmetry, and is called echinopluteus. It features bands of cilia allowing it to swim and feed on its own, and typically spends several months before its development is complete.

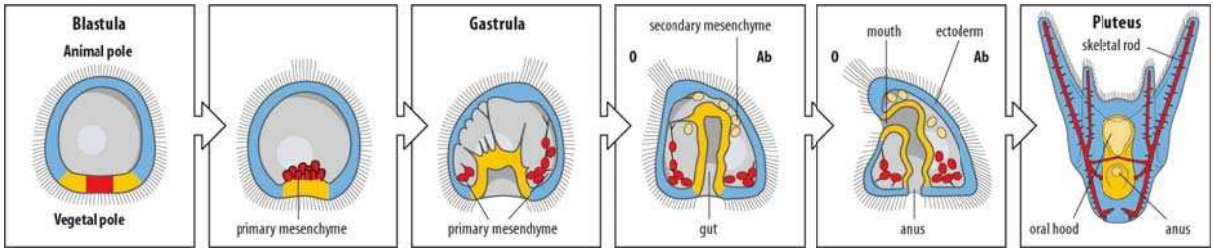

Figure IV.3. : *Gastrulation in the sea urchin embryo. The primary mesenchyme cells (depicted in red) are internalized and will form the skeleton of the larva. The vegetal membrane (depicted in yellow) invaginates and forms the anus, and then the mouth. The oral-aboral axis is indicated (O, Ab), the ectoderm-forming tissues are depicted in blue. (From (Staveley))*

During larval development, the juvenile sea urchin develops on the side of the echinopluteus (Figure IV.4.). This adult rudiment displays a five-fold radial symmetry. When fully developed, the larva sediments and starts the metamorphose process on the seabed. The larval gut and arms degenerate and only the juvenile remains, in a process that can be as quick as one hour. This young sea urchin, that already has all the characteristic of an adult, will then grow to its adult size. In some species, sea urchins continue to grow their whole life. Sexual maturity is usually reached in about five years, and the sea urchin life expectancy is rather long, reaching 100 years in some species.

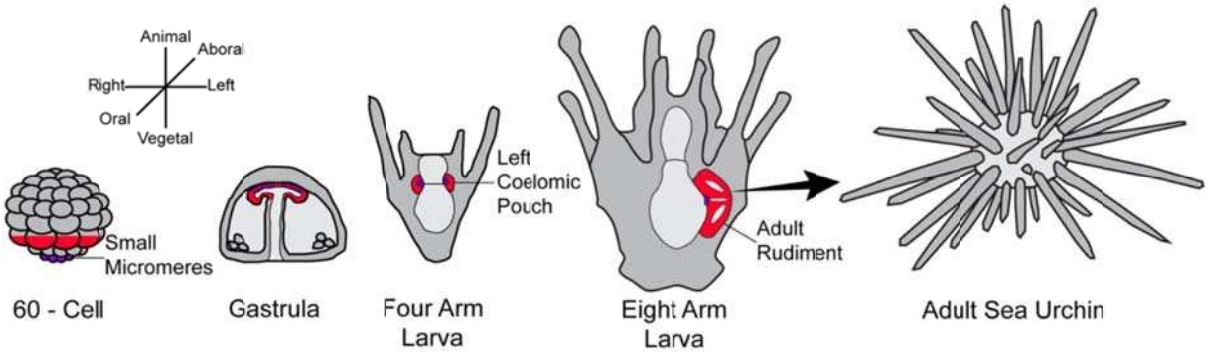

Figure IV.4. : *Development of the adult rudiment inside the larva. Tissues implied in the formation of the adult are shown in red and violet from the 60-cell stage. The juvenile sea urchin gets out of the larva after its sedimentation, and grows to become an adult sea urchin (From (Warner et al., 2012))*

2. Advantages and drawbacks

a. A minimal system

In addition to displaying an interesting five-fold symmetry, featuring an extremely complex non-adaptive immune system, and being closely related to chordates, making them a relevant model organism to study vertebrates and their evolution, sea urchin eggs and embryos are particularly adapted systems for studying early development and cell division in general. First, the model is relatively simple, as early embryos are small, with a restricted number of interacting cells, and are isolated systems since the external medium almost does not interact with the cleaving embryo. In contrast, models such as epithelial tissues are bigger, feature more cells, and are not isolated as cells migrate in and out the field of view. Moreover, the epithelial layer undergoes forces that cannot be assessed, coming from the sides, since the whole epithelium cannot generally be observed, and from the tissues underneath. The simplicity of the early embryo makes it an easier model to handle, in particular when it comes to numerical modeling.

In addition, the early development in the sea urchin embryo is simpler than in some other embryos in terms of biological effectors at play. These embryos appear to have a rather homogenous cytoplasm, with no clear yolk accumulation, and no obvious cytoplasmic or cortical rearrangements upon fertilization. The genome of the embryo is not expressed during early cleavage, so that it is easier to make hypotheses of self-organized cleavage and morphogens segregation based on the regulatory layers present at fertilization. The sea urchin embryo displays a stereotypical example of cortical polarity that is the maternal polarity cap at the vegetal pole. The cap has a precise spatial localization and appears to drive micromeres formation, which is an obvious phenotype. Thus, this embryo is an excellent model organism to elucidate the mechanisms of maternal polarity, through experiments challenging micromeres formation. Studying this simple polarized system is relevant to other cell types displaying cortical polarity (Chapter II.5.a.), yet possibly being more complicated systems. The embryos barely grow from the zygote to the blastula, and cleavage only divides the egg volume into numerous smaller cells, adding to the simplicity of numerical modeling.

Finally, the cleavage pattern of sea urchin embryos is highly reproducible, up to the 7^{th} round of divisions, facilitating both experiments and simulations, while in other species like Xenopus the 8-cell stage already displays noise in the pattern.

b. Technical advantages

In addition to being a minimal system, the sea urchin embryo has also many technical advantages. Sea urchins spawn unfertilized eggs and sperm directly into sea water, which makes it way more practical to obtain gametes and perform fertilization under the microscope than in the case of mammals for instance. The embryos do not need specific medium and simply develop in sea water. Unfertilized eggs can be kept for typically a day, and sperm for a week, and indefinitely if frozen. In some sea urchin species, the gametes are available at specific seasons, but for some others they are available all year long, especially as sea urchins can be bred in tanks and artificially synchronized by mimicking the moon cycle with light. A single female can generate millions of eggs in one batch, and these eggs can all be fertilized at the same time by adding sperm in the sea water. The eggs will then remain synchronized

during the early embryonic divisions, typically up to the 16-cell stage. Having a large number of synchrone eggs is a key asset to perform systematic experiments in a rather short time, and thus sea urchin embryos better allow to obtain statistically relevant data than other embryos such as mouse.

Moreover, the cell cycle is rapid, and divisions occur every 30 minutes in average, allowing to record the whole early embryonic development in less than a day. To make the sea urchin embryo even more imaging-friendly, the eggs are transparent, and relatively small (typically 100 µm), so that they fit in the field of view of a typical microscope up to 20x magnification, and can be completely imaged in depth with little optical deformation. By contrast, the large eggs of Xenopus or Zebrafish require lower resolution or mosaic imaging. The Xenopus eggs are not transparent, and must be sliced to allow deep imaging.

Finally, the sea urchin embryos allow to perform perturbation experiments. They are big enough to be micromanipulated with needles, and thus can be mechanically deformed and injected. Injection of proteins or mRNA is possible in these systems, and sea urchin eggs are able to absorb radioactive isotopes or fluorescent dyes readily, unlike Xenopus eggs for instance. They are also extremely robust, so that severe perturbation, like detergent treatment or cutting the egg in two with a needle, does not prevent cleavage. The sea urchin embryo is practical to manipulate and allows a great variety of experiments, thus making it a good system to explore the mechanisms and effectors of early cleavage and cell division in general.

c. Drawbacks

The life cycle of sea urchins is long, as they need several years to reach their sexual maturity. As a consequence, genetic studies on sea urchins are difficult, in comparison with organisms like fishes or mice where the time between two consecutive generations is about three months, or flies that can reproduce within two days. Moreover, male and female sea urchins cannot usually be distinguished, which does not facilitate genetic experiments. The adults, despite being able to live in aquariums, are very sensitive to environmental conditions, like ionic composition of the sea water. In particular, they do not survive well to a sudden change in water temperature of a few degrees, and must be kept at rather constant temperature (typically 15°C) all year long, which can be an additional constraint if animals must be kept for several generations.

Since the sea urchin model organism is not adapted to genetic studies, it has not been extensively studied in the past 50 years, and many tools of modern biology are lacking to perform experiments. In particular the genome has been way less documented that in the mouse, Drosophila or Zebrafish for instance, even though recent efforts have been made in that direction, in particular for immunology studies. The genome of *Strongylocentrotus purpuratus* was sequenced in 2006 (Sodergren et al., 2006), and initiatives such as the sea urchin genome database (Cameron et al., 2009) gather useful gene sequences and genetic tools to perform genetic perturbation experiments on sea urchins. However, to date, the sea urchin remains an old model organism with limited possibilities regarding modern genetic-related techniques.

3. History

a. Why echinoderm embryos ?

The question of cell division has long been acknowledged as a central question is cell biology, as dividing is a major event in the life of cells, and crucial to generate and maintain specific tissular shapes. As a consequence, cell division has been widely investigated, and the literature on the subject is extremely rich. In particular, the field originates back to the XIXth century, as simple experiments, easy to perform with the equipment available at that time, were sufficient for preliminary investigation on the core principles of cell division. The echinoderm embryos, especially the sea urchin and sand dollar embryos, have been extensively used as model systems to address these questions at that time, and the early literature of the field of cell division features many experiments performed on these embryos. Conceptually, division can be schematically viewed as a spherical cell centering its division apparatus and separating into two daughter cells of equal volume. This scheme is well illustrated by the first division of most embryos, where the cell that divides in two is isolated, and easy to see and manipulate in these systems as the zygote is a large cell. This conceptual reason explains that the early investigators on cell division were mainly embryologists. For many additional technical reasons listed in the previous chapter, the echinoderm egg has been the preferred biological system in the beginnings of the field. Ctenophores and amphibians unilateral cleavage and cultured vertebrate tissue cell division have also been extensively studied.

b. Early theories about cytokinesis

Initially, the mechanisms of cell division have led to a profusion of ideas and hypotheses, following observations. The mechanical forces driving shape, arrangement and division were considered of most interest to describe and theorize the observed events, in particular by German scientists who were at the forefront of developmental research at that time, although the importance of genetics was acknowledged. The huge amount of proposed theories, many of them by scientists interested in another field, as footnotes, does not reflect a chronological evolution of concepts and may rather be classified by the type of mechanism they suggest.

To explain cytokinesis, many theories postulate an active mitotic spindle as the main effector. The cytokinetic furrow would originate from astral traction fibers expanding from the centrosomes and pulling more on the surface at the equator, due to their longer lengths there. The nature of the traction fibers was various among authors, and could be whether made of contractile molecules (Heidenhain, 1897) or cytoplasmic flows toward the centrosomes (Rhumbler, 1903). The centrosome segregation would be a passive event in these models. Alternatively, cytokinesis has been proposed to be a consequence of active spindle elongation (Platner, 1886), in a process where the cytokinetic furrow would form passively with surface tension. A third hypothesis states that cytoplasm aggregates at the centrosomes (Morgan, 1899; Teichmann, 1903) or in the asters, the cytoplasmic aggregation being what forms viscous asters (Chambers, 1921), leading to a cytoplasm depletion at the furrow and to cytokinesis.

Other theories suggest that the cell surface actively shapes and separates the cells. The division has been proposed to originate from the contraction of the equatorial ring, whether from an increase of equatorial tension (Butschli, 1876; Just and others, 1939; Lewis, 1939; Ziegler, 1898), a decrease of polar tension (Chalkley, 1935; Lillie, 1903; Wolpert, 1960), or even an equatorial decrease or polar increase of tension, based on experiments affecting surface tension in oil droplets (Lillie, 1916; Robertson, 1909). The cell surface has also been suggested to separate the cell by a local surface growth and expansion. This process could be passive, and originate from the incorporation of new material first recruited at the equatorial plate (Andrews, 1897) and transported to the furrow by vesicles (MOTOMURA, 1940). Alternatively, the surface-mediated cytokinesis could rely on an active membrane expansion (Chambers, 1938; Swann and Mitchison, 1958).

Finally, some hybrid theories have been proposed, where several different mechanisms are working together, or in subsequent phases, going against the principle of parsimony, but allowing many possible explanations for cytokinesis. For instance the asters may first grow and generate pushing forces that elongate the cell and spindle, and in a second phase contract to form the furrow (Druner, 1894). The pushing forces may also indent the furrow as the cell volume is constant, and the second phase would consist in furrow ingression by material addition (Meves, 1897). Alternatively, the asters could contract first, pulling the centrosomes apart as well as indenting the furrow if the fibers connecting the centrosomes and cortex shrink or keep constant lengths while the spindle elongates. Then the cytokinesis would complete by cytoplasm aspiration (Dan, 1943) or formation of a constriction ring (Dan, 1988).

Regarding the stimulation that triggers cell division, some postulated a global stimulation localized by the mitotic apparatus. An agent that changes cortical tension (Painter, 1918), or a contractility activator (Scott, 1946) would be released in the whole cytoplasm, but the aster geometry would restrict its effects to the cytokinetic ring. Alternatively, the elongation of the cell could induce a higher surface stretching at the equator, where the membrane would become more permeable to calcium ions and lead to the contraction of the cytokinetic ring (Durham, 1974). However, most theories proposed the stimulation to be directly restricted whether to the equator or to the poles. In the case of a polar stimulation, a mint hypothesis is that the agent comes from the asters, centrosomes, or segregated chromosomes, and affects the nearest cortex, thus keeping away from the equator. The proposed effect of the agent is usually a decrease in surface tension (Lillie, 1903). Concerning the equatorial stimulation, the hypotheses generally involve a chemical or mechanical signal coming from the chromosomes, nucleus or spindle, and transmitted to the equator whether by aster interactions, by cytoplasmic currents or as the equator is the nearest cortex.

c. Experiments

These various and sometimes contradictory theories, even though each of them accounting efficiently for the observed phenomena, were somehow equivalent as they were not validated by perturbation experiments. Indeed, the simple observation of dividing cells, whether living or fixed, could not allow deciphering which of the observed events were active or passive. The systematic experimental testing of these speculations only occurred later.

The literature of perturbation experiments carried out on echinoderm eggs is vast (reviewed in (Rappaport, 1990)), but the early investigations mainly consisted in physically manipulating the eggs and blastomeres. Classical micromanipulation experiments included

compression of developing eggs and embryos, usually between glass slides or in microtubes (Figure IV.5.) (Dan, 1987; Hertwig, 1893), cutting of part or of the whole egg with needles, surface stretching by aspiration, tensile stress application, various shape alterations (Figure IV.5.), spindle displacement or segregation to a specific side of the egg, usually also performed with needles (Figure IV.5.), mitotic apparatus removal and other ablations, cytoplasm displacement, injection, surface relocation... Other classical perturbations consisted in separating blastomeres within an embryo (Dan, 1987), changing the number of asters or nuclei, removing chromosomes, affecting centrosomes attachment to nucleus, centrifuging eggs to segregate cytoplasmic components, treating cells with various chemicals (Dan and Ikeda, 1971), among others. The induction of polyspermy in eggs was also widely used to investigate on cellular organization during mitosis. The experiments carried out could combine several perturbative treatments, like needle cutting after centrifugation, to generate half eggs of different compositions for instance. The designs of these perturbative experiments were extremely various, and allowed to rule out many of the speculative theories about cleavage.

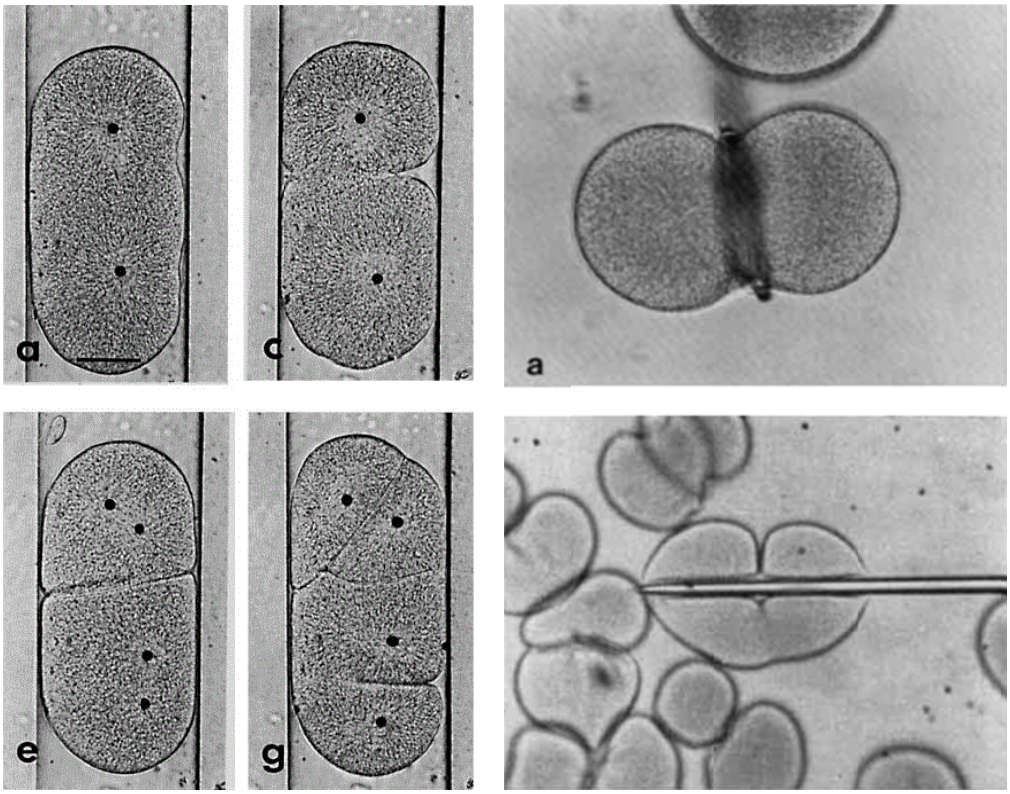

Figure IV.5. : *Examples of physical manipulation of echinoderms embryos.* ***Left :*** *compression of a developing sand dollar embryo to a flattened, cylindrical embryo. Aster centers are indicated by black dots, the cleavage pattern is modified. (Scale bar : 50 µm, adapted from (Rappaport, 1991))* ***Top right :*** *constriction of a dividing sand dollar egg. (From (Rappaport and Rappaport, 1984))* ***Bottom right*** *: Isolation of the telophase nuclei in the upper sides of a dividing sand dollar egg, with a microneedle. (From (Rappaport and Conrad, 1963))*

A typical example of such manipulation is the tore egg experiment performed by Rappaport on sand dollar eggs (Rappaport, 1961). The egg is compressed in its center, to be brought to a tore shape, with the nucleus getting pushed on the side (Figure IV.6.). As a result, the first cleavage occurred on the side where the nucleus was, and was incomplete since the opposite side remained uncleaved. In the next round of divisions, two spindles form, but there are three cleavage furrows, as the cell also divides between the two spindles. This classical experiment suggested that, in this system, the site of furrowing is determined by aster-aster interaction, whether the asters originate from the same spindle or from sister spindles.

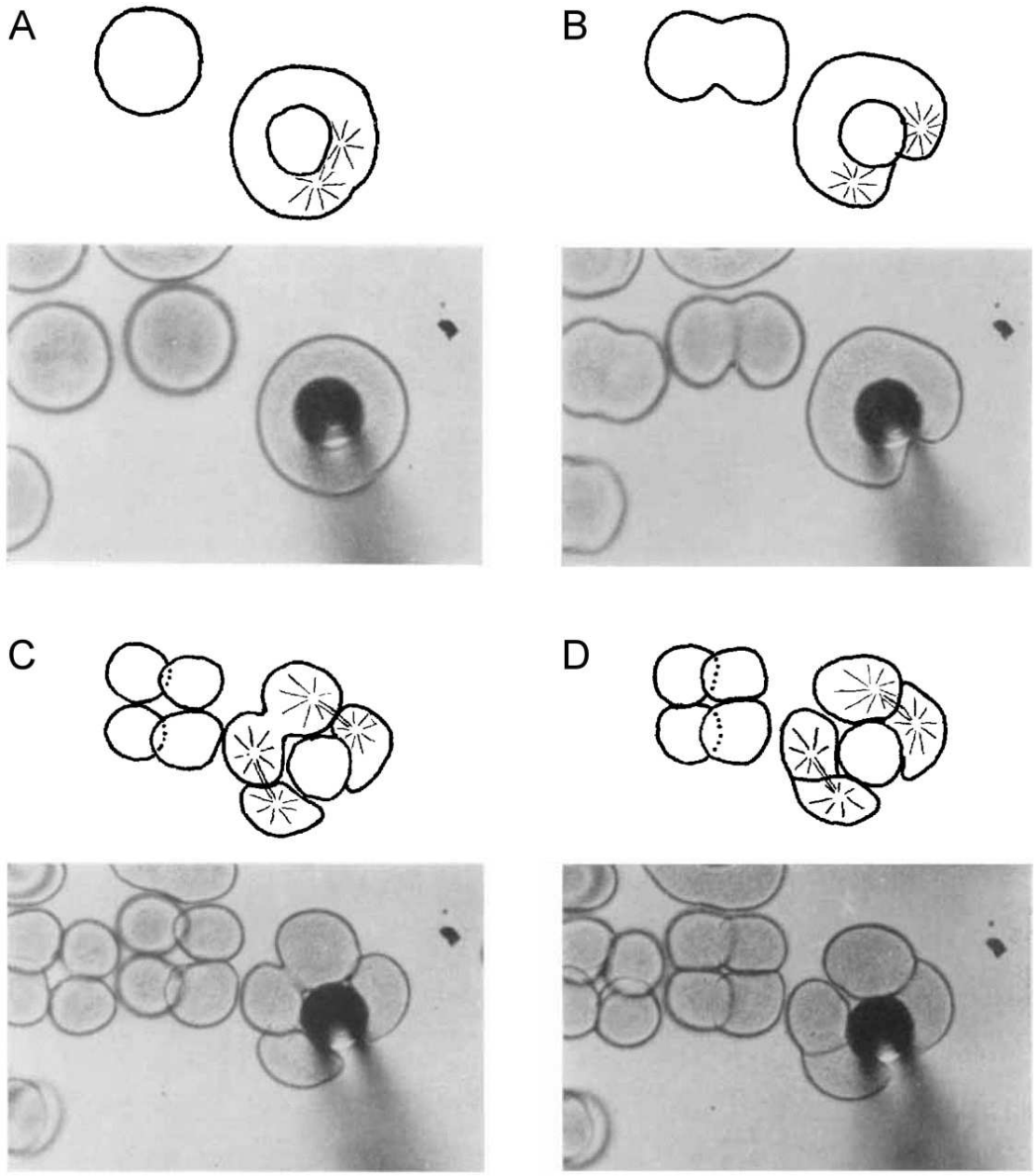

Figure IV.6. : *The classical tore-shaped egg experiment, performed on sand dollar eggs. Eggs are constricted to a tore shape, and form one cleavage furrow at the first division, and three at the second division. The time-lapse begins at fertilization. Upper panels are schematic views of the lower panels, with spindles indicated by parallel lines. (From (Rappaport, 1961))*

Echinoderm embryos have been extensively used to perform such perturbation experiments shedding light on the underlying mechanisms of cell division. At about the same time, and in order to bring some mechanistic insight on these experiments, echinoderm embryos also served for quantitative measurements (reviewed in (Rappaport, 1990)). Direct measurement of accessible values like volume ratios, centrosomes positions or cell cycle duration in the manipulated eggs were performed. The cells surface areas could be measured, and cortical movements during furrowing have been tracked by insertion of carbon particles. In addition, some intrinsic properties of the eggs have been assessed. For instance the forces at play, such as the contractile force of the furrow (Figure IV.7.), or cytoplasmic viscosity could be probed with needles. Surface tension of eggs and embryos was measured by pipette aspiration (Chapter III.2.a.) throughout the cell cycle.

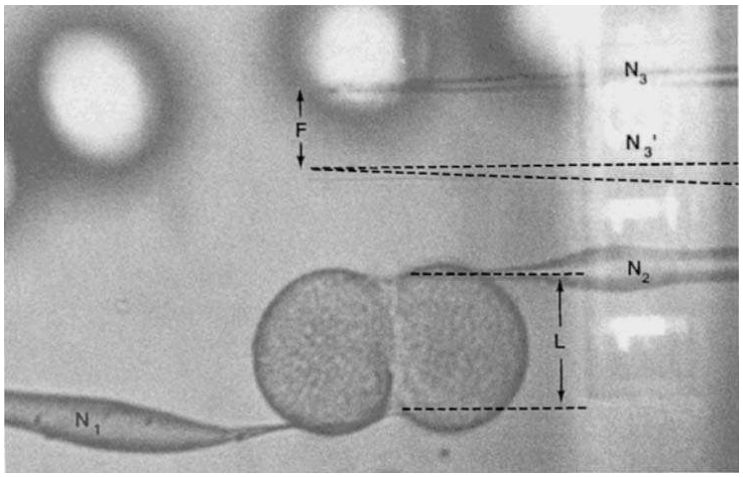

Figure IV.7. : *Measurement of the constriction force of the cleavage furrow with two microneedles N_1 and N_2. The bending of N_2, measured with a reference needle N_3, held by the same micromanipulator as N_2, allows to assess the furrowing force. The distance L between N_1 and N_2 is kept constant through the experiment, and an increase of force thus leads to a displacement F of N_3, that is proportional to the bending of N_2. (From (Hiramoto, 1979))*

Later on, with the apparition of the molecular tools of modern biology, the mechanisms of cell division in echinoderm embryos could be further investigated, by using fluorescent tags, protein and mRNA injection for instance. However, as these embryos are not well suited for genetic studies, the field of cell division rather shifted on more adapted systems such as drosophila epithelial tissues and mammal cultured cells, for instance. Yet, the echinoderm embryo still has many advantages (Chapter IV.2.) and remains a classic model organism to study cell division and early embryogenesis.

PROJECT

AIM OF THE WORK

As seen in introduction, the question of where a cell positions its nucleus, which will define the subsequent cleavage plane, is key to understand both cell division and the generation and maintenance of specific tissue shapes. Attempts have been made from up to 150 years ago to determine the rules that dictate division plane positioning, and several empirical rules have been proposed to predict the location and orientation of the division. Some of these generic rules, such as the long axis rule proposed by Oskar Hertwig in 1884, still stand today and show a striking accuracy in many cell types. Later on, more insight has been gained into the underlying mechanisms of nuclear positioning, in particular to explain the exceptions to the long axis rule that are asymmetric divisions. Many hypotheses have been made about the effectors of nuclear positioning, most of them relying on forces exerted by the cytoskeleton on the nucleus or on the pair of centrosomes. However, these mechanisms remain specific to an organism or cell type and a broad understanding of cell division plane positioning, integrating these various mechanisms and considering their possible competition, is still lacking.

More recently, numerical models for nuclear positioning have been implemented, that test and refine the proposed mechanisms. These models have various degrees of complexity, but generally feature a restricted number of mechanisms to allow characterizing their respective effects. Importantly, some of the proposed models are general and simulate nuclear positioning regardless of cell type, as a step further into the generic understanding of cell division.

The aim of this work is to propose a general model to predict division plane positioning, that integrates several cues for nuclear positioning. This model should account for Hertwig's long axis rule, but clarify its underlying mechanisms, as it will be based on existing hypotheses on the effectors of nuclear positioning. In addition, the model should explain the exceptions to the long axis rule, as it also takes into account cell polarity cues that have been proposed to drive nuclear decentration. The aim is to keep the model as simple and general as possible to extract the main principles of nuclear positioning at work in most systems. Importantly, this work should also allow assessing the competition between these main mechanisms, that may be system-specific, and thus give insight into a variety of cell behaviors.

CONTEXT AND METHODS

Early embryos are good minimal systems to study cell division, as they are isolated small systems featuring a limited number of cells, and do not display any growth or expression of the embryo's genome. In particular, in some embryos such as most deuterostomes embryos, the cleavage pattern is highly reproducible between related species, and is often invariant within a whole class of animals, suggesting little genetic regulatory layers. Such systems would rather rely on self-organization to define their division planes, and thus the default generic mechanisms for division plane positioning would possibly be the only ones at play in these embryos. As a result, these early embryos are easy systems to model, and allow extracting the core principles of nuclear positioning.

This work has been performed in the laboratory of Nicolas Minc, that has an expertise in using the sea urchin embryo as a model organism. These embryos are particularly suited for studying cell division, as discussed in the introduction. In particular, their early development is highly reproducible up to an advanced stage, they are imaging and manipulating-friendly, and easily available in numbers. In addition, they display a characteristic cleavage pattern with micromeres appearing on the vegetal pole at the fourth round of divisions, probably due to a vegetal cap of maternal polarity. The polarity cues have a simple and precise distribution, and are associated with a clear phenotype. As a result, the sea urchin embryo is an ideal system to study the effect of a maternal patch of polarity on nuclear positioning, and the competition between these polarity cues and other possible cues such as cell shape.

In order to extract the core mechanisms of nuclear positioning, and in particular the role of maternal polarity, the approach used in this work was a crosstalk between perturbation experiments challenging polarity or shape, and numerical simulations. Several tools for micromanipulation were available, such as photolithography, to confine cells in microchambers of specific shapes, or micromanipulators, that allow the injection, cutting or manipulation of embryos with microneedles. The idea was to affect polarity or shape cues to precise their effects on nuclear positioning, and to use these results to define and refine the model. In turn, the results of the simulations were useful to design experiments. In addition, this work included a major part of imaging, to quantitatively determine the relative position of the cues and effectors of interest and refine the model.

The model was developed from the static model designed by Nicolas Minc, which inputs a 2D cell shape and outputs the preferred orientation of a centered nucleus. The main hypotheses are that microtubules grow from the two centrosomes and reach the cell cortex, so that they span the whole cell volume in interphase. They are modelled straight, without branching and dynamics, and with a constant angular distribution within the asters. They undergo pulling forces, and the net contribution of these forces on the pair of centrosome generates a torque that rotates and orients the nucleus. The pulling force exerted by individual microtubules increases with microtubules lengths, supposedly as more motors attach to a longer microtubule. In agreement with previous findings from this 2D model, the expression of the force was supposed to follow a power law of the length, with an exponent set to 3, consistent with forces exerted in bulk cytoplasm by homogeneously distributed dyneins.

The model designed in this work adapts the previous 2D model in 3D, in order to perform division simulations on real blastomeres shapes. The new model is now designed to predict the position of the nucleus (and not only its orientation), and will then able to also address asymmetric divisions. Finally, additional cues such as polarity or yolk gradients are superimposed to shape in the model, allowing assessing the effects of these various cues on nuclear positioning, and their competition with cell shape. The aim is to come up with a complete generic model to predict the whole echinoderm cleavage pattern, and possibly other cleavage patterns, as well as divisions in other cell types.

CONTENT

The project was composed of two main parts, yielding two articles that are given in the next section.

The first part is purely theoretical. The model that predicts division positioning is run on artificial cell shapes obtained from surface simulations. This approach allows reproducing the whole early cleavage pattern with no need of experimental data, as the simulated shape is used as an input to the division prediction model, which in turn outputs the information required to generate the shapes of the next stage, and so on. This framework is valuable to study nuclear positioning in embryos that are too big or opaque to be easily imaged, like amphibians or fish embryos. This approach allowed to design a generic model that can predict division positioning in four representative deuterostome species (zebrafish, Xenopus, sea urchin and ascidian), and gives insights on the relative contributions of cell shape, maternal polarity and yolk gradients to define early cleavage patterns.

The second part of this work focuses on the sea urchin early embryo, and quantitatively explores the timely competition between maternal polarity and cell shape in this system. The approach is now a crosstalk between the model, broadly designed in the first part, and experiments. These experiments include quantitative imaging, both of live and stained embryos, and perturbative experiments challenging shape, size or polarity. The results serve to refine the model, precise the effects of polarity cues on nuclear positioning, and quantitatively assess their competition with shape cues and its evolution with time

.

RESULTS

GENERIC THEORETICAL MODELS TO PREDICT DIVISION PATTERNS OF CLEAVING EMBRYOS

Anaëlle Pierre[1], Jérémy Sallé[1], Martin Wühr[2] and Nicolas Minc[1,#,§]

Affiliation: [1] Institut Jacques Monod, 15 rue Hélène Brion, 75205 Paris cedex 13, France

Tel: +331-572-780-52, Fax : +331 572-780-26

[2] Lewis-Sigler Institute for Integrative Genomics and Department of Molecular Biology, Princeton University, Princeton, NJ 08544, USA

Corresponding author: Nicolas Minc, nicolas.minc@ijm.fr

§ Lead contact: Nicolas Minc, nicolas.minc@ijm.fr

Running Title: Predicting embryonic cleavage patterns

GRAPHICAL ABSTRACT

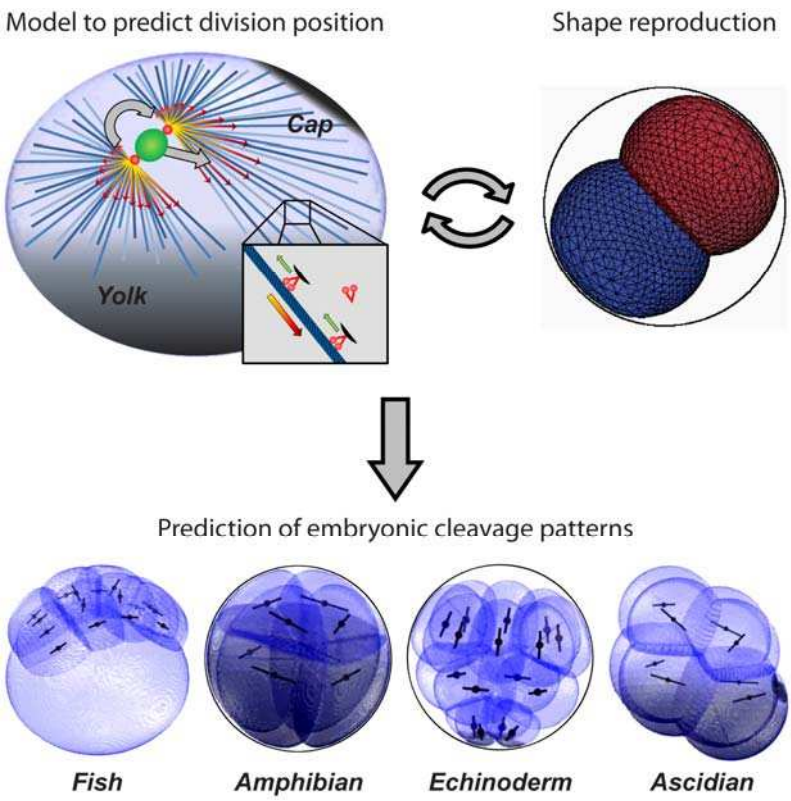

IN BRIEF

Pierre et al. develop computational models to make predictions on the positions and orientations of division axes in subsequent rounds of embryonic cleavages. The model reveals a set of simple self-organizing rules which can predict the morphogenesis of early developing embryos from different species.

HIGHLIGHTS

. A 3D model iteratively infers blastomere division positions and arrangements.

. The model can predict the embryonic cleavage patterns in multiple species.

. Cell shape is a default cue orienting division, biased by yolk or maternal polarity.

. Self-organization strongly contributes to pattern early embryo development.

SUMMARY

Life for all animals starts with a precise 3D-choreography of reductive divisions of the fertilized egg, known as cleavage patterns. These patterns exhibit conserved geometrical features and striking inter-species invariance within certain animal classes. To identify the generic rules that may govern these morphogenetic events, we developed a 3D-modelling framework that iteratively infers blastomere division positions and orientations, and consequent multicellular arrangements. From a minimal set of parameters, our model predicts detailed features of cleavage patterns in the embryos of fishes, amphibians, echinoderms and ascidians, as well as the genetic and physical perturbations that alter these patterns. This framework demonstrates that a geometrical system based on length-dependent microtubule forces that probe blastomere shape and yolk gradients, biased by cortical polarity domains, may dictate division patterns and overall embryo morphogenesis. These studies thus unravel the default self-organization rules governing early embryogenesis, and how they are altered by deterministic regulatory layers.

INTRODUCTION

A cleaving embryo serves as an excellent context to understand the emergence of diverse modes of division plane positioning in a single developing system. After fertilization, animal eggs undergo a precise series of subsequent reductive blastomere divisions called cleavage patterns. The geometry of these patterns may specify developmental axes, germ layers and cell fates (Gilbert, 2010). Blastomeres divide in a stereotyped manner, exhibiting symmetric or asymmetric divisions, oftentimes oriented with respect to embryonic axes or preceding divisions (Kimmel et al., 1995; Olivier et al., 2010; Summers, 1993; Tassy et al., 2010). The invariance and diversity of cleavage patterns has long attracted the attention of biologists, and several empirical rules were formulated. These include Balfour's, Sachs', or Hertwig's rules, that capture conserved features of blastomere division, such as the tendency of cells to divide along their long axis, or the orthogonal sequence of division axes typical of various species (Hertwig, 1893; Minc et al., 2011; Minc and Piel, 2012; Sachs, 1887; Wilson, 1925).

Division positioning is now known to involve the dynamic orientation of nuclei and spindles, which are moved and oriented from the forces exerted by microtubules (MT) and associated motors such as dynein (Minc and Piel, 2012). In eggs and early blastomeres, recent work suggested that division axes are pre-determined by interphase MT asters which fill the large volume of these cells. These asters are organized around the nucleus from a pair of centrosomes, and may be positioned and oriented from dynein-mediated MT forces exerted in the cytoplasm. These findings outline a geometrical model in which length-dependent MT forces may convert aster geometry into a net force and torque to specify division positioning (Hamaguchi and Hiramoto, 1986; Minc et al., 2011; Mitchison et al., 2012; Tanimoto et al., 2016; Wuhr et al., 2009; Wuhr et al., 2010). These designs contrast with deterministic inputs that guide division positioning from cortical polarity cues that influence MT forces by promoting dynein activity or MT depolymerization at the cortex (Gonczy, 2008; Grill and Hyman, 2005; Kozlowski et al., 2007). Although our basic understanding of these diverse mechanisms has emerged from detailed studies of one reproducible single-cell division in models such as the *C. elegans* zygote, how polarity and geometrical cues may cooperate or compete to pattern the wide diversity of division positioning events in a multi-cellular context remains an outstanding question.

Here, we develop a 3D-modelling framework to elucidate the generic rules that dictate subsequent division axes and overall morphogenesis of embryos from several deuterostome classes which exhibit invariant cleavage, including fishes, amphibians, echinoderms and

ascidians. These models iteratively predict division axes and blastomeres' arrangement, and thus allow full development of cleaving embryos *in silico*. Core hypotheses of the models are defined and tested using imaging data and experimental assays available in the literature, and performed by ourselves. Our findings support that aster geometry, set by cell boundaries, yolk gradients and/or neighboring asters, and probed by length-dependent MT pulling forces, serve as a basal cue for division positioning. This default mode may then be locally biased by maternal cortical domains that exert additional pulling forces on astral MTs. Thus, this quantitative analysis shows that complex multiple modes of division may be accounted for by a few simple rules, and begins to elucidate how self-organized and deterministic maternal traits intersect to pattern early embryogenesis.

RESULTS

Two complementary 3D models to predict division plane positioning, and consequent blastomere multicellular arrangement in cleaving embryos.

To understand the mechanisms that control cleavage patterns, we first developed a model to predict, in 3D, the position and orientation of interphase aster pairs which pre-specify the site of division in eggs and early blastomeres studied here (Minc et al., 2011; Sawada and Schatten, 1988; Wuhr et al., 2010). The model inputs simple MT aster nucleation parameters and assumes a certain spatial distribution of MT forces to output an equilibrium position and orientation of aster pairs (Bjerknes, 1986; Minc et al., 2011; Thery et al., 2007). Following recent studies, we assumed as a starting hypothesis that forces exerted by astral MTs depend on MT length, which may allow cells to divide with respect to their geometry (Minc et al., 2011; Wuhr et al., 2010) (Figure 1A). Length-dependency of MT forces is modeled using a scaling exponent δ, so that $F \sim L^{\delta}$, with L the MT length (Minc et al., 2011). The distribution of MT length in asters can be computed, depending on the system considered (see below), by assuming that MTs stop growing when touching the cell cortex, a sister aster, or from specific hypotheses on the influence of yolk density on MT growth.

The model computes a net force and torque on the pair of centrosomes at the center of asters for any position or orientation defined by the 5 space variables in 3D (x, y, z, θ, φ). The predicted mechanical equilibrium may be identified by assessing all possible positions or orientations (Minc et al., 2011; Thery et al., 2007). However, in 3D, this approach yielded overly long computing times, which led us to adopt a directed search for the mechanical equilibrium that follows the direction of force and torque up to the equilibrium position (Figure 1B, Experimental Procedure and Supplemental Information). Using a range of different input geometries, we first systematically confirmed that this model could account for the alignment of the division axis with cell shape in 3D (data not shown) (Minc et al., 2011). Next, we tested the influence of parameters on these predictions. The distance between centrosomes, D_c, did not impact predictions. The angular extension of MT asters, ψ, influenced aster positions, but only weakly affected their orientation. Finally, the force scaling exponent, δ had no major influence below a value of 5, and was set to 3 following recent estimations (Figure S1A-S1C, Experimental Procedure and Supplemental Information) (Minc et al., 2011).

Next, we sought to compute the resulting shapes and arrangement of divided blastomeres. We used the modeling software "The Surface Evolver", which iteratively minimizes surface energy under various constraints (Brakke, 1992; Xiong et al., 2014). We input the volumes of blastomeres, their initial topology based on previous division axes predicted from the abovementioned model, and values of surface tension at the site of cell-cell adhesion, γ_{int}, and cell-medium interface, γ_{ext}. Confinement by the fertilization envelope or other egg-surrounding layers can also be added as an additional factor contributing to blastomere shape and re-positioning (Figure 1C). The model ignores the complex mechanisms regulating cortical tension and cell-cell adhesion. Yet it allows generation of 3D blastomere shapes and arrangement from a minimal set of parameters, and subsequent testing of their contribution to cleavage patterns (Movie S1). For instance, a lower value of $\gamma_{ext}/\gamma_{int}$ yields more rounded blastomeres, while a higher value causes apposed blastomeres to adopt near-hemispherical shapes (Maitre et al., 2015) (Figure 1D). Similarly, an increased confinement tends to flatten cell sides and lengthen cell-cell interfaces (Figure 1E).

Using both models, we iteratively compute division position and blastomere shape and arrangement in subsequent cleavage stage, which provides us with a complete *in silico* modeling framework to predict and understand cleavage patterns (Figure 1F and Supplementary Item S1).

Cell geometry as a dominant cue to dictate a cleavage pattern: the case of fishes.

The geometry of eggs and blastomeres has been shown to influence division positioning in different cells and embryos (Minc et al., 2011; Minc and Piel, 2012), but whether it can serve as the prevalent cue to pattern early development is not known. In Zebrafish embryos, like in most fish species and several other vertebrates including birds and reptiles, cleavage is discoidal, as only a superficial part of the embryo, called the blastodisc, sitting on a large dense yolk layer, is being cleaved (Gilbert, 2010; Kimmel et al., 1995). Two conserved features of fish cleavage have been described: (i) Divisions up to the 4th cleavage all lie parallel to the yolk interface and are nearly orthogonal to the previous division axes and (ii) at the 5th cleavage, the four center-most blastomeres of the blastodisc switch to a division axis now orthogonal to the yolk interface, allowing tissue layering in the 3rd dimension (Kimmel et al., 1995; Mitchison et al., 2012; Olivier et al., 2010; Wuhr et al., 2010) (Figure 2A and 2C). Large interphase MT asters that fill the whole blastodisc, but do not penetrate the yolk, were

suggested to organize early fish cleavage through length-dependent MT forces (Figure S2A). Finally, centrosome separation in the next cell cycle occurs before cytokinesis within sister telophase asters, which repulse each other at an aster-aster interaction zone that marks the site of cleavage furrow ingression (Mitchison et al., 2012; Wuhr et al., 2010).

We modeled aster geometry by assuming that MTs stop growing at the cell cortex, at the yolk interface, and at aster-aster interaction zones. The shapes of dividing blastomeres were obtained by setting the value of $\gamma_{ext}/\gamma_{int}$ to match contact angles measured from images in the literature (Olivier et al., 2010). Confinement was neglected as the chorion which surrounds embryos is located far from the egg (Kimmel et al., 1995). Strikingly, a model solely based on length-dependent forces accounted for all stereotypical division orientations and positions up to the 5th cleavage, with no adjusted parameters between subsequent simulations (Figure 2B and 2D, Movie S2). The model robustly reproduced the planarity of division axes in the four initial rounds of divisions, the successive orthogonality of these division axes, and the switch in division orientation at the 5th cleavage in the four central blastomeres. In the model, this switch was caused by an elongation of these four cells perpendicular to the yolk-interface resulting from the compaction of neighboring blastomeres (Figure 2B, 2D and Figure S3A-S3D). By contrast, a model based on putative surface cues located at cell-cell adhesion sites was not able to reproduce the switch at the 5th cleavage (Figure S2B-S2D) (Goldstein, 1995).

To further test these findings, we assayed the impact of changing parameters that influence cell shape on the sequence of division axis alignments, and compared the results to published observations. We found that a decreased cell-cell tension or an increased cortical tension influenced blastomere shapes, and caused a precocious division orientation switch at the 4th cleavage. Conversely, a lower cortical tension caused cells to flatten, with a shorter cell-cell interface, and the 5th cleavage to remain planar. This simulation is consistent with defects in tissue layering observed in embryos treated with blebbistatin, which affects myosin activity and presumably reduces cortical tension (Figure 2E and S3I) (Urven et al., 2006). A similar effect was obtained by increasing cell-cell tension, which may account for weakened cell-cell adhesions. This simulation may correspond to the phenotype of a *nebel* mutant, which is defective in cell-cell adhesion, and predicts that the switch at the 5th cleavage should be less pronounced in this mutant (Figure 2F and S3J) (Pelegri et al., 1999; Webb et al., 1997). Finally, we found that a precocious separation of daughter cells induced earlier blastomeres arrangement and caused a significant bias in the angular distribution of division axes, consistent with experiments that challenge the cell cycle with heat shocks (Heier et al., 2015)

(Figure S3A-S3H). Together these data highlight how parameters that influence blastomere shape can give rise to various patterns, and demonstrate in a dose-dependent manner that a length-dependent MT pulling mechanism, which relies on pure geometrical effects, may account for early fish cleavage morphogenesis.

The gradual effect of yolk on length-dependent forces and cleavage patterns: the case of amphibians.

We next sought to test if variations in the length-dependent model could account for the development of mesolecithal eggs. A well-studied case is the cleavage pattern of the frog *Xenopus laevis*, which is stereotypical of hundreds of amphibian species (Desnitskiy, 2014). The 1st and 2nd division planes lie parallel to the A-V axis, and perpendicular to each other, and the cleavage furrow ingresses from the animal pole. The third cleavage is orthogonal to the A-V axis and asymmetric, generating small animal blastomeres (Figure 3A). Recent studies have suggested similar principles as in fish regarding large aster organization, cytoplasmic length-dependent MT forces, and the relative timing of centrosome duplication and furrow ingression (Wuhr et al., 2010). However, Xenopus eggs display a more gradual accumulation of yolk with increasing density towards the vegetal pole compared to zebrafish (Figure S4A). We asked if and how this yolk gradient could influence the length-dependent model to account for the cleavage patterns of amphibians.

To assess how MTs may be influenced by the yolk, we first performed immunostaining. This analysis confirmed a gradual accumulation of yolk towards the vegetal pole, and revealed that the relative density of MTs decreases as a function of yolk amount in a dose-dependent manner (Figure 3B and S4A). We thus used a model based on MT length-dependent forces but allowed MTs to penetrate the yolk. We tested several yolk distributions and hypotheses on the influence of yolk on MT growth, including one based on a threshold in yolk density that stops MT growth (Figure S4B-S4D and Supplemental Information). To reproduce the shapes of blastomeres reported in the literature, we assumed a strong confinement by the fertilization envelope and/or other coat layers around the egg (Danilchik et al., 2006; Gilbert, 2010). Given this confinement, tension values had little impact on blastomere shapes and arrangement.

The model accounted for Xenopus cleavage patterns up to the 8-cell stage (Figure 3C, Figure S4C and Movie S3). In contrast with zebrafish, altering the timing of furrow ingression had

no major effect on cleavage patterns, likely because, as a result of confinement, the shapes of divided blastomeres and preceding asters are similar (Figure S4E). Accordingly, removing the confinement yielded, with all other parameters fixed, a drastic change in blastomere shapes and an inhibition of the switch in orientation at the 3rd cleavage (Drechsel et al., 1997) (Figure S4F).

To further assay the influence of the yolk, we tested if our model could account for published experiments manipulating gravity and MT stability at the 3rd asymmetric cleavage (Neff et al., 1984; Yokota et al., 1992). Removing the effect of gravity by rolling the eggs yields a near symmetric 3rd cleavage, with similar orientation along the A-V axis. Conversely, placing eggs in 3*g* gravity by centrifuging them increases the amount of asymmetry. In the model, we tuned the sharpness of the yolk gradient to account for the effect of gravity, and could quantitatively reproduce these observed changes (Figure 3D). Another set of experiments consisted in exposing eggs to different treatments that presumably affect MT stability. Applying a 10 min cold shock to destabilize MTs prior to the 3rd cleavage, caused an increased asymmetry. Conversely, the use of heavy water (D_20) to stabilize MTs made division more symmetric than controls, and rescued the effects of cold shocks. By tuning the impact of yolk density on MT density in the model, we could account for these experimental results (Figure 3E).

Finally, we ran our models against Hertwig's experiments, in which eggs are deformed between glass slides either along or perpendicular to the A-V axis, by adding an asymmetric confinement in "The Surface Evolver" (Figures 3F-3G) (Hertwig, 1893). We found that when the egg was compressed along the A-V axis, the 3rd division now occurred perpendicular to the A-V axis, and the 4th division axis was nearly parallel to this axis, in agreement with Hertwig's findings (Figure 3F). A compression perpendicular to the A-V axis yielded, both in the simulation and in Hertwig's experiments, a premature switch of the 2nd cleavage axis parallel to the A-V axis (Figure 3G). We conclude that our hypothesis based on length-dependent forces combined with an influence of yolk on MT density may account for amphibians cleavage patterns and relevant perturbations of these patterns.

Integrating geometry and polarity to define a cleavage pattern: the case of echinoderms.

We next asked how geometrical cues may compete or cooperate with polarity cues that are known to promote asymmetric divisions in the cleavage of several embryos (Gonczy, 2008; Hörstadius, 1928). One remarkable example are echinoderms, such as sea urchin, sand dollar

or starfish (Gilbert, 2010; Raff, 1987). These embryos do not exhibit any yolk gradient, and cleave in a holoblastic manner. The first three cleavages are symmetric and orthogonal to each other, with the first and second ones parallel to the A-V axis. At the 4th cleavage, the four vegetal blastomeres undergo marked asymmetric divisions oriented along the A-V axis, to produce small micromeres, while animal blastomeres follow a symmetric pattern (Gilbert, 2010; Summers, 1993) (Figure 4A). Many past experiments have supported the existence of a single domain accumulated at the vegetal pole, which contains conserved polarity effectors, such as Dishevelled (Figure 4B) (Boveri, 1901; Dan, 1979; Hörstadius, 1928). This domain may influence MT forces to drive vegetal asymmetric divisions at the 4th cleavage (Dan, 1979; Leonard and Ettensohn, 2007; Peng and Wikramanayake, 2013; Tanaka, 1976). Yet, although this domain is assembled before fertilization, cell shape appears to override its effect in the first three rounds of cleavages, suggesting it only weakly influences MT forces in these stages (Minc et al., 2011). We sought to use echinoderm cleavage to understand how effects of length-dependent pulling and polarity on MT forces may be combined to pattern those various division events.

To generate blastomere shapes and arrangement, we tuned surface tensions and confinement to match shapes and adhesion angles in the literature (Summers, 1993). We first ran simulations solely based on length-dependent MT pulling. We found that at the 2-cell stage, the two division axes were not coplanar. At the 8-cell stage, the simulations yielded only symmetric divisions oriented near-perpendicular to the A-V axis. These simulations are in agreement with detergent treatment experiments, performed here and in published work (Dan, 1979; Tanaka, 1976), which presumably disrupt surface cues and inhibit division axes co-planarity at the 2-cell stage and cause 8-cell stage vegetal blastomeres to divide symmetrically (Figure 4C-4D). Thus, the vegetal domain may be required both to trigger asymmetric divisions and to orient the three first rounds of division with respect to the A-V axis.

To incorporate the influence of vegetal domains, we first added a “polarity” term in the MT force equation, following a previous hypothesis of dynein-dependent surface pulling limited by dynein (Grill and Hyman, 2005). This hypothesis implicates the force of MTs that contact the domain to be written as $F_P = \alpha L^3 + \beta L^2$, with β reflecting dynein concentration/activity at the domain. However, we found that this law systematically caused the division axis to point towards the cap already in the first cleavage (Figure S5A and S5B). We thus tested several other designs and compared simulations to published experimental data (Supplemental information). We found that a law in which the force exerted by MTs at the domain increases

exponentially with MT length could stabilize a division axis parallel to the domain (Figure S5C). Experimentally, we computed MT density in interphase asters, by performing immunostaining at various cleavage stages. This showed that branching properties of these asters caused MT density to increase exponentially in addition to dilution effects from the centrosomes to the cell cortex (Figure S5D-S5E) (Minc et al., 2011; Mitchison et al., 2012). We thus hypothesized that cortical pulling forces were limited by the number of MT tips, and subsequently used the law $F_P = \alpha L^3 + \gamma 2^{L/a}$, where γ accounts for the strength of the cap in this condition, and a is the distance between branches, estimated from staining images to be 6.9 ± 3 μm (Figure S5E), and set to 6.75 μm in all simulations. We speculate that this design could better reflect an end-on pulling mechanism mediated by other elements than dynein, such as depolymerization factors (Kozlowski et al., 2007; Kwon et al., 2015) (Figure 5A). Importantly, in simulations, this contribution yielded an orientation of the division axis parallel to the domain for a broad range of parameters (Figure S5F and Supplemental Information). However, it did not allow the generation of situations of centered aster pairs pointing towards the domain. However, 4-cell stage separated blastomeres are round and have been shown to divide symmetrically along the A-V axis (Dan, 1987), suggesting this law alone cannot account for the full range of reported experiments (Figure S5G-S5I).

Based on these analyses, we used a sum of both polarity terms, in addition to the length-dependent forces, but kept the polarity terms weak, so that they only modulated the potential landscape set by geometry in the three first cleavages (Figure 5A, Figures S6A-S6B and Supplemental Information). We could fully account for the normal sea urchin cleavage pattern, as well as blastomere dissections up to the 8-cell stage (Dan, 1987; Minc et al., 2011; Summers, 1993; Tanaka, 1976) (Figure 5Bi, and Figure S5C and S5I). These predictions were robust to parameter variations (Figure S6C-S6E). However, they could not produce asymmetric divisions of vegetal blastomeres at the 8-cell stage. We thus considered an additional hypothesis of an increase in motor activity, represented by an increase in the value of β. This was supported by Dan's retardation experiments (Dan, 1971). In those, eggs are treated at the 4-cell stage with UV or chemicals that presumably cause DNA damage and delay cell cycle progression, without affecting domain maturation. These treatments create a curious scenario in which the domain becomes attractive at the 4-cell stage, yielding four asymmetric divisions. A comparison of the model with Dan's observations and normal embryos suggested that an increase in β by a factor of ~ 10 would be sufficient to recapitulate experimental behavior (Figure 5C). With this additional hypothesis, the model could fully

reproduce cleavage patterns up to the 5th division, including micromere formation and radial divisions of animal blastomeres (Figure 5Bi and 5Bii and Movie S4).

To further validate our hypotheses, we compared the model to other published experiments assaying the competition between geometry and polarity. We first considered Hörstadius' experiments, which paused cell cycle-progression by incubating eggs in diluted sea water and assayed the consequence on cleavage patterns (Hörstadius, 1939) (Figure 6A). A treatment at the 1-cell stage caused the second pair of division axes to align along the A-V axis in a precocious manner. A treatment at the 4-cell stage yielded similar abnormal asymmetric divisions as in Dan's experiments. Finally, delaying the two first cell cycles of eggs cut into halves generated an asymmetric division at the 2-cell stage. Our model, using the exact same set of parameters as those used for controls, could account for all those variations in cleavage patterns (Figure 6B). Second, we ran our model against deformation experiments, in which eggs are flattened to assess the impact of cell shape on the location of micromere formation (Dan, 1987). The simulations reproduced these experiments, suggesting they can fully account for the titrated competition between cell geometry and polarity (Figure 6C and 6D). Thus, our model may capture all relevant designs for how a local surface cue could modulate the default geometrical rules to regulate echinoderms cleavage patterns.

Integrating several developmental axes: the case of ascidians.

Some embryos possess multiple cues oriented along different axes that may overlap to create complex patterns of divisions. One typical example are ascidians, which are tunicates that exhibit highly conserved cleavage patterns. Ascidian cleavage is organized along two independent axes, an Animal-Vegetal and an Antero-Posterior axis, which may be regulated independently (Gilbert, 2010; Negishi et al., 2007). A-V polarity has been suggested to be associated with the deposition of yolk and other organelles at the vegetal pole (Nishida, 1996). A polar domain, called CAB (Centrosome Attracting Body), may influence division positioning along the prospective A-P axis (Iseto and Nishida, 1999; Negishi et al., 2007; Nishikata et al., 1999). At fertilization, a cytoplasmic rotation creates a yolk crescent with most of the yolk accumulated at the vegetal part of the egg, and some at the incipient anterior pole (Figure 7A and 7B) (Conklin, 1931; Roegiers et al., 1999). The CAB then assembles on the posterior side and maturates to start influencing division positioning at the 2-cell stage (Negishi et al., 2007). The first two divisions are symmetric. The 2nd division axes are tilted

with an angle of ~35°, and only the two posterior blastomeres inherit the CAB at the 4-cell stage (Negishi et al., 2007). At the 3rd cleavage, blastomeres divide slightly asymmetrically towards the animal pole, with posterior blastomeres dividing at a different orientation than the anterior ones. Finally, at the 4th cleavage, the two most posterior blastomeres undergo an asymmetric division, while other blastomeres divide symmetrically (Figure 7A).

To reproduce the morphogenetic arrangement of blastomeres, we neglected the confining effect of the envelope, and used images from the literature to extract interface angles (Tassy et al., 2010). We noted that 4 and 8-cell stage blastomeres appear more adherent, and thus decreased cell-cell tension value after the 2-cell stage. To model division planes positioning, we assumed a model based on aster shape as above, on which we added the contributions of the CAB and yolk layers. We reproduced the yolk crescent at the 1-cell stage with two gradients. This, under the same hypotheses for the effect of yolk on MTs as in amphibians, predicted a division axis shifted towards the animal and posterior poles, and aligned perpendicular to the A-P axis, as in previous reports (Conklin, 1931; Roegiers et al., 1999) (Figure 7C). Following published experimental observations, we added a contribution of the CAB after the first cleavage (Negishi et al., 2007), and used a similar surface-based pulling hypothesis as for echinoderms. However, the exponential contribution to surface pulling did not appear to be required in this case (Figure S7).

We could predict the whole set of division positions observed in ascidians, and overall embryo morphogenesis, including the stereotypical posterior pointy shape of the embryo at the 16-cell stage (Figure 7C and Movie S5). As a further validation, we ran our model without the contribution of the CAB. As observed in published experiments where the CAB was ablated or made inactive with Morpholino against PEM mRNA (Negishi et al., 2007; Nishida, 1994; Nishikata et al., 1999), we obtained in the model a radialized embryo, which maintained an asymmetry along the A-V axis caused by yolk vegetal accumulation. In addition, as reported (Negishi et al., 2007), the position of the inactive CAB was different than in the wild-type as a result of altered division patterns and rearrangements (Figure 7D). We conclude that a competition between length-dependent MT forces influenced by the yolk and the presence of a single polarity domain may account for the cleavage patterns of ascidians.

DISCUSSION

A model to predict the developmental morphogenesis of early embryos

By systematically exploring the mechanisms that specify embryonic cleavage with a 3D model, we here identify and test the generic designs that may pattern multiple rounds of divisions in different species. The model is kept minimal to allow the rapid exploration of simple rules which can account for a broad range of experimental results. Inputs such as dynamic instabilities or details of MT arrangement in asters are ignored, as they are expected to only impact parameters values in the model. The quality of our prediction relative to experimental data in normal as well as manipulated embryos indicates that we may capture all dominant features regulating cleavage patterns. The opaqueness of some eggs, their large size or fragility renders 3D imaging of early embryogenesis limited to a few systems (Olivier et al., 2010; Summers, 1993; Tassy et al., 2010). In addition, embryonic cleavage relies on maternal proteins and mRNA, rendering the genetic dissection of underlying mechanisms difficult (Pelegri et al., 2004). In this context, our model, which can rapidly explore the impact of parameters connecting MT forces to spatial organization layers such as yolk or polarity domains, or assay the contribution of blastomere adhesion or tension to morphogenesis, may be valuable to guide the design of future experiments.

Generic designs regulating division positioning

In early embryos of fishes and amphibians, we find that a basal hypothesis in which MTs pull within asters that probe cell shape, sister asters and yolk layers with length-dependent forces may predict cleavage patterns up to the 32- and 16-cell stage respectively. Polarity domains do not appear to be required to polarize development. Rather, the natural deposition of dense yolk at the bottom of large eggs may represent a simple way of polarizing a shape-driven cleavage pattern. Whether yolk granules act as steric obstacles or affect MT growth by molecular means remains an important open question (Dogterom and Yurke, 1997; Wuhr et al., 2010). A significant output of these models is that parameters influencing blastomere shapes and arrangement, such as cortical tension, cell-cell adhesion, and fertilization membranes, are key to define cleavage patterns in these embryos (Minc et al., 2011; Minc and Piel, 2012; Mitchison et al., 2012; Wuhr et al., 2010). Further experimental work focusing on the factors controlling these shape-regulating elements shall bring important insights into early embryogenesis in these systems.

Geometrical cues alone, however, are not sufficient to account for the patterns of echinoderms and ascidians. In both systems, our modelling analysis suggests that the effect of polar domains are super-imposed on the default geometrical contribution (Negishi et al., 2007; Tanaka, 1976). In asymmetrically dividing *C. elegans* zygotes, inhibition of the PAR polarity system yields a symmetric division with a division aligned along the cell long axis (Tsou et al., 2003). This suggests that the competition between MT forces exerted in bulk cytoplasm and those localized at cortical sites may be a conserved feature of many cell divisions. How this competition may be titrated in different systems remains an important question to address experimentally (Minc and Piel, 2012; Mitchison et al., 2012).

Our analysis of the contribution of polar domains to division patterns in echinoderms indicates how cortical domains may contribute to produce not only asymmetric but also symmetric divisions, oriented parallel or perpendicular to the domain. We propose that overlapping contributions of dynein-based MT sliding/pulling at the surface, and a system limited by the number of MT tips touching the domain, for instance involving depolymerizing activities, may account for these diverse phenotypes (Kozlowski et al., 2007). These findings are in agreement with recent evidence showing that both systems act in concert to orient spindles in mammalian adherent cells (Kwon et al., 2015). Given that these division orientation phenotypes have been reported in a wide range of cell types and situations, we expect our model to be valuable beyond embryonic cleavage.

Self-organization vs. determinism for embryonic development

Finally, we demonstrate that simple self-organization rules for MT forces may predict diverse events of 3D division positioning in developing embryos. The near constant biochemistry of early embryos and their rapid cell cycle may explain why those systems may rely more on self-organization, in contrast with more regulated deposition of cortical layers in somatic cells (Bosveld et al., 2016; Thery et al., 2007). In considering different cleavage patterns studied over the years, we note, however, that more ancestral protostome species such as worms or mollusks exhibit cleavage patterns that are highly specified from the onset of fertilization (Gilbert, 2010; Wilson, 1925). Those patterns exhibit large variations between closely-related species, and some of them may have even evolved to improve the fitness of an organism to a given niche (Gilbert, 2010; Hejnol, 2010; Schierenberg, 2006). In contrast, cleavages of deuterostomes, which include those of vertebrate and some marine invertebrate species, are

invariant and more labile, relying more on self-organization than determinism (Mitchison et al., 2012; Wennekamp et al., 2013). More quantitative studies of the generic designs that regulate cleavage may unravel where and how self-organization has been selected over determinism in evolution.

EXPERIMENTAL PROCEDURES

Model for predicting division position and orientation in 3D

The model predicting division position and orientation consists in computing the net force and torque created by a pair of MT asters. Forces and torques are calculated from summing the contribution of all MTs in the aster pairs, based on hypotheses on single astral MT forces detailed in the main text. The search for the mechanical equilibrium is achieved by using a directed search of force and torque minima, to minimize computing times. The model is coded in Matlab (Mathworks), and inputs a 3D binary matrix that defines cell shape and another one for polarity domains, when relevant. The shape matrix is generated from a binary stack, in which the cell volume is labeled. This stack is created from "The Surface Evolver": the coordinates of the surface vertices in the output file of "The Surface Evolver" serve to generate a binary stack in which the cell surface is labeled, via a Matlab script. The volume of the cell is then filled with ImageJ. The polarity matrix comes from binary stacks created with ImageJ. A yolk gradient 3D matrix is directly generated in the Matlab program.

The directed search for the mechanical equilibrium loop is initiated from the center of mass of the shape matrix, with a random orientation. At each iteration of this loop, one of the coordinates x, y, z, θ or φ, randomly chosen, is changed according to the force/torque direction calculated at the previous iteration, with a step size of 1 pixel for x, y or z and 1° for θ and φ. If the force/torque does not change sign (or is smaller), the new position/orientation is kept. In order to avoid local minima due to pixel noise, a non-zero probability of keeping the new position anyways was set.

Details of the parameters used, how they are varied and may influence the results of simulations throughout this study are provided in great details in Supplemental Information. Briefly, the relevant parameters for this model are:

The aster extension ψ, the distance between centrosomes D_c, and the scaling exponent δ, which are the sole parameters used for the length-dependent contribution of MTs. For simulation accounting for yolk gradients, the parameters μ which represents the sharpness of the gradient and ε its offset from egg center serve to generate yolk gradients, and an additional parameter η is used to compute the sensitivity of MTs to yolk. Finally to incorporate a contribution from surface polarity domains, a parameter Δpol is used to represent the size of the domain, and the parameters β, γ and a are used for the laws which account for the contribution of polarity to MTs forces, as described in the main text.

Model to compute blastomere shapes and rearrangements

Blastomere shapes and arrangement were computed with "The Surface Evolver" (Brakke, 1992). Input files include the topology of the embryo (coordinates of faces and edges that define cell-cell contacts), the target volumes, which are both inferred from the previous division prediction, surface tensions values (γ_{ext} and γ_{int}) and confinement parameters. The calculations performed by the software are iterative, starting from cubic-like shapes (Movie S1). The calculation is stopped when the cells stop changing shapes, but before their complete rearrangement, to account for the effect of adhesion. Fast rearrangements and neighbor exchanges are however permitted.

Details of parameters used and how they are varied in simulations throughout this study are provided in great details in Supplemental Information. Briefly those are: the surface tension of the cell-medium interface γ_{ext}, the surface tension of the cell-cell interface γ_{int}, and the envelope confinement geometry R.

A starter package with models and brief notes on how to use them is included in Supplemental Information (Supplementary Item S1).

Immunostaining

Detailed protocols for fixation and immunostaining for Xenopus, and sea urchin are provided in (Minc et al., 2011; Wuhr et al., 2008) (Wuhr et al., 2008). The protocol for sea urchin was modified to include the addition of an antibody against Dishevelled, kindly provided by Pr Wikramanayake, used at 1/2000 (Peng and Wikramanayake, 2013). Zebrafish embryos expressing the microtubules marker EMTB-3xGFP, Tg(actb2:Hsa.MAP7-EGFP) (Wuhr et al., 2011), were fixed with (0.25 to 0.50% FA, 0.1% GA, 80 mM K Pipes, pH 6.8, 1 mM MgCl2, 5 mM EGTA, 0.2% Triton X-100) (slightly modified from (Becker and Gard, 2006) (Becker and Gard, 2006)). Embryos were cleared with 40% Quinoline, 32% glycerol, 28% water, 1% 2M Amonium Sulfate and stained with 1 µg/mL of Rhodamine-Phalloidin and 5 µg/mL ToPro3.

SDS detergent experiments

To test the effect of detergent on the coplanarity of divisions at the 2-cell stage in sea urchins, eggs were placed in a solution of 4.10^{-6} % SDS in sea water (40 ng/mL), from the end of sperm aster centration (10-15 min after fertilization). Embryos were fixed at the 2-cell stage interphase, and stained for Dishevelled, MTs and DNA.

Image Analysis

Correlation between Yolk and MT density

Intensity profiles were taken within the asters, from the yolk and MT channels of immunostaining images of 2-cell stage Xenopus embryos (from 149 to 160 min pf). Profiles were averaged on a 5 pixels width to reduce noise. For each profile, the correlative yolk and MT intensity ratios were plotted along the distance to the nucleus L, using a Matlab script.

Interphase aster branching

MT density was measured from immunostaining images of 1 to 8-cell stage sea urchin embryos, stained for MTs. Intensity profiles were taken from the centrosome to the maximum of MT intensity near the cell cortex (to circumvent staining artefacts that lower MT intensity close to the cell cortex), in several directions. Profiles were averaged on a 5 pixels width and on 1 to 4 z-slices (spaced by 2 µm) to reduce noise. They were corrected for size of the embryo and mean intensity of the image, averaged and fitted by $I = b\, 2^{L/a} / L^2 + c$ in Matlab. $L < 5$ µm and $L > 25$ µm ranges were excluded from the fit, because of averaging and staining artifacts respectively.

AUTHOR CONTRIBUTION

A.P. developed and performed models. A.P, J.S, M.W and N.M performed experiments. A.P. and N.M designed the research and wrote the manuscript.

ACKNOWLEDGMENTS

We thank present and past members of the Minc Laboratory for discussions, as well as our colleagues Yohanns Bellaiche, Michel Bornens, Arezki Boudaoud and Kimberley Laband for critical reading of the manuscript. A.P. was supported by an ASN fellowship from ENS Cachan. MW was supported by NIH grants HD073104 and GM39565. This work was supported by the CNRS, and grants from the “Mairie de Paris emergence” program, the FRM “amorçage” grant AJE20130426890 and the European Research Council (CoG FORCASTER N° 647073).

REFERENCES

Becker, B.E., and Gard, D.L. (2006). Visualization of the cytoskeleton in Xenopus oocytes and eggs by confocal immunofluorescence microscopy. Methods Mol Biol *322*, 69-86.

Bjerknes, M. (1986). Physical theory of the orientation of astral mitotic spindles. Science *234*, 1413-1416.

Bosveld, F., Markova, O., Guirao, B., Martin, C., Wang, Z., Pierre, A., Balakireva, M., Gaugue, I., Ainslie, A., Christophorou, N.*, et al.* (2016). Epithelial tricellular junctions act as interphase cell shape sensors to orient mitosis. Nature *530*, 495-498.

Boveri, T. (1901). Über die Polarität des Seeigel-Eies. Verhandl d Phys-Med GesellschaftWürzburg *34*.

Brakke, K.A. (1992). The Surface Evolver. Experimental Mathematics *1*, 141-165.

Conklin, E.G. (1931). The development of centrifuged eggs of ascidians. The Journal of Experimental Zoölogy *60*, 1-120.

Dan, K. (1979). Studies on unequal cleavage in sea urchins I. Migration of the nuclei to the vegetal pole. Development, Growth and Differentiation *21*, 527-535.

Dan, K. (1987). Studies on unequal cleavage in sea urchins III. Micromere formation under compression. Development, Growth and Differentiation *29*, 503-515.

Dan, K., Ikeda, M. (1971). On the system controlling the time of micromere formation in sea urchin embryos. Development, Growth and Differentiation *13*.

Danilchik, M.V., Brown, E.E., and Riegert, K. (2006). Intrinsic chiral properties of the Xenopus egg cortex: an early indicator of left-right asymmetry? Development *133*, 4517-4526.

Desnitskiy, A.G. (2014). On the classification of the cleavage patterns in amphibian embryos. Russian Journal of Developmental Biology *45*, 1-10.

Dogterom, M., and Yurke, B. (1997). Measurement of the force-velocity relation for growing microtubules. Science *278*, 856-860.

Drechsel, D.N., Hyman, A.A., Hall, A., and Glotzer, M. (1997). A requirement for Rho and Cdc42 during cytokinesis in Xenopus embryos. Curr Biol *7*, 12-23.

Gilbert, S. (2010). Developmental Biology. 9th edition., Vol 9th Ed (Sunderland (MA), Sinauer Associates).

Goldstein, B. (1995). Cell contacts orient some cell division axes in the Caenorhabditis elegans embryo. J Cell Biol *129*, 1071-1080.

Gonczy, P. (2008). Mechanisms of asymmetric cell division: flies and worms pave the way. Nat Rev Mol Cell Biol *9*, 355-366.

Grill, S.W., and Hyman, A.A. (2005). Spindle positioning by cortical pulling forces. Dev Cell *8*, 461-465.

Hamaguchi, M.S., and Hiramoto, Y. (1986). Analysis of the Role of Astral Rays in Pronuclear Migration in Sand Dollar Rggs by the Colcemid-UV Method. Develop Growth and Differ *28*, 143-156.

Heier, J., Takle, K.A., Hasley, A.O., and Pelegri, F. (2015). Ploidy manipulation and induction of alternate cleavage patterns through inhibition of centrosome duplication in the early zebrafish embryo. Dev Dyn *244*, 1300-1312.

Hejnol, A. (2010). A twist in time--the evolution of spiral cleavage in the light of animal phylogeny. Integr Comp Biol *50*, 695-706.

Hertwig, O. (1893). Ueber den Werth der ersten Furchungszellen fuer die Organbildung des Embryo. Experimentelle Studien am Frosch- und Tritonei. Arch mikr Anat *xlii* 662–807.

Hörstadius, S. (1928). Über die Determination des Keimes bei Echinodermen. Acta Zoologica, Stockholm *9*.

Hörstadius, S. (1939). The mechanics of sea urchin development, studied by operative methods. Biological Reviews *14*, 132-179.

Iseto, T., and Nishida, H. (1999). Ultrastructural studies on the centrosome-attracting body: electron-dense matrix and its role in unequal cleavages in ascidian embryos. Dev Growth Differ *41*, 601-609.

Kimmel, C.B., Ballard, W.W., Kimmel, S.R., Ullmann, B., and Schilling, T.F. (1995). Stages of embryonic development of the zebrafish. Dev Dyn *203*, 253-310.

Kozlowski, C., Srayko, M., and Nedelec, F. (2007). Cortical microtubule contacts position the spindle in C. elegans embryos. Cell *129*, 499-510.

Kwon, M., Bagonis, M., Danuser, G., and Pellman, D. (2015). Direct Microtubule-Binding by Myosin-10 Orients Centrosomes toward Retraction Fibers and Subcortical Actin Clouds. Dev Cell *34*, 323-337.

Leonard, J.D., and Ettensohn, C.A. (2007). Analysis of dishevelled localization and function in the early sea urchin embryo. Dev Biol *306*, 50-65.

Maitre, J.L., Niwayama, R., Turlier, H., Nedelec, F., and Hiiragi, T. (2015). Pulsatile cell-autonomous contractility drives compaction in the mouse embryo. Nat Cell Biol *17*, 849-855.

Minc, N., Burgess, D., and Chang, F. (2011). Influence of cell geometry on division-plane positioning. Cell *144*, 414-426.

Minc, N., and Piel, M. (2012). Predicting division plane position and orientation. Trends Cell Biol *22*, 193-200.

Mitchison, T., Wuhr, M., Nguyen, P., Ishihara, K., Groen, A., and Field, C.M. (2012). Growth, interaction, and positioning of microtubule asters in extremely large vertebrate embryo cells. Cytoskeleton (Hoboken) *69*, 738-750.

Neff, A.W., Wakahara, M., Jurand, A., and Malacinski, G.M. (1984). Experimental analyses of cytoplasmic rearrangements which follow fertilization and accompany symmetrization of inverted Xenopus eggs. J Embryol Exp Morphol *80*, 197-224.

Negishi, T., Takada, T., Kawai, N., and Nishida, H. (2007). Localized PEM mRNA and protein are involved in cleavage-plane orientation and unequal cell divisions in ascidians. Curr Biol *17*, 1014-1025.

Nishida, H. (1994). Localization of determinants for formation of the anterior-posterior axis in eggs of the ascidian Halocynthia roretzi. Development *120*, 3093-3104.

Nishida, H. (1996). Vegetal egg cytoplasm promotes gastrulation and is responsible for specification of vegetal blastomeres in embryos of the ascidian Halocynthia roretzi. Development *122*, 1271-1279.

Nishikata, T., Hibino, T., and Nishida, H. (1999). The centrosome-attracting body, microtubule system, and posterior egg cytoplasm are involved in positioning of cleavage planes in the ascidian embryo. Dev Biol *209*, 72-85.

Olivier, N., Luengo-Oroz, M.A., Duloquin, L., Faure, E., Savy, T., Veilleux, I., Solinas, X., Debarre, D., Bourgine, P., Santos, A.*, et al.* (2010). Cell lineage reconstruction of early zebrafish embryos using label-free nonlinear microscopy. Science *329*, 967-971.

Pelegri, F., Dekens, M.P., Schulte-Merker, S., Maischein, H.M., Weiler, C., and Nusslein-Volhard, C. (2004). Identification of recessive maternal-effect mutations in the zebrafish using a gynogenesis-based method. Dev Dyn *231*, 324-335.

Pelegri, F., Knaut, H., Maischein, H.M., Schulte-Merker, S., and Nusslein-Volhard, C. (1999). A mutation in the zebrafish maternal-effect gene nebel affects furrow formation and vasa RNA localization. Curr Biol *9*, 1431-1440.

Peng, C.J., and Wikramanayake, A.H. (2013). Differential regulation of disheveled in a novel vegetal cortical domain in sea urchin eggs and embryos: implications for the localized activation of canonical Wnt signaling. PLoS One *8*, e80693.

Raff, R.A. (1987). Constraint, flexibility, and phylogenetic history in the evolution of direct development in sea urchins. Dev Biol *119*, 6-19.

Roegiers, F., Djediat, C., Dumollard, R., Rouviere, C., and Sardet, C. (1999). Phases of cytoplasmic and cortical reorganizations of the ascidian zygote between fertilization and first division. Development *126*, 3101-3117.

Sachs, J. (1887). Lecture XXVII. Relations between growth and cell-division in the embryonic tissues. (Oxford, UK, Clarendon Press).

Sawada, T., and Schatten, G. (1988). Microtubules in ascidian eggs during meiosis, fertilization, and mitosis. Cell Motil Cytoskeleton *9*, 219-230.

Schierenberg, E. (2006). Embryological variation during nematode development. WormBook, 1-13.

Summers, R.G., Morrill J. B., Leith, A., Marko, M., Piston, D. W., Stonebraker, A. T. (1993). A stereometric analysis of karyokinesis, cytokinesis and cell arrangements during and following fourth cleavage period in he sea urchin, lytechinus variegatus. Development, Growth and Differentiation *35*, 41-57.

Tanaka, Y. (1976). Effects of the surfactants on the cleavage and further development of the sea urchin embryos 1. The inhibition of micromere formation at the fourth cleavage. Development, Growth and Differentiation *18*, 113-122.

Tanimoto, H., Kimura, A., and Minc, N. (2016). Shape-motion relationships of centering microtubule asters. J Cell Biol *212*, 777-787.

Tassy, O., Dauga, D., Daian, F., Sobral, D., Robin, F., Khoueiry, P., Salgado, D., Fox, V., Caillol, D., Schiappa, R.*, et al.* (2010). The ANISEED database: digital representation, formalization, and elucidation of a chordate developmental program. Genome Res *20*, 1459-1468.

Thery, M., Jimenez-Dalmaroni, A., Racine, V., Bornens, M., and Julicher, F. (2007). Experimental and theoretical study of mitotic spindle orientation. Nature *447*, 493-496.

Tsou, M.F., Ku, W., Hayashi, A., and Rose, L.S. (2003). PAR-dependent and geometry-dependent mechanisms of spindle positioning. J Cell Biol *160*, 845-855.

Urven, L.E., Yabe, T., and Pelegri, F. (2006). A role for non-muscle myosin II function in furrow maturation in the early zebrafish embryo. J Cell Sci *119*, 4342-4352.

Webb, S.E., Lee, K.W., Karplus, E., and Miller, A.L. (1997). Localized calcium transients accompany furrow positioning, propagation, and deepening during the early cleavage period of zebrafish embryos. Dev Biol *192*, 78-92.

Wennekamp, S., Mesecke, S., Nedelec, F., and Hiiragi, T. (2013). A self-organization framework for symmetry breaking in the mammalian embryo. Nat Rev Mol Cell Biol *14*, 452-459.

Wilson, E.B. (1925). The cell in development and heredity. (New-York, Macmillan).

Wuhr, M., Chen, Y., Dumont, S., Groen, A.C., Needleman, D.J., Salic, A., and Mitchison, T.J. (2008). Evidence for an upper limit to mitotic spindle length. Curr Biol *18*, 1256-1261.

Wuhr, M., Dumont, S., Groen, A.C., Needleman, D.J., and Mitchison, T.J. (2009). How does a millimeter-sized cell find its center? Cell Cycle *8*, 1115-1121.

Wuhr, M., Tan, E.S., Parker, S.K., Detrich, H.W., 3rd, and Mitchison, T.J. (2010). A model for cleavage plane determination in early amphibian and fish embryos. Curr Biol *20*, 2040-2045.

Xiong, F., Ma, W., Hiscock, T.W., Mosaliganti, K.R., Tentner, A.R., Brakke, K.A., Rannou, N., Gelas, A., Souhait, L., Swinburne, I.A.*, et al.* (2014). Interplay of cell shape and division orientation promotes robust morphogenesis of developing epithelia. Cell *159*, 415-427.

Yokota, H., Neff, A.W., and Malacinski, G.M. (1992). Altering the position of the first horizontal cleavage furrow of the amphibian (Xenopus) egg reduces embryonic survival. Int J Dev Biol *36*, 527-535.

FIGURES

Figure 1: A modelling framework to predict cleavage morphogenesis of early embryos.

(A) 3D model to predict division plane positioning and orientation from cell shape. Interphase MT asters exert forces and torques on centrosomes that scale to MT lengths (top). Definition of 3D positions and angles for the centrosome pair axis and individual MTs used to project forces and torques (Bottom, See Supplemental Information). **(B)** Principle of the directed search for mechanical equilibrium used to identify the position and orientation of aster pairs. The calculated force and torque directions lead the centrosome pair from a random starting point to its equilibrium position and orientation, that corresponds to a near-zero torque and force (center), and determines the position and orientation of the future division plane (right). **(C)** Shapes and arrangements of divided blastomeres are generated with "The Surface Evolver" software that minimizes surface energy under custom constraints, including cells volumes, surface tensions and confinement. **(D)** Influence of the ratio of cell-cell tension, γ_{int} over cell-medium tension, γ_{ext} on blastomere shapes. **(E)** Influence of confinement that mimics the impact of fertilization envelopes on blastomere shapes. **(F)** Iterative modelling framework subsequently predicting blastomere shape/arrangement and division position to develop embryos *in silico.*

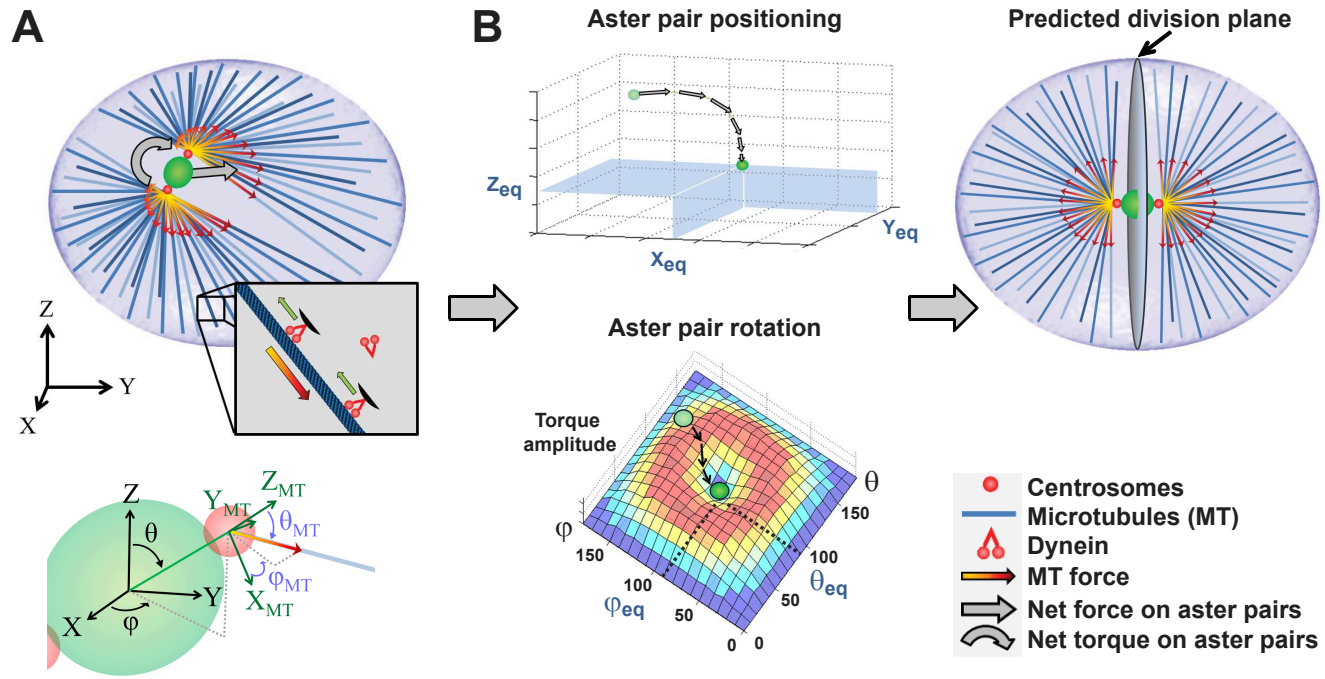
A
B
Aster pair positioning
Predicted division plane
Aster pair rotation
Torque amplitude
Centrosomes
Microtubules (MT)
Dynein
MT force
Net force on aster pairs
Net torque on aster pairs

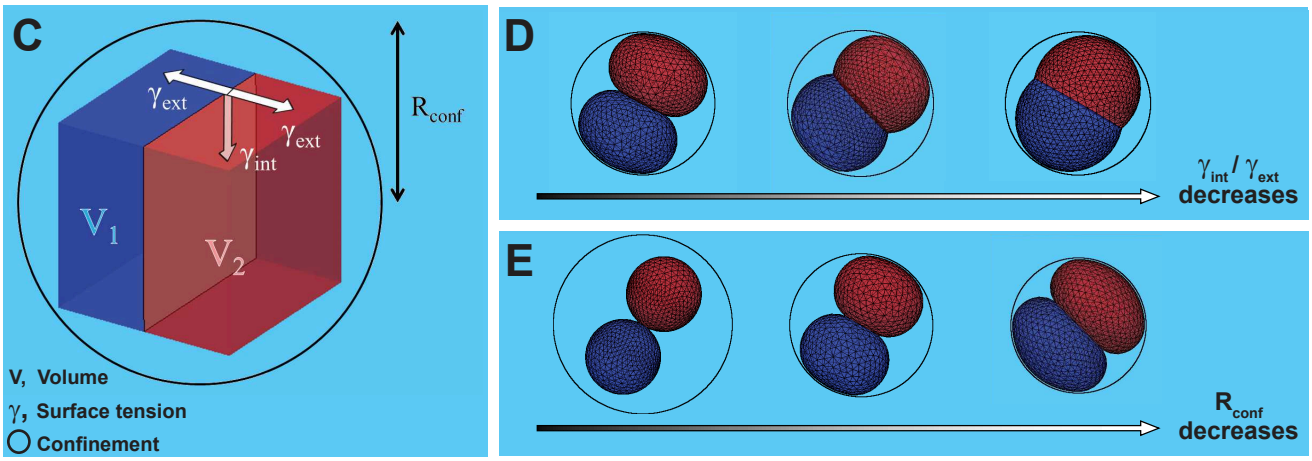
C
D
E
V, Volume
γ, Surface tension
Confinement
γint / γext decreases
Rconf decreases

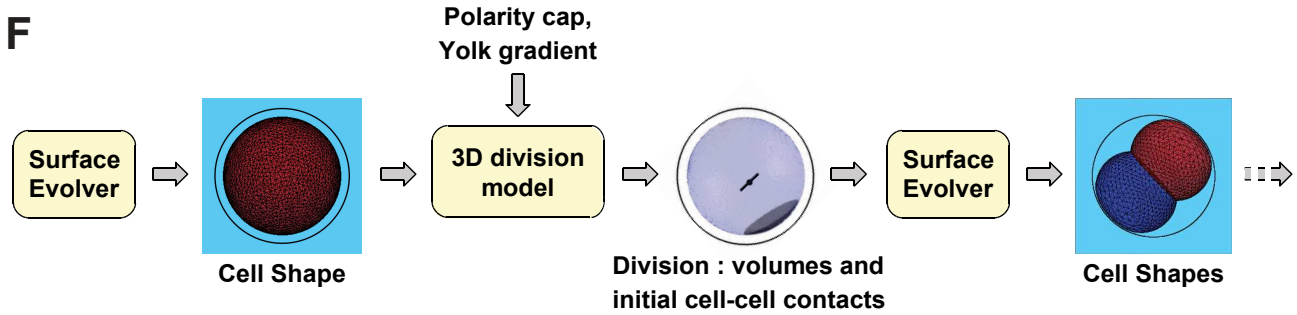
F
Polarity cap,
Yolk gradient
Surface Evolver
3D division model
Surface Evolver
Cell Shape
Division : volumes and initial cell-cell contacts
Cell Shapes

Figure 2: Division positioning based on aster shapes and MT length-dependent forces may account for fish early development.

(A) Cleavage patterns, and interphase aster position in zebrafish embryo (adapted from (Olivier et al., 2010; Wuhr et al., 2010)). A large fraction of the embryo is filled with yolk (yellow) that stops aster growth. (**B)** Model predictions of early embryo development. **(C)** Schematic subsequent 3D division positions and orientation (adapted from (Olivier et al., 2010)). Note the switch of division orientation in the 4 central blastomeres at the 5th cleavage (orange). Numbers represent the cleavage stage. **(D)** Predicted division patterns from the model solely based on length-dependent forces. **(E)** Effect of lowering cortical tension on morphogenesis and division patterns. Note the absence of switch at the 5th cleavage in the model. (Right) Schematic phenotype of controls and embryos treated with blebbistatin that reduces cortical tension (adapted from (Urven et al., 2006)). **(F)** Effect of increasing cell-cell tension on morphogenesis and division patterns. Note the spreading of blastomere on the yolk layer and the absence of division orientation switch at the 5th cleavage. (Right) Schematic phenotype of WT and *nebel* mutant embryos, defective in cell-cell adhesion (adapted from (Pelegri et al., 1999)).

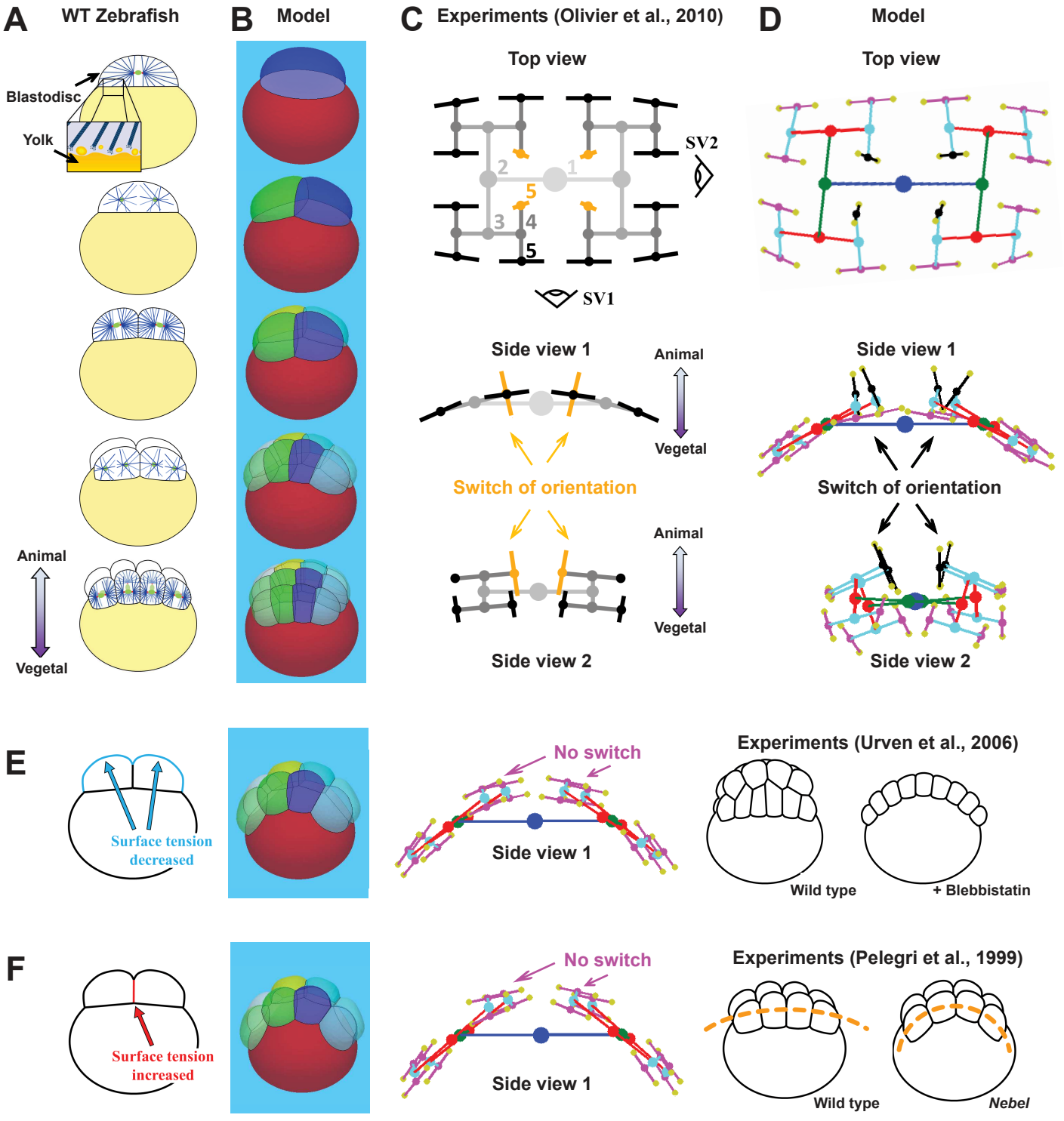
A
WT Zebrafish
Blastodisc
Yolk
Animal
Vegetal
B
Model
C
Experiments (Olivier et al., 2010)
Top view
SV2
SV1
1
2
3
4
5
Side view 1
Animal
Vegetal
Switch of orientation
Animal
Vegetal
Side view 2
D
Model
Top view
Side view 1
Switch of orientation
Side view 2
E
Surface tension decreased
No switch
Side view 1
Experiments (Urven et al., 2006)
Wild type
+ Blebbistatin
F
Surface tension increased
No switch
Side view 1
Experiments (Pelegri et al., 1999)
Wild type
Nebel

Figure 3: Gradual influence of yolk concentration on MT length and consequent forces may account for early amphibian cleavage pattern.

(A) Early developmental patterns and aster organization in Xenopus embryo (adapted from (Gilbert, 2010) and (Wuhr et al., 2010)). Yolk granules form a gradient in the cytoplasm, and the model now posits that MTs angular density decreases as a function of yolk concentration. **(B)** Immunostaining image showing the organization of interphase MTs (green) around yolk granules (red) in a Xenopus 2-cell stage embryo. Scale bar: 40µm. **(C)** Model predictions, the yolk is depicted in black inside the embryos. **(D)** Influence of gravity on yolk gradient and consequence on the asymmetry of the 3rd divisions computed by the AVCR (Animal-Vegetal Cleavage Ratio) in experiments (Yokota et al., 1992) and in the model (crosses, numbered red circles corresponding to bottom images). **(E)** Influence of MT stability in yolk on AVCR in experiments (Yokota et al., 1992) and in the model (crosses, numbered red circles corresponding to bottom images). **(F and G)** Hertwig's egg compression experiments (Hertwig, 1893). **(F)** Impact of compression orthogonal to the animal-vegetal axis in experiments and in the model. **(G)** Impact of compression along the animal-vegetal axis in experiments and in the model.

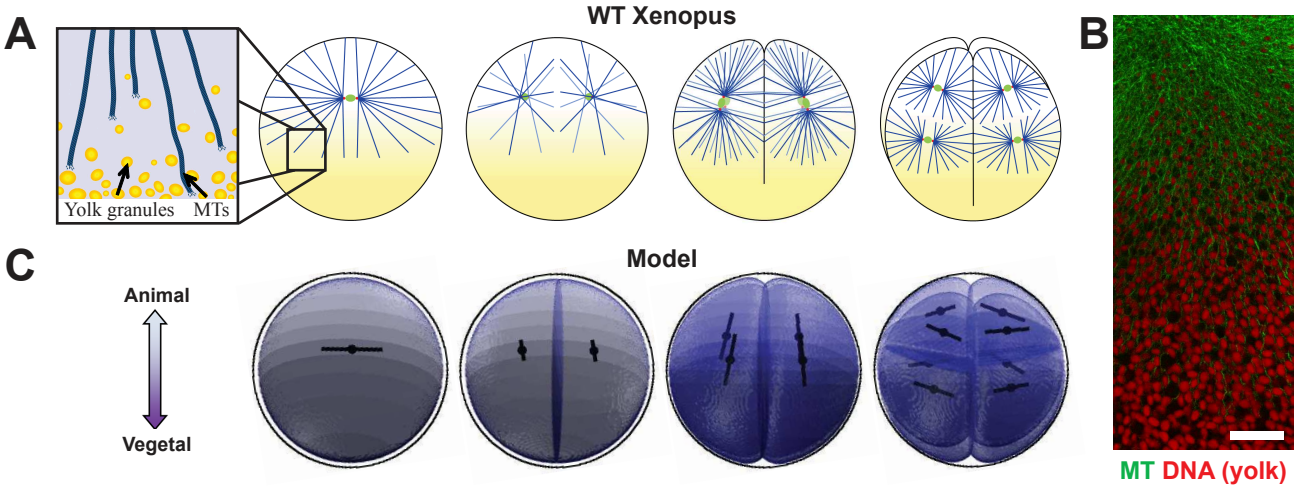
A
WT Xenopus
Yolk granules
MTs
B
MT DNA (yolk)
C
Model
Animal
Vegetal

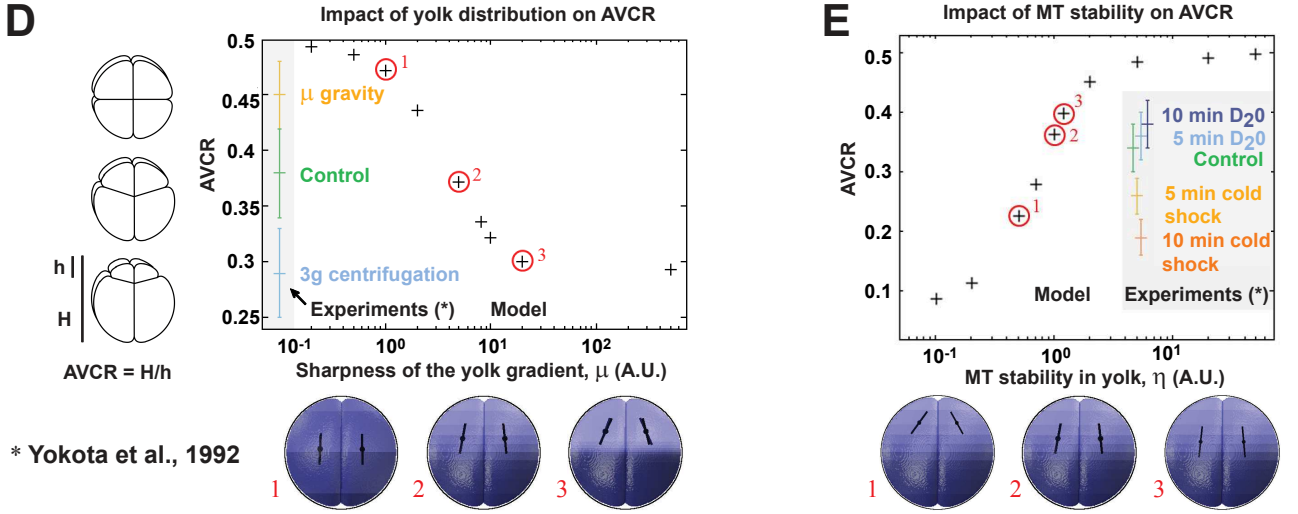
D
Impact of yolk distribution on AVCR
AVCR = H/h
μ gravity
Control
3g centrifugation
Experiments (*)
Model
AVCR
Sharpness of the yolk gradient, μ (A.U.)
* Yokota et al., 1992
E
Impact of MT stability on AVCR
10 min D20
5 min D20
Control
5 min cold shock
10 min cold shock
MT stability in yolk, η (A.U.)

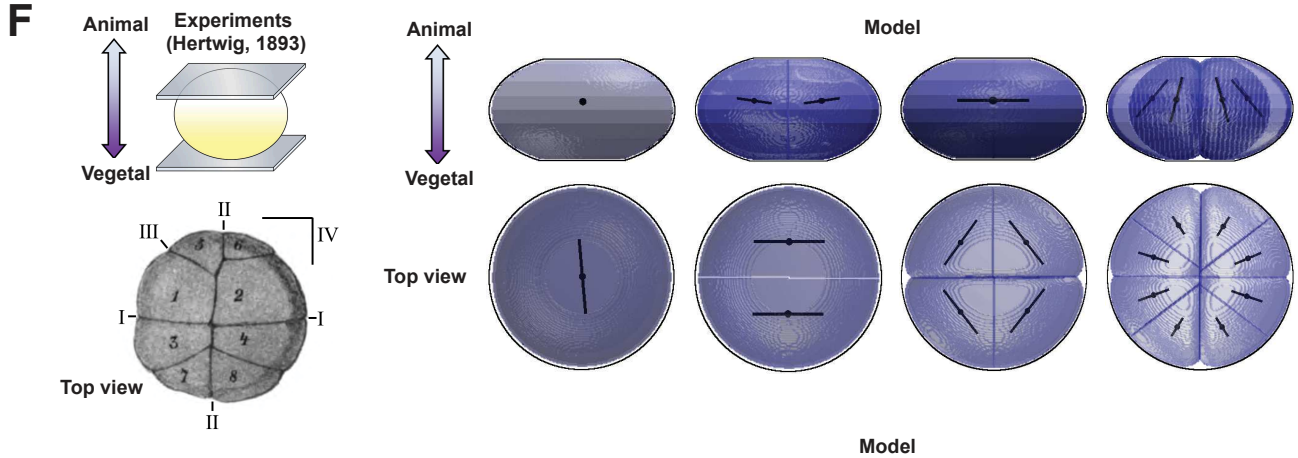
F
Animal
Experiments (Hertwig, 1893)
Vegetal
Top view
Model
G
Side view

Figure 4: A single maternal cortical domain may superimpose on cell geometry to orient divisions with respect to the A-V axis in echinoderms.

(A) Early developmental patterns and interphase aster organization of sea urchin embryos (adapted from (Gilbert, 2010; Minc et al., 2011; Peng and Wikramanayake, 2013)). **(B)** Immunostaining images of sea urchin early development, showing MT interphase asters (green), Dishevelled (red, arrows) and DNA (blue). Scale bar: 20µm. **(C)** Geometry alone is not sufficient to account for the co-planarity of the 2-cell stage division axes. (Left) Simulation of the 2nd round of divisions, solely based on cell shape. (Middle) Immunostaining image of SDS-treated 2-cell stage embryos, showing MT interphase asters (green) and DNA (blue). The two division axes are not coplanar. Scale bar: 20 µm. (Right) Quantification of the co-planarity of division axes in 2-cell stage SDS-treated embryos (N = 37), as compared to control embryos (N = 17). **(D)** A model solely based on geometry with no input from the vegetal polar domain cannot account for the asymmetric divisions in vegetal blastomeres at the 8-cell stage, but may account for symmetric patterns seen in embryos treated with SLS detergent that may inhibit effects of the cortical domain, depicted as a scheme on the right (Dan, 1979).

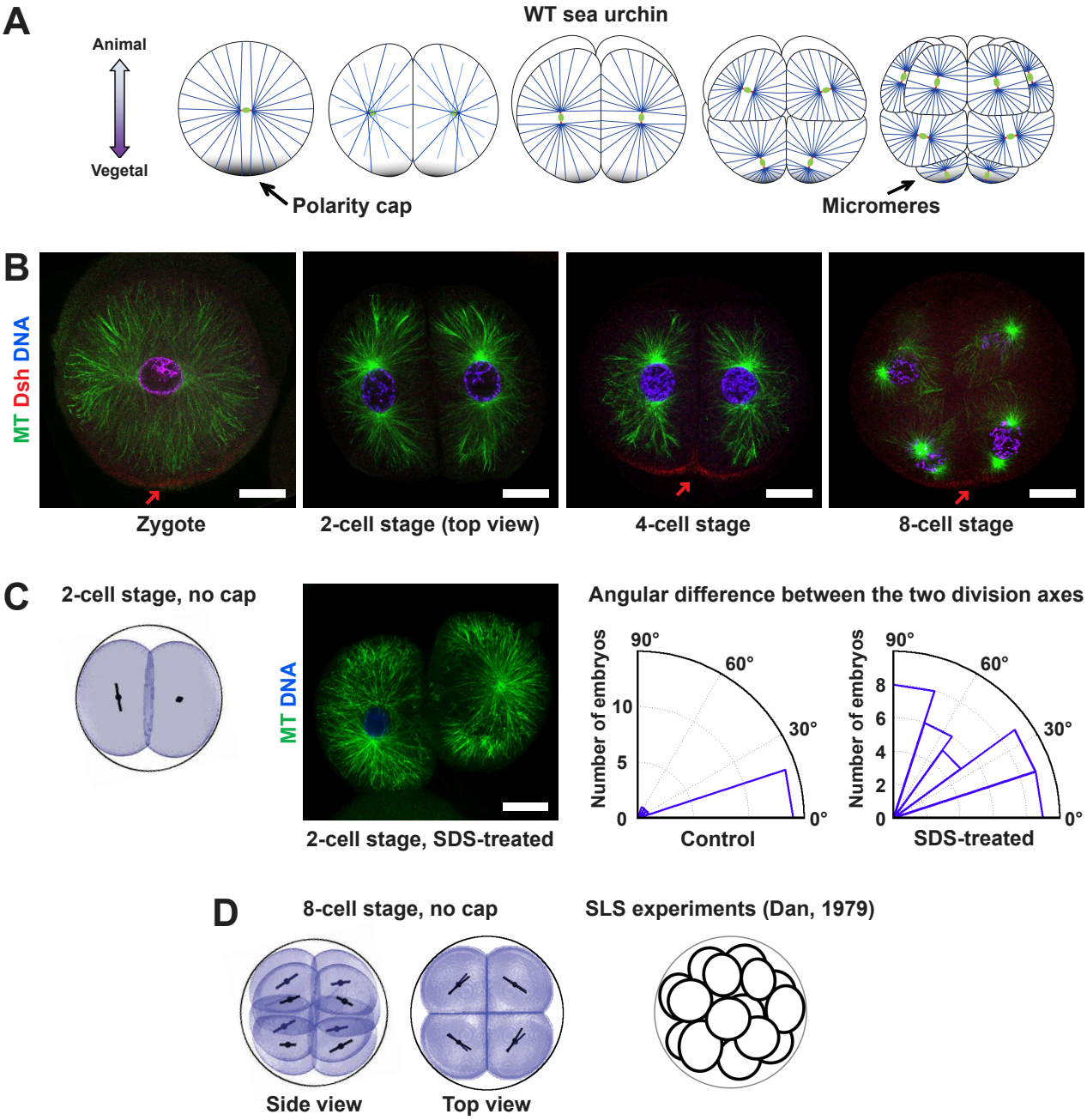
A
WT sea urchin
Animal
Vegetal
Polarity cap
Micromeres
B
MT Dsh DNA
Zygote
2-cell stage (top view)
4-cell stage
8-cell stage
C
2-cell stage, no cap
MT DNA
2-cell stage, SDS-treated
Angular difference between the two division axes
Number of embryos
90°
60°
30°
0°
10
5
0
Control
8
6
4
2
SDS-treated
D
8-cell stage, no cap
Side view
Top view
SLS experiments (Dan, 1979)

Figure 5: Cleavage-stage dependent competition between geometry and two distinct cortical mechanisms on MT forces may underlie echinoderm cleavage patterns.

(A) Additional hypothesis for the division model: in addition to MT length-dependent pulling, MTs contacting the polar domain may pull by two distinct mechanisms: (1) a sliding mechanism limited by dynein concentration/activity at the cap; and (2) an end-on mechanism that depends on the number of MT tips reaching the cap, which, as a result of MT branching, depends on MT length in an exponential manner. **(B)** Model predictions with polar domains represented in black. In the first 3 rounds of divisions, contribution (1) is small (i), and increases in strength in the 4th and 5th cleavages to promote asymmetric division (ii). More precisely for MTs extending from the centrosome to the polar domain along the A-V axis the relative contribution of the geometry term (αL^3), the sliding mechanism (βL^2) and the end-on mechanism ($\gamma 2^{L/a}$) are: (40-45%, <10%, 50-55%) for the 1 and 2-cell stage, (30-50%, <40%, 30-50%) for the 4-cell stage and (2.6%, 93.1%, 4.3%) for the 8-cell stage. **(C)** Evidence for a timing associated with an increase in strength of the cap promoting asymmetric division, in cell-cycle delay experiments (Dan, 1971) and in the model (crosses, numbered red circles corresponding to bottom images).

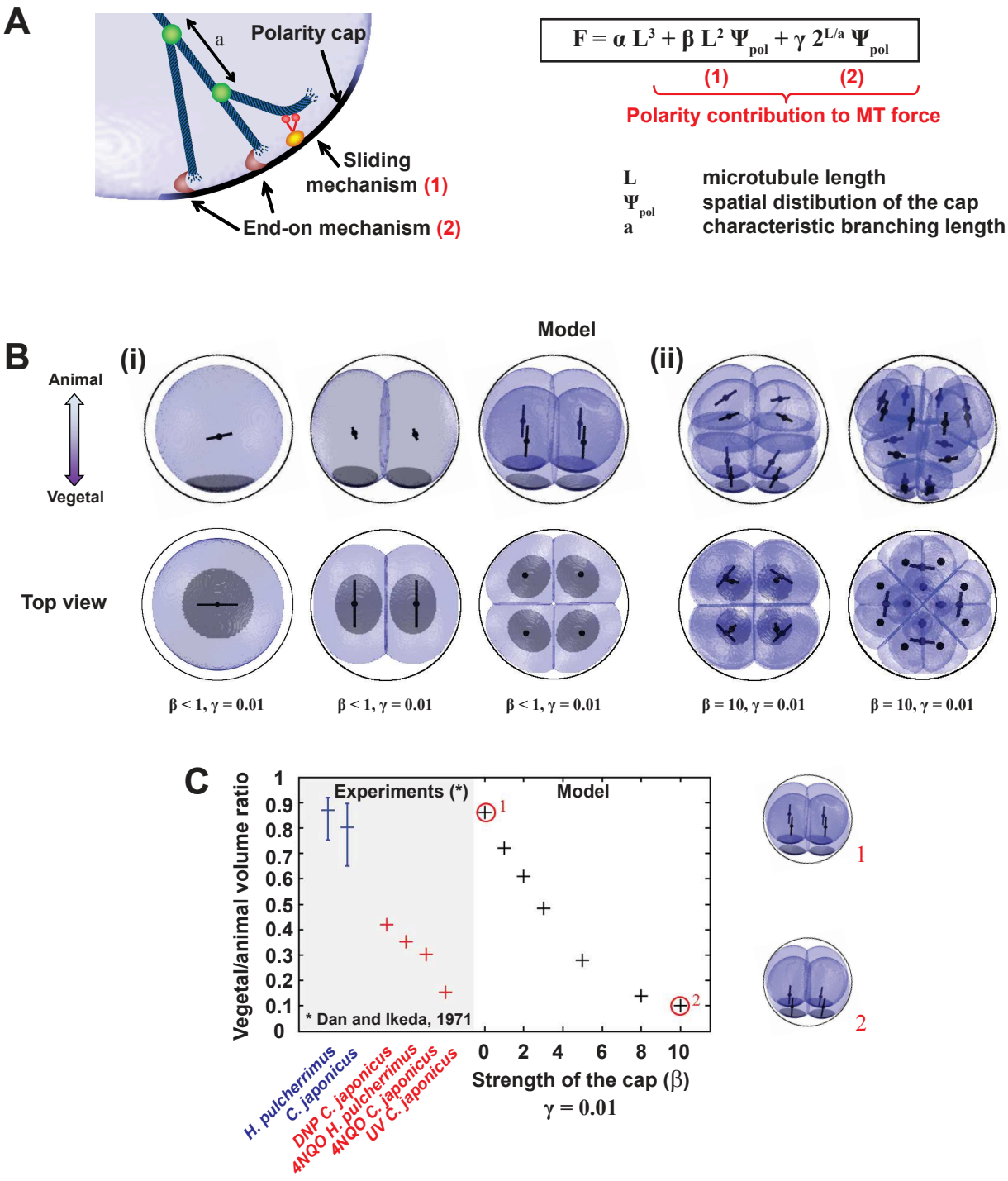
A
a
Polarity cap
Sliding mechanism (1)
End-on mechanism (2)
F = α L³ + β L² Ψpol + γ 2^(L/a) Ψpol
(1)
(2)
Polarity contribution to MT force
L microtubule length
Ψpol spatial distibution of the cap
a characteristic branching length
B
Model
(i)
(ii)
Animal
Vegetal
Top view
β < 1, γ = 0.01
β < 1, γ = 0.01
β < 1, γ = 0.01
β = 10, γ = 0.01
β = 10, γ = 0.01
C
Experiments (*)
Model
* Dan and Ikeda, 1971
Vegetal/animal volume ratio
Strength of the cap (β)
γ = 0.01
H. pulcherrimus
C. japonicus
DNP C. japonicus
4NQO H. pulcherrimus
4NQO C. japonicus
UV C. japonicus
1
2

Figure 6: Comparison of model prediction and experiments assaying the competition between polarity and geometry in echinoderms.

(A-B) : Hörstadius' experiment assaying the impact of delays in cleavage on division patterns (Hörstadius, 1939). **(A)** Cell cycle delay is induced by placing embryos in diluted sea water. **(B)** Variation of this assay and corresponding predictions of the model obtained by solely changing the value of cap strength β, at various cleavage stages. **(C)** Dan's egg compression experiments (Dan, 1987). **(D)** Impact of egg flattening on the appearance and location of micromeres in experiments and models.

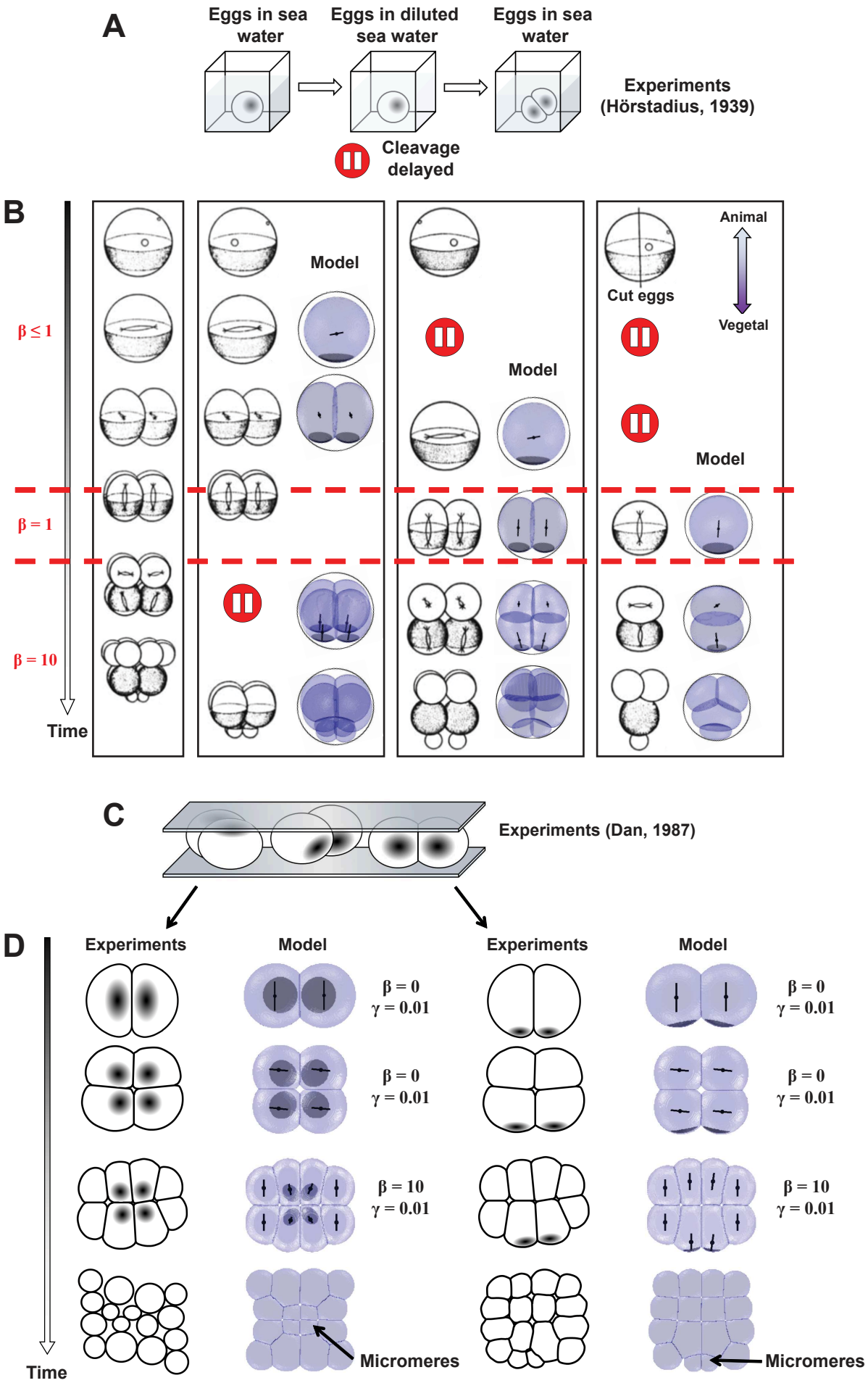
A
Eggs in sea water
Eggs in diluted sea water
Eggs in sea water
Experiments (Hörstadius, 1939)
Cleavage delayed
B
β ≤ 1
β = 1
β = 10
Time
Model
Model
Model
Cut eggs
Animal
Vegetal
C
Experiments (Dan, 1987)
D
Experiments
Model
Experiments
Model
β = 0 γ = 0.01
β = 0 γ = 0.01
β = 10 γ = 0.01
β = 0 γ = 0.01
β = 0 γ = 0.01
β = 10 γ = 0.01
Micromeres
Micromeres
Time

Figure 7: Ascidians bilateral cleavage pattern may integrate both influence of yolk on MT length-dependent forces, and the effect of a single polar domain.

(A) Cleavage patterns and aster organization in ascidian embryos (adapted from (Negishi et al., 2007)). Cytoplasm rotation in the zygote contributes to the accumulation of yolk at the presumptive vegetal and anterior poles. The polar domain (CAB, Centrosome Attracting Body) assembles at the presumptive posterior pole and influences aster position from the 2nd cleavage. **(B)** Cut top view of an egg which highlights the yolk accumulation at the anterior pole and the position of aster shifted away from the yolk (Conklin, 1931). **(C)** Model predictions using the same equations as in Figure 5A for the contribution of the polar domain, with a strength increasing at the 2-cell stage, and the same assumptions on the yolk gradients as in Figure 3. (Right) 16-cell stage blastomeres arrangement and typical embryo pointy shape predicted with "The Surface Evolver". **(D)** Cleavage radialization achieved by CAB physical ablation (Nishida, 1994; Nishikata et al., 1999) or PEM-mRNA knock-down (Negishi et al., 2007), and its simulation with a non-pulling cap.

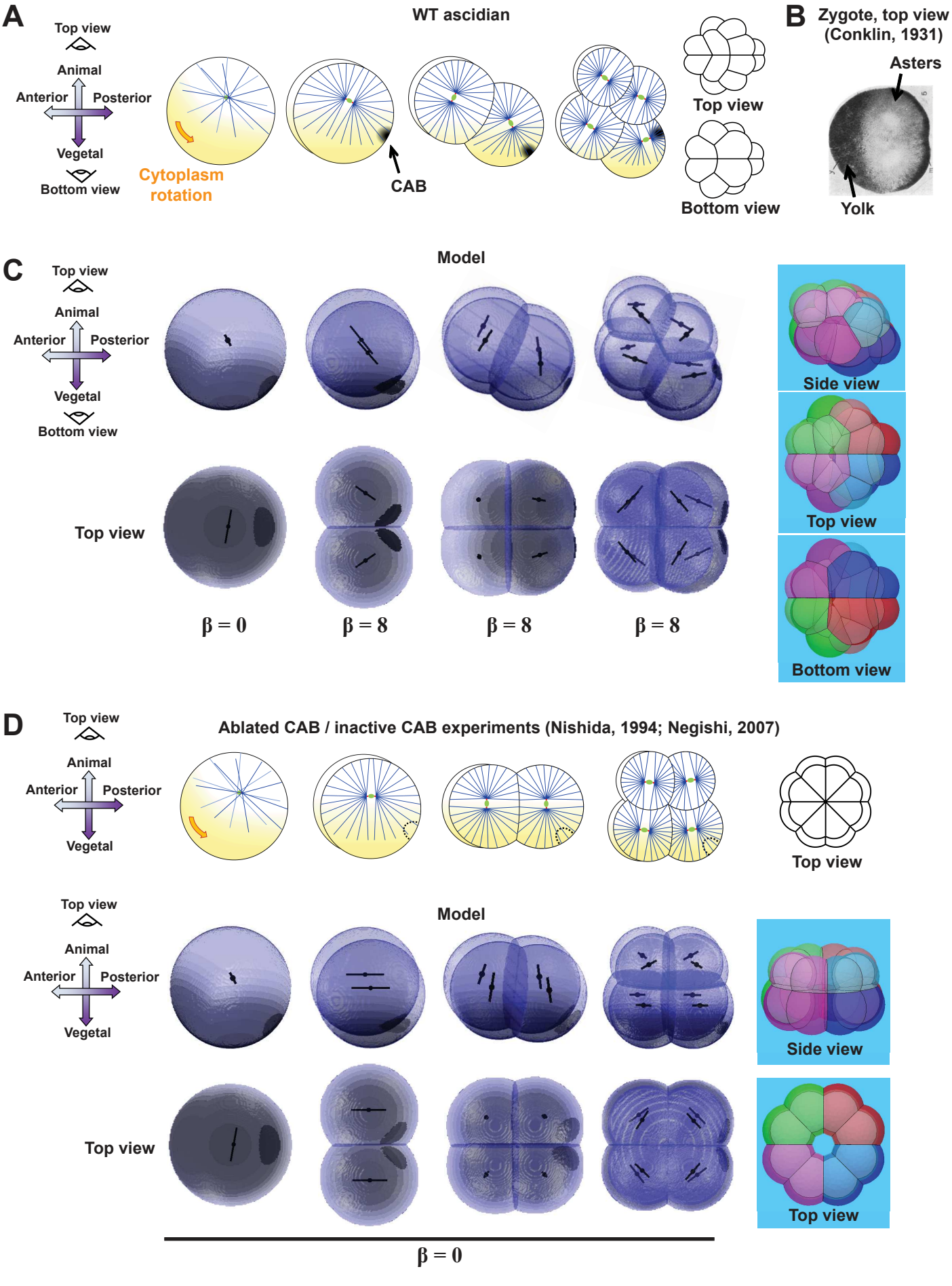
A
Top view
Animal
Anterior
Posterior
Vegetal
Bottom view
WT ascidian
Cytoplasm rotation
CAB
Top view
Bottom view
B
Zygote, top view (Conklin, 1931)
Asters
Yolk
C
Top view
Animal
Anterior
Posterior
Vegetal
Bottom view
Model
Top view
β = 0
β = 8
β = 8
β = 8
Side view
Top view
Bottom view
D
Top view
Animal
Anterior
Posterior
Vegetal
Ablated CAB / inactive CAB experiments (Nishida, 1994; Negishi, 2007)
Top view
Top view
Animal
Anterior
Posterior
Vegetal
Model
Top view
Side view
Top view
β = 0

Supplemental Materials Inventory:

I. Supplementary Figures

Figure S1 (related to Figure 1): Influence of different parameters on the length-dependent model in 3D

Figure S2 (related to Figure 2): Tests of hypotheses and parameters for zebrafish cleavage patterns.

Figure S3 (related to Figure 2): Influence of shape parameters on the prediction of zebrafish cleavage and embryo morphogenesis.

Figure S4 (related to Figure 3): Influence of yolk and shape parameters on the prediction of Xenopus cleavage and embryo morphogenesis.

Figure S5 (related to Figure 4, 5 and 6): Evidence and characteristics of MT branching in interphase asters in sea urchin embryos.

Figure S6 (Related to Figure 4, 5 and 6) : Influence of different parameters on the prediction of sea urchin cleavage patterns and early embryogenesis.

Figure S7 (Related to Figure 7): Influence of surface polarity conditions on ascidians cleavage pattern.

II. Supplementary Table

Table S1 (Related to all Figures): Parameters used to generate blastomere shapes throughout the manuscript from the Surface Evolver.

III. Supplementary Movie Legends

Movie S1 (Related to Figure 1). Typical sequence for the computation of blastomere shapes by "The surface Evolver". Example taken here correspond to the 4-cell stage zebrafish embryo.

Movie S2 (Related to Figure 2)3D rotation of model predictionsfor the cleavage pattern of fish embryos.

Movie S3(Related to Figure 2) 3D rotation of model predictionsfor the cleavage pattern of amphibiansembryos.

Movie S4(Related to Figure 2) 3D rotation of model predictionsfor the cleavage pattern of echinodermembryos.

Movie S5(Related to Figure 2) 3D rotation of model predictionsfor the cleavage pattern of ascidiansembryos.

IV. Description of the starter package (Supplementary Item S1, download separately, related to experimental methods)

V. Supplementary Methods

VI. Supplementary References

3-Supplemental Figures and Figure legends

Figure S1 (related to Figure 1): Influence of different parameters on the length-dependent model in 3D.

(A) Influence of the distance between centrosomes D_c. Test cell: zebrafish 2nd division. (Top Left) Predicted position and orientation of the spindle for every value of D_c. (Right) Torque amplitude profiles for different values of D_c. The (θ, φ) orientations where the torque amplitude is close to zero correspond to the equilibrium of the aster pair. The value of the stable equilibrium position does not change but the noise increases when D_c becomes small. (Bottom left) Noise quantification: Roughness of the torque profile vs D_c. **(B)** Influence of the asters angular extent ψ. Test cell: zebrafish 2nd division. (Bottom Left) Predicted positions of the aster pair center for different values of ψ. The center of the cell's center of mass is better found for asters that probe the whole cell (larger values of ψ). (Right) Side and top views of the predicted positions of the aster pair center (black dot) for different values of ψ. Asters are depicted in darker blue. **(C)** Influence of length-dependent exponent δ, on division axis position and orientation (for $\psi = 157.5°$), and phase diagram of stable orientations, for different values of δ and ψ.

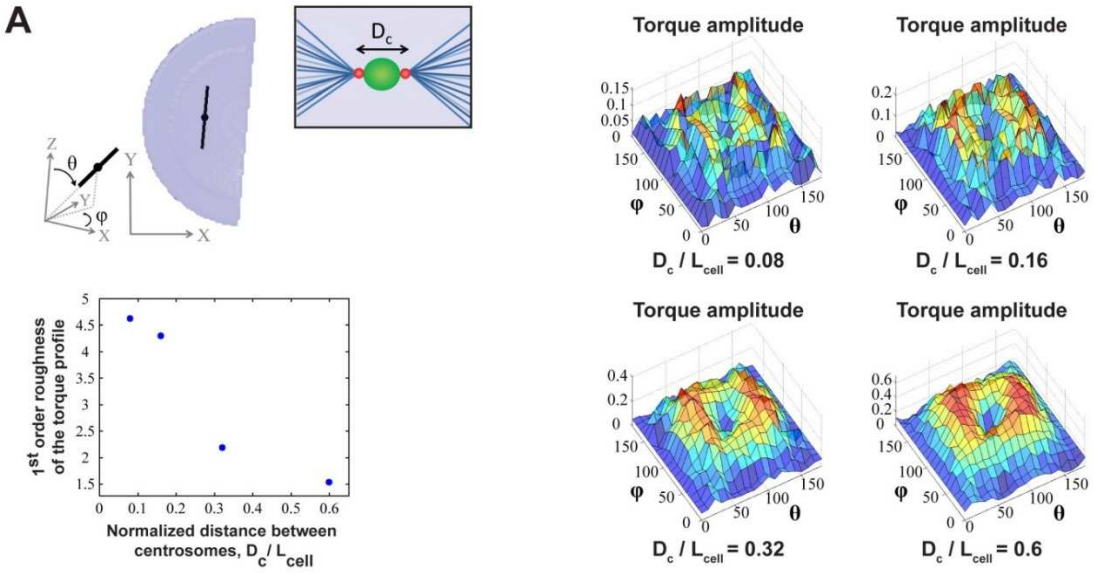
A
D_c
Z
θ
Y
φ
X
Y
X
1st order roughness of the torque profile
Normalized distance between centrosomes, D_c / L_cell
Torque amplitude
D_c / L_cell = 0.08
Torque amplitude
D_c / L_cell = 0.16
Torque amplitude
D_c / L_cell = 0.32
Torque amplitude
D_c / L_cell = 0.6
φ
θ

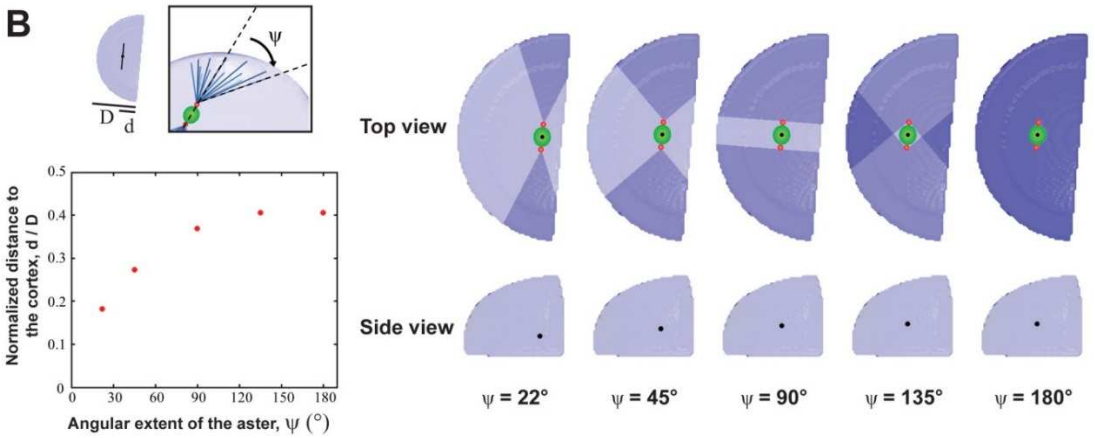
B
ψ
D
d
Normalized distance to the cortex, d / D
Angular extent of the aster, ψ (°)
Top view
Side view
ψ = 22°
ψ = 45°
ψ = 90°
ψ = 135°
ψ = 180°

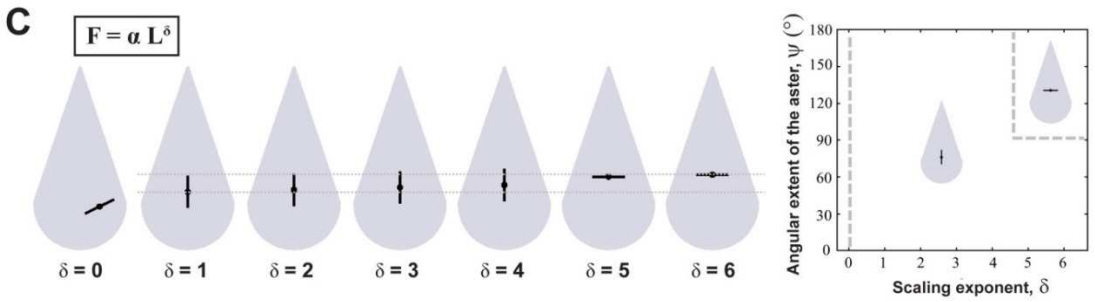
C
F = α L^δ
δ = 0
δ = 1
δ = 2
δ = 3
δ = 4
δ = 5
δ = 6
Angular extent of the aster, ψ (°)
Scaling exponent, δ

Figure S2 (related to Figure 2): Tests of hypotheses and parameters for zebrafish cleavage patterns.

(A) 4-cell stage zebrafish embryo expressing the MT marker ensconsin-GFP, fixed and labeled for actin and DNA, and imaged parallel to the A-V axis. Yolk granules fluoresce in the actin channel, and appear to exclude MTs. Scale bar: 50 μm, 10 μm (inset). **(B and C)** Predictions of the model, under the hypothesis that MT forces orienting the division axis arise from sites of cell-cell adhesion. Pulling interfaces (arrows) are depicted in darker blue. **(D)** The predicted cell division orientation lineage under this hypothesis. Note the absence of orientation switch at the 5^{th} Cleavage.

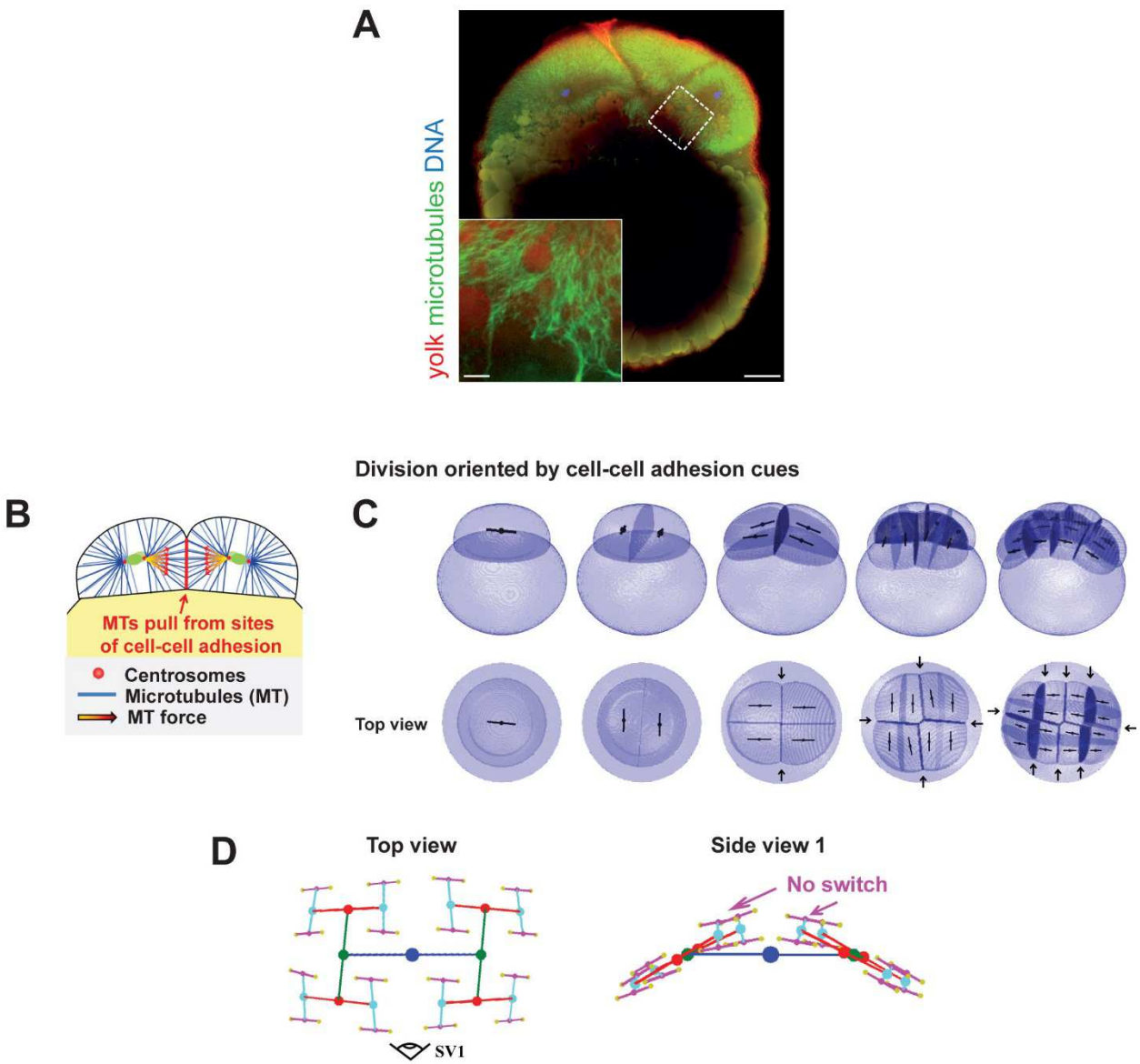
A
yolk microtubules DNA
B
MTs pull from sites of cell-cell adhesion
Centrosomes
Microtubules (MT)
MT force
Division oriented by cell-cell adhesion cues
C
Top view
D
Top view
Side view 1
No switch
SV1

Figure S3 (related to Figure 2): Influence of shape parameters on the prediction of zebrafish cleavage and embryo morphogenesis.

(A-H) Test of the importance of delayed furrow ingression on cleavage patterns in fish. **(B-C)** Model predictions under a delayed cytokinesis hypothesis (also shown in figure 2). **(D)** Predicted orientation of the fifth division of a lateral external cell (highlighted in red) under this hypothesis, and corresponding torque amplitude profile, smoothed from half-size mesh (see Supplemental Information, p.3). **(E-H)** Test of a hypothesis of immediate furrow ingression preceding division axis setting in the next cell-cycle. **(F and G)** Predicted cleavage patterns. Note the different orientations at the 16 cell stages as compared to Figures S3B-S3C. **(H)** Predicted orientation of the 5^{th} division of a lateral external cell (highlighted in red) under this hypothesis, and corresponding torque amplitude profile, smoothed from half-size mesh. **(I)** The surface tension of the cell-medium interface γ_{ext}, is increased in the "Surface Evolver" model. This yields blastomeres that are too high already at the 4-cell stage and a consequent division orientation along the A-V axis. **(J)** The surface tension of the cell-cell interface γ_{int}, is decreased in the "Surface Evolver" model. This yields blastomeres that are too high already at the 4-cell stage and a consequent division orientation along the A-V axis.

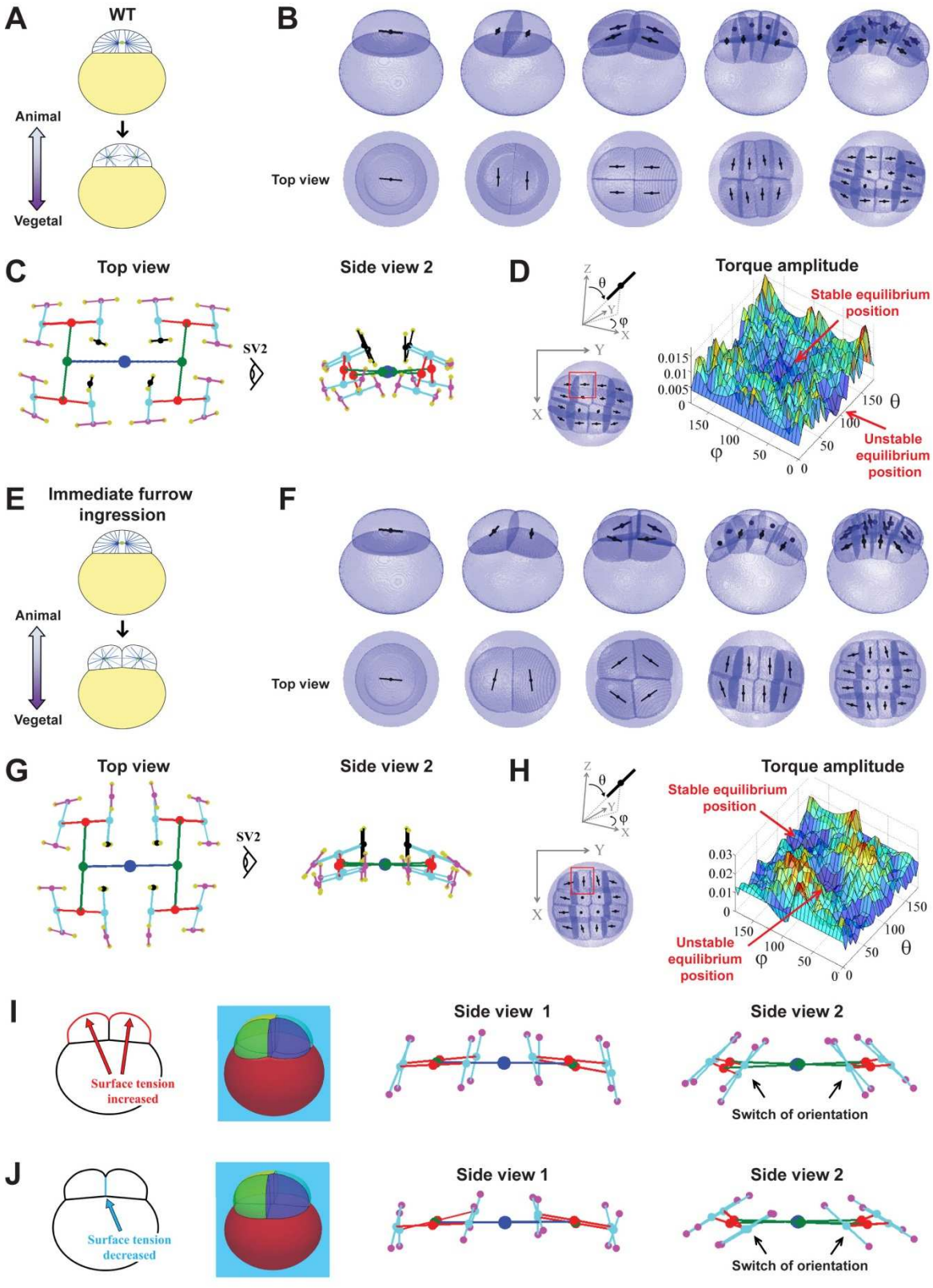
A
WT
Animal
Vegetal
B
Top view
C
Top view
SV2
Side view 2
D
Torque amplitude
Stable equilibrium position
Unstable equilibrium position
E
Immediate furrow ingression
Animal
Vegetal
F
Top view
G
Top view
SV2
Side view 2
H
Torque amplitude
Stable equilibrium position
Unstable equilibrium position
I
Surface tension increased
Side view 1
Side view 2
Switch of orientation
J
Surface tension decreased
Side view 1
Side view 2
Switch of orientation

Figure S4 (related to Figure 3): Influence of yolk and shape parameters on the prediction of Xenopus cleavage and embryo morphogenesis.

(A) Influence of yolk on MT density. (Left) Immunostaining images of a 2-cell stage Xenopus embryo, imaged near parallel to the A-V axis, depicting yolk (which fluoresces in the DNA channel) and MTs. Intensity profiles were extracted within the asters (boxes). Scale bar: 200 µm. (Right) Correlation between yolk and MT intensities, computed with regards to the distance to centrosomes, to avoid MT branching artefacts. $N_{profiles} = 45$, $N_{embryos} = 11$. Error bars are standard deviation. **(B)** Computed influence of yolk on MT density. (Left) Plot of the density of MTs as a function of the distance to the centrosomes, caused by pure dilution effects (no yolk). (Middle) Plot of yolk concentration as set in the model, and consequent evolution of the effect of yolk on MT density, based on a linear effect of yolk (red) or a threshold (blue). (Right) Combined effect of dilution and yolk on MT density, based on a linear effect of yolk (red) or a threshold (blue). **(C-D)** Test of different hypotheses for the impact of yolk on MT stability. **(C)** MT growth is inhibited in a dose-dependent manner by yolk concentration. (similar to Figure 3C) **(D)** MTs fully penetrate in the yolk up to a threshold in yolk concentration that stops MT growth. Note that the predicted cleavage pattern is similar to the one obtained in the previous hypothesis. **(E)** Test of a hypothesis of immediate furrow ingression preceding division axis re-orientation in the next cell-cycle on predicted cleavage patterns. Note that the pattern is similar to the one obtained in Figure 3C. **(F)** Predictions of the model with no confinement by the fertilization envelope in "The Surface Evolver". Note that blastomere shapes are completely different, and as a result, division axes do not switch orientation along the A-V axis at the 3rd cleavage.

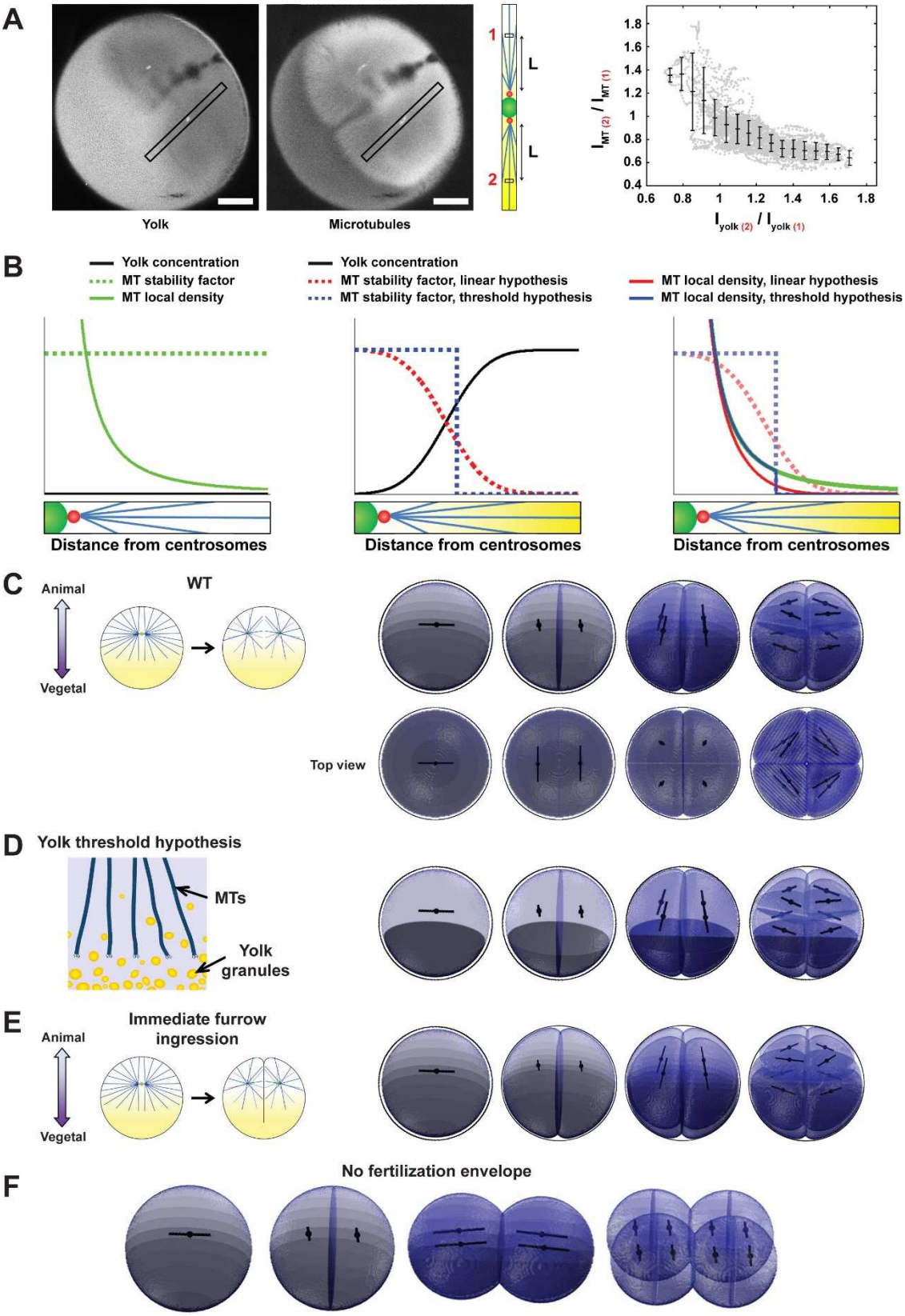
A
Yolk
Microtubules
1
2
L
L
1.8
1.6
1.4
1.2
1
0.8
0.6
0.4
0.6
0.8
1
1.2
1.4
1.6
1.8
I MT (2) / I MT (1)
I yolk (2) / I yolk (1)
B
Yolk concentration
MT stability factor
MT local density
Yolk concentration
MT stability factor, linear hypothesis
MT stability factor, threshold hypothesis
MT local density, linear hypothesis
MT local density, threshold hypothesis
Distance from centrosomes
Distance from centrosomes
Distance from centrosomes
C
Animal
Vegetal
WT
Top view
D
Yolk threshold hypothesis
MTs
Yolk granules
E
Animal
Vegetal
Immediate furrow ingression
F
No fertilization envelope

Figure S5 (related to Figure 4, 5 and 6): Evidence and characteristics of MT branching in interphase asters in sea urchin embryos.

(A-C) Requirement of the exponential term (condition 2) for the influence of polar domain on MT force to obtain division axis oriented parallel to the domain. **(B)** Prediction of the 1st division relative to the polar domain, using only the dynein-limited hypothesis (condition 1). Note that increasing the parameter β causes division center to come closer to the domain, but does not create an orientation parallel to the domain. **(C)** Adding the exponential term (condition 2) allows to stabilize the parallel configuration. **(D)** Immunostaining image of a 2-cell stage sea urchin embryo in interphase, showing MTs (green) and DNA (blue). Scale bar: 20 μm (left), 5 μm (right). **(E)** MT intensity profiles show an exponential increase in MT density, which compensates dilution of MTs and is independent on cleavage stage. (Left) MT intensity profiles from the centrosome in 1-cell stage interphase embryos (gray), mean and standard deviation (black). $N_{profiles}$ = 368, $N_{embryos}$ = 10. Fit by L^2 cytoplasmic dilution with exponential increase (red). L^2 cytoplasmic dilution alone is shown in green. (Middle) Mean MT intensity profiles from the centrosome in 1 to 8-cell stage interphase embryos. $N_{profiles}$ = 368, 325, 117, 96, $N_{embryos}$ = 10, 10, 4, 10. (Right) Fits of MT intensity profiles in 1 to 8-cell stage by L^2 cytoplasmic dilution with exponential increase. The branching parameter, a, does not vary significantly between different stages. **(F)** Phase diagram of the predicted division positioning with only the exponential term in the model, for the 1^{st} and 2^{nd} divisions. **(G)** 4-cell stage blastomere separation experiment, suggests that rounded separated blastomere may orient their division axis along the A-V axis even without the influence of an elongated cell shape (Dan, 1987). **(H)** Prediction of the model for a separated 4-cell stage blastomere (round cell with size and β as in 4-cell stage), using condition 2 alone can only produce divisions parallel to the domain or asymmetric divisions. **(I)** The use of both conditions allows to produce symmetric divisions oriented towards the domain.

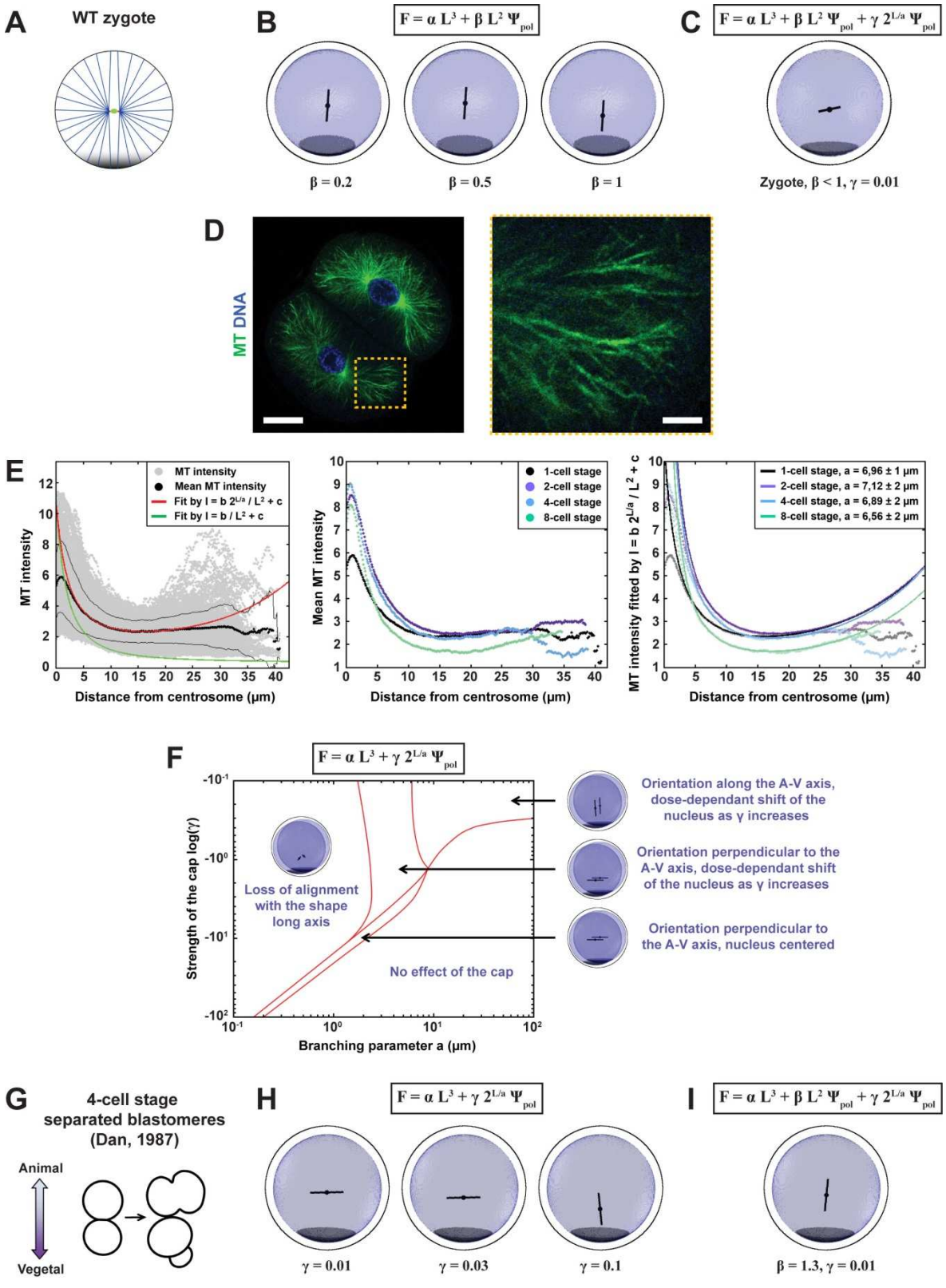
A
WT zygote
B
$F = \alpha L^3 + \beta L^2 \Psi_{pol}$
β = 0.2
β = 0.5
β = 1
C
$F = \alpha L^3 + \beta L^2 \Psi_{pol} + \gamma 2^{L/a} \Psi_{pol}$
Zygote, β < 1, γ = 0.01
D
MT DNA
E
MT intensity
Mean MT intensity
Fit by I = b 2^{L/a} / L² + c
Fit by I = b / L² + c
MT intensity
Distance from centrosome (µm)
1-cell stage
2-cell stage
4-cell stage
8-cell stage
Mean MT intensity
Distance from centrosome (µm)
1-cell stage, a = 6,96 ± 1 µm
2-cell stage, a = 7,12 ± 2 µm
4-cell stage, a = 6,89 ± 2 µm
8-cell stage, a = 6,56 ± 2 µm
MT intensity fitted by I = b 2^{L/a} / L² + c
Distance from centrosome (µm)
F
$F = \alpha L^3 + \gamma 2^{L/a} \Psi_{pol}$
Strength of the cap log(γ)
Loss of alignment with the shape long axis
No effect of the cap
Branching parameter a (µm)
Orientation along the A-V axis, dose-dependant shift of the nucleus as γ increases
Orientation perpendicular to the A-V axis, dose-dependant shift of the nucleus as γ increases
Orientation perpendicular to the A-V axis, nucleus centered
G
4-cell stage separated blastomeres (Dan, 1987)
Animal
Vegetal
H
$F = \alpha L^3 + \gamma 2^{L/a} \Psi_{pol}$
γ = 0.01
γ = 0.03
γ = 0.1
I
$F = \alpha L^3 + \beta L^2 \Psi_{pol} + \gamma 2^{L/a} \Psi_{pol}$
β = 1.3, γ = 0.01

<u>Figure S6 (Related to Figure 4, 5 and 6)</u>: Influence of different parameters on the prediction of sea urchin cleavage patterns and early embryogenesis.

(A) Predicted torque landscape at the 2-cell stage with no contribution from the polarity domain. Not that several stable equilibrium orientations are available, and as a result the two division axis are not necessarily coplanar. **(B)** Predicted torque landscape at the 2-cell stage with a relatively small contribution from the polarity domain, which allows to modulate the potential landscape so that only one orientation parallel to the cap is now stable, yielding co-planar division axes. **(C)** Influence of the asters angular extent ψ, on the effect of polarity domain in the condition 1+2. The two asters must overlap to produce the 1st division orientation (parallel to the cap). Test cell: sea urchin zygote. **(D-E)** Influence of polarity domain size on division positioning, in the zygote **(D)** and in a separated round 4-cell stage blastomere **(E)**. Predicted orientation does not depend on cap size as long as the cap covers less than half of the solid angular surface seen by the aster center. **(F)** Model predictions are similar without confinement from the fertilization envelope. The same equation and parameters as in figure 5B are used.

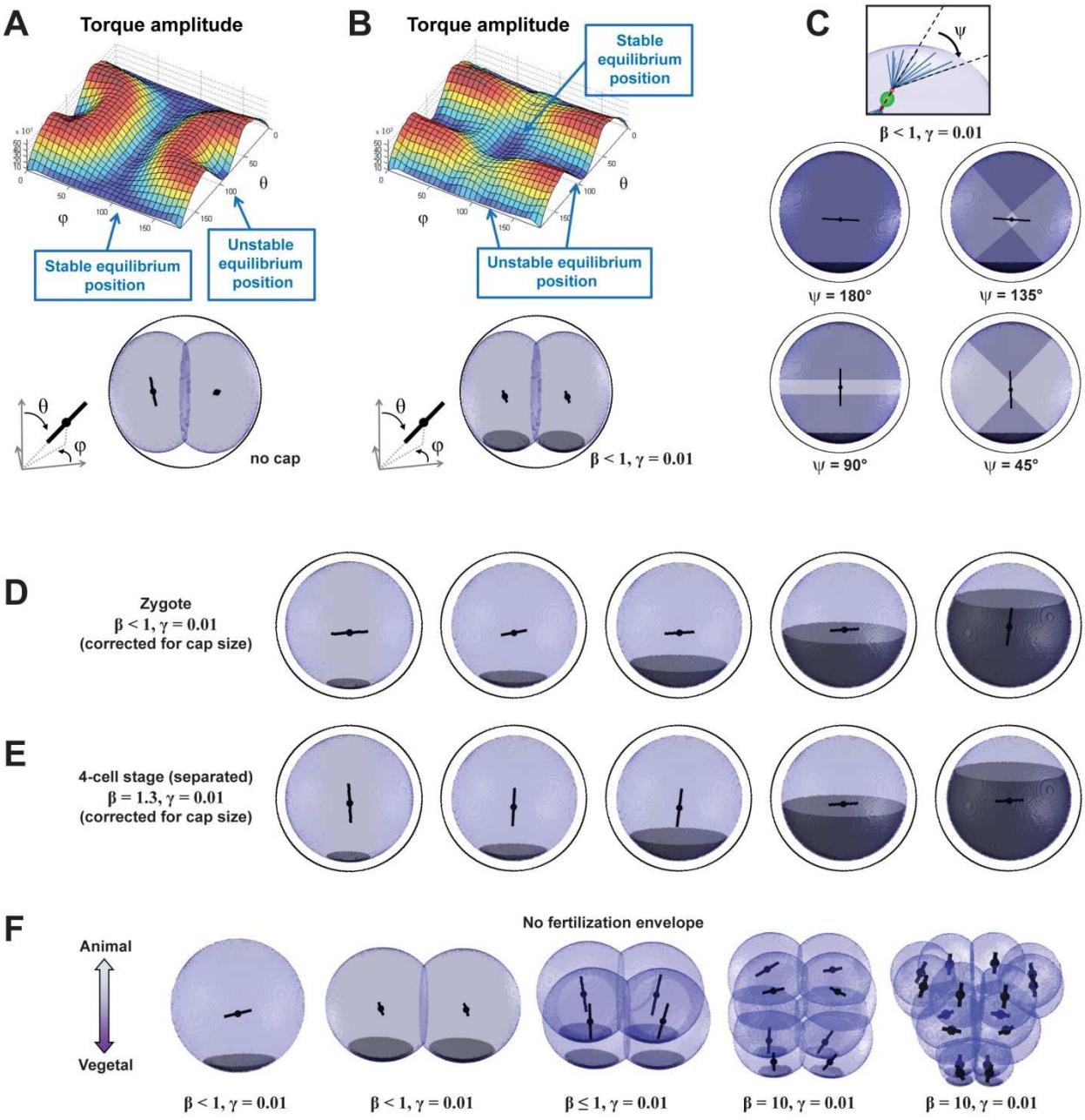
A
Torque amplitude
Stable equilibrium position
Unstable equilibrium position
θ
φ
no cap
B
Torque amplitude
Stable equilibrium position
Unstable equilibrium position
β < 1, γ = 0.01
C
ψ
β < 1, γ = 0.01
ψ = 180°
ψ = 135°
ψ = 90°
ψ = 45°
D
Zygote
β < 1, γ = 0.01
(corrected for cap size)
E
4-cell stage (separated)
β = 1.3, γ = 0.01
(corrected for cap size)
F
No fertilization envelope
Animal
Vegetal
β < 1, γ = 0.01
β < 1, γ = 0.01
β ≤ 1, γ = 0.01
β = 10, γ = 0.01
β = 10, γ = 0.01

<u>Figure S7 (Related to Figure 7)</u>: Influence of surface polarity conditions on ascidians cleavage pattern.

The predictions of the model using only the condition (1) (dynein-limiting pulling) for domain influence on MT force is similar as when using both conditions (see Figure 7C).

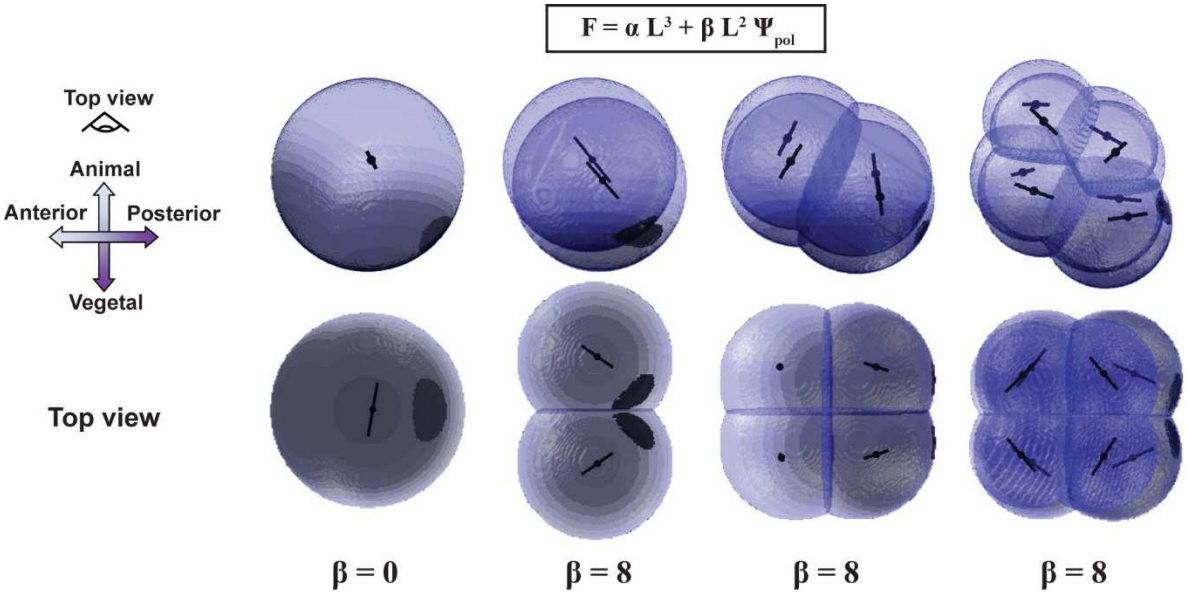

2- Supplementary Tables and legends

	Confinement parameters	γ_{ext}	γ_{int}	γ_{int} new neighbors	γ_{cell_yolk}	$\gamma_{ext\ yolk}$
WT zebrafish (all cleavage stages) (Figures 2B and 2D)	R=0.684	2.4	1.5	1.9	3.3	3.5
Zebrafish, γ_{ext} decreased (Figure 2E)	R=0.684	1.4	1.5	1.9	3.3	3.5
Zebrafish, γ_{int} increased (Figure 2F)	R=0.684	2.4	3	3.8	3.3	3.5
Zebrafish, γ_{ext} increased (Figure S3I)	R=0.684	4.4	1.5	1.9	3.3	3.5
Zebrafish, γ_{int} decreased (Figure S3J)	R=0.684	2.4	0.375	0.475	3.3	3.5
WT Xenopus 1, 2 cells (Figure 3C)	R=0.624	0.65	-	1	-	-
WT Xenopus 4, 8 cells (Figure 3C)	R=0.624	0.65	1	1	-	-
Hertwig, horizontal compression (Figure 3F)	Z = ± 0.4 R=0.75 (r=1.7)	0.65	0.8	1	-	-
Hertwig, vertical compression (Figure 3G)	Y = ± 0.35 R=0.78 to 0.81 (r=1.85)	0.65	0.8	1	-	-
Xenopus without envelope (Figure S4F)	-	0.65	1	1	-	-
WT sea urchin 1, 2, 16 cells (Figure 5B)	R=0.684	0.75	1.1	1.1	-	-
WT sea urchin 4, 8 cells (Figure 5B)	R=0.684	0.75	1.1	1.3 – 0.9	-	-

Hörstadius experiment 1, 2 cells, final shapes (Figure 6B)	R=0.684	0.75	1.1	1.1	-	-
Hörstadius experiment 4 cells (Figure 6B)	R=0.684	0.75	1.1	1.3 – 0.9	-	-
Dan experiment 2-cell stage (Figure 6D)	Z = ± 0.37	0.75	-	1.1	-	-
Dan experiment 4-cell stage (Figure 6D)	Z = ± 0.29	0.75	1.1	1.3 – 0.9	-	-
Dan experiment 8-cell stage (Figure 6D)	Z = ± 0.23	0.75	1.1	1.3 – 0.9	-	-
Dan experiment 16-cell stage (Figure 6D)	Z = ± 0.18	0.75	1.1	1.1	-	-
Sea urchin without envelope, 1, 2, 16 cells (Figure S6F)	-	0.75	1.1	1.1	-	-
Sea urchin without envelope, 4, 8 cells (Figure S6F)	-	0.75	1.1	1.3 – 0.9	-	-
WT and no CAB ascidian, 1, 2 cells (Figures 7C, 7D and S7)	-	0.75	-	1	-	-
WT and no CAB ascidian, 4, 8, 16 cells (Figures 7C, 7D and S7)	-	0.9	1	1	-	-

Where the elliptic confinement is $R^2 = X^2 + Y^2 + (Z * r)^2$, and the total volume of the embryo is 1.

Table S1 (Related to all Figures): Parameters used to generate blastomere shapes throughout the manuscript from the Surface Evolver.

3- -Supplementary Movie legends

Movie S1 (Related to Figure 1). Typical sequence for the computation of blastomere shapes by "The surface Evolver". Example taken here correspond to the 4-cell stage zebrafish embryo.

Movie S2 (Related to Figure 2) 3D rotation of model predictions for the cleavage pattern of fish embryos.

Movie S3 (Related to Figure 2) 3D rotation of model predictions for the cleavage pattern of amphibians embryos.

Movie S4 (Related to Figure 2) 3D rotation of model predictions for the cleavage pattern of echinoderm embryos.

Movie S5 (Related to Figure 2) 3D rotation of model predictions for the cleavage pattern of ascidians embryos.

4- Description of the starter package (Supplementary Item S1)

A starter package which includes explanation text files, Matlab scripts, and examples to implement both division predictions and "Surface Evolver" is associated to this work (Supplementary Item S1). This package contains the Matlab programs that were used to predict the position of the cell division plane in 3D, as well as a typical input folder. It also contains indications and tools to generate the shape and polarity inputs to this program from a Surface Evolver output file.

5- Supplementary Methods

a- Parameters used in the division axis prediction model:

The model predicting division position and orientation consists of computing the net force and torque created by a pair of MT asters (Figure 1A and 1B). Forces and torques are calculated from summing the contribution of all MTs in the aster pairs, based on hypotheses on single astral MT forces detailed in the main text. The positions of the centrosomes are first computed from a given division axis orientation and centrosome-centrosome distance, Dc (Figure S1A). The intersection

between MTs and the cell surface, and the consequent length of MTs and polarity effect are calculated for every 1° x 1° solid angle within the angular extent of the asters, ψ, by assuming a constant angular MT density (Figure S1B).

Directed search loop:

The search for mechanical equilibrium is done using a directed search strategy, initiated from the center of mass of the cell shape matrix with a random orientation. At each iteration MT forces are summed up to compute a net force and torque on aster pairs, and one of the coordinates of the aster pair axis and position, x, y, z, θ or φ, randomly chosen, is changed according to the force / torque direction calculated at the previous iteration, with a step size of 1 pixel for x, y or z and 1° for θ and φ. As the total egg diameter is ~140 pixels, pixel size is ~ 4.3 µm for zebrafish, ~ 8.6 µm for Xenopus, ~ 0.7 µm for sea urchins, and ~ 1.2 µm for ascidians. After calculation of the new force and torque, the force and torque vectors are decomposed into the coordinate system associated with the cell (see p.4). The force / torque component corresponding to the changed coordinate x, y, z, θ or φ is compared to its value before the change. If it does not change sign, or if it changes sign but becomes smaller in absolute values, the new position / orientation is kept as a starting point for the next iteration. Conversely, if it changes sign but becomes larger in absolute values, then the simulation comes back to the previous position/orientation to change randomly another coordinate. To prevent the search loop to remain trapped in non-relevant local minima, we assumed a non-zero probability (typically 2%) to maintain the new position and orientation even if not favorable. The correct equilibrium is then identified when a certain number of iterations (~ 500) yields similar position and orientation. The equilibrium position is usually reached within 2000 iterations. A maximum total number of 10000 iterations is allocated to the program to reach the correct equilibrium. If the equilibrium is not found passed this number, the simulations are re-started from a different initial orientation. If needed, the simulations can also be initiated from a different starting position than the center of mass of the cell. Due to pixel noise, the intrinsic error in the division simulation is about 5 pixels in position and 5° in orientation. As the modeling framework is iterative, the overall error may be slightly amplified at every round of divisions.

In order to validate the directed search strategy and to avoid metastable equilibrium positions, the torque amplitude profile can be computed after the search for the equilibrium position. The net torque is calculated for every 3D orientation (θ and φ, with a mesh size of typically 10° x 10°), at

the equilibrium position. If needed, the mesh size can be reduced (between 3° x 3° and 5° x 5°) to allow smoothing of the torque profile and reduce noise. We note that the zeros of the torque can correspond to stable or unstable orientations (Figure S5A and S5B). The unstable orientations are excluded by looking at the direction of the torque vector.

To predict the cleavage orientation based on a hypothesis of cell-cell contact-oriented division in zebrafish (Figure S2B-S2D), we kept the equilibrium position given by our model based on length-dependent pulling; and assayed orientation. We then varied only θ and φ in the directed search, to search for the equilibrium in orientation, assuming the MT force to be now proportional to L^2 for MTs that reach a cell-cell interface, and 0 otherwise.

Calculation of the net force and torque:

For a spindle orientation (θ, φ), the MT force vector is calculated for every 1° x 1° solid angle (θ_{MT}, φ_{MT}), with θ_{MT} varying between 0 and the aster extension ψ (Figure 1A). The MT length and the polarity contribution ψ_{pol} (when relevant) are obtained by computing the intersection of this solid angle with the cell surface. The pulling force of one MT is then:

$$\vec{F} = (\alpha L^3 + \beta L^2 \psi_{pol} + \gamma 2^{L/a} \psi_{pol}) \vec{u}_{MT}$$

where $\vec{u}_{MT}$ is the unit vector along the MT axis. The force is applied in the point C which marks the centrosome. The torque at the point O, which marks the center of the nucleus, is then written as:

$$\vec{T} = \overrightarrow{OC} \wedge \vec{F} = F D_c/2 \ \vec{u}_{ZMT} \wedge \vec{u}_{MT}$$

where (X_{MT}, Y_{MT}, Z_{MT}) is the coordinate system associated with the aster (Figure 1A). In order to direct the search for the equilibrium position, the force vector is decomposed into the coordinate system associated with the cell (X, Y, Z). $\vec{F}$ is first decomposed into the coordinate system associated with the aster (X_{MT}, Y_{MT}, Z_{MT}):

$$\vec{F}_{XMT} = F \sin(\theta_{MT}) \cos(\varphi_{MT}) \vec{u}_{XMT}$$
$$\vec{F}_{YMT} = F \sin(\theta_{MT}) \sin(\varphi_{MT}) \vec{u}_{YMT}$$
$$\vec{F}_{ZMT} = F \cos(\theta_{MT}) \vec{u}_{ZMT}$$

Similarly, the torque vector in (X_{MT}, Y_{MT}, Z_{MT}) is written as:

$\vec{T}_\theta = F_{XMT}\, D_c/2\ \ \vec{u}_{ZMT} \wedge \vec{u}_{XMT} = F_{XMT}\, D_c/2\ \ \vec{u}_{YMT}$
$\vec{T}_\varphi = F_{YMT}\, D_c/2\ \ \vec{u}_{ZMT} \wedge \vec{u}_{YMT} = -\, F_{YMT}\, D_c/2\ \ \vec{u}_{XMT}$

$\vec{F}$ is then decomposed into (X, Y, Z):

$\vec{F}_X = (\, F_{XMT} \cos(\theta) \cos(\varphi) - F_{YMT} \sin(\varphi) + F_{ZMT} \sin(\theta) \cos(\varphi))\, \vec{u}_X$
$\vec{F}_Y = (\, F_{XMT} \cos(\theta) \sin(\varphi) + F_{YMT} \cos(\varphi) + F_{ZMT} \sin(\theta) \sin(\varphi))\, \vec{u}_Y$
$\vec{F}_Z = (-F_{XMT} \sin(\theta) + F_{ZMT} \cos(\theta))\, \vec{u}_Z$

As $(\vec{u}_{XMT\_aster1},\ \vec{u}_{YMT\_aster1}, \vec{u}_{ZMT\_aster1}) = -(\vec{u}_{XMT\_aster2},\ \vec{u}_{YMT\_aster2}, \vec{u}_{ZMT\_aster2})$ and (θ, φ) define the direction of $\overrightarrow{OC}_1$ with C_1 the centrosome of aster 1, the previous equations are written for a MTs in aster 2 as:

$\vec{F}_X = (-F_{XMT} \cos(\theta) \cos(\varphi) + F_{YMT} \sin(\varphi) - F_{ZMT} \sin(\theta) \cos(\varphi))\, \vec{u}_X$
$\vec{F}_Y = (-F_{XMT} \cos(\theta) \sin(\varphi) - F_{YMT} \cos(\varphi) - F_{ZMT} \sin(\theta) \sin(\varphi))\, \vec{u}_Y$
$\vec{F}_Z = (\, F_{XMT} \sin(\theta) - F_{ZMT} \cos(\theta))\, \vec{u}_Z$

The net force and torque is the sum of the contributions of all MTs, so that:

$\vec{T}_{\theta\_net} = \Sigma_{\theta MT,\, \varphi MT} \,|\, \cos(\theta_{MT}) - \cos(\theta_{MT} - 1°) \,|\, (\ \vec{T}_{\theta\_aster1} + \vec{T}_{\theta\_aster2}\ )$
$\vec{T}_{\varphi\_net} = \Sigma_{\theta MT,\, \varphi MT} \,|\, \cos(\theta_{MT}) - \cos(\theta_{MT} - 1°) \,|\, (\ \vec{T}_{\varphi\_aster1} + \vec{T}_{\varphi\_aster2}\ )$
$\vec{F}_{X\_net} = \Sigma_{\theta MT,\, \varphi MT} \,|\, \cos(\theta_{MT}) - \cos(\theta_{MT} - 1°) \,|\, (\ \vec{F}_{X\_aster1} + \vec{F}_{X\_aster2}\ )$
$\vec{F}_{Y\_net} = \Sigma_{\theta MT,\, \varphi MT} \,|\, \cos(\theta_{MT}) - \cos(\theta_{MT} - 1°) \,|\, (\ \vec{F}_{Y\_aster1} + \vec{F}_{Y\_aster2}\ )$
$\vec{F}_{Z\_net} = \Sigma_{\theta MT,\, \varphi MT} \,|\, \cos(\theta_{MT}) - \cos(\theta_{MT} - 1°) \,|\, (\ \vec{F}_{Z\_aster1} + \vec{F}_{Z\_aster2}\ )$

Where $|\cos(\theta_{MT}) - \cos(\theta_{MT} - 1°)|$ is a correction factor introduced to keep a constant MT angular density within the aster.

Comparing F_{X_net} (respectively F_{Y_net}, F_{Z_net} _net, T_{θ_net}, _T_{φ_net}) before and after a change in the coordinate x (respectively y, z, θ, φ) allows to direct the search for the equilibrium position.

Calculation of the torque amplitude profile:

The torque amplitude profile was calculated along the two degrees of freedom, by varying θ and φ from 0 to 180°:

$$T = \sqrt{\left(\overrightarrow{T_{\theta\_net}}\right)^2 + \left(\overrightarrow{T_{\varphi\_net}}\right)^2}$$

In order to reduce noise, the mesh size could be narrowed and $\vec{T}_{\theta\_net}$ and $\vec{T}_{\varphi\_net}$ averaged over two or three angular steps (typically steps of 5° or 3° respectively, in both θ and φ) before calculating T.

Parameters of the length-dependent force contribution:

In the length-dependent force model, the dominant parameter for division plane specification is the shape of the cell, which influences the shape of asters; that we input from "the Surface Evolver" simulation. The size of the embryo is about 140x140x140 pixels, and normalized to the egg size in the MT length calculation (so that sizes of all stages are consistent). We note that the embryo is not resized to its actual size in µm (all lengths in the force calculation remain between 0 and 1). As a consequence, and for consistency with the starter package (Supplementary Item S1), parameters α, β and γ are given without resizing correction in the main text. However, the branching parameter *a*, which represents a biological length-scale, is corrected in the text to provide a value in µm. In the case of a delayed furrow ingression (zebrafish and Xenopus), the shapes generated with the Surface Evolver are divided in two to account for aster-aster repulsion. Using a Matlab script, the aster-aster interface plane is inferred from the position of the spindle in the previous division prediction (bisecting it perpendicular), and the corresponding voxels from the Surface Evolver simulation are labeled, allowing to define and separate the two half-cells via an ImageJ treatment.

The distance between centrosomes D_c appears to have no significant influence on the position and the orientation of the division axis (Figure S1A). It was generally set to 20 pixels (for an egg diameter of L_{cell} ~140 pixels), and reduced for smaller blastomeres: in the zebrafish blastodisc (Figure 2, D_c = 16 to 10 for 2-cell stage to 16-cell stage), the 8-cell stage cells in Hertwig's experiments (Figure 3F and 3G, D_c = 16), and the sea urchin micromeres (Figure 5, D_c = 16 and D_c = 12 for 8-cell stage and 16-cell stage).

The aster extension ψ has little influence on division axis position and orientation in the length-dependent forces model (Figure S1B). However, an overlap of the two asters ($\psi > 90°$) is required to orient the division axis parallel to the polarity domain in echinoderms (Figure S6C). ψ was thus

set to 157.5° for all simulations, except for Xenopus where it was set to 112.5° to better account for aster-aster repulsion (Figure 3A). For simplicity, the angular density of MTs was assumed to be constant within the aster.

The absolute MT nucleation angular density is a silent parameter in the model. The MT force was calculated in every 1° x 1° solid angle, within the aster. Using smaller angular steps did not affect the results of simulations (data not shown).

In the length-dependent MT force expression, $F = \alpha L^{\delta}$, α is a silent parameter, fixed to 1. The parameter δ has little influence on division axis determination, if strictly positive and inferior to 5 (Figure S1C, and data not shown). It was set to 3 in all simulations following reported estimations in the literature. In this report, this cubic term was suggested to be a putative result of limiting amount of dynein in the cytoplasm as compared to MT density, which makes portion of asters sensitive to the volume they explore rather than their length or surface (Minc et al., 2011).

Parameters for yolk gradients and influence on MT lengths:

For the simulations which account for a dose-dependent influence of yolk on MT stability and length (amphibians and ascidians), the yolk spatial concentration was simulated using an "error function" along the gradient axis, x: $[\text{ yolk }] = (1 - \text{erf}(\mu (x - \varepsilon) / (2 L_{cell}))) / 2$; with L_{cell}, the diameter the egg (~140 pixels), μ the sharpness of the gradient and ε its offset from the center of the egg. A linear gradient was also tested, which did not impact the results (data not shown). An additional parameter η was used to compute the sensitivity of MTs to yolk, which impacts the local angular density of MTs: $d_{angle}(x) = 1 - [\text{ yolk }] / \eta(x)$. As default we used a linear assumption for the input of yolk on MT stability, so that $\eta(x) = 1$. To assess a threshold hypothesis, we directly changed the yolk input to a near-Heaviside function, which is equivalent to changing the MT density to a Heaviside function.

In the force and torque calculation, the local yolk-related MT concentration was used to modulate the effective mean length of MTs in each 1°x1° solid angle.

The parameters μ and ε for the yolk gradient were inferred from the literature: in Xenopus, ε parameter was set from the AVCR of centrifuged embryos, and μ was then inferred from the AVCR in controls (Neff et al., 1984; Yokota et al., 1992). In ascidians, μ and ε were estimated from

previous reports, and then adjusted to fit the asymmetry of the 2nd and 3rd cleavages (Conklin, 1931; Negishi et al., 2007). μ and ε were chosen from a 2-parameters phase diagram going from 0.2 to 500 for μ and from -10 to 50 pix for ε (data not shown). The parameter μ was set to 5 in Xenopus and 10 in ascidians (also for the additional 45° gradient at the 1st division). To test the influence of gravity on AVCR in Xenopus, μ was varied from 0.2 to 500 (Figure 3D). The parameter ε was set to 0 in Xenopus and 30 pixels in ascidians (25 for the additional 45° gradient at the 1st division). To test the influence of MT stability on AVCR in Xenopus, η was varied from 0.1 to 50 (Figure 3E). It was set to 1 in all other simulations. When testing the threshold hypothesis in Xenopus, μ was set to 5000 and ε to 20 pixels, to get a near-Heaviside yolk distribution (Figure S4D).

Alternative hypotheses tested to account for echinoderms cleavage patterns (data not shown):

In order to model the division orientations in sea urchin embryos, we tested several hypotheses that could potentially define an A-V polarity.

We first looked at the possible mechanisms for micromeres formation.- We showed that a volumic attractive domain, gradually accumulating close to the vegetal pole had the same effect as a surfacic one, yielding a switch of orientation at the 4-cell stage and an asymmetric division at the 8-cell stage when the strength of the domain was increased. This attractive domain being equivalent to a repulsive domain at the animal pole, we modeled it using a yolk-like gradient as in Xenopus. However, we could only reproduce the sea urchin development by increasing the amplitude of the gradient (which may correspond to an increase of the quantity of attracting effectors), and not by sharpening the gradient (recruitment of diffuse effectors). Despite those findings, we chose to model polarity with a surfacic domain as this is more in agreement with detergent treatment experiments (Dan, 1979; Tanaka, 1976).

- We then asked if micromeres formation could result from a pure sizing effect, associated with an increase in blastomere surface/volume ratio as the embryo cleaves, potentially rendering surface polarity effects stronger as blastomeres become smaller. Micromeres could be generated, but the shift of the nucleus towards the vegetal domain was progressive and did not occur as abruptly as in experiments at the 8-cell stage. The range of parameters allowing a rather abrupt shift of the

nucleus was extremely narrow, suggesting poor biological robustness. We thus chose to introduce a timing in the strength of the polarity, which is largely supported by retardation experiments and cut-egg experiments (Dan and Ikeda, 1971; Hörstadius, 1939).

Next, we tested several hypotheses which could potentially account for the orientations of the 1st two divisions parallel to the cap.

- Setting a power law ($F = \alpha L^3 + \beta L^2 \Psi_{pol} + \gamma L^n \Psi_{pol}$) instead of an exponential law for MT pulling could reproduce the division orientations parallel to the cap for $n \geq 4$. The switch of orientation and the asymmetric positioning of the nucleus were not sharp enough for $n \sim 4$, but tended to occur more abruptly as n increased. We found that a value of $n > 10$ would be close to experimental behavior. In light of those analyses, we chose to use an exponential law, which is supported by the evolution of MT density with the distance from the centrosome, likely associated with MT branching (Figure S5D and S5E).

- We next considered a hypothesis based on a slight deformation of the egg that would orient the 2 first axes along the A-V axis because of geometric effects. Experimentally we computed shape anisotropies of many eggs, and found that it was smaller than 3%, and that the division axis was not correlated with this slight shape deformation.

- As shown in Xenopus, yolk gradients may also modulate aster shape, and influence division positioning. Although echinoderm do not show any known accumulation of yolk or internal vesicles, we tested the combined effect of a volumic repellant using a yolk-like gradient as in Xenopus and a polarity domain. We note that a volumic repellant on one side of the embryo is equivalent to a volumic attractant on the other side. A slight repelling gradient at the animal pole or at the vegetal pole was sufficient to reproduce the 1st two divisions. A strong repellant in the vegetal half of the embryo, in competition with an attractive polarity domain from the 1-cell stage also allowed to orient the divisions parallel to the domain. Then fading of the gradient could reproduce the switch of orientation at the 4-cell stage and the asymmetric divisions at the 8-cell stage, for a constant domain strength. Thus those designs could in principle account for echinoderm cleavage. However, given the results of detergent treatment experiments which inhibit coplanarity of the two first axes, we chose not to favor these hypotheses (Figure 4C) (Dan, 1979; Tanaka, 1976).

- We next modeled the effect of a surfacic repellant ($F = \alpha L^3 - \beta L^2 \Psi_{pol}$), in addition to the vegetal attractive domain. A repellant at the animal pole oriented the 1st two divisions parallel to the domain, but did not allow a switch of orientation at the 4-cell stage. We could reproduce the full normal developmental pattern of sea urchin embryos only when the repellant was also at the vegetal pole, through a cleavage stage-dependent competition between the two superimposed domains. Biologically, this design would amount to assume that a fraction of MTs may push at the domain and another fraction may pull; and that the ratio between those fractions evolve with cleavage stage. We consider this hypothesis still plausible, but we favored a hypothesis based on two different modes of pulling, as described in the main text, given the evidence that MT pulling dominates in this system (Minc et al., 2011; Tanimoto et al., 2016).

- Finally, we asked if a wide attracting surfacic domain ($F = \alpha L^3 + \beta L^2 \Psi_{pol}$) could account for the orientation of the 1st two divisions (similarly to Figure S6E). We could reproduce the whole sea urchin development with a cleavage stage-dependent competition between this wide cap and a vegetal attracting domain: either using a constant wide vegetal cap and a strengthening vegetal domain, or with a constant vegetal domain and a fading wide animal cap. Given that all experiments performed to date support the existence of a single vegetal domain of polarity in echinoderms, we did not favor this hypothesis.

Based on these analyses, we modeled the sea urchin early development using a single surfacic vegetal domain with two competing pulling contributions, as described in the main text.

Parameters for polarity domains and their influence on MT forces:

Polarity domains, used in the simulation for echinoderms and ascidians, were generated in the script by setting a center location for the domain and using a Heaviside profile to represent the distribution of concentration of polarity effectors from this center. Step or Gaussian profiles were also assessed, which did not influence the results (data not shown). The characteristic width of the domain, Δpol, is taken to match images in the literature, and performed by our means (Figure 4B) (Negishi et al., 2007; Peng and Wikramanayake, 2013). It is about 70x70 pixels in sea urchins zygote, and 20x30 pixels in the 2-cell stage ascidian (for an egg diameter L_{cell} ~140 pixels). In later stages, the position and size of the domain are inferred from the previous division in the simulation. Δpol had in general only a minor influence on the predictions (Figure S6D and S6E).

Astral MTs that contact the domain can pull with an additional force that arises from a contribution of a "sliding mechanism" and/or an "end-on mechanism" (see main text). The adjustable parameter for the sliding mechanism, β, is allowed to vary with cleavage stage to account for stage-dependent effects of the domain on aster positioning in both systems (Figures 5, 6 and 7). In sea urchins, we tested the influence of β on cleavage planes positions and orientations, by varying β from 0 to 100, for each stage, either with the L^2 mechanism alone or with both pulling mechanisms (for a = 6.75 µm and $\gamma = 0.01$) (data not shown). For the 1st and 2nd divisions, we noted that any value between 0 and 1 gave similar results. The simulations are shown for $\beta = 0$. The switch of division orientation at the 4-cell stage either requires a clear shape long axis (like in normal development), or a β parameter around 1 (like in dissociated 4-cell blastomeres). Thus, we set β to 1.3 for 4-cell stage separated sea urchins blastomeres (Figure S5G and S5H) and to 1 or 1.3 for mid stages in Hörstadius experiment (Figure 6B). For micromeres formation, the amount of asymmetry depended on β in a dose-dependent manner. According to the amount of asymmetry observed in the literature, we set β to 10 for both normal development and Hörstadius experiments. We note that the observed asymmetric divisions may also be reproduced by setting a higher value for β, but with assuming an additional steric exclusion between the nucleus and the cell cortex (data not shown).

In ascidians, β was set to 0 for the zygote and 8 from the 2-cell stage. As for sea urchins, β was varied from 0 to 100, for each stage, either with the L^2 mechanism alone or with both pulling mechanisms (for a = 6.75 µm and $\gamma = 0.01$) (data not shown). We note that β should be bigger than 5 for the CAB to have an effect on division orientation from the 2-cell stage. However, in the 2nd and 3rd division, it must not be higher than 10, not to completely override shape and yolk contributions. In the 4th division, the asymmetry depends on β parameter in a dose-dependent manner, and the observed asymmetry is reproduced for $\beta = 12 \pm 5$. In the inactive CAB simulations, β was set to 0.

The influence of the end-on mechanism parameters γ and a, were also tested in a dose-dependent manner and were fixed and kept small in order to modulate the geometrical effects without overriding it (Figures S6A and S6B). In echinoderms, the parameter a was set to 6.75 µm based on experimental results (using a px/µm size computed from the real egg size), and γ to 0.01 according to the a-γ phase diagram (Figures S5E and S5F). For simulations including only the dynein-limited

mechanism (Figure S5B), γ was set to 0. We note that *a* should be smaller than 8.5 µm to favor a parallel orientation of the division towards the cap. For a = 6.75 µm, γ must be between 0.005 and 0.02, so that the polarity has an effect on orientation, yet with the nucleus remaining as close to the cell center as observed in imaged embryos (Figures S5E and S5F). When testing the effect of the end-on mechanism alone, γ was varied from 0.01 to 0.1 (Figure S5H).

In ascidians, we kept the same values for parameters γ and *a*, as the end-on mechanism did not appear to have a dominant effect in this system (Figure S7). For the inactive CAB simulations, γ was set to 0 (Figure 7D).

b- Parameters used in The Surface Evolver to generate blastomere shapes and arrangements:

Three generic parameters influence the shape of blastomeres and their arrangement: the surface tension of the cell-medium interface γ_{ext}, the surface tension of the cell-cell interface γ_{int}, and the envelope confinement geometry (Maitre et al., 2015). In addition, to better account for certain observed blastomere arrangements, we sometimes used different values for the tension of cell-cell interfaces between newly formed neighbors ($\gamma_{int\ new\ neighbors}$) and old adhering neighbors. The values of parameters used for different embryos, cleavage stages and experimental set-ups are given in Table S1.

Additional specific settings:

- In zebrafish, we could not easily reproduce a flat yolk / blastodisc interface as in reported images (Olivier et al., 2010). The simulated interface tended to round up more, probably because active yolk / cytoplasm separation, adhesion and asymmetric ring constrictions cannot be reproduced by a surface equilibrium model. Thus, to accurately account for embryo morphogenesis, we modelled the yolk / cytoplasm interface as a membrane and allocated specific surface tension values: γ_{cell_yolk} and $\gamma_{ext\ yolk}$ to it. To reproduce the observed flattening of this interface and of the yolky part of the embryo, we then assumed different densities in the yolk (0.25) and in the blastodisc (0), and added gravity as an external force in “The Surface Evolver”. This causes the “yolk cell" to fall and slightly

flatten against the spherical confinement. The density of yolk and radius of confinement were adjusted so that the yolk flattening matches the experimental data, and that the confinement do not affect the blastodisc. In addition, we observed that the overall blastodisc appeared to slightly increase in size over the initial cleavage divisions, plausibly because of material transport from the yolk to the blastodisc in initial stages (Kimmel et al., 1995). Thus, the yolk/blastodisc ratio was set to 4 for the 1-cell stage, 3.34 for the 2-cell stage and 3 for the subsequent stages.

- In sea urchins, we kept a relatively mild confinement of the envelope, as removing the envelope does not appear to influence division patterns and blastomere shapes in experiments (Summers, 1993). Accordingly, removing the envelope in the model did not affect cleavage patterns (figure S6F). We also added a minor hypothesis on the spatial value of $\gamma_{\text{int new neighbors}}$ to better account for asymmetric new cell-cell adhesions observed at the 4 and 8-cell stage, which seems important to define the orientation of the symmetric division of animal blastomeres at the 8-cell stage. In the model, this amounts to set a cell-cell tension that is higher towards the center of the egg as towards the outside. For simplicity we used a step function centered in the mid-line between the inner and outer sides of the egg with two values $\gamma_{\text{int new neighbors max}}$ and $\gamma_{\text{int new neighbors min}}$.

6- Supplementary References

Conklin, E.G. (1931). The development of centrifuged eggs of ascidians. The Journal of Experimental Zoölogy *60*, 1-120.

Dan, K. (1979). Studies on unequal cleavage in sea urchins I. Migration of the nuclei to the vegetal pole. Development, Growth and Differentiation *21*, 527-535.

Dan, K. (1987). Studies on unequal cleavage in sea urchins III. Micromere formation under compression. Development, Growth and Differentiation *29*, 503-515.

Kimmel, C.B., Ballard, W.W., Kimmel, S.R., Ullmann, B., and Schilling, T.F. (1995). Stages of embryonic development of the zebrafish. Dev Dyn *203*, 253-310.

Maitre, J.L., Niwayama, R., Turlier, H., Nedelec, F., and Hiiragi, T. (2015). Pulsatile cell-autonomous contractility drives compaction in the mouse embryo. Nat Cell Biol *17*, 849-855.

Minc, N., Burgess, D., and Chang, F. (2011). Influence of cell geometry on division-plane positioning. Cell *144*, 414-426.

Neff, A.W., Wakahara, M., Jurand, A., and Malacinski, G.M. (1984). Experimental analyses of cytoplasmic rearrangements which follow fertilization and accompany symmetrization of inverted Xenopus eggs. J Embryol Exp Morphol *80*, 197-224.

Negishi, T., Takada, T., Kawai, N., and Nishida, H. (2007). Localized PEM mRNA and protein are involved in cleavage-plane orientation and unequal cell divisions in ascidians. Curr Biol *17*, 1014-1025.

Olivier, N., Luengo-Oroz, M.A., Duloquin, L., Faure, E., Savy, T., Veilleux, I., Solinas, X., Debarre, D., Bourgine, P., Santos, A.*, et al.* (2010). Cell lineage reconstruction of early zebrafish embryos using label-free nonlinear microscopy. Science *329*, 967-971.

Peng, C.J., and Wikramanayake, A.H. (2013). Differential regulation of disheveled in a novel vegetal cortical domain in sea urchin eggs and embryos: implications for the localized activation of canonical Wnt signaling. PLoS One *8*, e80693.

Summers, R.G., Morrill J. B., Leith, A., Marko, M., Piston, D. W., Stonebraker, A. T. (1993). A stereometric analysis of karyokinesis, cytokinesis and cell arrangements during and following fourth cleavage period in he sea urchin, lytechinus variegatus. Development, Growth and Differentiation *35*, 41-57.

Tanaka, Y. (1976). Effects of the surfactants on the cleavage and further development of the sea urchin embryos 1. The inhibition of micromere formation at the fourth cleavage. Development, Growth and Differentiation *18*, 113-122.

Tanimoto, H., Kimura, A., and Minc, N. (2016). Shape-motion relationships of centering microtubule asters. J Cell Biol *212*, 777-787.

Yokota, H., Neff, A.W., and Malacinski, G.M. (1992). Altering the position of the first horizontal cleavage furrow of the amphibian (Xenopus) egg reduces embryonic survival. Int J Dev Biol *36*, 527-535.

TITRATED COMPETITION BETWEEN CELL GEOMETRY AND CORTICAL POLARITY IN THE DETERMINATION OF ECHINODERM CLEAVAGE PATTERNS

Anaëlle Pierre, Jeremy Sallé, Nicolas Tissot, Orestis Faklaris and Nicolas Minc

Affiliation: Institut Jacques Monod, 15 rue Hélène Brion, 75205 Paris cedex 13, France
Tel: +331-572-780-52, Fax : +331 572-780-26

ABSTRACT.

Cells divide at stereotypical locations, symmetrically, asymmetrically, and/or with specific orientations relative to tissue axes. In general, asymmetric divisions are thought to arise from the activity of a cortical polarity domain, which clusters MT associated motors that pull or depolymerize MTs at the surface, yielding to a net force towards the domain. Centered divisions, may rely more on MT length-dependent mechanisms, either involving pulling in the cytoplasm or pushing. The competition between those MT-force generation systems is likely to produce the large diversity of division phenotypes observed in multicellular tissues. To date, however, we still lack a clear understanding on how those systems may be integrated *in vivo*. Here, we exploit the early division cycles of sea urchin embryos, which exhibit subsequent invariant patterns of blastomere divisions, some symmetrically oriented, and some asymmetric, to understand how cortical pulling and length-dependent systems may compete in time and space. We couple 3D live imaging of individual blastomere shapes and polarity, with cell manipulation experiments, and models for division orientation, to assay the titrated competition between different force-generation systems. These studies suggest that a sharp increase in polar cortical pulling may be responsible for the specific echinoderm cleavage pattern, by allowing polarity to override shape-related cues within two cell cycles and to become the dominant contribution to the nuclear positioning forces.

INTRODUCTION.

The proper positioning of the cell division plane is crucial for tissue homeostasis, layering and overall organization. In general cell divisions may be symmetric, oriented with a given tissue axis, or asymmetric (Minc and Piel 2012). Given its importance, for tissue morphogenesis in development and in organs repair, division orientation and position are tightly controlled events. Depending on cell types, the site of cell division follows the orientation of the nucleus or mitotic spindle, and in most cases the cleavage plane bisects the spindle axis at anaphase. This orientation is an output of the mechanics of cytoskeletal elements associated with the division machinery, such as actin and/or Microtubules (MTs) (Grill, Gonczy et al. 2001; Grill and Hyman 2005; Li, Guo et al. 2008).

In many animal cell types, astral MTs radiating from centrosomes around the nucleus or spindle exert forces and torques which position and orient the division figure. Signals that contribute to pattern these forces may be multiple. One largely accepted mechanism, for instance, is based on cortical domains which may cluster the activity of MT associated motors such as dynein or kinesin, which then pull or depolymerize MTs at a subcellular surface location, yielding a net force on the centrosome towards the domain for oriented or asymmetric divisions (Grill and Hyman 2005; Thery, Racine et al. 2005; Kozlowski, Srayko et al. 2007; Kwon, Bagonis et al. 2015). Another concurrent view, is that MTs may generate length-dependent forces, either from a mechanism based on pushing against the cortex limited by MT buckling, or from pulling forces that scale to MT length plausibly emerging from the collective accumulation of dynein pulling in bulk cytoplasm along the MT lattice (Tran, Marsh et al. 2001; Wuhr, Tan et al. 2010; Minc, Burgess et al. 2011; Mitchison, Wuhr et al. 2012).

A striking context during which the balance between those different modes of division may be essential is the early cleavage of embryos (Gilbert 2010; Mitchison, Wuhr et al. 2012). In many species, cleavage patterns exhibit stereotyped choreographies of oriented divisions. Blastomeres may divide symmetrically, with a particular orientation with embryonic axes or preceding divisions, or even asymmetrically. These modes of division entail fate specification and organization of embryonic layers. To date however, very little is known on how those subsequent division axes may be specified in time and space.

In this study, we focus on the early division patterns of echinoderms, using sea urchin as a model organism. Echinoderms eggs are round and possess a cortical domain/cap assembled before fertilization at the incipient vegetal pole of the embryo (Peng and Wikramanayake 2013). The first division plane is oriented along the A-V axis, and bisects the domain, so that the nuclei and spindles are oriented parallel to the domain. The second division axes are also parallel to the cap and co-planar. During the 3rd round of cleavage, nuclei and spindle now point towards the cap, and cells divide symmetrically, yielding four animal blastomeres devoid of polarity caps, and four vegetal blastomeres each possessing a single cortical domain. Finally at the 4th cleavage, animal blastomeres undergo a marked asymmetric division yielding the formation of small micromeres that inherit the domain, and undergo two more rounds of asymmetric

divisions. Animal blastomeres divide symmetrically along the meridional axis (Summers 1993).

In sea urchin embryos, as in many other embryos, division specification is set during interphase by large interphase asters which fill the cell and exert forces and torques (Minc, Burgess et al. 2011; Tanimoto, Kimura et al. 2016). These asters may be highly sensitive to cell geometry, and orient the division axis along the long axis of the cell through length-dependent MT forces exerted in the cytoplasm by dynein. The cortical domain, may also contribute to pattern those forces, at least for asymmetric divisions at the 8^{th} cell stage (Dan 1971; Dan 1979). This domain contains conserved dynein effectors such as Dishevelled and/or frizzled (Peng and Wikramanayake 2013).

Recently we have proposed a theoretical model combining division axes prediction with blastomere rearrangement to outline the required design needed to account for the cleavage patterns of different species (Pierre, Salle et al. 2016). To account for sea urchin patterns, we suggested a model in which MTs pull in the cytoplasm with length-dependent forces, and at the cap with an additional force. This cortical force involved two superimposed designs, one in which the force depended exponentially on the length of MTs, and one in which this force scales with the surface of the cap and with the concentration of effectors at the cap. Here we combine theoretical analysis compared directly to division orientation in individual dividing blastomeres imaged in 3D, and cell manipulation, to test and refine those designs. This study allows us to extract precise numbers which control the titrated competition between surface polarity and volume pulling that may have relevance to our general understanding of cell division.

RESULTS AND DISCUSSION.

3D arrangements of subsequent division axes relative to the vegetal polarity domain

To understand how division axes may be oriented with respect to the vegetal domain, we first fixed a large number of embryos at different cleavage stages, and imaged in 3D with 2-photon microscopy the position of MT asters, the nucleus and the cortical domain using an antibody against Dishevelled. We first focused on interphase cells, given that interphase asters have been proposed to guide spindle axis specification in these large cells (Minc, Burgess et al. 2011). We defined three angles to quantify the orientation of division. $\Phi_{polarity}$ represents the angle between the division axis (defined along the two centers of MT asters) and the center of the polarity domain, in the plane containing the two aster centers and the polarity domain center. $\Phi_{shape\ p}$ accounts for the angle between division axis and cell-cell interface, while $\Phi_{shape\ o}$ is the angle of the projected pair of centrosomes perpendicular to the A-V axis with the cell-cell interface. By analyzing those angles in mitosis, we found that at all cleavage stages considered here the division axis follows the same orientation with cell shape and polarity as in interphase. The angles in interphase were slightly noisier than in mitosis (Supplementary Figure 1), probably due to embryos in early interphase that have not yet defined their division axis. Considering the similarity of the angles in interphase and mitosis, we further analysed all angles together (Figure 1).

At the 1-cell stage, we found that $\Phi_{polarity}$ angles extracted from n = 98 individual eggs were clustered around 90° ($\Phi_{polarity}$ = 80.1 ± 7.8°) suggesting that the orientation of the division axis is robustly perpendicular to the incipient A-V axis (Figure 1A). At the second cell stage, $\Phi_{polarity}$ angles were similar than in the 1-cell stage ($\Phi_{polarity}$ = 75.8 ± 13.9°, N = 72 cells), suggesting a similar control of division orientation by the polarity domain as in the 1-cell stage. However, the division axis was now constrained in the plane perpendicular to the A-V axis, as $\Phi_{shape\ p}$ was close to 0° ($\Phi_{shape\ p}$ = 4.3 ± 5.9°), suggesting that both axes in the 2-cell stage embryo are parallel to the interface, and thus parallel to each other (Figure 1B). At the 4-cell stage, the division axis generally pointed along the A-V axis, but interestingly appeared to be more parallel to the cell-cell interfaces than aligned with the vegetal domain ($\Phi_{polarity}$ = 38.2 ± 8.8° and $\Phi_{shape\ p}$ = 9.72 ± 7.1°, N = 188 cells). In the plane perpendicular to the A-V axis, the division axis was randomly oriented and not necessarily pointing towards the domain (Figure 1C). This suggests that the division axis specification is likely dominated by geometrical effects, and that the effect of polarity remains weak at this stage.

At the 8-cell stage (Figure 1D), vegetal blastomeres exhibited the converse behavior, as division axes were now pointing more towards the domain than along the cell-cell interface ($\Phi_{polarity}$ = 17.4 ± 11.9° and $\Phi_{shape\ p}$ = 41.4 ± 9.5°, N = 112 cells). Accordingly, the projection of the division axis was close to 0° ($\Phi_{shape\ o}$ = 12.6 ± 14.5°) suggesting that the vegetal domain had a strong attraction of the cap. Animal blastomeres which do not inherit the polar domain aligned their division axis perpendicular to the A-V axis, and parallel to their cell-cell contacts ($\Phi_{shape\ p}$ = 63.3 ± 16.2° and $\Phi_{shape\ o}$ = 60.3 ± 24.5°). Together, these quantifications confirm that the

domain influences division axis position at all stages, with a clear enhancement of its effect in vegetal micromeres.

Comparison between a model purely based on cell geometry and experimental division axes.

A prominent model for the specification of division plane in zygotes and early blastomeres is that the geometry of each cell may guide division position and orientation. This model is based upon the assumption that MTs in interphase asters, which fill the cell, may pull with length-dependent forces. To directly test this contribution, we used live 3D imaging using a 2-photon microscope. Embryos were labeled with a yolk marker that fills the whole cytoplasm, and is extruded from aster centers, which allows to segment and extract both 3D cell shapes and division axis in subsequent rounds of cleavage. We then used the information from cell shapes as inputs for 3D simulations predicting the preferred division axis selected from length-dependent forces, and compared it directly with the experimental orientation in the same live cell (Figure 2A).

This analysis showed that cell shape alone can account for the division orientation of cells at the 4-cell stage, since the simulation, which is solely based on cell shape, predicted orientations close to the experimental ones (Figure 2B). However, the difference between the predicted and observed orientations was random at the 1-cell stage, 2-cell stage and for the vegetal blastomeres at the 8-cell stage, suggesting that shape alone is not sufficient to determine division orientation with the length-dependent pulling forces hypothesis. Interestingly, plotting the angular variations of the torque applied on the pair of centrosomes at the 1 and 2-cell stages revealed that blastomeres were still dividing with respect to cell shape, as the experimental orientation corresponded to a stable equilibrium orientation (Figure 2C). For instance at the 2-cell shape, both predicted and experimental division axes were parallel to the cell-cell interface. However, the symmetries of cell shape at these stages did not favor a unique equilibrium orientation, yielding a significant difference between predicted and experimental orientations. Importantly, with shape cues alone, the simulation could not predict the observed relative alignment of the two nuclei at the 2-cell stage (Figure 2C).

To test if those discrepancies are caused by the presence of the vegetal domain, we performed the same analysis in embryos treated with SDS detergent which may dissolve the polarity domain, and cause a radialization of the embryo and the loss of asymmetric divisions, without affecting other processes (Tanaka 1976). In embryos treated with SDS, the two division axes of the 2-cell stage were not aligned with each other, and their relative alignment was randomized (Figure 2D, data not shown). Interestingly, when the two division axes were not parallel to each other, the four daughter cells were undergoing a rearrangement, leading to a tetraedric configuration (Figure 2D). We measured the orientation of the pair of centrosomes in treated 2-cell stage embryos, and compared it to the possible equilibrium orientations predicted by the model. The division axis always lied within 5° of a predicted equilibrium orientation (Figure 2E). The accuracy of the model on 2-cell stage SDS-treated embryos and the randomness of the relative alignment of the two divisions axes suggest that shape may be the only cue determining

division positioning in these treated embryos. As detergent treatment is thought to only affect the cell surface, this analysis suggests that the default geometrical rules may be biased by surface polarity domains in sea urchin embryos.

In addition, we noted that in SDS treated embryos, the lack of alignment of the two division axes at the 2-cell stage, caused an unusual tetraedric rearrangement of blastomeres at the 4 cell stage (Figure 2D). This arrangement could be reproduced by using The Surface Evolver, a program that minimizes surface energy under various constraints (Brakke 1992), and suggested that the alignment of these two spindle has functional relevance to maintain embryonic organization.

Comparison between a model accounting for the presence of the polarity domain and experimental division axes.

Using time-lapse imaging, we next monitored the location of appearance of micromeres at the 8-cell stage, to mark the location of the A-V axis, and then analyzed all division axes in the model, by accounting for the presence of the polarity domain. We used a previously proposed design (Pierre, Salle et al. 2016), to add a polar cap as an input to the division prediction model, and to bias the length-dependent MT force by two polarity terms (Figure 3A). Using the same set of parameters (corrected for cap size), the refined model could better account for the observed division orientations (Figure 3C and 3D). We note that there are still several possible orientations at the 1-cell stage, as the sea urchin zygote displays a radial symmetry. Yet, the division axis always lied close to a predicted equilibrium orientation (Figure 3B). Adding a polarity cap thus improved the accuracy of the predictions, suggesting that our model can capture better the detailed featured of embryogenesis.

Manipulating the geometry of different blastomeres.

An important aspect of our model is that polarity and geometry may be competing in a dose dependent manner, and that this effect may change over cleavage stage. To test this, we manipulated cell shape of individual blastomeres at various cleavage stages. We first analyzed if dissociated 4-stage blastomeres align their axis along the domain. This stage is interesting because in the embryo, geometry and polarity are aligned in the same direction. Interestingly, we found that although the division axis was relatively aligned towards the domain, it was not precisely pointing to the center of the domain, with a $\Phi_{polarity} = 33.3 \pm 17.2°$ (N = 75 cells). A possible explanation is that the cap displays a circular gradient of Dishevelled intensity at the 4-cell stage, with the vegetal cortical pole appearing brighter on immunostaining images than the closely surrounding cortex areas (data not shown). Separated 4-cell stage cells would then display a "quarter gradient", with more Dishevelled on a side of the cap. The center of this non-circular gradient, as well as the effective center of motor activity at the cap, would then be difficult to determine, leading to a systematic error in the definition of the polarity center (Figure 4A). Simulations of the division in a quarter-sized cell with the same set of parameters as for normal embryos showed predicted the division axis to point toward the cap. These results suggest that polarity and shape favor the same nuclear orientation at this stage.

Next we shaped dissociated blastomeres at all subsequent cleavage stages in microfabricated PDMS wells having the same volume as blastomeres (Figure 5A). We found that 1-cell, 2-cell, 4-cell and half of the 8-cell blastomeres (presumably the animal blastomeres) all followed the long axis rule, dividing symmetrically and aligning their division axis with the major shape axis, with more alignment as the cell elongated more. In contrast half of the blastomeres 8-cell blastomeres (presumably the vegetal blastomeres) displayed a near-random orientation with cell shape and divided asymmetrically (Figure 5B). Importantly, a quantification of the number of asymmetric vs symmetric divisions suggested that high shape anisotropies did not prevent micromere formation. Interestingly, almost no asymmetric divisions have been observed making a 30 to 50° angle with the shape long axis. This can be due to the fast rearrangement of cells within the microchamber, as such angles yield a very unstable configuration.

We compared this analysis with a model in which the domain was randomly placed in the shape of the chamber (see Material and Methods), and could account for the distribution of division axis obtained experimentally (Figure 5D). For 2-cell separated blastomeres, the model gave three different outputs. In addition to blastomeres aligning with the shape long axis, closer as the shape anisotropy increased, some blastomeres were found to adopt an orthogonal orientation. This orientation perpendicular to the shape long axis was due to a competition between cell shape and polarity, and only happened in the cases when the polarity was at the tips of the shape ellipse/rectangle. The polarity cues could be stronger than the shape for low shape anisotropies, or for high shape anisotropies. This last configuration is due to the exponential increase of MT density with MT length, as the model supposes the MTs to be branched. In the case of highly elongated cells, with a long distance between the nucleus and the cap, this simple exponential model yields an overly strong polarity term, which probably does not reflect the biological values. Apart from this modeling artefact, all predictions are consistent with the experimental orientations. Thus this analysis validates the notion that geometry overrides polarity in early cleavage stages, and that polarity becomes prominent in vegetal blastomeres.

Manipulating egg size to test polarity timing

Our data on manipulated blastomere shapes, suggest that the domain becomes particularly attractive at the 8-cell stage. One possible scenario however, is that as blastomere size decreases as the egg divides, the surface effects become more important than volumetric ones, independently of an improved biochemistry. To directly test this, we sought to manipulate the size of eggs and test if they may undergo asymmetric division in a precautious manner. We sliced eggs with a microneedle, which yielded two mini eggs, one retaining the female nucleus and one not (Figure 4B). Both half-eggs could be fertilized and performed early cleavage, the absence of the female pronucleus only inducing a slight delay in division rate. Interestingly, in several instance, one part of the cut egg exhibited only symmetric divisions, while the other half generated micromeres which appeared similar to controls. Importantly those asymmetric divisions did not occur before the 8-cell stage, as the sizing hypothesis would predict. These data thus provide further support of a model in which the cap maturates to become attractive only at the 8-cell stage.

DISCUSSION.

Mechanisms of division positioning

In this study, we propose that the echinoderm early cleavage pattern mostly relies on self-organization principles. The accurate prediction of the cleavage of SDS-treated embryos by our model, based on real cell shapes and solely relying on length-dependent pulling forces, suggests that shape may be a default cue to orient divisions in this system. Cell shape has been suggested to be the default cue in division positioning in many systems, in particular in early embryos. For instance, in the nematode *C. elegans* that displays an asymmetric first division, inhibition of polarity PAR proteins in the zygote yields a symmetric division aligned with the shape long axis (Tsou, Ku et al. 2003). The cleavage patterns would then be defined by polarity cues superimposed on cell shape. In sea urchins, our study suggests that a polarity signal may be required to define the A-V axis, and to organize cleavage with respect with this axis. As shown in SDS-experiments and in blastomere arrangements simulations, a function of this domain is to keep the co-planarity of the division axes at the 2-cell stage to prevent blastomere tetraedric rearrangement at the 4 cell stage (Figures 2D and 2E). We note that those rearrangement are energetically favored, and are a hallmark of the cleavage patterns in several species including mammals. The nature of this polarity signal has been investigated in (Pierre, Sallé et al. 2016), in which various hypotheses for embryonic polarization have been explored, and the hypothesis of a single vegetal cap with two different cortical pulling contributions has been proposed. Here, through quantitative experiments challenging the competition between shape and such a polarity cap, and simulations of these experiments, we confirm the set of parameters and polarity evolution proposed in the previous theoretical study.

The design of the model and the required evolution of parameters give insights into the possible mechanisms at stake, for instance through the length-dependence of MT forces, but do not specify the exact nature of the molecular effectors. A mechanism where dynein pulls on MTs in bulk cytoplasm have been proposed (Kimura and Kimura 2011; Minc, Burgess et al. 2011; Kimura and Kimura 2014), and the cytoplasmic anchorage of dynein seems to be vesicles like lysosome or endosome (Kimura and Kimura 2011), but is still under investigation. At the cap, the Wnt pathway has been suggested to be implied in polarity determination (Peng and Wikramanayake 2013), but the effectors implied in both pulling mechanisms are poorly known in sea urchins, and neither are MT branching and dynamics. In addition, our model is voluntary kept simple to extract the core mechanisms at stake, but the aberrations observed in the prediction of divisions of 2-cell stage separated blastomeres in microchambers (Figure 5D) for instance suggest that there is room for refinement. In particular, MT dynamics are ignored, and a deeper understanding of the specific biology of this system should allow refining the modeling framework.

Finally, however our study quantitatively assesses the titrated competition between shape and polarity in sea urchins, the applicability of our results to other embryos and cell types remains to be tested. In particular, some embryos like nematodes or mollusks appear to have a more deterministic definition of their cleavage patterns, showing huge variations between closely

related species (Schierenberg 2006), in contrast with species like sea urchins or frogs that seem to rely more on self-organization (Mitchison, Wuhr et al. 2012). The interplay between shape and polarity in embryos with more regulatory layers may be different than in sea urchin, and require further investigation. In addition, other embryos and cell types may rely on other types of polarity than cortical pulling caps. For instance in large embryos like frogs or fishes, vegetal yolk deposition seems to bias nuclear positioning (Wuhr, Tan et al. 2010). The interaction of MTs with yolk and organelles is not clear, in particular the dynamics of their mutual exclusion, and how it would affect MT pulling at the cap remain open questions. The nuclear positioning mechanisms proposed in the present paper may also interfere with additional mechanisms such as MT pushing, which has been observed in smaller cells (Tran, Marsh et al. 2001). Here again the interplay between shape and polarity may be biased and require further investigation.

Symmetric versus asymmetric divisions

A major feature of echinoderm division pattern is the apparition of micromeres at the 16-cell stage. Interestingly, nuclear migration to the vegetal cortex that leads to micromere formation is achieved in two phases in the sea urchin 8-cell stage. During interphase, one of the centrosomes migrates toward the vegetal pole, and the nucleus and other centrosome rejoin it in the very end of interphase. The two asters of MTs do not seem to have the same structure (Dan 1971; Dan 1979; Dan 1987), and the mechanisms gathering the two centrosomes are unclear. The dynamics of micromere formation may be an important question to address, especially as the attraction of one centrosome by cortical MT pulling forces is also observed in other systems, such as the *C. elegans* zygote where the pair of asters centers at first, rotates, and decenters as one of the centrosomes moves toward the posterior pole.

In our model, the transition between symmetric and asymmetric divisions is mediated by an increase in attractivity of the vegetal cortical polarity cap. At this early stage of development, the embryo's DNA is not yet expressed and cleavage relies on maternal RNAs deposited in the egg. Although the microchambers experiments presented here, as well as previous experiments challenging the cell cycle (Hörstadius 1928; Hörstadius 1939), strongly suggest a timely expression of factors responsible for cortical pulling at the vegetal pole, the nature of the expression increase and its amplitude are not known. A first insight into the question has been provided by (Peng and Wikramanayake 2013), observing that Dishevelled is differently post-translationally modified in the micromeres. The effectors of local cortical pulling may be various across species, and further work will be required to identify the molecular basis of asymmetric divisions in specific systems. However, by generally showing how an increase of local cortical MT pulling may bias shape-determined nuclear positioning in the sea urchin embryo, our model may be valuable to other embryos and cell types.

MATERIAL AND METHODS.

2-photon microscopy

The fixed embryos, as well as the live control and SDS-treated embryos, were imaged using two-photon excitation with a pulsed laser (680-1300nm, Insight DeepSee, Spectra Physics) on an upright microscope stage (LaVision BioTec, Bielefeld, Germany), with a Carl Zeiss Plan-Apochromat 20× NA 1 water immersion objective.

Live embryos were dyed at a 1000X concentration with a yolk (cytoplasmic) far red fluorescent marker, Nile Blue, shortly before fertilization and without further rinsing. They were imaged in a dish containing sea water and Nile Blue. For SDS-treated embryos, Nile Blue was added after SDS, 15 min after fertilization. The excitation laser wavelength was set to 1100 nm (SDS-treated embryos), or 790 nm (untreated embryos). Emission was collected on a gallium arsenide phosphide photomultiplier tube detector (GaAsP-PMT). The step size in Z axis was set to 2 μm in all experiments. Image stacks were acquired typically at 10 min intervals.

Fixed embryos were also imaged in dish, free-floating in PBS. The excitation wavelength was set to 900 nm for normal embryos, and to 980 nm for embryos separated at the 4-cell stage. Two different laser lines were used to image DNA and Dsh (DeepSee Insight), and MTs (1040nm secondary output beam of DeepSee Insight). Emission light was collected on three different GaAsP-PMTs, using two dichroic mirrors (T560 LPX RTX and a T495 LPXR) and the green signal (Dsh) was collected through a 525/50 nm bandpass filter. For embryos separated at the 4-cell stage, only Dsh and MTs were imaged, using the main DeepSee-Insight laser line. The step size in Z was set to 2 μm for normal embryos and to 1 μm for separated blastomeres.

Image analysis

2-photon live images were analyzed with ImageJ to extract both blastomeres and asters shapes.

Blastomeres shapes were segmented manually to extract cell-cell interfaces, and using a light intensity threshold to extract the cell-medium contours. The threshold was applied after smoothing the images, and was adjusted throughout the Z-stack to compensate for the decrease of laser intensity with imaging depth. If needed, a last step of manual smoothing of the contours could be added to correct for imaging noise and dirt at the surface of the embryo. The shapes were filled to generate the input binary Z-stack for the division prediction program. To generate polarity stacks, a binary stack showing the surface of the blastomeres was extracted from the binary stack with filled volumes, using an ImageJ macro. The binary stack showing the polarity cap, and used as an input to the division prediction program, was generated by an intersection of the surface stack with a sphere or a threshold plane, using a Matlab script. The coordinates of the sphere/plane were set with regards to the position of micromeres formation.

Aster shapes were extracted with a light intensity threshold, after a slight smoothing of the images. Here again the threshold was adjusted in Z. The positions of the tips of the asters (the two extremities of the elongated zone formed by the two mitotic asters) were used to determine the orientation of the pair of centrosomes. They were inferred from an ImageJ 3D rotation of the aster binary stack, allowing finding the positions of the tips in two perpendicular views. The calculation of nuclear orientation from the projections of aster tips on these two perpendicular planes was performed with a Matlab script.

ImageJ 3D projections were also used to extract the positions of centrosomes (from the MT signal) and cap center of stained embryos. The positions were taken on two perpendicular planes, and converted back in XYZ coordinates with a Matlab script. When the signal was too dim to allow using this more precise technique, typically for interphase cells where MTs fill the whole cell and mask centrosomes in the 3D projection, XYZ coordinates were extracted directly from the Z-stack. Cell-cell contact planes were extracted from the Z-stack by taking 4 points on the edge of the contact at the 2-cell stage, and the two extremities of the midline and one point per lateral cell-cell contact at later stages. Relative angles of nuclear orientation with respect to shape/polarity were calculated from the XYZ coordinates of centrosomes, cap center and contact planes with a Matlab script.

Immunostainings

The protocol for fixation and immunostaining used for normal sea urchin embryos is provided in Minc et al. (2011). It was modified to include the addition of an antibody against Dishevelled, kindly provided by Prof. Wikramanayake, used at 1/2000 (Peng and Wikramanayake 2013). 4-cell stage separated embryos were separated 10-15 min after the onset of the second cytokinesis, and fixed 5 min after, directly on dishes coated with 1 % protamine.

SDS

To test the effect of detergent on the co-planarity of divisions at the 2-cell stage in sea urchins, the eggs were placed in a solution of 5 x 10^{-6}% SDS in sea water (50 ng/mL), from the end of sperm aster centration (10-15 min after fertilization). The embryos were stained with Nile Blue (X1000) shortly after, and imaged live with a 2-photon microscope.

Separated blastomeres

To separate blastomeres within an embryo, the eggs were treated with PABA sea water (2.74 10^{-2} % in sea water). From 10 seconds after fertilization, the eggs were continuously filtered through a 80 µm nylon mesh, for 2 min, in approximately equal volumes of PABA sea water and normal artificial sea water. They were then washed twice with sea water, and left to develop. Separation was done after the completion of the previous cytokinesis, typically 15 min after the onset of cytokinesis. The embryos were put in Mg-free Ca-free sea water for 2 min,

and agitated. They were then washed once with sea water. Mg-free Ca-free sea water was made of (for 100 ml) :
15 ml 3.0 M NaCl
10 ml 0.33 M Na2SO4
1.8 ml 0.50 M KCl
0.5 ml 0.50 M NaHCO3
1.0 ml 1.0 M Tris 0.25 M EDTA pH 8.0
71.7 ml water

Microchambers

Microfabrication of PDMS molds used to alter the shape of individual bleastomeres follows the same protocols as described in (Minc, Burgess et al. 2011). After separation of the blastomeres, Hoechst (X1000) was added to the final wash of the separation protocol, and let to stain the cells for about 20 seconds. The volume of the solution was then brought down to 2 drops, which were spread on a glass slide. The PDMS slab containing microwells, was applied on top of the slide, and the excess liquid was removed with a kimwipes. A further refinement consisted of putting an agar (2 %) pad on the glass slide before adding the blastomeres, and let the blastomeres divide in an agar/PDMS confinement. This tended to prevent excess drying and blastomere adhesion to the glass. The glass slide could be replaced by a plate, to further prevent drying. The divisions were observed in the plane of the nuclei, in bright field and fluorescence (Hoechst), every 5 min. Multi-position was used to image more blastomeres. The microscopes used were a Leica DMI6000B and a Nikon Ti inverted microscopes, equipped with a X10 air objective. The orientation of the division was inferred at cytokinesis, or from the DNA separation axis when the Hoechst signal was visible and in focus. As only the central plane of the cells was imaged, the measured angles were projections of the real division orientation on the imaging plane. The wells depth was small enough to slightly flatten the cells, and the observed divisions were mostly close to planar. Other orientations were not taken into account.

Cut eggs

Eggs were cut in a plate with a coverslip on the bottom, to allow imaging with an inverted microscope. A few drops of eggs in sea water were put onto the coverslip. The jelly layer around the eggs could be previously removed to make the eggs stickier and easier to cut. For this, the eggs were filtered 3 times through a 80 µm nylon mesh. Cutting was achieved with a microneedle fabricated by pulling a glass capillary, with a pipette puller. The needle was handled under a Leica DMI6000B inverted microscope with a X10 air objective, using a micromanipulator. The needle was usually making an angle of about 45° with the coverslip. The side of the needle was used to squeeze the eggs in two. If needed, the two brother eggs could be gathered with the glass needle, to be imaged together in the microscope field of view. The eggs were then let to rest for about 30 min before fertilization, to retrieve their round shapes. They were fertilized and imaged in bright field, every 30 seconds.

Division prediction program

The program to predict division positioning from shape and polarity was the same as (Pierre, Sallé et al. 2016), based on MT forces on the centrosomes that depend on MT lengths and two polarity cap contributions. To predict divisions from shapes generated with The Surface Evolver, the exact same program was used. To predict division positioning from real imaged 3D shapes, the program was modified for different XY resolutions and Z step sizes. All results were analyzed, compared to experiments and plotted with Matlab scripts.

The program performed a directed search for the equilibrium position and orientation. In the case of normal embryonic development simulated only from shapes (Figure 2B and 2C), as well as for the prediction of the divisions in cut eggs (Figure 4C) and separated 4-cell stage blastomeres (Figure 4A), the final position and orientation of the directed search were taken as the equilibrium position and orientation, and the angular variations of the torque amplitude (at the position given by the directed search) could be plotted afterwards to check the results. For instance the variations of the torque were plotted in the case of normal embryonic development simulated only from shapes (Figure 2C), but the plot was not used to infer the equilibrium orientation.

For the simulations of divisions in microchambers (Figure 5D), of SDS treated cells (Figure 2E) and of normal development with a cap (Figure 3), the angular variations of the torque were plotted after the directed search (at the position given by the directed search), and the equilibrium orientation was inferred from the plot. The curves were smoothed to reduce noise.

To determine the equilibrium orientation of divisions in microchambers, the torque was only calculated for planar orientations of the nucleus, after checking that the directed search yielded an almost planar orientation. In the case of several equilibrium orientations, only the main equilibrium orientation was selected, unless it was difficult to determine (then several orientations were taken). A Matlab script selecting the equilibrium orientations and sorting out the local/noise-related equilibrium orientations by curve smoothing helped processing the data.

Surface Evolver and other artificial shapes

The Surface Evolver simulated shapes used in division prediction for cut eggs and separated 4-cell stage blastomeres were those used in (Brakke 1992).

The shapes of eggs in microchambers were not computed with The Surface Evolver, but directly generated from the Autocad file used to make the microfabrication mask. With ImageJ, a binary stack of the cell volume was generated to be used as input to the division prediction program, as well as a binary stack of the surface. The binary stack showing the polarity cap was generated by an intersection of the surface stack with a sphere, using a Matlab script. The center of the sphere was calculated from the shape surface, so that 7 different polarity stacks were generated with a regular spacing on a quarter of the contour (given the symmetry of the shapes,

we only considered the situations where the polarity cap was making an angle ψ with the shape long axis between 0 and +90º).

The simulation of the tetraedric rearrangement of the cells in SDS-treated embryos was performed with The Surface Evolver. A first simulation was run to generate the starting shape, with the starting angles between the sister cell-cell interfaces fixed. The starting angle was set to 10.8º, as measured between the two pairs of asters at the two-cell stage mitosis in the embryo shown in figure 2D. The radius of confinement was set to 0.74 from a measurement on the images (total embryo volume is 1). Cell-cell surface tension was set to 1 and cell-medium surface tension to 0.65, to reproduce the observed shapes. Then the constraint on the starting interface angle was released, and the simulation was run from the starting shape, with no other parameter change. An image was taken at regular simulation steps. Simulation steps were: {r; u4; w0.0005; u4; g5; u4; w0.0006; u4; g5; u4; w0.0007; u4; g5; u4; w0.0008; u4; g5; u4; w0.001; u4; g40; u4; w0.001; u4; g5} (Surface Evolver syntax)

REFERENCES.

Brakke, K. A. (1992). "The Surface Evolver." Experimental Mathematics **1**(2): 141-165.

Dan, K. (1979). "Studies on unequal cleavage in sea urchins I. Migration of the nuclei to the vegetal pole." Development, Growth and Differentiation **21**(6): 527-535.

Dan, K. (1987). "Studies on unequal cleavage in sea urchins III. Micromere formation under compression." Development, Growth and Differentiation **29**(5): 503-515.

Dan, K., Ikeda, M. (1971). "On the system controlling the time of micromere formation in sea urchin embryos." Development, Growth and Differentiation **13**(4).

Gilbert, S. (2010). Developmental Biology. 9th edition. Sunderland (MA), Sinauer Associates.

Grill, S. W., P. Gonczy, et al. (2001). "Polarity controls forces governing asymmetric spindle positioning in the Caenorhabditis elegans embryo." Nature **409**(6820): 630-633.

Grill, S. W. and A. A. Hyman (2005). "Spindle positioning by cortical pulling forces." Dev Cell **8**(4): 461-465.

Hörstadius, S. (1928). "Über die Determination des Keimes bei Echinodermen." Acta Zoologica, Stockholm **9**(1).

Hörstadius, S. (1939). "The mechanics of sea urchin development, studied by operative methods." Biological Reviews **14**(2): 132-179.

Kimura, K. and A. Kimura (2011). "Intracellular organelles mediate cytoplasmic pulling force for centrosome centration in the Caenorhabditis elegans early embryo." Proc Natl Acad Sci U S A **108**(1): 137-142.

Kimura, K. and A. Kimura (2014). "A novel mechanism of microtubule length-dependent force to pull centrosomes toward the cell center." BioArchitecture **1**(2): 74-79.

Kozlowski, C., M. Srayko, et al. (2007). "Cortical microtubule contacts position the spindle in C. elegans embryos." Cell **129**(3): 499-510.

Kwon, M., M. Bagonis, et al. (2015). "Direct Microtubule-Binding by Myosin-10 Orients Centrosomes toward Retraction Fibers and Subcortical Actin Clouds." Dev Cell **34**(3): 323-337.

Li, H., F. Guo, et al. (2008). "Actin-driven chromosomal motility leads to symmetry breaking in mammalian meiotic oocytes." Nat Cell Biol **10**(11): 1301-1308.

Minc, N., D. Burgess, et al. (2011). "Influence of cell geometry on division-plane positioning." Cell **144**(3): 414-426.

Minc, N. and M. Piel (2012). "Predicting division plane position and orientation." Trends Cell Biol **22**(4): 193-200.

Mitchison, T., M. Wuhr, et al. (2012). "Growth, interaction, and positioning of microtubule asters in extremely large vertebrate embryo cells." Cytoskeleton (Hoboken) **69**(10): 738-750.

Peng, C. J. and A. H. Wikramanayake (2013). "Differential regulation of disheveled in a novel vegetal cortical domain in sea urchin eggs and embryos: implications for the localized activation of canonical Wnt signaling." PLoS One **8**(11): e80693.

Pierre, A., J. Salle, et al. (2016). "Generic Theoretical Models to Predict Division Patterns of Cleaving Embryos." Dev Cell **39**(6): 667-682.

Pierre, A., J. Sallé, et al. (2016). "Generic Theoretic Models to Predict Division Patterns of Cleaving Embryos." Developmental Cell **39**: 1-16.

Schierenberg, E. (2006). "Embryological variation during nematode development." WormBook: 1-13.

Summers, R. G., Morrill J. B., Leith, A., Marko, M., Piston, D. W., Stonebraker, A. T. (1993). "A stereometric analysis of karyokinesis, cytokinesis and cell arrangements during and following

fourth cleavage period in he sea urchin, lytechinus variegatus." Development, Growth and Differentiation **35**(1): 41-57.

Tanaka, Y. (1976). "Effects of the surfactants on the cleavage and further development of the sea urchin embryos 1. The inhibition of micromere formation at the fourth cleavage." Development, Growth and Differentiation **18**(2): 113-122.

Tanimoto, H., A. Kimura, et al. (2016). "Shape-motion relationships of centering microtubule asters." J Cell Biol **212**(7): 777-787.

Thery, M., V. Racine, et al. (2005). "The extracellular matrix guides the orientation of the cell division axis." Nat Cell Biol **7**(10): 947-953.

Tran, P. T., L. Marsh, et al. (2001). "A mechanism for nuclear positioning in fission yeast based on microtubule pushing." J Cell Biol **153**(2): 397-411.

Tsou, M. F., W. Ku, et al. (2003). "PAR-dependent and geometry-dependent mechanisms of spindle positioning." J Cell Biol **160**(6): 845-855.

Wuhr, M., E. S. Tan, et al. (2010). "A model for cleavage plane determination in early amphibian and fish embryos." Curr Biol **20**(22): 2040-2045.

FIGURES.

Figure 1 : Orientation of the pair of centrosomes with respect to shape and polarity in stained sea urchin embryos.

Figure 2 : Shape alone is not sufficient to predict cell division in live sea urchins embryos.

Figure 3 : The integration of shape and a polarity signal allows to predict cell division in live sea urchins embryos.

Figure 4 : Experiments to assess the shape/polarity competition in the determination of the cleavage plane : separated 4-cell stage blastomeres and cut eggs.

Figure 5 : Experiments to assess the shape/polarity competition in the determination of the cleavage plane : blastomeres in microchambers.

Supplementary Figure 1 : Fixed embryos fixed in interphase or during mitosis show similar orientations of their centrosome pair with regards to shape and polarity.

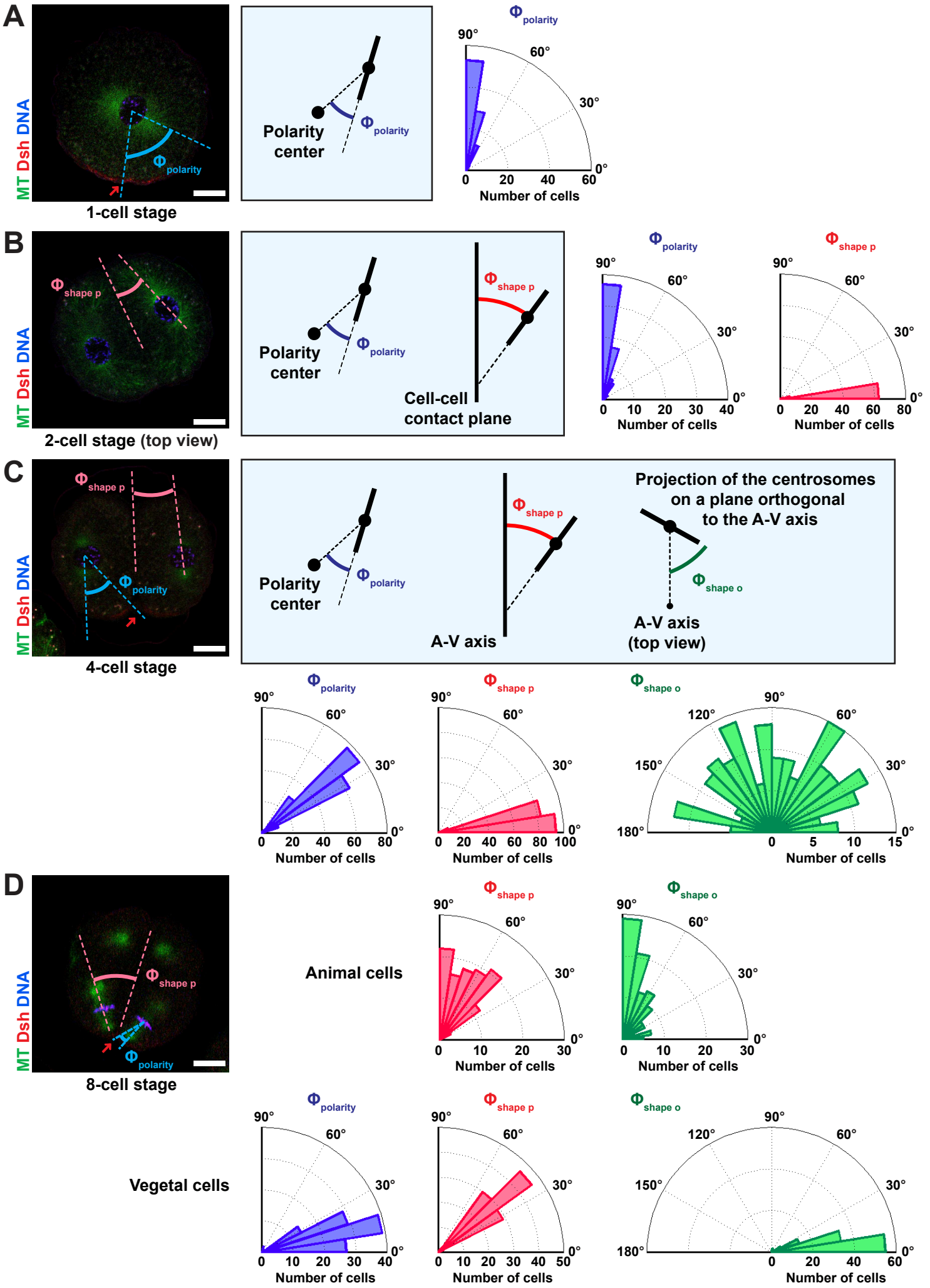
A
MT Dsh DNA
Φ polarity
1-cell stage
Polarity center
Φ polarity
Φ polarity
90°
60°
30°
0°
0 20 40 60
Number of cells
B
MT Dsh DNA
Φ shape p
2-cell stage (top view)
Polarity center
Φ polarity
Φ shape p
Cell-cell contact plane
Φ polarity
Φ shape p
0 10 20 30 40
0 20 40 60 80
Number of cells
C
MT Dsh DNA
Φ shape p
Φ polarity
4-cell stage
Polarity center
Φ polarity
Φ shape p
A-V axis
Projection of the centrosomes on a plane orthogonal to the A-V axis
Φ shape o
A-V axis (top view)
Φ polarity
Φ shape p
Φ shape o
0 20 40 60 80
0 20 40 60 80 100
0 5 10 15
Number of cells
D
MT Dsh DNA
Φ shape p
Φ polarity
8-cell stage
Animal cells
Vegetal cells
Φ shape p
Φ shape o
0 10 20 30
0 10 20 30 40 50
0 20 40 60
Number of cells

<u>Figure 1 :</u> Orientation of the pair of centrosomes with respect to shape and polarity in stained sea urchin embryos.

(A) 1-cell stage. **(Left)** Immunostaining of an egg in prophase, showing tubulin (green), Dishevelled (red) and DNA (blue). Red arrow indicates the center of the polarity cap. $\Phi_{polarity}$ is illustrated in blue. Scale bar : 20 µm. **(Middle)** Definition of $\Phi_{polarity}$. **(Right)** Quantification of $\Phi_{polarity}$ on both interphase and mitosis fixed zygotes (N = 75 cells in interphase, N = 23 cells in mitosis).

(B) 2-cell stage. **(Left)** Immunostaining of an embryo in 2-cell stage interphase, showing tubulin (green), Dishevelled (red) and DNA (blue). $\Phi_{polarity}$ is illustrated in blue, $\Phi_{shape\ p}$ in pink. Scale bar : 20 µm. **(Middle)** Definition of $\Phi_{polarity}$ and $\Phi_{shape\ p}$. At the 2-cell stage, $\Phi_{shape\ p}$ is defined with the cell-cell contact plane. **(Right)** Quantification of $\Phi_{polarity}$ and $\Phi_{shape\ p}$ on both interphase and mitosis 2-cell stage fixed embryos (N = 16 cells in interphase, N = 56 cells in mitosis).

(C) 4-cell stage. **(Top left)** Immunostaining of an embryo in 4-cell stage late interphase, showing tubulin (green), Dishevelled (red) and DNA (blue). Red arrow indicates the center of the polarity cap. $\Phi_{polarity}$ is illustrated in blue, $\Phi_{shape\ p}$ in pink. Scale bar : 20 µm. **(Top right)** Definition of $\Phi_{polarity}$, $\Phi_{shape\ p}$ and $\Phi_{shape\ o}$. From the 4-cell stage, $\Phi_{shape\ p}$ and $\Phi_{shape\ o}$ are defined with the embryo midline. **(Bottom)** Quantification of $\Phi_{polarity}$, $\Phi_{shape\ p}$ and $\Phi_{shape\ o}$ on both interphase and mitosis 4-cell stage fixed embryos (N = 84 cells in interphase, N = 104 cells in mitosis).

(D) 8-cell stage. **(Top left)** Immunostaining of an embryo in 8-cell stage metaphase, showing tubulin (green), Dishevelled (red) and DNA (blue). Red arrow indicates the center of the polarity cap. $\Phi_{polarity}$ is illustrated in blue, $\Phi_{shape\ p}$ in pink. The definitions of $\Phi_{polarity}$, $\Phi_{shape\ p}$ and $\Phi_{shape\ o}$ are the same as for the 4-cell stage. Scale bar : 20 µm. **(Top right)** Quantification of $\Phi_{shape\ p}$ and $\Phi_{shape\ o}$ on both interphase and mitosis animal cells of 8-cell stage fixed embryos (N = 12 cells in interphase, N = 100 cells in mitosis). **(Bottom)** Quantification of $\Phi_{polarity}$, $\Phi_{shape\ p}$ and $\Phi_{shape\ o}$ on both interphase and mitosis vegetal cells of 8-cell stage fixed embryos (N = 12 cells in interphase, N = 100 cells in mitosis).

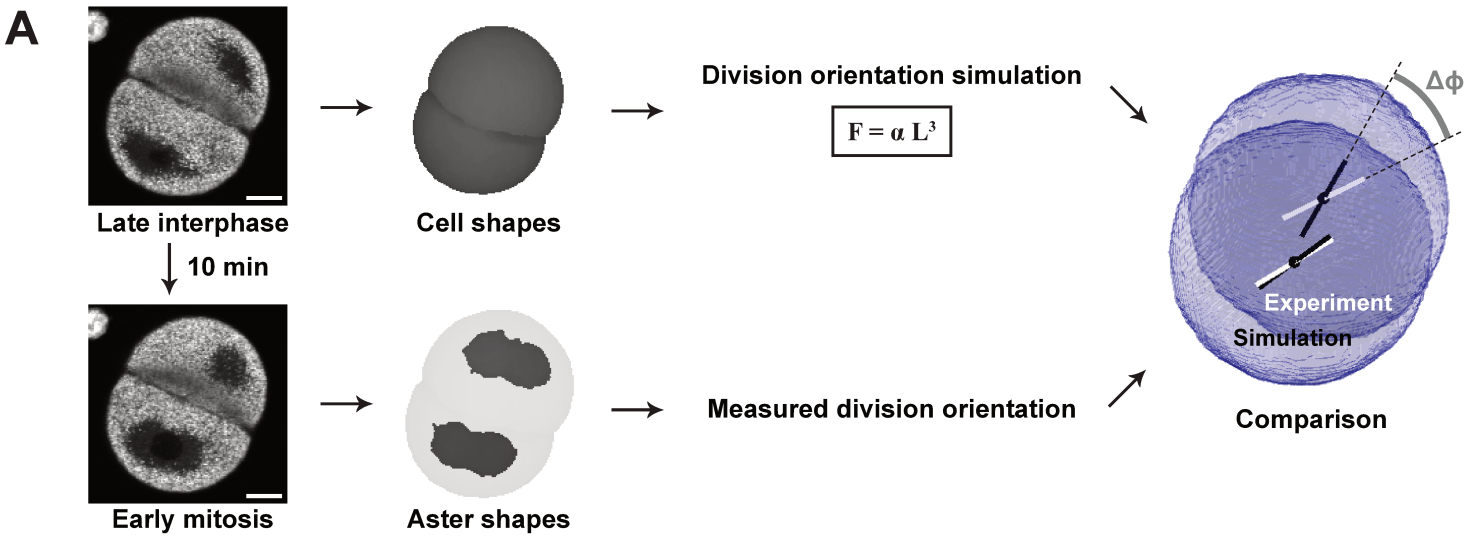
A
Late interphase
10 min
Early mitosis
Cell shapes
Aster shapes
Division orientation simulation
F = α L³
Measured division orientation
Δϕ
Experiment
Simulation
Comparison

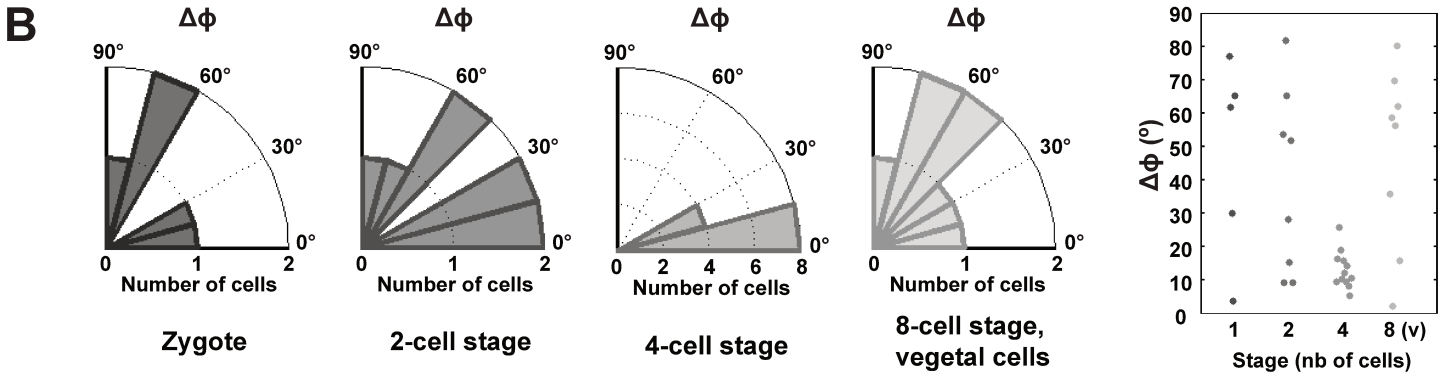
B
Δϕ
90°
60°
30°
0°
Number of cells
Zygote
2-cell stage
4-cell stage
8-cell stage, vegetal cells
Δϕ (°)
Stage (nb of cells)
1
2
4
8 (v)

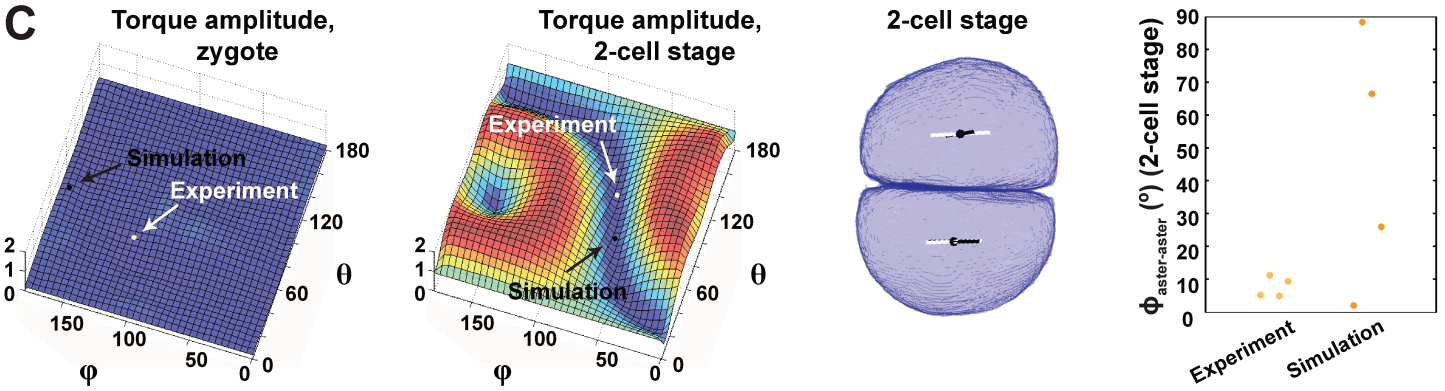
C
Torque amplitude, zygote
Simulation
Experiment
Torque amplitude, 2-cell stage
2-cell stage
θ
φ
$\phi_{aster-aster}$ (°) (2-cell stage)
Experiment
Simulation

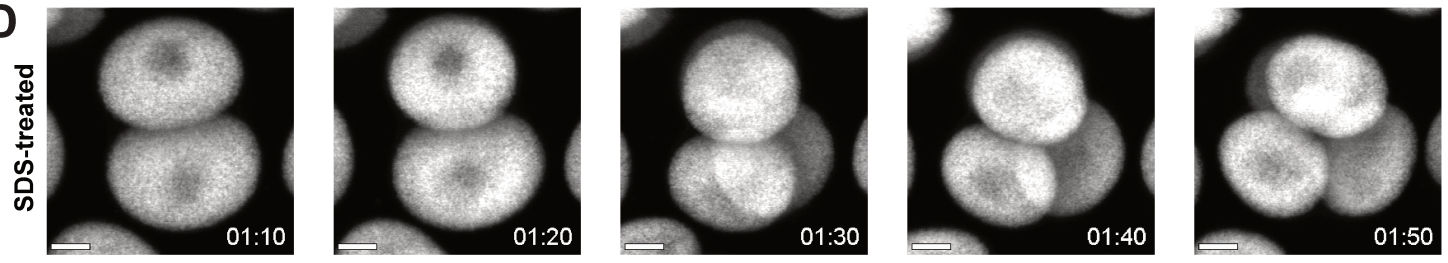
D
SDS-treated
01:10
01:20
01:30
01:40
01:50

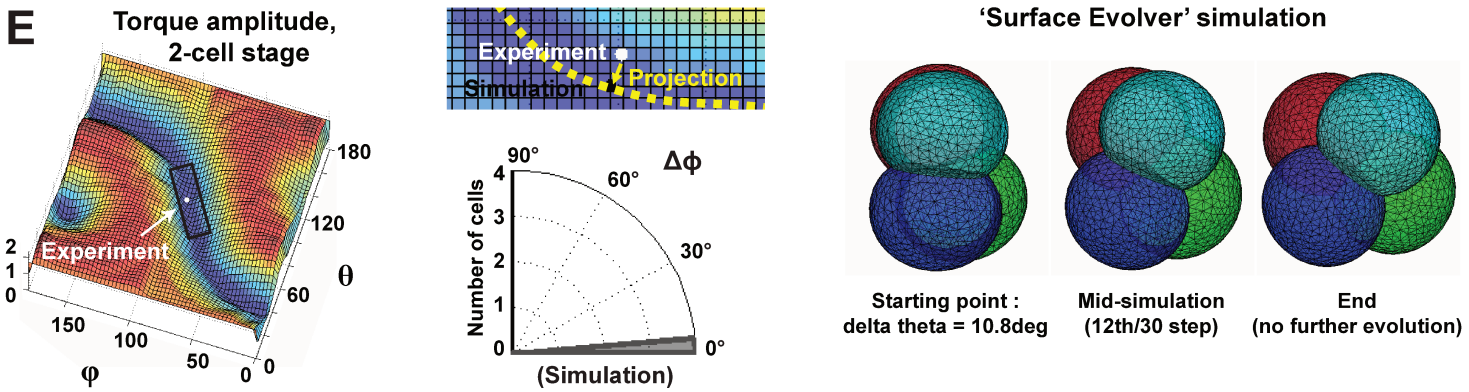
E
Torque amplitude, 2-cell stage
Experiment
Simulation
Projection
Δϕ
Number of cells
(Simulation)
'Surface Evolver' simulation
Starting point : delta theta = 10.8deg
Mid-simulation (12th/30 step)
End (no further evolution)

Figure 2 : Shape alone is not sufficient to predict cell division in live sea urchins embryos.

(A) Principle of the experiment/simulation crosstalk. **(Left)** 2-photon 3D images of embryos dyed with Nile Blue (cytoplasmic marker, excluded from the asters) are used to obtain cell shapes and aster shapes (See Material and Methods). Cell shapes serve as input to the division prediction program, and aster shapes allow measuring the experimental division orientation. **(Right)** Illustration of the angular difference $\Delta\phi$ (in gray) between the measured orientation (in white) and the simulated orientation (in black) of the pair of centrosomes (represented as a segment). Scale bar : 20 μm.

(B) Quantification of the angular difference $\Delta\phi$ for different stages (N = 5 cells at the 1-cell stage, N = 8 cells at the 2-cell stage, N = 12 cells at the 4-cell stage and N = 8 vegetal cells at the 8-cell stage,). The simulated orientation is the result of the directed search for the equilibrium position and orientation (not inferred from an analysis of the angular variations of the torque).

(C) (Left) Plot of the amplitude of the torque (smoothed) for all 3D orientations (θ,φ) of the nucleus, for zygote and 2-cell stage. Color code is consistent between the two panels. White dot shows the experimental orientation, and black dot shows the simulated orientation (resulting from the directed search for equilibrium). Both fall in zeros of the torque corresponding to a stable equilibrium orientation. **(Middle)** Example of a 2-cell stage shape, and the corresponding experimental (in white) and simulated (in black) nuclear orientations. Both orientations lie parallel to the cell-cell interface, according to the long axis rule. **(Right)** Angular difference between the two division axes of the two blastomeres at the 2-cell stage. The simulation does not reproduce the alignment of the two division axes observed in live embryos.

(D) Time-lapse of the second division of SDS-treated embryos, imaged in 3D by 2-photon microscopy with a cytoplasmic marker (Nile Blue). Z-projection, scale bar : 20 μm.

(E) Simulation of the SDS-treated embryos. **(Left)** Plot of the amplitude of the torque (smoothed) for all 3D orientations (θ,φ) of the nucleus in a 2-cell stage SDS-treated embryo. Observed orientation (white dot) falls in a stable equilibrium orientation. **(Top middle)** Inset from the torque plot, showing the definition of the simulated orientation from the torque calculation, as the nearest equilibrium orientation to the experimental orientation. **(Bottom middle)** Quantification of $\Delta\phi$ on SDS-treated embryos (N = 4 cells). **(Right)** Simulation of the tetraedric rearrangement of SDS-treated embryos at the 4-cell stage, from an angular difference between the two divisions axes, with The Surface Evolver.

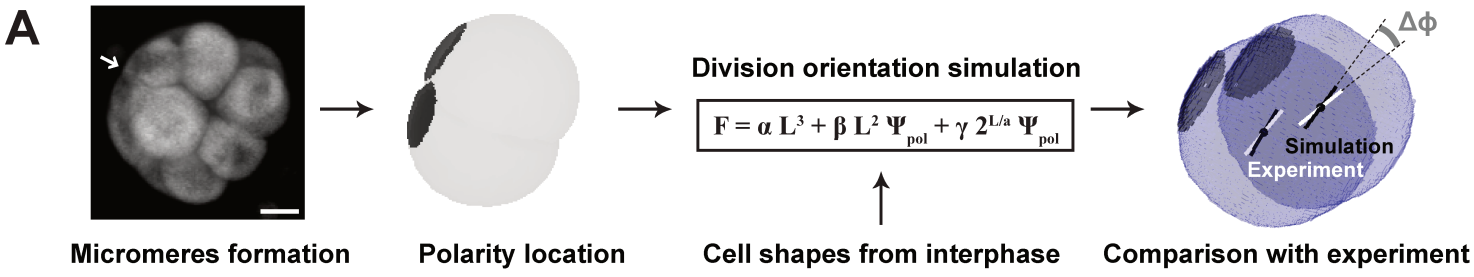
A
Division orientation simulation
$F = \alpha L^3 + \beta L^2 \Psi_{pol} + \gamma 2^{L/a} \Psi_{pol}$
Δϕ
Simulation
Experiment
Micromeres formation
Polarity location
Cell shapes from interphase
Comparison with experiment

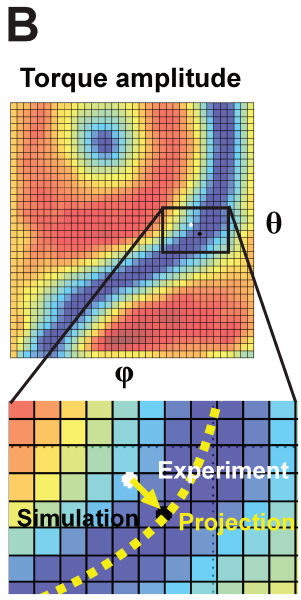
B
Torque amplitude
θ
φ
Experiment
Simulation
Projection

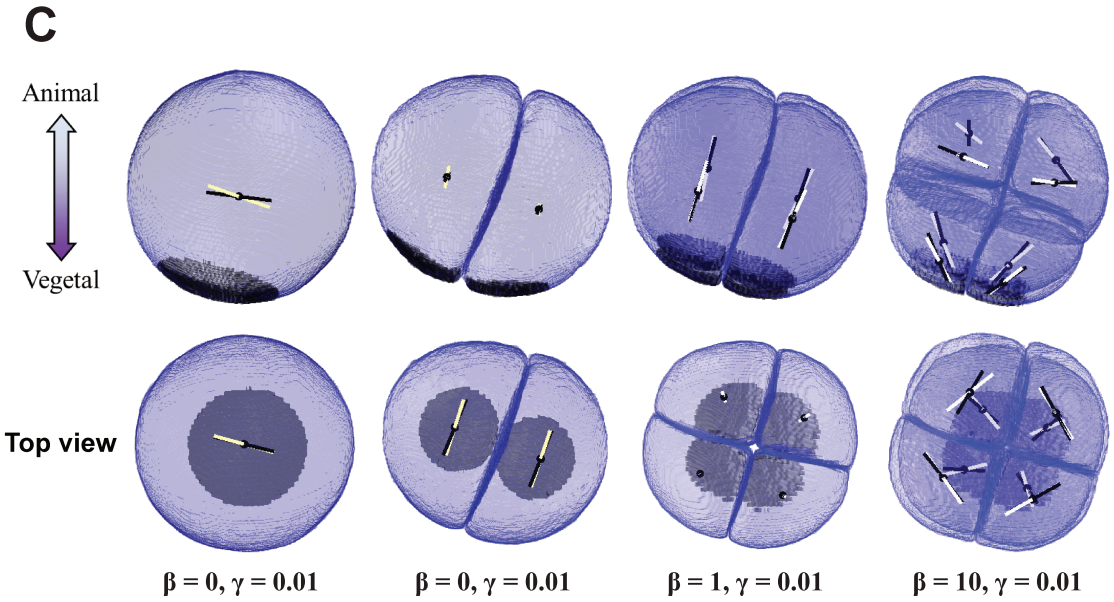
C
Animal
Vegetal
Top view
β = 0, γ = 0.01
β = 0, γ = 0.01
β = 1, γ = 0.01
β = 10, γ = 0.01

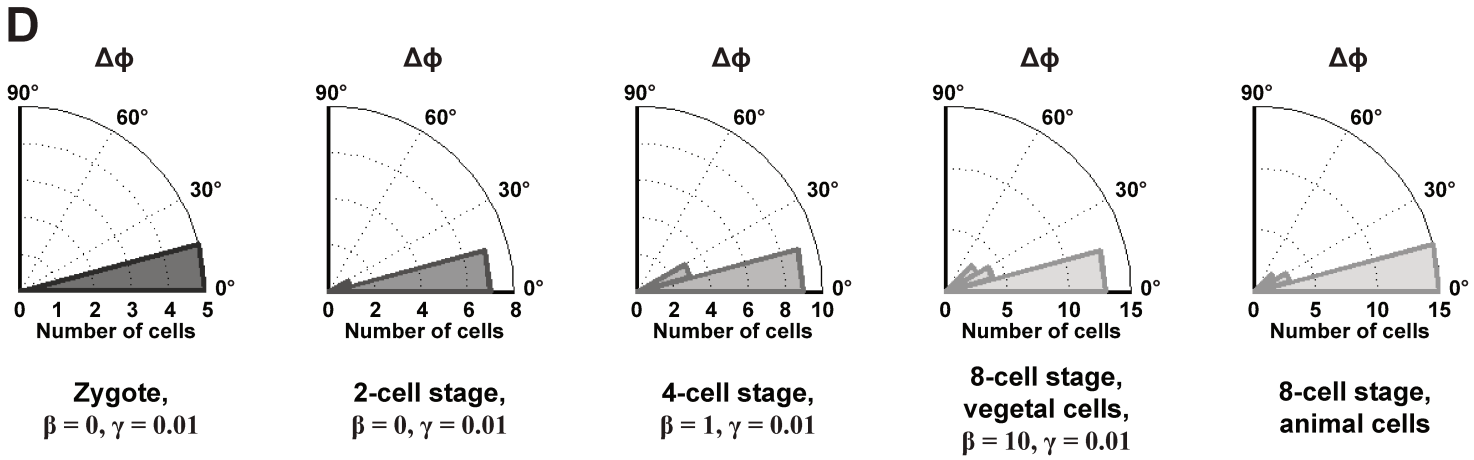
D
Δϕ
90°
60°
30°
0°
Number of cells
Zygote,
β = 0, γ = 0.01
2-cell stage,
β = 0, γ = 0.01
4-cell stage,
β = 1, γ = 0.01
8-cell stage,
vegetal cells,
β = 10, γ = 0.01
8-cell stage,
animal cells

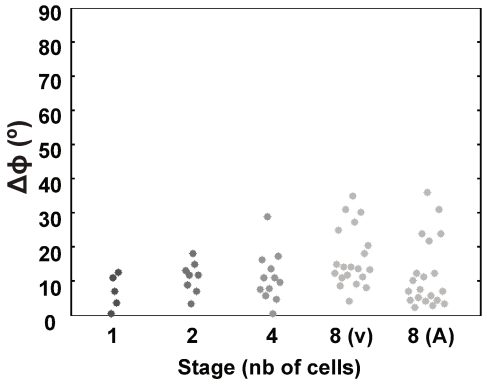
Δϕ (°)
Stage (nb of cells)
1
2
4
8 (v)
8 (A)

<u>Figure 3 :</u> The integration of shape and a polarity signal allows to predict cell division in live sea urchins embryos.

(A) Addition of a polarity signal as an input to the division prediction simulation, inferred from the side of micromere apparition. This side is indicated by a white arrow, on the Z-projection of a 3D 2-photon image of the 8-cell stage embryo (cytoplasmic dye : Nile Blue). Scale bar : 20 μm. Two polarity terms are added to the length-dependent expression of the individual MT force. The angular difference $\Delta\phi$ (in gray) between the measured orientation (in white) and the simulated orientation (in black) of the pair of centrosomes is calculated. Simulated orientations are inferred from the angular variations of the torque.

(B) Torque amplitude (smoothed) for all 3D orientations (θ,φ) of the nucleus in a zygote. Inset shows the definition of the simulated orientation in the case of several possible orientations, as the closest equilibrium orientation to the experimental orientation.

(C) 3D shapes of embryos from the zygote to the 8-cell stage, with the corresponding polarity cap (gray), experimental (white) and simulated (black) orientations of the nuclei.

(D) Quantification of $\Delta\phi$ for different stages (N = 5 cells for zygote, N = 8 cells for 2-cell stage, N = 12 cells for 4-cell stage, N = 20 cells for vegetal 8-cell stage and N = 20 cells for animal 8-cell stage).

A

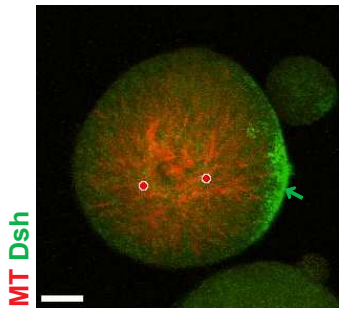

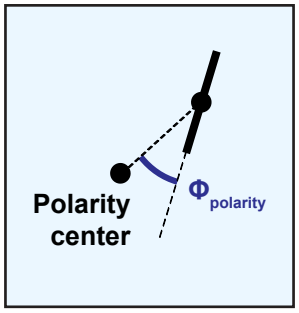

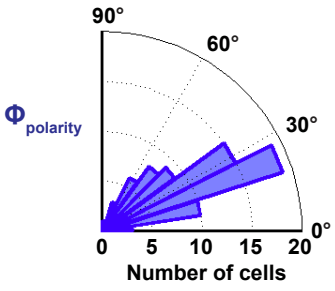

$$F = \alpha L^3 + \beta L^2 \Psi_{pol} + \gamma 2^{L/a} \Psi_{pol}$$

β = 1.3, γ = 0.01

B

Cut egg : development of the first half-egg

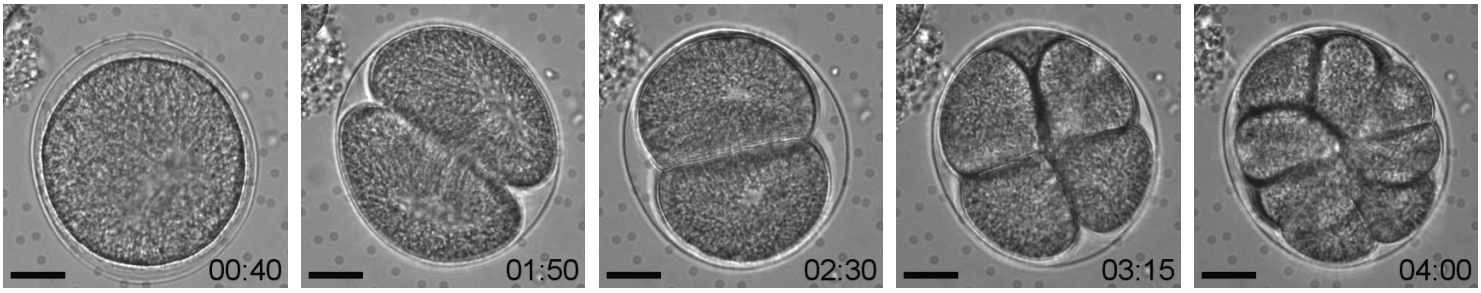

Cut egg : development of the second half-egg

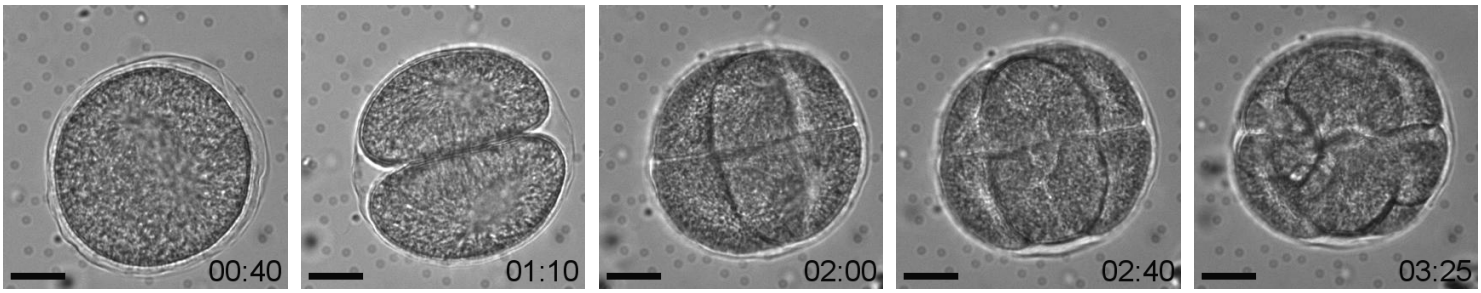

C

$$F = \alpha L^3 + \beta L^2 \Psi_{pol} + \gamma 2^{L/a} \Psi_{pol}$$

Half-sized embryos

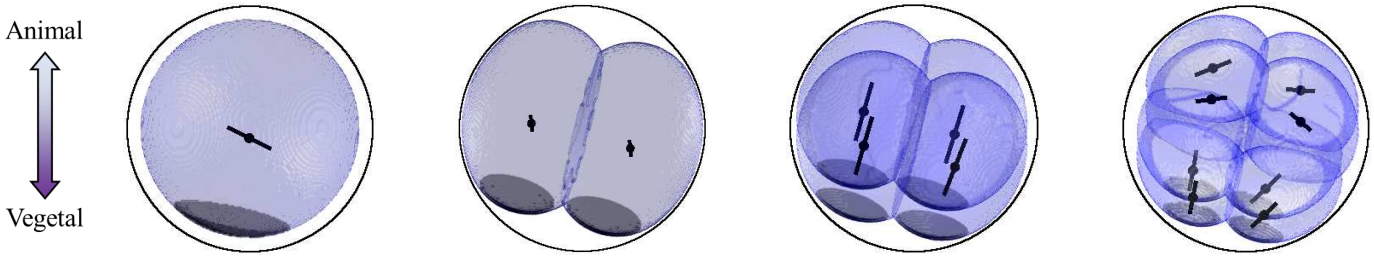

β = 0, γ = 0.01 | β = 0, γ = 0.01 | β = 1, γ = 0.01 | β = 10, γ = 0.01

<u>Figure 4 :</u> Experiments to assess the shape/polarity competition in the determination of the cleavage plane : separated 4-cell stage blastomeres and cut eggs.

(A) Nuclear orientation in 4-cell separated blastomeres. **(Left)** Immunostaining image (3D rotation) of a separated 4-cell stage blastomere, showing tubulin in red and Dishevelled in green. Red dots indicate centrosomes, green arrow indicates the center of the polarity cap chosen for the angular analysis. It corresponds to the center of the brightest area, but not of the whole cap. The centrosomes appear to point to the center of the whole cap. Scale bar : 10 µm. **(Middle)** Definition and quantification of $\Phi_{polarity}$ in separated blastomeres. **(Right)** Simulation of the division on quarter sized cells, with the shape and two polarity contributions to individual MT force. The shape originates from a Surface Evolver simulation. The division axis appears to point toward the cap.

(B) Time-lapse of cut eggs development. The top and bottom panels show the development of two half-eggs originating from the same egg. The top half-egg does not inherit the female pronucleus, and develops more slowly. It only performs symmetric divisions, while the bottom half-egg forms micromeres at the 16-cell stage. Scale bar : 20 µm.

(C) Simulation of half-egg cleavage with a polarity cap, on shapes generated with The Surface Evolver. Micromeres appear at the 16-cell stage.

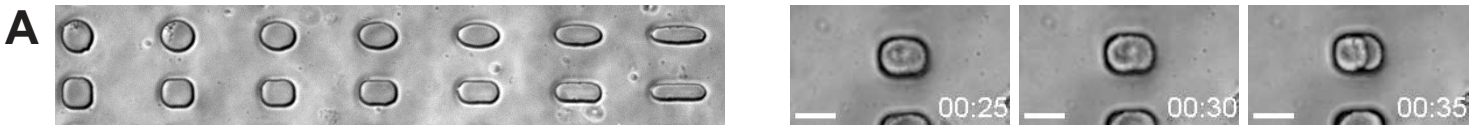
A
00:25
00:30
00:35

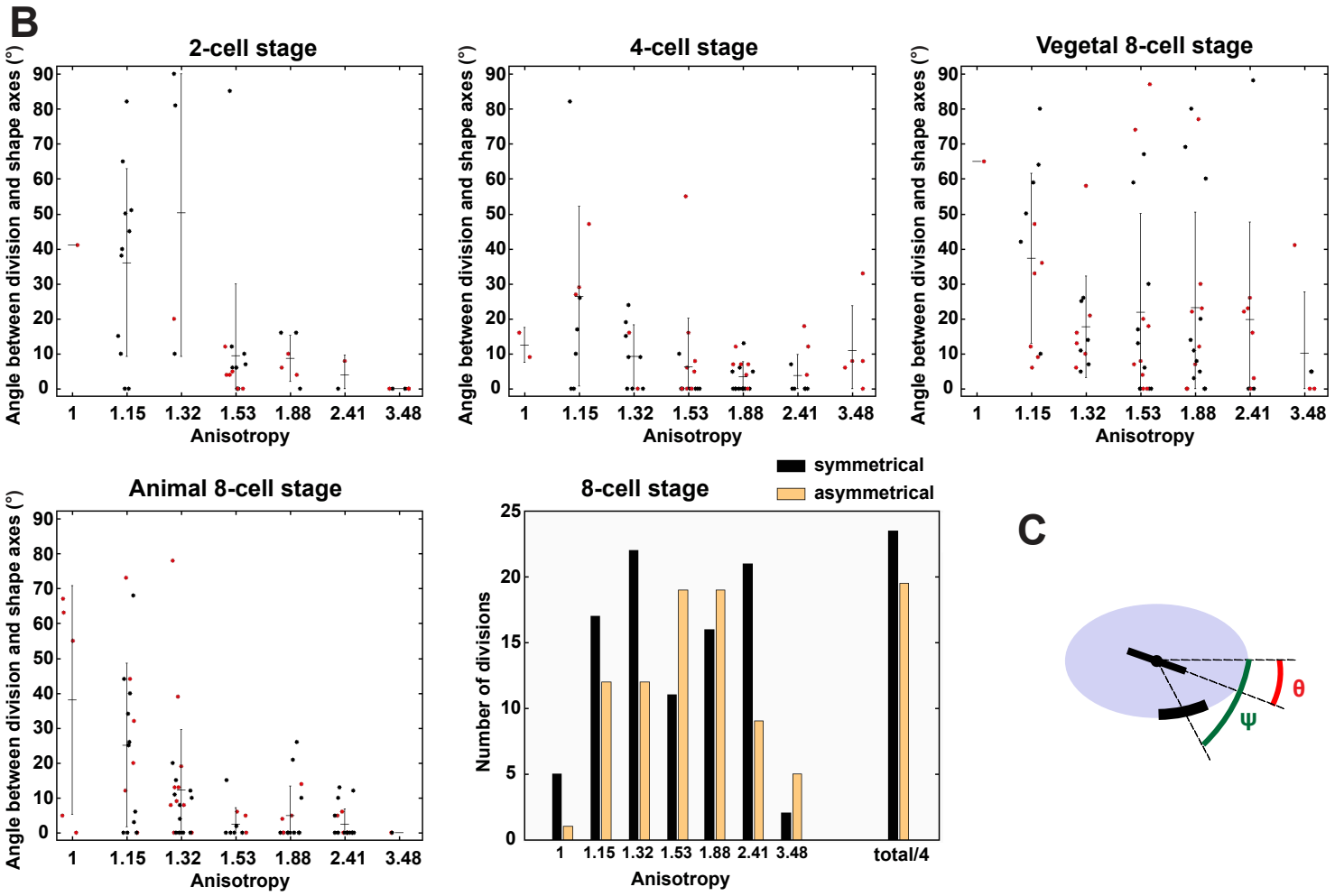
B
2-cell stage
4-cell stage
Vegetal 8-cell stage
Animal 8-cell stage
8-cell stage
symmetrical
asymmetrical
Angle between division and shape axes (°)
Anisotropy
Number of divisions
total/4

C
θ
ψ

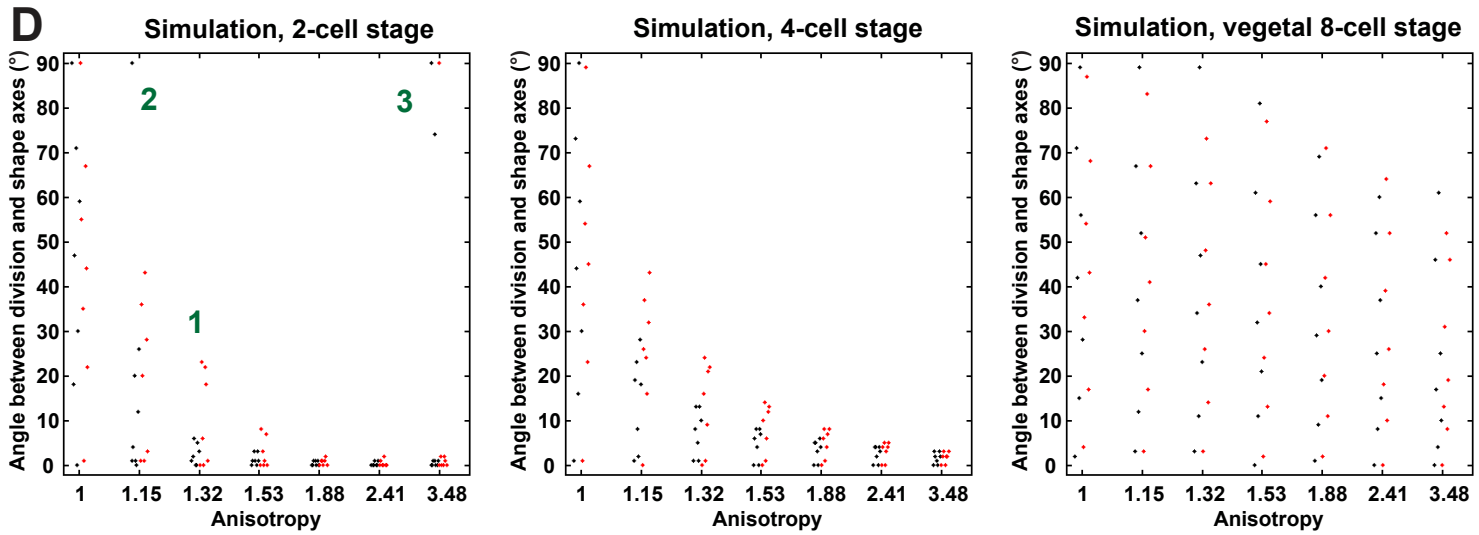
D
Simulation, 2-cell stage
Simulation, 4-cell stage
Simulation, vegetal 8-cell stage
Angle between division and shape axes (°)
Anisotropy
1
2
3

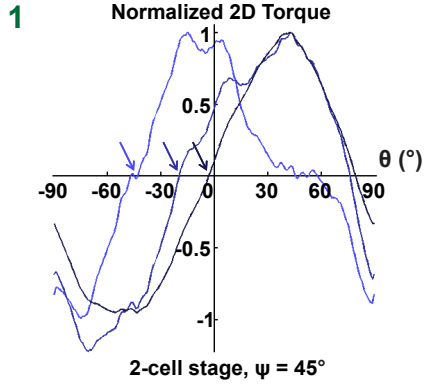
1
Normalized 2D Torque
θ (°)
2-cell stage, ψ = 45°
Anisotropy = 1; 1.15; 1.53

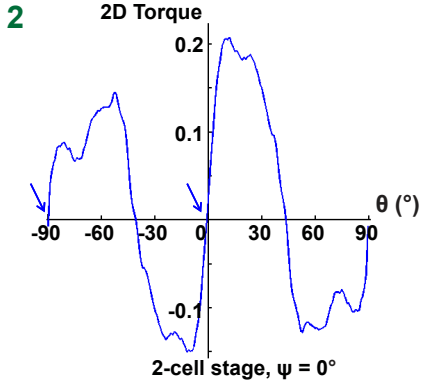
2
2D Torque
θ (°)
2-cell stage, ψ = 0°
Anisotropy = 1.15

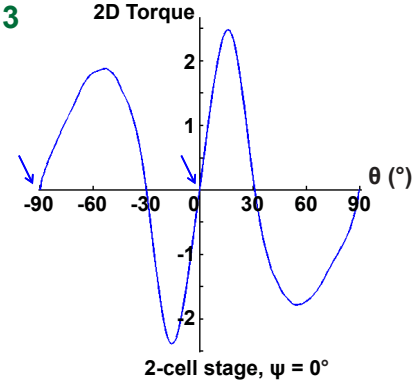
3
2D Torque
θ (°)
2-cell stage, ψ = 0°
Anisotropy = 3.48

<u>Figure 5 :</u> Experiments to assess the shape/polarity competition in the determination of the cleavage plane : blastomeres in microchambers.

(A) Microfabricated chambers. **(Left)** Image of the elliptic and rectangular wells with different shape anisotropies. **(Right)** Time-lapse of an 8-cell stage separated blastomere dividing in a microchamber. Scale bar : 20 μm.

(B) Angular difference between measured division axes and shape long axis in 2D, as a function of the anisotropy of the shape, for blastomeres separated at different stages. Black dots stand for elliptic wells and red dots for rectangular ones. Bars are standard deviation. Last panel shows the number of observed symmetrical and asymmetrical divisions as a function of shape anisotropy, for 8-cell stage separated blastomeres.

(C) The simulations were run on shapes of different anisotropies (corresponding to those of experiments), and for each shape, with different polarity locations defined by the angle ψ, at regular spacing on the surface (see Material and Methods). For each simulation the angular difference θ between the predicted division axis and the shape long axis was plotted.

(D) Results of the simulations. **(Top)** For all shape anisotropies and values of ψ, θ is plotted as a function of the anisotropy, for blastomeres separated at different stages. Black dots stand for elliptic wells and red dots for rectangular ones. **(Bottom)** Plots of the 2D torque (smoothed) as a function of θ, for representative simulations. Arrows indicate stable equilibrium orientations.

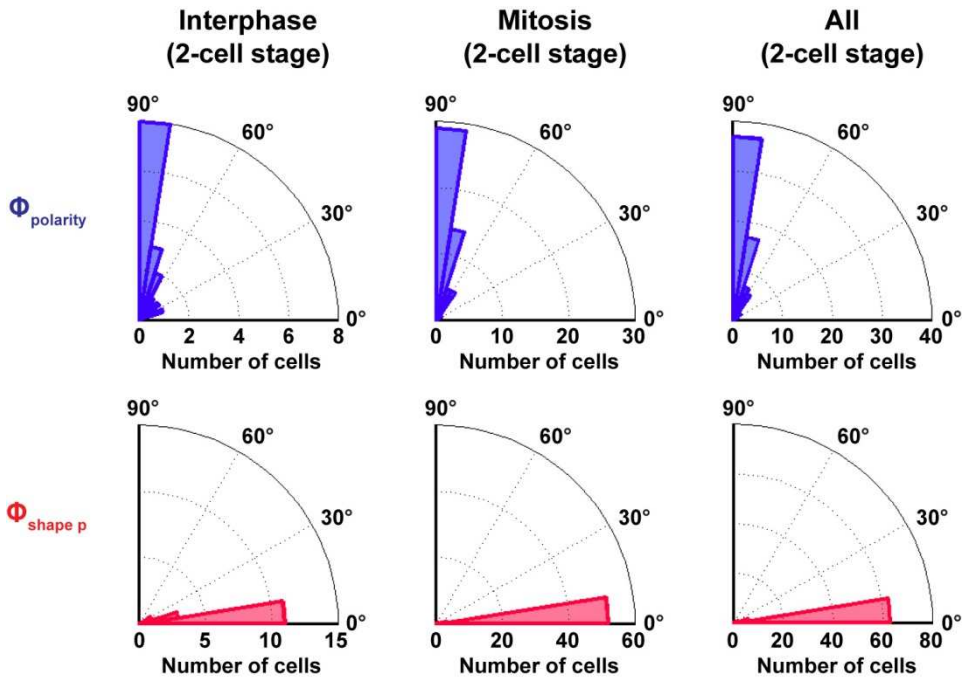

<u>Supplementary Figure 1 :</u> Fixed embryos fixed in interphase or during mitosis show similar orientations of their centrosome pair with regards to shape and polarity.

Quantification of $\Phi_{polarity}$ and $\Phi_{shape\ p}$ at the 2-cell stage. Left panels show only the interphase cells (N = 16), middle panels only the dividing cells (N = 56) and right panels show all. Orientations are similar, even though interphase orientations appear a bit noisier.

CONCLUSION

CONCLUSION

In the first part of this work, it has been possible to design a generic numerical model that allows predicting the positioning of the divisions that defines four representative deuterostome cleavage patterns. The model is based on length-dependent pulling forces exerted by microtubules on the pair of centrosomes, which are responsible for the positioning of the nucleus with regards to cell shape. This default contribution is then modulated by yolk gradients that bias microtubule lengths, and by maternal polarity cues that exert additional pulling forces. The contribution of these maternal polarity cues and their competition with cell shape have been quantitatively assessed in the second part of this work, and confirm the design hypotheses proposed in the first part.

In brief, these results show that the cleavage patterns of early embryos can be simulated with a rather simple modelling framework, requiring a limited number of hypotheses and little parameter adjustment, and thus suggest that these patterns originate from a few simple self-organization processes. In particular, the program is modular and the four cleavage patterns studied here can be predicted solely by adding or removing components that are not species-specific. This shows that the principles at play may be the same in all these systems, and that only the initial composition of the egg, with or without these components, may determine the whole subsequent cleavage pattern. The possible universality of the mechanism highlighted here would explain the remarkable conservation of these cleavage patterns within whole animal classes.

DISCUSSION AND PERSPECTIVES

Role of cell shape

An important point highlighted by this study is the role of cell shape in division plane positioning. As shown by simulations of cleavage in chemically or genetically manipulated zebrafish embryos, variations in the mechanical properties of cells or in their adhesion, that give rise to variations in cell shapes, can lead to dramatically different orientations of the cleavage planes. This result is confirmed by physical manipulations in sea urchin and frog embryos, that also alter the cleavage patterns. It may thus be important for further studies on cell division to take cell shape into account, and to quantitatively characterize the physical properties of cell surfaces, as well as cell-cell interactions. For instance, it would be interesting to see if variability in cortical tension or cell-cell adhesion, whether natural or induced, leads to a change in nuclear orientation in other embryos, in particular in the context of several superimposed cues for division plane positioning.

As seen in detergent-treated sea urchin embryos, maternal polarity seems to be responsible for the orientations of the nuclei with respect to the animal-vegetal axis. In treated embryos, the two division planes are not parallel to each other at the second division, and the four daughter cells rearrange to adopt a tetraedric configuration. The change in cell-cell adhesion induced by the detergent may be involved in this rearrangement. Indeed, untreated cells appear more adherent, and adhesion may hold the cells together and prevent conformation changes. This particular role of adhesion in maintaining stereotypical cleavage patterns by preventing cell movements would need to be examined. It is indeed interesting to note that embryos which display a spiral cleavage pattern rather seem to rely on rearrangement to adopt a stable cell packing. However, in the case of echinoderms, detergent-treated embryos that happen to have almost aligned nuclei at the 2-cell stage do not rearrange to a tetraedric configuration after the division. Another possibility is that the rearrangement is too slow to be complete before the next round of division, as suggested by Surface Evolver simulations, and thus cannot be observed. In any case, and even with little contribution of adhesion, the relative alignment of the two nuclei appears to prevent tetraedric rearrangement and to maintain the radial cleavage pattern. It is thus possible that both adhesion and polarity are involved in the definition of this cleavage pattern by preventing cell movements towards a more thermodynamically stable conformation. The question of the robustness of the cleavage pattern, through these mechanisms or by a compensation of the tetraedric configuration in the next series of nuclear orientations, remains an open question.

Variability in cleavage patterns

A similar question, which is only qualitatively addressed in this work, is the question of the noise of the patterns. The reproducibility of cleavage patterns in variable between species. For instance, frogs show variations in the pattern from the 16-cell stage, while echinoderms typically undergo two or three more rounds of divisions before showing variations. For a cellular approach such as the one developed in the present work, it is crucial to assess the biological noise in division positioning, as well as the simulation noise. The

iterative modeling framework used to predict division patterns *in silico* adds up noise at each step of simulation. This noise was typically smaller than the biological noise, allowing to efficiently predict nuclear orientation during the reproducible early stages. However, it would be necessary to perform a clean study of the variability of the system. Indeed, it would first allow testing the sensitivity of the pair of centrosomes to orientation cues, such as the anisotropy of the shape or the distribution of the polarity. Second, it would give insight into the robustness of cleavage patterns and further development. In particular, it would be interesting to know from which stage the precision of the pattern becomes less important, and how embryos cope with these variations in pattern at such an early stage. Finally, noise assessment would allow making the transition between the early stages of development, which are reproducible enough to be studied from a cellular point of view, and later stages that rather follow a tissular logic.

Self-organization versus determinism

The simulations of embryonic cleavage patterns performed here in four representative deuterostomes species, supported by perturbation experiments in sea urchin embryos, unravel a few generic principles for division plane positioning. The application of these principles to all embryonic cleavages and cell types remains however to discuss. It is possible that the mechanisms characterized in this study are main mechanisms, if not default mechanisms, playing a role in all systems. Yet, the observed variability of cleavage patterns between closely related species in other animal classes suggests that these embryos would rather rely on tight genetic control than on self-organization processes. The question of whether these regulatory layers would be working alone, or be superimposed on default organization principles, and in this case of how they would compete or interplay with them, is still to be addressed. It is however certain that the application of the generic principles described in this work to other embryos and cell types will require further adaptation of the model, in particular to include the effects of genetic factors.

It is interesting to note that self-organization appears to be a fast and direct way to define embryonic axes, in contrast to precise genetic control that seems more complex and may be requiring more time. Self-organization principles thus appear to be more adapted to the fast cell cycle of early embryos. In contrast, somatic cells that display a longer cell cycle rather seem to rely on determinism to define their division planes. In addition, adding many maternal regulatory layers might potentially take more time, be more costly and subject to more errors when it comes to generating oocytes. In line with these suppositions, the present study suggests that deuterostomes embryos may rely on self-organization principles, while the embryos which rather exhibit deterministic cleavage patterns, such as nematodes or mollusks, seem to belong to more ancestral lineages. The question of whether simpler self-organization has been selected over genetic control in evolution, when, how and on what grounds, remains open. It is possible that further quantitative studies on the mechanisms that positions divisions will bring insight on this point, in particular by assessing the amounts of effectors at stake and by energetic considerations.

Relevance of this study to different systems

As mentioned earlier, the applicability of the models developed here to different embryos and cell types remains questionable. It is not clear whether the principles highlighted

in this work are valid in embryos relying on determinism rather than on self-organization to define their cleavage patterns. In particular, how the competition between maternal polarity and cell shape is titrated has been explored in the sea urchin embryo, but may be different in deterministic cleavage patterns, in somatic cells, or even in some self-organized embryos. An adaptation of the model to the specificities of these systems may be required to understand how cell division is positioned there.

In particular, the role of cell-cell interaction has not been assessed. The four early patterns considered here do not seem to rely on cell-cell signaling, and the hypothesis of a nuclear orientation driven by cell-cell contacts has been ruled out by simulations in zebrafish in the first article. However many other embryos, like the nematode worm, rely on cell-cell signaling to determine cell fates, and possibly also division orientation. The study of planar division orientation in fly epithelial tissue, presented in annex, suggests that morphogens gradients that set the tissue axes may be dominant over cell shape to orient the nucleus. Moreover, these cells round up prior to mitosis, and it is not clear whether this change in shape is meant to erase shape information in order to divide with regards to tissue polarity, or whether tissue polarity helps keeping a trace of the previous cell shape to orient the division. In any case, the competition between polarity and shape appears different than in the sea urchin embryo. However, the effect of cell-cell contacts and signaling may be modeled similarly as maternal polarity, and it is possible that the adaptation of the model to such a system would only require some changes in parameters, but not in the generic design. To do so, it would be necessary to look at the details of cell-cell signaling, to determine the nature, localization and way of action of this type of polarity.

Details of the mechanisms

The model is kept simple in order to identify the minimal requirements to accurately predict cleavage patterns. The details of the described mechanisms are not considered here, and even their exact nature is sometimes only hypothesized, and potentially variable between species. For instance, the nature of the interaction between microtubules and yolk is not fully understood, as the inhibition of microtubule growth in yolk could originate whether from steric exclusion or from chemical destabilization. However, the exact mechanism of microtubule inhibition is not key to understand the effect of yolk on nuclear positioning.

When it comes to polarity, the pathways and molecular interactions at stake in force generation have not been thoroughly investigated. It is probable that these pathways are variable between species, but that the downstream effect is similar, allowing these differences between species to be accounted for simply with a slight change of parameter in the model, but no change in the design of the model. In particular, the stoichiometry of the reactions is not considered, and for instance the actual amount of dynein at the cap, and the order of magnitude of its variation, remain to be determined. Furthermore, the model developed here makes the hypothesis of an increase of pulling force at the cap during the early cleavage of the sea urchin embryo. This hypothesis is supported by several experiments from the literature, as well as from the second part of this work, but the model does not specify the nature of the increase in force. It is possible that the amount of dynein increases, but the increase in force could also originate from an increase in the amount of another effector, from the same pathway or from a different one, or from an increase in dynein activity, as suggested by recent observations showing that Dishevelled is differently post-translationally modified in the micromeres (Peng and Wikramanayake, 2013).

The structure of the microtubule network has not been closely investigated, and the exponential law accounting for microtubule branching in the model is an approximation and leaves room for refinement. So far, the model, voluntary kept simple, made the hypothesis that the details of the microtubule network structure could all be recapitulated in first approximation by an exponential term for pulling force, and that possible variations from the hypothesized simple regular branching would only be equivalent to changing the parameters of this term. The aberrations observed in the simulations for blastomeres constrained to highly elongated shapes by confinement in microchambers does not invalid this hypothesis, but rather suggests that it is only valid within a restricted range of sizes. When the characteristic length of microtubules is too high, typically higher than the diameter of the egg, the exponential term would be too strong in the model. Such a situation does not usually happen in normal embryos, explaining the accuracy of the simple exponential model to still predict division orientation in those normal embryos. However, microtubule density may reach a threshold in elongated blastomeres, that the exponential model does not account for, and would explain the aberrant simulations. A closer look to the details of the microtubule mesh may thus be interesting, to confirm the validity of the approximations made in the present model, or to propose a more accurate expression for microtubule force.

Importantly, the dynamics of the mechanisms described here are not considered. It would though be interesting to take them into account, for instance to evaluate the required force generation of each process, which would give insight into the interplay and competition between these several mechanisms. Similarly, the central role of dynein hypothesized in the model, in particular at the cap, may be quantitatively tested, for instance with disruptive experiments, overexpression, or injection of an ectopic polarity cap or local patch of dynein. It would also be interesting to explain some dynamic behaviors such as the decentration of the pair of centrosomes, responsible for the asymmetry of the first division of the nematode *C. elegans*. This decentration is accompanied with oscillations in orientation, and only occurs after the complete centration of the pair of centrosome that follows fertilization. These oscillations in the orientation of the pair of centrosomes are a clear sign that the mechanisms of force generation are dynamic, with possible instabilities, and that the use of a static model to predict the division in such a system remains a first step approximation. In the sea urchin embryo, the two centrosomes are dragged to the vegetal pole at different moments prior to micromeres formation, and do not appear to have the same structure, which is not taken into account by a static model that only considers the equilibrium position of a pair of identical centrosomes with a constant distance between them. It would be interesting to question the origin of the difference between the two centrosomes and its effect on centrosome behavior. A more accurate approach to the prediction of the following division may also take into account the dynamics of the pair of centrosomes and of their interaction with the nucleus.

Alternative mechanisms

Finally, this work only focuses on the core mechanisms, whose action alone allows explaining the observed phenotypes, and does not integrate smaller, possibly system-specific, contributions that may exist in these early embryos. Indeed, from all the mechanisms for nuclear positioning described in introduction, only three mechanisms have been considered in the present work : the cytoplasmic pulling, the motor-dependent surface pulling and the depolymerization-dependent surface pulling. Despite only those three mechanisms appear sufficient to accurately predict division positioning in the four systems considered here, other mechanisms may have a minor role to play. It is also important to note that not all

mechanisms have been tested, and that an alternative mechanism may work as well. However, the model was designed with regards to results from the literature, such as the colcemid experiment that favors cytoplasmic pulling over surface pushing in the sea urchin embryo (Hamaguchi and Hiramoto, 1986), to decipher between numerically working mechanisms. Moreover, some mechanisms proposed in introduction have been ruled out by simulations, like pulling forces at cell-cell contacts, ruled out in zebrafish in the first article, or several hypotheses for animal-vegetal axis specification in sea urchin, tested in Annexe 2. It is thus probable that the three mechanisms proposed in this work are the three main mechanisms at stake.

Yet, additional mechanisms such as surface pushing, that has been shown to be dominant in smaller cells (Tran et al., 2001) may play a minor role in larger cells. It would be interesting to evaluate the contribution of such additional mechanisms to nuclear positioning. Indeed, experiments such as the colcemid experiment only show that the main mechanisms considered here are sufficient to position the nucleus, but do not suggest that other mechanisms have no contribution. In particular, microtubule pushing at the membrane may exert length-dependence forces, mainly due to buckling, as discussed in introduction, and thus may contribute to nucleus centration. On the contrary, cytoplasmic pushing may decenter the nucleus. Experiments showing cytoplasmic centration as the main cytoplasmic contribution do not quantitatively investigate the contribution of cytoplasmic pushing, but only assess the balance between pulling and pushing. All these possible competing mechanisms are probably gathered into a single term in the model, with their combined effect described by one parameter. Getting insight into the molecular details of the effectors of nuclear positioning may allow specifying the mechanisms at play and their competition. Taking the dynamics of nuclear positioning into account may also help to assess the respective roles of the different mechanisms. Getting information on the mechanisms implied in the definition of cleavage planes and on their competition might be useful to propose a more complete and generic model that predicts cleavage in organisms, such as yeast, that may display the same mechanisms, but with a different balance between them. However, the model proposed here isolates a set of minimal requirements to predict nuclear positioning, and is thus expected to provide a broad quantitative understanding of the balance between forces that drive the nucleus, and thus to guide further work on these forces.

Conclusion

It is obvious that a full understanding of the early division patterns, and of the division in other cell types, would require adapting the simple model proposed here to the specificities of each system. In addition, the level of details may have to be increased, to refine the model or just to gain insight into the mechanisms it relies on. In particular, it would be interesting to assess the dynamics and the noise of nuclear positioning. However, the principles for nuclear positioning and their quantitative interplay depicted in this work may provide useful information to carry out further research. Notably, this model allows a rapid exploration of forces at play in a given system, which may be useful to determine the mechanisms of interest. Even though a complete study might be required in each case, this fast overview might provide some landmarks. Moreover, the model may be valuable in systems that are difficult to study, such as frog embryos which are hard to image. As a conclusion, the modeling framework designed here and the experiments performed in sea urchin highlight a set of possibly generic mechanisms for nuclear positioning and explore their competition, by integrating them in a single comprehensive model.

ANNEXES

ANNEXE 1 - SHAPE, POLARITY AND YOLK STACKS GENERATION

The following sections are adapted from the starter pack provided with the 1st article "Generic Theoretical Models to Predict Division Patterns of Cleaving Embryos", and explain how the generation of surfaces with the Surface Evolver was performed, as well as the processing of the Surface Evolver output file to create inputs to the division prediction program.

Generating a surface in the Surface Evolver

The Surface Evolver is a free software that iteratively finds the surface of minimal energy under given constraints.

The input files can be directly dragged and dropped in the surface evolver command window, or specified by path. Input format is .txt, see provided example (next page).

The input file specifies the constraints of the surface, and a list of :

- vertices with associated coordinates and constraints,
- edges defined by their two end vertices, with constraints
- faces defined by their edges (oriented), with constraints and surface tensions
- bodies (cells) defined by their faces (oriented), with target volumes, densities,…

The output file (command ‘d’ to print as text file) has the same properties. It can be used as an input file again. Input files were generated manually. Importantly, when the input file was defining three cells or more, contacts were made only between two adjacent cells, and tricellular contacts (or more) were avoided to allow cell rearrangement. When running the simulation, the apparition of tri-cellular vertices (that can happen when smaller faces are wed out to fasten/unblock the simulation) was avoided.

Some useful commands in the Surface Evolver (see the software website for further information) :

s : show the surface in graphics mode / enter graphics mode
q : quit
g : iteration step. Several iterations steps can be computed with : g20, g50,…
r : refine triangulation
w : weed out small surface triangles (threshold value to provide)
u : equitriangulate
d : dump surface to datafile

The topology and properties of the surface are set from the input file, but they can be changed during the energy minimization process, for instance by using commands like ‘facet_merge’ (merge two facets), ‘set’ (set new tension, color,… to a facet/edge).

The surface calculation is faster with a limited number of facets. However, in order to generate a readable input to the division prediction program, the equilibrium surface was refined as much as possible. This way, plotting the vertices (according to the list of coordinates) was resolutive enough to define a surface.

Example of Surface Evolver input text file (2-cell stage) :

```
constraint 1 nonpositive   // spherical confinement
formula: x^2 + y^2 + z^2 = 0.27*sqrt(3)

vertices
1  -0.5 -0.5 -0.5 constraint 1
2  0.5 -0.5 -0.5 constraint 1
3  0.5 0.5 -0.5 constraint 1
4  -0.5 0.5 -0.5 constraint 1
5  -0.5 -0.5 0.5 constraint 1
6  0.5 -0.5 0.5 constraint 1
7  0.5 0.5 0.5 constraint 1
8  -0.5 0.5 0.5 constraint 1
9  0 -0.5 -0.5 constraint 1
10 0 -0.5 0.5 constraint 1
11 0 0.5 -0.5 constraint 1
12 0 0.5 0.5 constraint 1

edges  // defined by endpoints
1    1  9   constraint 1
2    2  3  constraint 1
3    3  11  constraint 1
4    4  1  constraint 1
5    1  5  constraint 1
6    5  10 constraint 1
7    6  7  constraint 1
8    7  12 constraint 1
9    8  5  constraint 1
10   2  6  constraint 1
11   3  7  constraint 1
12   4  8  constraint 1
13   9  2  constraint 1
14   11 4  constraint 1
15   10 6  constraint 1
16   12 8  constraint 1
17   9  10  constraint 1
18   10 12  constraint 1
19   12 11  constraint 1
20   11 9  constraint 1

faces // defined by oriented edge loops to have outward normal
1   1 -20 14 4  opacity 0.5 color 4 tension 0.75  constraint 1
2   -6 -9 -16 -18  opacity 0.5 color 4  tension 0.75  constraint 1
3   -1 5 6 -17  opacity 0.5 color 4  tension 0.75  constraint 1
4   10 7 -11 -2  opacity 0.5 color 1  tension 0.75  constraint 1
5   11 8 19 -3  opacity 0.5 color 1  tension 0.75  constraint 1
6   -4 12 9 -5  opacity 0.5 color 4  tension 0.75  constraint 1
7   13 2 3 20  opacity 0.5 color 1  tension 0.75  constraint 1
8   -15 18 -8 -7  opacity 0.5 color 1  tension 0.75  constraint 1
9   -13 17 15 -10  opacity 0.5 color 1  tension 0.75  constraint 1
10  -19 16 -12 -14  opacity 0.5 color 4  tension 0.75  constraint 1
11  17 18 19 20 color 15  tension 1.1 constraint 1

bodies // defined by oriented face list
1   -1 -2 -10 -11 -6 -3   volume 0.5
2   -9 -4 -5 11 -7 -8   volume 0.5

Read   // commands to be automatically executed after loading the surface
```

Formatting a Surface Evolver output file to an input file to the division prediction program

The Surface Evolver outputs a text file providing a list of vertices, edges, faces and bodies, with associated definitions and properties (same format as the input file, see above).

For each cell of the embryo, these four lists were copied into four Matlab matrices (first copying into Excel to get rid of the text), named u1, u2, u3 and u4, and saved in the same .mat file :

u1 is a table of facets numbers (corresponding to the last list of the output file). It doesn't need to be sorted, and doublons are not a problem, but it must be rectangular.

Importantly, only the facets of one body (the considered cell) were copied. In case of a pluricellular embryo, all the formatting process and the division prediction were done for each cell.

u2 is a table of all the edges of the output file. Format is the same as in the output file : column 1 is the number of the facet and columns 2 to 4 are the corresponding edges.

u3 is a table of all the vertices of the output file. Format is the same as in the output file : column 1 is the number of the edge and columns 2 and 3 are the corresponding vertices.

u4 is a table of all the coordinates of the output file. Format is the same as in the output file : column 1 is the number of the vertex and columns 2 to 4 are the corresponding coordinates.

This Matlab file was then used as an input to a Matlab program that outputs a .tif Z-stack (separate images) of the surface, with black background and white vertices. To do so, the program identifies the set of coordinates belonging to the considered cell within the list of coordinates, by finding the edges in u2 from the one body copied in u1, then the corresponding vertices in u3 and coordinates in u4. It then projects the 3D coordinates on a 160x160x160 pixels matrix, to generate a binary stack with black background and white vertices. As the triangulation was refined to smaller than the Matlab pixel size in the Surface Evolver, the stack of the vertices defined the cell surface.

As the division prediction program inputs Z-stack images of cells volumes (white background and black cells), the images were then inverted and filled. If the mesh was not narrow enough (the triangulation was not refined enough in the Surface Evolver), there could be holes in the surface, that were filled manually. The stack was saved as an image sequence to be read by the division prediction program.

Generating a polarity stack from the shape stack

When needed, the polarity input stack was be created, from the shape stack. An imageJ macro allowed generating a surface of appropriate thickness from the shape images. The macro is based on the difference between two subsequent images of the 3D shape stack (cell volumes in black, white background), to generate a surface with no holes. As the macro was buggy and misdoing some images (too thin surface), it had to be run 2-3 times, and the 2-3 stacks were added to obtain a correct surface.

This surface (the surface of the whole cell) was then be carved to keep only the polarity cap, as the polarity input to the division prediction program was an image sequence (same size as shape image sequence) with white background and black polarity cap. This step was done with a Matlab script computing the intersection of the surface with a sphere of given center and diameter. Those two parameters were adjusted with regards to A-V axis and imaged Dishevelled in the literature[1]. Alternatively, the polarity cap could be carved with a Matlab script computing the intersection of the surface with a threshold plane. The stack was saved as an image sequence, with image numbers consistent with those of the shape image sequence.

[1] Peng and Wikramanayake, 'Differential Regulation of Disheveled in a Novel Vegetal Cortical Domain in Sea Urchin Eggs and Embryos'; Weitzel et al., 'Differential Stability of β-Catenin along the Animal-Vegetal Axis of the Sea Urchin Embryo Mediated by Dishevelled'.

Yolk gradients

The yolk gradients were generated directly by the division prediction program, based on three parameters : η, μ and ε. The yolk signal was computed as a 3D stack with the same dimensions as the shape and polarity stacks, allowing to simply define the local concentration of yolk along MTs in the length/force calculation loop.

Under the assumption that MTs are less stable in yolk, the MT stability factor (local angular density of MTs) was computed as : $d_{angle}(x) = 1 - [\ yolk(x)\ ] / \eta(x)$
where [yolk(x)] ranges between 0 (no yolk) and 1 (yolk packed at maximum density), and η(x) is a parameter for the sensitivity of MTs to yolk. x = 0 corresponds to the center of the 3D stack.

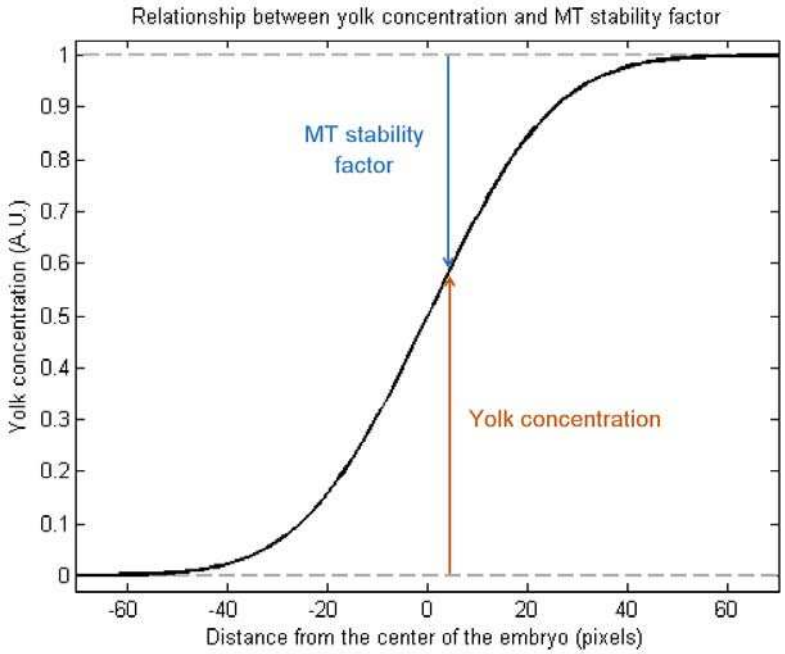

The real local MT density was then the MT density in the absence of yolk (depending solely on the distance from centrosome) multiplied by this MT stability factor (see figure S4B).

Parameter η(x) was computed as a constant in the program. By default, η(x) = 1.

Increasing parameter η(x) had the same effect as reducing [yolk(x)] :

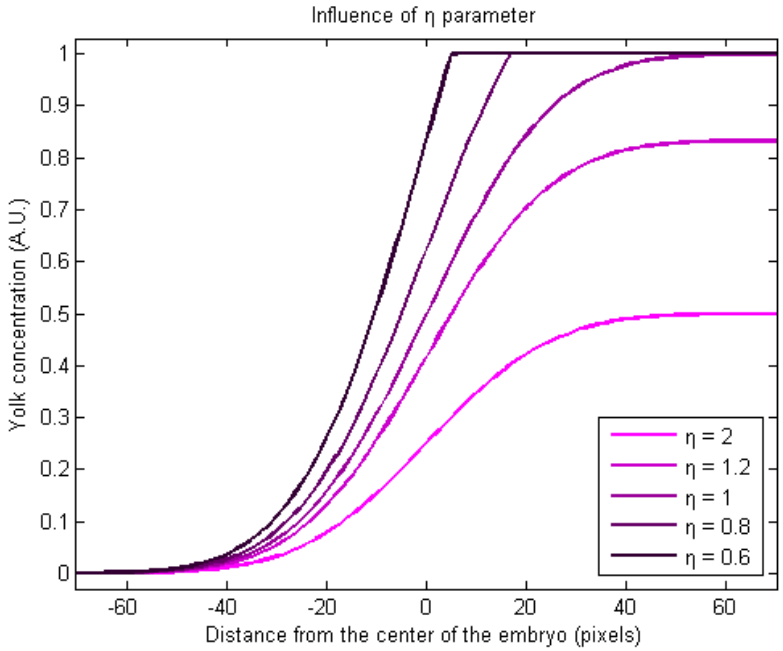

Note that in order to keep $d_{angle}(x)$ positive, [yolk(x)] / η(x) must be inferior to 1.

By default, the yolk gradient was simulated using an erf function :
[yolk(x)] = (1 – erf (μ (x – ε) / (2 L_{cell}))) / 2, with L_{cell} ~ 140 pixels (diameter of the egg).

The two following graphs show the effects of μ and ε on the yolk gradient :

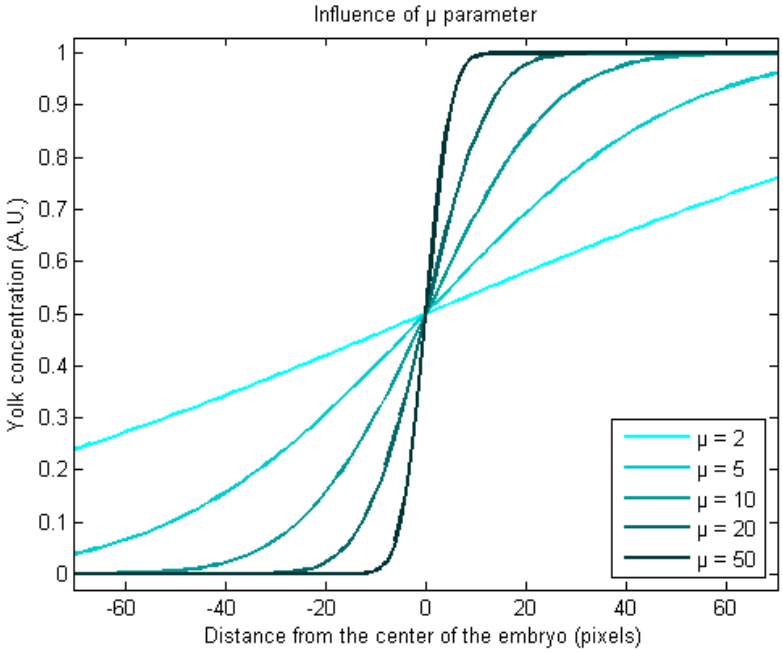

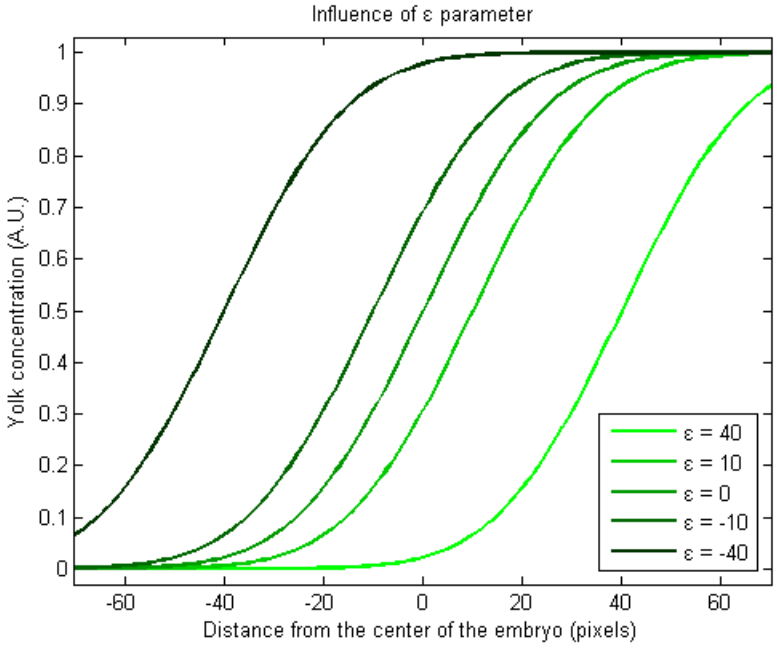
Influence of ε parameter
Yolk concentration (A.U.)
Distance from the center of the embryo (pixels)
ε = 40
ε = 10
ε = 0
ε = -10
ε = -40
0
0.1
0.2
0.3
0.4
0.5
0.6
0.7
0.8
0.9
1
-60
-40
-20
0
20
40
60

ANNEXE 2 - SUPPLEMENTAL FIGURES OF THE 1ST PAPER

These four figures are unpublished supplemental figures to the 1st article "Generic Theoretical Models to Predict Division Patterns of Cleaving Embryos". The first two figures show the influence of two parameters : the exponent δ of the length-dependence of the force, in the case where both shape and polarity compete for nuclear positioning, and the angular precision of the aster force calculation (MT spacing). The last two figures show alternative hypotheses than the vegetal cap with two force contributions to account for the sea urchin embryo cleavage pattern. These two figures refer to the paragraph in Supplemental Information "Alternative hypotheses tested to account for echinoderms cleavage patterns" (pages 136-138).

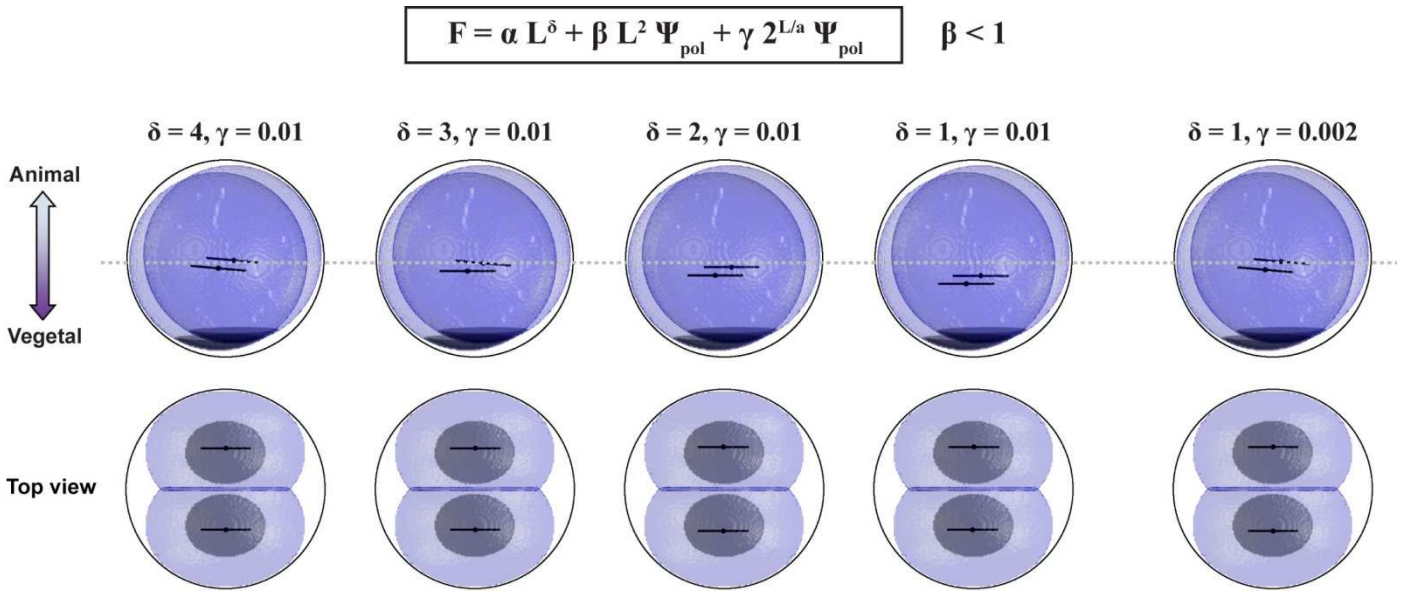

Figure S1: Influence of length-dependent exponent δ, on division axis position and orientation, in the context of a shape/polarity competition.

A change in the exponent δ (from 1 to 4) does not impact division orientation, but has a slight effect on division position. **(Right)** This effect can be corrected by adjusting the balance between α, β and γ parameters, without affecting the division orientation.

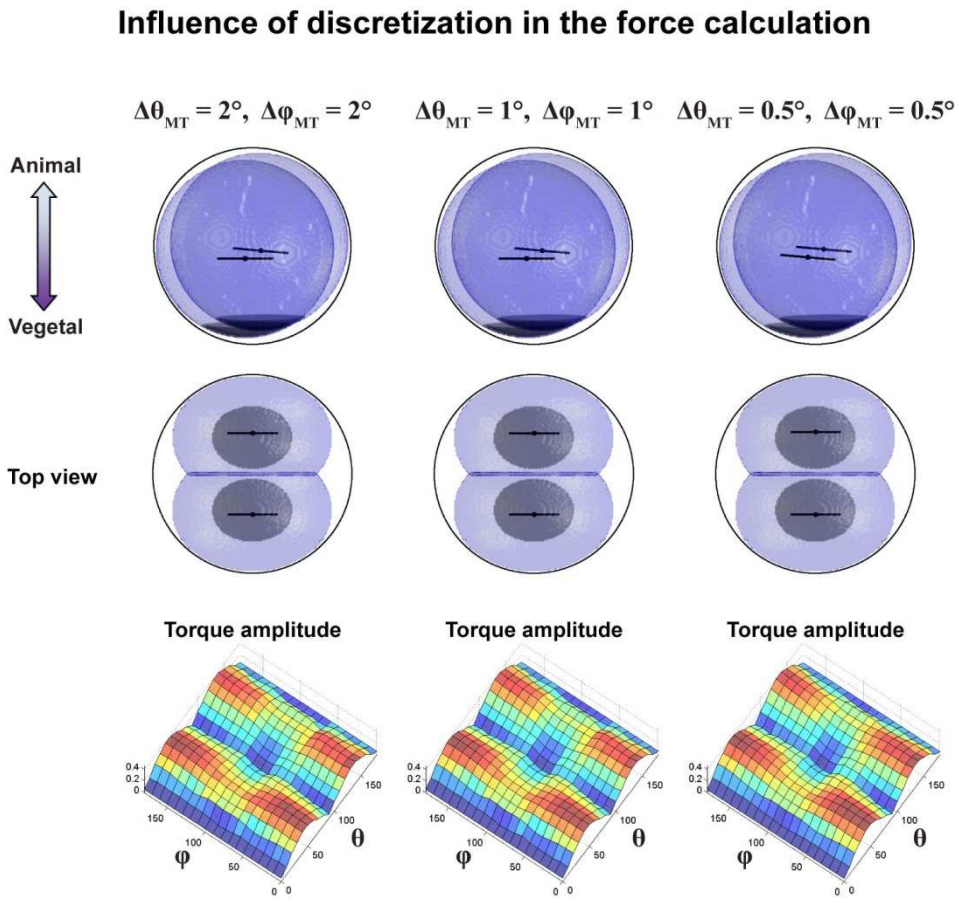

Figure S2: Influence of discretization in the aster force calculation.

The predictions of the model remain unchanged when the mesh size in MT orientations is reduced by half (four times more MTs are considered in the aster solid angle, net aster torque amplitude corrected for number of MTs). Torque amplitude profiles are smoothed from half-size mesh (see Supplemental Information p.134).

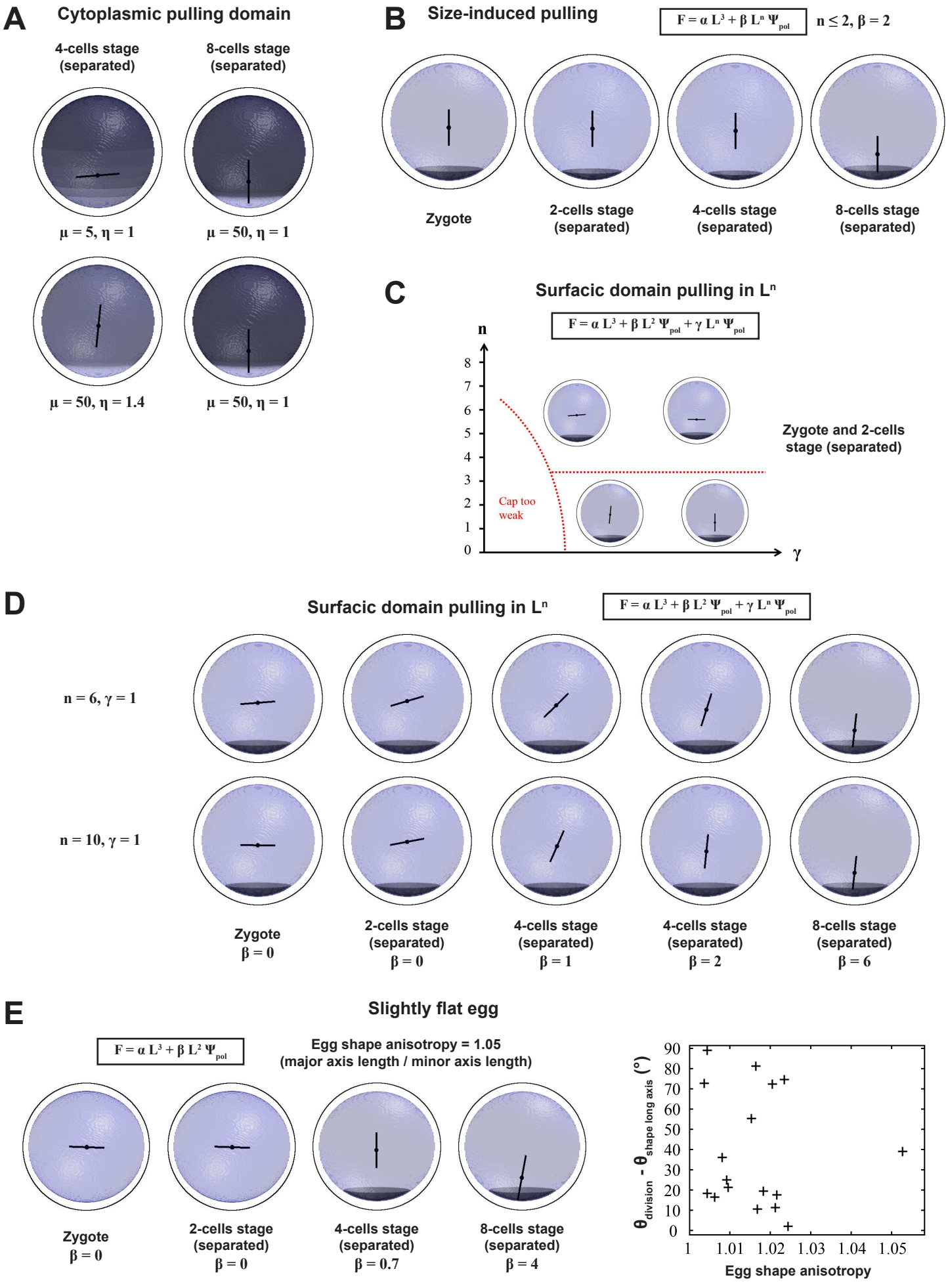
A
Cytoplasmic pulling domain
4-cells stage (separated)
8-cells stage (separated)
μ = 5, η = 1
μ = 50, η = 1
μ = 50, η = 1.4
μ = 50, η = 1
B
Size-induced pulling
F = α L³ + β Lⁿ Ψpol
n ≤ 2, β = 2
Zygote
2-cells stage (separated)
4-cells stage (separated)
8-cells stage (separated)
C
Surfacic domain pulling in Lⁿ
F = α L³ + β L² Ψpol + γ Lⁿ Ψpol
n
Cap too weak
γ
Zygote and 2-cells stage (separated)
D
Surfacic domain pulling in Lⁿ
F = α L³ + β L² Ψpol + γ Lⁿ Ψpol
n = 6, γ = 1
n = 10, γ = 1
Zygote β = 0
2-cells stage (separated) β = 0
4-cells stage (separated) β = 1
4-cells stage (separated) β = 2
8-cells stage (separated) β = 6
E
Slightly flat egg
F = α L³ + β L² Ψpol
Egg shape anisotropy = 1.05 (major axis length / minor axis length)
Zygote β = 0
2-cells stage (separated) β = 0
4-cells stage (separated) β = 0.7
8-cells stage (separated) β = 4
θdivision - θshape long axis (°)
Egg shape anisotropy

Figure S3: Tests of alternative hypotheses to model sea urchin cleavage pattern (Part 1).

(A and B) Alternative hypotheses that may account for a switch to an asymmetric division at the 8-cell stage for micromere formation. These simulations are performed on round cells (which correspond to experiments in dissected blastomeres) to eliminate the effects of cell shape.

(A) Hypothesis consisting of replacing a pure surface effect with a volumic effect gradually stronger towards the vegetal pole. Note that cytoplasmic pulling in the light zone is equivalent to cytoplasmic repelling in the dark zone. **(Top)** A strengthening of the pulling domain by changing the sharpness of the gradient does not allow to reproduce both 4 and 8-cell stage situations. **(Bottom)** A strengthening of the pulling domain by increasing the absolute strength but with a constant gradient may reproduce 4 and 8-cell stages. Although this hypothesis cannot be fully rejected, it is not supported by detergent treatment experiments suggesting effects restricted at the surface (Dan, 1979; Tanaka, 1976).

(B) Hypothesis of an effect associated to progressive cell size reduction which causes surfacic effects to become stronger as cell size decreases. Micromeres may be formed, but the shift of the nucleus is progressive and does not occur as abruptly at the 8-cell stage as in experiments. The range of parameters allowing a rather abrupt shift of the nucleus is extremely narrow, suggesting poor biological robustness. These also disagree with cut eggs experiments performed by Hörstadius, which suggests that initial egg size does not influence the apparition of an asymmetric division.

(C-E) Alternative hypotheses that may account for the co-planarity of the 2 first division axes. These simulations are performed on round cells (which correspond to experiments in dissected blastomeres) to eliminate the effects of cell shape.

(C and D) Test of a hypothesis of MT pulling based on a power law instead of an exponential law. **(C)** Phase diagram for the γL^n term shows that n must be higher than 4 to reproduce the 1^{st} and 2^{nd} division orientations. **(D)** The switch of orientation and the asymmetric positioning of the nucleus are not sharp enough with the L^n model, yet they tend to occur more abruptly as n increases.

(E) Hypothesis of a slight shape anisotropy with an egg flattened along the A-V axis. **(Left)** The shape anisotropy allows to reproduce the 1^{st} and 2^{nd} division orientations. A time-dependent surfacic pulling is then necessary to account for the switch in orientation and the asymmetric division. **(Right)** Experimental measurements performed by our mean on interphase 1-cell stage embryos show however that shape anisotropies are typically smaller than 3%. In addition the division axes in these experiments do not appear to align with the shape long axis, thus rejecting this hypothesis.

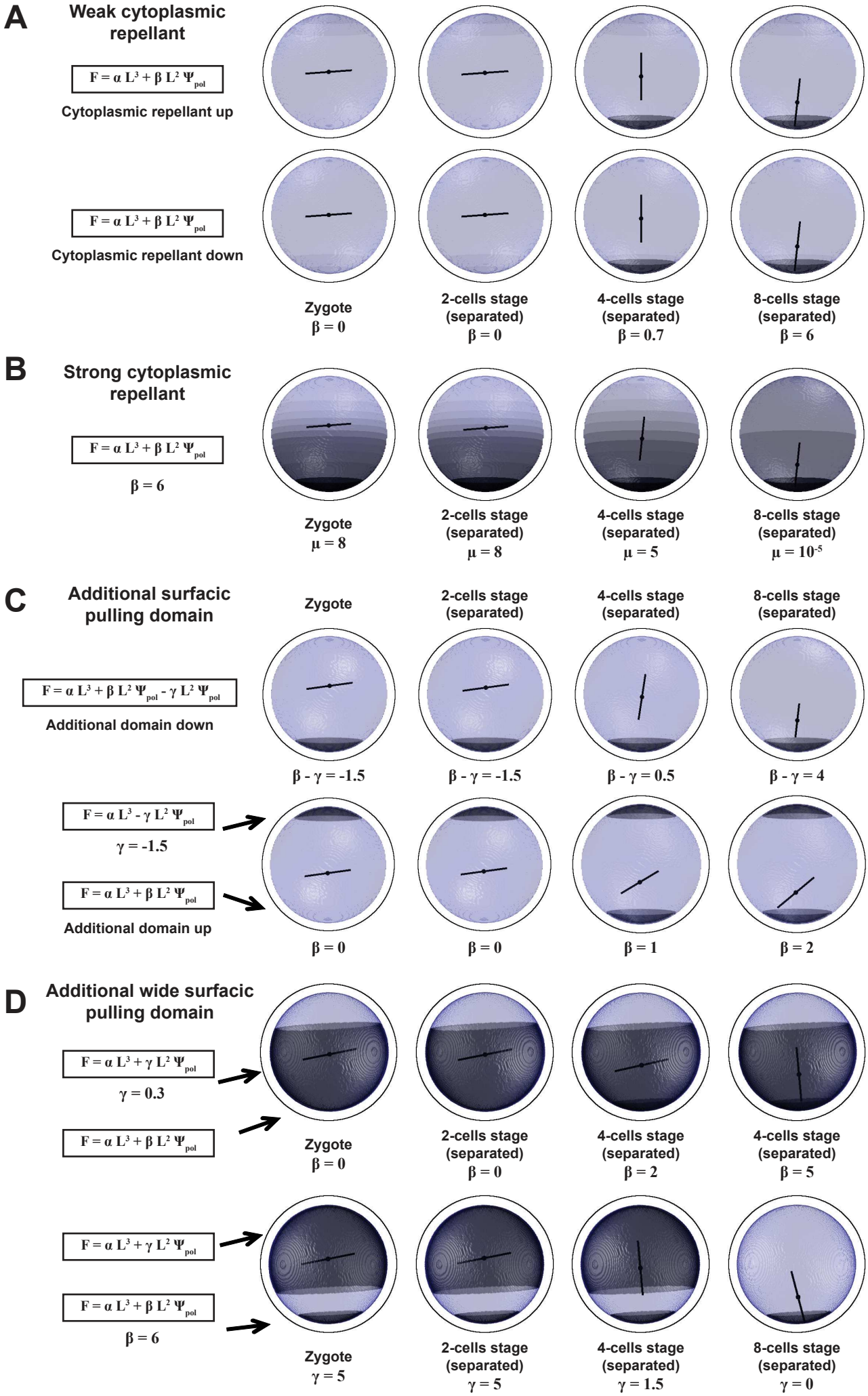
A
Weak cytoplasmic repellant
F = α L³ + β L² Ψpol
Cytoplasmic repellant up
F = α L³ + β L² Ψpol
Cytoplasmic repellant down
Zygote
β = 0
2-cells stage (separated)
β = 0
4-cells stage (separated)
β = 0.7
8-cells stage (separated)
β = 6
B
Strong cytoplasmic repellant
F = α L³ + β L² Ψpol
β = 6
Zygote
μ = 8
2-cells stage (separated)
μ = 8
4-cells stage (separated)
μ = 5
8-cells stage (separated)
μ = 10-5
C
Additional surfacic pulling domain
Zygote
2-cells stage (separated)
4-cells stage (separated)
8-cells stage (separated)
F = α L³ + β L² Ψpol - γ L² Ψpol
Additional domain down
β - γ = -1.5
β - γ = -1.5
β - γ = 0.5
β - γ = 4
F = α L³ - γ L² Ψpol
γ = -1.5
F = α L³ + β L² Ψpol
Additional domain up
β = 0
β = 0
β = 1
β = 2
D
Additional wide surfacic pulling domain
F = α L³ + γ L² Ψpol
γ = 0.3
F = α L³ + β L² Ψpol
Zygote
β = 0
2-cells stage (separated)
β = 0
4-cells stage (separated)
β = 2
4-cells stage (separated)
β = 5
F = α L³ + γ L² Ψpol
F = α L³ + β L² Ψpol
β = 6
Zygote
γ = 5
2-cells stage (separated)
γ = 5
4-cells stage (separated)
γ = 1.5
8-cells stage (separated)
γ = 0

<u>Figure S4:</u> Tests of alternative hypotheses to model sea urchin cleavage pattern (Part 2).

(A and B) Hypotheses of a cytoplasmic repellant to account for the 1st and 2nd division orientations. Note that cytoplasmic repelling in the dark zone is equivalent to cytoplasmic pulling in the light zone. These hypotheses work, but are not supported by detergent treatment experiments (Dan, 1979; Tanaka, 1976). **(A)** A weak repellant yields division axes orthogonal to the A-V axis at 1 and 2-cell stages. A cleavage-stage surface pulling is then necessary to account for the switch in orientation and the asymmetric division. **(B)** A strong repellant in competition with an attractive polarity domain from the 1-cell stage allows to reproduce the 1st and 2nd division orientations. Then the progressive smoothening of the repellant distribution (with a constant strength of the domain) could yield a switch in orientation and an asymmetric division.

(C-D) Hypotheses of an additional polarity domain to account for the 1st and 2nd division orientations. These hypotheses may work, but are not supported by experimental observations. **(C)** Hypothesis of an additional repelling surface domain. **(Top)** When both attracting and repelling domains are at the vegetal pole (even if not of the same size), their cleavage-stage dependent competition can yield the normal pattern of sea urchin embryos. **(Bottom)** When the repelling domain is at the animal pole, the model does not allow to reproduce the switch in orientation at the 4-cell stage. **(D)** Hypothesis of an additional wide attracting surfacic domain. When the competition of the two attracting domains depends on cleavage-stage progression, whether through **(Top)** an increase in the strength of the small domain, or **(Bottom)** a fading of the wide cap, this hypothesis allows to reproduce the normal developmental pattern of sea urchin embryos.

ANNEXE 3 - UNPUBLISHED DATA

This section shows unpublished experimental and theoretical results. The first figure presents shape simulations performed with the Surface Evolver, that illustrate cell rearrangements in the case of an anisotropic confinement and of the packing of cells in the spiral cleavage pattern. The second figure shows an experimental confirmation of the blastomeres separation experiments performed on echinoderm embryos in the literature[1], and the corresponding division simulations.

[1] Hörstadius and others, 'Experimental Embryology of Echinoderms', 1973.

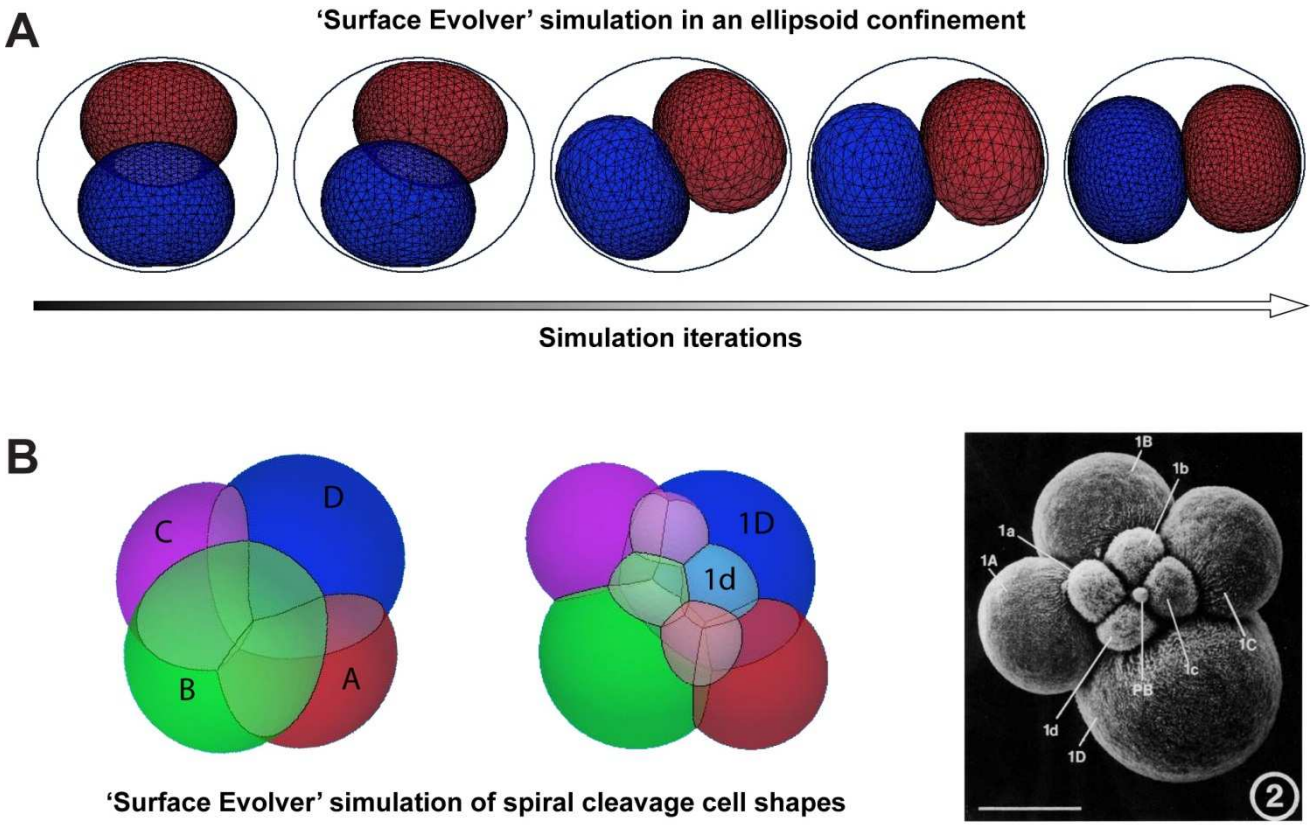

<u>Figure S5 :</u> Surface energy minimization with the Surface Evolver.

(A) Simulation of the rearrangement of two cells in an ellipsoid confinement. Images are taken at regular simulation steps. The ellipsoid is defined as $(|y| - 0.1)^2 + x^2 + z^2 = 0.52$, where the total volume of the embryo is 1. The cell-cell surface tension is 1 and the cell-medium surface tension is 0.5. **(B)** Spiral cell packing. **(Left)** Simulation of the cell arrangement with the Surface Evolver at the 4-cell stage and at the 8-cell stage. Cell names are indicated, colors are consistent. At the 8-cell stage the simulation was started with micromeres a bit shifted to the left to initiate a left-right asymmetry, the rearrangement process drove them further to the left. Parameters (surface tensions and cell volumes) were roughly adjusted with regards to the electron micrograph on the right, but it was not critical, since spiral pattern shows great variation between species. The simulations could account for the observed arrangement, suggesting that the packing of cells in spiral cleavage may be minimizing surface energy. **(Right)** Electron micrgraph of an embryo at the 8-cell stage, viewed from the animal pole. Polar body (PB) and cell names are indicated. Scale bar : 50 µm. From (Craig and Morrill, 1986[2]).

[2] Craig and Morrill, 'Cellular Arrangements and Surface Topography during Early Development in Embryos of Ilyanassa Obsoleta'.

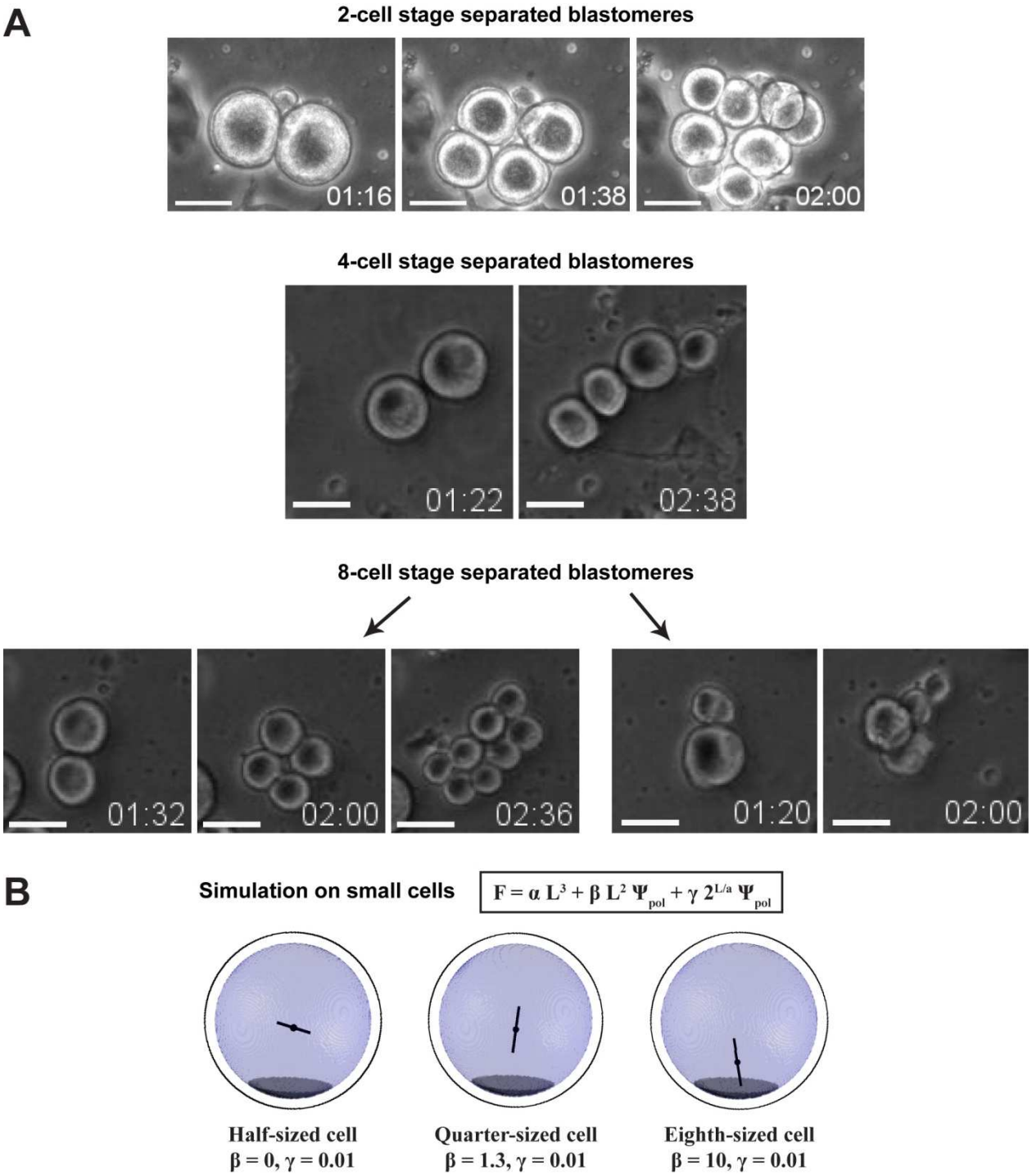

Figure S6 : Blastomere separation in the sea urchin early embryo.

(A) Development of sea urchin blastomeres separated at the 2, 4 and 8-cell stage. Micromeres appear at the 3rd and 2nd subsequent rounds of divisions for 2 and 4-cell stage separated blastomeres, respectively **(Top)**, and at the 1st round for half of the 8-cell stage separated blastomeres (presumably the vegetal blastomeres) **(Bottom right)**, suggesting that micromere formation does not depend on cell-cell interactions. The vegetal 8-cell stage blastomeres undergo one more round of asymmetric divisions, while the animal blastomeres only perform

symmetric divisions **(Bottom left)**. The 2 and 4-cell stage separated blastomeres developed into healthy half-sized and quarter-sized larvae, respectively. The 8-cell stage separated blastomeres died after a few division rounds. Time from the onset of the last division before blastomere separation is indicated. Scale bar : 40 μm. **(B)** Simulation of division positioning from a Surface Evolver-generated shape and a polarity cap, for half-sized, quarter-sized and eighth-sized blastomeres. Middle figure is the same as in Figure 4A of the second article. The results of the simulations are consistent with the observed divisions.

ANNEXE 4 - COLLABORATIONS

Our line of research gave rise to two main collaborations : with the laboratory of Carl-Philipp Heisenberg (IST Austria, Vienna) on ascidian early embryos and with the laboratory of Yohanns Bellaïche (Institut Curie, Paris) on drosophila embryos.

Ascidians

The work on ascidians, performed in particular in collaboration with Benoit Godard in CP Heisenberg's laboratory, remains preliminary. Simulations of division positioning were performed on 4-cell stage ascidian embryos imaged in 3D and segmented in CP Heisenberg's laboratory. The case of normal 4-cell stage was simulated both on interphase and anaphase images, and manipulated embryos, separated in two, whether along the left-right midline, or separating the two anterior cells from the two posterior, were simulated in anaphase. The position and orientation of divisions were simulated using the same division prediction program as in the first paper, adapted to input images of different XY resolution and Z step size.

The prediction of divisions based solely on cell shape did not allow to reproduce the slight asymmetry of the divisions at the 4-cell stage, even though the observed asymmetry is too slight to conclude. More importantly, the observed tilt of posterior spindles toward the CAB in anaphase was not reproduced from shape cues only. Another series of simulation was run with an imaged CAB signal, and a broad exploration of CAB attractivity parameter values suggested that the simulations could reproduce experimental spindle orientations from both shape and CAB cues. Finally, the 3D imaged yolk signal (Bodipy) was implemented in the program, by modifying the code to replace the yolk matrix generation from gradient parameters within the program by an input yolk matrix. Several parameters were tested for MT sensitivity to yolk, and for each parameter value, simulations were run for shape and yolk cues without the CAB contribution, and with the CAB for different parameters of CAB attractivity. The results are yet to be analyzed and compared to observed division positioning.

At first sight, the CAB + yolk simulation with a high sensitivity of MTs to yolk may give the better results, which is expected since yolk is distributed all around the cortex (with slightly more accumulation at the vegetal side) and excluded from the asters. Indeed, as yolk seems to be excluded from the asters, the only yolk-free volume is the astral volume. Under these conditions, a simulation where MTs are critically unstable in yolk will position the pair of asters in the middle of the yolk-free zone, which is the experimental spindle position. The

bias in yolk distribution induced by the asters thus makes it hard to conclude on the role of yolk in nuclear positioning in this system, especially as the animal-vegetal asymmetry is low, yielding little difference between the results of the different simulations, compared to biological noise. It may be necessary to take into account the dynamics of the mutual exclusion of yolk and MTs. Before concluding on further directions, the results need to be properly analyzed. In addition, experiments are being performed in CP Heisenberg laboratory to test a possible role of cell-cell contact signaling.

Drosophila

The work on drosophila morphogenesis during pupal stage was published in *Nature* (see next pages). Our implication in this work was to predict the division orientation of epithelial cells within the plane of the epithelium (in 2D), from cell shape and from polarity signal (Mud), and to compare the accuracy of these two simulations. The program predicting division orientation from cell shape was adapted from the one used in Minc et al.[1], searching for the equilibrium orientation in 2D with a centered nucleus. Torque potential was plotted, and the experimental orientation was reported on the graph, to assess the accuracy of the prediction (Figure 2). The program predicting division orientation from Mud signal was similar, but MT forces did not depend on MT lengths. Instead, Mud fluorescence intensity signal (at the cortex) was used, and MT forces depended on Mud intensity where the MT reaches the cortex. Again torque potential was plotted, and the predicted orientations were compared to experiment. The angular difference between the observed and the simulated division orientations suggested that divisions orient more with respect to Mud distribution than to cell shape.

[1] Minc, Burgess, and Chang, 'Influence of Cell Geometry on Division-Plane Positioning', 2011.

Epithelial tricellular junctions act as interphase cell shape sensors to orient mitosis

Floris Bosveld[1], Olga Markova[1], Boris Guirao[1], Charlotte Martin[1,#], Zhimin Wang[1], Anaëlle Pierre[2], Maria Balakireva[1], Isabelle Gaugue[1], Anna Ainslie[1,**], Nicolas Christophorou[1,*], David K. Lubensky[3,1], Nicolas Minc[2], Yohanns Bellaïche[1]

1. Polarity, Division and Morphogenesis Team, Institut Curie, CNRS UMR 3215, INSERM U934, 26 rue d'Ulm, 75248 Paris Cedex 05, France.
2. Institut Jacques Monod, CNRS UMR7592 15 rue Hélène Brion, 75205 Paris cedex 13, France.
3. Department of Physics, University of Michigan, Ann Arbor, MI 48109-1040, USA.

#: Present address: Institut Curie, CNRS UMR 3348, Université Paris Sud, Bâtiment 110, 91405 Orsay, France.

*: Present address: INRA, Institut Jean-Pierre Bourgin, UMR 1318, ERL CNRS 3559, Saclay Plant Sciences, RD10, Versailles, France.

**: Present address: The Francis Crick Institute, Lincoln's Inn Fields Laboratory, 44 Lincoln's Inn Fields, London WC2A 3LY, United Kingdom

Abstract

The orientation of cell division along the interphase cell long-axis, the century old Hertwig's rule, has profound roles in tissue proliferation, morphogenesis, architecture and mechanics[1,2]. In epithelial tissues, the shape of the interphase cell is influenced by cell adhesion, mechanical stress, neighbour topology, and planar polarity pathways[3-12]. At mitosis, epithelial cells usually round up to ensure faithful chromosome segregation and to promote morphogenesis[1]. The mechanisms underlying interphase cell shape sensing in tissues are therefore unknown. We found that in *Drosophila* epithelia, tricellular junctions (TCJ) localize microtubule force generators, orienting cell division via the Dynein associated protein Mud independently of the classical Pins/Gαi pathway. Moreover, as cells round up during mitosis, TCJs serve as spatial landmarks, encoding information about interphase cell shape anisotropy to orient division in the rounded mitotic cell. Finally, experimental and simulation data show that shape and mechanical strain sensing by the TCJ emerge from a general geometric property of TCJ distributions in epithelial tissues. Thus, in addition to their function as epithelial barrier structures, TCJs serve as polarity cues promoting geometry and mechanical sensing in epithelial tissues.

To understand how rounded mitotic cells tend to align their spindle along their interphase shape long-axis, we deciphered the mechanisms of spindle orientation in the *Drosophila* pupal notum epithelium. Within this tissue, more than ten thousand cells divide[13], and, as in many epithelial tissues, the division of rounded mitotic cells takes place in the plane of the tissue and is influenced by their interphase cell shape (Extended Data Fig. 1a,b). One possibility is that Pins (vertebrate LGN) or Gαi polarization orients division as found in single cells in culture or during asymmetric divisions[14]. However, Pins and Gαi were homogenous around the cortex (Extended Data Fig. 1c,d). In contrast, the distribution of the Dynein associated protein Mud (vertebrate NuMa) suggested a role in orienting the spindle according to the interphase cell shape. GFP:Mud was localized at the spindle poles and unexpectedly was also enriched at tricellular junctions (TCJs) where at least three cells meet (Fig. 1a, Extended Data Fig. 1e,h and Supplementary Video 1). Accordingly, in this tissue and other pupal or larval epithelial tissue GFP:Mud or endogenous Mud co-localized with Gliotactin (Gli), a septate TCJ marker[15] (Fig. 1b and Extended Data Fig. 1i-o). Furthermore, we established that in G2 phase GFP:Mud localizes at TCJs where it persists through mitosis (Extended Data Fig. 2). The TCJ localization of Mud was independent of Pins and Gαi in both interphase and mitotic cells (Fig. 1c-e and not shown). Accordingly, GFP:Mud lacking the Pins binding domain (GFP:MudΔPINS) localizes at TCJs (Fig. 1c). Whereas Mud loss of function did not affect Gli localization, loss of Gli led to a reduction of GFP:Mud localisation at the TCJs (Fig. 1d,e and Extended Data Fig. 3a). Likewise, loss of function of the Discs-large (Dlg) septate protein, which is necessary for Gli localization[15] caused the disappearance of both Gli and GFP:Mud from the TCJs (Fig. 1d,e and Extended Data Fig. 3b-d). Collectively, our results show that independently of the Pins/Gαi pathway, epithelial mitotic cells harbour a cortical TCJ Mud distribution inherited from interphase.

Since astral microtubules (MT) contacted ChFP:Mud patches at TCJ (Extended Data Fig. 4a and Supplementary Video 2), we asked whether TCJs recruit or activate force generators to orient the spindle. Following experiments in *C. elegans* zygote[16], we developed a laser ablation assay to estimate the relative magnitude and the direction of mechanical forces exerted by astral MTs on the centrosome within tissue (Extended Data Fig. 4b and 5). Astral MT ablation in wild-type (wt) cells caused the centrosomes to recoil away from the ablation site, suggesting that MTs predominantly exert pulling forces on spindle poles (Fig. 2a-b and Supplementary Video 3). The loss of Mud or Dynein minus-end directed motor

activity led to a reduction in centrosome recoil upon MT ablation (Fig. 2b). In agreement with the role of Gli and Dlg in promoting TCJ Mud localization, centrosome recoil velocities upon MT ablation were also reduced in *gli* and *dlg* mutant cells (Fig. 2b). Together, these results indicate that TCJs control the pulling forces exerted by astral MTs on the spindle via Mud and Dynein activities.

We then investigated whether the Mud distribution at TCJs accounts for the torque exerted by MTs on the spindle to dictate its orientation. To this end, we adapted a mechanical model predicting the spindle orientation according to cell shape[17,18]. In this model, developed to describe isolated and non-epithelial cells which do not round up at mitosis, the pulling forces exerted by astral MTs scale with MT length and, as a consequence, the model predicts the preferred spindle orientation along the cell long-axis (Fig. 2c). To account for the contribution of Mud to MT pulling forces in epithelia, we modified the model to assume that astral MTs instead pull with a force proportional to the cortical GFP:Mud intensity and independent of MT length (Fig. 2d). We then measured the metaphase distribution of cortical GFP:Mud and cell shapes to compare the predictions based on cell shape and GFP:Mud intensity models for cells in metaphase (Fig. 2e). Strikingly, the model based on GFP:Mud distribution along the cortex predicted spindle orientation and its predictions were significantly better than the ones based on the metaphase cell shape (Fig. 2f-h, Extended Data Fig. 6a-i and Supplementary Table 1). In agreement with the fact that Pins does not regulate Mud localization at TCJs, spindle orientation predictions were similar in wt and *pins* tissues (Extended Data Fig. 7). To further test the contribution of Mud-dependent MT pulling forces to spindle orientation, we characterized a GFP:Mud mutant deleted of its coiled-coil domain (GFP:MudΔCC, Extended Data Fig. 8). GFP:MudΔCC co-localizes with Gli in wt or *mud* tissues, but GFP:MudΔCC cannot restore astral pulling forces in *mud* tissue (Fig. 2i-k). Whereas the GFP:MudΔCC cortical localization predicted spindle orientation in wt tissue (Extended Data Fig. 8d), planar mitotic spindles were not oriented according to the distribution of GFP:MudΔCC in *mud* tissue (Fig. 2l). Collectively, these findings indicate that TCJ via Mud define the distribution of MT pulling forces specifying the spindle orientation in epithelial tissue.

Our finding that in metaphase the Mud distribution at TCJs is a better predictor of spindle orientation than is cell shape argues against a model where incomplete cell rounding

ensures interphase cell shape "memorization". We therefore hypothesized that the interphase TCJ distribution might explain the Hertwig's rule in tissues. Since our theoretical analysis indicated that spindle orientation is mainly dictated by the anisotropy of the TCJ distribution (Extended Data Fig. 6h,i), we introduced a TCJ bipolarity quantity characterized by an anisotropy (η_{TCJ}) and orientation (θ_{TCJ}) to describe the TCJ angular distribution in a given cell (Fig. 3a and Extended Data Fig. 6j). The TCJ bipolarity anisotropy and orientation can be similar to or distinct from the cell shape anisotropy (or elongation, η_{shape}) and the long-axis orientation (θ_{shape}) (Fig. 3a). We found that the anisotropy of TCJ bipolarity decreases much less than cell shape anisotropy during mitotic cell rounding (Fig. 3b). Also, division orientation predictions based on the TCJ distribution, unlike those based on cell shape, were similar in interphase and mitosis (Fig. 3c-c'). These findings support the notion that TCJ bipolarity is a persistent marker of the interphase cell elongation axis during mitotic rounding. We then measured each cell's average shape (θ_{shape}) and TCJ bipolarity (θ_{TCJ}) from 60 to 30 minutes prior to mitosis (from late G2 interphase to prior to mitotic rounding) as well as its division orientation ($\theta_{division}$). Apart from cases where TCJ and shape orientation are aligned ($\left|\theta_{TCJ} - \theta_{shape}\right|$<10°), TCJ gives better division orientation predictions than cell shape does, and this improvement increases as the difference between shape and TCJ orientation increases (Fig. 3d-e',g and Extended Data Fig. 9a). This finding applies for both rounded cells (low η_{shape}) and elongated cells (high η_{shape}) (Extended Data Fig. 9b-c). This raises the question of why cells tend to divide according to their interphase cell long-axis. The distribution of the angular difference between TCJ and shape orientation is broad in rounded cells (low η_{shape}) but narrow in elongated cells (high η_{shape}) (Fig. 3h). Accordingly, cell shape does not predict cell division axis in rounded cells, and as cell shape anisotropy increases, the predictions based on cell shape agree better and better with the predictions based on TCJ bipolarity (Fig. 3f-g and Extended Data Fig. 9b-c). Hence, in rounded cells TCJ bipolarity and cell shape orientations may be misaligned and division orientation follows TCJ bipolarity, whereas in elongated cells TCJ bipolarity and cell shape orientations are aligned in most cases, and the TCJ distribution ensures that cell division occurs along the former interphase cell shape long-axis. Lastly, cell division orientation along the interphase cell long-axis and TCJ distribution was strongly reduced in *mud* tissue (Fig. 3i and Extended Data Fig. 5f-g). Altogether, we propose that TCJ, via Mud, constitute the dominant mechanism of division orientation along the interphase cell long-axis.

Why are the orientations of cell long-axes and TCJ distributions aligned? This can be understood by picturing regular hexagonal cells, which are then pulled. The cell elongation leads to the alignments of cell shape and TCJ bipolarity orientations with the pulling direction (Fig. 4a). Computer simulation can then be used to model the disordered case of epithelial cells whose shapes depend on adhesion and cortical tension[19]. The simulations reproduce the alignment between cell shape long-axis and TCJ bipolarity orientations as cell shape anisotropy increases as well as the average alignment of the TCJ bipolarity and mechanical strain orientation (Fig. 4b,c Extended data Fig. 10d and Supplementary Video 4). Therefore generic properties of epithelial cells, adhesion and cortical tension, are sufficient to reproduce the alignment of TCJ bipolarity and cell shape as their anisotropy increases. Furthermore, in agreement with the fact that global mechanical stress tends to elongate cells[8,12], the alignment of TCJ bipolarity with mechanical stress increases as tissue stress anisotropy increases, thus accounting for orientation of divisions along the global mechanical stress orientation (Fig. 4d and Extended Data Fig. 10c). Our findings hence indicate that the alignment of TCJ distribution with cell elongation and mechanical stress axis is a core geometric property of epithelial tissues and accounts for a role of TCJ as spatial landmarks providing the information needed for cell shape and mechanical strain orientation sensing.

Altogether our findings provide evidence that TCJ can serve as built-in interphase shape sensors to orient division when the interphase cell shape is well defined. This mechanism is distinct from the ones involving extracellular matrix retraction fibres or signalling[17,20-23]. It accounts for the integration of two properties of epithelial division: orientation along the interphase cell shape and mitotic rounding (Fig. 4e). The packing of tissue promotes contacts between three (or more) cells and the formation of TCJs. In addition to TCJ proteins implicated in epithelial barrier function[24,25], several proteins are enriched at TCJs, including adhesion molecules, cytoskeleton regulators and Hippo pathway component[25-29]. The alignment of TCJ with cell shape or mechanical strain being a geometrical property of epithelia, TCJ might provide epithelial cells with an axial polarity (or bipolarity) to couple cell shape and tissue mechanics with adhesion, cytoskeleton organization and signalling.

FIGURES:

Fig. 1: Mud localizes at TCJ.

(**a**) GFP:Mud from interphase to telophase (t=0 min, anaphase). GFP:Mud at TCJ (arrows), spindle poles (arrowheads). *n*=21 cells.

(**b**) GFP:Mud and Gli co-localization in interphase (top, *n*=54 cells) and metaphase (bottom, *n*=8 cells).

(**c**) GFP:Mud localization in *mud* (*n*=15), *pins* (*n*=22), *Gαi* (*n*=5) cells and GFP:MudΔPINS in *mud* cells (*n*=18).

(**d**,**e**) GFP:Mud distribution (d, images representative of quantifications shown in e) and mean±s.e.m. TCJ intensities (e) in wt, *Gli*, *dlg* and *pins* cells. Fas3, cell contours. *t*-test (ns: not significant, ***:$p<0.0005$). *n*: cell numbers.

Scale bars: 1μm (a, b, c, d).

Fig. 2: TCJ regulate Mud-dependent MT pulling forces to orient divisions.

(**a**) Ablation of astral MTs (red line), *n*=21 cells quantified in b.

(**b**) Mean centrosome velocity relative to MT ablation site (left), mean velocity amplitude after ablation (mean±s.e.m, right) in wt, *mud*, *dlg* and *Gli* cells at 25°C and in wt and gl^{DN} cells at 29°C. *t*-test (*:$p<0.05$). Orientations are different in *mud*, *dlg and* gl^{DN} (Watson's U^2 test, $p<0.01$).

(**c**,**d**) Cell shape (c) and Mud intensity (d) models: pulling forces scale with MT length (blue arrows) or Mud cortical intensity (red arrows) to exert a torque (T, arrows).

(**e-g**) Experimental spindle orientation (green cross) and predictions based on cell shape (blue circles, f) or GFP:Mud intensity (red circles, g) potentials at t=-1min for cell in e (*n*=121 cells).

(**h**) Difference between theoretically predicted (θ_{theory}) (blue: shape, red: GFP:Mud intensity) and experimental ($\theta_{division}$) spindle orientation. Data are duplicated in a lighter colour relative to 0° line in this and subsequent plots. Kolmogorov-Smirnov test (*p* value).

(**i**) Localizations of GFP:Mud in wt (*n*=54) and *mud* (*n*=15) cells as well as of GFP:MudΔCC in wt (*n*=18) and *mud* (*n*=67) cells.

(**j**) Quantifications (mean±s.e.m) of GFP:Mud or GFP:MudΔCC co-localization with Gli in wt and *mud* cells. *t*-test. ns: not significant.

(**k**) Mean centrosome velocity relative to MT ablation (left), mean velocity amplitude after ablation (mean ± s.e.m, right) in wt and in *mud* tissues expressing GFP:Mud or GFP:MudΔCC.

t-test (**:p<0.005). Orientation is different in *mud*, *GFP:MudΔCC* (Watson's U^2 test, p<0.001).

(**l**) Difference between θ_{theory} (from cortical GFP intensity) and $\theta_{division}$ in *mud* cells expressing GFP:MudΔCC or GFP:Mud. GFP:Mud in *mud* and wt (h, red) tissue are similar (p=0.12). Kolmogorov-Smirnov test (p values).

Scale bars: 1μm (a, e, i), n: cell numbers (b, h, j, k, l).

Fig. 3: TCJ distribution accounts for division orientation along the interphase cell shape.

(**a**) TCJ (red dots) bipolarity and cell shape (blue) anisotropies η and orientations θ represented by the length and orientation of red and blue bars.

(**b**) η_{TCJ} and η_{shape} from interphase to anaphase (mean±s.e.m). Insets: time-lapse images of a cell from interphase to mitotic rounding (n=249 cells). *t*-test (*:p<0.05, ***:p<0.0005).

(**c-c'**) Difference between experimental ($\theta_{division}$) and predicted division orientations by the average (-20 to -10min interphase, -4 to -3min metaphase) cell long-axis (θ_{shape}) (c) or TCJ bipolarity (θ_{TCJ}) (c'). Kolmogorov-Smirnov test (p values).

(**d**) Top: θ_{shape} and θ_{TCJ} align with $\theta_{division}$. Bottom: only θ_{TCJ} aligns with $\theta_{division}$. Time-lapse images of 2 cells out of the 29388 cells analysed.

(**e-f'**) Difference between experimental ($\theta_{division}$) and predicted division orientations based on interphase TCJ bipolarity (θ_{TCJ}) or cell long-axis (θ_{shape}) for $|\theta_{TCJ} - \theta_{Shape}|$ intervals (e-e') and indicated η_{shape} intervals (f-f'). Kolmogorov-Smirnov test (p values), percentage of 29388 cells.

(**g**) TCJ bipolarity (θ_{TCJ}) prediction improvement over cell long-axis (θ_{Shape}) versus $|\theta_{TCJ} - \theta_{shape}|$. mean±s.e.m of three movies for a total of n=29388 cells analyzed.

(**h**) Differences (mean±s.d.) between θ_{shape} and θ_{TCJ} versus η_{shape}. Correlation coefficient $A_{experiment} = 0.88$.

(**i-i'**) Difference between experimental ($\theta_{division}$) and predicted division orientations based on interphase cell long-axis (θ_{shape}) (left) or the TCJ bipolarity (θ_{TCJ}) (right) in wt and *mud* cells. Kolmogorov-Smirnov test (p values).

Scale bars: 1μm (a, b), n: cell numbers (b, g, h).

Fig. 4: TCJ alignment with shape is a core geometric property.

(**a-b**) Regular hexagonal cells (a) and simulated cell lattice (b) before and after elongation.

(**c**) Differences (mean±s.d.) between θ_{shape} and θ_{TCJ} versus η_{shape} for experimental (Fig. 3g) and simulated cells. $A_{simulation} = 0.94$. n: cell numbers.

(**d**) Difference between θ_{TCJ} and principal strain axis (θ_{strain}) versus normal stress differences. n: ablation number.

(**e**) Upon mitotic rounding, Mud interphase localization is maintained at TCJs orienting the spindle along the interphase cell long-axis.

Acknowledgments

We thank V. Auld, A. Bardin, R. Basto, B. Edgar, S. Luschnig, F. Schweisguth, the Bloomington Stock Center and Developmental Studies Hybridoma Bank for reagents; M. Manil-Ségalen, S. Rigaud. T. Piolot, I. Bonnet for input and data analyses; the Developmental Biology Curie imaging facility; F. Graner, A. Guichet, S. Herszterg, J-L. Maître M. Piel, M. Thery for comments; ANR-MorphoDro, ERC Advanced, ARC (SL220130607097), Curie Mayent-Rothschild, Labex DEEP, NSF DMR1056456 and ICAM grants for funding.

Author contributions

F.B., N.M., Y.B. designed the project. F.B., M.B., A.A., N.C. performed experiments. C.M., Z.W., I.G. produced reagents. O.M., B.G., A.P., N.M. developed methods and scripts for data analysis. O.M. performed simulations. F.B., O.M., B.G., A.P., N.M., Y.B. analysed the data. D.K.L., N.M. developed theoretical models. F.B., O.M., D.K.L., N.M., Y.B. wrote the manuscript.

Author Information

The authors declare no competing financial interests. Correspondence and requests for material should be addressed to F.B. (floris.bosveld@curie.fr) and Y.B. (yohanns.bellaiche@curie.fr)

References

1. Cadart, C., Zlotek-Zlotkiewicz, E., Le Berre, M., Piel, M. & Matthews, H. K. Exploring the function of cell shape and size during mitosis. *Dev Cell* **29,** 159-169 (2014).

2. Hertwig, O. Das Problem der Befruchtung und der Isotropie des Eies, eine Theory der Vererbung. *Jenaische Zeitschrift fuer Naturwissenschaft.* (1884).

3. Baena-López, L. A., Baonza, A. & García-Bellido, A. The orientation of cell divisions determines the shape of Drosophila organs. *Curr Biol* **15,** 1640-1644 (2005).

4. Saburi, S., Hester, I., Fischer, E., Pontoglio, M., *et al.* Loss of Fat4 disrupts PCP signaling and oriented cell division and leads to cystic kidney disease. *Nat Genet* **40,** 1010-1015 (2008).

5. Aigouy, B., Farhadifar, R., Staple, D. B., Sagner, A., *et al.* Cell flow reorients the axis of planar polarity in the wing epithelium of Drosophila. *Cell* **142,** 773-786 (2010).

6. Gibson, W. T., Veldhuis, J. H., Rubinstein, B., Cartwright, H. N., *et al.* Control of the mitotic cleavage plane by local epithelial topology. *Cell* **144,** 427-438 (2011).

7. Mao, Y., Tournier, A. L., Bates, P. A., Gale, J. E., *et al.* Planar polarization of the atypical myosin Dachs orients cell divisions in Drosophila. *Genes Dev* **25,** 131-136 (2011).

8. Campinho, P., Behrndt, M., Ranft, J., Risler, T., *et al.* Tension-oriented cell divisions limit anisotropic tissue tension in epithelial spreading during zebrafish epiboly. *Nat Cell Biol* **15,** 1405-1414 (2013).

9. Le Goff, L., Rouault, H. & Lecuit, T. A global pattern of mechanical stress polarizes cell divisions and cell shape in the growing Drosophila wing disc. *Development* **140,** 4051-4059 (2013).

10. Mao, Y., Tournier, A. L., Hoppe, A., Kester, L., *et al.* Differential proliferation rates generate patterns of mechanical tension that orient tissue growth. *EMBO J* **32,** 2790-2803 (2013).

11. Xiong, F., Ma, W., Hiscock, T. W., Mosaliganti, K. R., *et al.* Interplay of cell shape and division orientation promotes robust morphogenesis of developing epithelia. *Cell* **159,** 415-427 (2014).

12. Wyatt, T. P., Harris, A. R., Lam, M., Cheng, Q., *et al.* Emergence of homeostatic epithelial packing and stress dissipation through divisions oriented along the long cell axis. *Proc Natl Acad Sci U S A* (2015).

13. Bosveld, F., Bonnet, I., Guirao, B., Tlili, S., *et al.* Mechanical Control of Morphogenesis by Fat/Dachsous/Four-Jointed Planar Cell Polarity Pathway. *Science* **336,** 724-727 (2012).

14. Kotak, S. & Gönczy, P. Mechanisms of spindle positioning: cortical force generators in the limelight. *Curr Opin Cell Biol* **25,** 741-748 (2013).

15. Schulte, J., Charish, K., Que, J., Ravn, S., *et al.* Gliotactin and Discs large form a protein complex at the tricellular junction of polarized epithelial cells in Drosophila. *J Cell Sci* **119,** 4391-4401 (2006).

16. Grill, S. W., Gönczy, P., Stelzer, E. H. & Hyman, A. A. Polarity controls forces governing asymmetric spindle positioning in the Caenorhabditis elegans embryo. *Nature* **409,** 630-633 (2001).

17. Théry, M., Jiménez-Dalmaroni, A., Racine, V., Bornens, M. & Jülicher, F. Experimental and theoretical study of mitotic spindle orientation. *Nature* **447,** 493-496 (2007).

18. Minc, N., Burgess, D. & Chang, F. Influence of cell geometry on division-plane positioning. *Cell* **144,** 414-426 (2011).

19. Morelli, L. G., Uriu, K., Ares, S. & Oates, A. C. Computational approaches to developmental patterning. *Science* **336,** 187-191 (2012).

20. Fink, J., Carpi, N., Betz, T., Bétard, A., *et al.* External forces control mitotic spindle positioning. *Nat Cell Biol* **13,** 771-778 (2011).

21. Kwon, M., Bagonis, M., Danuser, G. & Pellman, D. Direct Microtubule-Binding by Myosin-10 Orients Centrosomes toward Retraction Fibers and Subcortical Actin Clouds. *Dev Cell* **34,** 323-337 (2015).

22. Tamada, M. & Zallen, J. A. Square Cell Packing in the Drosophila Embryo through Spatiotemporally Regulated EGF Receptor Signaling. *Dev Cell* **35,** 151-161 (2015).

23. Machicoane, M., de Frutos, C. A., Fink, J., Rocancourt, M., *et al.* SLK-dependent activation of ERMs controls LGN-NuMA localization and spindle orientation. *J Cell Biol* **205,** 791-799 (2014).

24. Byri, S., Misra, T., Syed, Z. A., Bätz, T., *et al.* The Triple-Repeat Protein Anakonda Controls Epithelial Tricellular Junction Formation in Drosophila. *Dev Cell* **33,** 535-548 (2015).

25. Furuse, M., Izumi, Y., Oda, Y., Higashi, T. & Iwamoto, N. Molecular organization of tricellular tight junctions. *Tissue Barriers* **2,** e28960 (2014).

26. Lye, C. M., Naylor, H. W. & Sanson, B. Subcellular localisations of the CPTI collection of YFP-tagged proteins in Drosophila embryos. *Development* **141,** 4006-4017 (2014).

27. Rauskolb, C., Pan, G., Reddy, B. V., Oh, H. & Irvine, K. D. Zyxin links fat signaling to the hippo pathway. *PLoS Biol* **9,** e1000624 (2011).

28. Sawyer, J. K., Harris, N. J., Slep, K. C., Gaul, U. & Peifer, M. The Drosophila afadin homologue Canoe regulates linkage of the actin cytoskeleton to adherens junctions during apical constriction. *J Cell Biol* **186,** 57-73 (2009).

29. Oda, Y., Otani, T., Ikenouchi, J. & Furuse, M. Tricellulin regulates junctional tension of epithelial cells at tricellular contacts through Cdc42. *J Cell Sci* **127,** 4201-4212 (2014).

METHODS

Fly stocks and genetics.

Drosophila melanogaster stocks and associated references are listed in Supplementary Table 2. Flies were crossed and experiments were performed at 25°C unless specified otherwise. Male or female pupae were used. Experiments using the temperature-sensitive allele of p150/Glued, *D82glued*[30] were performed as previously described for temperature-controlled experiments in the *Drosophila* pupa[13]. Loss of function, gain of function and dual colored patches experiments were carried out using the FLP/FRT or the MARCM techniques[31-33]. Somatic clones were induced in the second instar larval stage by heat-shock (20 min at 37°C for FRT19A and FRT40A, 1 h at 37 °C for FRT42D) and analyzed 3-4 days after clone induction in 12-20 hours after pupa formation (hAPF) pupae. The analyses of dlg^{m52} loss of function clones were performed in small clones (3 days after induction) to avoid AB polarity defects[34].

Molecular biology.

To create the GFP:Mud or ChFP:Mud transgenes under the control of Mud endogenous promoter, we used recombineering[35,36] to introduce a GFP or ChFP tag at the ATG of the *mud* open reading frame in the CH322-147E14 BAC genomic clone (BACPAC Resources Center). This BAC clone contains ~19.5kb of X chromosome genomic region including ~3.3kb upstream of the *mud* mRNA 5' and 5.4kb downstream of the *mud* 3' mRNA and thus most of the coding regions of genes proximal and distal to *mud* locus.

First a galK cassette, amplified with primers F (5'-CATACATATACGGGCGCACACACACCCATAAAAACGCACAAAAATTCGCACCTG TTGACAATTAATCATCGGCA-3') and R (5'-GATTTACATACCCACTGGAGTAGGACCTTGCGCCAGCTGCGCGTGTCCATTCAGC ACTGTCCTGCTCCTT-3') (underscored letters for galK sequences), was inserted via recombination at the N-terminus of the *mud* open reading frame. After positive selection, the galK cassette was replaced with a GFP tag, primers F (5'-CATACATATACGGGCGCACACACACCCATAAAAACGCACAAAAATTCGCAATGG TGAGCAAGGGCGAGGA-3') and R (5'-GATTTACATACCCACTGGAGTAGGACCTTGCGCCAGCTGCGCGTGTCCATCTTGT ACAGCTCGTCCATGC -3') (underscored letters for GFP sequences) or with a ChFP tag, primers F (5'-CATACATATACGGGCGCACACACACCCATAAAAACGCACAAAAATTCGCAATGG TGAGCAAGGGCGAGGAGGATAACATG
3') and R (5'-GATTTACATACCCACTGGAGTAGGACCTTGCGCCAGCTGCGCGTGTCCATCTTGT ACAGCTCGTCCATGCCGCCGGTGGA-3') (underscored letters for ChFP sequences) via recombination and negative selection for galK[37]. The attB-P[acman-GFP:Mud]-CmR-BW was integrated into the PBac{y[+]-attP-9A}VK00030 landing site at 50E1, PBac{y[+]-attP-9A}VK00031 landing site at 62E1 and PBac{y[+]-attP-9A}VK00033 landing site at 65B2. The attB-P[acman-ChFP:Mud]-CmR-BW was integrated into the PBac{y[+]-attP-9A}VK00030 landing site at 50E1, PBac{y[+]-attP-9A}VK00031.

Deletions within the GFP:Mud genomic region were created by recombineering using a neomycin resistance cassette flanked by loxP sites[38], which were amplified by PCR (see below), at the amino acid positions shown in Extended Data Fig. 8a. Upon neomycin selection, the cassette was removed by Cre-mediated recombination[38] leaving behind a 78 bp loxP site

sequence. The following primers were used for PCR: MudΔCH: F (5'-CATACATATACGGGCGCACACACACCCATAAAAACGCACAAAAA TTCGCAGGCCTGGTGATGATGGCGGGATC-3') and R (5'-CTGCTGGGAAGACATGGGCTGACTGAGGTCGAAACCCCTTGTCGGTAAACTCAGA AGAACTCGTCAAGAAGGCG-3', Note that the MudΔCH is not tagged with GFP); GFP:MudΔCC: F (5'-GGCTGTTGACGCGCGAATATCTTAGCCAGGCGATCGCCAACGTTGCAGTTCGTTC CTTGTATACGGCGGAGGTGACGCGCATGAAGGAGAAGCAGGAACG-3') and R (5'-CGTTCCTGCTTCTCCTTCATGCGCGTCACCTCCGCCGTATACAAGGAACGAACTGC AACGTTGGCGATCGCCTGGCTAAGATATTCGCGCGTCAACAGCC-3'); GFP:MudΔPINS: F (5'-CCGTTTCGTCCAGTTCGTCGGCGCCGAACGATGACTGGCAGCCCTTCAAGCGCCA CTCCGGCTCCCAGATAAC-3') and R (5'-CTTACTTTGAGATCTTCGTCCTGGCTGCCCAAATCATATTGGGCAGCATAACTAGT GGATCCCCTCGAGGGACCTAATAAC-3') and GFP:MudΔTM: F (5'-AATTCACACAACTGGTGGCCGCCTCTTGCAGTAATATCACTACGACTAGCTAGAA GCGGCAACGAAAGCAATGGGAAACGCACAAATCTTGCTGATGATC-3') and R (5'-GATCATCAGCAAGATTTGTGCGTTTCCCATTGCTTTCGTTGCCGCTTCTAGCTAGT CGTAGTGATATTACTGCAAGAGGCGGCCACCAGTTGTGTGAATT-3').

The MudΔCH, GFP:MudΔPINS, GFP:MudΔCC and GFP:MudΔTM BAC constructs were integrated at the (PBac{y[+]-attP-9A}VK00030 landing site at 50E1 and at the PBac{y[+]-attP-9A}VK00033 landing site at 65B2.

A deletion of the C-terminal domain of Mud including the Pins and MT binding domains (MudΔC) (see Extended Data Fig. 8a) was created using the CRISPR/Cas9 system[39] at the endogenous *mud* locus. Two sgRNAs (upstream targeting sequence; 5'-CATCCAGTCTAACCAGGCGGAGG-3' and downstream targeting sequence: 5'-AGATGAGGCGCCGGTCATGTTGG-3') were inserted into pU6B-sgRNA-short[40] and co-injected with purified ssODN 5'-GGCTGCTTCTCGCTTCCAACCAAGAGTTGGAAGAACTAAATTCCATCCAGTCTAA CCAGGT-Δ-GACCGGCGCCTCATCTTGTACAGTCTATTCGATCGGCAGTGTGCACATGCAGCCG CTGC-3' (Δ denotes position of the deletion) in the *vas-Cas9* line[41]. Resulting F1 flies were screened for germline transmission of the deletion by single fly PCR. The F2 progeny was sequenced to confirm the deletion of the C-terminus domain.

Immunohistochemistry and fixed tissue imaging.

Pupae were dissected and fixed as previously described[42]. Primary antibodies were: rabbit anti-Gαi (1:500, provided by JA Knoblich, IMP), rabbit anti-Mud (aa375-549) (1:1000[43], mouse anti-Gli (1:250[44], mouse anti-Dlg (1:1000, DSHB, 4F3), mouse anti-FasIII (1:50, DSHB, 7G10), guinea-pig anti-Cora (1:2000[45], rabbit anti-GFP (1:2000, Molecular Probes). Fluorescent secondary antibodies were: alexa-488 goat-anti-rabbit IgG (1:500, Molecular Probes), Cy2, Cy3 and Cy5 donkey-anti-mouse IgGs (1:500, Jackson ImmunoResearch). Images were collected with confocal microscopes (LSM710NLO or LSM780, Carl Zeiss). All images are maximum projections of a *z*-stack unless otherwise indicated.

Live imaging microscopy.

Live imaging.

Pupae were prepared for live imaging as described previously[46]. Samples were imaged at 25°C or 29°C with either an inverted confocal spinning disk microscope from Nikon or Zeiss using either 40x NA1.3 OIL DIC H/N2 WD0.2 PL FLUOR, 60x NA1.4 OIL DIC N2 PL APO VC, 63x NA1.4 OIL DICII PL APO or 100x NA1.4 OIL DIC N2 PL APO VC objectives and either a CoolSNAP HQ2 (Photometrics), an EMCCD Evolve (Photometrics) or a CMOS (Hamamtsu) camera. Live images of FUCCI and GFP:Mud were acquired using a confocal microscope (LSM780, Carl Zeiss) and 63x NA 1.4 OIL DICII PL APO objective. To improve signal-to-noise ratio, videos and images for display and segmentation were either deconvolved using Huygens software (Scientific Volume Imaging b.v., NL) or denoised using Safir software[47]. Average projections of raw *z*-stack images were used for intensity measurements.

Unless specified otherwise, all experiments on dividing cells were performed during the first round of cell divisions in the notum tissue (12-20 hAPF). In the analyses (unless mentioned otherwise), the time (t) equals 0 was set at anaphase onset defined by the initial cell elongation and/or centrosome movements towards the cortex.

Photobleaching of GFP:Mud or GFP:MudΔCC in neighbouring cells.

Since the cortical GFP:Mud or GFP:MudΔCC signals at the TCJ has contributions from both the dividing cell and its neighbouring cells, we performed prediction of spindle orientation based on GFP:Mud or GFP:MudΔCC intensity upon photobleaching of GFP:Mud or GFP:MudΔCC in the neighbouring cells, the residual GFP:Mud or GFP:MudΔCC signal reflecting more faithfully the distribution of GFP:Mud or GFP:MudΔCC at the TCJ in the dividing cells. Having found by Fluorescence Recovery after Photobleaching (FRAP) that GFP:Mud turn-over at TCJ is on the order of tens of seconds ($t_{1/2}$=21±7 sec, data not shown), a region of approximately 2 cell diameters was photobleached (491 nm laser at 100% power, 12 iterations) around a dividing cell, which was identified by the accumulation of GFP:Mud or GFP:MudΔCC at the spindle poles. Following photobleaching of GFP:Mud or GFP:MudΔCC in neighbouring cells, confocal *z*-stacks of 14 slices (0.5 μm/slice) were acquired every 1 min. Cells were used for predictions of mitotic spindle orientation when their anaphase onset (t=0) occurred at least 4 minutes after photobleaching ensuring that the GFP:Mud or GFP:MudΔCC signal are mainly contributed by the dividing cells.

Segmentation and tracking of cells during tissue development.

To record cell division orientation, cell shape and TCJ bipolarity during development, maximal projected images of multiscale time-lapse videos of pupa notum tissue labelled with either E-Cad:GFP (16-28 *z*-stacks 0.5μm/slice, 0.322 μm/pixel, 5 min/acquisition, labelling of the apical adherens junctions) or Dlg:GFP (20 *z*-stacks 0.5μm/slice, 0.205 μm/pixel, 3 min/acquisition, labelling of the septate junctions) were segmented and cell divisions were tracked as in[13,48].

GFP:Mud kymograph from interphase to mitosis.

To generate the kymograph of the GFP:Mud signal around the cell contour from interphase to anaphase, the cell contour was manually segmented using the GFP:Mud signal. The GFP:Mud intensity of the fluorescence signal was recorded as a function of the angle θ of each contour pixel around the center of mass and then plotted as a line for each time point.

Laser ablations of astral MTs and estimation of cortical forces.

Laser ablation of astral MTs were performed in cells labelled with Jupiter:GFP or α-Tub:GFP (MT markers) and Sas-4:RFP, Spd-2:RFP or YFP:Asl (centrosome markers) as well as Dlg:GFP or Nrg:GFP (septate junction markers). Images were captured using a two-photon laser-scanning microscope (LSM710 NLO, Carl Zeiss) equipped with a 63x NA 1.4 OIL DICII PL APO objective (digital zoom 3X) in single-photon bidirectional scan mode lasting δt=756 ms. The astral MTs of mitotic spindles, which were parallel to the plane of the epithelial tissue were severed (t_3) using the Ti:Sapphire laser (Mai Tai DeepSee, Spectra Physics) at 890 nm with < 100 fs pulses with a 80 MHz repetition rate typically set at 60% power.

To measure the recoil velocity (amplitude and orientation) of the centrosomes upon astral MT ablation, all spindles were registered horizontally with the ablated astral MTs at the top right and the centrosome positioned at the origin. Centrosome movements were then manually tracked. The velocity (amplitude and orientation) was measured between t_2 and t_{20}.

Image quantifications and GFP:Mud and GFP:MudΔCC localization analyses.

To measure and compare the TCJ accumulation of GFP:Mud in wt, *pins*, *Gli* and *dlg* cells (Fig. 1e), confocal *z*-stack average projections at the level of the septate junction (labelled by FasIII, Cora, PH:ChFP or mRFP) were generated using ImageJ from fixed (*pins* and *dlg*) or live (wt and *Gli*) tissues harbouring wt, *Gli*, *dlg* and *pins* mutant cells. Using FasIII, Cora, PH:ChFP or mRFP labelling, the positions of the TCJs in each cell were manually determined. The FasIII, Cora, PH:ChFP or mRFP labelling were used to draw a mask (5 pixels wide) delineating the cell outline at the level of the mitotic spindle (as determined by GFP:Mud localization at the spindle poles) of (pro)metaphase cells. Following background subtraction, the mean intensity at TCJs (10° over each TCJ) was divided by the mean intensity along the rest of the cell outline to obtain the accumulation at TCJs. Significance was determined using the Student's *t*-test.

To compare the GFP:Mud or GFP:MudΔCC distributions at TCJ in wt, *pins* and *mud* tissues (Fig 2j or Extended Data Fig 7b), their co-localization with Gli were quantitatively compared as follows. Confocal *z*-stack average projections at the level of the septate junction of fixed (pro)metaphase cells (as determined by DAPI staining) expressing either GFP:Mud or GFP:MudΔCC and labelled with Gli and Coracle (Cora, a septate junction marker) were generated using ImageJ. Using the Cora staining, a mask of 5-pixels wide was manually drawn to measure the raw fluorescent intensity profiles of GFP:Mud or GFP:MudΔCC and Gli in (pro)metaphase cells (as determined by DAPI staining) which were normalised by their total fluorescence intensity upon subtraction of the background intensity. The colocalization factor (*C*, vertical axis Fig. 2j and Extended Data Fig. 7b) between GFP:Mud or GFP:MudΔCC and Gli was then determined by calculating the area between the GFP:Mud or GFP:MudΔCC and Gli normalized intensity curves.

$$C = 1 - \frac{1}{2}\int_0^{2\pi} |GFP(\theta) - Gli(\theta)|\, d\theta$$

C equals 1 if the two proteins perfectly co-localize and equals 0 if the two proteins do not colocalize. The comparisons of the distribution of GFP:Mud, GFP:MudΔCC in wt and *mud* tissues were performed blind (Fig 2j). Significance was determined using the Student's *t*-test.

Quantitative analyses of epithelial cell divisions orientation, cell shape and TCJ bipolarity.

Measurement of apical-basal (AB) angle of the spindle α_{AB}.

The AB orientations of the mitotic spindle (α_{AB}) in the different experimental conditions were determined by measuring the orientation of the centrosomes (marked by Spd-2:RFP, Sas-4:RFP or Sas-4:GFP) relative to the plane of the epithelial tissue (labelled by α-Tub:GFP, Jupiter:GFP or RFP:α-Tub) using a custom ImageJ plugin. Statistical significance was assessed using the Kolmogorov-Smirnov test.

Analyses of cell rounding and mitotic spindle prediction from interphase cell shape and TCJ bipolarity.

The analyses of cell rounding from t=-60 min to cytokinesis was performed using Dlg:GFP. The mitotic spindle being positioned at the level of the septate junction (Extended Data Fig. 1g-i), the segmentation of Dlg:GFP cortical signal recapitulates cell shape changes at the level of the spindle and the distributions of TCJ where GFP:Mud is enriched in interphase and mitosis. Due to the spreading of the Dlg:GFP cortical signal along the lateral domain of the cell, the accurate segmentation of the cortical Dlg:GFP signal was achieved by manual correction of each individual cell. This can only be performed on a limited number of cells during their cell cycle (*n*=249 cells from 2 distinct videos, 3 min temporal resolution).

In order to compare the prediction based on cell shape long-axis versus TCJ bipolarity, a very large number of segmented cells are needed. We therefore used E-Cad:GFP time-lapse videos (5 min temporal resolution) since the segmentation of the E-Cad:GFP signal can be readily automated and accurate segmentation of cell shapes and TCJ positions can be achieved for a very large number of cells. Quantifications shown in Fig. 3e-g and Extended Data Fig. 9 were obtained from 29388 cells analysed from 3 distinct videos.

To compare the prediction based on cell shape long-axis versus TCJ bipolarity in wt (6 videos, *n*=4860 cells) and *mud* (8 videos, *n*=7770 cells) mutant tissue predictions were performed in a specific region of the tissue were spindle misorientation along the AB is very weak (Extended Data Fig. 5f-g).

Upon Dlg:GFP signal or E-Cad:GFP signal segmentation and cell tracking, the following measurements were determined using Matlab:

(i) The experimental cell division orientation ($\theta_{division}$) was determined as the orthogonal of the interface between the two daughter cells upon cytokinesis. $\theta_{division}$, which correlates very well with cell division orientation measured by the positions of the two centrosomes at metaphase (R=0.91, *n*=127 cells, data not shown) as established using time-lapse videos of E:Cad:GFP and Spd-2:mRFP (centrosome marker) labelled epithelial tissue.

(ii) To characterize cell shape elongation (η_{shape}) and cell shape long-axis orientation (θ_{shape}), each cell region was used to construct its inertia matrix.

$$S = \frac{1}{n_{\text{pix}}} \sum_{p=1}^{n_{\text{pix}}} \overrightarrow{r_p} \otimes \overrightarrow{r_p} = \frac{1}{n_{\text{pix}}} \sum_{p=1}^{n_{\text{pix}}} \begin{pmatrix} x_p^2 & y_p x_p \\ x_p y_p & y_p^2 \end{pmatrix}$$

where n_{pix} is the number of pixels in the cell and $\vec{r}_p = (x_p, y_p)$ are the vectors pointing from the barycenter of the cell to each pixel of the cell, p. Its eigenvalues λ_S, Λ_S, with $0 < \lambda_S < \Lambda_S$, have the dimensions of a squared distance. Its eigenvector associated to Λ_S defines the direction of the cell's long-axis (θ_{shape}). The cell shape anisotropy was defined as a dimensionless number, which ranged from 0 for a cell perfectly circular, to 1 for an infinitely stretched cell: $\eta_{shape} = 1 - \lambda_S/\Lambda_S$.

(iii) To characterize the anisotropy (η_{TCJ}) and orientation of the TCJ (θ_{TCJ}) angular distribution, we built the "TCJ bipolarity" matrix V:

$$V = \sum_{v=1}^{n_{TCJ}} \overrightarrow{u_v} \otimes \overrightarrow{u_v}$$

where n_{TCJ} is the number of TCJs in the cell and the $\overrightarrow{u_v}$ are the unit vectors pointing from the barycenter of the cell to each cell TCJ, v (i.e. $\overrightarrow{u_v} = \overrightarrow{r_v}/\|\overrightarrow{r_v}\|$) (Extended Data Fig. 6j). Its eigenvalues λ_{TCJ}, Λ_{TCJ}, with $0 < \lambda_{TCJ} < \Lambda_{TCJ}$, are dimensionless numbers. Its eigenvector associated to Λ_{TCJ} defines the direction of the long-axis of the TCJ bipolarity (θ_{TCJ}). The TCJ distribution anisotropy was defined as a dimensionless number, ranging from 0 for TCJ uniformly distributed around the cell, to 1 for the theoretical case of TCJ split in two groups diametrically opposed: $\eta_{TCJ} = 1 - \lambda_{TCJ}/\Lambda_{TCJ}$.

Note that unlike the cell inertia S that is calculated using all the pixels making up the cell, the TCJ bipolarity V solely uses the unit vectors $\overrightarrow{u_v}$ pointing from the cell center to each cell TCJ. By doing so, the TCJ bipolarity disentangle the characterization of TCJ distribution from cell shape measurement, and any correlation observed between the two quantities is not due a shape bias in the TCJ bipolarity measurement. In the example shown in Extended Data Fig. 6j, although the two cells have different shape anisotropies, they share the same set of $\overrightarrow{u_v}$ vectors and have therefore the same TCJ bipolarity.

Both cell shape anisotropy and TCJ anisotropy were normalized to their respective averages over all the cells in the tissue. The cell shape and TCJ distribution anisotropies are represented with bars whose directions give the direction of their respective anisotropies and whose length is proportional to the magnitude of the normalized anisotropy.

To compare the orientations of the cell shape long-axis or the TCJ bipolarity axis with the cell division orientation, the cell shape and TCJ distribution tensors S and V were averaged during late interphase from 60 to 30 minutes prior to the end of cytokinesis. The orientations $\tilde{\theta}_{shape}$ and $\tilde{\theta}_{TCJ}$ of the resulting averaged tensors were then compared to the experimental cell division orientation, $\theta_{divison}$.
The improvement of spindle orientation prediction is calculated as $\left(\frac{N_{TCJ}}{N_S} - 1\right) * 100$. N_S is the number of cells for which $|\theta_{divison} - \tilde{\theta}_{shape}| \leq 15°$, and N_{TCJ} is the number of cells for which $\left|\theta_{division} - \tilde{\theta}_{TCJ}\right| \leq 15°$. The mean improvement and its standard deviation were calculated using the improvement values from three different videos. Similar improvement values are found when determining N_S and N_{TCJ} for $\left|\theta_{division} - \tilde{\theta}_{shape}\right|$ and $\left|\theta_{division} - \tilde{\theta}_{TCJ}\right|$ below 5°, 10°, 20° or 25°.

The correlation coefficient A between TCJ bipolarity and cell long-axis orientation is calculated as

$$A = \frac{2\sum_{i=1}^{N} \eta_i \cos^2(\Delta\theta_i)}{\sum_{i=1}^{N} \eta_i} - 1$$

where N is the total number of cells analyzed. For each cell, $\Delta\theta_i$ equals $\theta_{TCJ} - \theta_{shape}$ and η_i is the cell shape anisotropy. The correlation coefficient A ranged from -1 for complete anti-correlation to 1 for complete correlation. In between, a homogeneous distribution indicating an absence of correlation led to $A = 0$. The correlation coefficient was calculated over all 4504 simulated cells or over an equal number of experimental cells randomly picked (n=4505) among the 29388 cells analyzed in Fig. 3e-g and Extended Data Fig. 9.

As cell division is symmetric in size in the *Drosophila* notum we have focused on the anisotropy and the orientation of the distribution of the TCJ (bipolarity). The analysis of the asymmetry of TCJ distribution in epithelial tissue where epithelial cells undergo unequal size distribution might provide insights on how unequal daughter cells are generated in epithelial tissue.

Numerical simulations.

We used numerical simulations based on the cellular Potts model, which is particularly relevant in biology to describe variable cell shape, size, packing and irregular fluctuating interfaces of cells[48-50]. We consider a 2D square lattice. Each pixel i has an integer index σ_i The m-th cell is defined as the domain consisting of all pixels with the same index value $\sigma_i = m$. The number of pixels that cell has defines its cell area. A cell shape changes when one of its pixels is attributed to another cell. Here, the evolution is driven by the minimization of a total energy E, which has three physical ingredients: interfacial energy, area constraints and an external force applied to the patch of cells. Since the calculations are performed on a lattice, we have

$$E = \Lambda \sum_{i,j} [\,1 - \delta(\sigma_i, \sigma_j)] + \gamma \sum_{m} (A_m - A_0)^2 + k \sum_{i} (x_i - x_0)^2$$

The first term represents the contribution of the energy of the interfaces between the cells. Minimizing this term leads to perimeter minimization (δ is the Kronecker symbol and Λ is interfacial energy). The second term keeps each cell area A_m close to its predefined target value A_0 (γ is the compressibility). The balance between this term and the preceding one simulates a tissue relaxing towards mechanical equilibrium. The third term describes an energy gradient[51,52], i.e. an elastic force field, which pulls on the tissue in opposite directions (k is an elastic constant and x_0 is the x-position of the center of the simulated field).

The algorithm to minimize E uses Monte Carlo sampling and the Metropolis algorithm, as follows. We randomly draw (without replacement) a lattice pixel and one of its eight neighboring pixels. If both pixels belong to different cells, we try to copy the state of the neighboring pixel to the first one. If the copying decreases E, we accept it, and if it increases E, we accept it with probability $P = e^{-\Delta E/T}$, where $\Delta E = E_{after} - E_{before}$. The prefactor T is a fluctuation (random copying) allowance. Because all energy parameters are scalable with T, we can fix it without loss of generality; for numerical convenience, we choose numbers on the order of 10^3. We define one Monte Carlo time step (MCS) as the number of random drawings equal to the number of lattice pixels. We ran simulations during 600 MCS to reach a tissue shape that no longer evolves (initial image). We then applied a constant bulk force that stretched a tissue and run the simulations for 600 MCS (final image). To obtain a large range of cell anisotropies in the simulations we used simulations with an elastic constant, $k = [0; 0.5; 1; 2; 3; 4; 5; 10]$. For each value of k, 5 simulations (with about 170 cells in each simulation) were run. Using the initial and final images, the tissue elongation along the direction of stretching was calculated for each simulation as the relative increase in distances

between landmarks. On the final image, the segmented cell contours were used to determine the tensors V (TCJ bipolarity) and S (inertia matrix) for each cell as well as their averages over all cells in the simulation.

Mechanical stress estimation and TCJ bipolarity orientation.

To compare the mechanical stress and TCJ bipolarity orientations as a function of the normal mechanical stress difference ($\sigma_{yy} - \sigma_{xx}$), we used $\sigma_{yy} - \sigma_{xx}$ experimental values of the estimated mechanical stress obtained up to a prefactor by Bonnet et al.[53] measured from 12hAPF to 28hAPF in the medial region of the scutellum, where the mechanical stress is oriented along the medial-lateral axis ($\sigma_{xy} = 0$ and $\theta_{stress} = 0$). The experimental orientation of mechanical stress for each ablation was compared to the average TCJ bipolarity orientation determined using the segmented cell outlines of the E-Cad:GFP cells within the rim of ablated cells (Extended Data Fig. 10a,b).

Models for predicting spindle orientation.

Predictions based on experimental Mud distribution and cell shape.

For predictions of the mitotic spindle orientation based on GFP:Mud or GFP:MudΔCC signals (thereafter referred to as Mud fluorescence signal) in wt and *mud* tissues, average intensity (2-4 μm) projections centred around the plane of the centrosomes were generated using a custom ImageJ plugin for the t=-2 min and t=-1 min frames (t=0 corresponding to the anaphase onset). A 5 pixel mask that does not overlap with the GFP:Mud or GFP:MudΔCC centrosome signal was drawn around the cortex to determine using a Matlab script the shape of the dividing cell as well as the cortical Mud signal profiles. The experimental orientation of the mitotic spindle and the positions of the two centrosomes were manually determined using the GFP:Mud or GFP:MudΔCC accumulation at the spindle poles (Fig. 2e,i).

The model predicting spindle orientation from cell shape is similar to the one used in[8,18]. The model based on Mud fluorescence signal is adapted from this previous model and inputs the distribution of cortical intensity of GFP:Mud or GFP:MudΔCC obtained from a fluorescence image in a mitotic cell[17,18]. This intensity computed around the cell contour is renormalized, so that the sum of intensities around each treated cell is the same. For each cell, we aimed to compute the global torque T generated as a function of the spindle orientation angle θ (Fig. 2d,g). For each possible spindle orientation θ, (θ varying from 0 to π) we generate two asters of N MTs nucleated at a constant angular density ρ from centrosomes placed at a distance $\pm L/2$ from the spindle center along the axis θ. Both L, which represents the spindle length, and the spindle center are computed from the experimental position of the two centrosomes (Fig. 2e). An MT projecting at an angle ϕ with respect to the spindle contacts the cortex at a given location with a GFP:Mud or GFP:MudΔCC concentration C_{mud}; and is assumed to pull on the spindle pole it is connected to with a force $f[]$ that scales with C_{mud}: $f[C_{mud}\ (\theta, \phi)] \sim (C_{mud})^{\alpha}$, with the exponent α representing putative non-linearity in how Mud may influence astral MT pulling forces. This yields a torque, $\tau(\theta, \phi)$, at the spindle centre projected along the z-axis:

$$\tau(\theta, \phi) = \frac{L}{2} f[C_{mud}(\theta, \phi)] \sin(\phi) \qquad \text{(Eq. 1)}$$

The resultant total torque $T(\theta)$ generated by the two asters is then obtained by summing the projected torques over all MTs:

$$T(\theta) = \frac{L}{2}\int_{-\frac{\Phi}{2}}^{\frac{\Phi}{2}} f[C_{mud}(\theta,\phi)]\sin(\phi)\rho d\phi \qquad \text{(Eq. 2)}$$

where Φ is the total angular width of the aster. Initial tests of the model showed that, above a certain threshold, the number of MTs N (or equivalently the angular density: $\rho = N/\Phi$), does not significantly impact axis definition (Extended Data Fig. 6c-f). Thus, in the model, we keep N as a silent parameter, by normalizing the total torque with N. The stable theoretical axis orientation, θ_{theory} can be identified from the minima of the potential $U(\theta)$ computed as a primitive of $T(\theta)$, and compared with the experimental division axis $\theta_{division}$ (Fig. 2f-h and Extended Data Fig. 6g).

The quality of the prediction was computed based on the magnitude of the angular deviation between the model and the experiments, $|\theta_{theory} - \theta_{division}|$. Overall, the model based on the Mud distribution accounts for observed spindle orientation, with a mean angular deviation magnitude of 27.7° +/- 11.9° (n=140 cells). The shape-based model applied to these same cells predicted a higher mean deviation magnitude of 37.6° +/- 12.3° (n=140 cells). An open question is why the model based on Mud distribution predicts spindle orientation within only 27.7° For comparison, a previous model applied to dividing sea urchin eggs of various shapes made predictions within 15.6°. Although we cannot fully preclude the existence of Mud-independent secondary systems that contribute to spindle orientation, it is important to outline the structural differences in models and biological systems that could explain these differences. One first difference is that the Mud model infers a fluorescence signal distribution which could be in part affected by the imaging itself, yielding variations in Mud signal peak heights or widths which do not reflect the actual force field. In agreement with this, the same model run with cells where the neighbours are *not* photobleached makes predictions within 32.4°(n=241 cells, data not shown). Another probably more important difference is that in *Drosophila* epithelial cells the spindles jiggle and move with a time-scale close to mitosis duration (data not shown). In contrast, in large cells like zygotes and blastomeres, division axes are stably set for tens of minutes with negligible movement and rotation of the spindles[18,54]. Although the lack of a standardized Mud distribution precludes us from computing the effective temperature of the system, the difference in spindle movements suggests that the noise in the *Drosophila* epithelial system studied is much larger than in these other cell types previously analysed.

Predictions at the tissue scale based on TCJ anisotropy

In order to study spindle orientation across the entire tissue, we used the bipolarity axis of the TCJ distribution in each cell as a proxy for a prediction based on the full Mud protein distribution (see Fig. 3 and the discussion of the tensor V earlier in this Supplementary Information). This quantity has the advantages that it relies only on a marker (E-Cad:GFP or Dlg:GFP) that can be reliably imaged over the necessary length and time scales and that the predicted spindle orientations can be computed in a reasonable time, even for tens of thousands of cells. In this section, we show how the bipolarity axis arises naturally as an approximation to a more detailed description that explicitly calculates forces and torques.

We begin by examining in general terms how a cortical force distribution translates into a potential $U(\theta)$ governing the spindle orientation. In the context of this analytic formulation, we assume that the rounded, mitotic cells are approximately circles with radius R and center coinciding with the center of the spindle. Points on the cortex can then be labelled by their angle with the positive x axis. If the spindle makes an angle θ with the positive x axis, then a MT projecting from one of the spindle poles at an angle ϕ to the spindle contacts the cortex at an angle $\beta = \theta + \psi$ to the positive x axis, where ψ satisfies $\cot(\phi) = \cot(\psi) -$

$\epsilon/\sin(\psi)$ with $\epsilon = L/2R$. (Extended Data Fig. 6h). With this relation, one can translate the integral (2) over ϕ giving the net torque into an integral over the circle of the form

$$T(\theta) = \frac{\rho L}{2} \int_{-\pi}^{\pi} [f(\beta) + f(\beta + \pi)] \tilde{\tau}\,(\beta - \theta)\, \mathrm{d}\beta\ .$$

Similarly, the potential can be written as

$$U(\theta) = \frac{\rho L}{2} \int_{-\pi}^{\pi} [f(\beta) + f(\beta + \pi)] \tilde{u}(\beta - \theta)\, \mathrm{d}\beta\ .$$

Here, we have suppressed the explicit dependence of the force f on C_{mud}, and the kernel $\tilde{u}(\psi)$ is a 2π-periodic function given, for $-\pi < \psi \leq \pi$, by

$$\tilde{u}(\psi) = \begin{cases} \dfrac{\epsilon - \cos(\psi)}{\sqrt{1 + \epsilon^2 - 2\epsilon\cos(\psi)}}, |\psi| < \Psi \\ \dfrac{\epsilon - \cos(\Psi)}{\sqrt{1 + \epsilon^2 - 2\epsilon\cos(\Psi)}}, |\psi| \geq \Psi \end{cases},$$

where Ψ is related to Φ as $\cot(\Phi/2) = \cot(\Psi) - \epsilon/\sin(\Psi)$.

Importantly, $\tilde{u}(\psi)$ is hence a symmetric function whose magnitude peaks at $\psi = 0$. That is, within our model the net effect of the MTs is to act as a linear filter that smooths out the cortical Mud distribution without otherwise altering it. We therefore expect that the spindle should generally prefer to orient itself towards the direction of highest Mud concentration but that it is more sensitive to relatively wide, broad peaks of Mud than to the fine details of a rapidly varying Mud distribution. This idea can be expressed more formally by Fourier transforming the periodic functions *U, f,* and $\tilde{u}$. With $U(\theta) = \sum_n U_n \exp(in\theta)$, and similarly for *f* and $\tilde{u}$, we have $U_n = \rho L f_n \tilde{u}_n$ for *n* even and $U_n = 0$ for *n* odd. The magnitudes of the coefficients $\tilde{u}_n$ are plotted in Extended Data Fig. 6i. As expected, the filter decreases the importance of components with higher *n* relative to the dominant $n = 2$ mode. Thus, the orientation of the $n = 2$ mode of the force distribution $f(\beta)$ gives the natural, leading approximation to the location of the minimum of $U(\theta)$. For forces centered on the TCJs (where the Mud concentration is highest), the $n = 2$ mode of the TCJ distribution similarly gives the natural proxy for f_2 and thus for the orientation of the mitotic spindle. Moreover, the orientation of this bipolar mode can be computed far more efficiently than can the location of the global minimum of a potential including all Fourier modes. Indeed, it is a standard result that this orientation corresponds with the anisotropy axis of the second rank tensor V defined previously. This makes it especially appropriate for use in our tissue-scale calculations.

Statistics.

Sample sizes vary in each experiment. Every experiment was done at least three independent times. Statistical significances of protein distribution and velocity amplitude were assessed using Student *t*-tests: the distribution normalities were checked using Kolmogorov-Smirnov test. In cases where the variances were different, significance was assessed using the unequal variance *t*-test. The angular distribution of velocity was assessed using Watson's U^2 test for circular data. GFP:Mud localization at TCJ and GFP:Mud or GFP:MudΔCC co-localization with Gli in the different mutant backgrounds were analysed blindly. Kolmogorov-Smirnov tests were used to analyse differences in α_{AB} spindle orientations and differences in division orientation. P values superior to 0.05 are indicated as not significant (n.s.) in figure legends or

graphs. Predictions of division orientation based on GFP:Mud or GFP:MudΔCC in *mud* or wt tissues were performed blindly. Experiments were not randomized and every experiment was repeated at least three independent times.

Code availability.
Matlab code used to segment and track cells has been previously published[13]. Matlab code used to determine division orientation, cell shape and TCJ bipolarity upon cell segmentation and tracking are available upon request.

Method References

30. Allen, M. J., Shan, X., Caruccio, P., Froggett, S. J., *et al.* Targeted expression of truncated glued disrupts giant fiber synapse formation in Drosophila. *J Neurosci* **19,** 9374-9384 (1999).

31. Herszterg, S., Leibfried, A., Bosveld, F., Martin, C. & Bellaiche, Y. Interplay between the Dividing Cell and Its Neighbors Regulates Adherens Junction Formation during Cytokinesis in Epithelial Tissue. *Dev Cell* **24,** 256-270 (2013).

32. Xu, T. & Rubin, G. M. Analysis of genetic mosaics in developing and adult Drosophila tissues. *Development* **117,** 1223-1237 (1993).

33. Lee, T. & Luo, L. Mosaic analysis with a repressible cell marker for studies of gene function in neuronal morphogenesis. *Neuron* **22,** 451-461 (1999).

34. Nakajima, Y., Meyer, E. J., Kroesen, A., McKinney, S. A. & Gibson, M. C. Epithelial junctions maintain tissue architecture by directing planar spindle orientation. *Nature* **500,** 359-362 (2013).

35. Venken, K. J., He, Y., Hoskins, R. A. & Bellen, H. J. P[acman]: a BAC transgenic platform for targeted insertion of large DNA fragments in D. melanogaster. *Science* **314,** 1747-1751 (2006).

36. Venken, K. J., Carlson, J. W., Schulze, K. L., Pan, H., *et al.* Versatile P[acman] BAC libraries for transgenesis studies in Drosophila melanogaster. *Nat Methods* (2009).

37. Warming, S., Costantino, N., Court, D. L., Jenkins, N. A. & Copeland, N. G. Simple and highly efficient BAC recombineering using galK selection. *Nucleic Acids Res* **33,** e36 (2005).

38. Venken, K. J., Kasprowicz, J., Kuenen, S., Yan, J., *et al.* Recombineering-mediated tagging of Drosophila genomic constructs for in vivo localization and acute protein inactivation. *Nucleic Acids Res* **36,** e114 (2008).

39. Gratz, S. J., Cummings, A. M., Nguyen, J. N., Hamm, D. C., *et al.* Genome Engineering of Drosophila with the CRISPR RNA-Guided Cas9 Nuclease. *Genetics* (2013).

40. Ren, X., Sun, J., Housden, B. E., Hu, Y., *et al.* Optimized gene editing technology for Drosophila melanogaster using germ line-specific Cas9. *Proc Natl Acad Sci U S A* **110,** 19012-19017 (2013).

41. Gratz, S. J., Ukken, F. P., Rubinstein, C. D., Thiede, G., *et al.* Highly specific and efficient CRISPR/Cas9-catalyzed homology-directed repair in Drosophila. *Genetics* **196,** 961-971 (2014).

42. Ségalen, M., Johnston, C. A., Martin, C. A., Dumortier, J. G., *et al.* The Fz-Dsh planar cell polarity pathway induces oriented cell division via Mud/NuMA in Drosophila and zebrafish. *Dev Cell* **19,** 740-752 (2010).

43. Yu, J. X., Guan, Z. & Nash, H. A. The mushroom body defect gene product is an essential component of the meiosis II spindle apparatus in Drosophila oocytes. *Genetics* **173,** 243-253 (2006).

44. Auld, V. J., Fetter, R. D., Broadie, K. & Goodman, C. S. Gliotactin, a novel transmembrane protein on peripheral glia, is required to form the blood-nerve barrier in Drosophila. *Cell* **81,** 757-767 (1995).

45. Lamb, R. S., Ward, R. E., Schweizer, L. & Fehon, R. G. Drosophila coracle, a member of the protein 4.1 superfamily, has essential structural functions in the septate junctions and developmental functions in embryonic and adult epithelial cells. *Mol Biol Cell* **9,** 3505-3519 (1998).

46. David, N. B., Martin, C. A., Segalen, M., Rosenfeld, F., *et al.* Drosophila Ric-8 regulates Galphai cortical localization to promote Galphai-dependent planar orientation of the mitotic spindle during asymmetric cell division. *Nat Cell Biol* **7,** 1083-1090 (2005).

47. Boulanger, J., Kervrann, C., Bouthemy, P., Elbau, P., *et al.* Patch-based nonlocal functional for denoising fluorescence microscopy image sequences. *IEEE Trans Med Imaging* **29,** 442-454 (2010).

48. Bardet, P. L., Guirao, B., Paoletti, C., Serman, F., *et al.* PTEN Controls Junction Lengthening and Stability during Cell Rearrangement in Epithelial Tissue. *Dev Cell* **25,** 534-546 (2013).

49. Käfer, J., Hayashi, T., Marée, A. F., Carthew, R. W. & Graner, F. Cell adhesion and cortex contractility determine cell patterning in the Drosophila retina. *Proc Natl Acad Sci U S A* **104,** 18549-18554 (2007).

50. Graner, F. & Glazier, J. Simulation of biological cell sorting using a two-dimensional extended Potts model. *Phys. Rev. Lett.* **69,** 2013-2016 (1992).

51. Jiang, Y., Swart, P. J., Saxena, A., Asipauskas, M. & Glazier, J. A. Hysteresis and avalanches in two-dimensional foam rheology simulations. *Phys Rev E Stat Phys Plasmas Fluids Relat Interdiscip Topics* **59,** 5819-5832 (1999).

52. Raufaste, C., Dollet, B., Cox, S., Jiang, Y. & Graner, F. Yield drag in a two-dimensional foam flow around a circular obstacle: effect of liquid fraction. *Eur Phys J E Soft Matter* **23,** 217-228 (2007).

53. Bonnet, I., Marcq, P., Bosveld, F., Fetler, L., *et al.* Mechanical state, material properties and continuous description of an epithelial tissue. *J R Soc Interface* **9,** 2614-2623 (2012).

54. Wühr, M., Tan, E. S., Parker, S. K., Detrich, H. W. & Mitchison, T. J. A model for cleavage plane determination in early amphibian and fish embryos. *Curr Biol* **20,** 2040-2045 (2010).

55. Zielke, N., Korzelius, J., van Straaten, M., Bender, K., *et al.* Fly-FUCCI: A versatile tool for studying cell proliferation in complex tissues. *Cell Rep* **7,** 588-598 (2014).

56. Bergstralh, D., Lovegrove, H. & St Johnston, D. Discs Large Links Spindle Orientation to Apical-Basal Polarity in Drosophila Epithelia. *Current Biology* **23,** 1707-1712 (2013).

57. Morin, X. & Bellaïche, Y. Mitotic Spindle Orientation in Asymmetric and Symmetric Cell Divisions during Animal Development. *Dev Cell* **21,** 102-119 (2011).

58. Bowman, S. K., Neumüller, R. A., Novatchkova, M., Du, Q. & Knoblich, J. A. The Drosophila NuMA Homolog Mud regulates spindle orientation in asymmetric cell division. *Dev Cell* **10,** 731-742 (2006).

59. Izumi, Y., Ohta, N., Hisata, K., Raabe, T. & Matsuzaki, F. Drosophila Pins-binding protein Mud regulates spindle-polarity coupling and centrosome organization. *Nat Cell Biol* **8,** 586-593 (2006).

60. Siller, K. H., Cabernard, C. & Doe, C. Q. The NuMA-related Mud protein binds Pins and regulates spindle orientation in Drosophila neuroblasts. *Nat Cell Biol* **8,** 594-600 (2006).

Extended Data figure Legends.

Extended Data Figure 1: Mud, Pins, Gαi and Gli localization during symmetric epithelial cell division in the *Drosophila* notum.

Within the *Drosophila* pupal notum tissue cells divide according to their intephasic cell shape long-axis (a,b), thereby following the 130-year-old Hertwig rule. However, upon entry into mitosis cells round up (the cell shown in a, -15 to -2 min and Fig. 3b).

(**a**) Time-lapse images of Dlg:GFP in a dividing cell (out of 249 cells quantified in b) in the pupal notum tissue illustrating cell rounding during mitosis (The same cell is shown as inset in Fig. 3b.). Prior to mitosis (-30 min) the cell (marked by asterisk) is clearly elongated and divides according to its interphasic cell shape (5 min). Upon entry into mitosis (-15 min) the cell rounds up and reaches a minimal anisotropy just prior to anaphase (-2 min, see also Fig. 3b).

(**b**) Rose plot of the difference between the experimental ($\theta_{division}$) and predicted division orientations by the average (60-30 min prior to mitosis) interphase cell long-axis (θ_{shape}). The data are duplicated relative to 0° line (light green). Number of cells (*n*) analysed is indicated.

(**c,d,e**) Gαi localization in fixed epithelial dorsal thorax tissue (c), Pins:YFP localization in *pins* mutant tissue (d) and GFP:Mud localization (e) showing cells in G2 interphase (left) and mitosis (right). Gαi is hardly detected at the cell cortex in G2 phase and Gαi is mostly homogenously distributed around the cortex during mitosis. Pins:YFP is homogenously distributed around the cell cortex in both interphase and mitotic cells. In mitosis Pins:YFP also weakly localizes at the mitotic spindle. GFP:Mud localize at TCJs during interphase and mitosis (see also f). *n*=24 cells (c, left); *n*=19 cells (c, right); *n*=80 cells (d, left); *n*=12 cells (d, right); *n*=111 cells (e, left) and 54 cells (e, right).

(**f**) GFP:Mud time-lapse images from G2 interphase to telophase (*n*=21 cells). White arrows: GFP:Mud at TCJ (numbered at t=-22min). Red and yellow arrowheads: GFP:Mud on the spindle and its poles, respectively. The same panels -22min to 4min are shown in Fig.1a. See also Supplementary Video 1.

(**g**) Apical-basal (AB) sections of the cell in (f) at t=-22min (top) and t=-1min (bottom). White arrows: GFP:Mud at TCJ. *n*=21 cells.

(**h**) GFP:Mud kymograph along the cortex (x axis) from t=-22 to t=0 min of the cell in (f). TCJ numbered as in (f). The kymograph shows that during mitotic rounding GFP:Mud spread only modestly along the cortex of the dividing cell. *n*=21 cells.

(**i**) AB sections of GFP:Mud, adherens junction marker E-Cad and septate junction marker Dlg (top, *n*=16 cells) or septate TCJ marker Gli (bottom, *n*=30 cells).

(**j-m**) Localizations of GFP:Mud (white in j-m and green in j”-m”) and Gli (white in j’-m’ and red in j”-m”) in fixed pupal wing (j-k) and larval wing disc (l-m) tissues. GFP:Mud colocalizes with Gli at TCJ in G2 interphase and mitotic cells in both the pupal wing and larval wing disc epithelium. Asterisks mark Mud punctate structures present on the nuclear envelope of early G1 cells. Yellow arrows indicate GFP:Mud on the spindle poles. *n*=20 cells (j-j’’); *n*=5 cells (k-k’’); *n*=63 cells (l-l’’) and *n*=12 cells (m-m’’).

(**n-o**) Localizations of Mud (white in n, o and green in n”, o”) and Gli (white in n’, o’ and red in n”, o”) detected by antibody staining in G2 interphase and mitotic cells in the pupal dorsal thorax tissue. As observed for GFP:Mud (Fig. 1b and Extended data Fig. 1j-m), the endogenous Mud is enriched at TCJ where it co-localizes with Gli in G2 interphase and mitotic cells. Yellow arrows indicate Mud on the spindle poles. *n*=37 cells (n-n’’) and *n*=21 cells (o-o’’).

Scale bars: 1μm (a, c, d, e, f, g, i, j, k, l, m, n, o). 3 min (h).

Extended Data Figure 2: GFP:Mud localizes at TCJ from G2 interphase to mitosis.

(**a**) Scheme depicting the accumulation of the *Drosophila* FUCCI reporters during the cell cycle. ECFP:E2F1 accumulates during G1 phase, G2 phase and mitosis, whereas mRFP1:CycB accumulates during S phase, G2 phase and mitosis[55].

(**b**) Localization of GFP:Mud (green left column and white in the second column panels), mRFP1:CycB (red in the left column and white in the third column panels) and ECFP:E2F1 (blue in the left column and white in the right column panels) in epithelial cells of the pupal notum tissue. Confocal sections at the level of septate junctions are shown. Cells in G1 (n=21), S (n=6), G2 (n=35) phases and mitosis (n=6) are indicated in the left panels. During both G1 and S phase (upper two row panels), GFP:Mud is weakly localized at the nuclear envelope membrane, weakly localized at the cortex and at the apically localized centrioles (not shown). During G2 phase GFP:Mud becomes prominently localized at the TCJ (one cell in the 1st row panels and 2 cells in the 3rd row panels). Arrows indicate examples of TCJ GFP:Mud accumulation. During mitosis GFP:Mud remains localized at the TCJ and accumulates on the spindle and the spindle pole (bottom row panels). Similar results were obtained on fixed tissue for which the cell cycle phases were determined using the PCNA S-phase marker and the nucleus size to distinguish cells in G1 or G2 interphases (not shown).

(**c**) GFP:Mud (green arrows) and ChFP:Mud (red arrows) in adjacent tissue patches in G2 (n=31) and mitotic (n=8) cells. The FLP/FRT system was used to generate adjacent groups of cells labelled with either GFP:Mud or ChFP:Mud. By analysing the distribution of GFP:Mud in dividing cells adjacent to ChFP:Mud interphasic cells, we found that GFP:Mud was localized at the TCJs of the dividing cell from G2 through mitosis.

Scale bars: 1μm (b, c).

Extended Data Figure 3: Regulation of Dlg, Gli and Mud localization in epithelial tissue.
(**a,b**) Localizations of Gli (white in a and green in a', *n*=2 clones) and Dlg (white in b and green in b', *n*=3 clones) in fixed notum tissues harbouring *mud* clones (identified by loss of mRFP:nls, red in a'-b'). The loss of Mud function does not modify the Gli and Dlg localizations at septate junctions.
(**c**) Localization of Gli (white in c and green in c') in fixed notum tissue harbouring a clone of *dlg* (identified by the loss of mRFP:nls, red in c', *n*=13 clones). The loss of Dlg function results in a loss of Gli localization at TCJ.
(**d**) Localization of Dlg:GFP (white in d and green in d') in live epithelial dorsal thorax tissue harbouring a *Gli* clone (identified by expression of PH:ChFP, red in d', *n*=5 clones). The loss of Gli function does not affect the distribution of Dlg:GFP at the septate junctions.
Scale bars: 5μm (a, b, c, d).

Extended Data Figure 4: Astral MTs contact Mud at the TCJ.

(**a,a'**) Time-lapse images of ChFP:Mud (green in a and top panels a', white in bottom panel a') and of Jupiter:GFP (red in a and top panels a', white in middle panel a') in dividing cells (n=11) in the *Drosophila* pupal notum tissue. The panels in a' are magnifications of the boxed region in a. Yellow arrow points at an astral MT that contact ChFP:Mud at the cortex and shortens concomitant to the spindle pole movement towards the TCJ and spindle rotation. The dashed line corresponds to the initial spindle orientation and the solid lines correspond to its orientation at the final time point (see Supplementary Video 2). Similar results were obtained in cells expressing GFP:Mud and Tub:RFP to label the MTs (data not shown).

(**b**) Schematic of the laser-ablation assay used to estimate the origin and magnitude of forces on astral MT required for spindle orientation in the *Drosophila* pupal dorsal thorax epithelium. Upon ablation (red lines, top), pulling forces (green arrows, left column) or pushing forces (green arrows, right column) yield recoil away (grey arrow, left column) or toward the ablation site (grey arrow, right column), respectively.

Scale bars: 1μm (a).

Extended Data Figure 5: A large proportion of mitotic spindles remain planar in the absence of Mud, Dlg and Dynein function.

Loss of Mud activity is known to induce defects in mitotic spindle orientation relative to the apical-basal axis (AB) of the cell[31,34,56]. Nonetheless, in *mud*, *dlg*, *dynein* (gl^{DN}) mutant cells around 50% of the epithelial cell divide with an AB angle (α_{AB}) in the range of the wt tissue (a-e). Since a large proportion of the spindles remain within the plane of the tissue, all analyses reported in the manuscript were performed on cell divisions that occurred within the plane of the tissue. Furthermore, in a central region of the tissue (box in f and f'), 88% of the divisions in *mud* tissue occur with an α_{AB} in the range of the wt tissue (g). This region was analysed to compare TCJ bipolarity and cell shape based predictions of division orientation in wt and *mud* tissue (Fig. 3h-h').

(**a**) AB views of a dividing epithelial cell in a wt (left panel, out of 257 cells quantified in b) or *mud* (right panels, out of 176 cells quantified in b) tissue. The spindle is labelled using Jupiter:GFP (green) and the centrosomes using Sas-4:RFP (red). α_{AB} varies from 0° (spindle parallel to the plane of the tissue) to 90° (spindle perpendicular to the plane of the tissue).

(**b**) Quantification of α_{AB} in wt, *mud* and in *mud* tissue expressing GFP:Mud (*mud, GFP:Mud*). In wt tissue, α_{AB} varies between 0 and 22° (blue dashed line). In *mud* tissue, 56% of cells divide with a α_{AB} angle lower than 22° (dashed red lines). The expression of GFP:Mud in *mud* tissue rescues the spindle AB orientation phenotype caused by Mud loss of function. Numbers of cells (*n*) for each genotype are indicated. The distribution of angles in *mud* tissue is significantly different from wt ($p<10^{-4}$), and is restored in *mud, GFP:mud* ($p<10^{-4}$). *p* values, Kolmogorov-Smirnov test.

(**c**) Quantification of α_{AB} in wt , *Gαi* and *pins*. The loss of either Gαi or Pins function does not affect the orientation of the spindle relative to the plane of tissue ($p>0.3$) in agreement with our findings that Mud localization at TCJ is independent of Pins and Gαi. The analysis in *pins* tissue confirmed previously published findings[46]. Number of cells (*n*) are indicated. *p* value, Kolmogorov-Smirnov test.

(**d**, **e**) Quantification of α_{AB} in wt, *Gli* and *dlg* tissues at 25°C (d) and in wt and gl^{DN} tissues at 29°C (e). Gli loss of function does not affect α_{AB} orientation, whereas 46% of the *dlg* cells ($p<10^{-4}$) and 59% of the gl^{DN} cells ($p<10^{-4}$) divide with α_{AB} lower than 22° and 24°, respectively. Numbers of cells (*n*) are indicated. *p* values, Kolmogorov-Smirnov test.

(**f-f'**) Identification of a region of the notum where AB orientation of the spindle is not affected in *mud* mutant tissue. Defects in AB orientation of the mitotic spindle result in size asymmetry of the two daughter cells[57]. Therefore daughter cell size was initially used as a proxy for the magnitude of spindle misorientation along the AB axis in *mud* tissue. The maps of daughter cell size asymmetry in wt (f) and *mud* (f') tissues (green, no size asymmetry; purple strong size asymmetry) revealed that a region (highlighted by the black box, f, f') in the *mud* notum tissue exhibits almost no defects in daughter cell size asymmetry. Accordingly the quantification of spindle AB orientation within the region in wt and *mud* tissue revealed that 88% of the cells of the region divide within the range of the wt cells (see g).

Anterior is to the right and the dashed back line indicates the midline. Colour coding; purple: daughter cells with strong size asymmetry, green: daughter cells with normal size symmetry, cyan: cells for which no division was detected, grey: cells which left the field of view and were not analysed, yellow: macrocheatae, white: sensory organ precursors (SOPs).

(**g**) Quantification of α_{AB} in wt and *mud* tissue in the boxed regions in f-f' was performed as in b-e. Numbers of cells (*n*) for each genotype are indicated.

Scale bars:1 μm (a), 100 μm (f-f').

Extended Data Figure 6: Spindle orientation modelling.

(**a**) Mitotic cell in the *Drosophila* pupal notum labelled with Jupiter:GFP to label MTs (n=23 cells). White arrows point at astral MTs. Yellow arrowheads indicate spindle poles. Scale bar: 1μm.

(**b**) Representation of the different parameters that were varied for the predictions based on the GFP:Mud cortical intensity and shape model to estimate their contribution. L: length of the mitotic spindle, N: number of astral MTs, Φ: the angle covered by the astral MTs and α: the GFP:Mud intensity scaling factor. See also Supplementary Table 1.

(**c-f**) Cumulative plots of the differences between the theoretical spindle orientation (θ_{theory}) and the experimental spindle orientation ($\theta_{division}$) angles in GFP:Mud expressing cells (same cells as in Fig. 2h) for different spindle lengths (c), MT number (d), angular extension of astral MTs (e) and different scaling factor between the GFP:Mud intensity and mechanical pulling force (f). The GFP:Mud model predictions are mostly independent of spindle length, the number of astral MTs, the angle covered by the astral MTs or the scaling factor between GFP:Mud intensity and MT pulling force.

(**g**) Dependence of model prediction on shape or GFP:Mud effective potential depth (±s.e.m.). The y-axis quantitates the difference between the theoretical angle (θ_t) and experimental angle (θ_d) (1: aligned, -1: perpendicular). A larger potential depth corresponds to more deformed cells for the shape model, and to a sharp and anisotropic GFP:Mud distribution for the cortical model. Model predictions improve with potential depth, suggesting the model can capture the effect of GFP:Mud distributions in a dose-dependent manner. n=140 cells

(**h**) Definitions of the angles used in the analytical calculation of the contribution of different harmonics to the potential $U(\theta)$. The spindle (heavy black line) makes an angle θ with the positive x axis. An astral MT (thin black line indicated by the black arrow) projects to the cortex (circle) at an angle ϕ with respect to the spindle. The same MT contacts the cortex an angle $\beta = \psi + \theta$ above the positive x axis.

(**i**) Normalized magnitudes $|\tilde{u}_n|/|\tilde{u}_2|$ of the Fourier coefficients of the kernel $\tilde{u}(\psi)$ for n even. The magnitudes $|\tilde{u}_n|$ drop off substantially with increasing n, indicating that for many purposes it should be sufficient to approximate the function U by its lowest, $n = 2$ mode. To calculate numerical values for the Fourier coefficients, we took the average of the normalized spindle length $\epsilon = L/2R$ for the 140 cells (n) analysed in this paper, obtaining $\bar{\epsilon} \approx 0.76 \pm 0.03$; because it is difficult to precisely estimate Φ from the available data, coefficients are shown for $\Phi = 180°$ and $270°$ in agreement with the astral MT distribution observed in a.

(**j**) Schematic illustrating the difference between cell shape and cell TCJ bipolarity measurements. An elongated cell and a rounded cell are overlaid (left panels) and shown side-by-side (middle and right panels). In this example, although the two cells have distinct shapes, they have the same TCJ bipolarity. The upper panels illustrate the measurement of cell shape, which uses all the pixels making up the cell (blue bars). The lower panels illustrate the measurement of TCJ bipolarity (red bars), which is solely based on the angular distribution of the TCJs (red dots), only using the unit vectors $\overrightarrow{u_v}$ pointing from the cell center (black dot) to each cell TCJ. The TCJ bipolarity therefore characterizes TCJ distribution independently of cell shape, and a correlation observed between the two quantities is not due to a shape bias in the TCJ bipolarity measurement.

Extended Data Figure 7: Pins does not contribute to Mud-dependent epithelial cell division orientation.

(**a**) Rose plots of the difference between the theoretically predicted (θ_{theory}) and the experimental division ($\theta_{division}$) orientation of the mitotic spindle in *pins* tissue (orange left rose plot) and wt tissue (green right) based on the GFP:Mud intensity. To facilitate the comparison between the left and the right rose plots, the data are duplicated relative to 0° line (light orange and light green).Number of cells (*n*) analysed is indicated. *p* value, Kolmogorov-Smirnov test.

(**b**) Quantifications of the co-localization of GFP:Mud with Gli in *pins* in metaphase cells (±s.e.m.). Number of cells (*n*) analysed is indicated. ns: not significant (Student *t*-test).

Extended Data Figure 8: Structure-function analyses of the Mud protein in epithelial cells.

(**a**) Diagram of the domains of the Mud protein: putative actin binding calponin homology domain (CH, aa 1-246, blue), coiled-coil domain (CC, aa 246-1868, grey), conserved Numa/Lin-5/Mud domain (NLM, aa 1968-1998, red), putative transmembrane domain (TM, aa 2456-2499, yellow), 9x repeat domain (aa 1137-1515), MT binding domain (MT, aa 1850-2039) and Pins binding domain (aa 1928-1982)[58-60]. GFP or ChFP tagged deletion constructs and the MudΔCH constructs were generated by BAC recombineering (see Supplementary Methods for details). The MudΔC allele was generated at the *mud* locus using a CRISPR/Cas9 approach (see Supplementary Methods for details). For each mutant allele, its localization at the TJCs and its localization at the spindle pole are indicated.

(**b**) Localization of the GFP:Mud, MudΔCH, GFP:MudΔCC, GFP:MudΔPINS, GFP:MudΔTM and in G2 interphase and mitotic *mud* epithelial cells. GFP:Mud, GFP:MudΔCC, GFP:MudΔPINS, GFP:MudΔTM proteins were imaged in living tissue, whereas MudΔCH was localised on fixed tissue using Mud antibodies. GFP:Mud (n=56), MudΔCH (n=33), GFP:MudΔCC (n=165), GFP:MudΔPINS (n=42) and GFP:MudΔTM (n=67) interphase cells. GFP:Mud (n=15), MudΔCH (n=4), GFP:MudΔCC (n=67), GFP:MudΔPINS (n=18) and GFP:MudΔTM (n=11) mitotic cells.

(**c**) Localization of the $Mud^{\Delta C}$ protein (white in the left panels, green in the right panels), Gli (white in the panels in the middle and red in panels at the right) and Cora (magenta in the right panels) in fixed G2 interphase (n=71) and mitotic (n=6) cells. The $Mud^{\Delta C}$ protein is not enriched at TJCs and its localization at the spindle pole is strongly reduced.

(**d**) Rose plots of the difference between the theoretically predicted (θ_{theory}) and experimental ($\theta_{division}$) spindle orientation angles in wt (left rose plot, green) and *mud* (right rose plot, orange) tissues based on the distribution of GFP:MudΔCC. The right rose plot is identical to the one shown in Fig. 2l. To facilitate the comparison between the left and the right rose plots, the data are duplicated relative to 0° line (light green and light orange). Number of cells (n) analysed is indicated. p value, Kolmogorov-Smirnov test.

Scale bars: 1 μm (b, c).

Extended Data Figure 9: Predicting cell division based on TCJ distribution.

(**a-a"**) Rose plots of the magnitude of the difference between experimental ($\theta_{division}$) and predicted division orientations by the average (60-30 min prior to mitosis) interphase TCJ bipolarity (θ_{TCJ}) or cell long-axis (θ_{shape}) in cells for the indicated $\left|\theta_{TCJ} - \theta_{Shape}\right|$ intervals. To facilitate the comparison between the left and the right rose plots, the data are duplicated relative to 0° line (light blue and light red). Kolmogorov-Smirnov test (p values), percentage of total cells (n=29388). Panels b and b" are identical to panels e and e' in Fig. 3.

(**b-b"**) Rose plots of the magnitude of the difference between experimental ($\theta_{division}$) and predicted division orientations by the average (60-30min prior to mitosis) interphase TCJ bipolarity (θ_{TCJ}) or cell long-axis (θ_{shape}) for the indicated η_{shape} intervals. To facilitate the comparison between the left and the right rose plots, the data are duplicated relative to 0° line (light blue and light red). Kolmogorov-Smirnov test (p values), percentage of total cells (n=29388). Panels c and c" are identical to panels f and f' in Fig. 3.

(**c**) Plot of the spindle orientation prediction improvements (color-coded from dark blue to red) based on TCJ bipolarity over those based on cell shape versus the magnitude of their angular difference ($\left|\theta_{TCJ} - \theta_{shape}\right|$) and the cell shape anisotropy (η_{shape}). The plot height is the normalized cell number in each domain of the plot (29883 cell were analysed in total). As $\left|\theta_{TCJ} - \theta_{shape}\right|$ increases, the TCJ bipolarity predictions improve over cell shape prediction for both rounded (low η_{shape}) and elongated cells (high η_{shape}). Whereas the rounded cells are characterized by an even distribution along the $\left|\theta_{TCJ} - \theta_{shape}\right|$ axis, the elongated cells are mainly characterized by a strongly skewed distribution towards low $\left|\theta_{TCJ} - \theta_{shape}\right|$.

Extended Data Figure 10: TCJ bipolarity aligns with mechanical stress.

(**a**, **b**) Images of the scutellum tissue before and after ablation (ablated region in yellow) in early and late pupa characterized by small isotropic stress (a) and high anisotropic stress (b). Tissue stress was estimated by determining the initial recoiled velocity upon circular ablation in the x and y directions[53]. First and last images of two time-lapse movies out of the 18 quantified in c are shown. Scale bars: 10μm (a, b).

(**c**) Plot of the difference between the orientation of TCJ bipolarity (θ_{TCJ}) and principal strain axis (θ_{strain}) as a function of normal stress differences ($\sigma_{yy} - \sigma_{xx}$, note that $\sigma_{xy} = 0$) as estimated up to a prefactor by circular laser ablation. Number of ablations (n) analysed is indicated. The same plot is shown in Fig. 4d.

(**d**) Plot of the difference between the orientation of TCJ bipolarity (θ_{TCJ}) and the orientation of strain (θ_{strain}) as a function of the percentage of cell elongation applied to a simulated cell lattice. When cell elongation increases TCJ bipolarity orientation becomes aligned with the direction of cell elongation. Number of simulations (n) analysed is indicated.

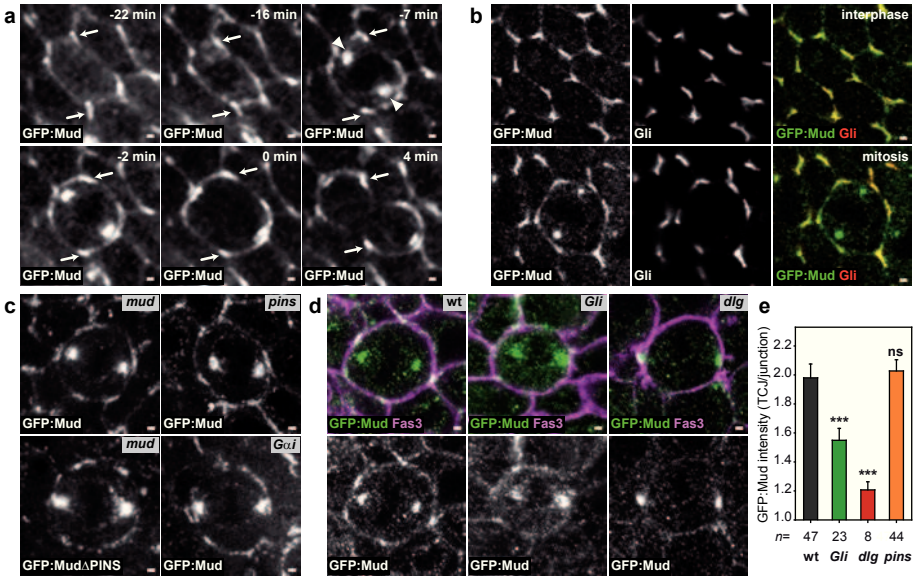
a
-22 min
-16 min
-7 min
GFP:Mud
-2 min
0 min
4 min
b
interphase
Gli
GFP:Mud Gli
mitosis
c
mud
pins
GFP:MudΔPINS
Gαi
d
wt
Gli
dlg
GFP:Mud Fas3
e
GFP:Mud intensity (TC:J/junction)
ns
***
n= 47 23 8 44
wt Gli dlg pins

Figure 1

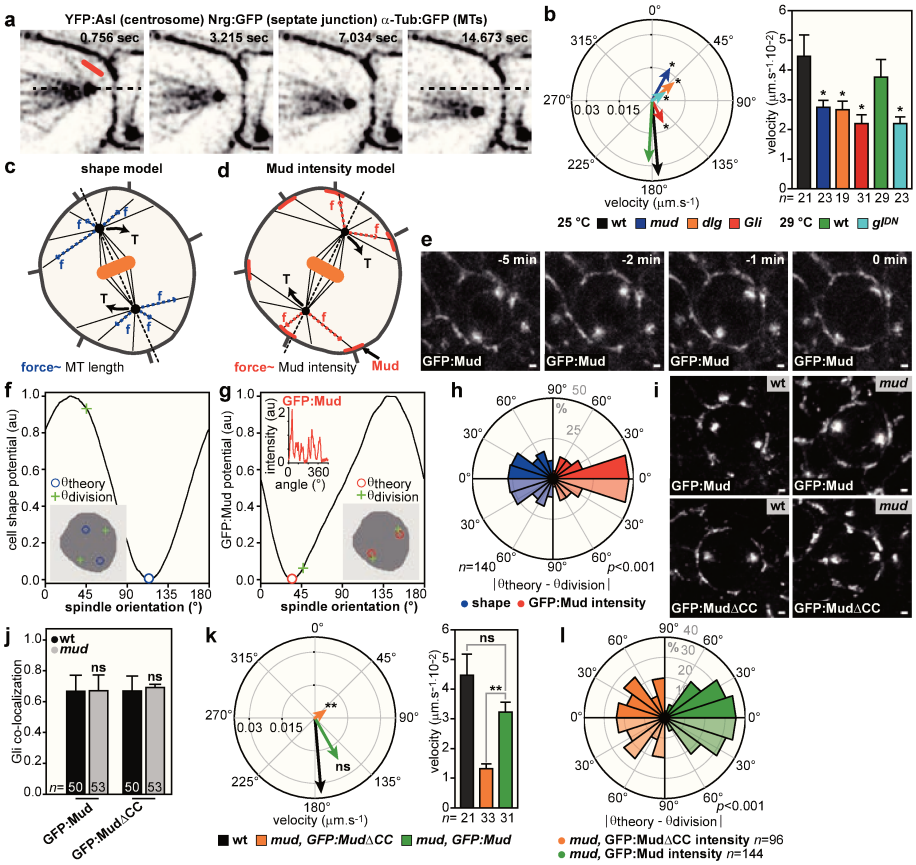
a
YFP:Asl (centrosome) Nrg:GFP (septate junction) α-Tub:GFP (MTs)
0.756 sec
3.215 sec
7.034 sec
14.673 sec
b
velocity (μm.s-1)
velocity (μm.s-1.10-2)
n= 21 23 19 31 29 23
25 °C wt mud dlg Gli
29 °C wt glDN
c
shape model
force~ MT length
d
Mud intensity model
force~ Mud intensity
Mud
e
-5 min
-2 min
-1 min
0 min
GFP:Mud
f
cell shape potential (au)
θtheory
+θdivision
spindle orientation (°)
g
GFP:Mud potential (au)
GFP:Mud
intensity (au)
angle (°)
h
n=140
p<0.001
|θtheory - θdivision|
shape GFP:Mud intensity
i
wt
mud
GFP:MudΔCC
j
wt
mud
Gli co-localization
ns
n= 50 53 50 53
GFP:Mud
GFP:MudΔCC
k
velocity (μm.s-1)
velocity (μm.s-1.10-2)
n= 21 33 31
wt mud, GFP:MudΔCC mud, GFP:Mud
l
p<0.001
|θtheory - θdivision|
mud, GFP:MudΔCC intensity n=96
mud, GFP:Mud intensity n=144

Figure 2

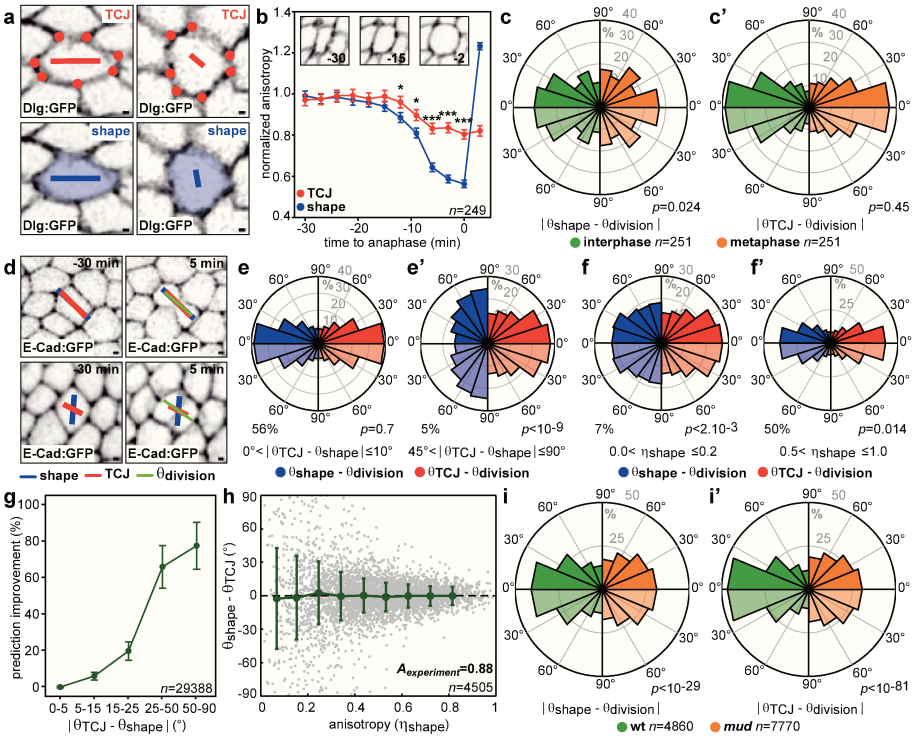
a
TCJ
Dlg:GFP
shape
b
normalized anisotropy
time to anaphase (min)
TCJ
shape
n=249
c
c'
p=0.024
p=0.45
interphase n=251
metaphase n=251
d
-30 min
5 min
E-Cad:GFP
shape
TCJ
θdivision
e
e'
56%
p=0.7
5%
p<10-9
0°<|θTCJ - θshape|≤10°
45°<|θTCJ - θshape|≤90°
f
f'
7%
p<2.10-3
50%
p=0.014
0.0< ηshape ≤0.2
0.5< ηshape ≤1.0
θshape - θdivision
θTCJ - θdivision
g
prediction improvement (%)
n=29388
|θTCJ - θshape| (°)
h
θshape - θTCJ (°)
Aexperiment=0.88
n=4505
anisotropy (ηshape)
i
i'
p<10-29
p<10-81
wt n=4860
mud n=7770

Figure 3

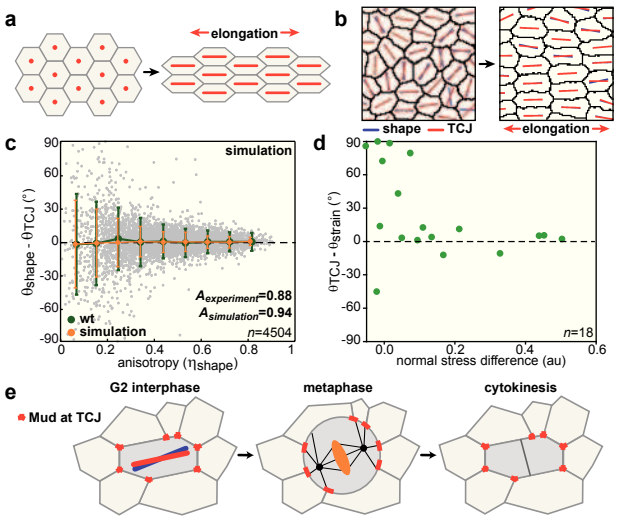
a
elongation
b
shape
TCJ
elongation
c
simulation
θshape - θTCJ (°)
anisotropy (ηshape)
wt
simulation
Aexperiment=0.88
Asimulation=0.94
n=4504
d
θTCJ - θstrain (°)
normal stress difference (au)
n=18
e
Mud at TCJ
G2 interphase
metaphase
cytokinesis

Figure 4

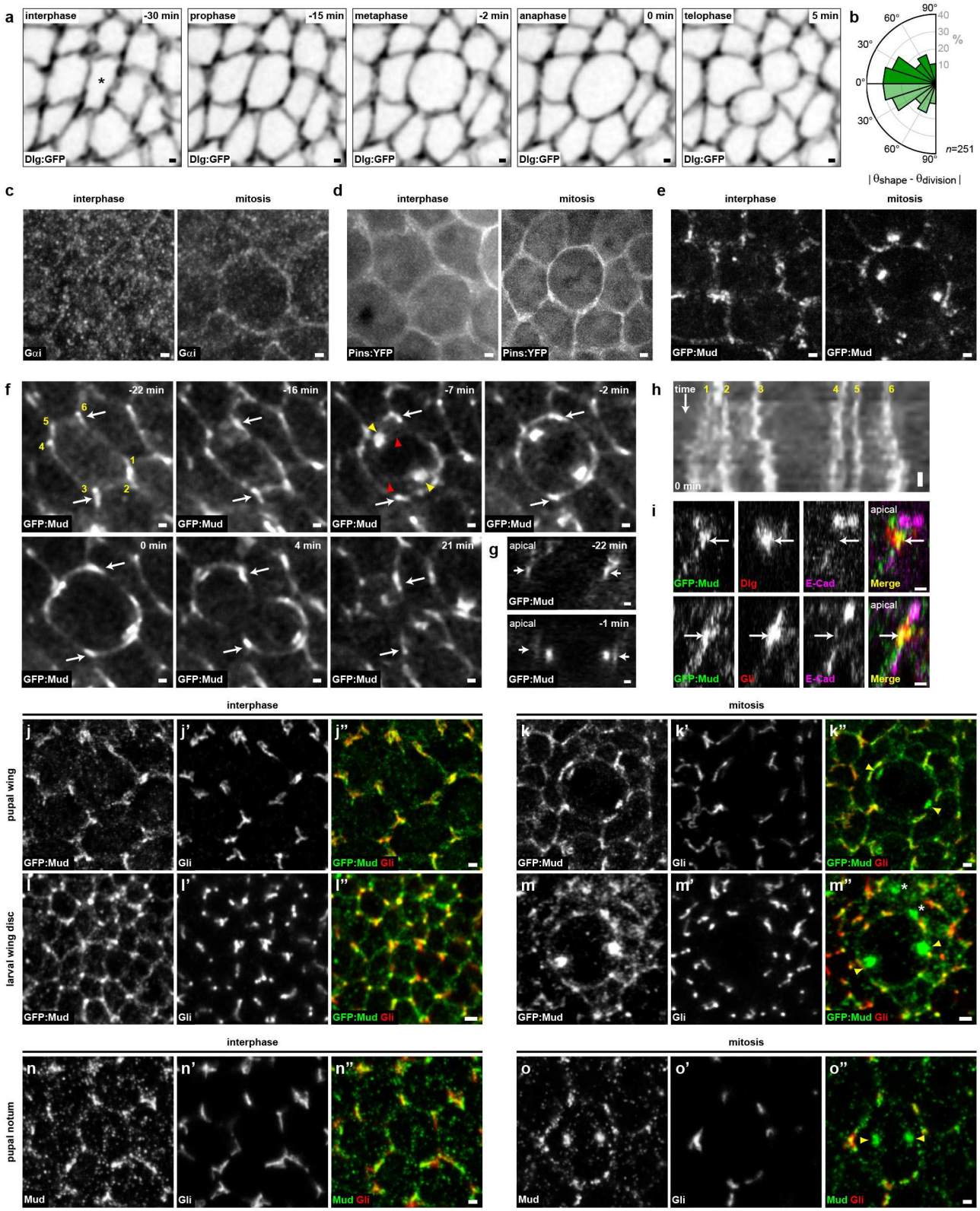

Extended Data Figure 1

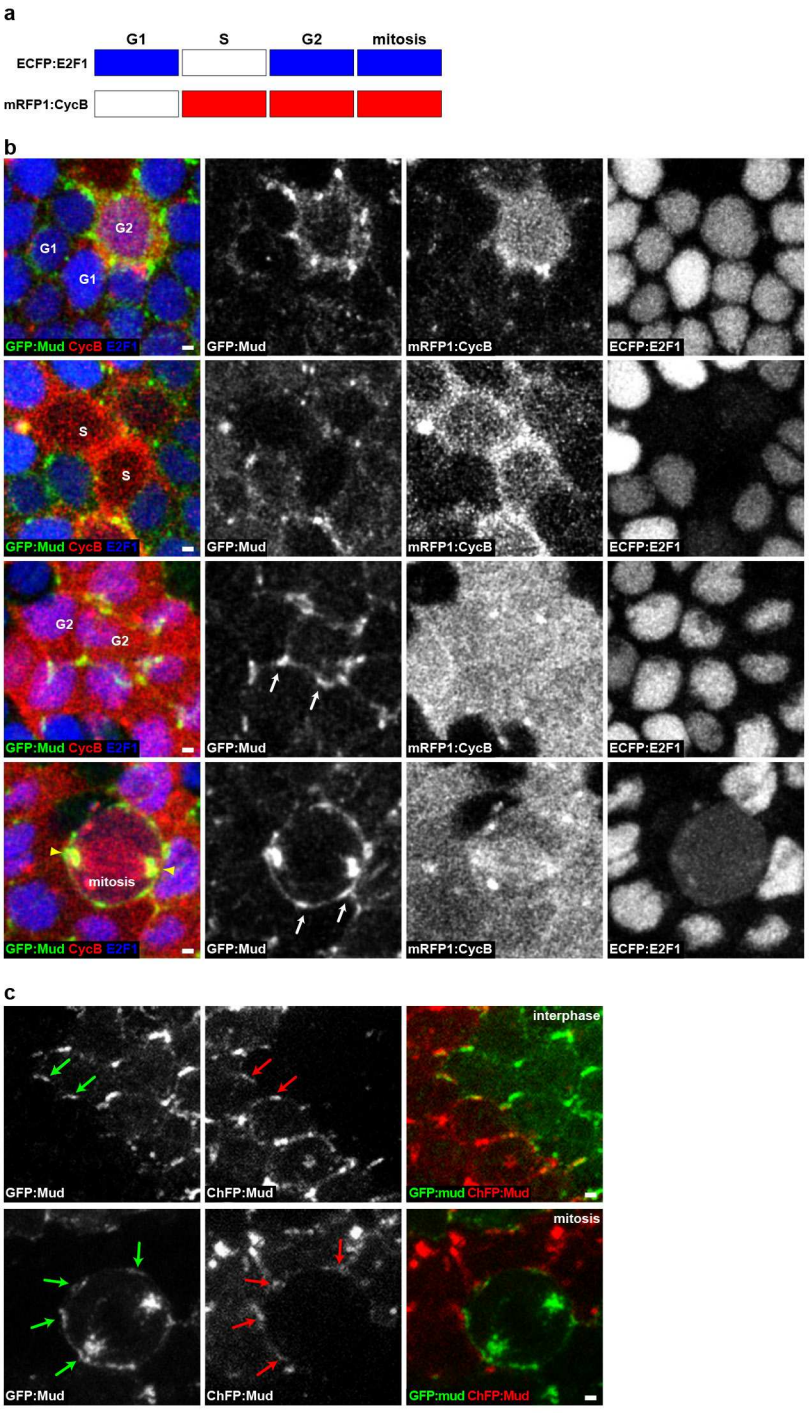
a
G1
S
G2
mitosis
ECFP:E2F1
mRFP1:CycB
b
G1
G2
G1
GFP:Mud CycB E2F1
GFP:Mud
mRFP1:CycB
ECFP:E2F1
S
S
GFP:Mud CycB E2F1
GFP:Mud
mRFP1:CycB
ECFP:E2F1
G2
G2
GFP:Mud CycB E2F1
GFP:Mud
mRFP1:CycB
ECFP:E2F1
mitosis
GFP:Mud CycB E2F1
GFP:Mud
mRFP1:CycB
ECFP:E2F1
c
GFP:Mud
ChFP:Mud
interphase
GFP:mud ChFP:Mud
GFP:Mud
ChFP:Mud
mitosis
GFP:mud ChFP:Mud

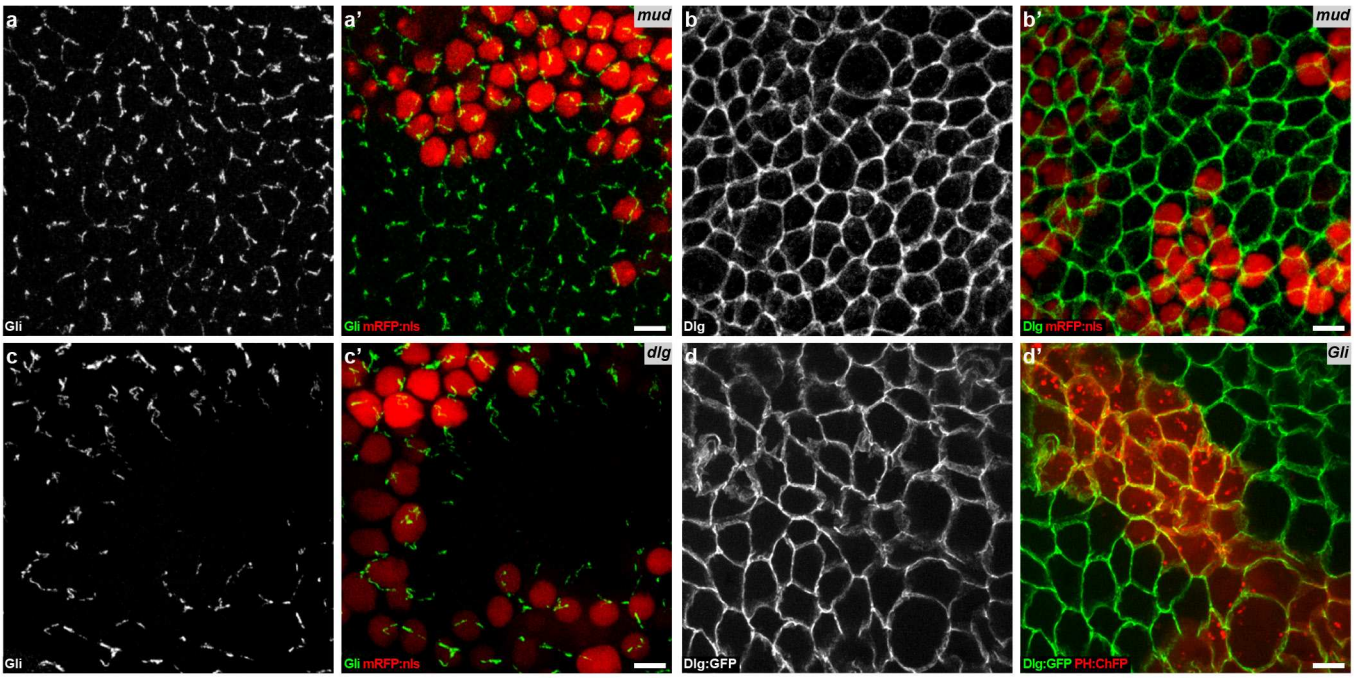

Extended Data Figure 3

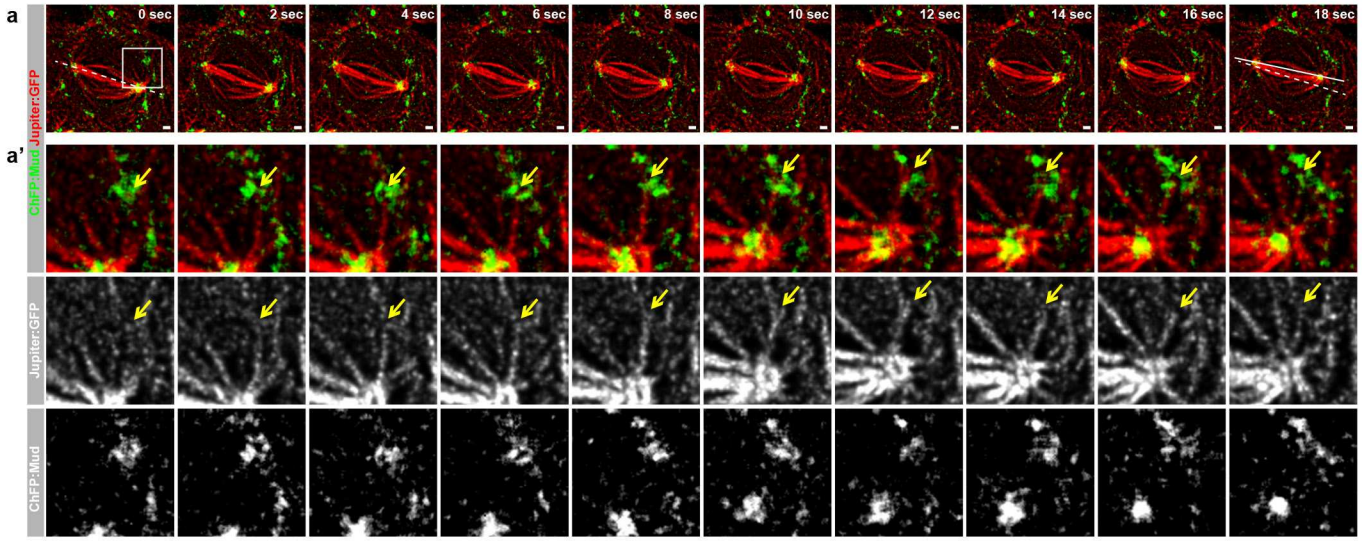

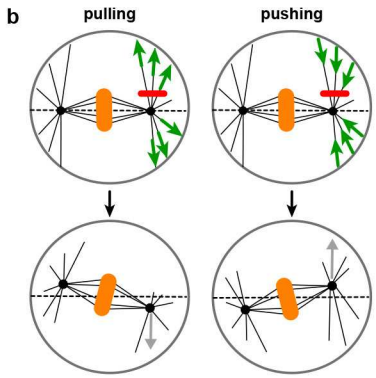

Extended Data Figure 4

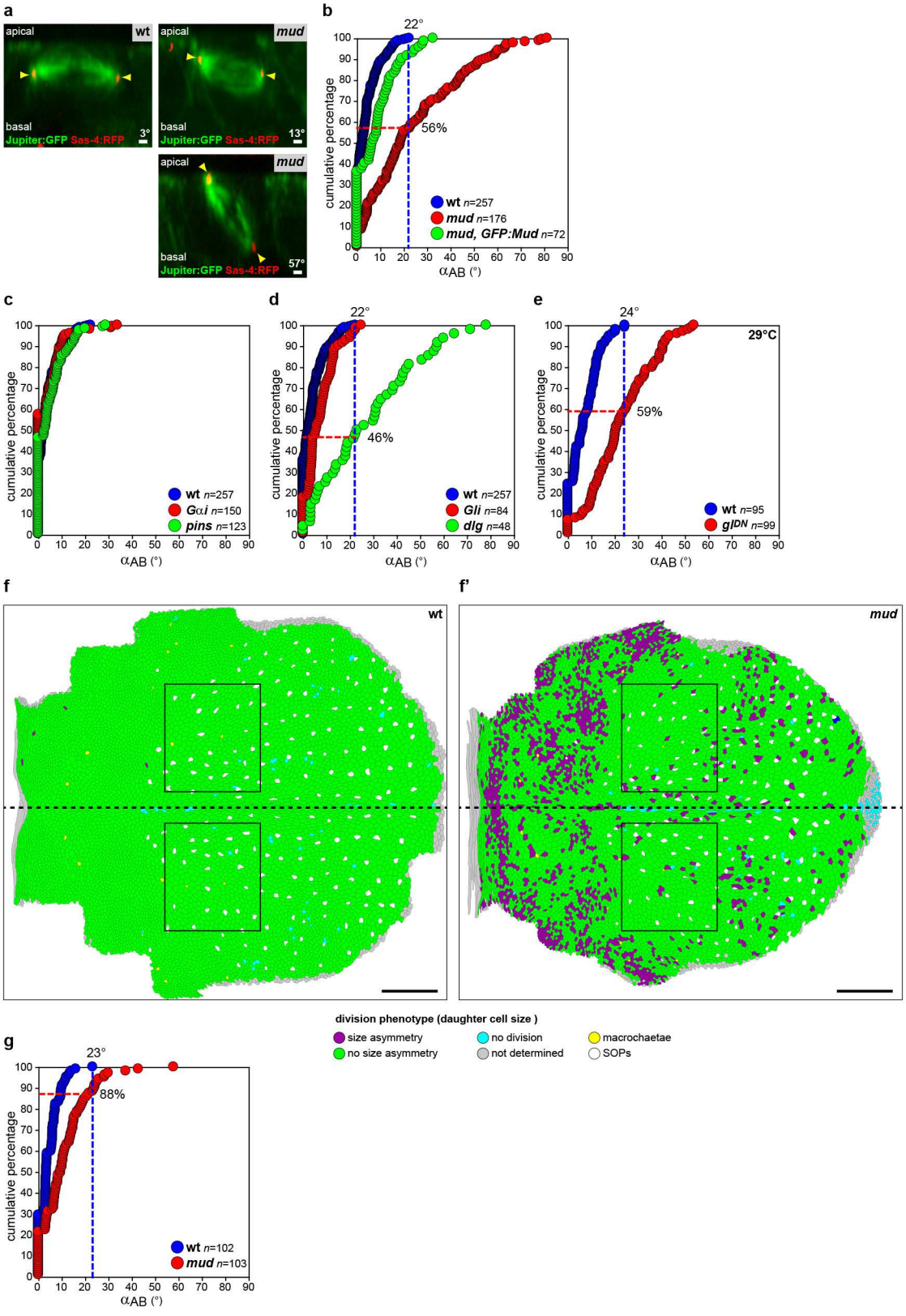
a
apical
wt
basal
Jupiter:GFP Sas-4:RFP
3°
apical
mud
basal
Jupiter:GFP Sas-4:RFP
13°
apical
mud
basal
Jupiter:GFP Sas-4:RFP
57°
b
22°
56%
cumulative percentage
αAB (°)
wt n=257
mud n=176
mud, GFP:Mud n=72
c
cumulative percentage
αAB (°)
wt n=257
Gαi n=150
pins n=123
d
22°
46%
cumulative percentage
αAB (°)
wt n=257
Gli n=84
dlg n=48
e
24°
29°C
59%
cumulative percentage
αAB (°)
wt n=95
glDN n=99
f
wt
f'
mud
division phenotype (daughter cell size)
size asymmetry
no size asymmetry
no division
not determined
macrochaetae
SOPs
g
23°
88%
cumulative percentage
αAB (°)
wt n=102
mud n=103

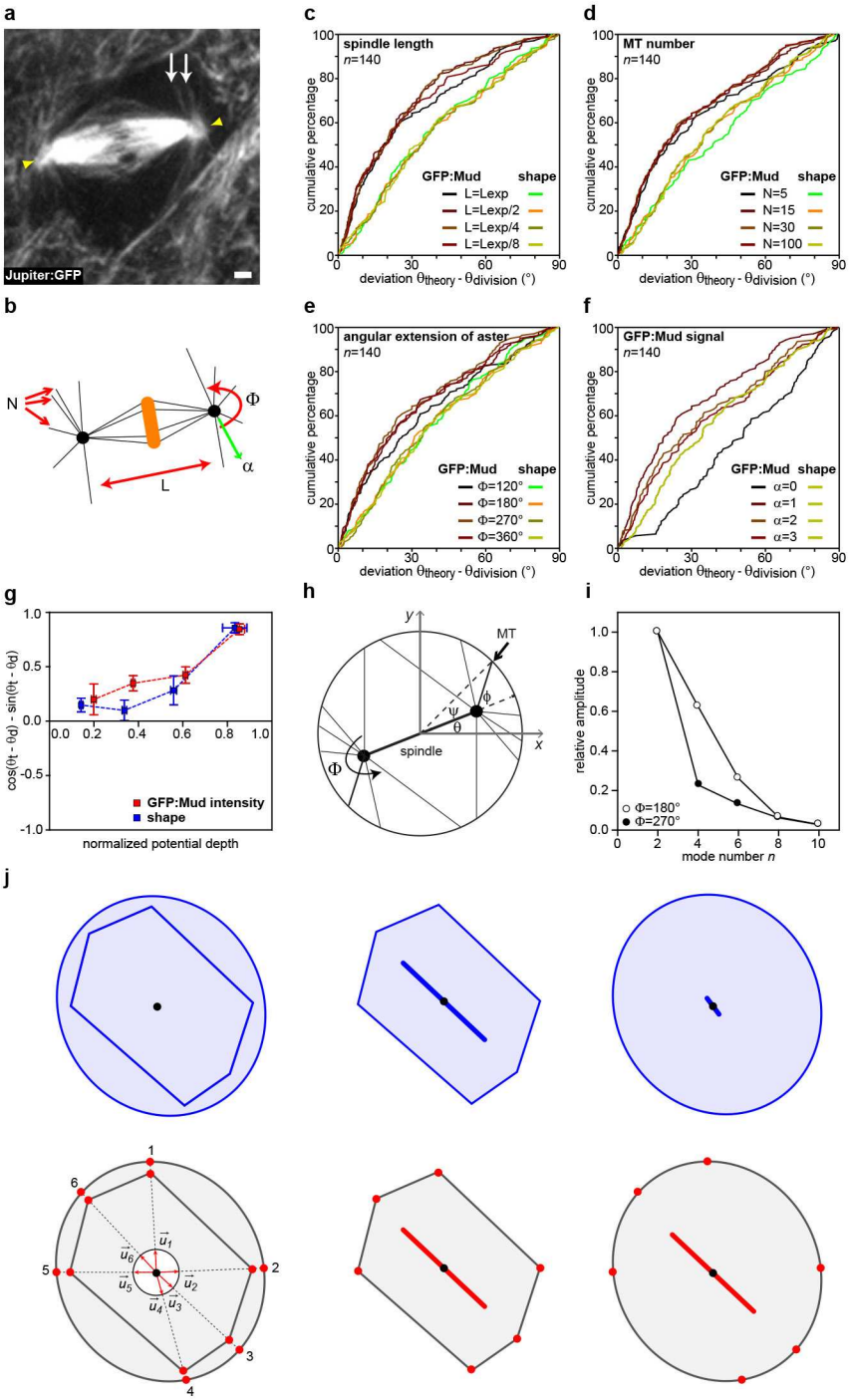

Extended Data Figure 6

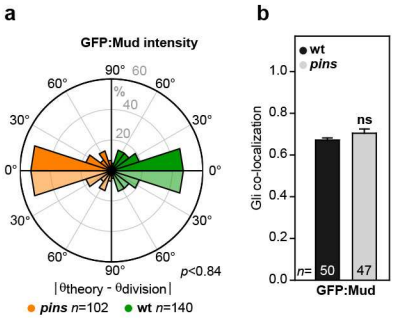

Extended Data Figure 7

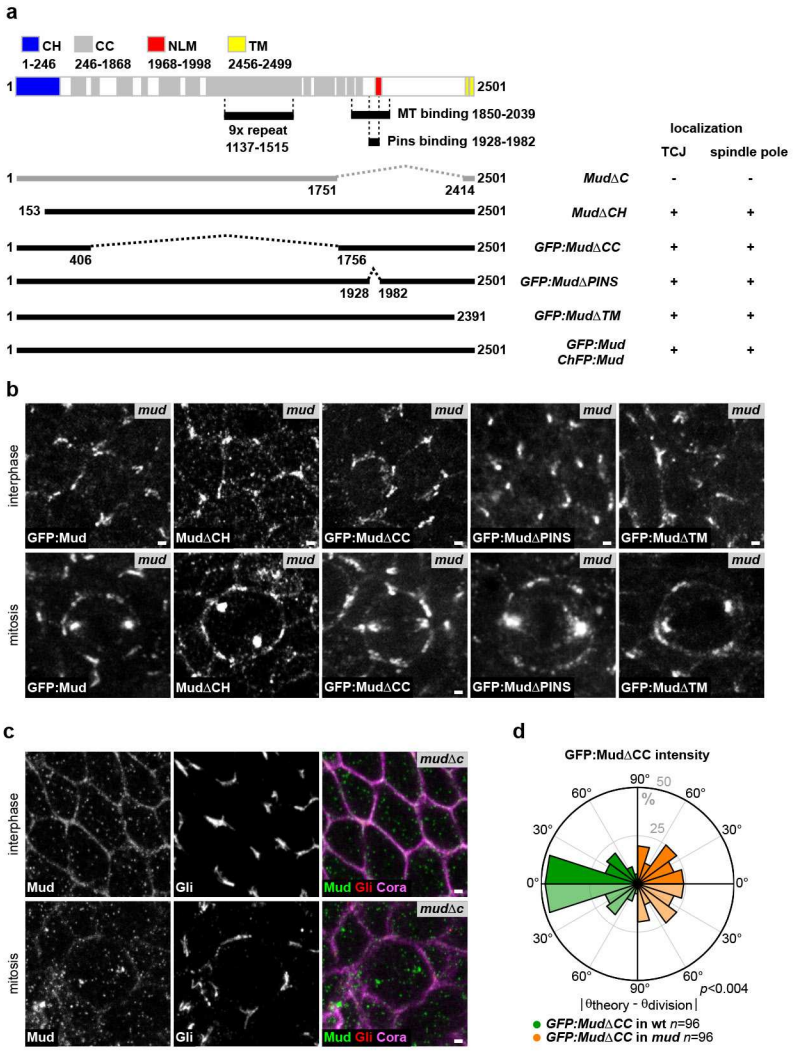
a
CH
CC
NLM
TM
1-246
246-1868
1968-1998
2456-2499
1
2501
9x repeat
1137-1515
MT binding 1850-2039
Pins binding 1928-1982
localization
TCJ
spindle pole
1751
2414
MudΔC
153
MudΔCH
406
1756
GFP:MudΔCC
1928
1982
GFP:MudΔPINS
2391
GFP:MudΔTM
GFP:Mud
ChFP:Mud
b
mud
interphase
mitosis
GFP:Mud
MudΔCH
GFP:MudΔCC
GFP:MudΔPINS
GFP:MudΔTM
c
mudΔc
Mud
Gli
Mud Gli Cora
d
GFP:MudΔCC intensity
90°
60°
30°
0°
50
%
25
p<0.004
|θtheory - θdivision|
GFP:MudΔCC in wt n=96
GFP:MudΔCC in mud n=96

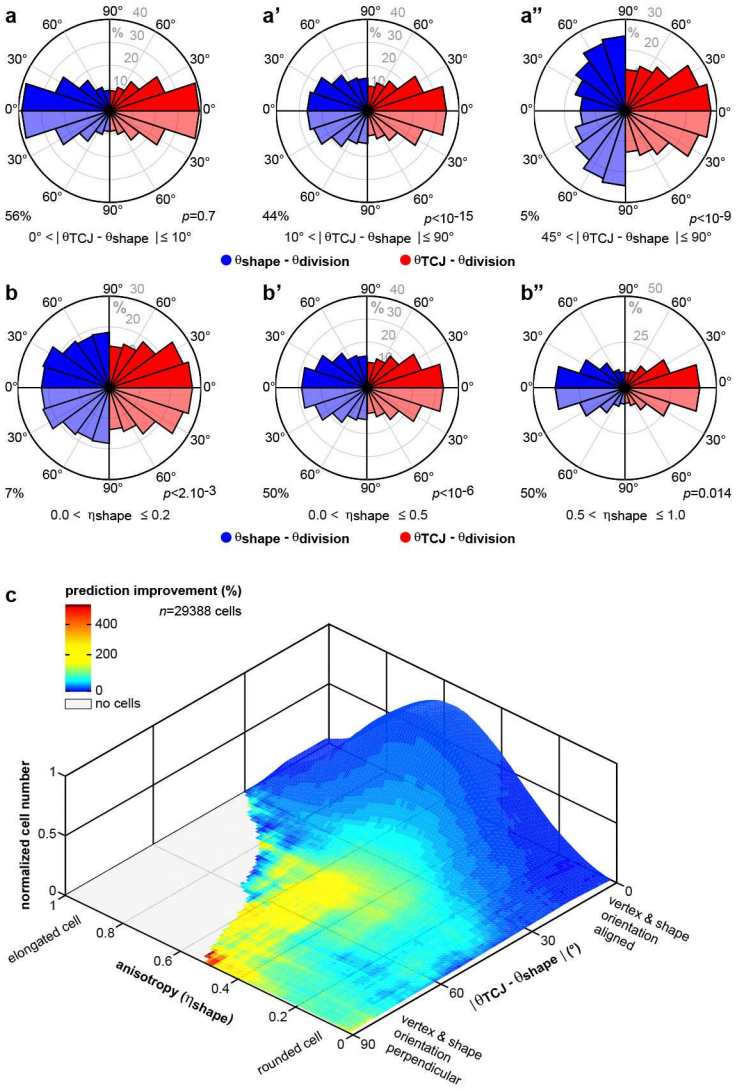

Extended Data Figure 9

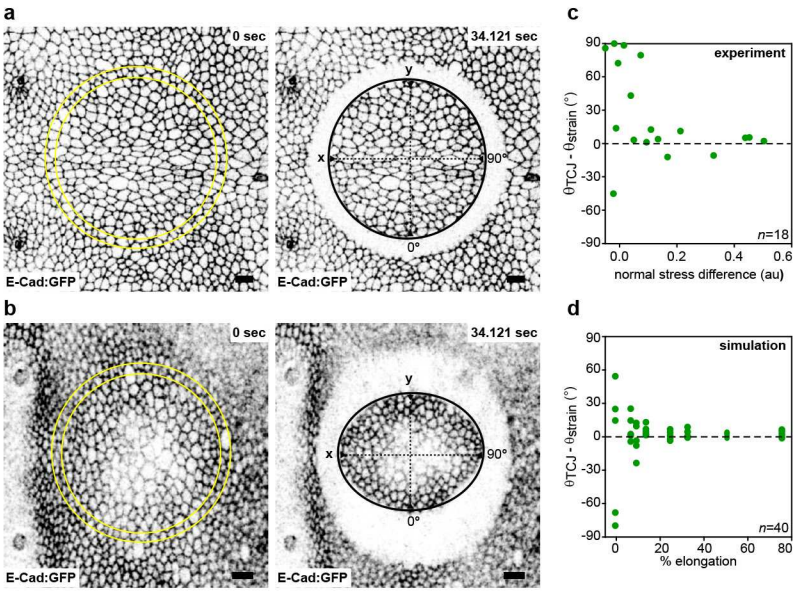

Extended Data Figure 10

Supplementary Information Guide.

The Supplementary Information includes Supplementary Tables 1 and 2, Supplementary Videos 1 to 8, Supplementary Theory Notes and Supplementary Codes.

2. SUPPLEMENTARY VIDEOS

Supplementary Video 1: 3D organisation of the dividing and neighbouring cell membranes.

3D segmentation of a PH::GFP expressing cell neighbouring a PH::ChFP dividing cell upon co-ingression of both cells' membranes during cytokinesis. White arrow: indicates the ingression of the PH::GFP neighbour in between the dividing cell membranes (see Extended Data Fig. 1a,b).

Scale bar: 5µm

Supplementary Video 2: Lowering contractile ring pulling forces in the dividing cell affects Myosin II accumulation in the neighbours.

(a) E-Cad::GFP and MyoII::mChFP localization in the dividing (D) cell and its neighbours (N) upon contractile ring laser ablation after MyoII::mChFP accumulation. Dashed box: ablated region. Time was set to 0s at the ablation time (see Fig. 1c).

(b) E-Cad::GFP and MyoII::mChFP localization in cells neighbouring *wt*, $pnut^{RNAi}$, rok^{RNAi} and ani^{RNAi} dividing cells (D) (see Fig. 1d-e and Extended Data Fig. 1p).

White arrows: MyoII::mChFP accumulation in the neighbouring cells. White open arrows: absence or decrease of MyoII::mChFP accumulation in the neighbouring cells.

Scale bars: 5µm

Supplementary Video 3: Myosin II accumulation in the neighbouring cells is preceded by cortex detachment and a decrease of E-Cad concentration at the ingressing AJ.

E-Cad::GFP and MyoII::mChFP localization in the dividing (D) cell and its neighbours (N). Time was set to 0s at cytokinesis onset. White asterisks: separation of the MyoII::mChFP and the E-Cad::GFP signals at the ingressing AJ. Yellow arrows: decrease of E-Cad::GFP signal at the ingressing AJs. White arrows: MyoII::mChFP accumulation in the neighbouring cells (see Fig. 2a,b).

Scale bar: 5µm

Supplementary Video 4: Cortex detachment is not sufficient to sustain MyoII accumulation in the neighbouring cells.

(a) E-Cad::GFP and MyoII::mChFP localization upon laser ablation of the initially detached cortical MyoII. Orange box: ablated region at t=0s. White arrows: MyoII::mChFP accumulation in the neighbouring cells upon laser ablation of the initially detached cortex (see Fig. 2d).
(b) E-Cad::GFP and MyoII::mChFP localization in cells neighbouring (N) $pnut^{RNAi}$ dividing cells (D). White asterisks: separation of cortical MyoII::mChFP from the ingressing AJs (see Extended Data Fig. 3g).
(c,d) MyoII::mChFP dynamics in moe^{RNAi} neighbouring cells (N, marked by the lack of cytosolic GFP; highlighted in (d) with white dots) during cytokinesis. Time was set to 0s at cytokinesis onset. (c) White asterisk: separation of MyoII::mChFP from the ingressing AJ. Yellow open arrow: decrease of E-Cad::GFP signal at the ingressing AJ. White arrow: MyoII::mChFP accumulation in the neighbouring cells (see Extended Data Fig. 3h). (d) White dashed boxes: inset regions. White arrowheads: detached cortical MyoII::mChFP coalesces with the MyoII::mChFP accumulation localized at the boundary of the high-low E-Cad::GFP signal. Open arrowheads: detached cortical MyoII::mChFP disassembles, while MyoII accumulates at the base of the ingressing AJ (see Extended Data Fig. 3i,j).
Scale bars: 5µm

Supplementary Video 5: Photoactivated E-Cadherin is diluted along the ingressing membrane during cytokinesis.
MyoII::3XmKate2 and a photoactivatable version of E-Cad, E-Cad::3XPAGFP during cytokinesis. The ingressing AJ is photoactivated at the rim of the contractile ring at the interface between the dividing (D) cell and its neighbour (N) (dashed box). Time is set to 0s at the time of E-Cad::3XPAGFP photoactivation (see Extended Data Fig. 5a,b).
Scale bar: 5µm

Supplementary Video 6: Lowering E-Cad concentration at the ingressing AJ triggers MyoII accumulation in cells neighbouring a *pnut* dividing cell.
E-Cad::3XGFP and MyoII::3XmKate2 distribution in a *pnut* mutant dividing (D) cell, marked by 2 copies of E-Cad::3XGFP, and its *E-Cad* mutant neighbour (N), marked by the absence of E-Cad::3XGFP. Time is set to 0s at cytokinesis onset. White dashed line: indicates the boundary with *E-Cad* mutant cells. White asterisk: separation of the MyoII::3XmKate2 and the E-Cad::3XGFP signals at the ingressing AJ. Bracket: decrease of E-Cad::3XGFP signal at the ingressing AJ. White arrow: MyoII::3XmKate2 accumulation in the neighbouring cells (see Fig. 3i-k).

Scale bar: 5µm

Supplementary Video 7: Actomyosin flows in the neighbouring cells.

(a) MyoII::RFP dividing (D) cell facing a MyoII::GFP neighbouring cell (N) upon photobleaching of the MyoII::GFP accumulation in the neighbours. Orange dashed box: photobleached region at t=0s. Arrowheads: MyoII::GFP speckles moving along the ingressing AJ and accumulating at its base (see Fig. 4d,e).

(b) MyoII::Dendra2 photoconversion at the rim of the contractile ring during cytokinesis. D: Dividing cell. N: Neighbouring cell. Red dashed box: photoconverted region at t=0s. Arrowhead: photoconverted MyoII::Dendra2 speckle moving with the ingressing AJ. White arrow: accumulation of photoconverted MyoII::Dendra2 in the neighbouring cells (see Fig. 4f).

(c,d) Lifeact::GFP (c) or Lifeact::Ruby (d) expressing neighbouring cells (N) facing a dividing cell (D) in a MyoII::3XmKate2 (c) or MyoII::3XGFP (d) tissue. Time was set to 0s at cytokinesis onset. Dashed Box: region shown in the insets (d). White Arrows: MyoII and Lifeact accumulation in the neighbours (see respectively (c) Fig. 4g,h and (d) Extended Data Fig. 9a,b) .

(e) Lifeact::Ruby expressing cell neighbouring a dividing cell (D) in a Dlg::GFP tissue at the level of the AJs (left panel) and of the Septate Junctions (right panel - 2µm below the apical plane). N: Neighbouring cell. Time was set to 0s at cytokinesis onset. F-Actin flows are observed apically, at level of the AJs (arrow) and not more basally, at the level of the Septate junctions (open arrow; see Extended Data Fig. 9e-g).

Scale bars: 5µm

Supplementary Video 8: Actomyosin flows are reduced in cells neighbouring a *pnut* dividing cell and in *rok* neighbouring cells facing a *wt* dividing cell.

(a) Lifeact::Ruby expressing neighbours (N) facing a $pnut^{RNAi}$ dividing (D) cell in a MyoII::3XGFP tissue. $pnut^{RNAi}$ cells express Lifeact::Ruby. White asterisks: separation of the MyoII::3XGFP signal at the tip of the ingressing AJ, highlighted by the contractile ring. White open arrows: reduced Lifeact::Ruby and MyoII::3XGFP flows in cells facing a $pnut^{RNAi}$ dividing cell (see Fig. 4i-l).

(b) *rok* neighbour (N), marked by Lifeact::GFP expression (white dots), facing a *wt* dividing (D) cell in a MyoII::3XmKate2 tissue. Time was set to 0s at cytokinesis onset. White open arrows: reduced Lifeact::GFP flows in *rok* neighbours (see Fig. 4m-p).

Scale bars: 5µm

3. SUPPLEMENTARY CODES

The three Supplementary Codes are provided as a single zip file.

Supplementary Code 1: E-Cad dilution.

Numerical integration of the dynamics of E-Cadherin on an elongating junction (written for Mathematica).

Supplementary Code 2: Actomyosin dynamics in one-dimension.

Numerical integration of the dynamics of actomyosin on a junction with variable friction in one-dimension (written for Mathematica).

Supplementary Code 2: Actomyosin dynamics in two-dimensions.

Numerical integration of the dynamics of actomyosin on a domain with variable friction in two-dimensions (written for Freefem++).

SUPPLEMENTARY REFERENCES

38. Bardet, P. L., Guirao, B., Paoletti, C., Serman, F., *et al.* PTEN Controls Junction Lengthening and Stability during Cell Rearrangement in Epithelial Tissue. *Dev Cell* **25,** 534-546 (2013).

39. Tabdanov, E., Borghi, N., Brochard-Wyart, F., Dufour, S. & Thiery, J. P. Role of E-cadherin in membrane-cortex interaction probed by nanotube extrusion. *Biophys J* **96,** 2457-2465 (2009).

40. Turlier, H., Audoly, B., Prost, J. & Joanny, J. F. Furrow constriction in animal cell cytokinesis. *Biophys J* **106,** 114-123 (2014).

41. Prost, J., Jülicher, F. & Joanny, J. F. Active gel physics. *Nature Physics* **11,** 111-117 (2015).

42. Brochard-Wyart, F. & de Gennes, P. -G. Unbinding of adhesive vesicles. *Comptes Rendus Physique* **4,** 281-287 (2003).

43. Fehon, R. G., McClatchey, A. I. & Bretscher, A. Organizing the cell cortex: the role of ERM proteins. *Nat Rev Mol Cell Biol* **11,** 276-287 (2010).

44. Grusche, F. A., Hidalgo, C., Fletcher, G., Sung, H. H., *et al.* Sds22, a PP1 phosphatase regulatory subunit, regulates epithelial cell polarity and shape [Sds22 in epithelial morphology]. *BMC Dev Biol* **9,** 14 (2009).

45. Lee, A. & Treisman, J. E. Excessive Myosin activity in mbs mutants causes photoreceptor movement out of the Drosophila eye disc epithelium. *Mol Biol Cell* **15,** 3285-3295 (2004).

46. Baum, B. & Perrimon, N. Spatial control of the actin cytoskeleton in Drosophila epithelial cells. *Nat Cell Biol* **3,** 883-890 (2001).

47. Truebestein, L., Elsner, D. J., Fuchs, E. & Leonard, T. A. A molecular ruler regulates cytoskeletal remodelling by the Rho kinases. *Nat Commun* **6,** 10029 (2015).

48. Simões, S. d. e. . M., Mainieri, A. & Zallen, J. A. Rho GTPase and Shroom direct planar polarized actomyosin contractility during convergent extension. *J Cell Biol* **204,** 575-589 (2014).

49. Munjal, A., Philippe, J. M., Munro, E. & Lecuit, T. A self-organized biomechanical network drives shape changes during tissue morphogenesis. *Nature* **524,** 351-355 (2015).

50. Lammel, U., Bechtold, M., Risse, B., Berh, D., *et al.* The Drosophila FHOD1-like formin Knittrig acts through Rok to promote stress fiber formation and directed macrophage migration during the cellular immune response. *Development* **141,** 1366-1380 (2014).

51. Oda, H., Tsukita, S. & Takeichi, M. Dynamic behavior of the cadherin-based cell-cell adhesion system during Drosophila gastrulation. *Dev Biol* **203,** 435-450 (1998).

52. Huang, J., Zhou, W., Dong, W., Watson, A. M. & Hong, Y. Directed, efficient, and versatile modifications of the Drosophila genome by genomic engineering. *Proc Natl Acad Sci U S A* **106,** 8284-8289 (2009).

53. Lye, C. M., Naylor, H. W. & Sanson, B. Subcellular localisations of the CPTI collection of YFP-tagged proteins in Drosophila embryos. *Development* **141,** 4006-4017 (2014).

54. Buszczak, M., Paterno, S., Lighthouse, D., Bachman, J., *et al.* The carnegie protein trap library: a versatile tool for Drosophila developmental studies. *Genetics* **175,** 1505-1531 (2007).

55. Kanca, O., Caussinus, E., Denes, A. S., Percival-Smith, A. & Affolter, M. Raeppli: a whole-tissue labeling tool for live imaging of Drosophila development. *Development* **141,** 472-480 (2014).

56. Winter, C. G., Wang, B., Ballew, A., Royou, A., *et al.* Drosophila Rho-associated kinase (Drok) links Frizzled-mediated planar cell polarity signaling to the actin cytoskeleton. *Cell* **105,** 81-91 (2001).

57. Matusek, T., Djiane, A., Jankovics, F., Brunner, D., *et al.* The Drosophila formin DAAM regulates the tracheal cuticle pattern through organizing the actin cytoskeleton. *Development* **133,** 957-966 (2006).

58. Bécam, I. E., Tanentzapf, G., Lepesant, J. A., Brown, N. H. & Huynh, J. R. Integrin-independent repression of cadherin transcription by talin during axis formation in Drosophila. *Nat Cell Biol* **7,** 510-516 (2005).

59. Neufeld, T. P. & Rubin, G. M. The Drosophila peanut gene is required for cytokinesis and encodes a protein similar to yeast putative bud neck filament proteins. *Cell* **77,** 371-379 (1994).

60. Strutt, D. I., Weber, U. & Mlodzik, M. The role of RhoA in tissue polarity and Frizzled signalling. *Nature* **387,** 292-295 (1997).

61. Yan, S., Lv, Z., Winterhoff, M., Wenzl, C., *et al.* The F-BAR protein Cip4/Toca-1 antagonizes the formin Diaphanous in membrane stabilization and compartmentalization. *J Cell Sci* **126,** 1796-1805 (2013).

62. Zallen, J. A., Cohen, Y., Hudson, A. M., Cooley, L., *et al.* SCAR is a primary regulator of Arp2/3-dependent morphological events in Drosophila. *J Cell Biol* **156,** 689-701 (2002).

63. Langevin, J., Morgan, M. J., Rosse, C., Racie, V., *et al.* Drosophila Exocyst Components Sec5, Sec6, and Sec15 Regulate DE-Cadherin Trafficking from Recycling Endosomes to the Plasma Membrane. *Dev Cell* **9,** 365-376 (2005).

64. Tepass, U., Gruszynski-DeFeo, E., Haag, T. A., Omatyar, L., *et al.* shotgun encodes Drosophila E-cadherin and is preferentially required during cell rearrangement in the neurectoderm and other morphogenetically active epithelia. *Genes Dev* **10,** 672-685 (1996).

65. Simões, S. d. e. . M., Blankenship, J. T., Weitz, O., Farrell, D. L., *et al.* Rho-kinase directs Bazooka/Par-3 planar polarity during Drosophila axis elongation. *Dev Cell* **19,** 377-388 (2010).

66. Emmons, S., Phan, H., Calley, J., Chen, W., *et al.* Cappuccino, a Drosophila maternal effect gene required for polarity of the egg and embryo, is related to the vertebrate limb deformity locus. *Genes Dev* **9,** 2482-2494 (1995).

67. Rosales-Nieves, A. E., Johndrow, J. E., Keller, L. C., Magie, C. R., *et al.* Coordination of microtubule and microfilament dynamics by Drosophila Rho1, Spire and Cappuccino. *Nat Cell Biol* **8,** 367-376 (2006).

68. Dietzl, G., Chen, D., Schnorrer, F., Su, K. C., *et al.* A genome-wide transgenic RNAi library for conditional gene inactivation in Drosophila. *Nature* **448,** 151-156 (2007).

69. Perkins, L. A., Holderbaum, L., Tao, R., Hu, Y., *et al.* The Transgenic RNAi Project at Harvard Medical School: Resources and Validation. *Genetics* **201,** 843-852 (2015).

70. Dollar, G., Gombos, R., Barnett, A. A., Sanchez Hernandez, D., *et al.* Unique and Overlapping Functions of Formins Frl and DAAM During Ommatidial Rotation and Neuronal Development in Drosophila. *Genetics* **202,** 1135-1151 (2016).

REFERENCES

Ahmad, F.J., and Baas, P.W. (1995). Microtubules released from the neuronal centrosome are transported into the axon. J. Cell Sci. *108 (Pt 8)*, 2761–2769.

Ajduk, A., Biswas Shivhare, S., and Zernicka-Goetz, M. (2014). The basal position of nuclei is one pre-requisite for asymmetric cell divisions in the early mouse embryo. Dev. Biol. *392*, 133–140.

Akhmanova, A., and Steinmetz, M.O. (2008). Tracking the ends: a dynamic protein network controls the fate of microtubule tips. Nat. Rev. Mol. Cell Biol. *9*, 309–322.

Akiyama, M., Tero, A., and Kobayashi, R. (2010). A mathematical model of cleavage. J. Theor. Biol. *264*, 84–94.

Alford, L.M., Ng, M.M., and Burgess, D.R. (2009). Cell polarity emerges at first cleavage in sea urchin embryos. Dev. Biol. *330*, 12–20.

Allan, V. (1995). Protein phosphatase 1 regulates the cytoplasmic dynein-driven formation of endoplasmic reticulum networks in vitro. J. Cell Biol. *128*, 879–891.

Alvarez, I.S., and Navascués, J. (1990). Shaping, invagination, and closure of the chick embryo otic vesicle: Scanning electron microscopic and quantitative study. Anat. Rec. *228*, 315–326.

Amack, J.D., and Manning, M.L. (2012). Knowing the Boundaries: Extending the Differential Adhesion Hypothesis in Embryonic Cell Sorting. Science *338*, 212–215.

Amano, M., Ito, M., Kimura, K., Fukata, Y., Chihara, K., Nakano, T., Matsuura, Y., and Kaibuchi, K. (1996). Phosphorylation and Activation of Myosin by Rho-associated Kinase (Rho-kinase). J. Biol. Chem. *271*, 20246–20249.

Andrews, G.F. (1897). The Living Substance as such: and as Organism (Ginn & Company).

Aplin, A.E., Howe, A., Alahari, S.K., and Juliano, R.L. (1998). Signal Transduction and Signal Modulation by Cell Adhesion Receptors: The Role of Integrins, Cadherins, Immunoglobulin-Cell Adhesion Molecules, and Selectins. Pharmacol. Rev. *50*, 197–264.

Arendt, D., and Nübler-Jung, K. (1999). Rearranging gastrulation in the name of yolk: evolution of gastrulation in yolk-rich amniote eggs. Mech. Dev. *81*, 3–22.

Arnal, I., Heichette, C., Diamantopoulos, G.S., and Chrétien, D. (2004). CLIP-170/Tubulin-Curved Oligomers Coassemble at Microtubule Ends and Promote Rescues. Curr. Biol. *14*, 2086–2095.

Asnes, C.F., and Schroeder, T.E. (1979). Cell cleavage. Ultrastructural evidence against equatorial stimulation by aster microtubules. Exp. Cell Res. *122*, 327–338.

Baker, J., Theurkauf, W.E., and Schubiger, G. (1993). Dynamic changes in microtubule configuration correlate with nuclear migration in the preblastoderm Drosophila embryo. J. Cell Biol. *122*, 113–121.

Bellion, A., Baudoin, J.-P., Alvarez, C., Bornens, M., and Métin, C. (2005). Nucleokinesis in Tangentially Migrating Neurons Comprises Two Alternating Phases: Forward Migration of the Golgi/Centrosome Associated with Centrosome Splitting and Myosin Contraction at the Rear. J. Neurosci. *25*, 5691–5699.

Belmont, L.D., Hyman, A.A., Sawin, K.E., and Mitchison, T.J. (1990). Real-time visualization of cell cycle-dependent changes in microtubule dynamics in cytoplasmic extracts. Cell *62*, 579–589.

Bertet, C., Sulak, L., and Lecuit, T. (2004). Myosin-dependent junction remodelling controls planar cell intercalation and axis elongation. Nature *429*, 667–671.

Bettencourt-Dias, M., and Glover, D.M. (2007). Centrosome biogenesis and function: centrosomics brings new understanding. Nat. Rev. Mol. Cell Biol. *8*, 451–463.

van den Biggelaar, J.A. (1977). Development of dorsoventral polarity and mesentoblast determination in Patella vulgata. J. Morphol. *154*, 157–186.

Bjerknes, M. (1986). Physical theory of the orientation of astral mitotic spindles. Science *234*, 1413–1416.

Borghi, N., and James Nelson, W. (2009). Intercellular adhesion in morphogenesis: molecular and biophysical considerations. Curr. Top. Dev. Biol. *89*, 1–32.

Boveri, T. (1888). Über partielle Befruchtung (Naturforschende Gesellschaft).

Bowerman, B., Tax, F.E., Thomas, J.H., and Priess, J.R. (1992). Cell interactions involved in development of the bilaterally symmetrical intestinal valve cells during embryogenesis in Caenorhabditis elegans. Development *116*, 1113–1122.

Bowman, S.K., Neumüller, R.A., Novatchkova, M., Du, Q., and Knoblich, J.A. (2006). The Drosophila NuMA Homolog Mud regulates spindle orientation in asymmetric cell division. Dev. Cell *10*, 731–742.

Boyd, L., Guo, S., Levitan, D., Stinchcomb, D.T., and Kemphues, K.J. (1996). PAR-2 is asymmetrically distributed and promotes association of P granules and PAR-1 with the cortex in C. elegans embryos. Development *122*, 3075–3084.

Braude, P., Bolton, V., and Moore, S. (1988). Human gene expression first occurs between the four- and eight-cell stages of preimplantation development. Nature *332*, 459–461.

Bringmann, H., and Hyman, A.A. (2005). A cytokinesis furrow is positioned by two consecutive signals. Nature *436*, 731–734.

Bringmann, H., Skiniotis, G., Spilker, A., Kandels-Lewis, S., Vernos, I., and Surrey, T. (2004). A Kinesin-like Motor Inhibits Microtubule Dynamic Instability. Science *303*, 1519–1522.

Brinkley, B.R., Cox, S.M., Pepper, D.A., Wible, L., Brenner, S.L., and Pardue, R.L. (1981). Tubulin assembly sites and the organization of cytoplasmic microtubules in cultured mammalian cells. J. Cell Biol. *90*, 554–562.

Brust-Mascher, I., and Scholey, J.M. (2011). Mitotic motors and chromosome segregation: the mechanism of anaphase B. Biochem. Soc. Trans. *39*, 1149–1153.

Burdsal, C.A., Alliegro, M.C., and McClay, D.R. (1991). Tissue-specific, temporal changes in cell adhesion to echinonectin in the sea urchin embryo. Dev. Biol. *144*, 327–334.

Burke, R.D., Murray, G., Rise, M., and Wang, D. (2004). Integrins on eggs: the βC subunit is essential for formation of the cortical actin cytoskeleton in sea urchin eggs. Dev. Biol. *265*, 53–60.

Butschli, O. (1876). Studien über die ersten Entwicklungsvorgänge der Eizelle, die Zelltheilung und die Conjugation der Infusorien (C. Winter).

Cahu, J., and Surrey, T. (2009). Motile microtubule crosslinkers require distinct dynamic properties for correct functioning during spindle organization in Xenopus egg extract. J. Cell Sci. *122*, 1295–1300.

Cai, D., McEwen, D.P., Martens, J.R., Meyhofer, E., and Verhey, K.J. (2009). Single Molecule Imaging Reveals Differences in Microtubule Track Selection Between Kinesin Motors. PLOS Biol. *7*, e1000216.

Callaini, G., and Riparbelli, M.G. (1990). Centriole and centrosome cycle in the early Drosophila embryo. J. Cell Sci. *97 (Pt 3)*, 539–543.

Cameron, R.A., Samanta, M., Yuan, A., He, D., and Davidson, E. (2009). SpBase: the sea urchin genome database and web site. Nucleic Acids Res. *37*, D750–D754.

Campbell, E.J., MacKinlay, S.A., and MacRae, T.H. (1989). Cross-linking of microtubules by microtubule-associated proteins (MAPs) from the brine shrimp, Artemia. J. Cell Sci. *93 (Pt 1)*, 29–39.

Canman, J.C., Lewellyn, L., Laband, K., Smerdon, S.J., Desai, A., Bowerman, B., and Oegema, K. (2008). Inhibition of Rac by the GAP Activity of Centralspindlin Is Essential for Cytokinesis. Science *322*, 1543–1546.

Carmena, M., Wheelock, M., Funabiki, H., and Earnshaw, W.C. (2012). The chromosomal passenger complex (CPC): from easy rider to the godfather of mitosis. Nat. Rev. Mol. Cell Biol. *13*, 789–803.

Carminati, J.L., and Stearns, T. (1997). Microtubules orient the mitotic spindle in yeast through dynein-dependent interactions with the cell cortex. J. Cell Biol. *138*, 629–641.

Carroll, D.J., Albay, D.T., Hoang, K.M., O'Neill, F.J., Kumano, M., and Foltz, K.R. (2000). The Relationship between Calcium, MAP Kinase, and DNA Synthesis in the Sea Urchin Egg at Fertilization. Dev. Biol. *217*, 179–191.

Chaigne, A., Campillo, C., Gov, N.S., Voituriez, R., Azoury, J., Umaña-Diaz, C., Almonacid, M., Queguiner, I., Nassoy, P., Sykes, C., et al. (2013). A soft cortex is essential for asymmetric spindle positioning in mouse oocytes. Nat. Cell Biol. *15*, 958–966.

Chaigne, A., Campillo, C., Voituriez, R., Gov, N.S., Sykes, C., Verlhac, M.-H., and Terret, M.-E. (2016). F-actin mechanics control spindle centring in the mouse zygote. Nat. Commun. *7*, 10253.

Chalkley, H.W. (1935). The mechanism of cytoplasmic fission in Amoeba proteus. Protoplasma *24*, 607–621.

Chambers, E.L. (1939). The Movement of the Egg Nucleus in Relation to the Sperm Aster in the Echinoderm Egg. J. Exp. Biol. *16*, 409–424.

Chambers, R. (1921). The formation of the aster in artificial parthenogenesis. J. Gen. Physiol. *4*, 33–39.

Chambers, R. (1938). Structural and kinetic aspects of cell division. J. Cell. Comp. Physiol. *12*, 149–165.

Chandler, D.E., and Heuser, J. (1979). Membrane fusion during secretion: cortical granule exocytosis in sex urchin eggs as studied by quick-freezing and freeze-fracture. J. Cell Biol. *83*, 91–108.

Cheeseman, I.M., and Desai, A. (2008). Molecular architecture of the kinetochore-microtubule interface. Nat. Rev. Mol. Cell Biol. *9*, 33–46.

Cheng, N.N., Kirby, C.M., and Kemphues, K.J. (1995). Control of cleavage spindle orientation in Caenorhabditis elegans: the role of the genes par-2 and par-3. Genetics *139*, 549–559.

Choi, J.K., and He, X. (2013). In vitro maturation of cumulus-oocyte complexes for efficient isolation of oocytes from outbred deer mice. PloS One *8*, e56158.

Ciani, L., Krylova, O., Smalley, M.J., Dale, T.C., and Salinas, P.C. (2004). A divergent canonical WNT-signaling pathway regulates microtubule dynamics: dishevelled signals locally to stabilize microtubules. J. Cell Biol. *164*, 243–253.

Clark, A.G., Wartlick, O., Salbreux, G., and Paluch, E.K. (2014). Stresses at the Cell Surface during Animal Cell Morphogenesis. Curr. Biol. *24*, R484–R494.

Clement, A.C. (1968). Development of the vegetal half of the Ilyanassa egg after removal of most of the yolk by centrifugal force, Compared with the development of animal halves of similar visible composition. Dev. Biol. *17*, 165–186.

Clift, D., and Schuh, M. (2013). Restarting life: fertilization and the transition from meiosis to mitosis. Nat. Rev. Mol. Cell Biol. *14*, 549–562.

Colombo, K., Grill, S.W., Kimple, R.J., Willard, F.S., Siderovski, D.P., and Gönczy, P. (2003). Translation of polarity cues into asymmetric spindle positioning in Caenorhabditis elegans embryos. Science *300*, 1957–1961.

Conklin, E.G. (1905). Mosaic development in ascidian eggs. J. Exp. Zool. *2*, 145–223.

Conklin, E.G. (1912). Experimantal Studies on Nuclear and Cell Division in the Eggs of Crepidula (Academy of Natural Sciences of Philadelphia).

Conklin, E.G. (1917). Effects of centrifugal force on the structure and development of the eggs of Crepidula. J. Exp. Zool. *22*, 311–419.

Conrad, G.W., Williams, D.C., Turner, F.R., Newrock, K.M., and Raff, R.A. (1973). Microfilaments in the polar lobe constriction of fertilized eggs of Ilyanassa obsoleta. J. Cell Biol. *59*, 228–233.

CRAMPTON, H.E. (1894). V.—Reversal of Cleavage in a Sinistral Gasteropod. Ann. N. Y. Acad. Sci. *8*, 167–170.

Culver–Hanlon, T.L., Lex, S.A., Stephens, A.D., Quintyne, N.J., and King, S.J. (2006). A microtubule-binding domain in dynactin increases dynein processivity by skating along microtubules. Nat. Cell Biol. *8*, 264–270.

Dai, J., and Sheetz, M.P. (1999). Membrane tether formation from blebbing cells. Biophys. J. *77*, 3363–3370.

Dan, K. (1943). Behavior of the cell surface during cleavage. VI. On the mechanism of cell division. J Fac Sci Tokyo Imp Univ *6*, 323–368.

Dan, K. (1979). Studies on Unequal Cleavage in Sea Urchins I. Migration of the Nuclei to the Vegetal Pole. Dev. Growth Differ. *21*, 527–535.

DAN, K. (1984). The Cause and Consequence of Unequal Cleavage in Sea Urchins. Zoolog. Sci. *1*, 151–160.

Dan, K. (1987). Studies on Unequal Cleavage in Sea Urchins III. Micromere Formation under Compression. Dev. Growth Differ. *29*, 503–515.

Dan, K. (1988). Mechanism of equal cleavage of sea urchin egg: transposition from astral mechanism to constricting mechanism. Zool Sci *5*, 507–517.

Dan, K., and Ikeda, M. (1971). On the System Controlling the Time of Micromere Formation in Sea Urchin Embryos. Dev. Growth Differ. *13*, 285–302.

Dan, K., and Ito, S. (1984). Studies of Unequal Cleavage in Molluscs: I. Nuclear Behavior and Anchorage of a Spindle Pole to Cortex as Revealed by Isolation Technique. Dev. Growth Differ. *26*, 249–262.

von Dassow, G. (2009). Concurrent cues for cytokinetic furrow induction in animal cells. Trends Cell Biol. *19*, 165–173.

von Dassow, G., and Schubiger, G. (1994). How an actin network might cause fountain streaming and nuclear migration in the syncytial Drosophila embryo. J. Cell Biol. *127*, 1637–1653.

David, R., Ninomiya, H., Winklbauer, R., and Neumann, A.W. (2009). Tissue surface tension measurement by rigorous axisymmetric drop shape analysis. Colloids Surf. B Biointerfaces *72*, 236–240.

David, R., Luu, O., Damm, E.W., Wen, J.W.H., Nagel, M., and Winklbauer, R. (2014). Tissue cohesion and the mechanics of cell rearrangement. Dev. Camb. Engl. *141*, 3672–3682.

Davidson, L.A., Ezin, A.M., and Keller, R. (2002). Embryonic wound healing by apical contraction and ingression in Xenopus laevis. Cell Motil. Cytoskeleton *53*, 163–176.

Davis, G.S., Phillips, H.M., and Steinberg, M.S. (1997). Germ-layer surface tensions and “tissue affinities” in Rana pipiens gastrulae: quantitative measurements. Dev. Biol. *192*, 630–644.

Desnitskiy, A.G. (2014). On the classification of the cleavage patterns in amphibian embryos. Russ. J. Dev. Biol. *45*, 1–10.

Dimitrov, A., Quesnoit, M., Moutel, S., Cantaloube, I., Poüs, C., and Perez, F. (2008). Detection of GTP-Tubulin Conformation in Vivo Reveals a Role for GTP Remnants in Microtubule Rescues. Science *322*, 1353–1356.

Dodding, M.P., and Way, M. (2011). Coupling viruses to dynein and kinesin-1. EMBO J. *30*, 3527–3539.

Dogterom, M., and Yurke, B. (1997). Measurement of the Force-Velocity Relation for Growing Microtubules. Science *278*, 856–860.

Drewes, G., Ebneth, A., Preuss, U., Mandelkow, E.M., and Mandelkow, E. (1997). MARK, a novel family of protein kinases that phosphorylate microtubule-associated proteins and trigger microtubule disruption. Cell *89*, 297–308.

Druner, L. (1894). Studien über den Mechanismus der Zellteilung. Jena. Z Naturwiss *29*.

Duguay, D., Foty, R.A., and Steinberg, M.S. (2003). Cadherin-mediated cell adhesion and tissue segregation: qualitative and quantitative determinants. Dev. Biol. *253*, 309–323.

Dupin, I., Sakamoto, Y., and Etienne-Manneville, S. (2011). Cytoplasmic intermediate filaments mediate actin-driven positioning of the nucleus. J Cell Sci *124*, 865–872.

Durham, A.C.H. (1974). A unified theory of the control of actin and myosin in nonmuscle movements. Cell *2*, 123–135.

Ebneth, A., Drewes, G., Mandelkow, E.M., and Mandelkow, E. (1999). Phosphorylation of MAP2c and MAP4 by MARK kinases leads to the destabilization of microtubules in cells. Cell Motil. Cytoskeleton *44*, 209–224.

Edgar, B.A., and Schubiger, G. (1986). Parameters controlling transcriptional activation during early drosophila development. Cell *44*, 871–877.

Elad, N., Abramovitch, S., Sabanay, H., and Medalia, O. (2011). Microtubule organization in the final stages of cytokinesis as revealed by cryo-electron tomography. J Cell Sci *124*, 207–215.

Endow, S.A., and Waligora, K.W. (1998). Determinants of Kinesin Motor Polarity. Science *281*, 1200–1202.

Epel, D., Patton, C., Wallace, R.W., and Cheung, W.Y. (1981). Calmodulin activates NAD kinase of sea urchin eggs: An early event of fertilization. Cell *23*, 543–549.

Errera, L. (1886). On a fundamental condition of equilibrium for living cells. CR Hebd Seances Acad Sci *103*, 822–824.

Erwin, D.H., Laflamme, M., Tweedt, S.M., Sperling, E.A., Pisani, D., and Peterson, K.J. (2011). The Cambrian Conundrum: Early Divergence and Later Ecological Success in the Early History of Animals. Science *334*, 1091–1097.

Etemad-Moghadam, B., Guo, S., and Kemphues, K.J. (1995). Asymmetrically distributed PAR-3 protein contributes to cell polarity and spindle alignment in early C. elegans embryos. Cell *83*, 743–752.

Evans, E., and Yeung, A. (1989). Apparent viscosity and cortical tension of blood granulocytes determined by micropipet aspiration. Biophys. J. *56*, 151–160.

Evans, T.C., Crittenden, S.L., Kodoyianni, V., and Kimble, J. (1994). Translational control of maternal glp-1 mRNA establishes an asymmetry in the C. elegans embryo. Cell *77*, 183–194.

Fankhauser, G. (1948). The organization of the amphibian egg during fertilization and cleavage. Ann. N. Y. Acad. Sci. *49*, 684–708.

Field, C.M., Groen, A.C., Nguyen, P.A., and Mitchison, T.J. (2015). Spindle-to-cortex communication in cleaving, polyspermic Xenopus eggs. Mol. Biol. Cell *26*, 3628–3640.

Fink, R.D., and McClay, D.R. (1985). Three cell recognition changes accompany the ingression of sea urchin primary mesenchyme cells. Dev. Biol. *107*, 66–74.

Fleming, T.P., Sheth, B., and Fesenko, I. (2001). Cell adhesion in the preimplantation mammalian embryo and its role in trophectoderm differentiation and blastocyst morphogenesis. Front. Biosci. J. Virtual Libr. *6*, D1000-1007.

Foe, V.E., and Alberts, B.M. (1983). Studies of nuclear and cytoplasmic behaviour during the five mitotic cycles that precede gastrulation in Drosophila embryogenesis. J. Cell Sci. *61*, 31–70.

Foe, V.E., and von Dassow, G. (2008). Stable and dynamic microtubules coordinately shape the myosin activation zone during cytokinetic furrow formation. J. Cell Biol. *183*, 457–470.

Forgacs, G., Foty, R.A., Shafrir, Y., and Steinberg, M.S. (1998). Viscoelastic properties of living embryonic tissues: a quantitative study. Biophys. J. *74*, 2227–2234.

Foty, R.A., and Steinberg, M.S. (1997). Measurement of tumor cell cohesion and suppression of invasion by E- or P-cadherin. Cancer Res. *57*, 5033–5036.

Foty, R.A., and Steinberg, M.S. (2005). The differential adhesion hypothesis: a direct evaluation. Dev. Biol. *278*, 255–263.

Foty, R.A., Forgacs, G., Pfleger, C.M., and Steinberg, M.S. (1994). Liquid properties of embryonic tissues: Measurement of interfacial tensions. Phys. Rev. Lett. *72*, 2298–2301.

Foty, R.A., Pfleger, C.M., Forgacs, G., and Steinberg, M.S. (1996). Surface tensions of embryonic tissues predict their mutual envelopment behavior. Dev. Camb. Engl. *122*, 1611–1620.

Foty, R.A., Corbett, S.A., Schwarzbauer, J.E., and Steinberg, M.S. (1998). Dexamethasone Up-Regulates Cadherin Expression and Cohesion of HT-1080 Human Fibrosarcoma Cells. Cancer Res. *58*, 3586–3589.

Freeman, G. (1983). The role of egg organization in the generation of cleavage patterns. Time Space Pattern Embryonic Dev. 171–196.

Freeman, G., and Lundelius, J.W. (1982). The developmental genetics of dextrality and sinistrality in the gastropodLymnaea peregra. Wilhelm Rouxs Arch. Dev. Biol. *191*, 69–83.

Gabriel, W.N., McNuff, R., Patel, S.K., Gregory, T.R., Jeck, W.R., Jones, C.D., and Goldstein, B. (2007). The tardigrade Hypsibius dujardini, a new model for studying the evolution of development. Dev. Biol. *312*, 545–559.

Gard, D.L. (1994). Gamma-tubulin is asymmetrically distributed in the cortex of Xenopus oocytes. Dev. Biol. *161*, 131–140.

Gard, D.L., and Kirschner, M.W. (1987). A microtubule-associated protein from Xenopus eggs that specifically promotes assembly at the plus-end. J. Cell Biol. *105*, 2203–2215.

Gilbert, S.F. (2000). Developmental Biology (Sinauer Associates).

Gillies, T.E., and Cabernard, C. (2011). Cell division orientation in animals. Curr. Biol. CB *21*, R599-609.

Gittes, F., Mickey, B., Nettleton, J., and Howard, J. (1993). Flexural rigidity of microtubules and actin filaments measured from thermal fluctuations in shape. J. Cell Biol. *120*, 923–934.

Goel, N.S., Doggenweiler, C.F., and Thompson, R.L. (1986). Simulation of cellular compaction and internalization in mammalian embryo development as driven by minimization of surface energy. Bull. Math. Biol. *48*, 167–187.

Goldstein, B. (1995). Cell contacts orient some cell division axes in the Caenorhabditis elegans embryo. J. Cell Biol. *129*, 1071–1080.

Goldstein, B. (2000). When cells tell their neighbors which direction to divide. Dev. Dyn. *218*, 23–29.

Goldstein, B., and Freeman, G. (1997). Axis specification in animal development. BioEssays *19*, 105–116.

Goldstein, B., and Hird, S.N. (1996). Specification of the anteroposterior axis in Caenorhabditis elegans. Dev. Camb. Engl. *122*, 1467–1474.

Gomes, E.R., Jani, S., and Gundersen, G.G. (2005). Nuclear Movement Regulated by Cdc42, MRCK, Myosin, and Actin Flow Establishes MTOC Polarization in Migrating Cells. Cell *121*, 451–463.

Gomes, J.E., Encalada, S.E., Swan, K.A., Shelton, C.A., Carter, J.C., and Bowerman, B. (2001). The maternal gene spn-4 encodes a predicted RRM protein required for mitotic spindle orientation and cell fate patterning in early C. elegans embryos. Dev. Camb. Engl. *128*, 4301–4314.

Gönczy, P. (2008). Mechanisms of asymmetric cell division: flies and worms pave the way. Nat. Rev. Mol. Cell Biol. *9*, 355–366.

Gönczy, P. (2015). Centrosomes and cancer: revisiting a long-standing relationship. Nat. Rev. Cancer *15*, 639–652.

Gönczy, P., Pichler, S., Kirkham, M., and Hyman, A.A. (1999). Cytoplasmic dynein is required for distinct aspects of MTOC positioning, including centrosome separation, in the one cell stage Caenorhabditis elegans embryo. J. Cell Biol. *147*, 135–150.

Gong, Y., Mo, C., and Fraser, S.E. (2004). Planar cell polarity signalling controls cell division orientation during zebrafish gastrulation. Nature *430*, 689–693.

Goshima, G., Mayer, M., Zhang, N., Stuurman, N., and Vale, R.D. (2008). Augmin: a protein complex required for centrosome-independent microtubule generation within the spindle. J. Cell Biol. *181*, 421–429.

Gotta, M., and Ahringer, J. (2001). Distinct roles for Galpha and Gbetagamma in regulating spindle position and orientation in Caenorhabditis elegans embryos. Nat. Cell Biol. *3*, 297–300.

Gotta, M., Dong, Y., Peterson, Y.K., Lanier, S.M., and Ahringer, J. (2003). Asymmetrically distributed C. elegans homologs of AGS3/PINS control spindle position in the early embryo. Curr. Biol. CB *13*, 1029–1037.

Grande, C., and Patel, N.H. (2009). Nodal signalling is involved in left–right asymmetry in snails. Nature *457*, 1007–1011.

Graner, F. (1993). Can Surface Adhesion Drive Cell-rearrangement? Part I: Biological Cell-sorting. J. Theor. Biol. *164*, 455–476.

Grill, S.W., and Hyman, A.A. (2005). Spindle positioning by cortical pulling forces. Dev. Cell *8*, 461–465.

Grill, S.W., Gönczy, P., Stelzer, E.H., and Hyman, A.A. (2001). Polarity controls forces governing asymmetric spindle positioning in the Caenorhabditis elegans embryo. Nature *409*, 630–633.

Grishchuk, E.L., Molodtsov, M.I., Ataullakhanov, F.I., and McIntosh, J.R. (2005). Force production by disassembling microtubules. Nature *438*, 384–388.

Guerrier, P. (1968). Origine et stabilité de la polarité animale végétative chez quelques Spiralia. Ann Embryol Morphog. *1*, 119–139.

Guharoy, M., Szabo, B., Contreras Martos, S., Kosol, S., and Tompa, P. (2013). Intrinsic structural disorder in cytoskeletal proteins. Cytoskelet. Hoboken NJ *70*, 550–571.

Gulyas, B.J. (1975). A reexamination of cleavage patterns in eutherian mammalian eggs: Rotation of blastomere pairs during second cleavage in the rabbit. J. Exp. Zool. *193*, 235–247.

Günzel, D., and Fromm, M. (2012). Claudins and other tight junction proteins. Compr. Physiol. *2*, 1819–1852.

Guyer, M.F. (Michael F. (1900). Spermatogenesis of normal and of hybrid pigeons : a dissertation, submitted to the faculty of the Graduate School of Arts, Literature, and Science, in candidacy for the degree of doctor of philosophy; Department of Zoology (Chicago : [s.n.]).

Hamaguchi, M.S., and Hiramoto, Y. (1986). Analysis of the Role of Astral Rays in Pronuclear Migration in Sand Dollar Eggs by the Colcemid-UV Method. Dev. Growth Differ. *28*, 143–156.

Hamaguchi, M.S., Hamaguchi, Y., and Hiramoto, Y. (1986). Microinjected Polystyrene Beads Move Along Astral Rays in Sand Dollar Eggs. Dev. Growth Differ. *28*, 461–470.

Hara, K. (1977). The cleavage pattern of the axolotl egg studied by cinematography and cell counting. Rouxs Arch. Dev. Biol. *181*, 73–87.

Hardin, J., and Keller, R. (1988). The behaviour and function of bottle cells during gastrulation of Xenopus laevis. Development *103*, 211–230.

Harrell, J.R., and Goldstein, B. (2011). Internalization of multiple cells during C. elegans gastrulation depends on common cytoskeletal mechanisms but different cell polarity and cell fate regulators. Dev. Biol. *350*, 1–12.

Harris, T.J.C., and Tepass, U. (2010). Adherens junctions: from molecules to morphogenesis. Nat. Rev. Mol. Cell Biol. *11*, 502–514.

Harvey, E.B. (1935). The mitotic figure and cleavage plane in the egg of parechinus microtuberculatus, as influenced by centrifugal force. Biol. Bull. *69*, 287–297.

Hausen, P., and Riebesell, M. (1991). The early development of Xenopus laevis: an atlas of the histology (Verlag Der Zeitschrift F'Ur Naturforschung).

Hayashi, T., and Carthew, R.W. (2004). Surface mechanics mediate pattern formation in the developing retina. Nature *431*, 647–652.

Hegedüs, B., Marga, F., Jakab, K., Sharpe-Timms, K.L., and Forgacs, G. (2006). The Interplay of Cell-Cell and Cell-Matrix Interactions in the Invasive Properties of Brain Tumors. Biophys. J. *91*, 2708–2716.

Heidemann, S.R., and Kirschner, M.W. (1975). Aster formation in eggs of Xenopus laevis. Induction by isolated basal bodies. J. Cell Biol. *67*, 105–117.

Heidenhain, M. (1897). Neue Erläuterungen zum Spannungsgesetz der centrirten Systeme. Morphol. Arb. *7*, 281–365.

Heifetz, Y., Yu, J., and Wolfner, M.F. (2001). Ovulation Triggers Activation of Drosophila Oocytes. Dev. Biol. *234*, 416–424.

Helfand, B.T., Chang, L., and Goldman, R.D. (2004). Intermediate filaments are dynamic and motile elements of cellular architecture. J. Cell Sci. *117*, 133–141.

Herrmann, H., and Aebi, U. (2004). Intermediate Filaments: Molecular Structure, Assembly Mechanism, and Integration Into Functionally Distinct Intracellular Scaffolds. Annu. Rev. Biochem. *73*, 749–789.

Hertwig, O. (1884). The problem of fertilization and of isotropy of the egg, a theory of heredity. Jena Z Naturwiss *18*, 21–23.

Hertwig, O. (1893). Ueber den Werth der ersten Furchungszellen für die Organbildung des Embryo Experimentelle Studien am Frosch-und Tritonei. Arch. Für Mikrosk. Anat. *42*, 662–807.

Hertzler, P.L., and McClay, D.R. (1999). αSU2, an Epithelial Integrin That Binds Laminin in the Sea Urchin Embryo. Dev. Biol. *207*, 1–13.

Hibino, T., Nishikata, T., and Nishida, H. (1998). Centrosome-attracting body: a novel structure closely related to unequal cleavages in the ascidian embryo. Dev. Growth Differ. *40*, 85–95.

Hidalgo-Carcedo, C., Hooper, S., Chaudhry, S.I., Williamson, P., Harrington, K., Leitinger, B., and Sahai, E. (2011). Collective cell migration requires suppression of actomyosin at cell-cell contacts mediated by DDR1 and the cell polarity regulators Par3 and Par6. Nat. Cell Biol. *13*, 49–58.

Hill, T.L. (1987). Linear Aggregation Theory in Cell Biology (Springer-Verlag).

Hinchcliffe, E.H., Li, C., Thompson, E.A., Maller, J.L., and Sluder, G. (1999). Requirement of Cdk2-cyclin E activity for repeated centrosome reproduction in Xenopus egg extracts. Science *283*, 851–854.

Hiramoto, Y. (1979). Mechanical properties of the dividing sea urchin egg. Cell Motil. Mol. Organ. 653–663.

Hofmeister, W. (1867). Die Lehre von der Pflanzenzelle (Engelmann).

Holy, J., and Schatten, G. (1991). Differential behavior of centrosomes in unequally dividing blastomeres during fourth cleavage of sea urchin embryos. J. Cell Sci. *98*, 423–431.

Holy, T.E., Dogterom, M., Yurke, B., and Leibler, S. (1997). Assembly and positioning of microtubule asters in microfabricated chambers. Proc. Natl. Acad. Sci. U. S. A. *94*, 6228–6231.

Horstadius, S. (1939). The Mechanics of Sea Urchin Development, Studied by Operative Methods. Biol. Rev. *14*, 132–179.

Hörstadius, S., and others (1973). Experimental embryology of echinoderms.

Howard, J. (2006). Elastic and damping forces generated by confined arrays of dynamic microtubules. Phys. Biol. *3*, 54–66.

Howard, J., and Hyman, A.A. (2007). Microtubule polymerases and depolymerases. Curr. Opin. Cell Biol. *19*, 31–35.

Hu, C.-K., Coughlin, M., Field, C.M., and Mitchison, T.J. (2011). KIF4 regulates midzone length during cytokinesis. Curr. Biol. CB *21*, 815–824.

Hutter, H., and Schnabel, R. (1994). glp-1 and inductions establishing embryonic axes in C. elegans. Development *120*, 2051–2064.

Hyman, A.A. (1989). Centrosome movement in the early divisions of Caenorhabditis elegans: a cortical site determining centrosome position. J. Cell Biol. *109*, 1185–1193.

Hyman, A.A., and White, J.G. (1987). Determination of cell division axes in the early embryogenesis of Caenorhabditis elegans. J. Cell Biol. *105*, 2123–2135.

Ichihara, K., Kitazawa, H., Iguchi, Y., Hotani, H., and Itoh, T.J. (2001). Visualization of the stop of microtubule depolymerization that occurs at the high-density region of microtubule-associated protein 2 (MAP2)1. J. Mol. Biol. *312*, 107–118.

Inoué, S., and Salmon, E.D. (1995). Force Generation by Microtubule Assembly/Disassembly in Mitosis and Related Movements. Mol. Biol. Cell *6*, 1619–1640.

Ishihara, K., Nguyen, P.A., Groen, A.C., Field, C.M., and Mitchison, T.J. (2014). Microtubule nucleation remote from centrosomes may explain how asters span large cells. Proc. Natl. Acad. Sci. U. S. A. *111*, 17715–17722.

Ishihara, K., Korolev, K.S., and Mitchison, T.J. (2016). Physical basis of large microtubule aster growth. eLife *5*.

Iwao, Y. (1989). An electrically mediated block to polyspermy in the primitive urodele Hynobius nebulosus and phylogenetic comparison with other amphibians. Dev. Biol. *134*, 438–445.

Izumi, Y., Ohta, N., Hisata, K., Raabe, T., and Matsuzaki, F. (2006). Drosophila Pins-binding protein Mud regulates spindle-polarity coupling and centrosome organization. Nat. Cell Biol. *8*, 586–593.

Jaarsma, D., and Hoogenraad, C.C. (2015). Cytoplasmic dynein and its regulatory proteins in Golgi pathology in nervous system disorders. Front. Neurosci. *9*, 397.

Janson, M.E., Loughlin, R., Loïodice, I., Fu, C., Brunner, D., Nédélec, F.J., and Tran, P.T. (2007). Crosslinkers and Motors Organize Dynamic Microtubules to Form Stable Bipolar Arrays in Fission Yeast. Cell *128*, 357–368.

Jeffery, W.R. (1982). Calcium ionophore polarizes ooplasmic segregation in ascidian eggs. Science *216*, 545–547.

Jourdain, L., Curmi, P., Sobel, A., Pantaloni, D., and Carlier, M.-F. (1997). Stathmin: A Tubulin-Sequestering Protein Which Forms a Ternary T2S Complex with Two Tubulin Molecules. Biochemistry (Mosc.) *36*, 10817–10821.

Just, E.E., and others (1939). biology of the cell surface.

Kaltschmidt, J.A., and Brand, A.H. (2002). Asymmetric cell division: microtubule dynamics and spindle asymmetry. J Cell Sci *115*, 2257–2264.

Kam, Z., Minden, J.S., Agard, D.A., Sedat, J.W., and Leptin, M. (1991). Drosophila gastrulation: analysis of cell shape changes in living embryos by three-dimensional fluorescence microscopy. Development *112*, 365–370.

Karr, T.L., and Alberts, B.M. (1986). Organization of the cytoskeleton in early Drosophila embryos. J. Cell Biol. *102*, 1494–1509.

Katow, H., and Solursh, M. (1980). Ultrastructure of primary mesenchyme cell ingression in the sea urchin Lytechinus pictus. J. Exp. Zool. *213*, 231–246.

Khodjakov, A., and Pines, J. (2010). Centromere tension: a divisive issue. Nat. Cell Biol. *12*, 919–923.

Kimura, A., and Onami, S. (2005). Computer simulations and image processing reveal length-dependent pulling force as the primary mechanism for C. elegans male pronuclear migration. Dev. Cell *8*, 765–775.

Kimura, K., and Kimura, A. (2011). Intracellular organelles mediate cytoplasmic pulling force for centrosome centration in the Caenorhabditis elegans early embryo. Proc. Natl. Acad. Sci. U. S. A. *108*, 137–142.

Kiyomoto, M., and Shirai, H. (1993). The Determinant for Archenteron Formation in Starfish: Co-Culture of an Animal Egg Fragment-Derived Cell Cluster and a Selected Blastomere. Dev. Growth Differ. *35*, 99–105.

Kollman, J.M., Merdes, A., Mourey, L., and Agard, D.A. (2011). Microtubule nucleation by γ-tubulin complexes. Nat. Rev. Mol. Cell Biol. *12*, 709–721.

Kozlowski, C., Srayko, M., and Nedelec, F. (2007). Cortical microtubule contacts position the spindle in C. elegans embryos. Cell *129*, 499–510.

Krieg, M., Arboleda-Estudillo, Y., Puech, P.-H., Käfer, J., Graner, F., Müller, D.J., and Heisenberg, C.-P. (2008). Tensile forces govern germ-layer organization in zebrafish. Nat. Cell Biol. *10*, 429–436.

Kroh, A., and Smith, A.B. (2010). The phylogeny and classification of post-Palaeozoic echinoids. J. Syst. Palaeontol. *8*, 147–212.

Kwon, M., Bagonis, M., Danuser, G., and Pellman, D. (2015). Direct Microtubule-Binding by Myosin-10 Orients Centrosomes toward Retraction Fibers and Subcortical Actin Clouds. Dev. Cell *34*, 323–337.

Lambert, J.D. (2010). Developmental Patterns in Spiralian Embryos. Curr. Biol. *20*, R72–R77.

Lambert, J.D., and Nagy, L.M. (2002). Asymmetric inheritance of centrosomally localized mRNAs during embryonic cleavages. Nature *420*, 682–686.

Lansky, Z., Braun, M., Lüdecke, A., Schlierf, M., ten Wolde, P.R., Janson, M.E., and Diez, S. (2015). Diffusible Crosslinkers Generate Directed Forces in Microtubule Networks. Cell *160*, 1159–1168.

Lapraz, F., Besnardeau, L., and Lepage, T. (2009). Patterning of the Dorsal-Ventral Axis in Echinoderms: Insights into the Evolution of the BMP-Chordin Signaling Network. PLoS Biol. *7*.

Lecuit, T., and Lenne, P.-F. (2007). Cell surface mechanics and the control of cell shape, tissue patterns and morphogenesis. Nat. Rev. Mol. Cell Biol. *8*, 633–644.

Leung, C.F., Webb, S.E., and Miller, A.L. (2000). On the mechanism of ooplasmic segregation in single-cell zebrafish embryos. Dev. Growth Differ. *42*, 29–40.

Lewis, W.H. (1939). The role of a superficial plasmagel layer in changes of form, locomotion and division of cells in tissue cultures. Arch Exp Zellforsch *23*.

Lewis, W.H. (1947). Mechanics of invagination. Anat. Rec. *97*, 139–156.

Lillie, R.S. (1903). Fusion of blastomeres and nuclear division without cell-division in solutions of non-electrolytes. Biol. Bull. *4*, 164–178.

Lillie, R.S. (1916). The physiology of cell-division. VI. Rhythmical changes in the resistance of the dividing sea-urchin egg to hypotonic sea water and their physiological significance. J. Exp. Zool. *21*, 369–402.

Lindeman, R.E., and Pelegri, F. (2012). Localized products of futile cycle/lrmp promote centrosome-nucleus attachment in the zebrafish zygote. Curr. Biol. CB *22*, 843–851.

Logan, C.Y., and McClay, D.R. (1998). The lineages that give rise to the endoderm and mesoderm in the sea urchin embryo. Cell Fate Lineage Determ. 41–58.

Lomakina, E.B., Spillmann, C.M., King, M.R., and Waugh, R.E. (2004). Rheological analysis and measurement of neutrophil indentation. Biophys. J. *87*, 4246–4258.

Longo, F.J., Lynn, J.W., McCulloh, D.H., and Chambers, E.L. (1986). Correlative ultrastructural and electrophysiological studies of sperm-egg interactions of the sea urchin, Lytechinus variegatus. Dev. Biol. *118*, 155–166.

Lüders, J., and Stearns, T. (2007). Microtubule-organizing centres: a re-evaluation. Nat. Rev. Mol. Cell Biol. *8*, 161–167.

Lutz, D.A., Hamaguchi, Y., and Inoué, S. (1988). Micromanipulation studies of the asymmetric positioning of the maturation spindle in Chaetopterus sp. oocytes: I. Anchorage of the spindle to the cortex and migration of a displaced spindle. Cell Motil. Cytoskeleton *11*, 83–96.

Lyczak, R., Gomes, J.-E., and Bowerman, B. (2002). Heads or tails: cell polarity and axis formation in the early Caenorhabditis elegans embryo. Dev. Cell *3*, 157–166.

Mahoney, N.M., Goshima, G., Douglass, A.D., and Vale, R.D. (2006). Making Microtubules and Mitotic Spindles in Cells without Functional Centrosomes. Curr. Biol. *16*, 564–569.

Maître, J.-L., Berthoumieux, H., Krens, S.F.G., Salbreux, G., Jülicher, F., Paluch, E., and Heisenberg, C.-P. (2012). Adhesion functions in cell sorting by mechanically coupling the cortices of adhering cells. Science *338*, 253–256.

Maître, J.-L., Niwayama, R., Turlier, H., Nédélec, F., and Hiiragi, T. (2015). Pulsatile cell-autonomous contractility drives compaction in the mouse embryo. Nat. Cell Biol. *17*, 849–855.

Maître, J.-L., Turlier, H., Illukkumbura, R., Eismann, B., Niwayama, R., Nédélec, F., and Hiiragi, T. (2016). Asymmetric division of contractile domains couples cell positioning and fate specification. Nature *536*, 344–348.

Manning, M.L., Foty, R.A., Steinberg, M.S., and Schoetz, E.-M. (2010). Coaction of intercellular adhesion and cortical tension specifies tissue surface tension. Proc. Natl. Acad. Sci. *107*, 12517–12522.

Mao, Y., Tournier, A.L., Bates, P.A., Gale, J.E., Tapon, N., and Thompson, B.J. (2011). Planar polarization of the atypical myosin Dachs orients cell divisions in Drosophila. Genes Dev. *25*, 131–136.

Marmottant, P., Mgharbel, A., Käfer, J., Audren, B., Rieu, J.-P., Vial, J.-C., van der Sanden, B., Marée, A.F.M., Graner, F., and Delanoë-Ayari, H. (2009). The role of fluctuations and stress on the effective viscosity of cell aggregates. Proc. Natl. Acad. Sci. U. S. A. *106*, 17271–17275.

Maro, B., Howlett, S.K., and Webb, M. (1985). Non-spindle microtubule organizing centers in metaphase II-arrested mouse oocytes. J. Cell Biol. *101*, 1665–1672.

Martin, A.C., and Goldstein, B. (2014). Apical constriction: themes and variations on a cellular mechanism driving morphogenesis. Dev. Camb. Engl. *141*, 1987–1998.

Martindale, M.Q., and Henry, J.Q. (1995). Modifications of cell fate specification in equal-cleaving nemertean embryos: alternate patterns of spiralian development. Development *121*, 3175–3185.

Maruyama, Y.K., Nakaseko, Y., and Yagi, S. (1985). Localization of cytoplasmic determinants responsible for primary mesenchyme formation and gastrulation in the unfertilized egg of the sea urchin Hemicentrotus pulcherrimus. J. Exp. Zool. *236*, 155–163.

Mayer, M., Depken, M., Bois, J.S., Jülicher, F., and Grill, S.W. (2010). Anisotropies in cortical tension reveal the physical basis of polarizing cortical flows. Nature *467*, 617–621.

Mello, C.C., Draper, B.W., and Prless, J.R. (1994). The maternal genes apx-1 and glp-1 and establishment of dorsal-ventral polarity in the early C. elegans embryo. Cell *77*, 95–106.

Merdes, A., Ramyar, K., Vechio, J.D., and Cleveland, D.W. (1996). A Complex of NuMA and Cytoplasmic Dynein Is Essential for Mitotic Spindle Assembly. Cell *87*, 447–458.

Meshcheryakov, V.N. (1978). Orientation of cleavage in pulmonate mollusks II. Role of structure of intercellular contacts in orientation of the third and fourth cleavage spindles. Ontogenez *9*, 567–575.

Meves, F. (1897). Über den Vorgang der Zelleinschnürung. Dev. Genes Evol. *5*, 378–386.

Minc, N., and Piel, M. (2012). Predicting division plane position and orientation. Trends Cell Biol. *22*, 193–200.

Minc, N., Burgess, D., and Chang, F. (2011). Influence of cell geometry on division-plane positioning. Cell *144*, 414–426.

Mishima, M., Kaitna, S., and Glotzer, M. (2002). Central spindle assembly and cytokinesis require a kinesin-like protein/RhoGAP complex with microtubule bundling activity. Dev. Cell *2*, 41–54.

Mishima, M., Pavicic, V., Grüneberg, U., Nigg, E.A., and Glotzer, M. (2004). Cell cycle regulation of central spindle assembly. Nature *430*, 908–913.

Mohri, H., Mohri, T., Mabuchi, I., Yazaki, I., Sakai, H., and Ogawa, K. (1976). Localization of Dynein in Sea Urchin Eggs During Cleavage*. Dev. Growth Differ. *18*, 391–398.

Mollinari, C., Kleman, J.-P., Jiang, W., Schoehn, G., Hunter, T., and Margolis, R.L. (2002). PRC1 is a microtubule binding and bundling protein essential to maintain the mitotic spindle midzone. J. Cell Biol. *157*, 1175–1186.

Moore, J.K., and Cooper, J.A. (2010). Coordinating mitosis with cell polarity: Molecular motors at the cell cortex. Semin. Cell Dev. Biol. *21*, 283–289.

Morgan, T.H. (1899). The action of salt-solutions on the unfertilized and fertilized eggs of Arbacia, and of other animals. Arch. Für Entwicklungsmechanik Org. *8*, 448–539.

Morgan, T.H. (1927). Experimental embryology.

Morin, X., and Bellaïche, Y. (2011). Mitotic spindle orientation in asymmetric and symmetric cell divisions during animal development. Dev. Cell *21*, 102–119.

MOTOMURA, I. (1940). Studies of cleavage. I. Changes in surface area of different regions of eggs of a sea urchin in the course of the first cleavage. Sci. Rep. Tôhoku Univ. *15*, 121.

Munro, E., Nance, J., and Priess, J.R. (2004). Cortical flows powered by asymmetrical contraction transport PAR proteins to establish and maintain anterior-posterior polarity in the early C. elegans embryo. Dev. Cell *7*, 413–424.

Murray, A.W., Desai, A.B., and Salmon, E.D. (1996). Real time observation of anaphase in vitro. Proc. Natl. Acad. Sci. U. S. A. *93*, 12327–12332.

Nance, J., and Zallen, J.A. (2011). Elaborating polarity: PAR proteins and the cytoskeleton. Development *138*, 799–809.

Nédélec, F. (2002). Computer simulations reveal motor properties generating stable antiparallel microtubule interactions. J. Cell Biol. *158*, 1005–1015.

Negishi, T., Takada, T., Kawai, N., and Nishida, H. (2007). Localized PEM mRNA and protein are involved in cleavage-plane orientation and unequal cell divisions in ascidians. Curr. Biol. CB *17*, 1014–1025.

Nelson, W.J., Dickinson, D.J., and Weis, W.I. (2013). Roles of cadherins and catenins in cell-cell adhesion and epithelial cell polarity. Prog Mol Biol Transl Sci *116*, 3–23.

Newport, J., and Kirschner, M. (1982). A major developmental transition in early xenopus embryos: I. characterization and timing of cellular changes at the midblastula stage. Cell *30*, 675–686.

Nguyen, P.A., Groen, A.C., Loose, M., Ishihara, K., Wühr, M., Field, C.M., and Mitchison, T.J. (2014). Spatial organization of cytokinesis signaling reconstituted in a cell-free system. Science *346*, 244–247.

Niethammer, P., Kronja, I., Kandels-Lewis, S., Rybina, S., Bastiaens, P., and Karsenti, E. (2007). Discrete States of a Protein Interaction Network Govern Interphase and Mitotic Microtubule Dynamics. PLOS Biol. *5*, e29.

Nishida, H. (1994). Localization of determinants for formation of the anterior-posterior axis in eggs of the ascidian Halocynthia roretzi. Development *120*, 3093–3104.

Nishida, H. (1996). Vegetal egg cytoplasm promotes gastrulation and is responsible for specification of vegetal blastomeres in embryos of the ascidian Halocynthia roretzi. Dev. Camb. Engl. *122*, 1271–1279.

Nishida, H. (2005). Specification of embryonic axis and mosaic development in ascidians. Dev. Dyn. Off. Publ. Am. Assoc. Anat. *233*, 1177–1193.

Nishikata, T., Hibino, T., and Nishida, H. (1999). The Centrosome-Attracting Body, Microtubule System, and Posterior Egg Cytoplasm Are Involved in Positioning of Cleavage Planes in the Ascidian Embryo. Dev. Biol. *209*, 72–85.

Nislow, C., Lombillo, V.A., Kuriyama, R., and Mclntosh, J.R. (1992). A plus-end-directed motor enzyme that moves antiparallel microtubules in vitro localizes to the interzone of mitotic spindles. Nature *359*, 543–547.

Nürnberg, A., Kitzing, T., and Grosse, R. (2011). Nucleating actin for invasion. Nat. Rev. Cancer *11*, 177–187.

O'Connell, K.F. (2000). The centrosome of the early C. elegans embryo: inheritance, assembly, replication, and developmental roles. Curr. Top. Dev. Biol. *49*, 365–384.

Okada, Y., and Hirokawa, N. (2000). Mechanism of the single-headed processivity: Diffusional anchoring between the K-loop of kinesin and the C terminus of tubulin. Proc. Natl. Acad. Sci. *97*, 640–645.

Oliferenko, S., Chew, T.G., and Balasubramanian, M.K. (2009). Positioning cytokinesis. Genes Dev. *23*, 660–674.

Olivier, N., Luengo-Oroz, M.A., Duloquin, L., Faure, E., Savy, T., Veilleux, I., Solinas, X., Débarre, D., Bourgine, P., Santos, A., et al. (2010). Cell Lineage Reconstruction of Early Zebrafish Embryos Using Label-Free Nonlinear Microscopy. Science *329*, 967–971.

Painter, T.S. (1918). Contributions to the study of cell mechanics. II. Monaster eggs and narcotized eggs. J. Exp. Zool. *24*, 445–497.

Paluch, E.K., and Raz, E. (2013). The role and regulation of blebs in cell migration. Curr. Opin. Cell Biol. *25*, 582–590.

Pasternak, C., Spudich, J.A., and Elson, E.L. (1989). Capping of surface receptors and concomitant cortical tension are generated by conventional myosin. Nature *341*, 549–551.

Pavin, N., Laan, L., Ma, R., Dogterom, M., and Jülicher, F. (2012). Positioning of microtubule organizing centers by cortical pushing and pulling forces. New J. Phys. *14*, 105025.

Pecreaux, J., Röper, J.-C., Kruse, K., Jülicher, F., Hyman, A.A., Grill, S.W., and Howard, J. (2006). Spindle oscillations during asymmetric cell division require a threshold number of active cortical force generators. Curr. Biol. CB *16*, 2111–2122.

Peng, C.J., and Wikramanayake, A.H. (2013). Differential Regulation of Disheveled in a Novel Vegetal Cortical Domain in Sea Urchin Eggs and Embryos: Implications for the Localized Activation of Canonical Wnt Signaling. PLOS ONE *8*, e80693.

Peskin, C.S., Odell, G.M., and Oster, G.F. (1993). Cellular motions and thermal fluctuations: the Brownian ratchet. Biophys. J. *65*, 316–324.

Petry, S., Pugieux, C., Nédélec, F.J., and Vale, R.D. (2011). Augmin promotes meiotic spindle formation and bipolarity in Xenopus egg extracts. Proc. Natl. Acad. Sci. *108*, 14473–14478.

Petry, S., Groen, A.C., Ishihara, K., Mitchison, T.J., and Vale, R.D. (2013). Branching Microtubule Nucleation in Xenopus Egg Extracts Mediated by Augmin and TPX2. Cell *152*, 768–777.

Peukes, J., and Betz, T. (2014). Direct Measurement of the Cortical Tension during the Growth of Membrane Blebs. Biophys. J. *107*, 1810–1820.

Piko, L., and Clegg, K.B. (1982). Quantitative changes in total RNA, total poly(A), and ribosomes in early mouse embryos. Dev. Biol. *89*, 362–378.

Platner, G. (1886). Die Karyokinese bei den Lepidopteren als Grundlage für eine Theorie der Zellteilung.

Pritchard, R.H., Huang, Y.Y.S., and Terentjev, E.M. (2014). Mechanics of biological networks: from the cell cytoskeleton to connective tissue. Soft Matter *10*, 1864–1884.

Rajasekaran, A.K., and Rajasekaran, S.A. (2003). Role of Na-K-ATPase in the assembly of tight junctions. Am. J. Physiol. - Ren. Physiol. *285*, F388–F396.

Ralston, E., Lu, Z., Biscocho, N., Soumaka, E., Mavroidis, M., Prats, C., Lømo, T., Capetanaki, Y., and Ploug, T. (2006). Blood vessels and desmin control the positioning of nuclei in skeletal muscle fibers. J. Cell. Physiol. *209*, 874–882.

Ramanathan, S.P., Helenius, J., Stewart, M.P., Cattin, C.J., Hyman, A.A., and Muller, D.J. (2015). Cdk1-dependent mitotic enrichment of cortical myosin II promotes cell rounding against confinement. Nat. Cell Biol. *17*, 148–159.

Rappaport, R. (1961). Experiments concerning the cleavage stimulus in sand dollar eggs. J. Exp. Zool. *148*, 81–89.

Rappaport, R. (1985). Repeated furrow formation from a single mitotic apparatus in cylindrical sand dollar eggs. J. Exp. Zool. *234*, 167–171.

Rappaport, R. (1990). Cytokinesis in Animal Cells. In Biomechanics of Active Movement and Deformation of Cells, N. Akkaş, ed. (Springer Berlin Heidelberg), pp. 1–34.

Rappaport, R. (1991). Enhancement of aster-induced furrowing activity by a factor associated with the nucleus. J. Exp. Zool. *257*, 87–95.

Rappaport, R., and Conrad, G.W. (1963). AN EXPERIMENTAL ANALYSIS OF UNILATERAL CLEAVAGE IN INVERTEBRATE EGGS. J. Exp. Zool. *153*, 99–112.

Rappaport, R., and Rappaport, B.N. (1984). Division of constricted and urethane-treated sand dollar eggs: a test of the polar stimulation hypothesis. J. Exp. Zool. *231*, 81–92.

Reck-Peterson, S.L., Yildiz, A., Carter, A.P., Gennerich, A., Zhang, N., and Vale, R.D. (2006). Single-Molecule Analysis of Dynein Processivity and Stepping Behavior. Cell *126*, 335–348.

Redemann, S., Pecreaux, J., Goehring, N.W., Khairy, K., Stelzer, E.H.K., Hyman, A.A., and Howard, J. (2010). Membrane Invaginations Reveal Cortical Sites that Pull on Mitotic Spindles in One-Cell C. elegans Embryos. PLOS ONE *5*, e12301.

Reinsch, S., and Gönczy, P. (1998). Mechanisms of nuclear positioning. J. Cell Sci. *111 (Pt 16)*, 2283–2295.

Reinsch, S., and Karsenti, E. (1997). Movement of nuclei along microtubules in Xenopus egg extracts. Curr. Biol. CB *7*, 211–214.

Rhumbler, L. (1903). Mechanische Erklärung der Ähnlichkeit zwischen magnetischen Kraftliniensystemen und Zelltheilungsfiguren. Arch. Für Entwicklungsmechanik Org. *16*, 476–535.

Roberts, A.J., Kon, T., Knight, P.J., Sutoh, K., and Burgess, S.A. (2013). Functions and mechanics of dynein motor proteins. Nat. Rev. Mol. Cell Biol. *14*, 713–726.

Robertson, T.B. (1909). Note on the chemical mechanics of cell-division. Dev. Genes Evol. *27*, 29–34.

Robinson, D.N., and Cooley, and L. (1997). Genetic Analysis of the Actin Cytoskeleton in the Drosophila Ovary. Annu. Rev. Cell Dev. Biol. *13*, 147–170.

Roegiers, F., McDougall, A., and Sardet, C. (1995). The sperm entry point defines the orientation of the calcium-induced contraction wave that directs the first phase of cytoplasmic reorganization in the ascidian egg. Development *121*, 3457–3466.

Roegiers, F., Djediat, C., Dumollard, R., Rouvière, C., and Sardet, C. (1999). Phases of cytoplasmic and cortical reorganizations of the ascidian zygote between fertilization and first division. Dev. Camb. Engl. *126*, 3101–3117.

Rogulja, D., Rauskolb, C., and Irvine, K.D. (2008). Morphogen control of wing growth through the Fat signaling pathway. Dev. Cell *15*, 309–321.

Rouse, G.W., Jermiin, L.S., Wilson, N.G., Eeckhaut, I., Lanterbecq, D., Oji, T., Young, C.M., Browning, T., Cisternas, P., Helgen, L.E., et al. (2013). Fixed, free, and fixed: the fickle phylogeny of extant Crinoidea (Echinodermata) and their Permian-Triassic origin. Mol. Phylogenet. Evol. *66*, 161–181.

Rouvière, C., Houliston, E., Carré, D., Chang, P., and Sardet, C. (1994). Characteristics of pronuclear migration in Beroe ovata. Cell Motil. Cytoskeleton *29*, 301–311.

Rusan, N.M., Tulu, U.S., Fagerstrom, C., and Wadsworth, P. (2002). Reorganization of the microtubule array in prophase/prometaphase requires cytoplasmic dynein-dependent microtubule transport. J. Cell Biol. *158*, 997–1003.

Sachs, J. (1878). Ein Beitrag zur Kenntniss des aufsteigenden Saftstroms in transpirirenden Pflanzen. Arb Bot Inst Wurzburg *2*, 148–184.

Saiki Hamaguchi, M., and Hiramoto, Y. (1980). Fertilization Process in the Heart-Urchin, Clypeaster Japonicus Observed with a Differential Interference Microscope*. Dev. Growth Differ. *22*, 517–530.

Salbreux, G., Charras, G., and Paluch, E. (2012). Actin cortex mechanics and cellular morphogenesis. Trends Cell Biol. *22*, 536–545.

Samejima, I., Lourenço, P.C.C., Snaith, H.A., and Sawin, K.E. (2005). Fission yeast mto2p regulates microtubule nucleation by the centrosomin-related protein mto1p. Mol. Biol. Cell *16*, 3040–3051.

Sardet, C., Dru, P., and Prodon, F. (2005). Maternal determinants and mRNAs in the cortex of ascidian oocytes, zygotes and embryos. Biol. Cell *97*, 35–49.

Sardet, C., Paix, A., Prodon, F., Dru, P., and Chenevert, J. (2007). From oocyte to 16-cell stage: cytoplasmic and cortical reorganizations that pattern the ascidian embryo. Dev. Dyn. Off. Publ. Am. Assoc. Anat. *236*, 1716–1731.

Sato, N. (Tohoku U. (1979). Visualization with scanning electron microscopy of cleavage pattern of the ascidian eggs. Bull. Mar. Biol. Stn. Asamushi - Tohoku Univ. Jpn.

Sawada, T., and Schatten, G. (1989). Effects of cytoskeletal inhibitors on ooplasmic segregation and microtubule organization during fertilization and early development in the ascidian Molgula occidentalis. Dev. Biol. *132*, 331–342.

Schatten, G. (1981). The movements and fusion of the pronuclei at fertilization of the sea urchin Lytechinus variegatus: Time-lapse video microscopy. J. Morphol. *167*, 231–247.

Schatten, G. (1983). Motility during fertilization. Endeavour *7*, 173–182.

Schatten, G., and Schatten, H. (1981). Effects of motility inhibitors during sea urchin fertilization: microfilament inhibitors prevent sperm incorporation and restructuring of fertilized egg cortex, whereas microtubule inhibitors prevent pronuclear migrations. Exp. Cell Res. *135*, 311–330.

Schatten, G., Simerly, C., and Schatten, H. (1985). Microtubule configurations during fertilization, mitosis, and early development in the mouse and the requirement for egg microtubule-mediated motility during mammalian fertilization. Proc. Natl. Acad. Sci. U. S. A. *82*, 4152–4156.

Schatten, H., Walter, M., Biessmann, H., and Schatten, G. (1988). Microtubules are required for centrosome expansion and positioning while microfilaments are required for centrosome separation in sea urchin eggs during fertilization and mitosis. Cell Motil. Cytoskeleton *11*, 248–259.

Schoetz, E.M. (2008). Dynamics and mechanics of zebrafish embryonic tissues—a study of the physical properties of zebrafish germlayer cells and tissues and cell dynamics during early embryogenesis (Saarbrücken, Germany: VDM publishing group).

Schötz, E.-M., Burdine, R.D., Jülicher, F., Steinberg, M.S., Heisenberg, C.-P., and Foty, R.A. (2008). Quantitative differences in tissue surface tension influence zebrafish germ layer positioning. HFSP J. *2*, 42–56.

Schroeder, M.M., and Gard, D.L. (1992). Organization and regulation of cortical microtubules during the first cell cycle of Xenopus eggs. Dev. Camb. Engl. *114*, 699–709.

Schulze, J., and Schierenberg, E. (2011). Evolution of embryonic development in nematodes. EvoDevo *2*, 18.

Scott, A. (1946). The effect of low temperature and of hypotonicity on the morphology of the cleavage furrow in Arbacia eggs. Biol. Bull. *91*, 272–287.

Seetapun, D., and Odde, D.J. (2010). Cell-Length-Dependent Microtubule Accumulation during Polarization. Curr. Biol. *20*, 979–988.

Shibazaki, Y., Shimizu, M., and Kuroda, R. (2004). Body Handedness Is Directed by Genetically Determined Cytoskeletal Dynamics in the Early Embryo. Curr. Biol. *14*, 1462–1467.

Shinar, T., Mana, M., Piano, F., and Shelley, M.J. (2011). A model of cytoplasmically driven microtubule-based motion in the single-celled Caenorhabditis elegans embryo. Proc. Natl. Acad. Sci. U. S. A. *108*, 10508–10513.

Siller, K.H., and Doe, C.Q. (2009). Spindle orientation during asymmetric cell division. Nat. Cell Biol. *11*, 365–374.

Siller, K.H., Cabernard, C., and Doe, C.Q. (2006). The NuMA-related Mud protein binds Pins and regulates spindle orientation in Drosophila neuroblasts. Nat. Cell Biol. *8*, 594–600.

Silljé, H.H.W., Nagel, S., Körner, R., and Nigg, E.A. (2006). HURP is a Ran-importin beta-regulated protein that stabilizes kinetochore microtubules in the vicinity of chromosomes. Curr. Biol. CB *16*, 731–742.

Sivasankar, S., Brieher, W., Lavrik, N., Gumbiner, B., and Leckband, D. (1999). Direct molecular force measurements of multiple adhesive interactions between cadherin ectodomains. Proc. Natl. Acad. Sci. U. S. A. *96*, 11820–11824.

Skop, A.R., and White, J.G. (1998). The dynactin complex is required for cleavage plane specification in early Caenorhabditis elegans embryos. Curr. Biol. *8*, 1110–1117.

Sodergren, E., Weinstock, G.M., Davidson, E.H., Cameron, R.A., Gibbs, R.A., Angerer, R.C., Angerer, L.M., Arnone, M.I., Burgess, D.R., Burke, R.D., et al. (2006). The Genome of the Sea Urchin Strongylocentrotus purpuratus. Science *314*, 941–952.

Speicher, S., Fischer, A., Knoblich, J., and Carmena, A. (2008). The PDZ protein Canoe regulates the asymmetric division of Drosophila neuroblasts and muscle progenitors. Curr. Biol. CB *18*, 831–837.

Srinivasan, D.G., Fisk, R.M., Xu, H., and van den Heuvel, S. (2003). A complex of LIN-5 and GPR proteins regulates G protein signaling and spindle function in C. elegans. Genes Dev. *17*, 1225–1239.

Staveley, B.E. Molecular & Developmental Biology (BIOL3530). Department of Biology, Memorial University of Newfoundland. http://www.mun.ca/biology/desmid/brian/BIOL3530/DEVO_06/devo_06.html.

Steinberg, M.S. (1978). Specific Cell Ligands and the Differential Adhesion Hypothesis: How do they fit together? In Specificity of Embryological Interactions, D.R. Garrod, ed. (Springer US), pp. 97–130.

Steinberg, M.S., and Takeichi, M. (1994). Experimental specification of cell sorting, tissue spreading, and specific spatial patterning by quantitative differences in cadherin expression. Proc. Natl. Acad. Sci. U. S. A. *91*, 206–209.

Steinhardt, R., Zucker, R., and Schatten, G. (1977). Intracellular calcium release at fertilization in the sea urchin egg. Dev. Biol. *58*, 185–196.

Stewart, M.P., Helenius, J., Toyoda, Y., Ramanathan, S.P., Muller, D.J., and Hyman, A.A. (2011). Hydrostatic pressure and the actomyosin cortex drive mitotic cell rounding. Nature *469*, 226–230.

Stewart-Savage, J., and Grey, R.D. (1982). The temporal and spatial relationships between cortical contraction, sperm trail formation, and pronuclear migration in fertilizedXenopus eggs. Wilhelm Rouxs Arch. Dev. Biol. *191*, 241–245.

Stirbat, T.V., Mgharbel, A., Bodennec, S., Ferri, K., Mertani, H.C., Rieu, J.-P., and Delanoë-Ayari, H. (2013). Fine Tuning of Tissues' Viscosity and Surface Tension through Contractility Suggests a New Role for α-Catenin. PLOS ONE *8*, e52554.

Strome, S., and Hill, D.P. (1988). Early embryogenesis in Caenorhabditis elegans: the cytoskeleton and spatial organization of the zygote. BioEssays News Rev. Mol. Cell. Dev. Biol. *8*, 145–149.

Strome, S., and Wood, W.B. (1983). Generation of asymmetry and segregation of germ-line granules in early C. elegans embryos. Cell *35*, 15–25.

Sturtevant, A.H. (1923). INHERITANCE OF DIRECTION OF COILLING IN LIMNAEA. Science *58*, 269–270.

Subramanian, R., Wilson-Kubalek, E.M., Arthur, C.P., Bick, M.J., Campbell, E.A., Darst, S.A., Milligan, R.A., and Kapoor, T.M. (2010). Insights into antiparallel microtubule crosslinking by PRC1, a conserved nonmotor microtubule binding protein. Cell *142*, 433–443.

Sulston, J.E., and Horvitz, H.R. (1977). Post-embryonic cell lineages of the nematode, Caenorhabditis elegans. Dev. Biol. *56*, 110–156.

Summers, R.G., Morrill, J.B., Leith, A., Marko, M., Piston, D.W., and Stonebraker, A.T. (1993). A Stereometric Analysis of Karyokinesis, Cytokinesis and Cell Arrangements during and following Fourth Cleavage Period in the Sea Urchin, Lytechinus variegatus. Dev. Growth Differ. *35*, 41–57.

Swann, M.M., and Mitchison, J.M. (1958). The mechanism of cleavage in animal cells. Biol. Rev. *33*, 103–135.

Sweeton, D., Parks, S., Costa, M., and Wieschaus, E. (1991). Gastrulation in Drosophila: the formation of the ventral furrow and posterior midgut invaginations. Development *112*, 775–789.

Szollosi, D., Calarco, P., and Donahue, R.P. (1972). Absence of Centrioles in the First and Second Meiotic Spindles of Mouse Oocytes. J. Cell Sci. *11*, 521–541.

Tanaka, Y. (1976). Effects of the Surfactants on the Cleavage and Further Development of the Sea Urchin Embryos 1. the Inhibition of Micromere Formation at the Fourth Cleavage*. Dev. Growth Differ. *18*, 113–122.

Tanimoto, H., Kimura, A., and Minc, N. (2016). Shape-motion relationships of centering microtubule asters. J. Cell Biol. *212*, 777–787.

Tatsumoto, T., Xie, X., Blumenthal, R., Okamoto, I., and Miki, T. (1999). Human Ect2 Is an Exchange Factor for Rho Gtpases, Phosphorylated in G2/M Phases, and Involved in Cytokinesis. J. Cell Biol. *147*, 921–928.

Teichmann, E. (1903). über die Beziehung zwischen AstrosphÄren und Furchen. Dev. Genes Evol. *16*, 243–327.

Telford, M.J., Lowe, C.J., Cameron, C.B., Ortega-Martinez, O., Aronowicz, J., Oliveri, P., and Copley, R.R. (2014). Phylogenomic analysis of echinoderm class relationships supports Asterozoa. Proc. R. Soc. Lond. B Biol. Sci. *281*, 20140479.

Théry, M., Racine, V., Pépin, A., Piel, M., Chen, Y., Sibarita, J.-B., and Bornens, M. (2005). The extracellular matrix guides the orientation of the cell division axis. Nat. Cell Biol. *7*, 947–953.

Théry, M., Jiménez-Dalmaroni, A., Racine, V., Bornens, M., and Jülicher, F. (2007). Experimental and theoretical study of mitotic spindle orientation. Nature *447*, 493–496.

Thorpe, C.J., Schlesinger, A., Carter, J.C., and Bowerman, B. (1997). Wnt Signaling Polarizes an Early C. elegans Blastomere to Distinguish Endoderm from Mesoderm. Cell *90*, 695–705.

Tinevez, J.-Y., Schulze, U., Salbreux, G., Roensch, J., Joanny, J.-F., and Paluch, E. (2009). Proc. Natl. Acad. Sci. *106*, 18581–18586.

Tirnauer, J.S., Grego, S., Salmon, E.D., and Mitchison, T.J. (2002). EB1–microtubule interactions in Xenopus egg extracts: role of EB1 in microtubule stabilization and mechanisms of targeting to microtubules. Mol. Biol. Cell *13*, 3614–3626.

Tirnauer, J.S., Salmon, E.D., and Mitchison, T.J. (2004). Microtubule Plus-End Dynamics in Xenopus Egg Extract Spindles. Mol. Biol. Cell *15*, 1776–1784.

Toba, S., Watanabe, T.M., Yamaguchi-Okimoto, L., Toyoshima, Y.Y., and Higuchi, H. (2006). Overlapping hand-over-hand mechanism of single molecular motility of cytoplasmic dynein. Proc. Natl. Acad. Sci. U. S. A. *103*, 5741–5745.

Toret, C.P., Collins, C., and Nelson, W.J. (2014). An Elmo-Dock complex locally controls Rho GTPases and actin remodeling during cadherin-mediated adhesion. J. Cell Biol. *207*, 577–587.

Tóth, J., Kovács, M., Wang, F., Nyitray, L., and Sellers, J.R. (2005). Myosin V from Drosophila reveals diversity of motor mechanisms within the myosin V family. J. Biol. Chem. *280*, 30594–30603.

Toyama, Y., Peralta, X.G., Wells, A.R., Kiehart, D.P., and Edwards, G.S. (2008). Apoptotic force and tissue dynamics during Drosophila embryogenesis. Science *321*, 1683–1686.

Tran, P.T., Marsh, L., Doye, V., Inoué, S., and Chang, F. (2001). A mechanism for nuclear positioning in fission yeast based on microtubule pushing. J. Cell Biol. *153*, 397–411.

Tsou, M.-F.B., Hayashi, A., and Rose, L.S. (2003). LET-99 opposes Gα/GPR signaling to generate asymmetry for spindle positioning in response to PAR and MES-1/SRC-1 signaling. Development *130*, 5717–5730.

Twitchett, R.J., and Oji, T. (2005). Early Triassic recovery of echinoderms. Comptes Rendus Palevol *4*, 531–542.

Uehara, R., Nozawa, R., Tomioka, A., Petry, S., Vale, R.D., Obuse, C., and Goshima, G. (2009). The augmin complex plays a critical role in spindle microtubule generation for mitotic progression and cytokinesis in human cells. Proc. Natl. Acad. Sci. U. S. A. *106*, 6998–7003.

Vallee, R.B., McKenney, R.J., and Ori-McKenney, K.M. (2012). Multiple modes of cytoplasmic dynein regulation. Nat. Cell Biol. *14*, 224–230.

Verde, F., Dogterom, M., Stelzer, E., Karsenti, E., and Leibler, S. (1992). Control of microtubule dynamics and length by cyclin A- and cyclin B-dependent kinases in Xenopus egg extracts. J. Cell Biol. *118*, 1097–1108.

Waddle, J.A., Cooper, J.A., and Waterston, R.H. (1994). Transient localized accumulation of actin in Caenorhabditis elegans blastomeres with oriented asymmetric divisions. Development *120*, 2317–2328.

Wallingford, J.B., Niswander, L.A., Shaw, G.M., and Finnell, R.H. (2013). The Continuing Challenge of Understanding, Preventing, and Treating Neural Tube Defects. Science *339*, 1222002.

Warner, J.F., Lyons, D.C., and McClay, D.R. (2012). Left-Right Asymmetry in the Sea Urchin Embryo: BMP and the Asymmetrical Origins of the Adult. PLOS Biol. *10*, e1001404.

Watanabe, N., Madaule, P., Reid, T., Ishizaki, T., Watanabe, G., Kakizuka, A., Saito, Y., Nakao, K., Jockusch, B.M., and Narumiya, S. (1997). p140mDia, a mammalian homolog of Drosophila diaphanous,is a target protein for Rho small GTPase and is a ligand for profilin. EMBO J. *16*, 3044–3056.

Waters, J.C., Cole, R.W., and Rieder, C.L. (1993). The force-producing mechanism for centrosome separation during spindle formation in vertebrates is intrinsic to each aster. J. Cell Biol. *122*, 361–372.

Wayne Brodland, G., and Chen, H.H. (2000). The mechanics of cell sorting and envelopment. J. Biomech. *33*, 845–851.

Weitzel, H.E., Illies, M.R., Byrum, C.A., Xu, R., Wikramanayake, A.H., and Ettensohn, C.A. (2004). Differential stability of β-catenin along the animal-vegetal axis of the sea urchin embryo mediated by dishevelled. Development *131*, 2947–2956.

White, E.A., and Glotzer, M. (2012). Centralspindlin: At the heart of cytokinesis. Cytoskeleton *69*, 882–892.

Whittaker, J.R. (1980). Acetylcholinesterase development in extra cells caused by changing the distribution of myoplasm in ascidian embryos. Development *55*, 343–354.

Wilson, E.B. (1901). Experimental studies in cytology. Arch. Für Entwicklungsmechanik Org. *12*, 529–596.

Wilson, E.B. (1904). Experimental studies on germinal localization. J. Exp. Zool. *1*, 1–72.

Wilson, E.B. (1925). Cell In Development And Heredity, 3rd. Rev. Ed. (Macmillan Company.; New York).

Winklbauer, R. (2015). Cell adhesion strength from cortical tension – an integration of concepts. J Cell Sci *128*, 3687–3693.

Winkler, M.M., Steinhardt, R.A., Grainger, J.L., and Minning, L. (1980). Dual ionic controls for the activation of protein synthesis at fertilization. Nature *287*, 558–560.

Wolpert, L. (1960). The mechanics and mechanism of cleavage. Int Rev Cytol *10*, 163–216.

Wolpert, L., Tickle, C., and Arias, A.M. (2015). Principles of Development (Oxford University Press).

Wong, J.L., Créton, R., and Wessel, G.M. (2004). The Oxidative Burst at Fertilization Is Dependent upon Activation of the Dual Oxidase Udx1. Dev. Cell *7*, 801–814.

Wühr, M., Chen, Y., Dumont, S., Groen, A.C., Needleman, D.J., Salic, A., and Mitchison, T.J. (2008). Evidence for an Upper Limit to Mitotic Spindle Length. Curr. Biol. CB *18*, 1256–1261.

Wühr, M., Dumont, S., Groen, A.C., Needleman, D.J., and Mitchison, T.J. (2009). How does a millimeter-sized cell find its center? Cell Cycle Georget. Tex *8*, 1115–1121.

Wühr, M., Tan, E.S., Parker, S.K., Detrich, H.W., and Mitchison, T.J. (2010). A model for cleavage plane determination in early amphibian and fish embryos. Curr. Biol. CB *20*, 2040–2045.

Wühr, M., Obholzer, N.D., Megason, S.G., Detrich, H.W., and Mitchison, T.J. (2011). Live imaging of the cytoskeleton in early cleavage-stage zebrafish embryos. Methods Cell Biol. *101*, 1–18.

Yamada, S., and Nelson, W.J. (2007). Localized zones of Rho and Rac activities drive initiation and expansion of epithelial cell–cell adhesion. J. Cell Biol. *178*, 517–527.

Yokota, H., Neff, A.W., and Malacinski, G.M. (2004). Altering the position of the first horizontal cleavage furrow of the amphibian (Xenopus) egg reduces embryonic survival. Int. J. Dev. Biol. *36*, 527–535.

York-Andersen, A.H., Parton, R.M., Bi, C.J., Bromley, C.L., Davis, I., and Weil, T.T. (2015). A single and rapid calcium wave at egg activation in Drosophila. Biol. Open BIO201411296.

Youssef, J., Nurse, A.K., Freund, L.B., and Morgan, J.R. (2011). Quantification of the forces driving self-assembly of three-dimensional microtissues. Proc. Natl. Acad. Sci. *108*, 6993–6998.

Ziegler, H.E. (1898). Experimentelle Studien über die Zelltheilung. Arch. Für Entwicklungsmechanik Org. *6*, 249–293.

SUMMARY

RESUME EN FRANCAIS

I. Introduction

a. Les patrons de clivage

Le développement des embryons chez les animaux commence par le clivage de la cellule-œuf. Après la fertilisation de l'ovule par le spermatozoïde, la cellule-œuf opère une série de divisions successives, rapides et généralement synchronisées. Ces divisions sont extrêmement reproductibles spatialement et temporellement entre les individus appartenant à une même espèce, voire à une même classe d'animaux, et les embryons suivent exactement le même patron de clivage typiquement jusqu'au stade 16 à 64 cellules selon les espèces. En effet chez la plupart des animaux le début du clivage embryonnaire détermine les axes de l'organisme, généralement définis successivement lors des premières divisions. Une régulation spatio-temporelle précise de ces divisions est alors cruciale pour le bon développement de l'embryon. Chez les espèces où les axes sont définis plus tard par réarrangement des cellules au sein de l'embryon, comme chez les rongeurs par exemple, les patrons de clivage sont bien moins reproductibles.

Il est intéressant de noter que la polarité de l'embryon émerge en général avant la première division. En effet, la composition de la cellule-œuf n'est pas homogène. En particulier le vitellus (jaune d'œuf) peut être accumulé dans une région particulière du cytoplasme, de même que les morphogènes et facteurs de polarité déposés par la mère dans l'ovocyte. A ce stade précoce de développement, le génome de l'embryon n'est pas encore exprimé et le clivage s'opère grâce aux ARN messagers maternels déposés dans l'ovocyte. Le point d'entrée du spermatozoïde peut aussi être impliqué dans la polarisation de l'œuf. Comme les morphogènes sont répartis de manière inhomogène initialement, à mesure que les divisions successives séparent le cytoplasme de la cellule-œuf en de plus en plus de petites cellules (la taille totale de l'embryon évolue en général peu lors du clivage précoce, à cause de la rapidité du cycle cellulaire), les différentes cellules contiennent différentes compositions en morphogènes, ce qui définit différents destins cellulaires.

Il existe sept principaux patrons de clivage, classés en fonction de la complétion des divisions, qui semble dépendre de la quantité et répartition du vitellus dans la cellule-œuf. Lorsque l'œuf contient une zone avec une haute densité de vitellus, au milieu chez les insectes (clivage centrolécithe) ou sur le côté chez les poissons, oiseaux et céphalopodes (clivage télolécithe), la division du cytoplasme (cytocinèse) est incomplète et la constriction de la membrane conduisant à la séparation des cellules-filles commence hors du vitellus et s'arrête dans le vitellus. Le clivage est appelé méroblastique. Chez les embryons contenant moins de vitellus, il est appelé holoblastique, et la cytocinèse est complète. Chez les amphibiens, l'œuf contient néanmoins beaucoup de vitellus, accumulé au pôle végétal, et la cytocinèse commence au pôle animal et progresse lentement vers le pôle végétal (clivage mésolécithe). Lorsque le vitellus est moins dense et réparti de manière homogène dans l'œuf, la cytocinèse est symétrique et le clivage est dit isolécithe. Il existe quatre principaux patrons de clivage isolécithes : le clivage radial, rencontré chez les échinodermes et des amphioxus, le clivage spiral, chez la plupart des mollusques, annélides et planaires, le clivage bilatéral,

caractéristique des ascidies, et le clivage rotationnel, rencontré chez les mammifères et les vers nématodes.

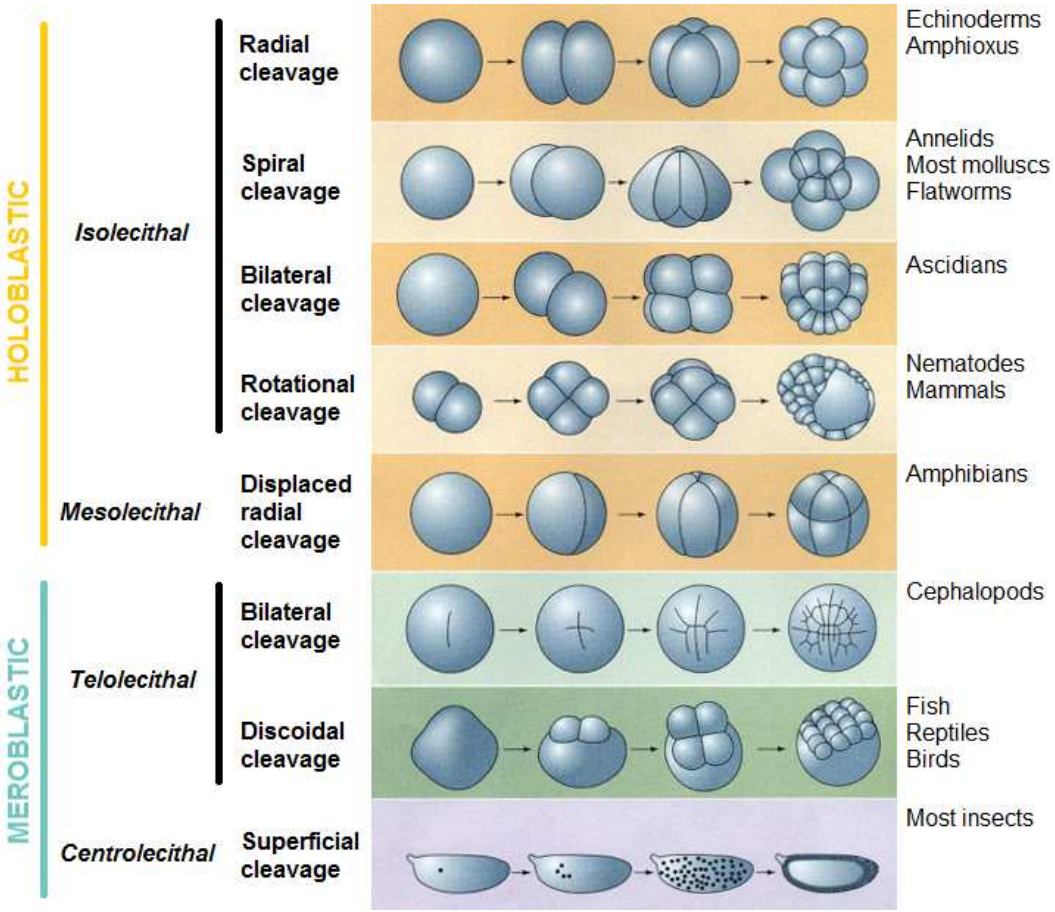

Les sept principaux patrons de clivage des embryons d'animaux, et les espèces où ils sont rencontrés (à droite). (Adapté de (Gilbert, 2000))

La question du positionnement du plan de division, en particulier dans les œufs et cellules de l'embryon, suscite un vif intérêt depuis près de deux siècles, car la division cellulaire est considérée comme un événement majeur du cycle cellulaire, et le bon positionnement du plan de division est nécessaire pour générer et maintenir des formes tissulaires spécifiques. Plusieurs lois empiriques ont été postulées pour prédire le positionnement des divisions, en particulier chez les végétaux. En 1878 Julius Sachs propose que le nouveau plan de division se forme perpendiculairement aux parois existantes, en formant deux cellules aux volumes égaux. En 1886 Léo Errera ajoute une condition de minimisation d'aire de la nouvelle paroi, par analogie avec les bulles de savon. Chez les animaux, Oskar Hertwig postule en 1884 que les cellules se scindent en deux parts égales perpendiculairement à leur axe long. Cette règle s'applique remarquablement bien aux divisions symétriques observées dans de nombreux tissus et organismes, même si elle ne permet pas de prédire les divisions asymétriques qui sont fréquentes dans les embryons, comme par exemple la première division du nématode *C. elegans*, ou la formation de micromères (plus petites cellules) au pôle végétal lors de la quatrième division de l'embryon d'oursin. En outre, la règle d'Hertwig reste empirique et n'explique pas les mécanismes de positionnement sous-jacents.

Les patrons de clivage sont extrêmement reproductibles, néanmoins ils peuvent être influencés par des manipulations de l'embryon. Par exemple un changement de forme, obtenu par exemple par compression, ou une perturbation de la membrane ou du cytoplasme (centrifugation, ablation,…) modifie le positionnement des divisions de l'embryon. Les embryons peuvent également être sensibles aux perturbations des contacts entre cellules ou du cycle cellulaire. La suppression de la polarité de l'œuf produit généralement une division symétrique selon l'axe long, en accord avec la règle d'Hertwig. Ces expériences suggèrent que les embryons précoces sont des systèmes plus ou moins auto-organisés, qui se divisent en fonction de leur forme par défaut, et d'un certain nombre de régulations additionnelles. Il est probable que les patrons de clivage largement conservés au sein d'une classe d'animaux (amphibiens, poissons, échinodermes,…) reposent davantage sur des principes d'auto-organisation que les patrons de clivage qui varient d'une espèce à l'autre (mollusques, nématodes,…) et qui dépendraient eux davantage d'une régulation génétique complexe.

b. Les mécanismes de positionnement du noyau

Le positionnement du plan de clivage dépend en général de la position du fuseau mitotique chez l'embryon animal. Le fuseau mitotique se compose de deux centrosomes, positionnés de part et d'autre du noyau, d'où polymérisent les microtubules qui se lient aux chromosomes et les séparent lorsque l'enveloppe nucléaire se rompt au début de la mitose. La cellule se divise dans un plan qui bissecte le fuseau perpendiculairement, de sorte que les deux centrosomes attachés à leur lot de chromosomes respectif soient répartis chacun dans une des deux cellules-filles. Le lien entre la position du fuseau et celle de l'anneau contractile qui sépare la cellule en deux semble variable selon les espèces, et dépendrait de la proximité des chromosomes et de la membrane, ou du cytosquelette. Le choix du plan de division est donc déterminé par le positionnement de la paire de centrosomes.

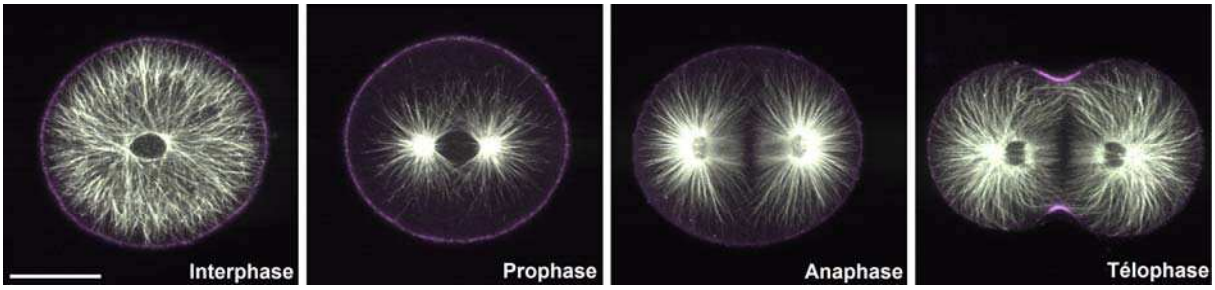

Oeuf d'oursin se divisant. Deux astres de microtubules (en blanc) grandissent depuis les deux centrosomes qui encadrent le noyau, et remplissent toute la cellule en interphase. Le noyau, encore visible en prophase, se rompt pour permettre la ségrégation des chromosomes dans les deux cellules-filles, que l'anneau contractile (en violet) sépare. (Barre d'échelle : 20 µm, adapté de (Foe and von Dassow, 2008))

Chez la plupart des embryons animaux, il a été suggéré que le positionnement de la paire de centrosomes dépendrait principalement des microtubules, qui rayonnent depuis le centrosome en interphase et remplissent tout le volume de la cellule. Ces deux astres de microtubules génèreraient des forces sur les centrosomes et les positionneraient. Plusieurs mécanismes ont été proposés quant à l'origine de ces forces. Les microtubules pourraient pousser contre la membrane ou tout autre obstacle auquel ils se heurtent en polymérisant. Les forces générées seraient transmises aux centrosomes via le réseau cytoplasmique de

microtubules, et dépendraient de la longueur des microtubules, principalement parce qu'un microtubule plus long flamberait plus facilement en compression et pourrait donc exercer moins de force. Ainsi, la paire de centrosomes serait poussée loin d'une membrane proche par les microtubules courts qui s'y heurtent, engendrant une centration du noyau en accord avec la règle d'Hertwig. D'autres mécanismes ont été proposés, qui reposent sur des forces de traction exercées à la membrane, soit par des moteurs moléculaires se déplaçant sur les microtubules (dynéines), soit par la dépolymérisation de microtubules attachés au cortex. Enfin, une dernière hypothèse consiste en des forces exercées directement dans le cytoplasme par des moteurs moléculaires traînant des cargos le long des microtubules. La friction des cargos dans le cytoplasme engendrerait une force sur le microtubule, de direction opposée à la direction de procession du moteur moléculaire. Dans le cas des dynéines, cela produirait une force de traction sur le centrosome, possiblement plus forte pour les longs microtubules qui recrutent davantage de dynéines (dans l'hypothèse d'une répartition cytoplasmique homogène des moteurs moléculaires), conduisant ici encore à la centration du noyau.

Plusieurs modèles théoriques ont été proposés pour simuler la centration de l'astre mâle après fertilisation et le positionnement du noyau lors des divisions successives. Ces modèles reposent sur les mécanismes de génération de forces par les microtubules décrits précédemment, et permettent de prédire le positionnement des astres de microtubules de manière statique ou dynamique, en prenant en compte divers paramètres tels que les propriétés mécaniques des microtubules, leur répartition ou encore la dynamique de leur polymérisation. En particulier, un modèle statique développé par Nicolas Minc prédit l'orientation du fuseau mitotique dans une cellule à deux dimensions, en supposant que deux astres de microtubules qui rayonnent à partir des centrosomes rencontrent des dynéines dans le cytoplasme et exercent des forces de traction sur les centrosomes. Dans ce modèle, les microtubules remplissent tout le volume de la cellule avec une répartition angulaire homogène. Les forces s'appliquant sur la paire de centrosomes sont calculées à partir de la longueur des microtubules, en supposant une loi en puissance, pour toutes les orientations possibles du fuseau, ce qui permet de déduire l'orientation d'équilibre. Les résultats des simulations sont notamment en accord avec les premières divisions de l'embryon d'oursin, à la fois dans des embryons normaux et des embryons déformés, et suivent la règle d'Hertwig. En particulier, les résultats montrent un meilleur accord entre simulation et expérience pour un exposant de la loi en puissance compris entre 3 et 5, ce qui suggère une force exercée dans le volume de la cellule, et une répartition volumique homogène des dynéines.

Enfin, plusieurs mécanismes additionnels ont été proposés, en particulier pour expliquer la polarité des divisions, à l'origine notamment des divisions asymétriques. L'exemple le plus frappant est la première division du nématode *C. elegans*, où le fuseau se décentre après la migration du noyau mâle au centre de l'œuf, pour former une cellule postérieure plus petite que la cellule antérieure. Les hypothèses les plus récentes impliquent des forces de traction corticales plus fortes dans la moitié postérieure de l'embryon dues à une répartition polarisée de protéines corticales (PAR, en particulier), induisant un déplacement de la paire de centrosomes vers le pôle postérieur de l'œuf. Un mécanisme similaire pourrait être à l'œuvre dans l'embryon d'oursin, où une accumulation des protéines Dishevelled et β-caténine a été observée au pôle végétal, là où se forment les micromères à la quatrième division. La polarité des divisions observée chez certains embryons pourrait également s'expliquer par des mécanismes cytoplasmiques, et résulter soit d'une répartition volumique inhomogène des effecteurs des forces s'appliquant sur les microtubules, soit d'une accumulation locale de vitellus ou d'organites créant un volume exclu pour les microtubules. Finalement, les facteurs de polarité semblent évoluer dans le temps, puisque des expériences

de retardation du cycle cellulaire chez les échinodermes ou les mollusques altèrent les patrons de clivage. De plus, ces facteurs peuvent dépendre des contacts cellulaires, soit via des processus de signalisation cellulaires ou tissulaires, soit via un recrutement spécifique d'effecteurs aux zones d'adhésion.

c. Les formes cellulaires

L'efficacité de la règle d'Hertwig pour prédire les divisions dans de nombreux types cellulaires suggère que la forme cellulaire est un facteur important, voire le facteur par défaut, pour déterminer la position et l'orientation de la division. La forme des cellules est déterminée par leur arrangement au sein de l'embryon, qui induit des contacts cellulaires maintenus par des adhésions membranaires. La forme est également modulée par la tension corticale des cellules, principalement due à la contractilité du cortex d'actine sous la membrane plasmique. En particulier, une tension corticale plus faible aux contacts cellulaires qu'aux surfaces externes de l'embryon permet d'augmenter la surface de contact entre cellules adjacentes, et donne aux cellules des formes plus complexes que de simples sphères adhérentes. Finalement, la contractilité corticale des cellules permet le réarrangement des cellules au sein de l'embryon, vers une configuration qui peut en général être relativement bien décrite par des considérations de minimisation d'énergie de surface.

II. Projet

Le modèle développé par Nicolas Minc prédit de manière remarquablement efficace l'orientation de la division en fonction de la forme cellulaire, à partir d'hypothèses relativement simples. Cependant, seule l'orientation de la division est prédite, pour un noyau centré, ce qui ne rend pas compte des divisions asymétriques. De plus, le modèle est en deux dimensions, et ignore les géométries tridimensionnelles complexes que peuvent prendre les cellules au sein d'un embryon. Enfin, seule la forme cellulaire est prise en compte, ce qui ne permet pas de prédire l'effet d'éventuelles polarités cytoplasmiques ou membranaires sur les patrons de clivage. En particulier la décentration du noyau à l'origine des divisions asymétriques ne peut être obtenue seulement à partir de la forme des cellules, en supposant une répartition homogène des microtubules et des dynéines.

Le but de ce projet est de proposer un modèle similaire, mais plus complet, en ce qu'il explore des formes cellulaires tridimensionnelles pour déterminer à la fois une orientation et une position d'équilibre de la paire de centrosomes. Surtout, le nouveau modèle doit intégrer non seulement la forme cellulaire mais également d'autres facteurs de polarité, et sonder la compétition entre ces différents facteurs dans la détermination du plan de division. Pour ce faire, la simulation est couplée à de l'imagerie, et à des expériences manipulant ces différents facteurs. L'objectif est de prédire complètement les patrons de clivages embryonnaires, y compris leurs divisions asymétriques. Au delà, il s'agit d'extraire les principaux mécanismes qui influencent le positionnement de la division, chez l'embryon et potentiellement dans d'autres types cellulaires.

III. Résultats

a. Un modèle pour prédire les divisions embryonnaires

Le modèle numérique a été développé sous Matlab, à partir du script de Nicolas Minc, mais adapté en trois dimensions. Le programme calcule la force et le couple nets appliqués sur la paire de centrosomes pour différentes positions et orientations du noyau en 3D, ce qui correspond à faire varier un jeu de trois coordonnées et deux angles. La force exercée par chaque microtubule est déduite de sa longueur, calculée géométriquement en supposant que le microtubule atteint la membrane depuis le centrosome, en ligne droite. La force varie comme le cube de la longueur, en accord avec les estimations du modèle en deux dimensions, bien que d'autres exposants aient été testés. La densité angulaire de microtubules est supposée constante dans l'astre, et l'étendue angulaire de l'astre permet un chevauchement des astres des deux centrosomes.

Afin de réduire les temps de calcul, trop longs pour pouvoir explorer systématiquement tous les jeux de coordonnées et d'angles, une recherche itérative de la position d'équilibre a été implémentée. Le noyau est positionné et orienté initialement avec un jeu de coordonnées aléatoires. A chaque itération, il est déplacé ou tourné en accord avec la direction de la force ou du couple calculée à la position précédente. Lorsqu'il stagne à une position donnée, celle-ci est considérée comme position d'équilibre. Enfin, à titre de confirmation de l'orientation d'équilibre, les variations du couple en fonction de l'orientation de la paire de centrosomes (exploration systématique de tous les jeux de coordonnées angulaires) peuvent être calculées à cette position d'équilibre. La position et l'orientation du plan de division sont déduites de la position et de l'orientation d'équilibre de la paire de centrosomes.

Le programme a d'abord été lancé sur des formes test, telles que des parallélépipèdes. La position d'équilibre était systématiquement centrée dans le volume, et l'axe de la paire de centrosome était aligné avec l'axe long de la forme, en accord avec la règle d'Hertwig. Le modèle montrait en outre une grande sensibilité à l'anisotropie de la forme.

De plus, un deuxième programme a été développé pour prédire l'orientation planaire de la division dans l'épithélium du thorax de la pupe de drosophile, dans le cadre d'une collaboration avec l'équipe de Yohanns Bellaïche. Le script a également été adapté du programme de Nicolas Minc, et calcule l'orientation de la division (centrée) en fonction de la forme 2D de la cellule ou de la répartition membranaire de la protéine Mud. Les deux prédictions ont été comparées à la division effective des cellules épithéliales, pour conclure que l'orientation se fait davantage en fonction de Mud que de la forme. Cette étude a été publiée dans un article paru dans la revue *Nature* en février 2016.

b. Génération des formes cellulaires

L'étape suivante consistait à générer les formes des cellules embryonnaires sur lesquelles tester le programme. Afin de s'approcher au plus près des formes réelles des cellules, en particulier chez des embryons difficiles à imager, car gros et/ou opaques, tels que le xénope ou le poisson-zèbre, une approche numérique a été adoptée. Les formes embryonnaires ont été simulées avec le logiciel « The Surface Evolver », qui effectue une recherche itérative de la surface de moindre énergie à partir d'une surface de départ, sous différentes contraintes.

Les principaux paramètres et contraintes utilisés sont les tensions de surfaces, les volumes, et un éventuel confinement, généralement sphérique. Les tensions de surfaces, évaluées par la mesure des angles de contact entre cellules adjacentes sur des images de la littérature, déterminent principalement les adhésions cellulaires. Une tension à l'interface entre deux cellules plus forte par rapport à la tension entre la surface de l'embryon et l'extérieur donne une zone de contact plus réduite et des cellules plus sphériques. Les volumes respectifs des différentes cellules au sein de l'embryon sont définis de manière itérative. La division précédente, prédite par le modèle, permet de définir les volumes des cellules filles à partir du positionnement du plan de division, et sert ainsi à la génération des formes cellulaires au stade suivant. De même, la topologie de l'embryon qui permet de définir une surface de départ vient de la simulation de la division précédente. De plus, un confinement peut éventuellement être imposé à la surface pour reproduire l'effet de la membrane de fertilisation qui entoure généralement l'embryon, ou encore des expériences de compression d'embryons. Les dimensions du confinement sont mesurées sur les images de la littérature. Enfin, des contraintes additionnelles telles que des densités cellulaires ou des gradients de tension de surface ont été ajoutées pour affiner la reproduction des formes cellulaires observées dans la littérature.

En plus d'ajuster les surfaces à partir d'une topologie de départ, les simulations des formes ont également permis de rendre compte des réarrangements cellulaires qui se produisent au sein de l'embryon. Par exemple, le réarrangement vers une configuration tétraédrique des quatre cellules de l'embryon d'oursin traité au détergent après la deuxième division est bien reproduit par « The Surface Evolver ». En particulier, l'utilisation de ce seul logiciel a permis de simuler l'arrangement des cellules dans les embryons de mollusques, où le clivage suit un patron en spirale qui génère un empilement thermodynamiquement stable des cellules.

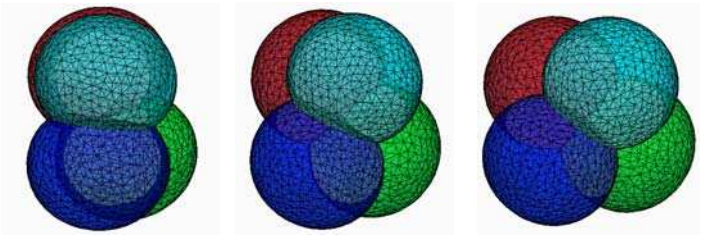

Réarrangement tétraédrique des cellules au sein d'un embryon d'oursin traité au détergent, simulé avec « The Surface Evolver ».

c. Premiers résultats

Les formes cellulaires générées ont été utilisées en entrée du programme Matlab qui prédit le positionnement de la division. Le résultat de la prédiction a ensuite servi à définir les volumes et l'arrangement des cellules au stade suivant, pour en prédire les formes, tous autres paramètres gardés constants. Ainsi, la boucle entre la simulation des formes et celle de la division a permis de prédire les premières divisions de manière intégralement numérique chez quatre organismes modèle que sont le poisson-zèbre, le xénope, l'oursin et l'ascidie.

Chez le poisson-zèbre, le clivage est télolécithe, et seule une petite partie de l'embryon se divise, le reste étant constitué de vitellus. Comme les microtubules qui rayonnent depuis les centrosomes en interphase ne grandissent pas dans cette masse de vitellus, les formes ont été générées en assimilant la réserve de vitellus à une grosse cellule, qui garde un volume

constant au cours des divisions des autres cellules. Ainsi, seul le volume des cellules, et non le vitellus, est sondé par leurs microtubules respectifs pendant la simulation de la division. Les résultats sont en accord avec le patron de clivage observé jusqu'à la cinquième série de divisions, où, après des divisions toujours dans le même plan, les quatre cellules centrales se divisent selon l'axe animal-végétal, pour donner une seconde couche de cellules. Le modèle prédit ce changement d'orientation, et également son inhibition ou son arrivée précoce dans le cas d'embryons perturbés génétiquement ou chimiquement. Dans ce dernier cas, les propriétés mécaniques des cellules sont perturbées, ce qui altère leur forme. En reproduisant ces changements par une modification des tensions de surface, le modèle permet de prédire les nouveaux patrons de clivage, suggérant un rôle majeur de la forme cellulaire pour le positionnement du plan de division dans ce système.

d. Polarités additionnelles

Cependant les patrons de clivage des amphibiens, des échinodermes et des ascidies comportent des divisions asymétriques que le modèle uniquement basé sur la forme cellulaire ne peut reproduire. Dans le cas du xénope, la troisième division clive l'embryon en quatre grosses cellules végétales et quatre petites cellules animales. L'asymétrie de cette division peut s'expliquer par une accumulation de vitellus du côté du pôle végétal. Le vitellus est moins concentré que chez le poisson-zèbre, et forme plutôt un gradient selon l'axe animal-végétal, mais là encore les microtubules grandissent plus difficilement dans le vitellus, ce qui se traduit par un volume exclu pour la centration de l'appareil mitotique. En incluant dans le modèle un gradient de vitellus, et une dépendance de la densité locale de microtubules avec la concentration en vitellus (moins de microtubules dans les zones plus denses en vitellus), le patron de clivage du xénope a pu être reproduit jusqu'à la quatrième série de divisions. Au delà, les divisions deviennent non reproductibles. Ainsi, l'axe animal-végétal serait défini dès la première division par l'accumulation par gravité de vitellus (plus dense). Cette hypothèse est confortée par des expériences de manipulation de la gravité (microgravité, centrifugation) qui altèrent l'asymétrie de la troisième division, et sont également reproduites par le modèle. Enfin, le modèle permet de prédire les résultats d'expériences classiques d'altération des patrons de clivage par compression des embryons de xénope. Dans ce système, l'orientation par défaut des divisions vis-à-vis de la forme serait donc modulée par des inhomogénéités dans la distribution du vitellus.

Chez l'embryon d'oursin, le vitellus est réparti de manière homogène dans le cytoplasme, ce qui ne permet pas d'expliquer par une accumulation locale de vitellus l'apparition de micromères au pôle végétal lors de la quatrième division. L'asymétrie de cette division trouverait plutôt son origine dans une accumulation de facteurs de polarité au pôle végétal (la protéine Dishevelled, notamment). La polarité serait surfacique, comme suggéré par des expériences où les embryons, traités avec du détergent, ce qui perturbe uniquement leur surface, perdent l'alignement de leurs divisions vis-à-vis de l'axe animal-végétal et font une quatrième division symétrique. En accord avec ces résultats, et après avoir testé de nombreuses hypothèses alternatives, le modèle a été complété en incluant une force de traction exercée sur les microtubules à la membrane du pôle végétal. La force exercée par un microtubule sur le centrosome est alors la somme du terme « de forme » utilisé précédemment qui varie comme le cube de la longueur, et de deux termes « de polarité » pour les microtubules qui atteignent le pôle végétal. Le premier terme de polarité varie comme le carré de la longueur, et correspondrait à l'action de dynéines (limitantes) à la surface. Le deuxième terme est exponentiel, et rendrait compte d'un mécanisme de traction basé sur la dépolymérisation de microtubules attachés à la surface. Dans ce second mécanisme, les

microtubules seraient limitants, et leur nombre à la surface dépendrait de leur longueur (de manière exponentielle) en les supposant branchés. Cette dernière hypothèse est en accord avec des expériences réalisées au laboratoire où les microtubules sont marqués par immunofluorescence et où l'intensité du signal est mesurée du centrosome à la surface.

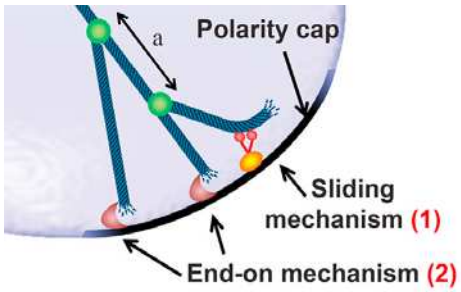

$$F = \alpha L^3 + \beta L^2 \Psi_{pol} + \gamma 2^{L/a} \Psi_{pol}$$

(1) (2)

Contribution de la polarité à la force des microtubules

L Longueur du microtubule
Ψ_{pol} Distribution spatiale de la polarité
a Longueur caractéristique entre deux branches

Expression de la force exercée par un microtubule, comportant un terme de forme et deux termes de polarité.

Avec cette nouvelle expression pour la force d'un microtubule, le modèle permet de prédire à la fois l'orientation des divisions vis-à-vis de l'axe animal-végétal et l'apparition des micromères à la quatrième série de divisions. Cependant les paramètres déterminant la contribution relative des trois termes de force doivent évoluer pour reproduire toutes les divisions. En effet, si le terme de forme domine jusqu'à la quatrième division pour avoir un noyau centré et des divisions quasiment symétriques, l'un au moins des termes de polarité doit l'emporter sur le terme de forme pour déplacer le noyau vers le pôle végétal et obtenir des micromères à la quatrième division. De plus, le terme exponentiel seul permet de reproduire les deux premières divisions, dont l'axe est orthogonal à l'axe animal-végétal, mais les deux divisions suivantes sont alignées avec l'axe animal-végétal, ce qui serait plutôt dû à une prédominance de l'autre terme de polarité sur le terme exponentiel. Plusieurs expériences classiques altérant le cycle cellulaire suggèrent une évolution de la polarité durant les premières divisions de l'embryon d'oursin. En accord avec ces résultats, le terme de polarité correspondant à l'action de dynéines à la surface a été augmenté du stade 2 cellules au stade 8 cellules dans le modèle, les deux autres termes restants constants. Ce seul ajustement a permis de reproduire le patron de clivage des échinodermes jusqu'au stade 32 cellules, ainsi que les résultats des expériences d'altération du cycle cellulaire et d'expériences de compression des embryons, sans autre changement de paramètres. Ceci suggère que les patrons de clivage sont déterminés dans ce système par une compétition évoluant dans le temps entre des forces volumiques dépendant de la forme cellulaire et des forces surfaciques dépendant d'une accumulation locale de facteurs de polarité.

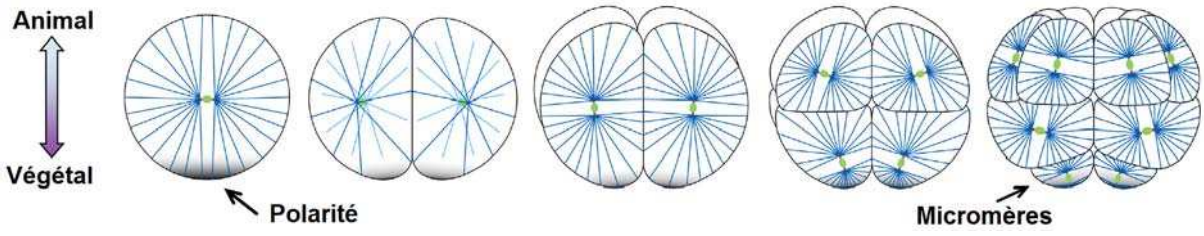

Patron de clivage de l'embryon d'oursin. Les microtubules sont en bleu et le noyau en vert.

Finalement, le modèle complet a été testé sur le patron de clivage des ascidies. Au stade 2 cellules, ces embryons assemblent une structure surfacique au pôle postérieur appelée CAB (Centrosome Attracting Body), et qui semble attirer le noyau pour donner des divisions asymétriques au pôle postérieur à partir du stade 8 cellules. De plus, suite à deux vagues de réorganisation cytoplasmique, la distribution du vitellus est inhomogène, avec une légère accumulation au pôle végétal, qui s'étend encore du côté antérieur lors de la première division. En incluant dans le modèle à la fois un gradient de vitellus modulant la densité en microtubules comme pour le xénope et les deux termes de polarité utilisés pour l'oursin dans la force des microtubules qui atteignent le CAB, le patron de clivage de l'ascidie a été reproduit jusqu'au stade 16 cellules. Le modèle a également pu reproduire le clivage d'embryons dont le CAB a été retiré ou inhibé. Ces résultats suggèrent que ces embryons se comportent comme des systèmes auto-organisés, où l'appareil de division est positionné via une compétition entre un signal de forme, modulé par des accumulations de vitellus ou d'organites, et un signal de polarité surfacique. Cette étude a donné lieu à une collaboration avec l'équipe de Carl-Philipp Heisenberg, pour simuler la division chez l'embryon d'ascidie à partir de la forme réelle des cellules et de la distribution de vitellus imagées par microscopie 3D.

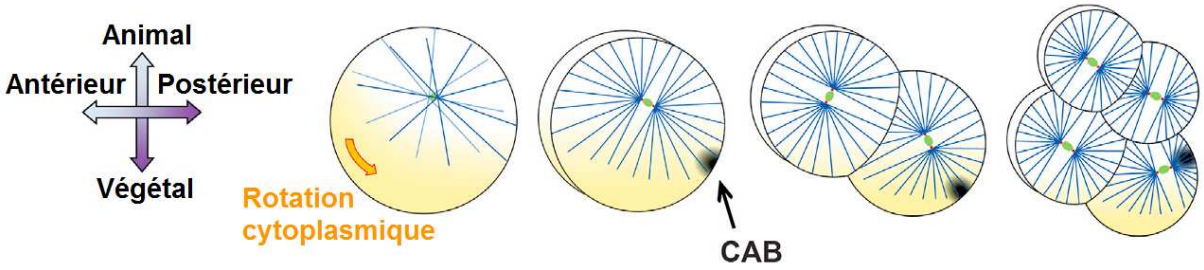

Patron de clivage de l'embryon d'ascidie. Les microtubules sont en bleu, le noyau en vert et le vitellus en jaune.

e. Etude de la polarité chez l'oursin

Comme vu précédemment, l'embryon d'oursin est un bon système pour étudier la compétition entre les signaux de forme et de polarité dans la détermination du plan de division, en ce qu'il présente un cytoplasme relativement homogène et une distribution simple et précise de polarité surfacique, associée à un phénotype clair (l'apparition de micromères). De plus, le contrôle génétique du développement semble minime dans ce système, contrairement à d'autres embryons comme les nématodes ou les mollusques qui montrent une grande variabilité des patrons de clivage entre espèces proches. Le caractère auto-organisé de l'embryon d'échinoderme, ainsi que la grande reproductibilité des patrons de clivage jusqu'à un stade relativement avancé ajoutent à la simplicité du système et permettent d'extraire plus facilement les principaux principes à l'œuvre dans le positionnement du noyau. En outre, l'embryon d'oursin comporte de nombreux avantages techniques. Les œufs sont pondus par millions, quasiment à toute saison, peuvent être fertilisés tous en même temps et se développent alors de manière synchrone simplement dans de l'eau de mer. Le cycle cellulaire est rapide, avec une division environ toutes les demi-heures, ce qui permet d'observer l'intégralité du développement précoce en moins d'une journée. Les embryons sont transparents, et assez petits pour être imagés facilement (environ 100 µm de diamètre). Ils

sont cependant assez gros pour pouvoir être manipulés (déformés, injectés,…), et assez robustes pour supporter de tels traitements et continuer à se diviser. Ils absorbent également facilement les isotopes radioactifs et les marqueurs fluorescents. En revanche, du fait de leur long cycle de vie, les échinodermes ne sont pas adaptés aux études génétiques. De plus, ils ont été abandonnés ces 50 dernières années au profit d'organismes modèles se prêtant mieux à la génétique, et leur génome n'est que peu documenté à ce jour, ce qui réduit les possibilités d'expériences de perturbation génétique.

Afin de déterminer les rôles respectifs de la polarité et de la forme dans le positionnement du plan de division, une première étude a consisté à caractériser précisément la position et l'orientation du noyau pendant les quatre premiers stades de développement des embryons d'oursin. Les microtubules, le noyau et la polarité ont été imagés par microscopie 2-photon sur des embryons marqués par immunofluorescence. Les résultats montrent une orientation du noyau davantage vis-à-vis de la forme jusqu'au stade 4 cellules, et davantage vis-à-vis de la polarité pour les cellules végétales au stade 8 cellules. Les orientations en interphase et en mitose ne semblent pas significativement différentes.

Ensuite, les formes des cellules ont été extraites à partir d'images d'embryons vivants, pour simuler la division avec le modèle à partir de formes cellulaires réelles. Les images ont été obtenues en 3D par microscopie 2-photon, avec un marqueur de vitellus (Nile Blue) qui marque ici tout le cytoplasme. Le résultat des simulations a ensuite été comparé à la division observée des cellules, extraite en début de mitose suivante à partir de la forme des astres. L'orientation prédite n'était en accord avec l'orientation observée de la paire de centrosomes qu'au stade 4 cellules, où l'axe long de la forme est aligné avec la polarité. En fait, à la fois l'orientation prédite et l'orientation observée suivent la règle d'Hertwig lors des trois premières divisions. Mais les symétries de la forme ne permettent pas de déterminer un unique axe long, et l'axe long choisi par le programme est alors aléatoire, ce qui explique les différences observées avec les données expérimentales. L'alignement des deux premières divisions orthogonalement à l'axe animal-végétal serait dû au signal de polarité présent au pôle végétal. Les embryons traités au détergent perdent cet alignement, mais se divisent toujours selon l'axe long, comme montré par la simulation de la division sur les formes de ces embryons imagées au 2-photon.

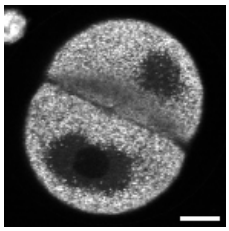

Exemple d'image (oursin au stade 2 cellules) obtenue par microscopie 2-photon. Le marqueur cytoplasmique est exclu des astres de microtubules et du noyau, ce qui permet de voir l'orientation de la future division. Barre d'échelle : 20 µm.

Pour prédire de manière satisfaisante l'orientation de la division, il a fallu, de même qu'avec les formes artificielles, ajouter un signal de polarité en entrée du programme. Ce signal a été généré artificiellement, et positionné à chaque stade de développement en fonction du site d'apparition des micromères à la quatrième division. L'expression de la force exercée par les microtubules qui atteignent la polarité était la même qu'avec les formes artificielles, et les paramètres n'ont pas eu à être changés pour permettre de reproduire les orientations observées de la paire de centrosomes.

Une première question concerne le stade 4 cellules, où les cellules suivent la règle d'Hertwig. Au stade précédent, la polarité favorisait une orientation de la paire de centrosomes orthogonale à l'axe animal-végétal, mais au stade suivant l'orientation favorisée est parallèle à cet axe. La contribution de la polarité n'est donc pas claire au stade 4 cellules, tant du point de vue de l'orientation qu'elle favorise que de sa compétition avec la forme cellulaire. Pour éclairer ce point, les cellules de l'embryon ont été séparées à ce stade, donnant des cellules sphériques en l'absence de contacts cellulaires, et annulant ainsi tout effet de la forme sur l'orientation de la division. Les microtubules et la polarité ont été imagés par microscopie 2-photon après un marquage par immunofluorescence. La paire de centrosomes pointe vers la polarité, suggérant que le changement dans l'orientation favorisée par la polarité, dû dans le modèle au terme dépendant de la dynéine devenant plus fort que le terme exponentiel, s'opère dès le stade 4 cellules.

Une deuxième question qui peut se poser concerne l'effet de la taille de l'embryon sur la compétition entre une force s'exerçant dans le volume de la cellule (le signal de forme) et une autre à la surface (la polarité). En particulier l'asymétrie des divisions végétales au stade 8 cellules pourrait correspondre à un seuil à partir duquel le signal surfacique devient prédominant sur le signal volumique à mesure que les tailles cellulaires rétrécissent. Pour déterminer le rôle de la taille des cellules dans l'apparition des micromères, les œufs ont été coupés en deux avec une micro-aiguille avant d'être fertilisés, pour donner des embryons plus petits. Comme le processus de clivage dépend uniquement du centrosome amené par le spermatozoïde, les deux moitiés d'œuf parviennent à se diviser. Typiquement, l'une des moitiés fait uniquement des divisions symétriques, suggérant qu'elle n'a pas hérité la polarité. L'autre moitié en revanche suit le patron de clivage exact des œufs entiers, et forme des micromères à la quatrième division, ce qui montre que l'apparition des divisions asymétriques dépend du temps plus que de la taille des cellules.

Enfin, la compétition entre la forme cellulaire et la polarité a été systématiquement testée en observant l'orientation en 2D de la division de cellules placées dans des microchambres de différentes formes. Les microchambres imposent ainsi aux cellules une forme rectangulaire ou elliptique d'une certaine anisotropie. La position de la polarité dans la microchambre est aléatoire. Les cellules de l'embryon ont été séparées à différents stades avant d'être placées dans des microchambres de taille adaptée. Il est intéressant de noter que les cellules séparées et non contraintes suivent le même patron de clivage que si elles avaient encore des voisines, suggérant que leur forme précise imposée par les contacts cellulaires n'a que peu d'influence sur le positionnement de la division. Placer les cellules dans des microchambres permet en revanche de leur imposer une forme pouvant être fortement anisotrope pour tester quantitativement l'influence de l'axe long sur la division. Aux stades 2 et 4 cellules, les divisions s'alignent systématiquement avec l'axe long de la forme dès que l'anisotropie de la forme augmente. Au stade 8 cellules, la moitié des cellules se divise symétriquement et s'aligne de même avec l'axe long. L'autre moitié se divise asymétriquement avec une orientation aléatoire même aux fortes anisotropies. Le fait que ces cellules soient aussi nombreuses que les cellules qui se divisent symétriquement suggère d'une part qu'il s'agit des cellules végétales et animales respectivement, et d'autre part qu'aucune division asymétrique des cellules végétales n'a été transformée en division symétrique à cause d'une forte anisotropie de la forme cellulaire. Avec le caractère aléatoire de l'orientation, cela montre que la polarité prédomine au stade 8 cellules, alors que la forme est la contribution dominante aux stades précédents.

Ces résultats ont été confirmés par la simulation des divisions dans les microchambres. L'orientation de la division a été prédite en 2D pour les différentes formes et anisotropies de l'expérience, et pour chaque forme avec différentes positions de la polarité. Avec les mêmes paramètres en fonction du stade cellulaire que pour la simulation avec les formes artificielles et réelles d'embryons entiers, le modèle permet de prédire l'alignement de la division avec l'axe long de la forme aux stades 2 et 4 cellules pour toutes les positions de la polarité, ainsi que l'alignement de la division vers la polarité quelle que soit la forme au stade 8 cellules. Ces résultats indiquent que le modèle, bien que volontairement gardé simple, rend compte de manière satisfaisante de la compétition entre les signaux de forme et de polarité et de son évolution dans le temps.

IV. Conclusion

Cette étude a mis en évidence l'existence de principes simples qui pourraient déterminer le positionnement du plan de division chez la plupart des deutérostomiens et permettre de le prédire à partir d'un nombre limité d'informations. L'application de ces résultats à d'autres embryons, qui reposent davantage sur des régulations génétiques que sur des principes d'auto-organisation, et à d'autres types cellulaires nécessitera sans doute des ajustements et la prise en compte de mécanismes additionnels. Cependant il est probable que les mécanismes isolés ici soient des mécanismes génériques, voire par défaut, communs à de nombreux types cellulaires, et sur lesquels viennent s'ajouter des mécanismes spécifiques aux différents types cellulaires ou espèces.

Le modèle proposé ici reste très général et la nature exacte des mécanismes décrits, possiblement variables entre différentes espèces, reste à élucider. En particulier l'identité des molécules et réactions en jeu, leur stœchiométrie et son évolution, les détails de la génération de force et la dynamique du positionnement du noyau ne sont qu'à peine considérés dans le cadre de cette étude. Une étude plus poussée, s'attachant aux spécificités de chaque système, sera probablement nécessaire à la compréhension du positionnement du plan de division, mais les principes mis en évidence ici donnent des pistes quant à la nature des phénomènes à investiguer.

Title : Architecture of cleavage planes during embryogenesis : a quantitative approach

Keywords : Embryogenesis, cell division, polarity

Abstract : Cells position their cleavage planes in a precise and predictable way. In particular, during the early embryogenesis, the cleavage pattern of the egg cell is extremely reproducible, yet sensitive to perturbation, which suggests an intrinsic plasticity of the system. The aim of this work is to determine the signals that set the positions of the cleavage planes in the early embryo, and their competition. First, a numerical model has been designed, to predict division positioning in four classical cleavage patterns (fishes, amphibians, echinoderms, ascidians). This model is based on pulling forces exerted by interphase astral microtubules on centrosomes, which depend on cell shape, cytoplasmic yolk gradients and cortical polarity cues. This model, coupled with a simulation of embryonic shapes by surface energy minimization, allows the accurate prediction of both cleavage patterns and their perturbation, completely *in silico*. Second, the competition between cell shape and polarity has been quantitatively assessed in the sea urchin embryo. This part comprises 3D imaging, as well as experiments assessing the roles of blastomere shape/size and of polarity. The results are compared to the predictions of the model, which now inputs the imaged blastomere shapes. The results suggest that the early embryos of most deuterostomes are self-organized systems, and that division plane positioning mainly depends on a limited number of signals.

Titre : Architecture des plans de clivage pendant l'embryogenèse : une approche quantitative

Mots clés : Embryogenèse, division cellulaire, polarité

Résumé : Les cellules positionnent leur plan de division de manière précise et prévisible. En particulier au tout début de l'embryogenèse, la cellule-œuf suit un patron de clivage extrêmement reproductible, mais néanmoins sensible aux perturbations, ce qui suggère une plasticité intrinsèque du système. Le but de cette thèse est de déterminer les signaux qui définissent la position des plans de division embryonnaires, et leur compétition. Dans un premier temps, un modèle numérique a été développé, pour simuler le positionnement de la division dans quatre patrons de clivage classiques (poissons, amphibiens, échinodermes, ascidies). Ce modèle est basé sur des forces de traction exercées par les microtubules des astres interphasiques sur les centrosomes, qui dépendent de la forme cellulaire, des gradients cytoplasmiques de vitellus et de signaux de polarité corticale. Couplé avec la simulation des formes embryonnaires par minimisation d'énergie de surface, ce modèle parvient à prédire les patrons de clivage et leurs perturbations, complètement *in silico*. Dans un second temps, la compétition entre la forme cellulaire et la polarité a été quantitativement étudiée chez l'embryon d'oursin. Cette étude comporte une part importante d'imagerie 3D, ainsi que des expériences visant à tester le rôle de la forme/taille des blastomères et de la polarité. Les résultats obtenus sont comparés aux prédictions du modèle, cette fois basées sur la forme imagée des blastomères. Les résultats suggèrent que les embryons de la plupart des deutérostomiens sont des systèmes auto-organisés et que la détermination du plan de division dépend principalement d'un nombre restreint de signaux.